湖南省地球物理地球化学调查所
GEOPHYSICALAND GEOCHEMICAL SURVEY INSTITUTE OF HUNAN PROVINCE

2023-2024年度
地质科技成果集
第一册论文集

科技合作室 组编
2024年12月

目 录

2023-2024年度地质科技论文

序号	论文名称	期刊	作者	单位	期刊级别	发表日期
1	Gradual Failure of a Rainfall-Induced Creep-Type Landslide and an Application of Improved Integrated Monitoring System: A Case Study	sensors	郭军、孟繁星、郭经纬	湖南省地球物理地球化学调查所（第一单位）	SCI 3区	2024.11
2	New Re-Os Geochronological Data from the Upper Doushantuo Formation: Age Constraint on the Shuram Excursion and Implication for the Ediacaran Fluctuated Continental Weathering	ACS Omega	谭昭昭、骆检兰、徐雪生、贾望鲁，李杰，陈礼然	湖南省地球化学过程与资源环境效应重点实验室(第一单位) 湖南省地球物理地球化学调查所（第二单位）	SCI 3区	2024.11
3	扩频激电法（SSIP）找矿效果分析-以湖南省永州市零陵区东湘桥锰矿床勘查为例	矿产勘查	廖凤初、刘桂元、周杰、黄建权、徐军伟、陈儒军	湖南省地球物理地球化学调查所（第一单位）	中文科技核心T3	2024.09
4	Geological Conditions of Shale Gas Accumulation in Coal Measures	processes	廖凤初、王克营、詹健、刘志伟、蔡宁波	湖南省地球物理地球化学调查所（第一单位） 湖南省地质新能源勘探开发工程技术研究中心（第二单位）	SCI 3区	2024.08
5	Dual-mineralization in the Woxi Au-Sb-W deposit, South China and its regional metallogenic significance: evidence from textures and in-situ trace elements and oxygen analysis of quartz	Ore Geology Reviews	李彬、徐德茹、白道元、池国祥、 何红生、邵拥军、邓滕、戴俊峰、邹绍浩、陈剑锋	湖南省地球物理地球化学调查所（第一单位）	SCI 2区	2024.07
6	湘东北虎形山钨铍矿区隐伏花岗岩体地球化学特征及成因研究	华南地质	徐军伟、王玉华、曾认宇、廖凤初、李素欣	湖南省地球化学过程与资源环境效应重点实验室(第一单位) 湖南省地球物理地球化学调查所（第二单位）	中文科技核心T3	2024.06
7	Synergistic Remediation of Cd-Contaminated Soil with Pure Natural Adsorption Material and Hyperaccumulator Plant	Agronomy	郭军、徐宏根、尹凤翔、曹建、徐雪生、李聪、黄凤寸、陈方炜、毛雄、廖琦	湖南省地球化学过程与资源环境效应重点实验室(第一单位) 湖南省地球物理地球化学调查所（第二单位）	SCI 3区	2024.06
8	湘南地区东湘桥沉积型锰矿床地球化学特征及成矿机理	矿床地质	廖凤初、刘湘华、徐军伟、熊伊曲、李斌、赖健清、骆检兰、陈雨林、罗益周、王勇	湖南省地球物理地球化学调查所（第一单位）	中文核心期刊T1	2024.04
9	湖南省热水圩地热田干热岩形成的热源机制与成因模式	煤田地质与勘探	杜江、蔡宁波、张保建、王克营、何立宏、廖凤初	湖南省地球物理地球化学调查所（第一单位）湖南省地质新能源勘探开发工程技术研究中心（第二单位）	中文核心期刊EI T1	2024.04
10	湘中冷水江矿区煤层气地质条件分析	煤炭技术	杜江、蔡宁波、张良平	湖南省地球物理地球化学调查所（第一单位） 湖南省地质新能源勘探开发工程技术研究中心（第二单位）	北大中文核心T2	2024.04
11	The Geology, Fluid Inclusions, and O-S Isotopes of the MibeiGold Deposit, Hunan Province, Southern China	Acta Geologica Sinica (English Edition)	XUE Wenhao, LIANG Yayun, 李晓峰, LI Mingyi, XIE Wenbo, PENG Xue, XIA Rui4, 5, HE Hongsheng2, 3 and XIAO Jincheng	湖南省地球物理地球化学调查所（第二单位） 湖南省地质新能源勘探开发工程技术研究中心（第三单位）	SCI 3区	2024.04
12	添加二氧化硅的煤石墨化高温高压模拟实验	矿业科学学报	陈高健、曹代勇、王安民、魏迎春、刘志飞、赵萌	湖南省地球化学过程与资源环境效应重点实验室(第二单位)	中文核心期刊T1	2024.04
13	思茅盆地页岩气地质条件及资源潜力分析	矿产与地质	杜江	湖南省地球物理地球化学调查所（第一单位）湖南省地质新能源勘探开发工程技术研究中心（第二单位）	中文科技核心T2	2024.02
14	中扬子地台宜昌地区寒武系水井沱组优质页岩储层发育特征及天然气富集机理研究	中国地质	蔡宁波、王琳霖、鲍一遥、李怡普、万泽鑫、康志梅、罗胜元	湖南省地质新能源勘探开发工程技术研究中心（第二单位）	中文核心期刊cscd T1	2024.01
15	桂中-南盘江地区黔水地1井打屋坝组页岩储层含气性及可压性评价	中国地质调查	郭军、苑坤、郭经纬、陈相霖、李岩	湖南省地球物理地球化学调查所（第一单位）	中文科技核心T3	2023.12
16	张家界市永定区地质灾害发育规律及易发性评价研究	中国地质调查	巩书华，王克营，蔡宁波，杜江，李少青，王焕银	湖南省地球物理地球化学调查所（第一单位）湖南省地质新能源勘探开发工程技术研究中心（第二单位）	中文科技核心T3	2023.12
17	湘东南东风岩体锆石 U-Pb 年代学、Hf 同位素组成及稀土矿床特征	矿床地质	张锦煦，林碧海，廖凤初，孙 骥，谭仕敏，何艳林，周 超，朱继华，熊 雄，李超，陈剑锋	湖南省地球物理地球化学调查所（第二单位）	中文核心期刊T1	2023.12
18	A method to classify coal pore system by using cumulative amplitude ratio and its dynamic variation	greenhouse gases science and technology	邹明俊、蔡宁波、王键英、Zibin Ding and Linlin Yao,	湖南省地质新能源勘探开发工程技术研究中心（第二单位） 湖南省地球物理地球化学调查所（第三单位）	SCI 4区	2023.07
19	南岭加里东期钨锡矿床成矿机制研究：以湘西南落家冲矿床为例	岩石学报	陈剑锋，杜云，熊伊曲，管申进，何红生，周立同，陆文，石金江	湖南省地球物理地球化学调查所（第一单位）湖南省地质新能源勘探开发工程技术研究中心（第五单位）	中文核心期刊T1	2023.06
20	Petrogenesis of Mesozoic Li-, Cs-, and Ta-rich (LCT) pegmatites from the Neoproterozoic Jiangnan Orogenic Belt,South China: An alternative origin model for the LCT type pegmatite	Ore Geology Reviews	陈剑锋、文春华、吕正航、黄建中、张金旭、唐勇、Yun Du, Chuang-Hua Cao	湖南省地球物理地球化学调查所（第一单位）	SCI 2区	2023.02

sensors

MDPI

Article

Gradual Failure of a Rainfall-Induced Creep-Type Landslide and an Application of Improved Integrated Monitoring System: A Case Study

Jun Guo [1,*], Fanxing Meng [2] and Jingwei Guo [1]

[1] Hunan Institute of Geophysics and Geochemistry, Changsha 410014, China
[2] Hunan Institute of Nuclear Geological Survey, Changsha 410011, China; qinym_dzy@163.com
* Correspondence: guoj_2023@126.com

Abstract: Landslides cause severe damage to life and property with a wide-ranging impact. Infiltration of rainfall is one of the significant factors leading to landslides. This paper reports on a phase creep landslide caused by long-term rainfall infiltration. A detailed geological survey of the landslide was conducted, and the deformation development pattern and mechanism of the landslide were analyzed in conjunction with climatic characteristics. Furthermore, reinforcement measures specific to the landslide area were proposed. To monitor the stability of the reinforced slope, a Beidou intelligent monitoring and warning system suitable for remote mountainous areas was developed. The system utilizes LoRa Internet of Things (IoT) technology to connect various monitoring components, integrating surface displacement, deep deformation, structural internal forces, and rainfall monitoring devices into a local IoT network. A data processing unit was established on site to achieve preliminary processing and automatic handling of monitoring data. The monitoring results indicate that the reinforced slope has generally stabilized, and the improved intelligent monitoring system has been able to continuously and accurately reflect the real-time working conditions of the slope. Over the two-year monitoring period, 13 early warnings were issued, with more than 90% of the warnings accurately corresponding to actual conditions, significantly improving the accuracy of early warnings. The research findings provide valuable experience and reference for the monitoring and warning of high slopes in mountainous areas.

Keywords: rainfall-induced landslide; field exploration; failure mechanism; LoRa Internet of Things; monitoring

Citation: Guo, J.; Meng, F.; Guo, J. Gradual Failure of a Rainfall-Induced Creep-Type Landslide and an Application of Improved Integrated Monitoring System: A Case Study. *Sensors* **2024**, *24*, 7409. https://doi.org/10.3390/s24227409

Academic Editor: Klaus Moessner

Received: 12 September 2024
Revised: 13 October 2024
Accepted: 15 November 2024
Published: 20 November 2024

1. Introduction

Landslides have always been one of the deadliest geological disasters distributed worldwide, leading to the collapse of houses and fatalities [1–5]. The primary driving force behind landslide disasters is the gravitational force acting on rock and soil masses, making landslides most prevalent in mountainous areas. Specifically, geological structures such as discontinuities and properties, rainfall, groundwater seepage, earthquakes, and other factors often play a key role in causing slope instability.

The investigation into the influential mechanisms of stability factors has become the most crucial approach to distinguish the development stage and failure mode of landslides. Generally, the triggering factors of a landslide are multiple [6,7]. Among these factors water is one of the most frequent causes of landslides. Landslides triggered by water can be categorized into two types: water seepage inside the soil mass and surface flow. The primary source of water is rainfall. When rainfall carries a substantial amount of rainwater that seeps into the receiving soil, it results in a decrease in soil suction and an increase in soil pore water pressure. This, in turn, decreases soil resistance and ultimately leads to slope failure [8–10]. Consequently, many landslides are caused by

rainfall [11,12]. The correlation between surface water flow and landslides lies in the erosion and damage to the slope surface, which further impacts the rock and soil structure of the slope, resulting in terrain and landforms conducive to instability [13,14].

As the soil mechanical properties decrease with surface water infiltration, various phenomena characterizing landslides occur, such as shear failure of rock and soil, groundwater outflow, surface fissures, and even the toppling of surface vegetation in the initial and evolution stages of landslides [15–19]. By monitoring these characteristics, the development stage of landslides can be predicted, and corresponding disposal measures can be taken to prevent further slope collapse [20,21]. Landslide prevention methods include brushing and reducing the load, gentle slope treatment, drainage, and backpressure at the foot of the slope, strengthening the foot of the slope, and reinforcing the slope body [22–26]. Drainage measures are particularly crucial for rainfall-induced landslides, including surface drainage and groundwater drainage. Therefore, drainage channels and pipes are commonly employed methods. Others include prestressed staggered anchor cables, retaining walls, anti-skid piles, pressure grouting, shotcrete, and grouting for seepage prevention. The monitoring of slope reinforcement measures includes surface deformation monitoring and internal monitoring. Surface deformation monitoring can be conducted through remote monitoring [27]. However, the variation of internal characteristics, such as deep displacement, groundwater pressure, and the stress and strain of piles or anchors, should be monitored using sensors [28,29]. In remote mountainous areas, the conditions for continuous on-site measurements are challenging, making it difficult to ensure the quality and consistency of monitoring data [30]. Additionally, conducting monitoring at multiple sites exacerbates the difficulties associated with on-site surveillance. Presently, the automation of landslide monitoring in remote mountainous regions remains a challenging task that is not easily accomplished.

In this study, we reported a landslide that happened in Yongshun County, Hunan Province in China. Through the collection of various surface features characterizing landslides, the destructive patterns and triggering mechanisms of slope landslides were analyzed. Based on this analysis, the stages of slope landslide occurrences were determined, and corresponding reinforcement and remediation measures were proposed. An intelligent monitoring and early warning system applicable to remote mountainous areas was developed. This system, based on Internet of Things (IoT) technology, integrated and developed a local IoT for key project monitoring devices such as surface displacement, deep deformation, groundwater level, and internal forces in anchored structures. The research findings can serve as an experiential reference for the monitoring and early warning of high slopes in mountainous areas.

2. General Characteristics of the Landslide

The Xianeyu landslide, situated in Aimin Village, Yongshun County in Hunan Province of China (109°59′12″ E, Latitude: 29°15′22″ N), represents a considerable geological hazard with an estimated volume of approximately 10.5 × 104 m^3, as shown in Figure 1. Once the landslide slides down, it directly threatens the life and property safety of over 220 people. This landslide was initially documented in June 1984, triggered by persistent heavy rainfall, leading to deformation of the landslide mass and the development of cracks in houses situated at its rear edge. In the 2003 monsoon season, heavy rainfall caused the displacement of approximately 3500 m^3 of soil and rocks, resulting in damage to 12 houses.

Figure 1. Distribution of landslide and the threatened area: (**a**) remote sensing image, (**b**) threatened building, (**c**) topographic of the landslide area.

In recent years, the Xianeyu landslide has exhibited more pronounced deformation, aggravated by the increasing frequency of extreme weather events. The mass of the landslide has significantly subsided, causing a noticeable tilt in wooden structures on its slope, localized shear cracks at the front edge of the landslide, and multiple instances of dry-stone retaining walls collapsing. Additionally, to the north of this landslide, there is an unstable sloped area. Field observations have indicated gradual subsidence in the cultivated fields on the slope, although it does not pose an immediate threat to structures. Therefore, it is recommended to enhance monitoring efforts for this unstable slope.

2.1. Geological Characteristics

Based on surface deformation characteristics and micro-topographic features, the rear and front edges of the landslide are demarcated by steep slopes, while the lateral boundaries of the landslide are determined by the presence of fissures and the ridge line. The plan view of the landslide exhibits a round-chair shape, and its longitudinal profile appears as a broken-line pattern with the main sliding direction oriented at 85°. The elevation of the landslide's rear edge ranges from approximately 616.75 to 627.52 m, while the front edge's elevation is between 579.59 and 583.78 m, resulting in a relative height difference of about 40 m. The landslide has an inclined length of approximately 142 m and a lateral width of about 210 m, covering an area of approximately 23,600 square meters. The thickness of the landslide ranges from 3 to 5 m, with an estimated volume of approximately 105,000 cubic meters. It is classified as a medium-sized shallow translational landslide composed of soil material.

According to the on-site survey results as shown in Figure 2, the predominant geological strata in the affected area consist of Quaternary residual slope deposits (Q), as depicted in Figure 2b, which include fine-grained clay and gravelly soil. Additionally, there are Silurian upper Shamao Group (S3sh, Figure 2c) formations characterized by gray-green, gray–white, and purple–red mudstone, sandy shale, and quartz sandstone. The Silurian middle Luoreping Group (S2Lr, Figure 2d) is also presented as siltstone and

sandstone. The geomorphological type of the landslide area falls under the category of low mountain fold-valley terrain, with an overall west-high and east-low topography (Figure 2). The composition of the landslide's soil includes gravelly clay and soil forming a single-layer structure with relatively loose characteristics. The rock formations in the area range from weak to moderately hard and vary in thickness including laminated clastic rocks such as shale, slab-like shale, sandy shale, and mudstone. The rocks exhibit a strongly weathered condition, and there is extensive development of joint fractures within the rock layers, resulting in considerable fragmentation. Consequently, the rock strata exhibit relatively low resistance to deformation.

Figure 2. (**a**) Exploratory pit, (**b**) Quaternary residual layer, (**c**) the Upper Silurian Gauze Hat Group, (**d**) the Middle Silurian Luojiaping Group.

2.2. Weather Conditions

The study area experiences a humid mid-subtropical monsoon climate, characterized by an annual average temperature of 16.5 °C and precipitation totaling 1344.6 mm per year. However, since autumn 2009, the area has been facing an unprecedented series of droughts, causing extensive cracking in both the bedrock and soil. Meteorological data from the Yongshun County weather station reveal an average of 164.0 rainy days annually, with the longest consecutive rainy period lasting 20 days in May 2005. The annual rainfall is concentrated from April to September, accounting for 75% of the total annual rainfall. The average annual rainfall is 1344.6 mm. A 50-year maximum rainfall record is 95.8 mm/h. The highest annual rainfall recorded was 1837.7 mm in 1995, with a peak daily rainfall of 344.1 mm on 31 May of the same year. There are noticeable variations in rainfall distribution across Yongshun County, with higher rainfall occurring along the Longjiazhai syncline axis and the mountain township line in the north and west, while lower rainfall is observed in the south and east regions. Three times of extreme weather events were recorded, 167.0 mm rainfall on 23 July in 1993, 344.1 mm rainfall on 31 May in 1995. and 235.2 mm rainfall on 9 July in 2003. These precipitation patterns significantly impact soil saturation and water infiltration, which contribute to landslide formation.

Over time, continuous rainfall infiltration has gradually exacerbated slope deformation, leading to the hazardous conditions observed today.

2.3. Deformation Development Characteristics

As shown in Figures 3–6, numerous cracks of varying sizes are now visible in the site located at the rear of the landslide. These cracks typically measure between 1 and 5 cm in width and 3 and 10 m in length. Among them, the most severe crack spans about 5 m in length and 0.5 m in width, causing noticeable leaning in the central part of the housing affected by the landslide. Additionally, tensile cracks emerged at the rear and sides of the landslide, ranging from 5 to 20 m in length, 0.1 to 0.2 m in width, and with displacement distances ranging from 0.1 to 0.3 m. At the front, shear cracks have become apparent, leading to the bulging and collapse of several dry-stone walls. These cracks are distributed around the landslide and form the sliding range on the surface after coalescence. At the top of the landslide, tensile cracks are the main type (Figure 3), while tensile shear cracks are more common on both sides of the landslide body (Figure 4). At the front edge of the landslide body, soil swelling cracks are the main type (Figure 6). And obvious inclination could be seen in the buildings on the landslide (Figure 5). All these phenomena indicate that the landslide was in a sliding stage. When cracks rapidly expand, it indicates that the landslide is accelerating its sliding.

The signs of deformation on the landslide mass are quite prominent, indicating that it is currently experiencing overall creep deformation. Tension cracks have emerged at the rear and sides of the landslide, with noticeable cracks appearing in houses situated at the rear of the landslide, as well as numerous dry-stone walls along the slope and at the front showing signs of bulging and collapsing. Local monitoring personnel have reported that the width of ground and house cracks is progressively increasing year by year. These observations strongly suggest that the Xianeyu landslide in Aimin Village is facing increased downslope force and reduced resistance, thereby further compromising its stability, especially during heavy rainfall or rainy conditions. Looking ahead, considering the influence of rainfall and human engineering activities, the trend of landslide deformation and rupture is expected to escalate, heightening the risk of landslide movement in the future.

Figure 3. Cracks induced by landslide: (**a**) Cracks in rear edge of landslide, (**b**) Cracks in front edge of landslide**.**

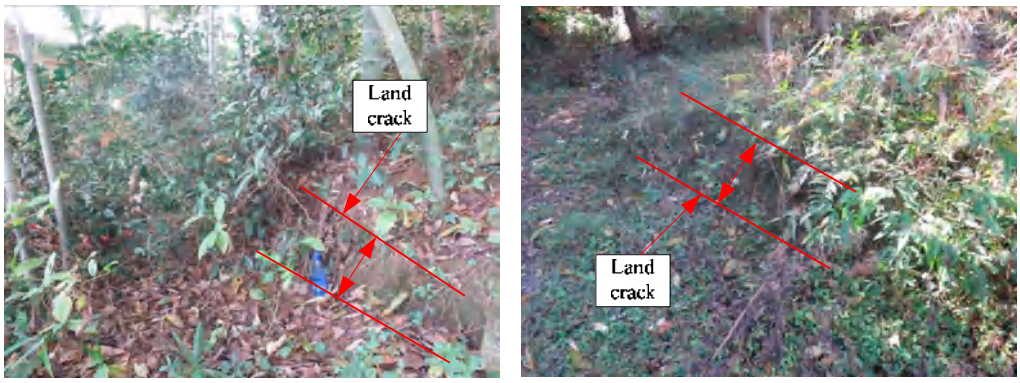

Figure 4. Cracks in side edge of landslide.

Figure 5. Cracks on wall and ground.

Figure 6. Phenomenon in front of landslide, (**a**) Building inclination, (**b**) Wall swelling.

3. Failure Mechanism of the Landslide

The mechanism of landslide destruction is influenced by a combination of internal and external factors. Internal factors encompass geological elements such as terrain, lithology, and structure, whereas external factors consist of continuous heavy rainfall and human activities.

In the specific area under consideration, the landscape features a karst hilly terrain with a moderately dissected topography and ground slopes typically ranging from 25° to 40°, providing favorable terrain conditions for landslide occurrence. The landslide mass primarily consists of residual soil mixed with a substantial amount of gravel. This soil

type is characterized by its loose structure, mixed particle sizes, good permeability, and relatively low cohesion, rendering the slope vulnerable to instability after rainfall. Such susceptibility to rainfall-induced instability is considered one of the primary internal factors contributing to landslides in the area.

Additionally, meteorological factors play a crucial role in influencing landslide stability. In this region, the frequent occurrence of heavy rainfall, combined with the relatively large pores in the landslide mass soil, facilitates rapid infiltration of rainwater into the slope. This influx increases both the self-weight and downward force of the slope. Furthermore, intense rainfall can create hydraulic flow paths within the soil, leading to softening and saturation of the soil near these paths. Consequently, the soil's shear strength decreases, diminishing its internal friction and cohesion, thereby heightening the risk of slope instability and sliding. Moreover, the presence of numerous houses within the landslide mass introduces additional load to the slope. Moreover, the steep slopes formed by road construction and other activities at the front edge of the landslide serve as significant contributing factors to landslide formation.

Based on investigations and field surveys, the primary deformation characteristics of the landslide mass manifest as cracks at the rear (Figure 3), sides (Figure4), and bulging (Figure 6) at the front edge. The mechanism behind this formation primarily includes several factors: unstable slopes formed due to human-induced slope cutting at the front, the loading of residential houses at the rear and on the landslide mass, saturation of the soil due to rainfall and water infiltration, and increased weight of the landslide mass resulting in decreased shear strength, leading to gradual creeping towards the free edge under its own weight. This process exerts pressure on the soil at the front edge, causing it to press against the dry-stone retaining walls and resulting in their bulging. Additionally, the soil at the rear edge of the landslide mass, under the influence of gravity and artificial structures, pushes against the soil at the front edge, resulting in tension cracks at the rear and partial cracking at the front, thereby forming potential geological hazard points.

Further observations indicate that the deformation and destruction mode of the landslide belongs to the translational type. The deformation characteristics generally involve rapid shear sliding of the landslide towards the free edge under the pushing of soil mass at the rear edge while the shear surface is controlled by weak structural planes. The deformation progresses gradually from deep potential shear surfaces to the surface, with the rear edge of the landslide and the shear exit located at the terrain change turning point. Therefore, the deformation and destruction mode of the landslide belongs to the translational type.

4. Reinforcement Measures

The design of reinforcement engineering should adhere to the principles of safety, rationality, and economy. The focus should be on ensuring convenience in construction, minimizing environmental impact, and adopting the most cost-effective structural form while guaranteeing safety and normal functionality [31]. Moreover, it is crucial to align these principles with the goal of protecting the local ecological environment. Considering that the landslide mass in this area is primarily composed of soil and that there are numerous buildings and crops within the sliding range, the slope stabilization must ensure that the displacement of the slope is effectively controlled after reinforcement. The stabilization measures should be systematically arranged, with minimal land occupation. Therefore, a comprehensive stabilization approach combining anti-slide piles, retaining walls, and drainage (interception) systems is adopted. Comparatively, if anchor rods or anchor cables were used, the required land area would be larger, and the slope could still experience displacement after reinforcement, which would not adequately ensure the safety of the buildings above. This integrated approach ensures a balanced strategy that effectively mitigates landslide risks while also considering environmental conservation efforts.

Figure 7 illustrates the plan for slope retaining treatment. Given the extensive length and significant pushing force of the landslide mass, anti-sliding piles are chosen for anti-sliding support. Considering the dense housing at the rear edge of the landslide mass and the limited construction space, anti-sliding pile engineering is implemented at the front edge of the landslide mass to provide necessary support against sliding. The anti-slide piles are deeply embedded and arranged to pass through the sliding surface, effectively preventing further movement of the slope soil mass. Moreover, the anti-slide piles can efficiently control the local deformation and displacement of the landslide and transmit the stresses generated by sliding to the more stable deep soil or bedrock. By using anti-slide piles in this scenario, the sliding forces from the upper sliding body can be resisted, achieving the effect of controlling the slope movement.

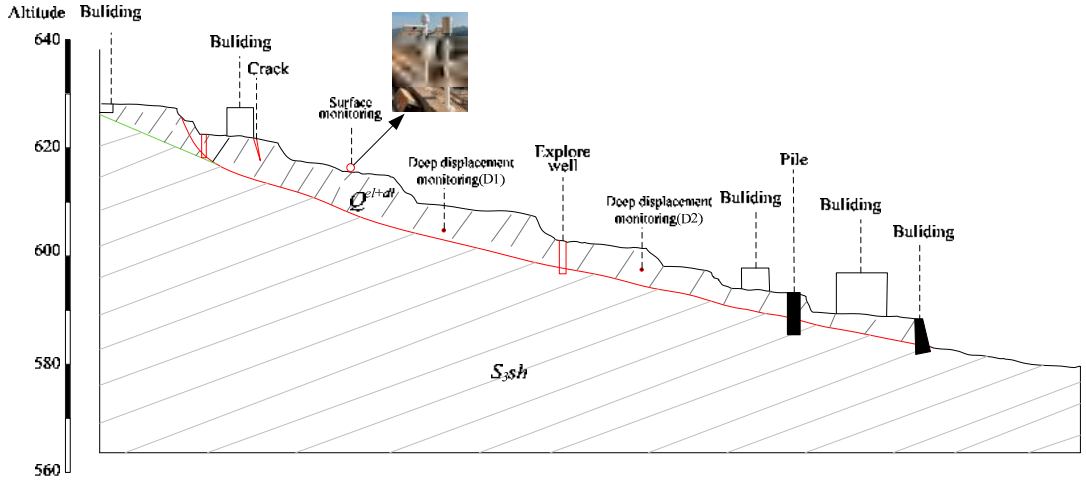

Figure 7. Site treatment of the landslide.

Retaining walls are predominantly positioned at the front edge of the landslide mass. Due to steep slopes resulting from road construction or house cutting, soil erosion and local bulging are common occurrences. Hence, retaining walls are strategically designed to be erected at the front of these steep slopes to stabilize the landslide mass. The retaining wall is installed at the front edge of the landslide mass to prevent further sliding of the landslide body. In combination with anti-slide piles, this creates a slope retaining system that ensures the safety of the structures located above.

Furthermore, cut-off and drainage ditches are strategically placed around the landslide to redirect seasonal surface water from atmospheric rainfall and domestic water usage by villagers into nearby valleys. Drainage ditches are constructed to facilitate the efficient discharge of surface water within the landslide area during the rainy season. This measure effectively reduces soil erosion and minimizes rainfall infiltration within the landslide area, which may contribute to enhanced stability.

5. Monitoring

5.1. Optimization and Deployment of Monitoring Systems

To effectively monitor landslides, it is crucial to conduct safety risk identification through typical high-risk slope assessment. This involves employing various monitoring terminals to achieve comprehensive real-time online monitoring of slope displacement, rainfall, surface water, groundwater, stress, macro deformation, and other relevant factors. These monitoring tools enable continuous and real-time safety monitoring of high-risk slopes, ensuring timely detection and response to potential landslide hazards. The principle of IoT monitoring technology involves collecting physical data through sensors, transmitting the data via wireless communication technologies, and processing it in real time using edge computing or cloud computing. This is combined with intelligent

analysis and decision-making models to provide scientific support for the management and control of monitored objects. This technology is widely applied in various fields, including industrial equipment monitoring, environmental monitoring, intelligent transportation, and building safety monitoring, significantly enhancing monitoring efficiency and accuracy.

In addition to the traditional monitoring system, on-site network communication among various devices using LoRa wireless self-organizing network technology is explored. This enables devices to function independently of remote servers, allowing the collection, calculation, and transmission of Beidou monitoring data directly from high-risk slopes at the project site. This approach reduces overall data transmission requirements, lowers the system's demands for on-site communication environments, and unlocks cloud computing capabilities. It fosters integrated collaborative operation of terminal edge management cloud network, thereby enhancing the system's adaptability and intelligence. Moreover, an integrated approach is implemented, along with high-performance batteries and solar panels, to create a self-powered Internet of Things composite sensor monitoring unit.

Specifically, for the on-site self-organizing network scheme, the LoRa gateway incorporates a digital baseband chip based on SX1301, featuring an eight-channel single gateway capable of accommodating 300 terminals, with a total power consumption of approximately 6 W. It boasts a coverage area of up to a 3 km radius in an open environment, offering superior anti-interference and link stability compared to FSK technology. By integrating a 160 W monocrystalline solar panel, a 120 AH lead-acid gel battery, a solar controller, and other self-built photovoltaic power supply systems, we achieve 24-h power supply with uninterrupted power for 15 consecutive rainy days. The LoRa nodes utilize the LoRaWAN protocol with DSSS modulation and operate in the half-duplex communication mode. Each node has a built-in microcontroller with an integrated transceiver program, supporting common baud rates ranging from 1200 to 57,600. The gateway based on the SX1301 chip adopts an eight-channel parallel data transmission and reception scheme. This approach significantly improves data throughput compared to traditional LoRa polling methods while also reducing data congestion and minimizing transmission conflicts.

The composite sensor monitoring units communicate using the IEEE802.15.4 standard signal[32], with a transmission range of 50–100 m, enabling low-power self-organizing networks. For each composite sensor monitoring unit or a group of adjacent units, an intelligent data acquisition system is developed. This system can simultaneously collect data from various sensors, including GNSS, fixed inclinometers, rain gauges, anchor rod load cells, anchor cable load cells, piezometers, strain gauges for lattice structures, retaining wall earth pressure cells, and more. The collected data are then integrated and transmitted at predefined data transmission intervals.

The fusion calculation technology of Beidou and gyroscope is adopted (Figure 8), involving the integration of a gyroscope device into the low-power Beidou device. The monitoring data from both devices are fused, and the gyroscope monitoring results are incorporated as constraints when fixing the ambiguity of the Beidou solution algorithm. Additionally, adaptive Kalman filtering and wavelet denoising processing are applied to the monitoring results of both devices to yield stable monitoring outcomes. This approach effectively addresses challenges such as ambiguity fixation difficulties, low accuracy, and instability in monitoring.

Considering the large volume of real-time monitoring data and the communication challenges in mountainous high-slope areas, especially during heavy rainfall when the probability of landslides significantly increases, it is a critical moment for slope monitoring and early warning. Therefore, localized deployment of data acquisition and processing systems is necessary, providing on-site computation capabilities. This approach enables data collection, real-time computation, post-processing, and transmission of results based on LoRa IoT networks. By shortening the data acquisition

chain and improving reliability, this method enhances the efficiency of monitoring and early warning systems.

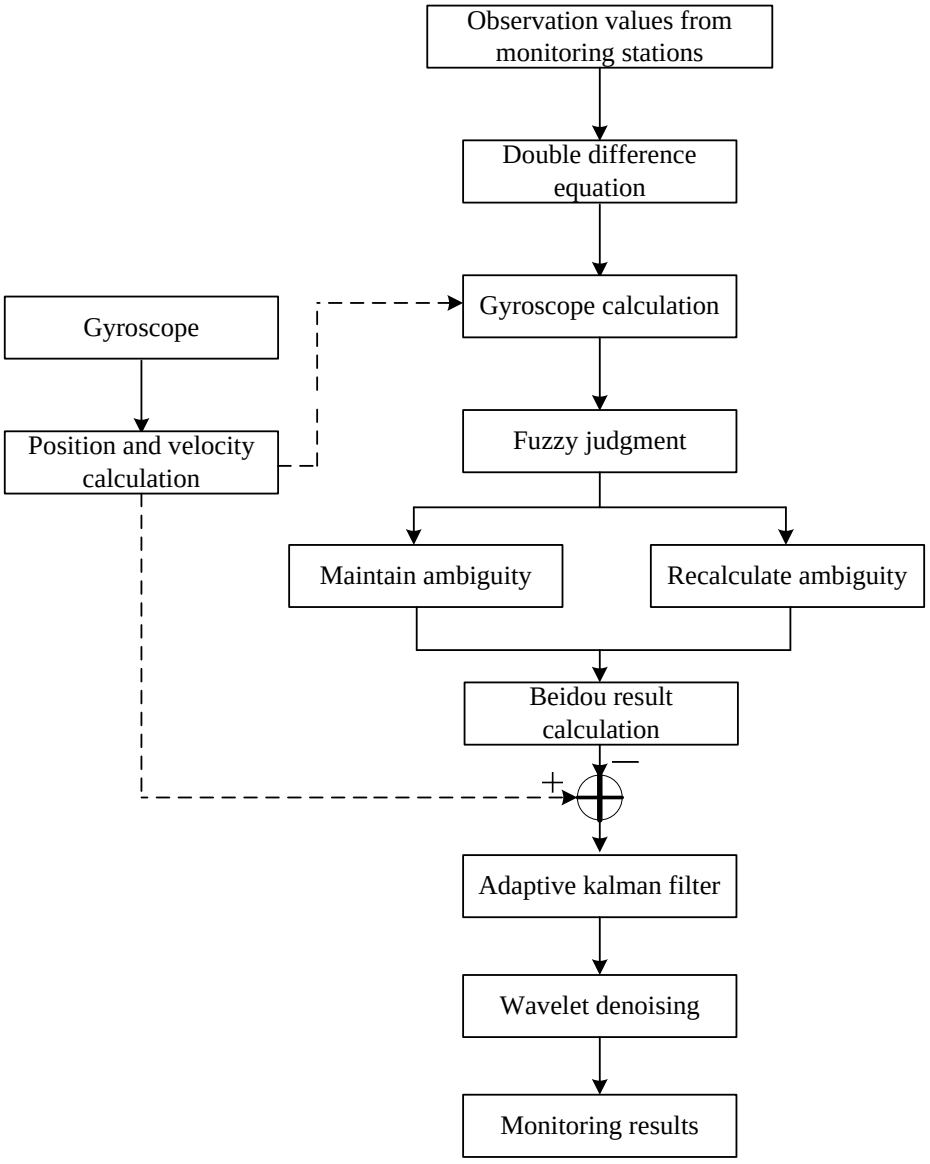

Figure 8. Algorithm for gyroscope fusion**.**

5.2. Results

As shown in Figure 7, surface and deep-seated displacement monitoring is consistently conducted on the slope to facilitate long-term real-time monitoring and early warning. Furthermore, recognizing the significant correlation between rainfall and landslides in this area, rainfall gauges are strategically installed.

Since the initiation of the site treatment project in 2022, the on-site monitoring instruments have been sequentially deployed and put into operation. Consequently, the monitoring system has been operating continuously and reliably. Data forecasting adheres to a daily reporting strategy and is accessible in real time via the internet cloud platform. In the event that monitored data surpass preset threshold values, the system automatically issues alerts and delivers varying levels of warning messages based on the magnitude of the monitored values. Moreover, it provides on-site disposal recommendations.

Figures 9–12 exhibit the monitoring and forecasting data of select monitoring instruments from the commencement of their operation until the present. An examination of these figures reveals that since the slope's construction, surface displacement, deep-seated deformation, and stress of the pile reinforcement have exhibited gradual increases in the initial stage, followed by stabilization over time.

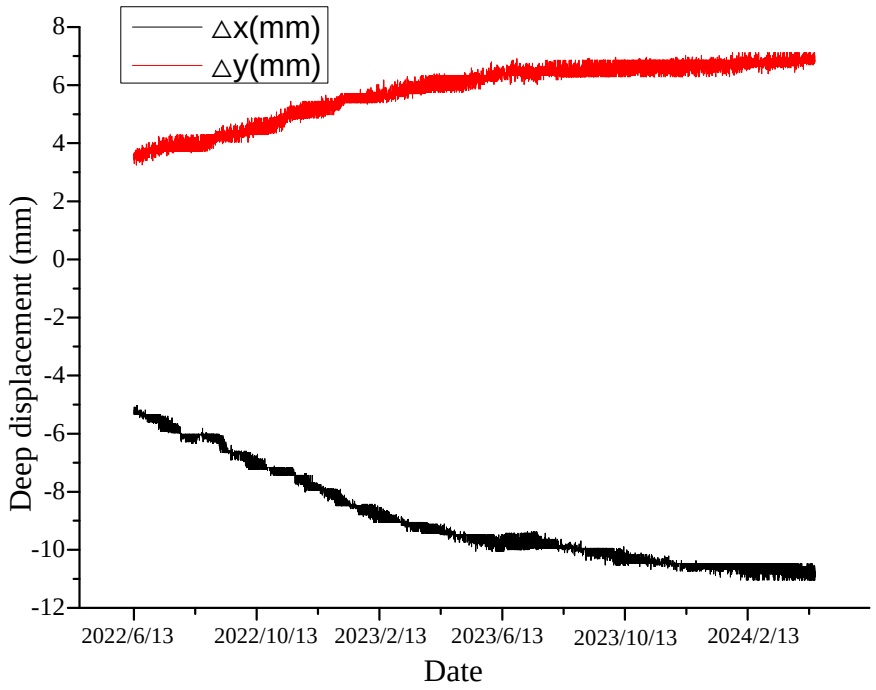

Figure 9. Deep displacement.

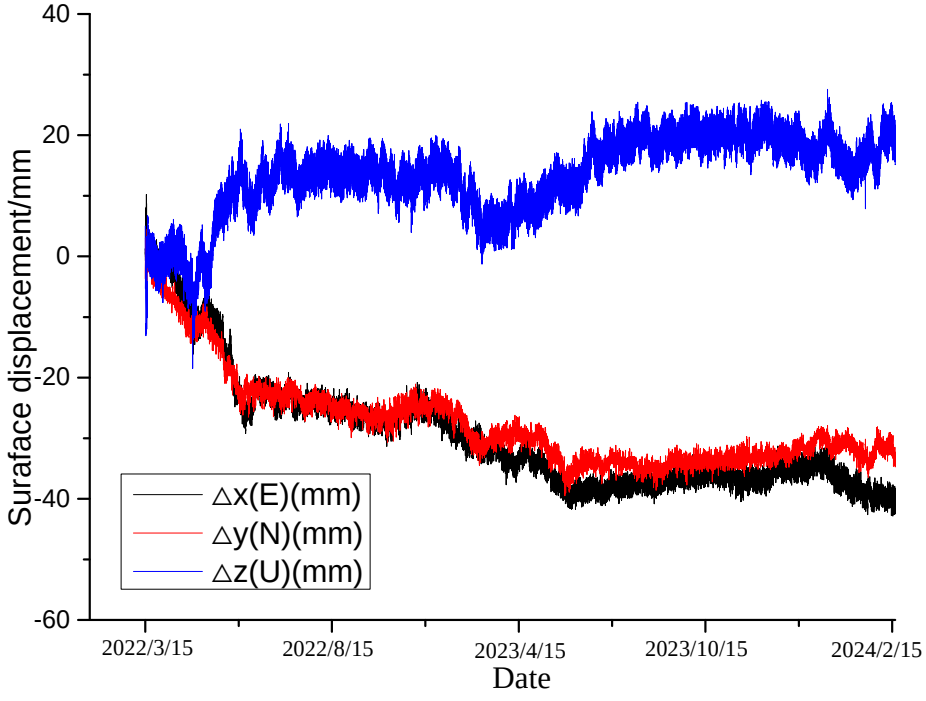

Figure 10. Surface displacement.

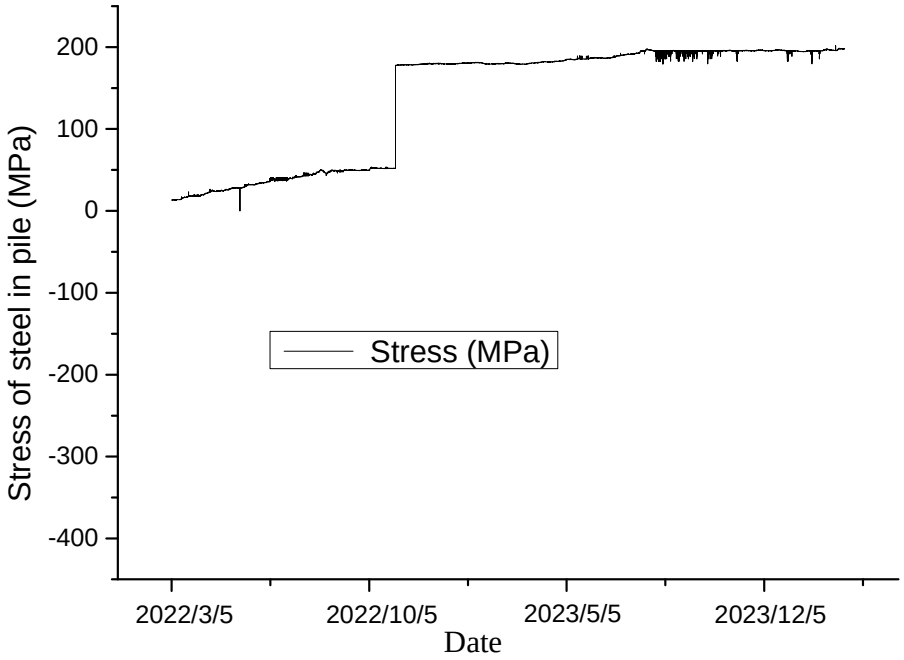

Figure 11. Stress of steel in pile.

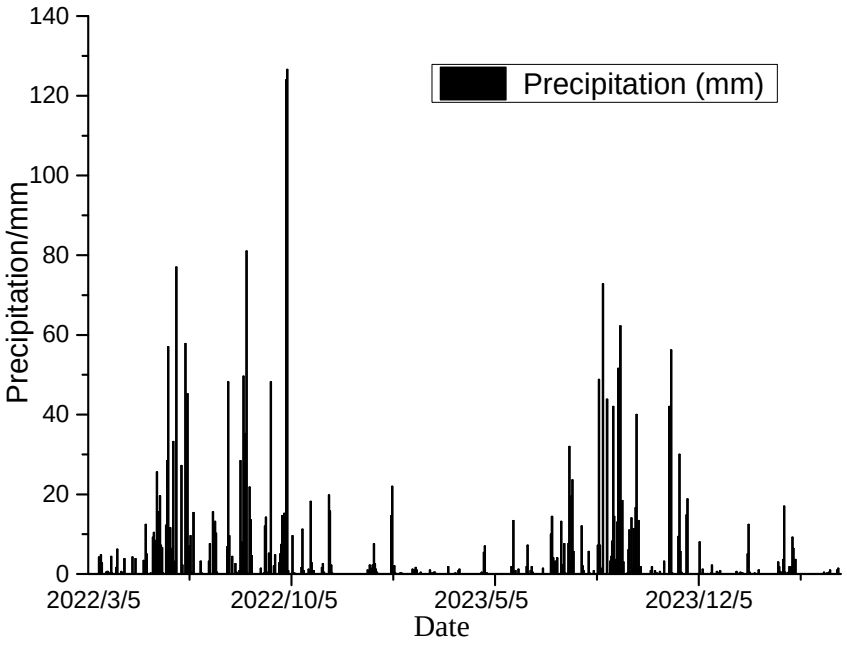

Figure 12. Monitored precipitation.

As shown in Figure 9, illustrating the deep-seated displacement–time curve, and Figure 10, showing the surface displacement curve, both the surface and deep-seated displacements of the rock–soil mass have continuously increased over time following the disturbance caused by excavation, gradually stabilizing afterward. This suggests that the deformation of the deep-seated rock–soil mass was effectively controlled following the completion of the supporting structure. At this juncture, all reinforcement facilities of the slope amalgamated into an organic whole, successfully regulating the displacement rate of the slope. The change pattern of the monitoring system data can accurately reflect the real-time working status of each reinforcement facility. The monitoring results of the stress monitoring (Figure 11) indicate that it began to exert the most significant effect after

the completion of the anti-sliding pile. A considerable change in stress was observed in early November 2023, followed by gradual stabilization. This suggests a reduction in slope deformation under the support of the anti-sliding piles and approaching a stable state.

The rainfall monitoring results depicted in Figure 12 automatically trigger warning messages when the rainfall exceeds the predefined threshold value within a short period. The threshold values for daily rainfall are set as follows: 55 mm for a blue alert, 60 mm for a yellow alert, 80 mm for an orange alert, and 100 mm for a red alert. Since its establishment, the system has issued warnings 13 times, each corresponding to rainfall exceeding 55 mm. Following the issuance of the warning, the system automatically provides recommendations for on-site observation of the slope status, along with continuous warning alerts. On-site observations reveal that the slope boasts a well-functioning drainage system. Although rainfall does have some influence on surface displacement, it has not reached a level that threatens the overall stability of the slope.

6. Conclusions

The performance of a case study on a landslide that occurred in Yongshun County, Hunan Province, China was reported. The investigation involved geological surveys of the landslide, analysis of regional climatic characteristics, and historical analysis of landslide development to understand its mechanism. The findings indicate that the landslide in this area is a shallow translational soil landslide primarily caused by long-term creep influenced by rainwater infiltration. To address the layout of houses, topography, and characteristics of the landslide within the area, reinforcement measures including the use of anti-sliding piles and retaining walls were implemented. Recognizing the influence of environmental factors on monitoring signals in remote mountainous areas, low-power, low-cost, high-precision Beidou receiving devices were developed based on existing Beidou monitoring equipment. The application of LoRa self-organizing network technology in the intelligent transformation of the monitoring system enabled the integration of end edge management cloud network operations, enhancing the adaptability and intelligence of the system and addressing the issue of decentralized data in slope engineering monitoring. Utilizing a fusion of Beidou and gyroscope-based calculation techniques for local preliminary data processing, the integration and upgrade of monitoring data were achieved, enabling data collection, real-time calculation, post-processing, and transmission of calculation results based on LoRa IoT technology. This streamlined data collection process enhances the reliability of deformation monitoring and early warning for typical high slopes in mountainous regions, demonstrating reliable results and significant potential for widespread application.

Author Contributions: Conceptualization, J.G. (Jun Guo); Methodology, J.G. (Jun Guo); Software, J.G. (Jun Guo); Validation, J.G. (Jun Guo); Formal analysis, F.M.; Investigation, F.M.; Resources, F.M.; Data curation, F.M.; Writing—original draft, J.G. (Jun Guo); Writing—review and editing, F.M. and J.G. (Jingwei Guo); Visualization, J.G. (Jingwei Guo); Supervision, J.G. (Jingwei Guo); Project administration, J.G. (Jingwei Guo); Funding acquisition, J.G. (Jun Guo). All authors have read and agreed to the published version of the manuscript.

Funding: This study is financially supported by Special Fund Project of Safety Production Prevention and Emergency in Hunan Province (2023YJT003).

Institutional Review Board Statement: Not applicable.

Informed Consent Statement: Not applicable.

Data Availability Statement: All data used in the study was shown in the manuscript.

Acknowledgments: We thank the two anonymous reviewers for their constructive comments.

Conflicts of Interest: The authors declare no conflict of interest.

References

1. Tang, H.M.; Wasowski, J.; Juang, C.H. Geohazards in the three Gorges Reservoir Area, China–lessons learned from decades of research. *Eng. Geol.* **2019**, *261*, 105267.
2. Wolter, A.; Stead, D.; Clague, J.J. A morphologic characterisation of the 1963 Vajont Slide, Italy, using long-range terrestrial photogrammetry. *Geomorphology* **2014**, *206*, 147–164.
3. Zhou, G.G.D.; Roque, P.J.C.; Xie, Y.; Song, D.; Zou, Q.; Chen, H. Numerical study on the evolution process of a geohazards chain resulting from the Yigong landslide. *Landslides* **2020**, *17*, 2563–2576.
4. Yang, C.; Shi, W.; Peng, X.; Zhang, S.; Wang, X. Numerical simulation of layered antiinclined mining slopes based on different free face characteristics. *Bull. Eng. Geol. Environ.* **2022**, *81*, 359.
5. Shao, C.; Li, Y.; Lan, H.; Li, P.; Zhou, R.; Ding, H.; Yan, Z.; Dong, S.; Yan, L.; Deng, T. The role of active faults and sliding mechanism analysis of the 2017 Maoxian postseismic landslide in Sichuan, China. *Bull. Eng. Geol. Environ.* **2019**, *78*, 5635–5651.
6. Greco, R.; Comegna, L.; Damiano, E.; Marino, P.; Olivares, L.; Santonastaso, G.F. Recurrent rainfall-induced landslides on the slopes with pyroclastic cover of Partenio mountains (Campania, Italy): Comparison of 1999 and 2019 events. *Eng. Geol.* **2021**, *288*, 106160.
7. Komac, M.; Holley, R.; Mahapatra, P.; Van der marel, H.; Bavec, M. Coupling of GPS/GNSS and radar interferometric data for a 3D surface displacement monitoring of landslides. *Landslides* **2015**, *12*, 241–257.
8. Ng, C.W.W.; Shi, Q. A numerical investigation of the stability of unsaturated soil slopes subjected to transient seepage. *Comput. Geotech.* **1998**, *22*, 1–28.
9. Zhu, L.; Deng, Y.; He, S. Characteristics and failure mechanism of the 2018 Yanyuan landslide in Sichuan, China. *Landslides* **2019**, *16*, 2433–2444.
10. Komolvilas, V.; Tanapalungkorn, W.; Latcharote, P.; Likitlersuang, S. Failure analysis on a heavy rainfall-induced landslide in Huay Khab Mountain in Northern Thailand. *J. Mt. Sci.* **2021**, *18*, 2580–2596.
11. Guzzetti, F. Landslide fatalities and the evaluation of landslide risk in Italy. *Eng. Geol.* **2000**, *58*, 89–107.
12. Salvati, P.; Petrucci, O.; Rossi, M.; Bianchi, C.; Pasqua, A.A.; Guzzetti, F. Gender, age and circumstances analysis of flood and landslide fatalities in Italy. *Sci. Total Environ.* 2018, 610–611, 867–879.
13. Dong, J.; Zhang, L.; Li, M.; Yu, Y.; Liao, M.; Gong, J.; Luo, H. Measuring precursory movements of the recent Xinmo landslide in Mao County, China with Sentinel-1 and ALOS-2 PALSAR-2 datasets. *Landslides* **2017**, *15*, 135–144.
14. Egholm, D.L.; Knudsen, M.F.; Sandiford, M. Lifespan of mountain ranges scaled by feedbacks between landsliding and erosion by rivers. *Nature* **2013**, *498*, 475–478.
15. Fiorucci, F.; Cardinali, M.; Carlà, R.; Rossi, M.; Mondini, A.; Santurri, L.; Ardizzone, F.; Guzzetti, F. Seasonal landslide mapping and estimation of landslide mobilization rates using aerial and satellite images. *Geomorphology* **2011**, *129*, 59–70.
16. Huang, R. Mechanisms of large-scale landslides in China. *Bull. Eng. Geol. Environ.* **2012**, *71*, 161–170.
17. Xing, A.; Yin, Y.; Jiang, Y.; Wang, G.; Yang, S.; Dai, D.; Zhu, Y.; Dai, J. Dynamic analysis and field investigation of a fluidized landslide in Guanling, Guizhou. *China Eng. Geol.* **2014**, *181*, 1–14. (In Chinese)
18. Ma, K.; Wang, L.; Peng, Y.; Long, L.; Wang, S.; Chen, T. Permeability characteristics of fractured rock mass: A case study of the Dongjiahe coal mine. *Geomat. Nat. Hazards Risk* **2020**, *11*, 1724–1742.
19. Liu, G.; Zhong, Z.; Ma, K.; Bo, W.; Zhao, P.; Li, Y.; Zhang, Z.; Zhang, P. Field experimental verifications of 3D DDA and its applications to kinematic evolutions of rockfalls. *Int. J. Rock Mech. Min. Sci.* **2024**, *175*, 105687.
20. Segoni, S.; Piciullo, L.; Gariano, S.L. A review of the recent literature on rainfall thresholds for landslide occurrence. *Landslides* **2018**, *15*, 1483–1501.
21. Napolitano, E.; Fusco, F.; Baum, R.L.; Godt, J.W.; De Vita, P. Effect of antecedent-hydrological conditions on rainfall triggering of debris flows in ash-fall pyroclastic mantled slopes of Campania (southern Italy). *Landslides* **2016**, *13*, 967–983.
22. Cogan JGratchev, I. A study on the effect of rainfall and slope characteristics on landslide initiation by means of flume tests. *Landslides* **2019**, *16*, 2369–2379.
23. Sun, H.-Y.; Pan, P.; Lü, Q.; Wei, Z.-L.; Xie, W.; Zhan, W. A case study of a rainfall-induced landslide involving weak interlayer and its treatment using the siphon drainage method. *Bull. Eng. Geol. Environ.* **2019**, *78*, 4063–4074.
24. Park, H.I.; Jang, J.Y.; Lee, J.H. Assessment of rainfall-induced landslide susceptibility at the regional scale using a physically based model and fuzzy-based Monte Carlo simulation. *Landslides* **2019**, *16*, 695–713.
25. Cho, S.E. Failure distribution analysis of shallow landslides under rainfall infiltration based on fragility curves. *Landslides* **2020**, *17*, 79–91.
26. Yang, M.; Deng, B. Stability study of slope reinforced with piles under steady unsaturated flow conditions. *Comput. Geotech.* **2019**, *109*, 89–98.
27. Takafumi, H.K. Influence of the spatial variability of shear strength parameters on rainfall induced landslides: A case study of sandstone slope in Japan. *Arab. J. Geosci.* **2017**, *10*, 369.
28. Coe, J.A. Regional moisture balance control of landslide motion: Implications for landslide forecasting in a changing climate. *Geology* **2012**, *40*, 323–326.
29. Zakharov, V.N.; Malinnikova, O.N.; Trofimov, V.A.; Filippov, Y.A. Stability and Creeping of Landslide Slope. *J. Min. Sci.* **2014**, *50*, 1007–1016.
30. Forte, G.; Pirone, M.; Santo, A.; Nicotera, M.V.; Urciuoli, G. Triggering and predisposing factors for flow-like landslides in pyroclastic soils: The case study of the Lattari Mts. (southern Italy). *Eng Geol.* **2019**, *257*, 105137.

31. Ma, K.; Wang, L.; Long, L.; Peng, Y.; He, G. Discrete element analysis of structural characteristics of stepped reinforced soil retaining wall. Geomatics. *Nat. Hazards Risk* **2020**, *11*, 1447–1465.
32. Pucci, R.; Del Re, E.; Boschetti, D.; Ronga, L. Performance Evaluation of an IEEE802.15.4 Standard Based Wireless Sensor Network in Mars Exploration Scenario. In Proceedings of the 2009 1st International Conference on Wireless Communication, Vehicular Technology, Information Theory and Aerospace & Electronic Systems Technology IEEE, Aalborg, Denmark, 17–20 May 2009.

ACS OMEGA

http://pubs.acs.org/journal/acsodf
Article

New Re−Os Geochronological Data from the Upper Doushantuo Formation: Age Constraint on the Shuram Excursion and Implication for the Ediacaran Fluctuated Continental Weathering

Zhaozhao Tan,* Jianlan Luo, Xuesheng Xu, Wanglu Jia, Jie Li, and Liran Chen

Cite This: https://doi.org/10.1021/acsomega.4c05072

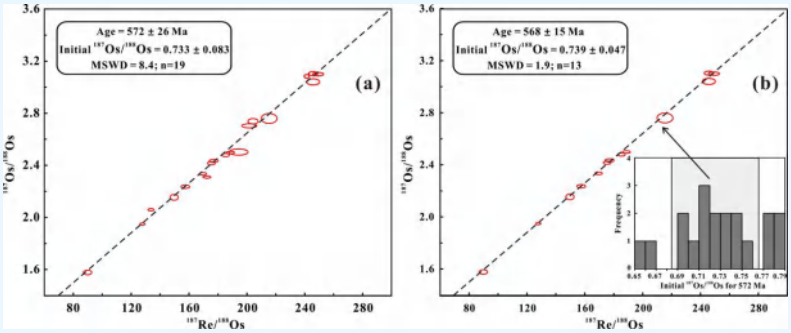

ABSTRACT: The largest negative carbon-isotope excursion in geological history has been reported by several studies of the upper Doushantuo Formation of South China, which has been correlated to the middle Ediacaran-Shuram excursion (SE). Due to a scarcity of radiometric age constraints on the excursion in South China, however, global correlations and comparisons of this event remain a debate. Here, we present Re−Os and carbon isotope data on organic-rich sediments obtained from a drill-core sample in the Chengkou area, the northeastern margin of the Yangtze Platform, and South China. The Re−Os geochronology yields a depositional age of 568 ± 15 Ma (Model 3, MSWD = 1.9, n = 13; 2σ), indicating a middle-late Ediacaran age for the upper Doushantuo Formation. This is supported by a negative $\delta^{13}C_{carb}$ excursion, which can be reliably correlated to the SE sequences. This age is consistent with the Re−Os radioisotopic dates bracketing the Shuram peaks in Northwest Canada and Oman. A compilation of $^{187}Os/^{188}Os$ and $^{87}Sr/^{86}Sr$ isotope ratios as well as the contents of redox-sensitive elements (RSE) from organic-rich sediments deposited between 635 and 540 Ma shows that the radiogenic $^{187}Os/^{188}Os$ ratios (>1.0) associated with enhanced oxidative weathering occurred at ca. 635, 580, and 560 Ma. As a result, accelerated influxes of nutrients stimulated primary productivity, promoting organic carbon burial and leading to ocean oxygenation. Additionally, elevated continental weathering could have delivered high fluxes of oxidants (e.g., sulfates) to oceans, resulting in transient ocean oxygenation. Corresponding to elevated radiogenic Os and Sr isotope ratios, the significant RSE enrichments at these three times indicate the presence of large marine RSE reservoirs and an oxygenated ocean. Therefore, the Re−Os age and initial Os isotope composition of organic-rich shale can be a sensitive tool for constraining the time interval of enhanced continental weathering and resulting pulses of ocean oxygenation during the Neoproterozoic era.

1. INTRODUCTION

The Ediacaran Period (ca. 635−541 M) has recorded the largest global carbon cycle perturbation event in geological history, known as the "Shuram Excursion (SE)"[1,2] and has been believed to be the result of Ediacaran atmospheric−oceanic oxidation.[2−6] Furthermore, large amounts of geochemical data have demonstrated that the SE was also accompanied by globally parallel negative shifts of $\delta^{34}S$ of pyrite and carbonate-associated sulfate (CAS) and an increased $^{87}Sr/^{86}Sr$ ratio.[4,5,7−9] These prominent changes imply that the onset of the SE was associated with enhanced continental weathering that delivered radiogenic strontium as well as sulfates acting as an oxidizing agent to the Ediacaran Ocean. Therefore, a primary seawater origin associated with the oxidation of dissolved organic carbon in the ocean has been advanced to account for the uniquely high amplitudes of Neoproterozoic $\delta^{13}C$ excursions during the past 20 years.[2−6,9−12]

Received: June 4, 2024
Revised: November 22, 2024
Accepted: November 26, 2024

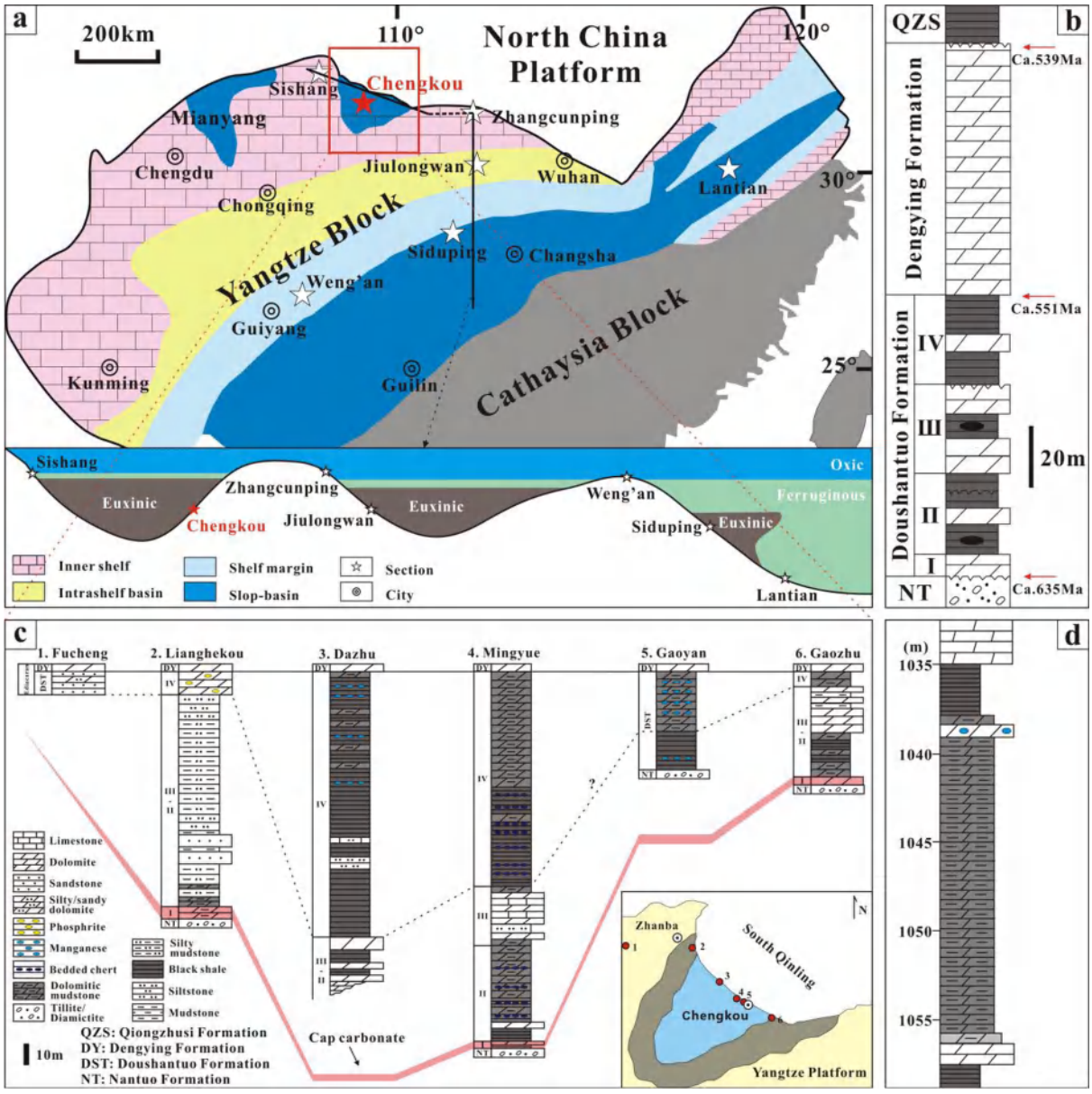

Figure 1. Paleogeographic maps and lithostratigraphic columns of the studied sections. (a) Paleogeographic reconstruction of the late period of the Ediacaran Doushantuo Formation in South China (modified from Jiang et al.,[37] Lu et al.,[15] and Och et al.[38]). (b) Typical stratigraphic column of the Yangtze Block, modified from Jiang et al.[37] and Cui et al.[9] Radiometric ages are from Condon et al.[14] and Zhu et al.[39] (c) Stratigraphic correlation of the Doushantuo Formation in the Chengkou sub-basin (modified from Wang et al.[36] and Tan et al.[40]). Red star shows the location of the studied drill core. (d) The lithology of the studied drill core from Chengkou County (referenced from Tan et al.[40]).

A primary origin would imply that the largest Neoproterozoic $\delta^{13}C$ excursion is globally synchronous, which means that the age and duration of the SE should be identical throughout its worldwide development. Recently, Rooney et al.[13] presented Re−Os ages bracketing the SE between 574.0 ± 4.7 and 567.3 ± 3.0 Ma on two separate paleocontinents, i.e., Oman and Northwest Canada. The DOUNCE (DOUshantuo Negative Carbon isotope Excursion),[1] which is regarded as an equivalent to the SE, has been widely observed from outcrop sections and drilling cores in the Yangtze Block of the South China Craton, one of the most well-developed areas of the Ediacaran strata.[1,4,14−17] Although numerous chemostratigraphic studies have been conducted in South China,[1,9,15−18] there have been few radioisotopic ages constraining the timing of the excursion, hampering the worldwide correlation and comparison of this event.

Zircon U−Pb dating of tuff beds has been widely used to constrain the age of sedimentary rocks. However, its application is limited due to a lack of tuff in many areas. Over the past three decades, the Re−Os isotope system has been developed as a convenient approach for dating the deposition of organic-rich sediments.[13,19−27] Previous studies have shown that postdepositional processes do not appreciably disturb the Re−Os system in sediments, i.e., the thermal maturation of organic matter, igneous intrusions, and lower greenschist metamorphism.[20,21,24] Thus, the Re−Os system can be an ideal geochronological tool to determine the depositional age of organic-rich sedimentary rocks. In addition to geochronology, the initial $^{187}Os/^{188}Os$ ratio can mirror temporal variations in the $^{187}Os/^{188}Os$ ratio of

https://doi.org/10.1021/acsomega.4c05072
ACS Omega XXXX, XXX, XXX−XXX

contemporary seawater.[19,28] The seawater Os isotope composition is a mix of radiogenic Os flux from oxidative weathering of the upper continental crust ($^{187}Os/^{188}Os$ = ∼1.4) and nonradiogenic Os input from the mantle and extraterrestrial sources (∼0.126).[29,30] Therefore, the significant increase in seawater $^{187}Os/^{188}Os$ ratios recorded in organic-rich sedimentary rocks may reflect a combination of increasing atmosphere-ocean oxygenation and weathering of more radiogenic continental crust.[31,32] Previous studies suggested that the SE should be attributed to the elevated sulfate flux into oceans resulting from continental weathering, which has been demonstrated by $^{87}Sr/^{86}Sr$ ratios and $\delta^{34}S$ values (both pyrite and CAS).[2−6] However, variations in the seawater isotope composition, which can be applied to indicate weathering intensity, have received little attention for the Ediacaran epochs.

In this study, we provide new geochemical data on the Upper Ediacaran sedimentary rocks from a drill core in the Chengkou area, the northwestern Yangtze Block, South China, including Re−Os isotopic systematics, carbon isotopes, and major element concentrations. With these fresh samples, we aim to (1) provide a new Re−Os age for the less studied area and (2) interpret the Ediacaran Ocean environment variations with marine Os isotope composition coupled with other geochemical indices.

2. GEOLOGICAL SETTING

The South China Craton consists of the Yangtze Block in the northwest and the Cathaysia Block in the southeast (Figure 1a), which amalgamated during the early Neoproterozoic Jinning orogeny (1.0−0.8 Ga).[33] The stratigraphy and paleogeographic reconstructions of the Ediacaran Yangtze Block indicate an increase in water depth from proximal intertidal environments in the northwest to distal deep basin settings in the southeast (Figure 1a). The postglacial Ediacaran marine carbonate and shale successions of the Doushantuo Formation and Dengying Formation in the Yangtze Block were deposited on a passive continental margin. The Doushantuo Formation is generally divided into four members, from bottom to top (Figure 1b).[2,34] The cap dolomite (Member I) at the bottom of the Doushantuo Formation overlies the Cryogenian Nantuo tillite, which is equivalent to global Marinoan glaciation deposition. Member II is predominantly composed of interbedded shale and thin-bedded muddy dolomite with pea-sized chert nodules. The overlying Member III consists mainly of thinly to moderately bedded dolomite and limestone, from which the upper part is characterized by a pronounced negative $\delta^{13}C_{carb}$ excursion.[2,9,15,34] Member IV is predominantly composed of <10 m thick, organic-rich black shales with manganese- and phosphorite-bearing rocks.[9,34−36] The depositional interval of the Doushantuo Formation was constrained by U−Pb zircon ages of 635.2 ± 0.6 Ma from the cap carbonate (Member I) and 551.1 ± 0.7 Ma for the Doushantuo/Dengying boundary (Member IV) (Figure 1b).[14]

Our main study area is located in the Chengkou sub-basins and palaeogeographically belongs to the northwestern margin of the Yangtze Block (Figure 1a).[36,40] The stratigraphic units, including the Cryogenian Nantuo Formation, Ediacaran Doushantuo Formation, and Dengying Formation, can be observed in this area (Figure 1c). The Nantuo Formation is a typical sequence of glacial tuffaceous siliciclastic rocks, and there is a regional exposure of unconformity between the Nantuo and Doushantuo Formations, manifesting as obvious variations in color, thicknesses, and grain sizes. The Doushantuo Formation varies laterally in thickness. In relatively uplifted areas, such as Fucheng and Zhengba, the stratum is thin and is not completely developed. For instance, the Doushantuo Formation in the Fucheng section is only 12 m thick and directly unconformably overlies Precambrian basement metamorphic rocks. It mainly consists of alternating sandy dolomites and dolomitic sandstones (Figure 1c). In the relatively depressed areas of Lianghekou, Dazhu, and Mingyue, however, this formation is thicker, up to 125−500 m. The typical cap dolomite, though missing in some places, overlies the tuffaceous tillites of the Nantuo Formation. Overlying the cap carbonate, this formation consists of dolomite, limestone, black carbonaceous shale, mudstone, argillaceous siltstone, and bedded chert from the bottom to the top with a small amount of phosphorite in the middle and manganese-bearing rocks at the top (Figure 1c). Although several geochemical characteristics were reported on this formation in the northwestern margin of the Yangtze Block,[17,36,40−42] the high-precision geochronology is still unclear.

3. SAMPLES AND METHODS

A total of 33 samples of the Upper Doushantuo Formation were collected from a drill core employed as part of a local manganese ore exploration in Chengkou County, Chongqing, China (Figure 1a,d). The lower part of this section is dominated by fine-grained sandstones and black shales. The upper section is mainly composed of phosphorus-containing muddy dolomite interbedded with manganese- and phosphorite-bearing carbonate. About 3 m thick black shale at the top of the Doushantuo Formation is overlaid by Dengying dolomite (Figure 1d).

3.1. Carbonate Carbon and Oxygen isotopes. Carbonate carbon and oxygen isotope ($\delta^{13}C_{carb}$ and $\delta^{18}O_{carb}$) analyses were carried out using a Kiel IV carbonate device connected to a Finnegan MAT 253 mass spectrometer. CO_2 produced from the reaction of 100% H_3PO_4 with the powder samples was introduced to the mass spectrometer for isotopic measurements. The Chinese national standard GBW-04405, with a $\delta^{13}C_{carb}$ value of 0.57 ± 0.03‰ and $\delta^{18}O$ value of −8.49 ± 0.13‰ (relative to VPDB), was used for analytical calibration. The analytical precision was better than 0.1‰ for $\delta^{13}C_{carb}$ and 0.1‰ for $\delta^{18}O_{carb}$. All samples underwent duplicate carbon isotope analysis at the Nanjing Institute of Geology and Palaeontology, Chinese Academy of Sciences.

3.2. Re−Os Isotopes. Measurements of the Re−Os isotopes were performed at the Guangzhou Institute of Geochemistry, Chinese Academy of Sciences. Rock powder (0.3−0.5 g) was digested together with a mixed $^{185}Re-^{190}Os$ tracer in 12 mL of an H_2O_2/HNO_3 solution (2 mL 12 M HNO_3 plus 10 mL 30% H_2O_2) in a Carius tube at 220 °C for 24 h. To minimize the impact of any nonhydrogenous Re and Os on the true isochronous age of our samples, the more suitable digestion procedure described by Li et al.[43] and Yin et al.[44] was applied in this study.

The Re content was determined by inductively coupled plasma-mass spectrometry (with Thermo Fisher Scientific Inc.). Os loaded onto Pt filaments was analyzed using the electron multiplier mode on the Thermo Fisher thermal ionization mass spectrometer (TIMS). The procedural blanks for the Re analyses were 9 ± 3 pg (n = 6), and that for the Os analyses were 1.0 ± 0.2 pg (2SD), with an average $^{187}Os/^{188}Os$ ratio of 0.1534 ± 0.0036. Blank contributions were typically <2% for Re and <5% for Os. Isoplot v. 3.0 was used for the regression analyses with a ^{187}Re decay constant of 1.666×10^{-11} yr^{-1}.[45,46]

https://doi.org/10.1021/acsomega.4c05072
ACS Omega XXXX, XXX, XXX−XXX

In the present work, the uncertainties for the $^{187}Re/^{188}Os$ and $^{187}Os/^{188}Os$ ratios were comprehensively determined by several factors, including uncertainties from Re and Os mass spectrometer measurements, total blank abundances and isotopic compositions, spike calibrations, and the reproducibility of standard Re and Os isotopic values.

4. RESULTS

The $\delta^{13}C_{carb}$ values vary between −6.7 and +0.5‰, displaying a decreasing trend bottom up, with extremely low values in the uppermost section (mean of −5.3‰; n = 4, Table 1). In contrast, the $\delta^{18}O_{carb}$ data show constantly low values in the lowermost section (average −9.3‰; n = 26, Table 1) and an increasing trend in the upper part of the section (Figure 2).

Table 1. Carbon Geochemical Data of the Study Section

sample	depth (m)	$\delta^{13}C_{carb}$ (‰)	$\delta^{18}O_{PDB}$ (‰)
DST-1	1036.22	−5.6	−6.6
DST-2	1037.25	−3.1	−8.3
DST-3	1037.95	−5.7	−5.6
DST-4	1038.81	−6.7	−6.2
DST-5	1039.61	−1.0	−6.3
DST-6	1040.31	−2.7	−7.9
DST-7	1041.01	−2.1	−8.3
DST-8	1041.99	−1.6	−9.3
DST-9	1042.54	−2.0	−8.9
DST-10	1043.39	−1.9	−9.0
DST-11	1043.87	−1.9	−9.0
DST-12	1044.07	−2.0	−8.7
DST-13	1045.25	−2.4	−9.1
DST-14	1045.55	−2.2	−9.3
DST-15	1046.09	−2.0	−9.1
DST-16	1048.2	−2.2	−9.2
DST-17	1048.65	−2.2	−9.5
DST-18	1049.11	−2.0	−9.4
DST-19	1049.11	−2.1	−9.3
DST-20	1049.81	−1.8	−9.4
DST-21	1050.46	−1.8	−9.6
DST-22	1051.43	−2.0	−9.5
DST-23	1051.68	−1.2	−9.7
DST-24	1052.23	−1.0	−9.8
DST-25	1052.61	−1.1	−9.6
DST-26	1052.91	−0.8	−9.9
DST-27	1053.41	−2.0	−8.5
DST-28	1053.71	−0.4	−9.6
DST-29	1054.41	−0.3	−9.7
DST-30	1054.75	−0.21	−9.1
DST-31	1055.45	−0.0	−9.5
DST-32	1055.75	−0.3	−8.3
DST-33	1056.21	0.5	−8.7

The Re−Os concentrations and isotopic compositions of the studied samples are listed in Table 2. These samples exhibit large variations in Re and Os contents of 17.86−46.59 and 0.580−2.942 ppb, respectively, which are much higher than average continental crustal values (e.g., 0.2−2 ppb for Re and 0.03−0.05 ppb for Os),[47,48] suggesting a predominantly hydrogenous origin for Re and Os. The $^{187}Re/^{188}Os$ ratios of these samples range from 91 to 249, in correspondence with their $^{187}Os/^{188}Os$ ratios (from 1.60 to 3.11). A linear regression (Isoplot v 3.0) of the Re−Os data yielded an age of 572 ± 26 Ma for an $^{187}Os/^{188}Os$ ratio of 0.733 ± 0.083 (Model 3; mean squared weighted deviation (MSWD) = 8.4; n = 19; 2σ) (Figure 3a).

5. DISCUSSION

5.1. Chemostratigraphic Correlations between the Chengkou Drill Core and Other Sections. Based on the marker layer of the special lithology division and comparisons, the correlation interval in this study can be roughly correlated to the upper Doushantuo Formation in the other regions of the Yangtze Block. Three phosphorus-bearing layers are identified in the most shallow-water sediments, which occur in the bottom, middle, and top of the Doushantuo Formation.[35] The first phosphorus formation event occurred in the early Doushantuo period. For example, in the Zhangcunping section of Hubei Province, a phosphorus-bearing rock series developed at the bottom of the Doushantuo Formation, whose U−Pb age is 614 ± 7.6 Ma (Figure 4).[50] Pb−Pb isochron ages of 599 ± 4.2 Ma for the dolomitic phosphorite of the middle Doushantuo Formation and 576 ± 14 Ma for the phosphatic dolostone of the upper Doushantuo Formation were reported by Barfod et al.[51] and Chen et al.,[52] respectively, in the Weng'an area (Figure 4). In Lianghekou, and our studied drill cores obtained in Zhenba County and Chengkou County, phosphorus-containing organic material distributed as bands in a thick layered dolomite bed (2−10 m in thickness) were observed at the upper Doushantuo Formation (Figures 1c,d and 2),[36] which should be correlated to the phosphatic dolostone in the upper portion of the Doushantuo Formation based on the lithologic and stratigraphic characteristics. Furthermore, manganese- and phosphorus-containing rocks are also considered marker layers of Members IV of the Doushantuo Formation on the northern margin of the Yangtze Platform (Figure 2).[17,35,36]

Carbon isotopic chemostratigraphy has also been widely used in Ediacaran stratigraphic correlations.[1,8,11] In recent years, more and more carbon isotope curves from the Yangtze Block have shown a large negative $\delta^{13}C_{carb}$ shift in the upper Doushantuo Formation.[1,9,15−17] Several types of mechanisms have been proposed to explain its origin: a disturbance of the global ocean dissolved inorganic carbon reservoir caused by the oxidation of organic carbon or methane,[2−4,6,10] precipitation of ^{13}C-depleted authigenic carbonates,[8,53,54] and the diagenetic alteration of primary $\delta^{13}C_{carb}$ signatures.[55,56] Although the proposed theories controversially explain its origin, complexity, age, and duration, there is consensus in the academic community that the SE is an important Ediacaran stratigraphic comparison symbol.[18,57]

The upper Doushantuo Formation in the Jiulongwan profile is a perfect illustration of the SE event in the Yangtze Platform (Figure 4). The negative $\delta^{13}C_{carb}$ excursion in this section could be as low as −10‰, which is remarkably stable and continues for nearly 50 m through the upper half of Member III and large carbonate concretions in Member IV.[2,34] However, a previous study suggested that the high spatial heterogeneity of the SE occurred in different depositional settings.[4] For instance, the magnitude of the negative $\delta^{13}C_{carb}$ shifts at the upper Doushantuo Formation is much larger in the Jiulongwan section than in the Zhangcunping and Siduping sections (Figure 4).[4] The Sishang section in the northern margin of the Yangtze Platform (Figure 1), showing a large negative drift of $\delta^{13}C_{carb}$ in the upper part of the Doushantuo Formation, is similar to the Jiulongwan profile in terms of drift amplitude (Figure 4).[15] The lower portion of the ca. 30 m limestone generally has positive $\delta^{13}C_{carb}$ values, followed by ca. 3-m dolostone with $\delta^{13}C_{carb}$

https://doi.org/10.1021/acsomega.4c05072
ACS Omega XXXX, XXX, XXX−XXX

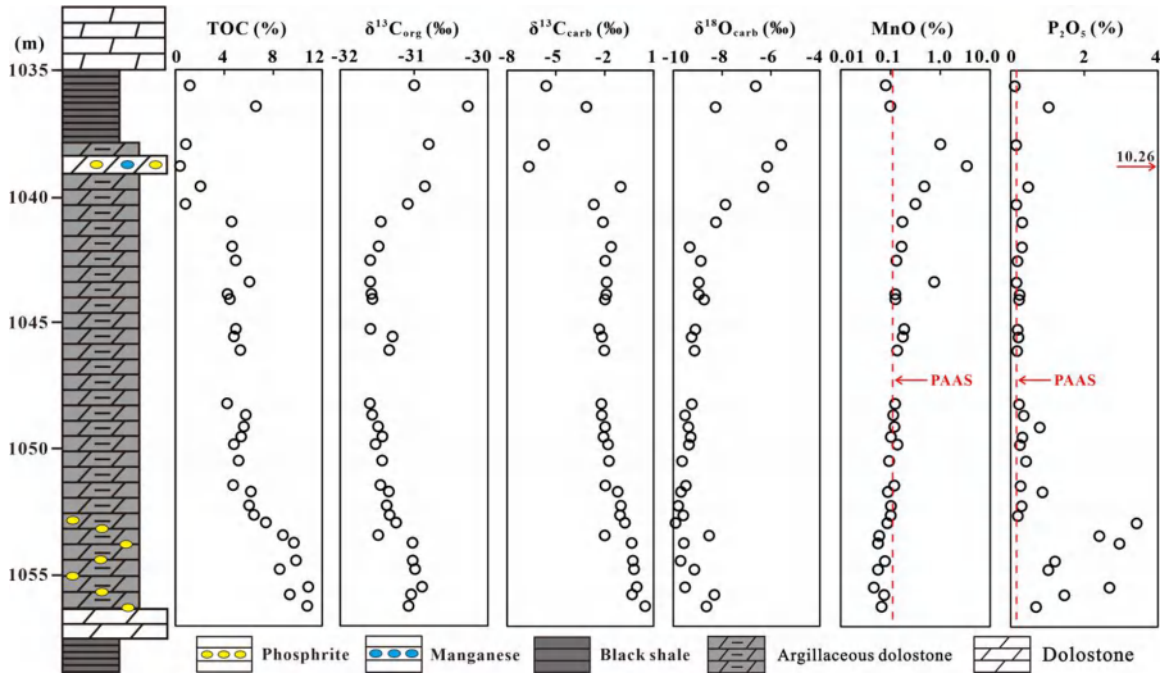

Figure 2. Chemostratigraphic profiles of the Chengkou drill core. The lithological column, TOC, $\delta^{13}C_{org}$, MnO, and P_2O_5 are referenced from Tan et al.[40] and Wu et al.[42] PAAS is the Post-Archean Average Australian Shale composition of Taylor and McLennan.[49]

Table 2. Re−Os Contents and Isotope Data for the Studied Samples[a]

sample	Re (ppb)	2SD	Os (ppb)	2SD	$^{187}Re/^{188}Os$	2SD	$^{187}Os/^{188}Os$	2SD	$(^{187}Os/^{188}Os)^a_i$	$(^{187}Os/^{188}Os)^b_i$
DST-2	46.59	0.44	2.942	0.071	90.9	2.4	1.5989	0.014	0.73	0.73
DST-5	23.12	0.20	1.074	0.007	128.6	1.4	1.9661	0.007	0.73	0.74
DST-7	18.66	0.21	0.669	0.004	172.7	2.2	2.3218	0.008	0.67	0.68
DST-10	33.57	0.30	0.914	0.005	245.5	2.6	3.1059	0.012	0.76	0.77
DST-11	19.81	0.23	0.724	0.003	169.9	2.1	2.3465	0.008	0.72	0.73
DST-12	20.48	0.27	0.831	0.007	150.3	2.3	2.1682	0.018	0.73	0.74
DST-13	17.86	0.33	0.580	0.011	194.4	5.3	2.5119	0.019	0.65	0.66
DST-15	23.95	0.10	0.663	0.003	241.1	1.4	3.0853	0.011	0.78	0.79
DST-17	23.51	0.32	0.915	0.006	157.9	2.4	2.2488	0.011	0.74	0.75
DST-19	22.43	0.24	0.799	0.005	175.7	2.2	2.4267	0.010	0.74	0.76
DST-20	19.56	0.20	0.664	0.003	185.6	2.1	2.4889	0.010	0.71	0.72
DST-22	21.73	0.24	0.726	0.004	188.9	2.3	2.5079	0.008	0.70	0.71
DST-23	22.95	0.14	1.031	0.012	134.3	1.7	2.0743	0.007	0.79	0.80
DST-25	29.20	0.20	0.791	0.010	245.5	3.6	3.0434	0.019	0.69	0.71
DST-27	34.08	0.32	1.078	0.011	204.3	2.9	2.7444	0.016	0.79	0.80
DST-28	28.07	0.30	0.992	0.010	177.4	2.6	2.4448	0.009	0.75	0.76
DST-29	26.15	0.39	0.786	0.011	215.4	4.4	2.7659	0.030	0.70	0.72
DST-30	24.87	0.29	0.668	0.002	249.0	3.0	3.1016	0.010	0.72	0.73
DST-31	27.78	0.52	0.887	0.008	201.7	4.2	2.7109	0.013	0.78	0.79

[a]Note: "$(^{187}Os/^{188}Os)^a_i$" and "$(^{187}Os/^{188}Os)^b_i$": initial $^{187}Os/^{188}Os$ ratios calculated at 572 and 568 Ma, respectively, using the ^{187}Re decay constant of 1.666 e^{-11} $year^{-1}$.[46] "2SD": Two standard deviations, determined from the uncertainties of the mass spectrometer measurements, blank contents, ^{187}Re decay constant, and spike calibration.

values declining dramatically. Subsequently, the $\delta^{13}C_{carb}$ data within a 25-m limestone interval in the middle of the profile display stably negative values around −8.5‰ (Figure 4). The Chengkou drilling profile, located near the Sishang section, shows $\delta^{13}C_{carb}$ values that vary from positive to negative in the upper Doushantuo Formation. Despite only a 6‰ negative shift in $\delta^{13}C_{carb}$ values in this section, such isotope variability suggests that the SE occurred within a stratigraphically equivalent interval (Figure 4).

5.2. Re−Os Geochronology of Organic-Rich Rocks of the Upper Doushantuo Formation. The Re−Os data of the Doushantuo organic-rich rocks from the studied drill core (n = 19) yielded an age of 572 ± 26 Ma (Model 3, MSWD = 8.4, initial $^{187}Os/^{188}Os = 0.733 \pm 0.083$). Previous studies concluded that the requirements for precise Re−Os dating of sedimentary rocks include the following three aspects: (1) the Re−Os system has not been modified by postdepositional processes, (2) the initial $^{187}Os/^{188}Os$ (Os_i) ratios are uniform, and (3) there is sufficient spread in $^{187}Re/^{188}Os$ ratio.[19,23,58] The Re−Os system

https://doi.org/10.1021/acsomega.4c05072
ACS Omega XXXX, XXX, XXX−XXX

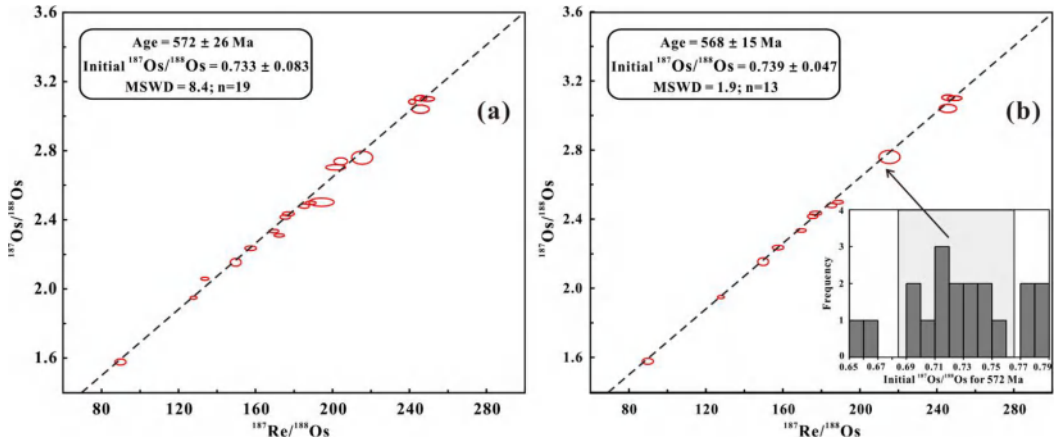

Figure 3. (a) Re−Os isochron of organic-rich sediments from the upper Doushantuo Formation, northeastern margin of the Yangtze Block. (b) Re−Os isochron for selected samples (shown in the gray box of the inset) after excluding samples with relatively low and high initial $^{187}Os/^{188}Os$ ratios (calculated for a depositional age of 572 Ma).

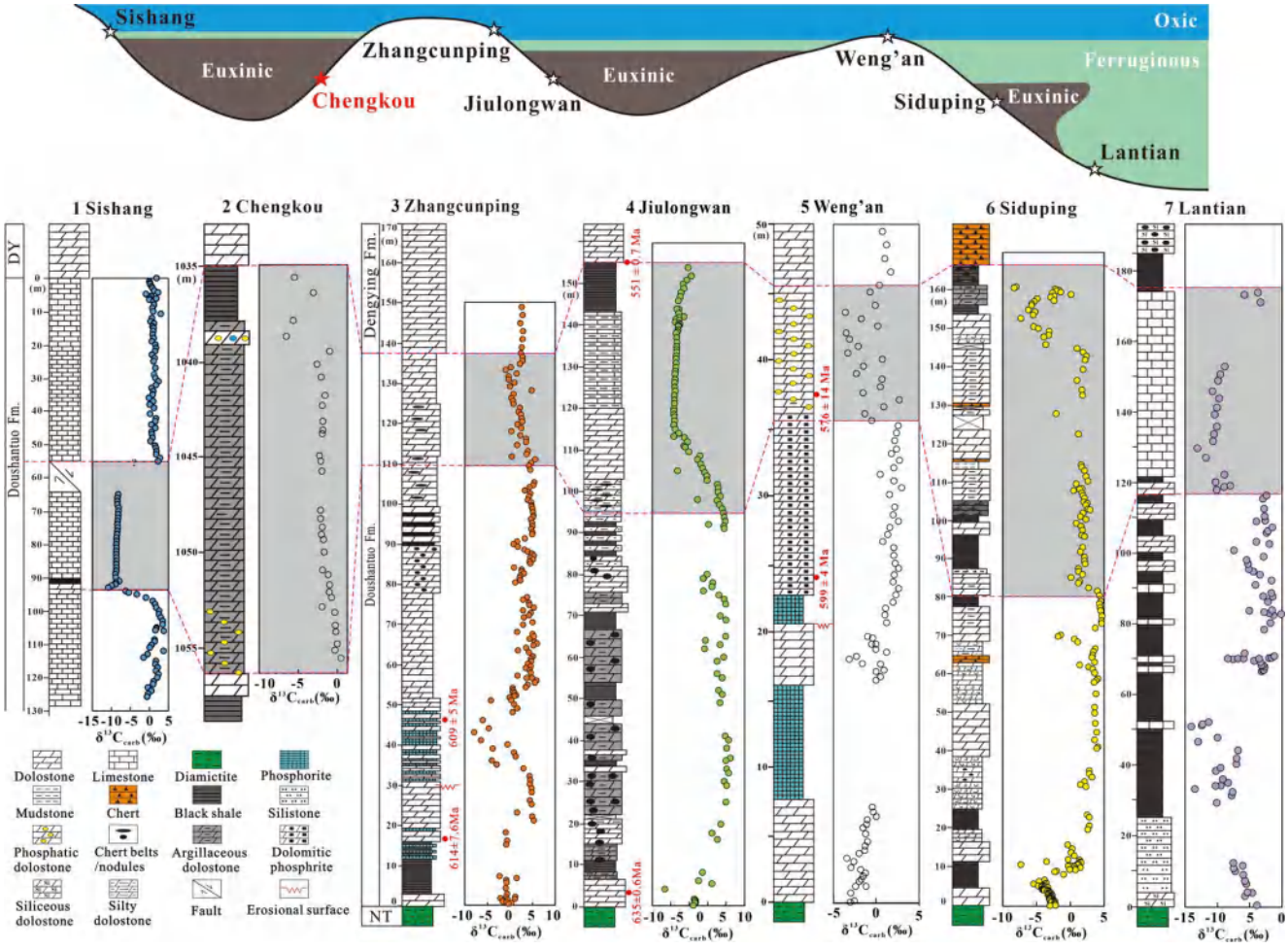

Figure 4. Carbonate carbon isotope ($\delta^{13}C_{carb}$) chemostratigraphic correlations of the Ediacaran Doushantuo Formation. Gray shades in $\delta^{13}C$ profiles identify $\delta^{13}C$ excursions. Data source: Zhangcunping section;[4] Jiulongwan section;[4,61] Weng'an section;[34,62] Sishang section;[15] Chengkou (this study); Siduping section;[4] Lantian section.[63] Radiometric ages are from Barfod et al.,[51] Chen et al.,[52] Condon et al.,[14] Liu et al.,[50] and Zhou et al.[62]

can be affected by hydrothermal fluid interaction with sedimentary strata and chemical weathering through the mobilization of Re and Os from sedimentary rocks.[25,59,60] Samples affected by hydrothermal fluids are usually characterized by variable and mostly negative Os_i isotope composition; however, the disturbance of the Re−Os system by hydrothermal fluid is unlikely in our samples. Second, disturbance of the Re−Os system by surficial weathering is unlikely, for our samples were collected from a drilling core. Using 572 Ma as the depositional age of the samples, the Os_i values of the samples

https://doi.org/10.1021/acsomega.4c05072
ACS Omega XXXX, XXX, XXX−XXX

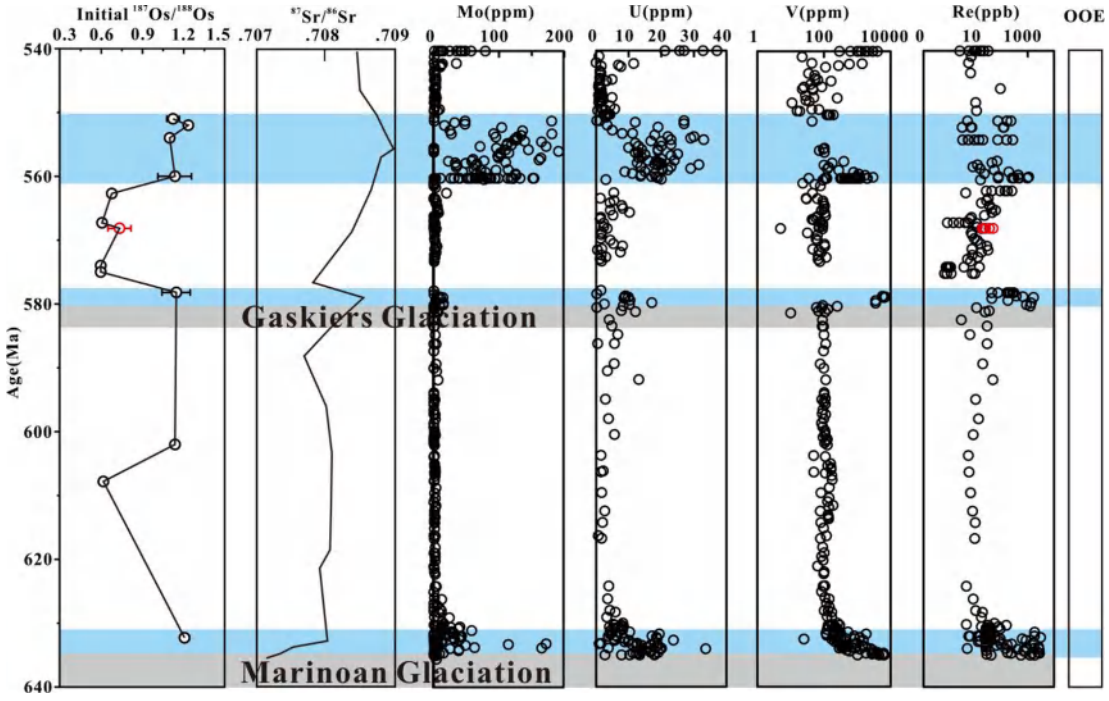

Figure 5. Compilation of the initial $^{187}Os/^{188}Os$, $^{87}Sr/^{86}Sr$, and redox-sensitive elements data during 640 to 540 Ma. The initial $^{187}Os/^{188}Os$ data are from Singh et al.,[73] Kendall et al.,[21] Rooney et al.,[13,27] Zhu et al.,[74] Yang et al.[75] and this study (red circles). The $^{87}Sr/^{86}Sr$ ratio curve is referenced from Macdonald et al.[8] The redox sensitive element data are from Ugidos et al.,[76] Singh et al.,[73] Li et al.,[61] Sahoo et al.,[77,78] Zhu et al.,[74] Johnston et al.,[79] Chen et al.,[80] Kendall et al.,[81] Kurzweil et al.,[82] Rooney et al.[13] and this study. Previously identified Ediacaran Ocean oxygenation events are identified by blue boxes.[72,77,78]

were back-calculated using a ^{187}Re decay constant of 1.666×10^{-11} yr^{-1} and showed somewhat variable values ranging from 0.66 to 0.80 (Table 2). To obtain a more precise age through the $^{187}Re-^{187}Os$ chronometer requires homogeneity of the Os_i ratios, therefore, we also plotted the Re−Os isochron for selected samples with relatively small variations in Os_i isotope composition (ranging from 0.69 to 0.76) (Figure 3b). The Re−Os isochron for these 13 samples defines a more precise depositional age of 568 ± 15 Ma (MSWD = 1.9; 2σ) with smaller uncertainties on Os_i = 0.739 ± 0.047 (Figure 3b). We speculate that the Os_i heterogeneity caused by changes in the $^{187}Os/^{188}Os$ ratio in seawater explains the larger uncertainties if all samples are regressed together as in Figure 3a. Additionally, the sampling interval also affects the Re−Os age. For example, the Re−Os data of the samples from the Waipawa Formation in the Taylor White section yielded an age of 58.3 ± 7.7 Ma (MSWD = 28.8). This Re−Os age is very consistent with those derived from the Orui-1A samples of the Waipawa Formation (Re−Os age of 58.1 ± 3.9 Ma; MSWD = 4.1) but with larger uncertainties. Therefore, Rotich et al.[58] argued that the large uncertainty of 58.3 ± 7.7 Ma was related to the large stratigraphic interval (50 m). Similarly, our stratigraphic interval represented by the samples, reaching up to ∼18 m, may likely be related to the uncertainties of the 568 ± 15 Ma value found here.

The 568 ± 15 Ma age calculated by the regression analysis of the Re−Os isotopic data for these 13 samples implies a reliable depositional age for the organic-rich sediments in the upper Doushantuo Formation. Several viewpoints support the reliability of this interpretation. First, even though high-to-moderate uncertainties occurred for all samples (572 ± 26 Ma, Figure 3a) and selected samples (568 ± 15 Ma, Figure 3b), the slight difference and very small variations in the Os_i values indicate that Re−Os systematics of these organic-rich samples were not significantly undermined by postdepositional processes such as late diagenesis, weathering, or other geological processes. Second, our Re−Os age of 568 ± 15 Ma is well bracketed within the uncertainties of the onset and end of the Doushantuo Formation constrained by the two U−Pb zircon ages of 635.2 ± 0.6 and 551.1 ± 0.7 Ma from two ash beds in the Wuhe-Gaojiaxi and Jijiawan sections, respectively.[14] A Pb−Pb age of 576 ± 14 Ma (MSWD = 0.4) from the upper phosphorite layers (Member III) of the Doushantuo Formation has been provided in the Weng'an section, located 750 km to the southwest of the Three Gorges region (Figure 4).[52] This estimated age is consistent with the Re−Os age of 568 ± 15 Ma of the phosphorus-containing layer from Chengkou ZK-01. Additionally, as the largest amplitude negative carbon isotopic excursion in Earth's history and a critical chemostratigraphic mark for Ediacaran global correlations,[6,18,53] the Ediacaran SE and its isochronous feature have been reported in many places around the world. Based on the Re−Os geochronology bracketing the SE on the Northwest Canada and Oman paleocontinents, Rooney et al.[13] reported that the SE was a synchronous global event occurring between 574.0 ± 4.7 and 567.3 ± 3.0 Ma. The Re−Os age of the $\delta^{13}C_{carb}$ excursion in the upper Doushantuo Formation in the Chengkou section is nearly consistent with these ages.

5.3. Late Neoproterozoic Seawater Os Isotope Composition and Implications for Continental Weathering and Fluctuated Oceanic Oxygenation. Reducing marine sediments has the potential to track Os isotopic composition variations in contemporaneous seawater,[64−66] which is supported by observations of approximate $^{187}Os/^{188}Os$ ratios between modern organic-rich mudstone

https://doi.org/10.1021/acsomega.4c05072
ACS Omega XXXX, XXX, XXX−XXX

and present-day seawater.[67,68] The seawater Os isotope composition is jointly constrained by the supply of the radiogenic Os flux from oxidative weathering of the upper continental crust ($^{187}Os/^{188}Os = \sim 1.4$), nonradiogenic Os input from the hydrothermal alteration of oceanic crustal rocks, and the dissolution of cosmic dust ($^{187}Os/^{188}Os = \sim 0.12$).[29,30] For instance, modern seawater has a high $^{187}Os/^{188}Os$ ratio of approximately 1.06 due to the substantial radiogenic osmium input resulting from oxidative weathering of the upper continental crust. In contrast, the marine shales have consistently low Os_i ratios of ∼0.1 from 2.5 Ga to ca. 1.4 Ga,[60,64,69−71] which suggests that these nonradiogenic Os may have resulted from significant Os input from magmatic, hydrothermal, or extraterrestrial sources,[32] but low oxidative weathering of more radiogenic continental crust. Furthermore, recent compiling studies showed that the increasing Os_i ratios of marine shales were roughly coupled with the atmospheric oxygen content during the Proterozoic Eon,[31] suggesting that an increase in a highly radiogenic Os supply must be from enhanced weathering of the continent.[30−32] Nevertheless, whether the Os_i ratios of marine shales are sensitive to multiple, transiently increased weathering of the continents, which were common in the Ediacaran period, needs to be demonstrated.

Figure 5 presents a compilation of Ediacaran seawater osmium isotope compositions inferred from the Re−Os isochron regression of organic-rich sediments in this study and previous studies. Despite the limited availability of Os_i data, the existing data suggests that the seawater $^{187}Os/^{188}Os$ ratio fluctuated frequently during the Ediacaran period. The data is characterized by radiogenic $^{187}Os/^{188}Os$ ratios (>1.0) at ca. ∼635, ∼580, and ∼560 Ma (Figure 5), indicating that substantial amounts of radiogenic Os were transported by rivers and groundwater to the oceans during these short intervals. Similar to $^{187}Os/^{188}Os$ ratios, the Ediacaran seawater $^{87}Sr/^{86}Sr$ ratios, as inferred from marine carbonates, also show pulsed contributions of highly radioactive ^{87}Sr in these three periods (Figure 5). These radiogenic seawater $^{187}Os/^{188}Os$ and $^{87}Sr/^{86}Sr$ ratios indicate multiple enhanced continental weathering events during the Ediacaran, which was attributed to either climate changes (glacial−interglacial interactions) or plate tectonic reorganizations.[32,72] The Sheepbed Formation following Marinoan glaciation (∼635 Ma) and the Khufai Formation following Gaskiers glaciation (∼580 Ma) have typical radiogenic Os_i isotopic signatures with corresponding values of 1.21 ± 0.04 and 1.15 ± 0.1, respectively.[13,27] This information indicates that increased intensity of oxidative weathering combined with the exposure of easily leached glacial deposits released more radiogenic ^{187}Os into the oceans,[32] thus causing a transient rise in seawater $^{187}Os/^{188}Os$ ratio during the deglaciation. This is supported by observed concordant increasingly radiogenic $^{87}Sr/^{86}Sr$ compositions.[7] By contrast, the highly radiogenic Os_i for the black shales of Doushantuo Member IV (560−550 Ma) was tied to the highest $^{87}Sr/^{86}Sr$ ratios for the Ediacaran carbonates (Figure 5), suggesting relatively long-lasting and stronger continental weathering than the two older enhanced-weathering events. An enhanced weathering rate might be attributed to the continental collision that built the Trans-Gondwana mountain chains.[72]

Once the Gaskiers glacial period (∼580 Ma) ended, however, there was a noticeable decline in the isotopic composition of $^{187}Os/^{188}Os$ in seawater (Figure 5). The Re−Os isochron for the Chengkou organic-rich rocks yields a moderate initial Os isotopic composition ranging from 0.65 to 0.79, which is in accordance with the sediments Os_i ratios (0.60 to 0.68) from Northwest Canada and Oman of the same period.[13] Three separate paleocontinents exhibit similar ∼0.7 Os_i ratios, indicating that the ∼0.7 isotope ratio in seawater was homogeneous between ∼575 and ∼562 Ma, approximately 0.7. Obviously, the isotopic composition of seawater during this period is significantly lower than ∼580 Ma. This decline in seawater $^{187}Os/^{188}Os$ ratios during the SE period may result from a significant reduction in the input from the weathering of Gaskiers glacial deposits. Nevertheless, the Shuram interval shows a more radiogenic $^{187}Os/^{188}Os$ of ∼0.7 compared with the seawater $^{187}Os/^{188}Os$ ratio (∼0.3) in the Archean and pre-Ediacaran Proterozoic time bins.[31,32] Hence, the weathering of more radiogenic continental crust and an oxygenated atmosphere most likely is responsible for the overall higher Os_i ratios in the Shuram anomaly compared to the pre-Neoproterozoic era.[32]

Oxidative weathering of the upper continental crust not only brings a substantial amount of radiogenic osmium to the ocean but also plays an important role in inputting soluble redox-sensitive elements (RSE) to the oceans through riverine transport.[32,83] In an oxidized atmosphere with high partial pressure of oxygen, the global seawater concentrations of these RSEs will be abundant.[84] As a corollary, a large magnitude of RSE enrichments of euxinic sediments will be observed in ancient basins with access to the open ocean.[77,78] Thus, the magnitude of RSE enrichments in the sedimentary rocks can be applied for tracking Earth's oxygenation history, specifically the extent of anoxia in the ocean. Interestingly, three major RSE enrichments of marine shales occurring at ca. 635, 580, and 560 Ma are comparable to the levels found in modern euxinic shales,[77,78,83] and the timing of these three episodes of RSE enrichments coincides with the radiogenic increase of Os isotopes in seawater (Figure 5). Therefore, the three pronounced changes in Osi of the Ediacaran shales seem to mirror the variations in the RSE concentration. This suggests that the elevated levels of these metals in seawater are primarily related to an increase in riverine inputs, which is a result of enhanced continental weathering activities occurring over multiple short periods.

The late Neoproterozoic period was marked by a significant rise of atmospheric and dynamic oceanic oxygenation. An increasing number of studies have demonstrated that oceanic oxygenation was not a unidirectional process.[2,3,12,77,78,81] The temporary ocean oxygenations immediately following the Sturtian and Marinoan glaciations, interpreted from uranium, iron, and sulfur isotope records and trace metal (Mo, U, and V) enrichments, are generally attributed to enhanced continental weathering.[5,77,78,85,86] On the one hand, subglacial weathering fertilized the oceans with phosphate, stimulating oceanic productivity and organic carbon burial, which finally promoted more oxidizing conditions in the global ocean.[12,84] On the other hand, elevated continental weathering delivered high fluxes of oxidants (e.g., sulfates) to the oceans, leading to transient ocean oxygenation.[2−6] However, the global oceans were still dominated by widespread anoxia after these transient oxygenation events.

6. CONCLUSIONS

Organic-rich samples from a new upper Doushantuo section have been analyzed using a combined geochemical tool. Based on manganese- and phosphorus-bearing layers and a negative $\delta^{13}C_{carb}$ excursion, we conclude that the studied interval should

https://doi.org/10.1021/acsomega.4c05072
ACS Omega XXXX, XXX, XXX−XXX

be correlated to SE sequences in the Doushantuo Formation. Furthermore, the Re−Os age of 568 ± 15 Ma (Model 3, MSWD = 1.9, n = 13; 2σ) obtained for these samples is consistent with the Re−Os geochronology from Northwest Canada and Oman.

A compilation of initial $^{187}Os/^{188}Os$ values from marine shales spanning the period between ∼640 and ∼540 Ma reveals that the Os isotope record broadly correlates with those of the Sr isotope and RSE, pointing to a dominant control on these geochemical indices. Transiently increased initial $^{187}Os/^{188}Os$ ratios of shales occurred immediately after ca. 635, 580, and 560 Ma, suggesting multiple, short-time enhancements of continental oxidative weathering. As a result, the inputs of both RSE and oxidants from the continents to the ocean were enhanced, leading to transient RSE enrichments in the anoxic shales and pulsed ocean oxygenation thoroughly documented in previous studies. Therefore, high-precision Re−Os isotope analysis could be a powerful tool to trace enhanced continental weathering events in low-oxygen atmospheres like the Neoproterozoic era.

AUTHOR INFORMATION

Corresponding Author

Zhaozhao Tan − *Hunan Provincial Key Laboratory of Geochemical Processes and Resource Environmental Effects, Changsha, Hunan 410014, China; Geophysical and Geochemical Survey Institute of Hunan Province, Changsha, Hunan 410014, China; State Key Laboratory of Organic Geochemistry, Guangzhou Institute of Geochemistry, Chinese Academy of Sciences, Guangzhou 510640, China;* orcid.org/0000-0002-4022-0433; Email: 15621039296@163.com

Authors

Jianlan Luo − *Hunan Provincial Key Laboratory of Geochemical Processes and Resource Environmental Effects, Changsha, Hunan 410014, China; Geophysical and Geochemical Survey Institute of Hunan Province, Changsha, Hunan 410014, China*

Xuesheng Xu − *Hunan Provincial Key Laboratory of Geochemical Processes and Resource Environmental Effects, Changsha, Hunan 410014, China; Geophysical and Geochemical Survey Institute of Hunan Province, Changsha, Hunan 410014, China*

Wanglu Jia − *State Key Laboratory of Organic Geochemistry, Guangzhou Institute of Geochemistry, Chinese Academy of Sciences, Guangzhou 510640, China;* orcid.org/0000-0003-1715-4279

Jie Li − *State Key Laboratory of Isotope Geochemistry, Guangzhou Institute of Geochemistry, Chinese Academy of Sciences, Guangzhou 510640, China*

Liran Chen − *Hunan Provincial Key Laboratory of Geochemical Processes and Resource Environmental Effects, Changsha, Hunan 410014, China; Geophysical and Geochemical Survey Institute of Hunan Province, Changsha, Hunan 410014, China*

Complete contact information is available at: https://pubs.acs.org/10.1021/acsomega.4c05072

Notes

The authors declare no competing financial interest.

ACKNOWLEDGMENTS

This study was financially supported by the National Key Research and Development Program of China (2017YFC0603101), the State Key Laboratory of Organic Geochemistry (SKLOG2020-1) and the Hunan Province Key Research and Development Program (2023SK2066).

REFERENCES

(1) Zhu, M.; Zhang, J.; Yang, A. Integrated Ediacaran (Sinian) chronostratigraphy of South China. *Palaeogeogr. Palaeoclimatol. Palaeoecol.* **2007**, *254* (1−2), 7−61.

(2) McFadden, K. A.; Huang, J.; Chu, X.; Jiang, G.; Kaufman, A. J.; Zhou, C.; Yuan, X.; Xiao, S. Pulsed oxidation and biological evolution in the Ediacaran Doushantuo Formation. *Proc. Natl. Acad. Sci. U. S. A.* **2008**, *105*, 3197−3202.

(3) Fike, D. A.; Grotzinger, J. P.; Pratt, L. M.; Summons, R. E. Oxidation of the Ediacaran ocean. *Nature.* **2006**, *444*, 744−747.

(4) Li, C.; Hardisty, D. S.; Luo, G.; Huang, J.; Algeo, T.; Cheng, M.; Shi, W.; An, Z.; Tong, J.; Xie, S.; Jiao, N.; Lyons, W. Uncovering the spatial heterogeneity of Ediacaran carbon cycling. *Geobiology* **2017**, *15*, 211−224.

(5) Shi, W.; Li, C.; Luo, G.; Huang, J.; Algeo, T. J.; Jin, C.; Zhang, Z.; Cheng, M. Sulfur isotope evidence for transient marineshelf oxidation during the Ediacaran Shuram Excursion. *Geology* **2018**, *46*, 267−270.

(6) Shields, G. A.; Mills, B. J. W.; Zhu, M.; Raub, T. D.; Daines, S. J.; Lenton, T. M. Unique Neoproterozoic carbon isotope excursions sustained by coupled evaporite dissolution and pyrite burial. *Nat. Geosci.* **2019**, *12*, 823−827.

(7) Sawaki, Y.; Ohno, T.; Tahata, M.; Komiya, T.; Hirata, T.; Maruyama, S.; Windley, B. F.; Han, J.; Shu, D.; Li, Y. The Ediacaran radiogenic Sr isotope excursion in the Doushantuo Formation in the Three Gorges area. *South China. Precambrian Res.* **2010**, *176*, 46−64.

(8) Macdonald, F. A.; Strauss, J. V.; Sperling, E. A.; Halverson, G. P.; Narbonne, G. M.; Johnston, D. T.; Kunzmann, M.; Schrag, D. P.; Higgins, J. A. The stratigraphic relationship between the Shuram carbon isotope excursion, the oxygenation of Neoproterozoic oceans, and the first appearance of the Ediacara biota and bilaterian trace fossils in northwestern Canada. *Chem. Geol.* **2013**, *362*, 250−272.

(9) Cui, H.; Kaufman, A. J.; Xiao, S.; Zhu, M.; Zhou, C.; Liu, X. M. Redox architecture of an Ediacaran ocean margin: Integrated chemostratigraphic ($\delta^{13}C-\delta^{34}S-^{87}Sr/^{86}Sr-Ce/Ce^*$) correlation of the Doushantuo Formation South China. *Chem. Geol.* **2015**, *405*, 48−62.

(10) Rothman, D. H.; Hayes, J. M.; Summons, R. E. Dynamics of the Neoproterozoic carbon cycle. *Proc. Natl. Acad. Sci. U. S. A.* **2003**, *100*, 8124−8129.

(11) Cañadas, F.; Papineau, D.; Leng, M.; Li, C. Extensive primary production promoted the recovery of the Ediacaran Shuram excursion. *Nat. Commun.* **2022**, *13*, 148.

(12) Shi, W.; Mills, B. J. W.; Li, C.; Poulton, S. W.; Krause, A. J.; He, T.; Zhou, Y.; Cheng, M.; Shields, G. A. Decoupled oxygenation of the Ediacaran Ocean and atmosphere during the rise of early animals. *Earth Planet. Sci. Lett.* **2022**, *591*, No. 117619.

(13) Rooney, A. D.; Cantine, M. D.; Bergmann, K. D.; Gómez-Pérez, I.; Al Baloushi, B.; Boag, T. H.; Busch, J. F.; Sperling, E. A.; Strauss, J. V. Calibrating the co-evolution of Ediacaran life and environment. *Proc. Natl. Acad. Sci. U. S. A.* **2020**, *117*, 16824−16830.

(14) Condon, D.; Zhu, M. Y.; Bowring, S.; Wang, W.; Yang, A.; Jin, Y. U-Pb ages from the Neoproterozoic Doushantuo Formation. *China. Science* **2005**, *308* (5718), 95−98.

(15) Lu, M.; Zhu, M. Y.; Zhang, J. M.; Shields-Zhou, G.; Li, G.; Zhao, F.; Zhao, X.; Zhao, M. The DOUNCE event at the top of the Ediacaran Doushantuo Formation, South China: Broad stratigraphic occurrence and non-diagenetic origin. *Precambrian Res.* **2013**, *225*, 86−109.

(16) Zhou, C. M.; Xiao, S. H.; Wang, W.; Guan, C. G.; Ouyang, Q.; Chen, Z. The stratigraphic complexity of the middle Ediacaran carbon isotopic record in the Yangtze Gorges area, South China, and its implications for the age and chemostratigraphic significance of the Shuram excursion. *Precambrian Res.* **2017**, *288*, 23−38.

(17) Zhang, Y.; Liao, Z. W.; Cao, J.; Gary, G.; Wei, Y.; Shi, Q.; Zhang, B.; Kuang, H.; Liu, Y.; Huang, Q. Climate variability during the late

Ediacaran: Insights from episodic deposition of black shale-hosted Mn-carbonates in South China. *Chem. Geol.* **2024**, *646*, No. 121910.
(18) Xiao, S.; Narbonne, G. M.; Zhou, C.; Laflamme, M.; Grazhdankin, D. V.; Moczydlowska-Vidal, M.; Cui, H. Towards an Ediacaran Time Scale: Problems, protocols, and prospects. *Episodes* **2016**, *39*, 540−555.
(19) Cohen, A. S.; Coe, A. L.; Bartlett, J. M.; Hawkesworth, C. J. Precise Re-Os ages of organic-rich mudrocks and the Os isotope composition of Jurassic seawater. *Earth Planet. Sci. Lett.* **1999**, *167* (3−4), 159−173.
(20) Creaser, R. A.; Sannigrahi, P.; Chacko, T.; Selby, D. Further evaluation of the Re-Os geochronometer in organic-rich sedimentary rocks: a test of hydrocarbon maturation effects in the Exshaw Formation, Western Canada sedimentary basin. *Geochim. Cosmochim. Acta* **2002**, *66* (19), 3441−3452.
(21) Kendall, B.; Creaser, R. A.; Ross, G. M.; Selby, D. Constraints on the timing of Marinoan Snowball Earth glaciation by $^{187}Re-^{187}Os$ dating of a Neoproterozoic, post-glacial black shale in Western Canada. *Earth Planet. Sci. Lett.* **2004**, *222*, 729−740.
(22) Kendall, B.; Creaser, R. A.; Selby, D. Re−Os geochronology of post-glacial black shales in Australia: constraints on the timing of "Sturtian" glaciation. *Geology* **2006**, *34*, 729−732.
(23) Selby, D.; Creaser, R. A. Direct radiometric dating of the Devonian- Mississippian time scale boundary using the Re-Os black shale geochronometer. *Geology* **2005**, *33* (7), 545−548.
(24) Rooney, A. D.; Selby, D.; Houzay, J.; Renne, P. R. Re−Os geochronology of a Mesoproterozoic sedimentary succession, Taoudeni basin, Mauritania: implications for basin wide correlations and Re−Os organic-rich sediments systematics. *Earth Planet. Sci. Lett.* **2010**, *289* (3−4), 486−496.
(25) Rooney, A. D.; Chew, D. M.; Selby, D. Re-Os geochronology of the Neoproterozoic Cambrian Dalradian Supergroup of Scotland and Ireland: Implications for Neoproterozoic stratigraphy, glaciations and Re−Os systematics. *Precambrian Res.* **2011**, *185* (3−4), 202−214.
(26) Rooney, A. D.; Macdonald, F. A.; Strauss, J. V. Re-Os geochronology and coupled Os-Sr isotope constraints on the Sturtian snowball Earth. *Proc. Natl. Acad. Sci. U. S. A.* **2014**, *111*, 51−56.
(27) Rooney, A. D.; Strauss, J. V.; Brandon, A. D.; Macdonald, F. A. A Cryogenian chronology: Two long-lasting synchronous Neoproterozoic glaciations. *Geology* **2015**, *43*, 459−462.
(28) Ravizza, G.; Turekian, K. K. Application of the ^{187}Re-^{187}Os system to black shale geochronometry. *Geochim. Cosmochim. Acta* **1989**, *53* (12), 3257−3262.
(29) Peucker-Ehrenbrink, B.; Ravizza, G. The marine osmium isotope record. *Terra Nova.* **2000**, *12*, 205−219.
(30) Cohen, A. S. The rhenium-osmium isotope system: applications to geochronological and palaeoenvironmental problems. *J. Geol. Soc.* **2004**, *161*, 729−734.
(31) Tripathy, G. R.; Singh, S. K. Re−Os depositional age for black shales from the Kaimur Group, Upper Vindhyan. *India. Chem. Geol.* **2015**, *413*, 63−72.
(32) Lu, X.; Kendall, B.; Stein, H. J.; Hannah, J. L. Temporal record of osmium concentrations and $^{187}Os/^{188}Os$ in organic-rich mudrocks: Implications for the osmium geochemical cycle and the use of osmium as a paleoceanographic tracer. *Geochim. Cosmochim. Acta* **2017**, *216*, 221−241.
(33) Wang, J.; Li, Z. X. History of Neoproterozoic rift basins in South China: implications for Rodinia break-up. *Precambrian Res.* **2003**, *122*, 141−158.
(34) Zhou, C.; Xiao, S. Ediacaran $\delta^{13}C$ chemostratigraphy of South China. *Chem. Geol.* **2007**, *237* (1−2), 89−108.
(35) Yang, A. H.; Zhu, M. Y.; Zhang, J. M.; Zhao, F. C.; Lu, M. Sequence stratigraphic subdivision and correlation of the Ediacaran (Sinian) Doushantuo Formation of Yangtze Plate South China. *J. Palaeogeography* **2015**, *17*, 1−20.
(36) Wang, H.; Li, Z. W.; Liu, S. G.; Ran, B.; Song, J. M.; Li, J. X.; Ye, Y. H.; Li, N. Ediacaran extension along the northern margin of the Yangtze Platform, South China: Constraints from the lithofacies and geochemistry of the Doushantuo Formation. *Mar. and Petro. Geol.* **2020**, *112*, No. 104056.
(37) Jiang, G. Q.; Shi, X. Y.; Zhang, S. H.; Wang, Y.; Xiao, S. H. Stratigraphy and paleogeography of the Ediacaran Doushantuo formation (ca. 635−551 Ma) in south China. *Gondwana Res.* **2011**, *19*, 831−849.
(38) Och, L. M.; Cremonese, L.; Shields-Zhou, G. A.; Poulton, S. W.; Struck, U.; Ling, H.; Li, D.; Chen, X.; Manning, C.; Thirlwall, M. Palaeoceanographic controls on spatial redox distribution over the Yangtze Platform during the Ediacaran−Cambrian transition. *Sedimentology* **2016**, *63*, 378−410.
(39) Zhu, M. Y.; Yang, A. H.; Yuan, J. L.; Li, G. X.; Zhang, J. M.; Zhao, F. C.; Ahn, S.; Miao, L. Y. Cambrian integrative stratigraphy and timescale of China Sci. *China Earth Sci.* **2019**, *62*, 25−60.
(40) Tan, Z.; Wu, J.; Jia, W.; Li, J.; Kendall, B.; Song, J.; Peng, P. Molybdenum isotope evidence from restricted-basin mudstones for an intermediate extent of oxygenation in the late Ediacaran Ocean. *Chem. Geol.* **2023**, *623*, No. 121410.
(41) Chen, Y. L.; Huang, J.; Zhong, Y.; Zhang, X. L.; Zhai, M. G.; Chu, X. L. Suboxic dominated conditions in the Ediacaran shallow ocean: Geochemistry of pelitic siltstones in the Doushantuo Formation South China. *Palaeogeogr. Palaeoclimatol. Palaeoecol.* **2020**, *546*, No. 109658.
(42) Wu, J. X.; Jia, W. L. Nitrogen isotopic compositions of organic-rich shales (∼560 Ma) in the Chengkou region, South China: Implications for a stable and relatively large nitrate reservoir of the late Ediacaran ocean. *J. Asian Earth Sci.* **2024**, *260*, No. 105969.
(43) Li, J.; Zhao, P. P.; Liu, J.; Wang, X. C.; Yang, A. Y.; Wang, G. Q.; Xu, J. F. Reassessment of hydrofluoric acid desilicification in the Carius tube digestion technique for Re−Os isotopic determination in geological samples. *Geostand. Geoanal. Res.* **2015**, *39*, 17−30.
(44) Yin, L.; Li, J.; Liu, J.; Li, C.; Sun, S. L.; Liang, H. Y.; Xu, J. F. Precise and accurate Re−Os isotope dating of organic-rich sedimentary rocks by thermal ionization mass spectrometry with an improved H_2O_2-HNO_3 digestion procedure. *Int. J. Mass Spectrom.* **2017**, *421*, 263−270.
(45) Ludwig, K. R. *ISOPLOT, a Geochronological Toolkit for Microsoft Excel 3.00*; Berkeley Geochronology Center: Berkeley, 2003, vol *5*, pp 1−75.
(46) Smoliar, M. I.; Walker, R. J.; Morgan, J. W. Re-Os ages of group IIA, IIIA, IVA, and IVB iron meteorites. *Science* **1996**, *271*, 1099−1102.
(47) Esser, B. K.; Turekian, K. K. The osmium isotopic composition of the continental crust. *Geochim. Cosmochim. Acta* **1993**, *57*, 3093−3104.
(48) Peucker-Ehrenbrink, B.; Jahn, B. M. Rhenium-osmium isotope systematics and platinum group element concentrations: loess and the upper continental crust. *Geochem. Geophys. Geosyst.* **2001**, *2*, 22−1061.
(49) Taylor, S. R.; McLennan, S. M. *The continental crust: its composition and evolution*; Blackwell Scientific Publications: Oxford, 1985.
(50) Liu, P. J.; Yin, C. Y.; Gao, L. Z.; Tang, F.; Chen, S. M. New material of microfossils from the Ediacaran Doushantuo Formation in the Zhangcunping area, Yichang, Hubei Province and its zircon SHRIMP U−Pb age. *Chin. Sci. Bull.* **2009**, *54*, 1058−1064.
(51) Barfod, G. H.; Albarede, F.; Knoll, A. H.; Xiao, S.; Telouk, P.; Frei, R.; Baker, J. New Lu−Hf and Pb−Pb age constraints on the earliest animal fossils. *Earth Planet. Sci. Lett.* **2002**, *201*, 203−212.
(52) Chen, D. F.; Dong, W. Q.; Zhu, B. Q.; Chen, X. P. Pb−Pb ages of Neoproterozoic Doushantuo phosphorites in South China: constraints on early metazoan evolution and glaciation events. *Precambrian Res.* **2004**, *132* (1−2), 123−132.
(53) Grotzinger, J. P.; Fike, D. A.; Fischer, W. W. Enigmatic origin of the largest-known carbon isotope excursion in Earth's history. *Nat. Geosci.* **2011**, *4*, 285−292.
(54) Schrag, D. P.; Higgins, J. A.; Macdonald, F. A.; Johnston, D. T. Authigenic carbonate and the history of the global carbon cycle. *Science* **2013**, *339*, 540−543.
(55) Knauth, L. P.; Kennedy, M. J. The late Precambrian greening of the Earth. *Nature* **2009**, *460*, 728−732.
(56) Derry, L. A. A burial diagenesis origin for the Ediacaran Shuram-Wonoka carbon isotope Anomaly. *Earth Planet. Sci. Lett.* **2010**, *294*, 152−162.

https://doi.org/10.1021/acsomega.4c05072
ACS Omega XXXX, XXX, XXX−XXX

(57) Zhou, C. M.; Yuan, X. L.; Xiao, S. H.; Chen, Z.; Hua, H. Ediacaran integrative stratigraphy and timescale of China. *Sci. China Earth Sci.* **2019**, *62*, 7−24.
(58) Rotich, E. K.; Handler, M. R.; Naeher, S.; Selby, D.; Hollis, C. J.; Sykes, R. Re−Os geochronology and isotope systematics, and organic and sulfur geochemistry of the middle late Paleocene Waipawa Formation, New Zealand: Insights into early Paleogene seawater Os isotope composition. *Chem. Geol.* **2020**, *536*, No. 119473.
(59) Jaffe, L. A.; Peucker-Ehrenbrink, B.; Petsch, S. T. Mobility of rhenium, platinum group elements and organic carbon during black shale weathering. *Earth Planet. Sci. Lett.* **2002**, *198* (3−4), 339−353.
(60) Kendall, B.; Creaser, R. A.; Selby, D. ^{187}Re-^{187}Os geochronology of Precambrian organic-rich sedimentary rocks. *Geol. Soc. London Spec. Publ.* **2009**, *326*, 85−107.
(61) Li, C.; Love, G. D.; Lyons, T. W.; Fike, D. A.; Sessions, A. L.; Chu, X. A stratified redox model for the Ediacaran ocean. *Science* **2010**, *328*, 80−83.
(62) Zhou, C.; Li, X. H.; Xiao, S.; Lan, Z.; Ouyang, Q.; Guan, C.; Chen, Z. A new SIMS zircon U-Pb date from the Ediacaran Doushantuo Formation: age constraint on the Weng'an biota. *Geol. Mag.* **2017**, *154*, 1193−1201.
(63) Wang, W.; Guan, C. G.; Zhou, C. M.; Peng, Y. B.; Pratt, L. M.; Chen, X.; Chen, L.; Chen, Z.; Yuan, X. L.; Xiao, S. H. Integrated carbon, sulfur, and nitrogen isotope chemostratigraphy of the Ediacaran Lantian Formation in South China: spatial gradient, ocean redox oscillation, and fossil distribution. *Geobiology* **2017**, *15*, 552−571.
(64) Hannah, J. L.; Bekker, A.; Stein, H. J.; Markey, R. J.; Holland, H. D. Primitive Os and Ma age for marine shale: implications for Paleoproterozoic glacial events and the rise of atmospheric oxygen. *Earth Planet. Sci. Lett.* **2004**, *225*, 43−52.
(65) Ravizza, G.; Paquay, F. Os isotope chemostratigraphy applied to organic-richmarine sediments from the Eocene-Oligocene transition on the West African margin (ODP Site 959). *Palaeoceanography* **2008**, *23*, PA2204.
(66) Kendall, B.; Creaser, R. A.; Gordon, G. W.; Anbar, A. D. Re−Os and Mo isotope systematics of black shales from the Middle Proterozoic Velkerri and Wollogorang Formations, McArthur Basin, northern Australia. *Geochim. Cosmochim. Acta* **2009**, *73* (9), 2534−2558.
(67) Oxburgh, R. Variations in the osmium isotope composition of sea water over the past 200,000 years. *Earth Planet. Sci. Lett.* **1998**, *159*, 183−191.
(68) Dalai, T. K.; Suzuki, K.; Minagawa, M.; Nozaki, Y. Variations in seawater osmium isotope composition since the last glacial maximum: a case study from the Japan sea. *Chem. Geol.* **2005**, *220*, 303−314.
(69) Hannah, J. L.; Stein, H. J.; Zimmerman, A.; Yang, G.; Melezhik, V. A.; Melezhikm, V. A. Precise 2004 ± 9 Ma Re-Os age for Pechenga black shale: comparison of sulfides and organic material. *Geochim. Cosmochim. Acta* **2008**, *70*, A228.
(70) Anbar, A. D.; Duan, Y.; Lyons, T.; Arnold, G.; Kendall, B.; Creaser, R.; Kaufman, A.; Gordon, G.; Scott, C.; Garvin, J.; Buick, R. A whiff of oxygen before the great oxidation event. *Science* **2007**, *317* (5846), 1903−1906.
(71) Sperling, E.; Rooney, A.; Hays, L.; Sergeev, V.; Vorobeva, N.; Sergeeva, N.; Selby, D.; Johnston, D.; Knoll, A. Redox heterogeneity of subsurface waters in the Mesoproterozoic ocean. *Geobiology* **2014**, *12*, 373−386.
(72) Och, L. M.; Shields-Zhou, G. A. The Neoproterozoic oxygenation event: Environmental perturbations and biogeochemical cycling. *Earth-Sci. Rev.* **2012**, *110*, 26−57.
(73) Singh, S. K.; Trivedi, J. R.; Krishnaswami, S. Re−Os isotope systematics in black shales from the Lesser Himalaya: their chronology and role in the ^{187}Os/^{188}Os evolution of seawater. *Geochim. Cosmochim. Acta* **1999**, *63*, 2381−2392.
(74) Zhu, B.; Becker, H.; Jiang, S.; Pi, D. Re−Os geochronology of black shales from the Neoproterozoic Doushantuo Formation, Yangtze platform, South China. *Precambrian Res.* **2013**, *225*, 67−76.
(75) Yang, C.; Li, Y.; Selby, D.; Wan, B.; Guan, C.; Zhou, C.; Li, X. H. Implications for Ediacaran biological evolution from the ca. 602 Ma Lantian biota in China. *Geology* **2022**, *50*, 562−566.
(76) Ugidos, J. M.; Armenteros, I.; Barba, P.; Valladares, M. I.; Colmenero, J. R. Geochemistry and petrology of recycled orogen-derived sediments: a case study from Upper Precambrian siliciclastic rocks of the Central Iberian Zone, Iberian Massif Spain. *Precambrian Res.* **1997**, *84*, 163−180.
(77) Sahoo, S. K.; Planavsky, N. J.; Kendall, B.; Wang, X.; Shi, X. Y.; Scott, C.; Anbar, A. D.; Lyons, T.; Jiang, G. Ocean oxygenation in the wake of the Marinoan glaciation. *Nature* **2012**, *489*, 546−549.
(78) Sahoo, S. K.; Planavsky, N. J.; Jiang, G.; Owens, J. D.; Wang, X.; Shi, X.; Anbar, A. D.; Lyons, T. Oceanic oxygenation events in the anoxic Ediacaran ocean. *Geobiology* **2016**, *14*, 457−468.
(79) Johnston, D. T.; Poulton, S. W.; Tosca, N. J.; Obrien, T.; Halverson, G. P.; Schrag, D. P.; Macdonald, F. A. Searching for an oxygenation event in the fossiliferous Ediacaran of northwestern Canada. *Chem. Geol.* **2013**, *362*, 273−286.
(80) Chen, X.; Ling, H.; Vance, D.; Shields-Zhou, G. A.; Zhu, M.; Poulton, S. W.; Och, L. M.; Jiang, S.; Li, D.; Cremonese, L.; Archer, C. Rise to modern levels of ocean oxygenation coincided with the Cambrian radiation of animals. *Nat. Commun.* **2015**, *6*, 7142.
(81) Kendall, B.; Komiya, T.; Lyons, T. W.; Bates, S. M.; Gordon, G. W.; Romaniello, S. J.; Jiang, G.; Creaser, R. A.; Xiao, S.; Mcfadden, K. Uranium and molybdenum isotope evidence for an episode of widespread ocean oxygenation during the late ediacaran period. *Geochim. Cosmochim. Acta* **2015**, *156*, 173−193.
(82) Kurzweil, F.; Drost, K.; Pašava, J.; Wille, M.; Taubald, H.; Schoeckle, D.; Schoenberg, R. Coupled sulfur, iron and molybdenum isotope data from black shales of the Teplá-Barrandian unit argue against deep ocean oxygenation during the Ediacaran. *Geochim. Cosmochim. Acta* **2015**, *171*, 121−142.
(83) Scott, C.; Lyons, T. W.; Bekker, A.; Shen, Y.; Poulton, S. W.; Chu, X.; Anbar, A. D. Tracing the stepwise oxygenation of the Proterozoic ocean. *Nature* **2008**, *452* (7186), 456−459.
(84) Mills, B.; Watson, A. J.; Goldblatt, C.; Boyle, R.; Lenton, T. Timing of Neoproterozoic glaciations linked to transport-limited global weathering. *Nat. Geosci.* **2011**, *4*, 861−864.
(85) Lau, K. V.; Macdonald, F. A.; Maher, K.; Payne, J. Uranium isotope evidence for temporary ocean oxygenation in the aftermath of the Sturtian Snowball Earth. *Earth Planet. Sci. Lett.* **2017**, *458*, 282−292.
(86) Zhang, F. F.; Zhu, X. K.; Yan, B.; Kendall, B.; Peng, X.; Li, J.; Algeo, T.; Romaniello, S. Oxygenation of a Cryogenian ocean (Nanhua Basin, South China) revealed by pyrite Fe isotope compositions. *Earth Planet. Sci. Lett.* **2015**, *429*, 11−19.

https://doi.org/10.1021/acsomega.4c05072
ACS Omega XXXX, XXX, XXX−XXX

doi:10.20008/j.kckc.202409014

扩频激电法(SSIP)找矿效果分析——以湖南省永州市零陵区东湘桥锰矿床勘查为例

廖凤初[1],刘桂元[1],周杰[1],黄建权[1],徐军伟[1],陈儒军[2,3,4,5]

(1. 湖南省地球物理地球化学调查所 湖南 长沙 410116;2. 中南大学地球科学与信息物理学院, 湖南 长沙 410083;3. 中南大学 AIoT(人工智能物联网)与地质地球物理创新创业教育中心, 湖南 长沙 410083;4. 有色金属成矿预测与地质环境监测教育部重点实验室, 湖南 长沙 410083;5. 有色资源与地质灾害探查湖南省重点实验室, 湖南 长沙 410083)

摘 要 本文在充分研究勘查区地质背景的基础上,首次采用扩频激电法在祁零盆地开展锰矿资源的探测。通过双边三极测深反演结果分析,发现了一条较连续的相对高极化异常带,异常带强度与围岩相差10倍,突出而稳定;电阻率反演结果则表现为"U"型盆状高阻基底包裹低阻的特征,推测其高极化异常带由地下矿床引起;而高阻盆底包裹低阻则指示地层受向斜构造控制,与已知的向斜构造一致。经钻探勘探,发现2条较为连续的锰矿矿脉,厚0.9~2.8 m,品位9.3%~15.2%,与黄铁矿成伴生关系,一同赋存于灰岩中。通过SSIP实验成果以及钻探验证情况,得出视极化率异常与矿脉揭露深度、形态轮廓十分吻合,视电阻率异常较好地反应矿区地层展布信息,扩频激电法在碳酸锰矿产资源勘查方面的有效性得到验证。

关键词 双边三极测深;扩频激电法;锰矿;激电异常

中图分类号:P631 **文献标志码**:A **文章编号**:1674-7801(2024)09-1691-09

Analysis of exploration effect of spread spectrum induced polarization (SSIP) method——Taking the exploration of Dongxiangqiao manganese deposit in Lingling district, Yongzhou City, Hunan Province as an example

LIAO Fengchu[1], LIU Guiyuan[1], ZHOU Jie[1], HUANG Jianquan[1], XU Junwei[1], CHEN Rujun[2,3,4,5]

(*1. Hunan Institute of Geophysics and Geochemistry, Changsha 410116, Hunan, China; 2. School of Geoscience and Info-Physics, Central South University, Changsha 410083, Hunan, China; 3. AIoT Innovation and Entrepreneurship Education Center for Geology and Geophysics, Central South University, Changsha 410083, Hunan, China; 4. Key Laboratory of Nonferrous Metal Mineralization*)

[收稿日期]2024-08-30; [修回日期]2024-10-11

[基金项目]本文受自然资源部新一轮找矿突破战略行动科技支撑项目(ZKKJ202407)和湖南省地质院科研项目(HNGSTP202402)联合资助。

[第一作者简介]廖凤初,男,1969年生,正高级工程师,长期从事矿产勘查和地质工作;E-mail: liaofengchuhunanwuhuasuo@hnwhs.work。

[通讯作者简介]周杰,男,1983年生,高级工程师,长期从事地球物理勘查工作;E-mail:452428218@qq.com。

[引用格式]廖凤初,刘桂元,周杰,黄建权,徐军伟,陈儒军. 2024. 扩频激电法(SSIP)找矿效果分析——以湖南省永州市零陵区东湘桥锰矿床勘查为例[J]. 矿产勘查,15(9):1691-1699.

Liao Fengchu, Liu Guiyuan, Zhou Jie, Huang Jianquan, Xu Junwei, Chen Rujun. 2024. Analysis of exploration effect of spread spectrum induced polarization (SSIP) method——Taking the exploration of Dongxiangqiao manganese deposit in Lingling district, Yongzhou City, Hunan Province as an example[J]. Mineral Exploration, 15(9): 1691-1699.

Prediction and Geological Environment Detection of Ministry of Education, Changsha 410083, Hunan, China; 5. Hunan Key Laboratory of Non-ferrous Resources and Geological Disaster Exploration, Changsha 410083, Hunan, China)

Abstract: On the basis of fully studying the geological background conditions of the exploration area, this article first uses spread-spectrum induced polarization (SSIP) to explore manganese ore resources in the Qiling Basin. Through the analysis of the inversion results of SSIP sounding using the forward and inversion pole-dipole array, a relatively continuous high polarization anomaly zone was discovered, with an intensity 10 times higher than that of the surrounding rock, protruding and stable; The inversion results of apparent resistivity show the characteristic of U-shaped basin shaped high resistive basement enveloping low resistive zone, suggesting that its high polarization anomaly zone is caused by underground mineral deposit; The inclusion of high resistive basin bottom and low resistive zone indicates that the strata are controlled by syncline structures, consistent with known syncline structures. Through drilling and exploration, two relatively continuous manganese ore veins were discovered, with a thickness of 0.9 m to 2.8 m and a grade of 9.3% to 15.2%. They are associated with pyrite and coexist in limestone. Through experimental results of SSIP survey and drilling verification, it was found that the polarization anomaly is very consistent with the depth and shape of the ore vein exposure, and the resistivity anomaly reflects the distribution of the mining area strata well. Therefore, the effectiveness of the SSIP method in the exploration of manganese carbonate mineral resources is verified.

Keywords: forward and inverse pole-dipole sounding; spread spectrum induced polarization method; manganese ore; induced polarization anomaly

0　引言

地球物理勘探可以在深部隐伏矿勘探中发挥重要作用。尤其是地质情况复杂的地区,采用多种地球物理勘探方法相结合,可以起到较好找矿效果(程华等,2024;赵磊等,2024)。这是因为在矿石品位高低含量不同、规模大小不一、矿床不连续等情况下,往往使得矿石自身电阻率与围岩差异不大,仅仅依靠电阻率测量无法取得较好的找矿效果(谭义东,1991;刘涛等,2011;殷保全,2014;吴新刚等,2016;吕玉增等,2023)。相比于单一的视电阻率测量方法,可以同时测量视电阻率和激电参数的激电法在大多情况下能够探测到浸染状金属硫化物引起的异常(向晓松和贾继标,2014;张晓东等,2017;郝海强等,2023;农观海等,2023)。由于激电法受地形影响相对较小,激电异常可靠性比电阻率异常更高(陈颖祥和梁鸿喜,1977;刘晓宇,2018;吕翔,2022;Revil et al., 2022)。

然而,目前大量激电测量为时间域脉冲式供电,深部目标体二次场是否能充分达到饱和而被探测感知,与充电时长密不可分(石昆法和莫焰玉,1982;陆学村,2012);加之需要人工多次改变AB供电极距,以达到不同深度的探测目的(张彦和陈兴峰,2019;郭洪娟等,2022)。这一技术现状使得传统的激电测量方法具有施工难度大、效率低、成本高、深部信号微弱、探测深度有限等不足之处。

针对以上缺陷,陈儒军等(2020)在仪器和方法上进行了大量创新,独创性地结合扩频通信信号处理技术和微弱地球物理信号采集技术,研发出扩频激电探测技术与装备,并将这项技术命名为扩频激电(SSIP)。该项探测技术具有大深度、高精度、抗干扰、成本低、效率高等特点,在1000 m以浅的探测范围内可以测得激电参数,能有效识别有色金属矿致异常(Liu et al., 2016, 2017)。该技术已在国内西藏、甘肃、云南、贵州、河南和江苏等地多个矿产勘查项目进行了有效应用(刘卫强和陈儒军,2016;陈儒军等,2020;Ahmad et al., 2024)。

目前,扩频激电三级测深技术在碳酸型锰矿探测应用较少,笔者以湖南省永州市零陵区东湘桥矿区锰矿勘查为例,引入扩频激电测量技术对锰矿矿床进行了勘探。经后期多个钻孔揭露,有效验证了激电异常,异常特征与矿床地下埋深、形态特征高度吻合性,为后期在相似地质背景下采用该技术方法进行地质找矿起到了较好的示范作用。因此,采用扩频激电法在祁零盆地开展碳酸锰矿勘探研究具有重要的应用价值。

1　地质与地球物理特征

1.1　矿区地质特征

矿区位于祁零盆地荞麦冲—东湘桥复式向斜的中南部(图1),整体构造为一向斜,地层东西两翼基本对称发育,出露地层主要有石炭系(C)、二叠系(P)及第四系(Q_4)。其中,石炭系地层为壶天群(CPH),分布于矿区东西侧,即向斜左右两翼,主要为白云岩和白云质灰岩。二叠系地层有上统龙潭组(P_3l)、中统孤峰组(P_2g)、小江边组(P_2x)和栖霞组(P_2q)。上统龙潭组(P_3l)地层岩性以泥岩和页岩为主,位于矿区中部,亦为向斜核部地层;中统孤峰组(P_2g)—栖霞组(P_2q)地层则呈平行整合接触关系,对称分布于向斜两翼。中统孤峰组(P_2g)地层为一套碳酸盐岩相,为碳酸锰矿的主要赋存层位;小江边组(P_2x)和栖霞组(P_2q)地层主要岩性为硅质岩、硅质灰岩和白云质灰岩;第四系(Q)地层呈风化残坡积物多沿山坡及沟谷分布,一般厚0~20 m。

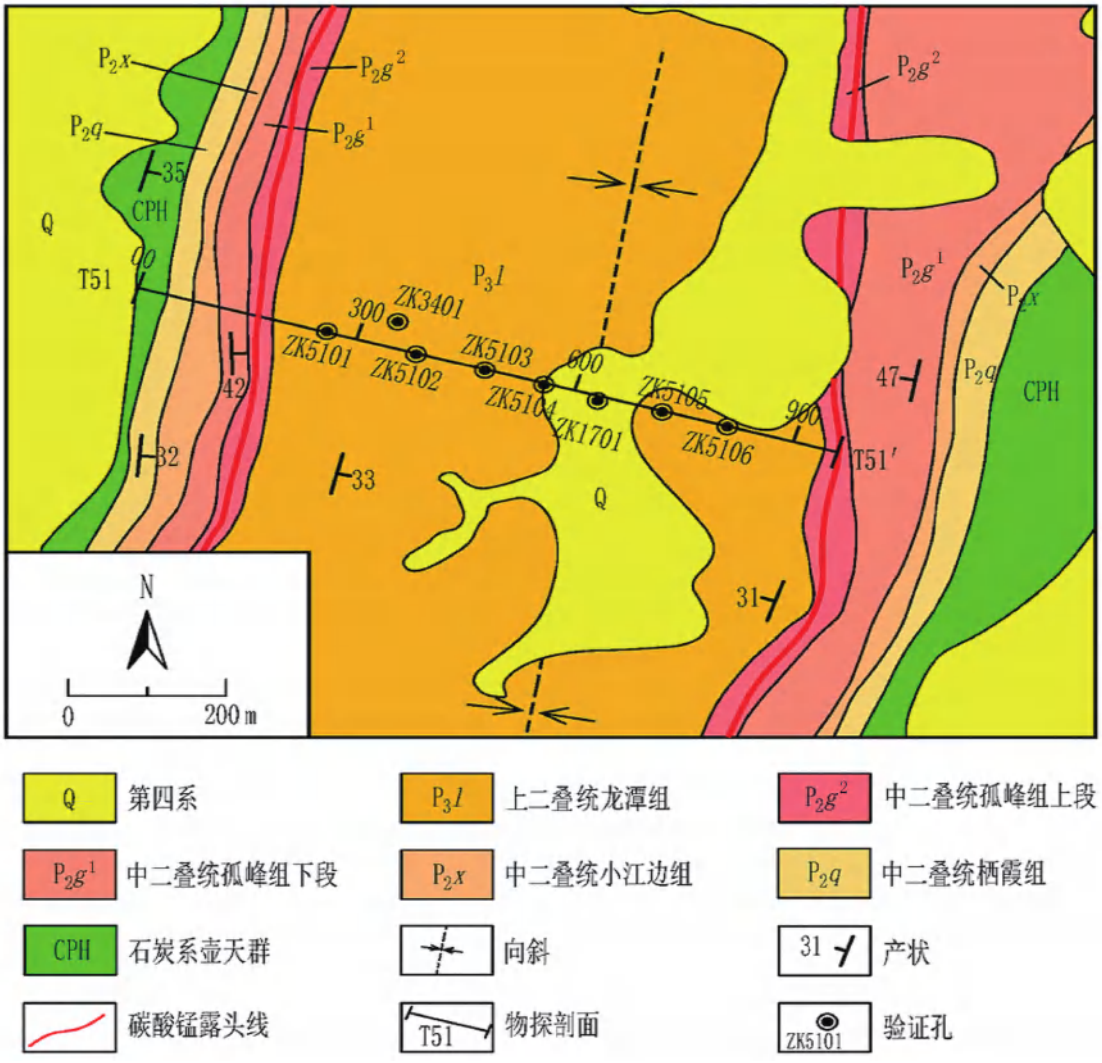

图1　研究区地质图

矿区构造较简单,总体为一轴向北东的东湘桥向斜,伴随零星规模较小的近东西向断裂构成了区内总体构造框架。东湘桥向斜在区域上位于荞麦冲—东湘桥复式向斜的南段,该向斜构造控制了区内锰矿的展布。

1.2　矿体地质特征

(1)地层层位对碳酸锰矿的控制

有利的赋矿地层存在,是区内碳酸锰矿产出的基本条件之一。区内碳酸锰矿主要赋存于二叠系

孤峰组上段上部地层中，岩性为一套富含泥质和藻类生物的含泥灰岩、泥灰岩；向下一套地层为含硅质的较纯灰岩，锰含量较低，基本未见碳酸锰矿层的发育。因此，二叠系孤峰组上段地层含生物屑的不纯碳酸盐岩控制了碳酸锰矿的产出和分布。

(2)构造对碳酸锰矿的控制

构造对碳酸锰矿的控制，不仅表现在区域成矿上，而且对特定矿床的控制上也起到了重要作用。据该区域地质资料表明，在区域上祁零盆地属于成锰盆地，该盆地的发育和形成受多组深大断裂控制。在盆地内发育一组呈雁列产出的近南北向次级向斜构造，向斜构造控制了区内锰矿床的产出，同时也控制了赋锰岩系和碳酸锰矿层的分布及矿层的产状、形态。由此可见，构造对区内锰矿床具有分级控制的特点。

(3)沉积相对区内锰矿床的控制

孤峰期沉积了一套富含铁锰质的硅质岩、碳酸盐岩和泥岩，由于相邻古陆(江南古陆和雪峰古陆)及火山活动区的物质经强烈化学分解形成氧化硅、锰、铁流入海盆，加之海水表层、海底分别繁育大量放射虫、硅质海绵，故形成锰(铁锰)矿。矿石中的菱锰矿多与藻类生物呈球粒状分布，显示出两者的密切关系。区内孤峰期为泻湖潮坪沉积环境。

1.3　地球物理电性特征

区内由浅至深不同地层主要岩性分别为第四系(Q_4)含砾黏土；上二叠统龙潭组(P_3l)泥岩、页岩夹砂岩；中二叠统孤峰组上段(P_2g^2)泥灰岩、黄铁矿、锰矿；下段(P_2g^1)硅质灰岩、白云质灰岩；中二叠统小江边组(P_2x)硅质岩、硅质灰岩；中二叠统栖霞组(P_2q)钙质灰岩夹页岩；石炭系壶天群组(CPH)白云质灰岩等。不同地层岩性电性特征如表1所示。

表1　测区地层电阻率和激电参数统计

地层名称	主要岩性	电阻率范围/(Ω·m)	平均电阻率/(Ω·m)	地层综合电阻率/(Ω·m)	极化率范围/%	平均极化率/%	地层综合极化率/%
第四系Q_4	含砾黏土	5 ~ 100	30	30	0.2 ~ 1.6	0.8	0.8
上二叠统龙潭组(P_3l)	泥岩	250 ~ 800	525	650	0.3 ~ 2.0	1.1	1.0
	页岩	365 ~ 1200	780		0.2 ~ 1.7	0.9	
中二叠统孤峰组上段(P_2g^2)(含矿地层)	泥灰岩	900 ~ 2650	1775	1280	0.4 ~ 2.3	1.3	14.2
	黄铁矿	10 ~ 200	135		5.0 ~ 31.0	18.0	
	含锰灰岩	400 ~ 3450	1925		3.5 ~ 43.2	23.3	
中二叠统孤峰组下段(P_2g^1)	硅质灰岩	1600 ~ 4200	2860	2540	0.3 ~ 2.1	1.7	1.3
	白云质灰岩	1200 ~ 3500	2350		0.2 ~ 1.5	0.8	
中二叠统小江边组(P_2x)	硅质岩	1700 ~ 5500	3300	3025	0.3 ~ 1.8	1.1	1.4
	硅质灰岩	1600 ~ 4200	2860		0.3 ~ 2.1	1.7	
中二叠统栖霞组(P_2q)	钙质灰岩	950 ~ 2840	1900	1900	0.1 ~ 1.4	0.7	0.7
石炭系壶天群组(CPH)	白云质灰岩	1200 ~ 3500	2350	2350	0.2 ~ 1.5	0.85	0.85

据表1可知，含矿地层由于不同岩石电阻率差异较大，致该地层综合电阻率与上下相邻地层有一定的差异。若仅仅依靠单一视电阻率测量，则很难判断含矿地层在地下深部的埋藏特征，其找矿效果也将大受影响。但含锰灰岩和与之伴生的黄铁矿均表现为极为突出的高极化特征，致赋矿地层综合极化率达14.2%，而其余地层综合极化率均在1.4%及以下，两者形成10倍的差异。

因此，含矿地层具有中阻、高极化的电性特征，为采用激电测量进行深部找矿奠定了良好的物性前提。

2　基本原理

扩频激电(SSIP)系统采集方式为无线分布式高精度阵列采集，发送频率范围为1/256 ~ 8192 Hz，根据调制阶数的不同频率数量范围为4 ~ 256。系统通过发送机发送M序列伪随机扩频信号，大大提高了频域分辨率及信号抗干扰能力；通过无线分布式阵列高精度接收系统实现了大深度、高效率和高精度扩频激电信号检测。在方法上，利用相对相位谱

法对电磁耦合感应进行校正(王书民和雷达,2002;陈儒军等,2004;李栋等,2019),获取激电相位响应和 Cole-Cole 模型参数;通过扩频信号发射、Robust 和相关技术压制电磁干扰,增强信噪比;通过带地形的多频点多装置组合精密反演,实现探测目标的精密成像,得到丰富的地电结构信息;最后通过多频点多参数反演结果的分析,得到勘探成果与地质体的最佳耦合,实现成矿有利区的高可信度预测。

3　技术参数设置与反演

扩频激电三极测深装置,数据采用无线分布式阵列接收。施工时,先根据剖面长度和点距计算出测点数量,然后一次性在整条剖面上布置全部测量电极和采集站,再根据设计的供电点逐点供电,每次供电时,所有通道同时测量,当所有设计供电点完成后,整条剖面测量完成。其采集的数据量为常规人工跑极方式的10倍以上,大大提高了反演精度和可靠性,实现地下目标的精细探测,具体工作布设如图2所示。

其中,测点距为 10 m,测量极距 MN 为 20 m,最小—最大供电极距 A0 为 15 ~ 1500 m。发送组合频率为4个的5阶扩频全方波信号,基准频率 1/16 Hz,供电电流 1.0 ~ 8.5 A。

扩频激电数据采集完成后,由 ZondRes2D 软件反演。该软件针对扩频激电观测方式进行了多次改进,可以对任意供电电极和测量电极组合的扩频激电数据进行反演。本次选择的反演方法为 Occam 反演,迭代次数为 10。根据视极化率的变化范围及测区岩矿石电性参数测量结果,本文将极化率的上限设置为 10%。在剖分方面,第一层厚度为 10 m,增加因子为 10%,总层数为 30 层,最大反演深度为 823 m。反演结果表明电阻率和极化率反演误差都在可接受范围内,可以将电阻率和极化率反演结果用于解释和钻孔定位。

4　成果推断解释

由于探测目标体极化率特征相比电阻率更加明显,其异常推断解释以极化率反演结果为主,电阻率反演结果为辅。

从极化率反演剖面图(图3)中可以看出:在平距 125 m(标高+150 m)、200 m(标高+50 m)、300 ~ 450 m 测段(标高-100 m)、600 m(标高 0 m)、725 m(标高+50 m)和 800 m(标高+175 m)处,出现了多个断断续续的高极化异常体,异常强度达 10.0%,而背景围岩平均为 1.0%,两者相差 10 倍。异常体强烈稳定,整体上呈下凹带状特征。

在电阻率剖面图(图4)中的平距 100 ~ 900 m,标高-50 m 至地表区域,为连续稳定的低阻区域,-50 m 标高以下,则为高阻区域。其连续稳定的低阻区为向斜核部的上二叠统龙潭组(P_3l)地层;盆状高阻基底则指示中二叠统孤峰下段—石炭系壶天群组多个高阻地层;其高—低过渡区域(500 ~ 800 Ω·m),则为含矿地层(中二叠统孤峰上段)埋深处。

5　钻探揭露情况

对T51号勘探剖面布设了 ZKT5101 ~ ZKT5106、

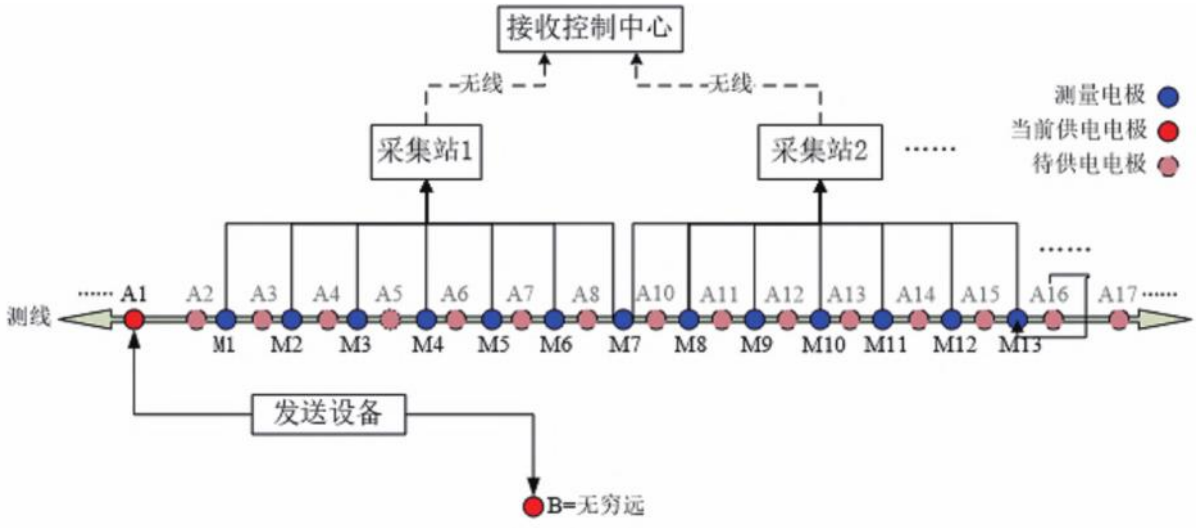

图2　扩频激电双边三极测深示意图

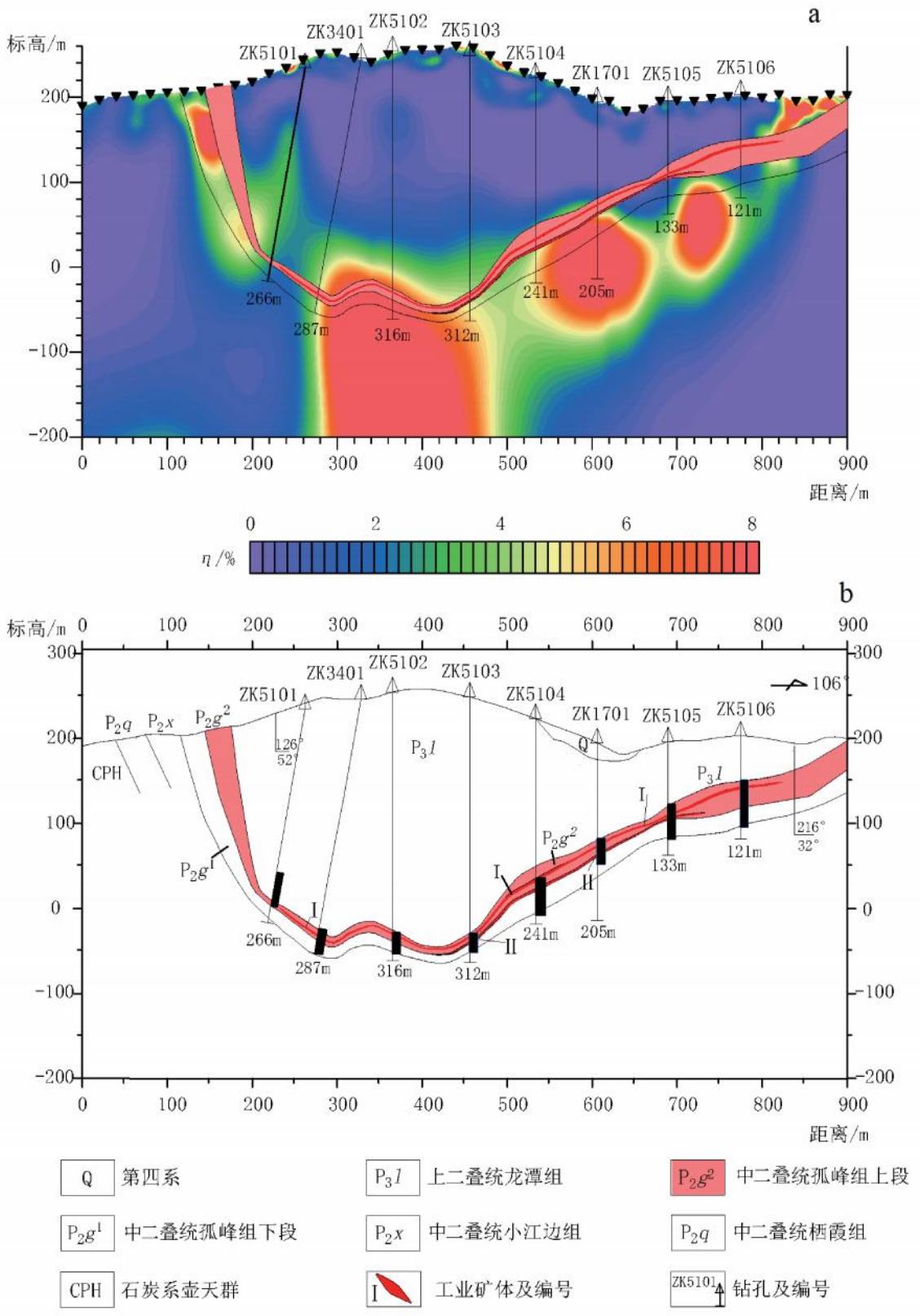

图 3　T51 线扩频激电极化率(a)与地质剖面图(b)

1696

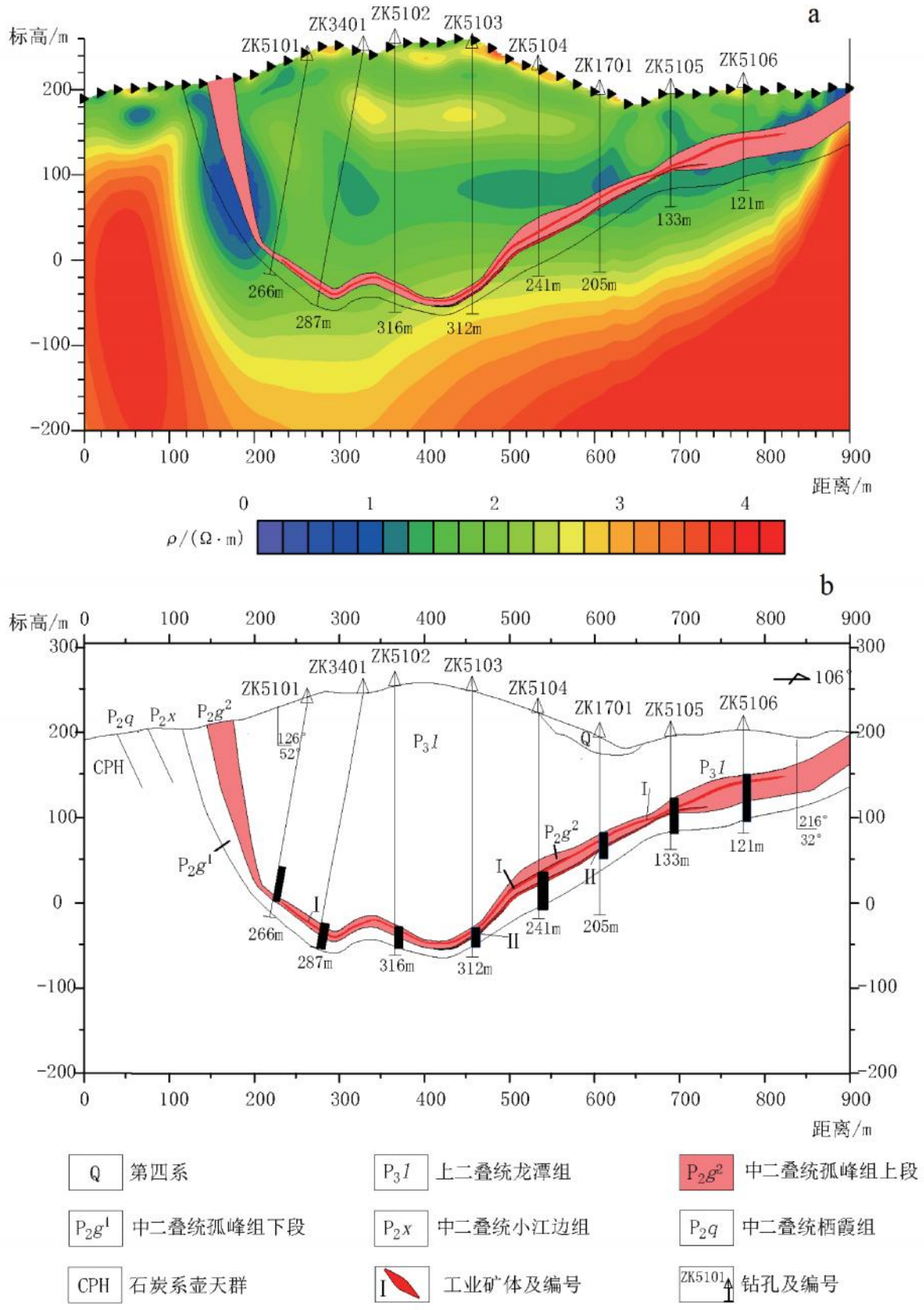

图 4　T51 线扩频激电电阻率(a)和地质剖面图(b)

ZK1701、ZK3401等8个钻孔，孔深在121.5～316.2 m。分别在埋深222.5 m、284.0 m、281.2 m、187.7 m、85.0 m、59.6 m、281.5 m和117.9 m处的灰岩中，揭露到厚0.9～2.8 m锰矿体，经样品测试分析（表2），其品位9.3%～15.2%锰矿矿脉2条。所揭露的矿脉较为连续稳定，其埋藏范围和形态与激电异常带基本吻合。

表2　T51线岩心测试分析结果

孔号	矿层号	矿层厚度/m	测试分析结果/%							
			Mn	TFe	P	SiO_2	CaO	Mg0	Al_2O_3	烧失量
ZKT5101	Ⅰ1	0.76	9.10	2.53	0.289	14.48	28.86	2.41	3.38	31.11
ZKT5102	Ⅰ1	0.91	9.29	3.69	0.316	10.87	30.51	2.55	2.97	31.86
ZKT5103	Ⅰ1	1.78	9.15	3.32	0.284	5.44	31.88	3.04	2.85	35.04
	$Ⅱ_1$	2.25	11.92	4.87	0.274	30.84	14.12	2.33	3.55	23.30
ZKT5104	$Ⅰ_1$	2.36	9.23	3.40	0.178	11.89	28.42	2.73	2.97	32.05
	$Ⅱ_1$	2.25	13.30	2.41	0.219	37.98	10.41	1.88	4.09	20.81
ZKT5105	$Ⅰ_1$	2.12	9.45	3.17	0.208	9.94	28.89	2.91	2.63	33.32
	$Ⅱ_1$	1.77	14.43	2.19	0.223	39.56	9.68	1.53	5.06	19.00
ZKT5106	$Ⅰ_1$	2.80	11.45	3.16	0.199	36.66	12.04	1.57	4.84	21.18
ZKT1710	$Ⅰ_1$	1.4	9.44	7.50	0.19	9.86	27.58	2.71	2.71	31.89
	$Ⅱ_1$	2.8	15.24	2.54	0.21	33.02	8.52	1.55	3.67	23.84
ZKT3401	$Ⅰ_1$	1.50	10.59	4.03	0.85	32.18	8.15	2.18	4.99	26.00

6　结论

（1）区内锰矿的产出和分布与多种成矿因素有关，与成矿关系密切的主要有地层岩性、岩相和构造等因素。其中地层产状决定了矿床的大致空间分布范围，岩性组分的复杂程度影响了矿石的综合物性特征，而构造则对矿床在地下的形态起到了重塑作用。

（2）由于电阻率相对于围岩差异较小，与整个含矿层相比其厚度比例极小，在无法形成一定规模电阻率异常情况下，结合极化率参数，能较好的识别矿层的空间展布。因此，多参数测量是寻找锰矿矿藏的有效途径。

（3）经钻探验证，扩频激电法在寻找碳酸岩型锰矿矿床方面是有效的，极化率异常与矿脉揭露深度、形态轮廓十分吻合，电阻率异常较好的反应矿区地层展布信息，同时，扩频激电法工作与传统激电测量方法相比效率快、成本低、激电异常可靠，值得推广使用。

参考文献

Ahmad J, Chen R J, Ijaz A, Muhammad Y, Shahid A S, Osama A R, Farid U, Shah F, Li R. 2024. Spread Spectrum Induced Polarization (SSIP) Survey for the Qiushuwan Copper-Molybdenum Deposits in Southern Henan Province, China[J]. Minerals, 14(9): 934-947.

Liu W Q, Chen R J, Cai H Z, Luo W B, André R. 2017. Correlation analysis for spread-spectrum induced-polarization signal processing in electromagnetically noisy environments[J]. Geophysics, 82(5): 243-256.

Liu W Q, Chen R J, Cai H Z, Luo W B. 2016. Robust statistical methods for impulse noise suppressing of spread spectrum induced polarization data, with application to a mine site, Gansu Province, China[J]. Journal of Applied Geophysics, 135: 397-407.

Revil A, Pierre V, Su Z Y, Chen R J. 2022. Induced polarization as a tool to assess mineral deposits: A review[J]. Minerals, 12(5): 571-584.

陈儒军，何继善，白宜诚，汤井田. 2004. 多频激电相对相位谱研究[J]. 中南大学学报(自然科学版)，(1)：106-111.

陈儒军，刘春明，何兰芳，唐冬春，柳卓，杨云见. 2020. 阵列式扩频激电法关键技术研究及应用[D]. 长沙：中南大学.

陈颖祥，梁鸿喜. 1977. 起伏地形条件下激电异常的定性分析和定量计算[J]. 地质与勘探，(1)：67-72.

程华，李水平，白德胜，曹杰，孙进，谢彦军，荆鹏，宋永利. 2024. 河南省嵩县九仗沟—东湾金矿区深部地球物理特征与找矿预测[J]. 矿产勘查，15(4)：600-611.

郭洪娟，聂冀强，赵卫东. 2022. 洪山岩体多金属成矿远景区激电测深探测深度浅析[J]. 世界有色金属，(20)：101-103.

郝海强，刘志远，杨闪，王建国，张明科，谢静博. 2023. 激发极化法在西非加纳某锰矿勘查中的应用[J]. 矿产勘查，14(7)：1106-

1113.
李栋,杨帆,高鹏举. 2019. 相位激电法电磁耦合效应的校正[J]. 矿产勘查,10(2): 316-320.
刘涛,陈卫,陈伟民,侯朝勇. 2011. 内蒙古嘎仙镍钴矿区物探找矿方法技术组合及应用[J]. 矿产勘查,2(6): 772-779.
刘卫强,陈儒军. 2016. 稳健统计用于扩频激电数据预处理与脉冲噪声压制[J]. 地球物理学进展,31(3): 1332-1341.
刘晓宇. 2018. 激电测深中的地形改正[D]. 北京: 中国地质大学(北京).
陆学村. 2012. 激电二次场衰减分布规律实验研究[D]. 邯郸: 河北工程大学.
吕翔. 2022. 浅谈激电中梯及激电测深物探方法在地形复杂、切割剧烈地区的实用性[J]. 世界有色金属,(15): 226-228.
吕玉增,程一鸣,卢光辉,姚双秋. 2023. 综合物探技术在桂西沉积型铝土矿勘查中的应用[J]. 矿产与地质,37(5): 1039-1045.
农观海,黄凯,邓耀辉,卢卯,杜蔺. 2023. 黔西北大坪子铅锌矿区电法组合异常特征及找矿潜力分析[J]. 矿物学报,43 (6): 903-911.
石昆法,莫焰玉. 1982. 对激电二次场时间特性影响因素的实验研究[J]. 地质与勘探,(1):53-57.
谭义东. 1991. 物探找金模式的建立和研究[J]. 地质与勘探,(1):55.
王书民,雷达. 2002. 相位激电法(偶极—偶极)单频电磁耦合校正方法[J]. 物探与化探,(1):57-59,63.
吴新刚,陆桂福,杨亚斌. 2016. 铁锌矿床物探异常特征及勘查实例[J]. 物探化探计算技术,38(3): 347-352.
向晓松,贾继标. 2014. 双频激电法在新疆金沙滩金矿勘查中的应用[J]. 矿产勘查,5(1): 53-57.
殷保全. 2014. 综合物探方法在斑岩铜矿中的应用效果[J]. 新疆有色金属,37(5): 20-22.
赵磊,李香资,谢国兴,权知心,岑朝正,郜朋飞,张猛. 2024. 内蒙古索家沟银多金属矿床地球物理特征及找矿前景[J]. 矿产勘查,15(2): 264-272.
张晓东,方捷,张定源,谢恩才,凌其怀,孙瑛,冯海林. 2017. 激发极化法在东溪金矿接替资源勘查中的应用[J]. 物探与化探,41(3): 445-451.
张彦,陈兴峰. 2019. 五极纵轴测深和对称四极激电测深在多金属找矿中的对比研究[J]. 世界有色金属,(3): 61-62.

processes

MDPI

Article

Geological Conditions of Shale Gas Accumulation in Coal Measures

Fengchu Liao [1], Keying Wang [1,2,3,*], Jian Zhan [1,2], Zhiwei Liu [1,2], Jiang Du [1,2], Shuhua Gong [1,2], Ningbo Cai [1,2,3], Jianglun Bai [4] and Junjian Zhang [4]

1 Geophysical and Geochemical Survey Institute of Hunan Province, Changsha 410014, China; liaofc123456@163.com (F.L.); zhanjian0822@163.com (J.Z.); liuzhiwei6657@163.com (Z.L.); dujiangcumt@163.com (J.D.); shgong10@126.com (S.G.); cainb666@163.com (N.C.)
2 Hunan Geological New Energy Exploration and Development Engineering Technology Research Center, Changsha 410014, China
3 Institute of Advanced Study, China University of Geosciences (Wuhan), Wuhan 430070, China
4 College of Earth Sciences & Engineering, Shandong University of Science and Technology, Qingdao 266590, China; 18803661662@163.com (J.B.); junjianzhangcumt@126.com (J.Z.)
* Correspondence: wangjx3327225@163.com

Abstract: The shale of different potential layers is studied by using rock pyrolysis analysis, total organic carbon determination (TOC), kerogen microscopic component identification, mineral X-ray diffraction, scanning electron microscopy, and low-temperature nitrogen adsorption experiments. The results are as follows: (1) Shishui Formation of the Lower Carboniferous and Longtan Formation of the Upper Permian are the two most important shale gas reservoirs in the Chenlei Depression. The sedimentary environment of the target shale is a marine land interaction facies coastal bay lagoon swamp sedimentary system. Two sedimentary facies of tidal flat facies, subtidal zone, and lagoon swamp facies are developed. (2) The organic matter types of shale are Type III and II_2, with TOC content greater than 1%. The maturity of shale samples is relatively higher ($R_{o,max}$ is above 2%), which means they have entered the stage of large-scale gas generation. The overall brittle mineral content of the target shale sample is relatively higher (above 40%), which is conducive to artificial fracturing and fracture formation in the later stage, while an appropriate amount of clay minerals (generally stable at 40%) is conducive to gas adsorption. (3) The overall pore structure of the water measurement group and Longtan group is good, with a higher specific surface area and total pore volume (average specific surface area is 12.21 and 8.36 m^2/g, respectively), which is conducive to the occurrence of shale gas and has good adsorption and storage potential. The gas content of the water measurement group and the Longtan Formation varies from 0.42 to 5 cm^3/g, with an average of 2.1 cm^3/g. It indicates that the water measurement group and the Longtan Formation shale gas in the study area have good resource potential.

Keywords: shale gas; physical property; gas content; pore structure; resource potential

Citation: Liao, F.; Wang, K.; Zhan, J.; Liu, Z.; Du, J.; Gong, S.; Cai, N.; Bai, J.; Zhang, J. Geological Conditions of Shale Gas Accumulation in Coal Measures. *Processes* **2024**, *12*, 1734. https://doi.org/10.3390/pr12081734

Academic Editors: Youguo Yan and Carlos Sierra Fernández

Received: 7 June 2024
Revised: 17 July 2024
Accepted: 13 August 2024
Published: 18 August 2024

1. Introduction

With the development of oil and gas exploration in China, shale gas as an important strategic alternative energy has received more and more attention [1]. The geological conditions for shale gas accumulation are the theoretical basis for achieving breakthroughs in shale gas exploration [2–6]. Related literature has systematically evaluated the geological conditions for shale gas accumulation in different regions from the perspectives of sedimentary environment, shale thickness, organic matter content, mineral composition, and gas content [7–9]. Based on this, the main controlling factors affecting the enrichment of shale gas reservoirs have also been determined [10,11].

Breakthroughs have been made in marine shale gas exploration in southern China in the upper Yangtze region [12–14]. However, multiple rounds of exploration have been

carried out in the middle and lower Yangzi regions over the years, but there have been no large-scale gas fields [15–18]. As a key area of marine shale gas in the middle and lower Yangzi regions of China, shale gas exploration in the Chenlei Sag, southeast of Hunan Province, is still lower. In recent years, related literature has shown that the possibility of shale gas accumulation in the Chenlei Depression in terms of hydrocarbon source conditions, reservoir characteristics, and structural evolution [12,19]. Cao et al. studied the hydrocarbon source and porosity of shale in the lower carboniferous Yanguanjie Formation [20]. Luo et al. and Cao et al. studied the mud shale of the Longtan Formation and concluded that the mud shale of the Longtan Formation has good reservoir properties [2]. Yin et al. studied the relationship between geological structural characteristics and coal seams [21]. Shi et al. discussed the tectonic evolution of the area and its relationship with oil and gas accumulation [22].

Above all, some research has been done on the geological conditions for shale gas reservoir formation. However, there are still several issues that need to be addressed. Firstly, the method for determining the main controlling factors of shale gas reservoir formation and geological conditions needs to be explored. In addition, further research is needed on the geological conditions for shale gas accumulation in this study area. Finally, the target shale rock layers in the study area are not yet clear.

In this paper, geological conditions for the formation of shale gas reservoirs in the coal bearing strata of Chenlei Depression, Hunan Province, have been studied. The main target layer for shale gas occurrence has been determined through shale thickness and sedimentary facies analysis. Rock pyrolysis analysis, total organic carbon determination (TOC), kerogen microscopic component identification, mineral X-ray diffraction, scanning electron microscopy, and low-temperature nitrogen adsorption experiments are used to study the geological conditions of shale gas. On this basis, the sedimentary environment/thickness/physical properties (porosity and permeability)/gas content of shale reservoirs in different formations are studied, the basic geological conditions of shale gas in the target rock layers are determined, and favorable areas for shale gas development are determined.

2. Geological Setting and Experimental Methods

2.1. Geological Setting

The study area is located in the southeastern margin of the southeastern Hunan Depression. The Chenlei Depression is a secondary tectonic unit of the southeastern Hunan Depression. It is bounded by a fault zone to the northwest and adjacent to the Hengshan uplift zone, separated by a fault zone to the north and east from the Cathaysia fold belt, and gradually transitioning to the Ningjiang bulge in the southwest in the form of a slope zone (Figure 1). The southeast Hunan Depression is located in the southeast of Hunan Province, geotectonically situated in the south china plate and Yangzi plate junction, as a whole is part of the south china fold system [23]. The study area has experienced the superimposed influence of multi-stage tectonic cycles, and the tectonic lines are crisscrossing and extremely complex, and the folds and faults are developed. The southeastern part of the Chenlei Depression in the Linwu area is a Caledonian fold belt, with structural lines mainly trending NNE~SSW and dipping southeast. It is a tight anticline with a reverse fault parallel to the fold axis, accompanied by the intrusion of granodiorite and diorite. In the central and western parts of the depression, there is an Indonesian fold belt that runs through the entire area from north to south [24–27].

The study area is well developed and distributed from the Proterozoic to Cenozoic (Figure 1). The basement is built of flysch in the Proterozoic and Lower Paleozoic. The lithology is mainly slate and carbonate. From the Devonian Period of the Late Paleozoic Era to the Early Triassic Period of the Mesozoic Era, the deposits were platform-type littoral-shallow marine strata, the lithology was carbonate rock and coal-bearing clastic rock, and a variety of shale strata were developed. The study area entered the continental sedimentary period from the Middle Triassic. Only the Middle Jurassic strata remain today.

The lithology is interbedded sandstone and mudstone. After the Late Mesozoic Cretaceous period, multiple phases of fault depression occurred due to extensional movements caused by mantle uplift, resulting in the deposition of a set of red clastic rocks. The fourth department is the residual slope, and the accumulation layer is not developed [17]. Dark mudstones and shales developed in the Middle to Upper Devonian, Lower Carboniferous, and Upper Permian of the Late Paleozoic within cratonic platform-type coastal shallow marine and coal-bearing clastic rock formations of marine–terrestrial transitional facies.

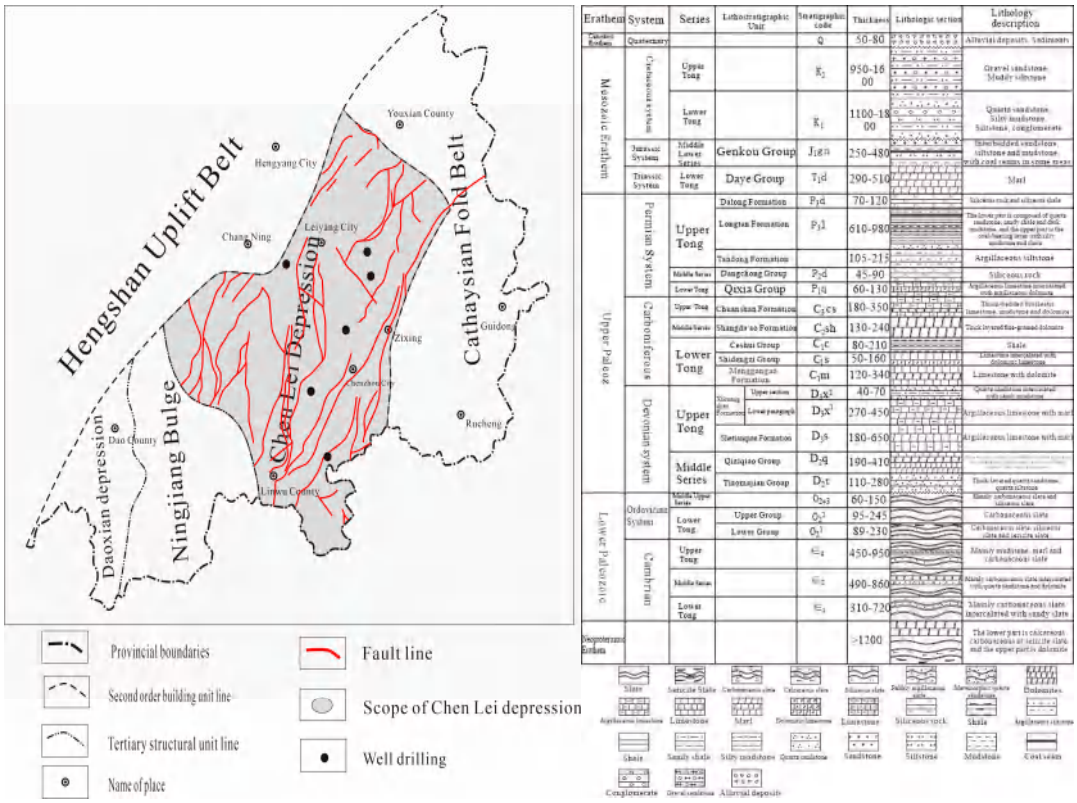

Figure 1. Study area location and stratum formation.

2.2. Experimental Methods

High-pressure mercury intrusion test (HPMI). The most commonly used method to analyze the seepage pore structure of coal reservoirs is the HPMI method. It determines essential information such as porosity, pore structure, pore connectivity, and the pore compression coefficient of coal. This test overcomes capillary forces by gradually increasing the pressure of the mercury injection. The maximum mercury inlet pressure for this test is 14.7 MPa, covering a test pore size range of 3~10,000 nm.

Low-temperature carbon dioxide/nitrogen adsorption test ($LTCO_2/N_2$ GA). In this test, 20 g of each sample is selected and ground to a particle size of 40–60 mesh. $LTCO_2/N_2$ GA is the prevailing method for analyzing the adsorption pore structure of coal reservoirs, providing insights into parameters such as porosity, pore structure, and pore connectivity. The TriStar III 3020 surface area and pore size distribution analyzer was used to detect the surface morphology of adsorption pores at 77 K. The PV and SSA of meso-pores (2~100 nm) are determined using the Barrett–Joyner–Halenda (BJH) model, whereas the PV and SSA of micro-pores (<2 nm) are determined using the density function theory (DFT) model.

3. Results and Discussion

3.1. Sedimentary and Distribution of Shale

From the Late Paleozoic to the Middle Triassic of the Mesozoic, the tectonic environment was stable, and the clastic rock was widely accepted as the main clastic rock.

Several sets of mud shale formations were developed. Among them, the thick dark black carbonaceous shale is developed in the Lower Cambrian Formation of the Carboniferous and upper Longtan Formation of the Permian, and the target shale is the most important potential source of shale gas in the Chenlei Depression.

The sedimentary environment of the Lower Carboniferous Water (LCW) Formation is the sea–land interlocking marina bay lagoon swamp sedimentary system, which develops two sedimentary facies: tidal flat facies subtidal zone and lagoon swamp facies. The subtidal zone of the tidal flat facies is composed of gray siltstone, silty mudstone, and gray black mud shale; it could also contain thin coal seams, which developed in the eastern part of the study area (Figures 2a and 3a). The lagoon swamp facies are composed of fine sandstone, siltstone, sandy mudstone, and thick coal seams interbedded with gray-black to black shale. It is developed in the western part (Figures 2b and 3a). The shale of the Ceshui Formation is distributed in most parts of the depression, but the thickness is thinner, with an average thickness of about 30 m, and the thickness is above the maximum in the southern part of the center of the depression (up to nearly 70 m), corresponding to the lagoon swamp facies deposits, which gradually thin to the north until they peak out.

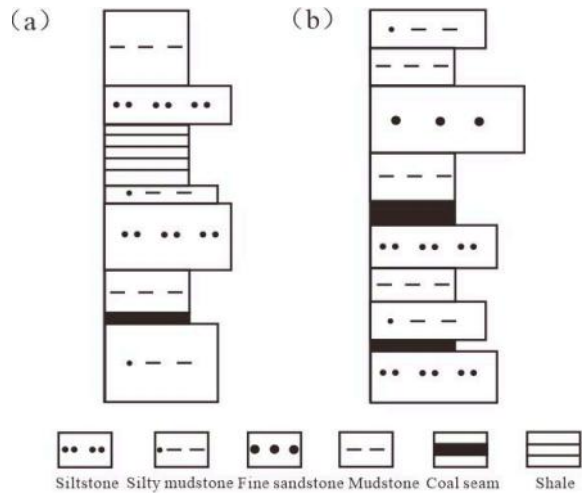

Figure 2. Lithologic combination of different sedimentary facies of Ceshui Formation. ((**a**) Tidal flat facies subtidal zone; (**b**) lagoon swamp facies).

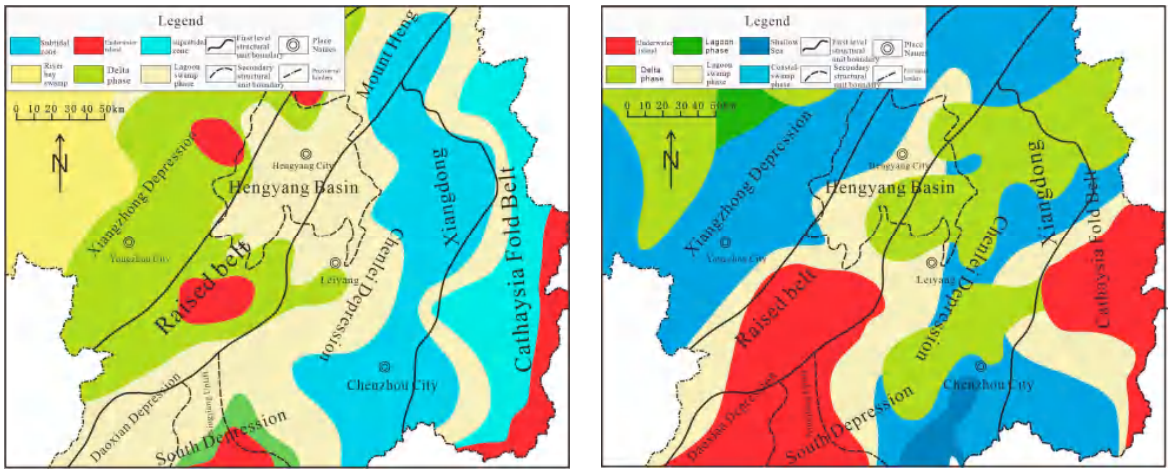

Figure 3. Sedimentary facies plan of Lower Carboniferous Ceshui and Upper Permian Longtan Formation. ((**a**) Ceshui Formation; (**b**) Longtan Formation).

The development types of the Longtan Formation in the Upper Permian include two types: continental sedimentation dominated by delta facies and transitional sedimentation represented by shallow marine, underwater island, lagoon swamp, and coastal swamp facies (Figure 3b). The delta facies are developed in the northwest of the study area, forming a bird-foot-shaped pattern from northeast to southwest. The lithology is composed of thick layers of siltstone and mudstone interbedded with coal seams (Figure 4a). The shallow marine shelf facies are mainly distributed in the southeast. They are primarily affected by the intrusion of seawater from the southeast. The lithology is composed of high calcium content sandy mudstone and mudstone, and the overall thickness of the shale is higher (Figure 4b). The underwater island facies are mainly distributed in the southwest, influenced by ancient landforms, and they are composed of quartz sandstone, medium to fine sandstone, and sand bar facies sedimentation (Figure 4c). The lagoon swamp facies are developed in the central southern part of the Chenlei Depression, and the underwater island facies are northeast. The overall grain size becomes finer, mainly composed of black sandy mudstone, muddy siltstone, and mudstone. The mud shale is thick, with siderite nodules visible (Figure 4d). The coastal swamp facies are distributed in the upper part of the coastline before the ancient continent and are products of the marshification of the coastal plain. They are developed in the eastern and northern parts of the depression, northeast of the lagoon swamp facies, and the lithology is mainly black-gray mud shale and sandy mudstone. The mud shale is thick and is the main environment for mud shale deposition (Figure 4e). The underwater island sand bar is developed from the southwest. The deltaic sediments developed from lagoon-swamp facies to land-facies in the NW direction, indicating a gradual retreat from marine facies to the NE direction of land (Figure 3b).

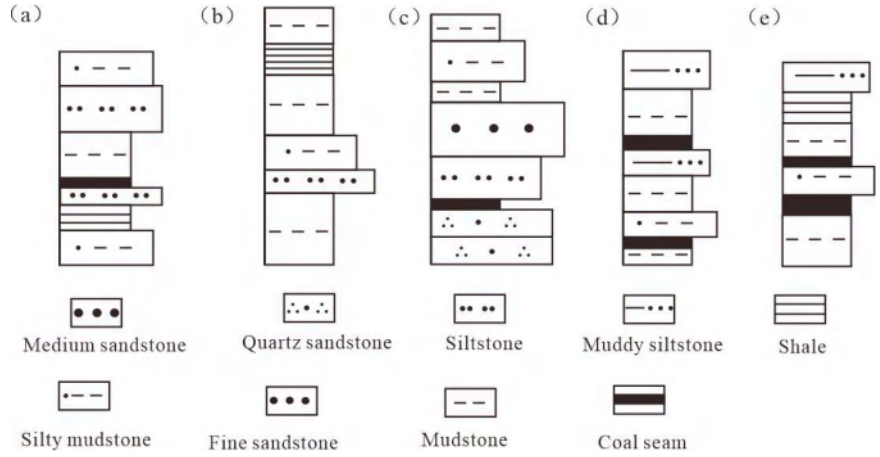

Figure 4. Lithologic combination of different sedimentary facies of Ceshui Formation. ((**a**) Delta facies; (**b**) shallow sea shelf facies; (**c**) underwater island facies; (**d**) lagoon swamp facies; (**e**) coastal swamp facies).

The shale of the Longtan Formation is composed of sandy shale, black shale, carbonaceous shale, etc., and it contains abundant siderite nodules and bands, coexisting with coal seams. The mud shale is almost distributed throughout the entire depression, with a cumulative thickness of large and an average thickness of 100 m(Figure 5a). It is the stratum with the highest thickness of mud shale in the target layer. The thickness of shale in the Longtan Formation matches well with the distribution of sedimentary facies, mainly developed in coal-accumulating environments such as lagoon swamp facies, coastal swamp facies, and delta facies. The maximum thickness of shale in the area between Leiyang and Chenzhou exceeds 200 m (Figure 5b), and it gradually decreases towards the northwest–southeast edges of the depression, with a thickness from 0–50 m.

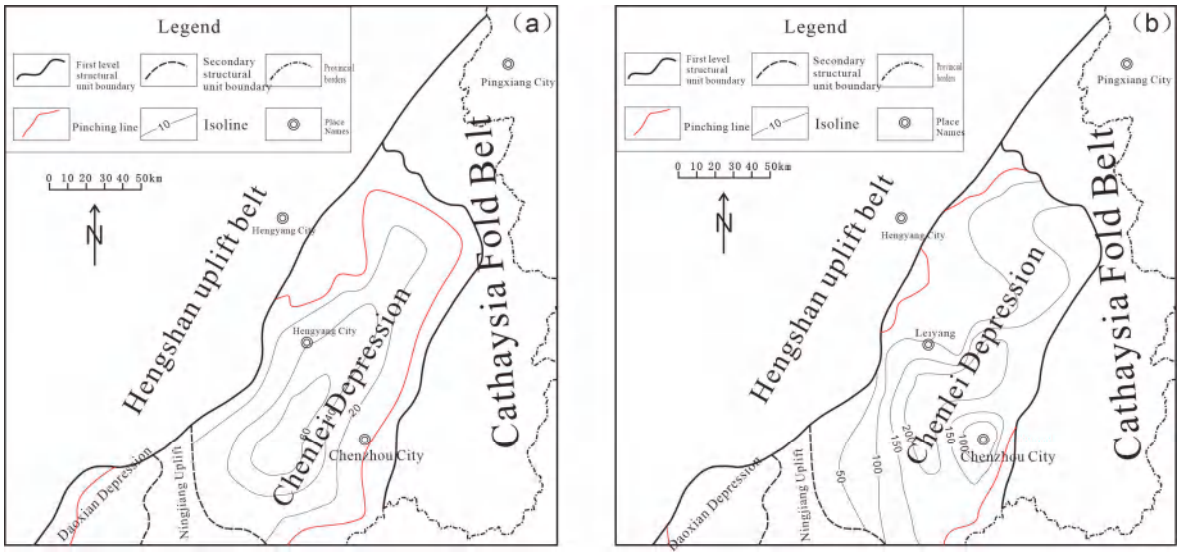

Figure 5. Shale thickness map of geological survey Ceshui and Longtan Formation in Chenlei Sag. ((**a**) Ceshui Formation; (**b**) Longtan Formation).

3.2. Geochemical Characteristics of Shale

3.2.1. Organic Matter Abundance

Based on the total organic carbon (TOC) content of shale in the study area, the TOC values of shale collected from Ceshui and Longtan formations in the Chenlei Depression, southeastern Hunan, are higher (greater than 1%). The TOC of other layers is all below 0.4%, which are source rocks. Therefore, the main hydrocarbon source rock series in the study area belongs to the Ceshui and Longtan formations (Figure 6). Among them, the TOC value of the shale in the Ceshui Formation is the highest, followed by the Longtan Formation. However, they belong to good to excellent high-quality source rocks and have good hydrocarbon generation potential.

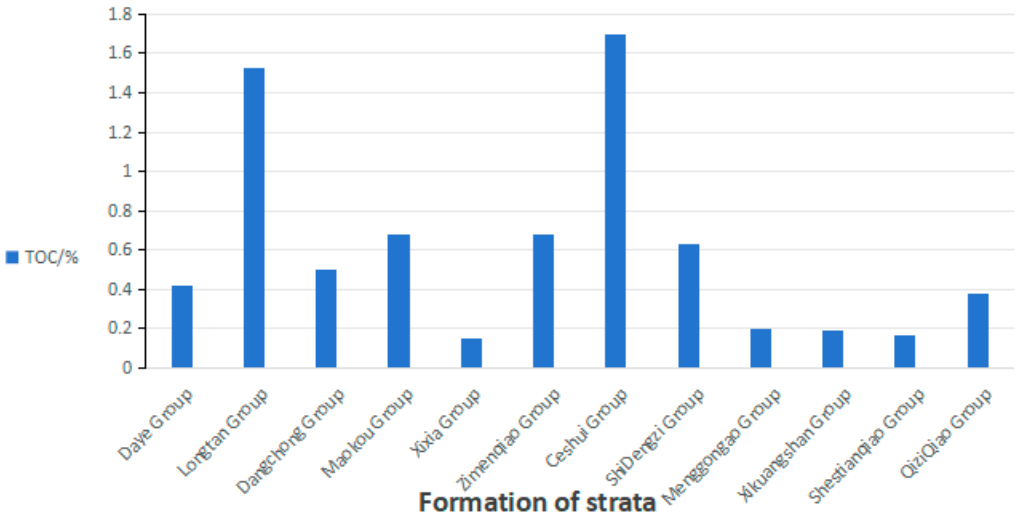

Figure 6. Distribution of organic matter abundance of source rocks in Chenlei Sag.

3.2.2. Organic Matter Type

Based on microscopic identification of components, shale organic matter types in the Chenlei Sag and Longtan Formation are mainly type III and type II_2 (Table 1), and the kerogen type of a small number of samples is type II_1. The Carboniferous-Permian period was a major period of transition from marine to terrestrial phases in geological history. Organisms in the marine and terrestrial transitional phases were unprecedentedly

prosperous. In their chemical composition, lignin, cellulose, and other abundant parent materials were deposited in large quantities, forming a quantitatively superior Type III kerogen, but the contribution of local, deeper organisms evolving into organic matter cannot be ruled out [28,29]. This also shows that the types of organic matter in marine–terrestrial transitional shale are not single. Humic type is the main type, supplemented by mixed type, which provides multiple organic matter for shale hydrocarbon generation.

Table 1. Kerogen macerals of organic-rich shale in Chenlei Sag.

Sampling Layer	Microscopic Component Content/%					Kerogen Type Index (TI)	Kerogen Type
	Sapropel Group	Resin Body	Exinite	Vitrinite	Inert Group		
Ceshui Formation	25	/	56	15	4	37.75	II_2
	21	/	62	14	3	38.5	II_2
Longtan Formation	12	/	66	16	6	27	II_2
	82	/	14	4	/	86	II_1
	64	/	34	2	/	79.5	II_1
	8	/	28	40	24	−32	III
	5	/	20	54	21	−46.5	III
	6	/	30	48	16	−31	III
	8	/	28	50	14	−29.5	III

Rock pyrolysis experiment results show that the Ceshui and Longtan formation shales have TOC values ranging from 1.22 to 10.79 mg/g, with an average of 6.88 mg/g. The hydrogen index values are low, indicating that the organic matter is type III kerogen (Table 2). The reason is that it is the source of humic organic matter. This is related to the excessive maturation of shale (T_{max} is greater than 500 °C) and large-scale occurrences related to hydrocarbon generation. Based on the analysis of kerogen microcomponents and rock pyrolysis, the lithofacies, paleogeography, and geological evolution processes of the region have been studied. The results show that the main source of organic matter in shale is input from terrestrial higher plants, and the main types of organic matter are II_2 and III, which are favorable for the generation of natural gas.

Table 2. Pyrolysis and $R_{o,max}$ data of shale samples from Ceshui and Longtan formations in Chenlei Sag.

Sampling Layer	Sampling No.	Maximum Temperature T_{max} (°C)	Soluble Hydrocarbons S_1 (mg/g)	Pyrolysis Hydrocarbons S_2 (mg/g)	HI (mg/g TOC)	$R_{o,max}$ (%)	Maturity Assessment
Ceshui Formation	CLZH-06	584	0.03	0.84	9.23	2.91	Overmature
	DCLC-03	587	0.04	0.35	9.54	2.99	Overmature
	XJZ-04	585	0.03	0.05	4.39	2.95	Overmature
	ZK3206-87	587	0.03	0.11	4.33	2.37	Overmature
	XDY-74	540	0.04	0.12	15.38	3.51	Overmature
	KJC-68	539	0.05	0.03	1.92	2.75	Overmature
	GML-63	553	0.02	0.08	5.82	2.80	Overmature
	JZC-41	532	0.08	0.52	6.14	3.23	Overmature
	TMC-27	536	0.04	1.1	7.20	3.00	Overmature
	LMQ-08	563	0.03	0.68	5.34	3.12	Overmature

Table 2. *Cont.*

Longtan Formation	WBD-01	586	0.05	0.09	6.72	2.86	Overmature
	WBD-05	595	0.03	0.11	4.20	2.99	Overmature
	MT-YP-09	585	0.02	0.09	9.47	2.16	Overmature
	MT-YP-11	582	0.02	0.15	10.79	2.08	Overmature
	MT-YP-19	587	0.01	0.03	3.90	2.19	Overmature
	MT-YP-21	593	0.02	0.13	7.10	2.55	Overmature
	MT-YP-25	589	0.01	0.06	5.00	2.36	Overmature
	MT-YP-35	528	0.12	5.97	10.14	2.08	Overmature
	MT-YP-38	591	0.01	0.36	7.88	2.23	Overmature
	MT-YP-40	595	<0.01	0.01	1.22	2.37	Overmature

3.2.3. Maturity

In order to become a potential shale gas exploration target, the maturity of shale must enter the gas-producing window [30,31]. $R_{o,max}$ of shale samples indicate that the shale collected from Ceshui and Longtan formations has entered the large-scale gas production stage. The $R_{o,max}$ value of shale from the Ceshui Formation is between 2.37 and 3.51%, with an average of 2.95%. The $R_{o,max}$ value of all samples is greater than 2%. It indicates that the samples of the Ceshui Formation are all in the overmature stage. The sample $R_{o,max}$ of the Longtan Formation was lower than that of the Ceshui Formation, ranging from 1.34 to 2.99%, with an average of 2.16%. Most of the samples' $R_{o,max}$ is above 2%, indicating that most of the samples are in the over-mature stage.

In short, the shale of the Chenlei Sag's hydrometric and Longtan Formation has a high organic matter abundance, and its types are humic, such as II_2 and III types. The overall maturity is high and has exceeded the high-mature to over-mature stage. It has begun to generate large-scale gas and has a certain thickness. It is a favorable source rock for large-scale shale gas generation in the study area.

3.3. Shale Reservoir Characteristics

3.3.1. Mineral Composition Characteristics

Shale gas is generally adsorbed on the surface of organic matter, kerogen, and clay minerals, or is free in micropores and microfractures. The mineral composition is the basis for an in-depth study of the adsorption capacity and matrix porosity of shale reservoirs [32]. The mineral components of shale mainly include brittle minerals (quartz, calcite, feldspar, etc.) and clay minerals such as illite, kaolinite, chlorite, and illite mixed layers. Brittle minerals mainly control the development of fractures and affect the reservoir space and permeability of the reservoir, which in turn determines the effect of reservoir fracturing. A certain amount of clay minerals can adsorb gas [33,34]. Therefore, the key to shale gas research is to find mud shale with high organic matter content, high brittle mineral content, moderate clay mineral content, and crack development that is easy to artificial fracturing.

The whole rock mineral composition of the Ceshui Formation in Chenlei Depression is mainly quartz and clay minerals; some samples are rich in calcite, and the content of feldspar is low. The brittle mineral content is 30–80% and the clay mineral content is 10–40% (Figure 7). The whole rock mineral composition of the Longtan Formation is mainly quartz and clay minerals (Figure 8). Some samples are rich in calcite; the content of brittle minerals is 20–60%; and the content of clay minerals is 20–70%, which is not conducive to the formation of fractures but is conducive to the adsorption of shale gas. The content of brittle minerals in the shale of the Ceshui and Longtan formations in the Chenlei Depression is more than 40%, which is conducive to artificial fracturing in the later stage. Appropriate clay minerals are beneficial to gas adsorption.

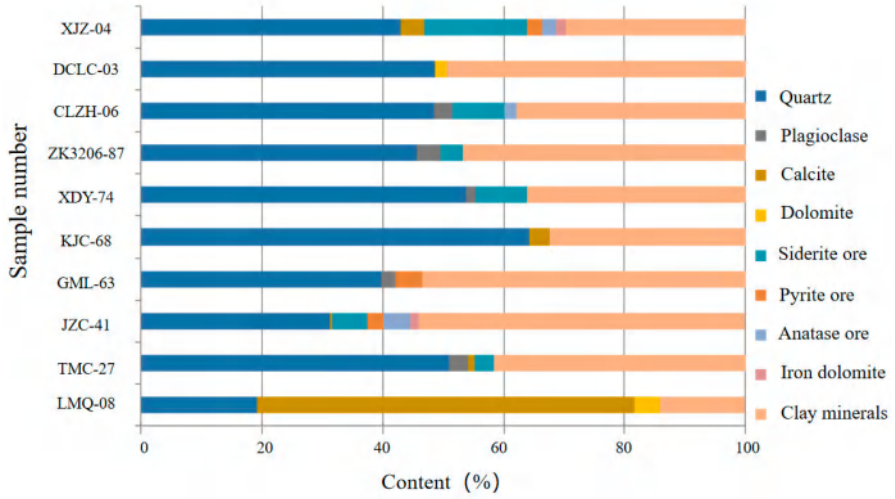

Figure 7. Bar chart of X-ray diffraction (whole rock) test results of organic-rich shale of Ceshui Formation in the study area.

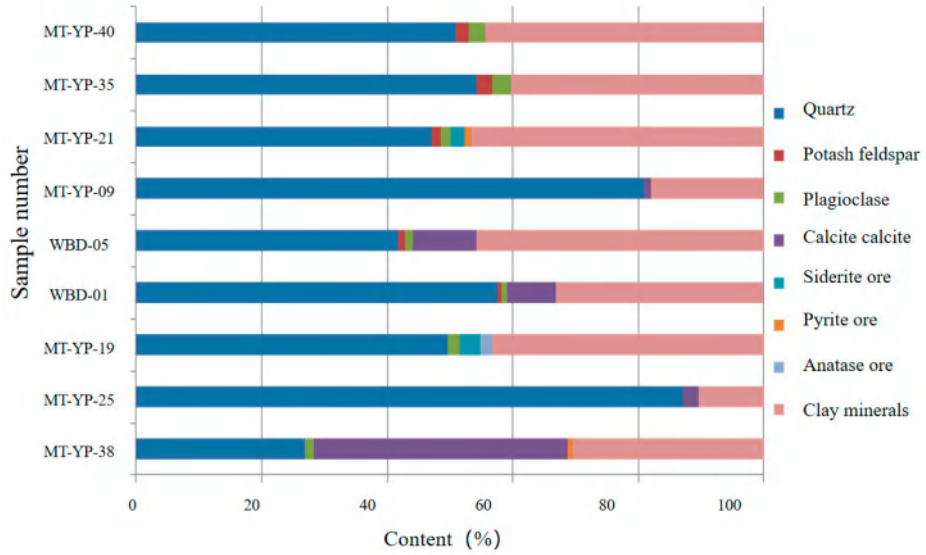

Figure 8. Bar chart of X-ray diffraction (whole rock) test results of organic-rich shale of Longtan Formation in Chenlei Sag.

3.3.2. Porosity and Permeability Characteristics

Shale reservoirs have typical characteristics of low porosity and low permeability [35], with porosity often less than 10% and permeability generally less than 1×10^{-3} μm^2. Physical property analysis of shale samples from the Ceshui and Longtan formations in the Chenlei Sag shows that the porosity and permeability of the shale from the Ceshui and Longtan formations are generally low (Figure 9), among which the porosity of the shale from the Ceshui Formation is 0.5~5.4%, with an average of 2.8%. Samples with porosity less than 3% account for more than 65% of the total samples. The permeability is 0.0002~1×10^{-3} μm^2, with an average of 0.013×10^{-3} μm^2, and more than 50%. The sample permeability is lower than 0.01×10^{-3} μm^2. The Longtan Formation mud shale has good porosity and permeability characteristics, with a porosity between 1.1% and 4.8%, with an average of 26%, and a permeability of 0.004–0.46×10^{-3} μm^2, with an average of 0.045×10^{-3} μm^2. In contrast, the porosity of major gas-producing shale reservoirs in the United States is concentrated at 4.22% to 6.51%, and the permeability is generally lower than 0.1×10^{-3} μm^2 [36]. The porosity of the mud shale in the Chenlei Sag is slightly lower than that in the Longtan Formation, and the permeability is not much different, indicating that the mud shale reservoir characteristics in the study area are better.

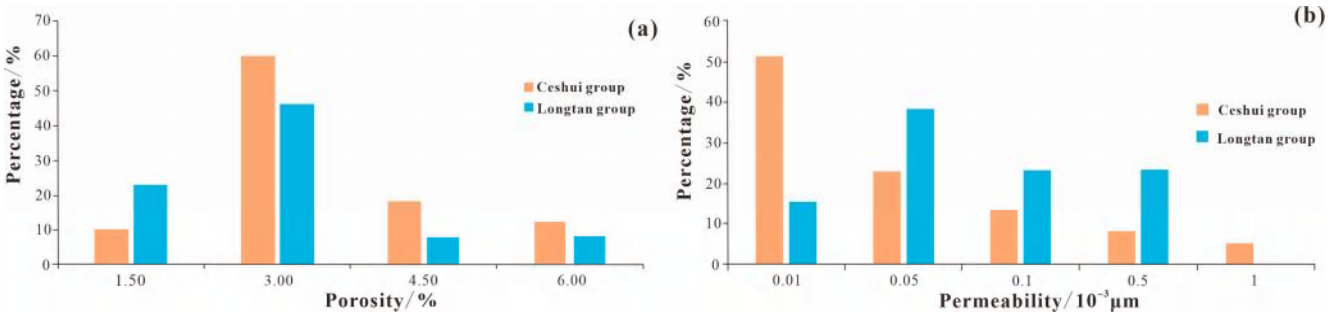

Figure 9. Distribution of porosity and permeability of Ceshui and Longtan formations in Chenlei Sag. ((**a**) Porosity Characteristics; (**b**) Permeability Characteristics).

The low-temperature nitrogen adsorption experimental data also show (Table 3) that the overall pore structure of the shale in the Chenlei Sag's Ceshui and Longtan formations is better, and its specific surface area and total pore volume are both higher (the average specific surface area is 12.21 m^2/g, respectively) and 8.36 m^2/g. The total pore volumes are 24.87 × 10^{-3} cm^3/g and 14.32 × 10^{-3} cm^3/g, respectively, and the most probable pore diameters are larger (7.05 and 4.07 nm, respectively), which is beneficial to the development of shale gas. It has good adsorption and storage potential.

Table 3. Statistics of experimental data of low-temperature nitrogen adsorption of shale samples.

Sampling Layer	Sampling No.	Specific Surface Area/m^2/g	The Most Probable Aperture/nm	Total Pore Volume/10^{-3} cm^3/g
Ceshui Formation	CLZH-06	12.61	4.05	20.49
	DCLC-03	11.38	4.07	16.33
	XJZ-04	12.84	4.04	20.64
	ZK3206-87	15.64	18.80	39.12
	XDY-74	10.81	18.79	47.21
	KJC-68	12.59	18.88	27.54
	GML-63	12.79	5.87	18.63
	JZC-41	12.88	5.37	20.04
	TMC-27	13.97	3.71	13.52
	LMQ-08	12.87	4.84	16.85
Longtan Formation	WBD-01	16.698	4.042	26.07
	WBD-05	13.073	4.065	19.65
	MT-YP-09	6.987	4.066	14.87
	MT-YP-11	7.602	4.3	11.53
	MT-YP-19	2.83	4.03	5.947
	MT-YP-21	7.668	4.068	16.23
	MT-YP-25	7.017	4.048	16.4
	MT-YP-35	8.489	4.037	11.58
	MT-YP-38	5.368	4.059	11.34
	MT-YP-40	7.533	4.063	18.41

3.3.3. Pore and Crack Characteristics

The development of shale pores and fractures in the reservoir directly affects the storage performance of the reservoir and has a great impact on the accumulation, later

preservation, and reservoir modification of shale gas [37]. This paper divides the pores in the Chenlei Sag Ceshui and Longtan formations into inorganic pores, organic pores, and micro-cracks based on their development locations and pore origins. Inorganic pores are further divided into intergranular pores, intercrystalline pores, and intragranular pores.

Intergranular pores in shale are developed at the contact point of mineral particles, which are mainly lamellar clay minerals (Figure 10a,b). They are characterized by concentrated development, complex cementation, poor sorting, and diverse pore shapes, with polygonal shapes and elongated strip shapes being the main ones. In the shale samples, the pyrite intergranular pores are well developed (Figure 10c), and the pyrite is mostly in the form of a regular cube or pentagonal dodecahedron. Organic matter and partial symbiosis. The integrate pores developed in the particles, and the integrate pores developed well in the clay mineral layer, mainly the Imon mixed layer. (Figure 10d). The pores formed by other minerals are few, and the dissolution pores of carbonate minerals can be seen under the microscope (Figure 10e).

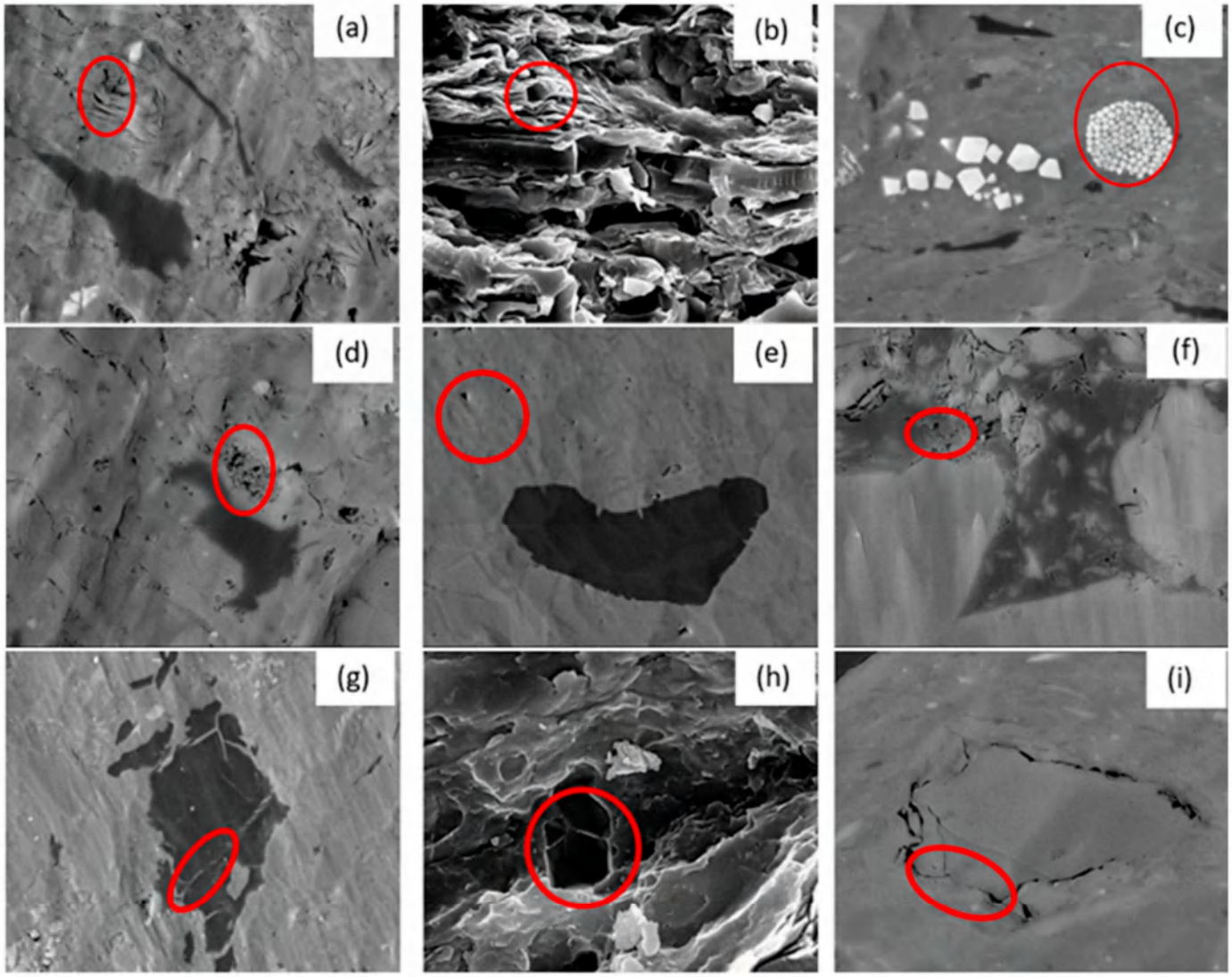

Figure 10. Pore morphology and characteristics of shales from the Ceshui and Longtan formations in Chenlei Sag. ((**a**) Flaky clay mineral interstices; (**b**) illite intergranular pores; (**c**) strawberry pyrite, intergranular pores; (**d**) mineral dissolution pores; (**e**) carbonate mineral dissolution pores; (**f**) organic matter pores; (**g**) organic matter micro-cracks are filled; (**h**) asphaltene body mold pores; (**i**) Micro-cracks).

Organic matter pores are ubiquitous in shale [38], with pore sizes ranging from a few nanometers to hundreds of nanometers. The connectivity between pores is excellent, and most organic matter pores are distributed in circular or elliptical shapes (Figure 10f). In some samples, an organic matter particle with a diameter of several microns can contain many nanopores, but some organic matter does not develop pores. Asphaltene mold pores formed by mineral exfoliation were found in some samples (Figure 10h).

Microfractures play an important role in the seepage of shale gas and are the bridge connecting microscopic pores and macroscopic fractures, which are generally micron-scale [39]. Experiments have found that both organic matter particles and clay minerals can develop micro-cracks. Micro-cracks developed inside organic matter are generally straight, small, and do not extend long. Some organic matter micro-cracks are filled with minerals (Figure 10g). The shapes of micro-cracks between minerals are diverse (Figure 10i). Some of them may be formed due to dehydration and shrinkage of the mineral matrix. They are densely developed, mostly obtuse triangle shapes, with large pore sizes and good connectivity.

3.4. Gas-Bearing Characteristics of Shale

Gas-bearing property is an important criterion for evaluating shale gas resource potential and whether it has development value [40]. The desorption method was used to perform on-site analysis on the shale cores of the Ceshui and Longtan formations obtained from four drilling wells in the study area. The results showed that the gas content of the shale in the Ceshui Formation varied from 0.31 to 2.6 cm^3/g, with an average of 1.6 cm^3/g. The gas content of the Longtan Formation shale varies from 0.42 to 5 cm^3/g, with an average of 2.1 cm^3/g. The overall gas content is high, confirming that the shale gas of the Ceshui and Longtan formations in the study area has good resource potential. The isothermal adsorption experiment shows that the maximum adsorption volume of the shale Ceshui Formation is balanced at 1~2 MPa, and the maximum adsorption capacity is between 1.2~6 cm^3/g, showing good adsorption capacity (Figure 11a,b). The Longtan Formation of shale samples maximum adsorption volume in the balance of 1.5 MPa, adsorption capacity of 0.5~5.2 cm^3/g (Figure 11c,d). The shale of the Ceshui and Longtan formations is the lowest industrial standard at 1 cm^3/g under pressure less than 2 MPa, showing good mining potential.

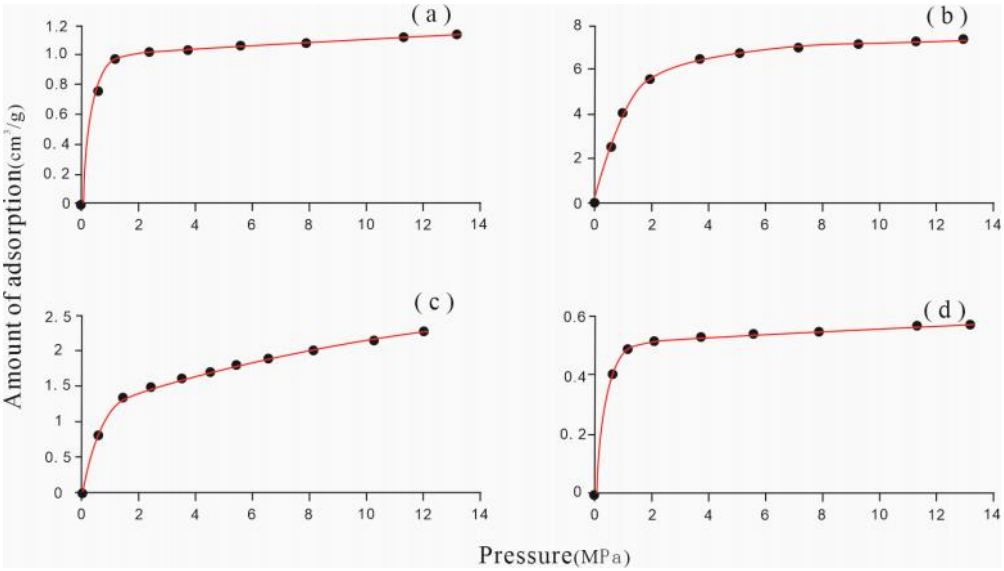

Figure 11. Typical isotherm adsorption curve of shales in Cehui and Longtan formations of Chenlei Sag. ((**a**) the shale Ceshui Formation a; (**b**) the shale Ceshui Formation b; (**c**) the Longtan Formation of shale sample c; (**d**) the Longtan Formation of shale sample d).

Based on the isothermal adsorption results and analytical gas content results, there are good shale gas displays in the study area, which has the potential to form a good shale gas reservoir.

4. Conclusions

In this paper, we discuss total organic carbon determination (TOC), kerogen microscopic component identification, mineral X-ray diffraction, scanning electron microscopy, and low-temperature nitrogen adsorption experiments. The geological conditions for the formation of shale gas reservoirs in the coal bearing strata of Chenlei Depression, Hunan Province, have been studied in detail. Moreover, the main shale gas-bearing strata and their physical characteristics in the coal bearing strata of Chenlei Depression, Hunan Province, have been studied. On this basis, the gas content of shale in the water and Longtan formations has been determined by using high-temperature and high-pressure isothermal adsorption tests. The results are as follows:

(1) The shale thickness of the water measuring group is lower, with an average thickness of about 30 m. The thickness is highest in the southern part of the depression center (nearly 70 m), then decreases towards the north. In the Leiyang and Chenzhou areas, the shale thickness of the Longtan Formation is the highest (up to 200 m), decreasing towards the northwest and southeast edges of the depression with a thickness from 0–50 m.

(2) The TOC values of the water measurement group and the Longtan group are higher, both greater than 1%, while the other layers are below 0.4%. The organic matter types are type III and II_2, and kerogen in a small amount of samples belongs to type II_1. The maturity of shale is higher, and it has entered the stage of large-scale gas generation. The Ro of the sample collected from the water measurement group is 2.37–3.51%, with an average of 2.95%.

(3) The mineral composition of the water measurement group is composed of quartz and clay minerals, with some samples rich in calcite and a low content of feldspar. The content of brittle minerals is higher, distributed in 30~80%, while the content of clay minerals is moderate, mostly distributed at 10~40%. The mineral composition of the Longtan Formation is composed of quartz and clay minerals.

(4) The overall pore structure of the water measurement group and Longtan group shale is good, with a higher specific surface area and total pore volume (average specific surface area is 12.21 and 8.36 m^2/g, respectively), which is conducive to the occurrence of shale gas and has good adsorption and storage potential. The gas content of the water measurement group varies from 0.31 to 2.6 cm^3/g, with an average of 1.6 cm^3/g; the gas content of the Longtan Formation varies from 0.42 to 5 cm^3/g, with an average of 2.1 cm^3/g. It indicates that the water measurement group and the Longtan Formation shale gas in the study area have good resource potential.

Author Contributions: Methodology, F.L.; Software, K.W.; Formal analysis, Z.L. and J.D.; Resources, S.G.; Data curation, N.C.; Writing—review & editing, J.B.; Supervision, J.Z. (Junjian Zhang); Project administration, J.Z. (Jian Zhan). All authors have read and agreed to the published version of the manuscript.

Funding: This research was sponsored by the Research Project of Hunan Institute of Geology, Study on Geological Carbon Sequestration Potential of Lianshao Basin (HNGSTP202310).

Data Availability Statement: Data are contained within the article.

Conflicts of Interest: The authors declare no conflict of interest.

References

1. Chandra, D.; Bakshi, T.; Bahadur, J.; Hazra, B.; Vishal, V.; Kumar, S.; Sen, D.; Singh, T.N. Pore morphology in thermally-treated shales and its implication on CO_2 storage applications: A gas sorption, SEM, and small-angle scattering study. *Fuel* **2023**, *331*, 125877. [CrossRef]
2. Luo, X.; Li, Y.; Wu, C. Characteristics of mud shale reservoirs in Upper Permian Longtan Formation of Southeast Hunan depression, China. *J. Chengdu Univ. Technol. (Sci. Technol. Ed.)* **2013**, *40*, 588–594.

3. Wang, E.; Guo, T.; Li, M.; Li, C.; Dong, X.; Zhang, N.; Feng, Y. Exploration potential of different lithofacies of deep marine shale gas systems: Insight into organic matter accumulation and pore formation mechanisms. *J. Nat. Gas Sci. Eng.* **2022**, *102*, 104563. [CrossRef]
4. Li, J.; Li, H.; Yang, C.; Wu, Y.; Gao, Z.; Jiang, S. Geological Characteristics and Controlling Factors of Deep Shale Gas Enrichment of the Wufeng-Longmaxi Formation in the Southern Sichuan Basin, China. *Lithosphere* **2022**, *2022*, 4737801. [CrossRef]
5. Zhang, J.; Wang, H.; Vandeginste, V.; Miao, H.; Guo, Y.; Ji, Y.; Liu, P.; Peng, Y. Effect of litho-facies on nano-pore structure of continental shale in shuinan formation of Jiaolai Basin. *Geoenergy Sci. Eng.* **2023**, *228*, 212020. [CrossRef]
6. Tang, Q.; Zhou, L.; Chen, L.; Tan, X.; Wang, G. Development Characteristics of Shale Lithofacies in the Longmaxi Formation and their Main Controlling Factors in the Changning Area, South Sichuan Basin, SW China. *Front. Earth Sci.* **2021**, *9*, 775657. [CrossRef]
7. Li, J.; Li, H.; Yang, C.; Ren, X.; Li, Y. Geological Characteristics of Deep Shale Gas and Their Effects on Shale Fracability in the Wufeng-Longmaxi Formations of the Southern Sichuan Basin, China. *Lithosphere* **2023**, *2023*, 4936993. [CrossRef]
8. Fang, R.; Jiang, Y.; Sun, S.; Luo, Y.; Qi, L.; Dong, D.; Lai, Q.; Luo, Y.; Jiang, Z. Controlling factors of organic matter accumulation and lacustrine shale distribution in Lianggaoshan Formation, Sichuan Basin, SW China. *Front. Earth Sci.* **2023**, *11*, 1218215. [CrossRef]
9. Zhang, P.; Lu, S.; Li, J.; Wang, J.; Zhang, J.; Chen, G.; Huang, H.; Zhi, Q.; Yin, Y. Microscopic characteristics of pore-fracture system in lacustrine shale from Dongying Sag, Bohai Bay Basin, China: Evidence from scanning electron microscopy. *Mar. Pet. Geol.* **2023**, *150*, 106156. [CrossRef]
10. Wang, E.; Li, Y.; Guo, T.; Xiong, L.; Dong, X.; Wang, T.; Shi, K. Geological Features, Paleosedimentary Environment, and Organic Matter Accumulation Mechanisms of the Lacustrine Shale Oil System: A Case Study of the Jurassic Dongyuemiao Member in the Sichuan Basin. *Processes* **2023**, *11*, 2638. [CrossRef]
11. Xu, H.; Madina, M.; Yu, S.; Wang, Z.; Cheng, H.; Jiang, T. Geological Characteristics of Shale Reservoir of Pingdiquan Formation in Huoshaoshan Area, Junggar Basin. *Processes* **2023**, *11*, 2126. [CrossRef]
12. Cai, Z.; Huang, Q.; Xia, B.; Xiang, J. Differences in shale gas exploration prospects of the upper Yangtze Platform and the lower Yangtze Platform: Insights from computer modelling of tectonic development. *J. Nat. Gas Sci. Eng.* **2016**, *36*, 3642–3653. [CrossRef]
13. Shi, W.; Wang, X.; Wang, Z.; Shi, Y.; Feng, A.; Chen, N. A study on the relationship between graptolites and shale gas enrichment in the Wufeng–Longmaxi Formations of the Middle–Upper Yangtze region in China. *Arab. J. Geosci.* **2020**, *13*, 205–217. [CrossRef]
14. Zhao, L.; Li, Y.; Zou, C.; Zhao, S.; Wu, C. Palaeoweathering Conditions, Provenance, and Tectonic Setting of the Early Silurian Longmaxi Formation in the Upper Yangtze Region (Southern China): Evidence from Geochemistry. *Minerals* **2023**, *13*, 576. [CrossRef]
15. Wang, T.; Xu, Z.; Yuan, K.; Wang, X.; Ge, M. Paleoenvironment and shale gas potential of the Carboniferous Dawuba and the Cambrian Niutitang shales in the Upper Yangtze Platform, South China. *Front. Earth Sci.* **2024**, *12*, 1404178. [CrossRef]
16. Liu, W.; Gao, P.; Xiao, X.; Zhao, Y.; Xing, Y.; Li, J. Variable depositional environments and organic matter enrichment of Early Cambrian shales in the Middle Yangtze region, South China. *J. Asian Earth Sci.* **2024**, *259*, 105874. [CrossRef]
17. Qian, J.; Ma, R.; Bu, S.; Xu, F. Lithofacies-paleogeographical characteristics of marine shale series of strata in Xiangzhong and Xiangdongnan depressions, Hunan, China. *J. Chengdu Univ. Technol. (Sci. Technol. Ed.)* **2013**, *40*, 688–695.
18. Lin, D.; Xi, Z.; Tang, S.; Lash, G.G.; Guo, Q.; Wang, H.; Zhu, Y. Organic matter enrichment in shale deposited proximal to paleo-uplifts and its impact on shale gas exploration.Palaeogeography, Palaeoclimatology. *Palaeoecology* **2024**, *633*, 111900. [CrossRef]
19. Zhang, B.; Yao, S.; Hu, W.; Wu, Y.; Yu, W.; Yu, H. Hydrocarbon source rock characteristics and shale gas potential of Permian marine shales in the Lower Yangtze region of South China. *AAPG Bull.* **2024**, *108*, 719–749. [CrossRef]
20. Taotao, C.; Mo, D.; Hu, L.; Yanran, H.; Hurssthouse, S. Shale gas potential of Yanguanjie Formation and Longtan Formation in central and southeastern Hunan Province. *Coal Geol. Explor.* **2019**, *47*, 94–103.
21. Yin, S.; Xiao, J. Relationship between Geological Structure Characteristics and Coal Seams in Chenlei and Lianshao Coal-bearing Areas. *West-China Explor. Eng.* **2014**, *26*, 138–141.
22. Shi, W.; Li, Q.; Li, J. Structural evolution and hydrocarbon accumulation in Southeast Hunan Depression. *Land Resour. Her.* **2006**, *S1* (Suppl. S1), 15–21.
23. Xu, G.S.; Zhang, Z.; Luo, X.P.; Zhang, W.; Bu, S.F. Gas-bearing characteristics and affected factors of Upper Paleozoic shale in depressions of Central Hunan and Southeast Hunan, China. *J. Chengdu Univ. Technol. (Sci. Technol. Ed.)* **2013**, *40*, 577–587.
24. Ahmadi, Y.; Mansouri, M.; Jafarbeigi, E. Improving Simultaneous Water Alternative Associate Gas Tests in the Presence of Newly Synthesized γ-Al2O3/ZnO/Urea Nano-Composites: An Experimental Core Flooding Tests. *ACS Omega* **2023**, *8*, 1443–1452. [CrossRef]
25. Zhang, P.F.; Wu, H.; Lu, S.F.; Wang, J.J.; Li, W.B.; Yin, Y.J.; Zhou, N.W.; Zhang, J.J.; Chen, G.H.; Yi, Y.J.; et al. The occurrence of pore fluid in shale-oil reservoirs using nuclear magnetic resonance: The Paleogene Funing Formation, Subei Basin, Eastern China. *Mar. Pet. Geol.* **2024**, *167*, 106986. [CrossRef]
26. Xu, J.; Guo, W.; Yang, B.; Ma, D.; Zhao, L.; Liu, H.; Ji, H.; Tao, H. Nanopore Characteristics of the Cambrian Niutitang Formation Organic-Rich Shales in the Middle Yangtze Region and Its Formation Controlling Factors. *Geofluids* **2023**, *2023*, 2070913. [CrossRef]
27. Hu, L.; Xue, X.; Zhang, Y.; Ma, Y.; Yunnan CBM Resources Exploration and Development Co., Ltd. Accumulation Conditions Analysis of Shale Gas of Upper Permian Longtan Formation of Xuanwei Area in Eastern Yunnan. *Unconv. Oil Gas* **2018**, *5*, 29–33.

28. Wang, Z.; Xiao, Z.; Yang, R.; Huang, Y. A Study on Carboniferous Ceshui Formation Shale Gas Generation Material Basis in Central Hunan. *Coal Geol. China* **2013**, *25*, 19–21+31.
29. Zhou, N.; Lu, S.; Zhang, P.; Wang, M.; Xiao, D.; Li, J.; Chen, G.; Wang, J.; Zhang, Y.; Lin, Z. Continental shale gas dynamic enrichment and evolution over geological time. *Int. J. Coal Geol.* **2021**, *251*, 103914. [CrossRef]
30. Zhang, P.; Lu, S.; Wang, J.; Li, W.; Yin, Y.; Chen, G.; Zhou, N.; Wu, H. Microscopic occurrence and distribution of oil and water in situ shale: Evidence from nuclear magnetic resonance. *Petrol. Sci.* **2024**, 1995–8226. [CrossRef]
31. Zhang, H.; Wang, X.; Jia, C.; Li, J.; Meng, Q.; Jiang, L.; Wang, Y.; Bai, X.; Zheng, Q. Whole petroleum system and hydrocarbon accumulation model in shallow and medium strata in northern Songliao Basin, NE China. *Pet. Explor. Dev. Online* **2023**, *50*, 784–797. [CrossRef]
32. Qi, P.; Xue, P.; Zhao, Q. Research on evaluation methods and characteristics of shale gas reservoirs in Shanxi formation in Xiasiwan area, Ordos basin. *Unconv. Oil Gas* **2019**, *6*, 10–17.
33. Zou, C.; Dong, D.; Wang, S.; Li, J.; Li, X.; Wang, Y.; Li, D.; Cheng, K. Geological characteristics, formation mechanism, and resource potential of shale gas in China. *Pet. Explor. Dev.* **2010**, *37*, 641–653. [CrossRef]
34. Ma, B.; Hu, Q.; Yang, S.; Zhang, T.; Qiao, H.; Meng, M.; Zhu, X.; Sun, X. Pore structure typing and fractal characteristics of lacustrine shale from Kongdian Formation in East China. *J. Nat. Gas Sci. Eng.* **2021**, *85*, 103709. [CrossRef]
35. Lan, B.; Zhao, F.; Li, S.; Jiang, H.; Liu, S.; Zhang, Z. Investigation of the Enrichment and Accumulation of Normal Pressure Shale Gas in Anchang Syncline Outside of Sichuan Basin. *Front. Earth Sci.* **2022**, *9*, 802142. [CrossRef]
36. Dong, C.Y.; Xie, Z.Y.; Zhu, H.; Guo, J.Y.; Zhang, L.; Dai, X.; Yang, C.L. New Insight for Gas Source and Gas Accumulation Modes of Middle Permian in Central Sichuan Basin. *J. Xi'an Shiyou Univ. (Nat. Sci.)* **2017**, *32*, 18–23, 31.
37. Wu, C. Study on fractal features of shale pore based on low-temperature nitrogen absorption experiment. *Unconv. Oil Gas* **2018**, *5*, 14–20.
38. Zhang, T.; Zhang, X. Comparative study on qualitative and quantitative methods for shale pore characterization. *Nat. Gas Explor. Dev.* **2017**, *40*, 34–43.
39. Xiao, D.; Lu, S.; Fang, D. Pore connectivity of marine high-maturity shale gas reservoirs: A case study in Longmaxi formation, Pengshui area. *Reserv. Eval. Dev.* **2019**, *9*, 45–53.
40. Long, P.Y.; Zhang, J.C.; Tang, X.; Nie, H.K.; Liu, Z.J.; Han, S.B.; Zhu, L.L. Feature of Muddy Shale Fissure and Its Effect on Shale Gas Exploration and Development. *Nat. Gas Geosci.* **2011**, *22*, 525–532.

Ore Geology Reviews 171 (2024) 106172

Contents lists available at ScienceDirect

Ore Geology Reviews

journal homepage: www.elsevier.com/locate/oregeorev

Dual-mineralization in the intracontinental Jiangnan Orogen, South China: Evidence from textures and in-situ trace elements and oxygen analysis of quartz from the Woxi Au-Sb-W deposit

Bin Li [a,c,d,*], Deru Xu [b], Daoyuan Bai [c], Guoxiang Chi [e], Hongsheng He [a], Yongjun Shao [d], Teng Deng [b], Junfeng Dai [b], Shaohao Zou [b], Jianfeng Chen [c]

[a] Geophysical and Geochemical Survey Institute of Hunan Province, Changsha 410116, China
[b] State Key Laboratory of Nuclear Resources and Environment, East China University of Technology, Nanchang 330013, China
[c] Geological Survey Institute of Hunan Province, Changsha 410114, China
[d] Key Laboratory of Metallogenic Prediction of Nonferrous Metals and Geological Environment Monitoring, Ministry of Education, Central South University, Changsha 410083, China
[e] Department of Geology, University of Regina, Regina, SK S4S 0A2, Canada

ARTICLE INFO

Keywords:
Quartz texture
LA-ICP-MS trace elements
SIMS oxygen isotopes
Woxi Au-Sb-W deposit
Jiangnan Orogen

ABSTRACT

The Jiangnan Orogenic Belt (JOB), situated in the interior of the South China Block (SCB), harbors numerous gold-polymetallic deposits, but the ore genesis has been a long-standing controversy. This study examines the Woxi super-large gold deposit in the middle JOB, which is characterized by simultaneous large-scale antimony-tungsten mineralization. The investigation shows that the Woxi ore deposit have developed multiple-stage quartz, i.e., Qz1 (early quartz-carbonate, stage I), Qz2 (quartz-wolframite-scheelite, stage II), Qz3a (quartz-gold-pyrite, early stage III), Qz3b (quartz-stibnite-scheelite, late stage III) and Qz4 (late quartz-carbonate, stage IV). We conducted SEM-CL texture imaging, LA-ICP-MS trace element, and SIMS oxygen isotope analysis on the quartz samples from the main mineralization stages (mainly Qz2 and Qz3). The results reveal a dual mineralization process of the Woxi gold-antimony-tungsten deposit. In the initial stage, the quartz (Qz2) exhibits intense brightness in CL imaging and spiderweb-like texture, shows high concentrations of trace elements, especially Ge, Al and Ti, and has $\delta^{18}O_{fluid}$ values ranging from 10.84 ‰ to 11.64 ‰. These characters are consistent with a magmatic fluid that is acidic (pH<3), reducing, and of relatively high-temperature. In the second stage, the quartz (including Qz3a, Qz3b and Qz4) shows relatively darker CL image and band texture or cobweb mosaic coexistence texture, low concentrations of trace elements, especially Al and Ti, and a low $\delta^{18}O_{fluid}$ values (8.01 ‰ to 9.19 ‰ for Qz3a and 5.83 ‰ to 6.51 ‰ for Qz3b) consistent with characteristics of mantle-derived fluids. The results of this study supports an "intracontinental reactivation metallogenic model", in which the gold-polymetallic deposits in the JOB formed from a dual-stage mineralization related to tectono-magmatic activities in a back-arc setting. The dual ore-forming processes revealed in this study provide important insights for a comprehensive understanding of the gold-polymetallic deposits in the JOB, and it may be a significant mechanism in the formation of large to super-large gold-polymetallic deposits in this region, which is indicative perspective for exploration of the gold-polymetal deposits. Our work also demonstrates that quartz is an effective tool for identifying the mineralization in the JOB.

1. Introduction

Intracontinental mineralization refers to mineralization that occurs within continental plates, far from active continental margins. It is of great interest due to the unclear relationship between the driving mechanisms, processes, and the diversity of mineralization (Mao et al., 2005; Pirajno et al., 2009; Zhai and Santosh, 2013; Hu et al., 2024). The Jiangnan orogenic belt (JOB) on the southeast margin of the Yangtze plate (Fig. 1a) is one of the important gold mining areas in South China (Mao et al., 2013; Xu et al., 2017), and it is formed by the collision

* Corresponding author.
E-mail address: cuglibin@163.com (B. Li).

https://doi.org/10.1016/j.oregeorev.2024.106172
Received 20 March 2024; Received in revised form 22 June 2024; Accepted 20 July 2024
Available online 22 July 2024

between the Yangtze and Cathysia plates during Neoproterozoic (Zhang et al., 2013; Wang et al., 2017). Afterwards, it underwent two intracontinental orogenies in the early Paleozoic and early Mesozoic formed a complex intracontinental composite orogen (Raimondo et al., 2014; Shu et al., 2021), generating extensive deformation, metamorphism and magmatism (Zhang et al., 2013; Shu et al., 2021). The JOB, as an ancient intracontinental suture, experienced multiple episodes of magmatic activity and polymetallic mineralization events (Xu et al., 2017; Zeng et al., 2023; Hu et al., 2024), and it is known for its abundant polymetallic deposits (Fig. 1b), mainly including hydrothermal gold, gold-antimony, and gold-antimony-tungsten deposits, with a total gold content exceeding 1000 t (Xu et al., 2017).

Extensive research has been conducted on the gold-polymetallic deposits in the JOB, and some consensus has been reached: 1) the deposits mainly occur in the Neoproterozoic low-grade metamorphic volcanic-sedimentary rocks, with most deposits/points not developing magmatic rocks (Xu et al., 2017); and mineralization is generally controlled by different scales of structures, with early structural activation being crucial for mineralization (Zhang et al., 2019a; Bai et al., 2021; Zhou et al., 2021; Li et al., 2022a); 2) multi-stage mineralization occurs, including the early Paleozoic (423–397 Ma) gold, Triassic (ca. 235 Ma) gold-antimony-tungsten, Jurassic (176–170 Ma) copper–gold-tungsten, and Early Cretaceous (148–126 Ma) gold-antimony-tungsten (Xu et al., 2017; Zhang et al., 2019a; Li et al., 2020a; Bai et al., 2021; Zhu et al., 2023; Li et al., 2023a; Li et al., 2024); However, there are still significant debates on the sources of ore-forming materials and the origins of ore deposits: 3) there are divergent views on the ore-forming fluids and metal sources, including metamorphic, magmatic and mantle-derived sources (Li et al., 2024 and its references); nevertheless, the contribution of mantle-derived fluids to mineralization is increasingly recognized (Mao and Li, 1997; Dai et al., 2022; Li et al., 2024); 4) various scholars have proposed different genetic models, including orogenic (Zhu and Peng, 2015; Wang et al., 2020a), epithermal (Wang et al., 2021a), intrusive rock-related (Jia et al., 2019), and

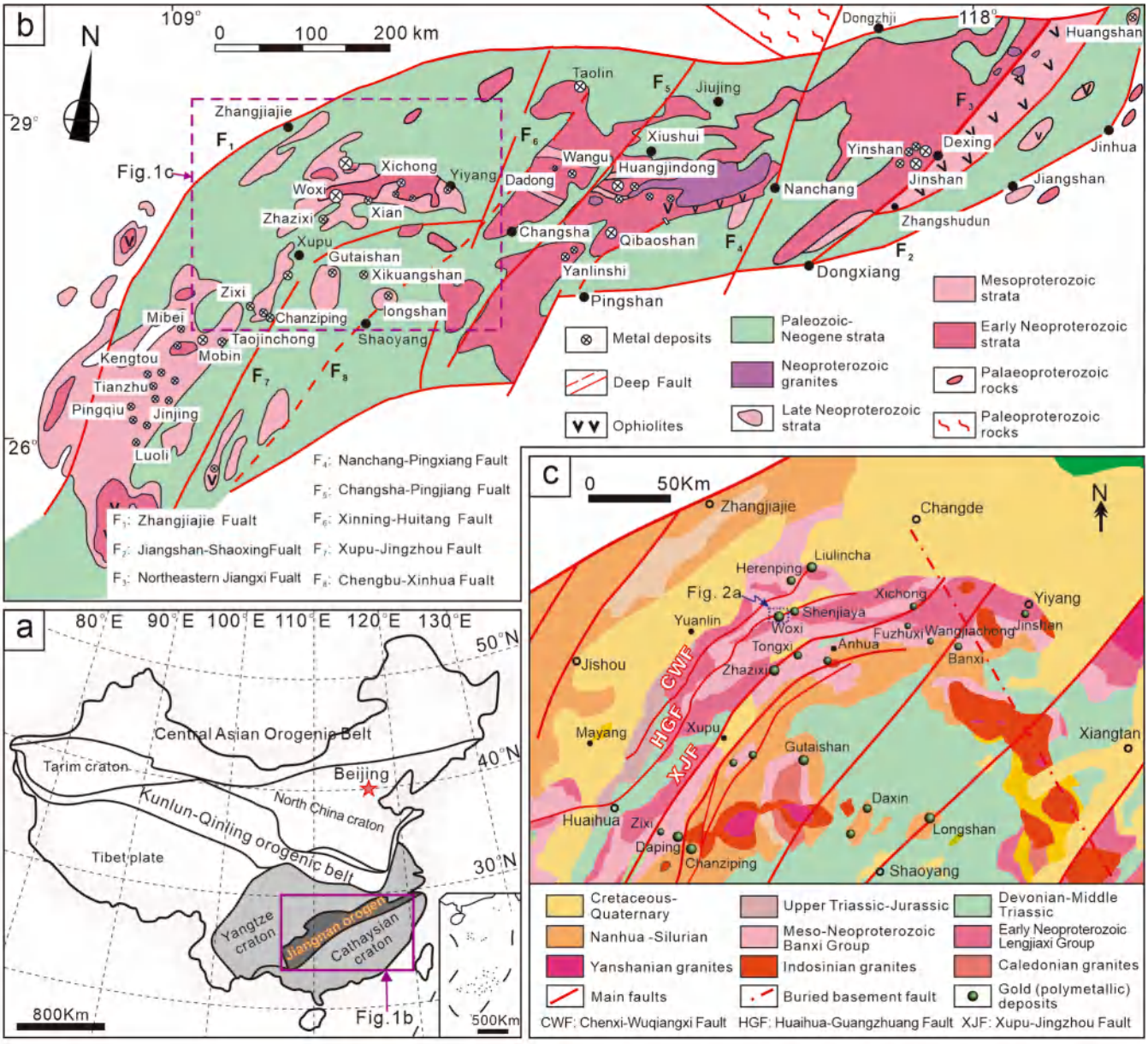

Fig. 1. (a) The outline of China tectonics shows the position of Jiangnan Orogen; (b) Distribution diagram of the Proterozoic strata, structures, magmatic rocks and metallic deposits in the JOB (modified from Xu et al., 2017); (c) Simplified map of the geological structures and gold-polymetallic deposits in the Xuefeng tectonic zone in northwestern Hunan province (modified from Li et al., 2022a; Bai et al., 2021).

intracontinental activation (Xu et al., 2017; Li et al., 2022a) types. The main issue stems from the complex mineralization in gold polymetallic deposits within the JOB, making it challenging to ascertain their origin. In fact, superimposed mineralization can promote the improvement of deposit grade, the increase of reserves and the diversification of ore-forming elements. For example, the early mineral veins of the Madrid deposit in the Hope Bay Greenstone Belt in Canada were enriched by new gold mineralization from late-stage magmatic-hydrothermal fluids (Kerr et al., 2018); late-stage antimony mineralization in the La Bellière gold district in France overprinted early deep-seated orogenic gold deposits (Cheval-Garabédian et al., 2020); and the Laowan super-large gold deposit in the Tongbai orogenic belt in China has early molybdenum mineralization and late-stage gold mineralization (Yang et al., 2021). In the JOB, previous studies have noticed the superimposed mineralization through the study of ore-formming structures or mineral interpenetration (Zeng et al., 2017; Deng et al., 2020a; Li et al., 2022a; Li et al., 2022b;Bai et al., 2023). However, the metallogenic process and formation mechanism are still unknown.

The Woxi deposit is located in the middle of the JOB (Fig. 1c). It is a super large gold deposit with large-scale antimony-tungsten mineralization. The ore bodies are mainly hosted in the NEE-trending interlayer fractures of the Neoproterozoic slate strata (Li et al., 2022a). As for the metallogenic epoch, some studies suggested that there were two stages mineralization in Caledonian and Yanshanian (Peng et al., 2003; Zhu et al., 2023), or Indosinian mineralization (Peng and Frei, 2004). Recently, more accurate ages supported Yanshanian Mineralization (Dai et al., 2022; Li et al., 2022a;Li et al., 2023a; Li et al., 2024); For the genesis of the deposit, some of the most controversial views include that it is related to metamorphic hydrothermal fluids during the orogenic period (Luo et al., 1984; Ma and Liu, 1991; Zhu and Peng, 2015; Li et al., 2018), concealed intrusions (Peng and Frei, 2004), and concealed intrusions but emphasizing mantle-derived materials and tectonic activation (Xu et al., 2017; Dai et al., 2022; Li et al., 2022a). In a word, the genesis of the Woxi deposit is still uncertain, and there is no effective identification or fine constraint on the multi-stage and multi-stage mineralization, which provides an ideal window for us to study the superimposed mineralization in the JOB.

In hydrothermal mineral deposits, quartz is one of the most important vein minerals, often spanning the entire mineralization process (Monecke et al., 2018), and can record processes or pulses on scales of millions or thousands of years (Rottier et al., 2021; Li and Li, 2023; Li et al., 2023b). Previous studies have conducted research on the textures and in-situ chemistry of quartz in different gold deposits, such as Orogenic(Kerr et al., 2018), Carlin (Yan et al., 2020; Li et al., 2020b), Porphyry (Monecke et al., 2018; Cernuschi et al., 2023), and Epithermal deposits (Rottier et al., 2021), finely delineating the evolution and origin of ore-forming fluids in these deposits, and showing the advantage of quartz minerals in revealing multiple stages of mineralization history and their potential as economic indicators (Müller et al., 2018; Gao et al., 2022).This study focuses on the Woxi deposit in JOB, dividing the quartz into different metallogenic stages and analyzing the textures of quartz using SEM-CL. Based on this, LA-ICP-MS and SIMS were used to conduct in-situ analysis of trace elements and O isotopes in quartz separately in the primary ore-forming stages, aiming to trace changes in fluid physicochemical conditions and sources during the ore-forming process. Through our research, we identified the two-stage metallogenic process of the Woxi Au-Sb-W deposit, and discussed the metallogenic tectonic setting in conjunction with existing data, providing new insights on the genetic mechanism of the Woxi deposit and intracontinental mineralization in SCB.

2. Geological setting

The JOB is located in the central part of the SCB (Fig. 1a) and is generally considered as the suture between the Yangtze and Cathaysia blocks during the Neoproterozoic (Wang et al., 2017). The belt mainly consists of Neoproterozoic low-grade metamorphic volcanic debris rocks and sedimentary rocks, while the rest includes Paleozoic marine sediments (including shale, siliceous rocks, sandstone, siltstone and carbonate rocks), early to middle Mesozoic continental shelf sediments (including sandstone, siltstone, and minor carbonate rocks), late Mesozoic rift basin sediments, and Cenozoic continental rift basin sediments (including conglomerate, gravelly sandstone, sandstone and mudstone) (Zhang et al., 2013; Shu et al., 2021). The structural deformation in the region mainly includes E-W-trending structures involving pre-Silurian strata formed during the Caledonian movement and NE~NNE-trending folds and thrust faults extending up to 1500 km generated by the Indosinian and Yanshanian movements (Li and Li, 2007; Zhang et al., 2013; Shu et al., 2021). Magmatic rocks include collisional granites in the early Neoproterozoic and later extensional A-type granites (860–760 Ma), Late Silurian to Early Devonian S-type granites (440–420 Ma), Early Mesozoic S-type granites (240–220 Ma), and Late Mesozoic magmatism (155–95 Ma) (Wang et al., 2013; Shu et al., 2021; Cao et al., 2021).

The JOB hosts a series of gold-dominant and gold-polymetallic deposits. In the eastern segment, there are porphyry-type, skarn-type Cu-Au, and iron deposits, which are associated with Paleo-Pacific plate subduction (Mao et al., 2021). In the central segment, the main deposits are gold, antimony and tungsten, predominantly occurrence in the form of quartz vein and altered rocks, which are related to multiple tectonic magmatic activities (Xu et al., 2017; Zhang et al., 2019a). In the western segment, tin, gold, silver, lead, and zinc are the dominant minerals, mainly occurring as greisen and MVT deposits, driven by tectono-magmatic hydrothermal processes (Hu et al., 2017). The mineralized host rocks of these deposits mainly consist of low-grad metamorphosed volcanic and clastic rocks from the Neoproterozoic era, with the ore-forming ages mainly spanning from the Late Jurassic to the Early Cretaceous, followed by the Late Silurian and Late Triassic (Xu et al., 2017; Bai et al., 2021).

Previous studies mostly believed that the Yangtze and Cathaysia plates underwent rift tectonics and glacial events in the late Neoproterozoic after the formation of the SCB (Zhang et al., 2013; Shu et al., 2021), which may be associated with post collision extension or mantle plume (Wang et al., 2017; Li et al., 2019a). In the Early Paleozoic, a large-scale intracontinental orogeny event (the Caledonian Orogeny) occurred in the region, possibly influenced by the aggregation of the Gondwana supercontinent (Du and Xu, 2012; Zhang et al., 2015; Shu, 2021). In the Early Mesozoic, SCB successively collided with the Indochina and North China cratons, leading to another intense intracontinental folding orogeny event (the Indosinian orogeny) in the region (Zhang et al., 2013; Shu et al., 2021). During the late Triassic to early Jurassic, the SCB may have been influenced by subduction of the paleo-Pacific plate (Li et al., 2017; Zhu and Xu, 2019), but the transition of tectonic regime from the Tethyan tectonic domain to the paleo-Pacific tectonic domain occurred in the early Jurassic (170 ± 5 Ma) (Zhang et al., 2009; Dong et al., 2018). During the Jurassic-Cretaceous period, due to the westward subduction of the paleo-Pacific plate (Li et al., 2014; Zhu and Xu, 2019), the Yanshanian orogeny occurred in the region, causing multiple episodes of compression and extension events. Around 55 Ma years ago, as the Pacific plate once again subducted beneath East Asia, SCB was under the joint control of the India-Eurasia collision dynamics system and the Pacific subduction dynamics system (Dong et al., 2018; Zhu and Xu, 2019).

The Woxi Au-Sb-W deposit is located in the middle section of the JOB (Fig. 1c) where the tectonic lines exhibit a northward trend from south to north. The area is mainly composed of Neoproterozoic to lower Paleozoic metasediments, with small amounts of upper Paleozoic and early Mesozoic rocks. Multiple large-scale faults are present in the region, and the deposits are mainly distributed near these faults, indicating a close relationship between deep-seated faults and mineralization (Xu et al., 2017; Zhang et al., 2019a). Additionally, the distribution of the deposits is associated with tectonic uplifts, including

basement uplifts (Neoproterozoic Lengjiaxi Group), structural domes, and magmatic uplift areas (Bai et al., 2021; Li et al., 2022a). Granites are not widely developed in the area, but there are large-scale Late Yanshanian and Mesozoic intrusions on the southeastern margin (Fig. 1c). The granitic intrusion closest to the Woxi deposit is located in Anhua, with a smaller scale and a distance of over 50 km.

3. Deposit Geology and mineralization

The Woxi Au-Sb-W deposit is located in Guanzhuang Town, western Hunan. It has a mining history of over 130 years and confirmed gold resources exceeding 68 tons (Xu et al., 2017). In recent decades, extensive exploration and research have been conducted in order to discover new resources and supple the diminishing ore reserves. The mining area is situated on the northeastern side of the Xianebaodan basement uplift (Fig. 2a) and comprises five mine sections: Hongyanxi, Yuershan, Liaojiashan, Shiliupenggong, and Shangwoxi. The stratigraphic sequence consists of the Neoproterozoic Lengjiaxi and Banxi groups, as well as Cretaceous units (Fig. 2a, b). Among them, the purple-red sericite slate or calcareous slate interval (with a thickness of 70–800 m) in the Madiyi Formation of the Banxi Group is the ore-bearing unit (Yang and Blum, 1999; Chen et al., 2008).

The structural framework in mining area consists of NE-SW and NE ~ NNE-trending structures (Fig. 2a). Prior research has suggested that the

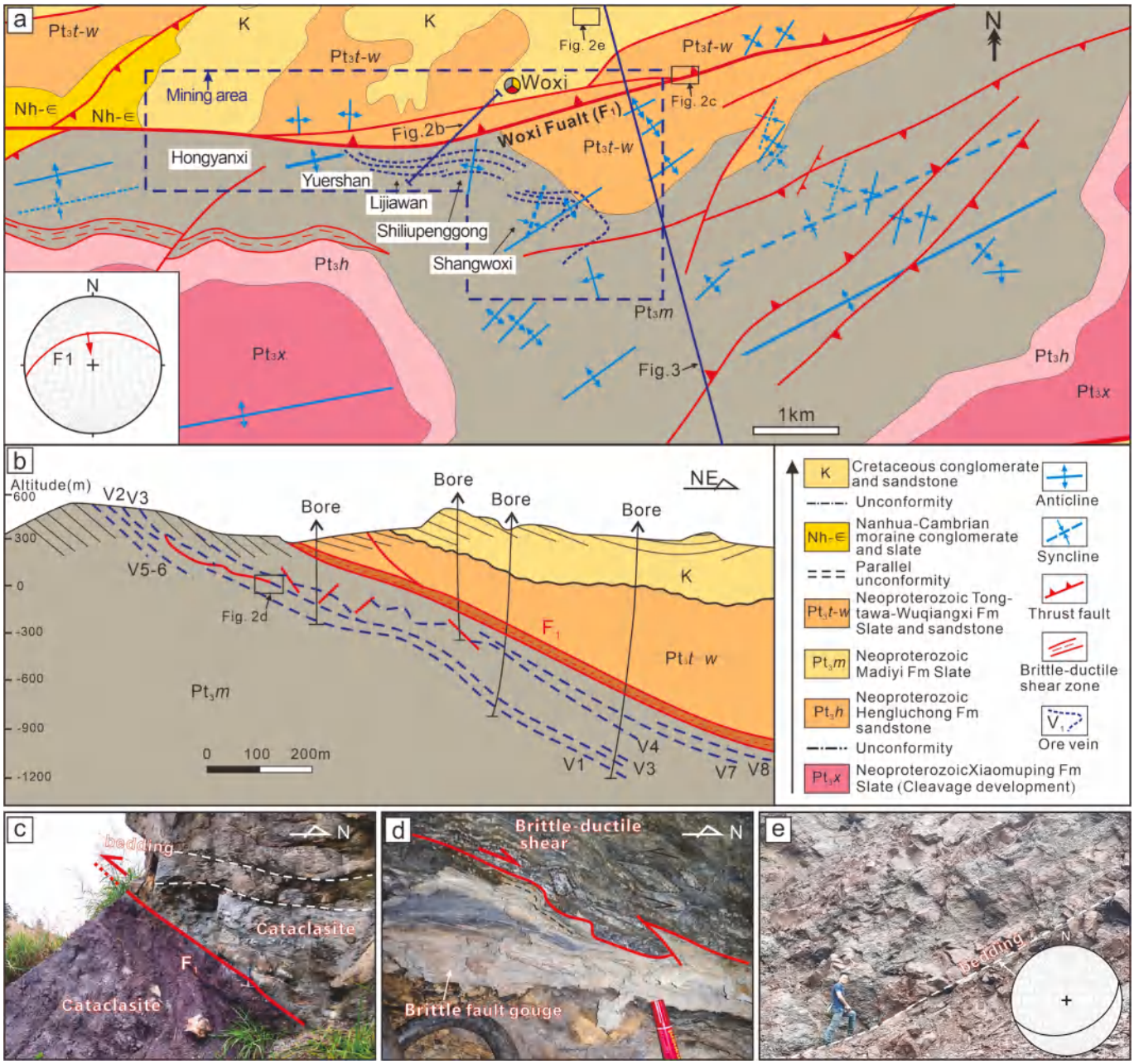

Fig. 2. (a) Presents the geological structural diagram of the Woxi Au-Sb-W deposit (modified from Li et al., 2022a), with the stereographic projection (lower hemisphere) showing the main occurrence of the Woxi Fault (F_1); (b) Typical exploration cross-section profile of the mining area (modified from Xu et al., 2017), displaying the distribution of ore veins and their spatial relationship with the F_1; (c) Outcrop features of the Woxi fault, developed cataclastic rock of brittle domain; (d) Interlayer shear fractures developed at an elevation of −25 m underground, with quartz σ-cracks indicating early brittle-ductile thrusting and small extensional folds in fault mud indicating late normal slip; (e) Red glutenite in the F_1-controlled basin during the Cretaceous extension period. (For interpretation of the references to color in this figure legend, the reader is referred to the web version of this article.)

NE-trending structures formed during the Indochina orogeny, while the NE ~ NNE-trending structures are associated with the subduction of the paleo-Pacific plate during Yanshanian (Li et al., 2022; Li et al., 2022a; Bai et al., 2023). The Woxi fault (F_1) is the most important fault in the mining area, dipping gently to the north and trending nearly east–west, and shows a fractured zone with a width of more than 10 m in outcrop (Fig. 2c). The F_1 shows multi-stage deformation characteristics (Li et al., 2022a), including the superposition of early brittle-ductile deformation and late brittle deformation (Fig. 2d). These observations indicate significant crustal uplift during the early stage of tectonic deformation, followed by a later extensional event that controlled the Cretaceous continental basin sedimentation in the hanging wall (Fig. 2e). Currently, the industrial ore bodies that have been discovered are all situated in the footwall of F_1, within a series of shear fractured zones between the layers of the Madiyi Formation, and they include eight main ore bodies (Fig. 2b). Moreover, these ore bodies are commonly controlled by NE ~ NNE-trending folds and are more concentrated in the core of the folds, such as the Shiliupenggong and Shangwoxi mine sections (Chen et al., 2008; Li et al., 2022a). No large-scale granites have been observed in the mining area, but recent geophysical studies suggest the presence of large intrusive bodies at a depth of < -2km underground (Fig. 3).

The primary type of mineralization is the quartz veins of more than 50 cm, which occurs in the interlayer shear zones (Fig. 4b, c, d, e), accounting for 70 % of the total mineral resources (Luo et al., 1984; Chen et al., 2008; Yi, 2012). This type of mineralization has been the main high-grade veins exploited in the past, with grades reaching up to 20 g/t, such as V3-1. The network vein type, altered shale type, and fragmented breccia type in the secondary fractures on both sides of the interlayer shear zones (Fig. 4f, g) account for about 30 % of the total mineral resources. These lower-grade veins (generally less than 3 g/t) have been increasing in proportion in recent years. The main thick interlayer veins are generally trending approximately east–west and dip gently to the north (dipping angle 20° to 30°). The dip direction tends to extend deeper than the strike extension, and their attitude changes locally with folding (Chen et al., 2008; Xu et al., 2015). The main types of ore include gold-quartz type, antimony-gold-quartz type, tungsten-gold-quartz fine vein type, and gold-antimony-tungsten altered slate type (Fig. 4h, i, j, k).

Metallic minerals mainly include scheelite, stibnite, native gold, pyrite and wolframite (Fig. 4; Fig. 5), with small amounts of arsenopyrite, sphalerite and galena (Chen et al., 2008; Yi, 2012). Gold is mainly present in native gold, followed by pyrite (Dai et al., 2022; Li et al., 2024). Stibnite is mainly associated with quartz-scheelite-gold, occurring as layered or banded shapes (Fig. 4b, c). Wolframite is mainly found in vein-like form (Fig. 5 a-d), with internal development of joints, filled or cut by later-stage stibnite (Fig. 5 b, c). Three types of pyrite can be identified in the hydrothermal stage: coarse pyrite in milky white quartz or altered slate adjacent to the quartz vein (Fig. 4k), fine-grained pyrite in the surrounding rocks near the quartz vein (Fig. 5l), and fine-grained pyrite in band-shaped or massive form closely related to stibnite (Fig. 4j). Gangue minerals mainly include quartz, with small amounts of muscovite, carbonate,

illite and chlorite (Peng et al., 2008; Yi, 2012). In the third stage of vein formation, the earlier formed veins are generally fragmented and often infiltrated by later-stage milky white quartz (Fig. 3c, d). Mineralization alteration are featured with bleaching (Fig. 4l), including silicification, pyritization, carbonatization (Fig. 4a, m-p) and chloritization. Among them, bleaching has the thickness generally greater than that of the ore bodies, usually ranging from 0.2 to 2 m. Additionally, the spatial variation and intensity of discoloration alteration are closely related, making it an important indicator for prospecting in the mining area and regionally (Chen et al., 2008).

Previous research has indicated that the ore formation in this mine occurs at medium to low temperatures (140-300℃) and low salinity (<7.0 wt% NaCl), with ore-forming fluids rich in CO_2, N_2 and H_2O (Zhu and Peng, 2015; Yi, 2012). In terms of the mineralizing stages, this study aligns with previous research (Yi, 2012; Zhu and Peng, 2015; Dai et al., 2022; Li et al., 2022a), identifying four stages: quartz-calcite, quartz-wolframite-scheelite (with minor pyrite and gold mineralization), quartz-pyrite-stibnite-natural gold-(scheelite), and quartz-carbonate. These four stages are supported by observed mineral associations, such as cross-cutting relationships between quartz-stibnite veins in the third stage and quartz-wolframite veins in the second stage (Fig. 4a, b, c), late-stage quartz-calcite veins cutting early-stage quartz veins (Fig. 4a), and early-stage angular ore (Fig. 5l).

4. Sampling and analytical methods

4.1. Sampling

We have collected dozens of samples from tunnels being mined or previously mined of the Woxi deposit. We have chosen 6 representative quartz samples (Table 1) for research, which cover different mineralization stages, ores and depths. The hand specimens were thoroughly observed initially, and appropriate areas were selected to make thin sections of the rocks. Based on the constraints of optical microscopy and scanning electron microscopy (SEM) on their microstructure characteristics, ideal particles were selected for in-situ LA-ICP-MS trace element and SIMS O isotope analysis.

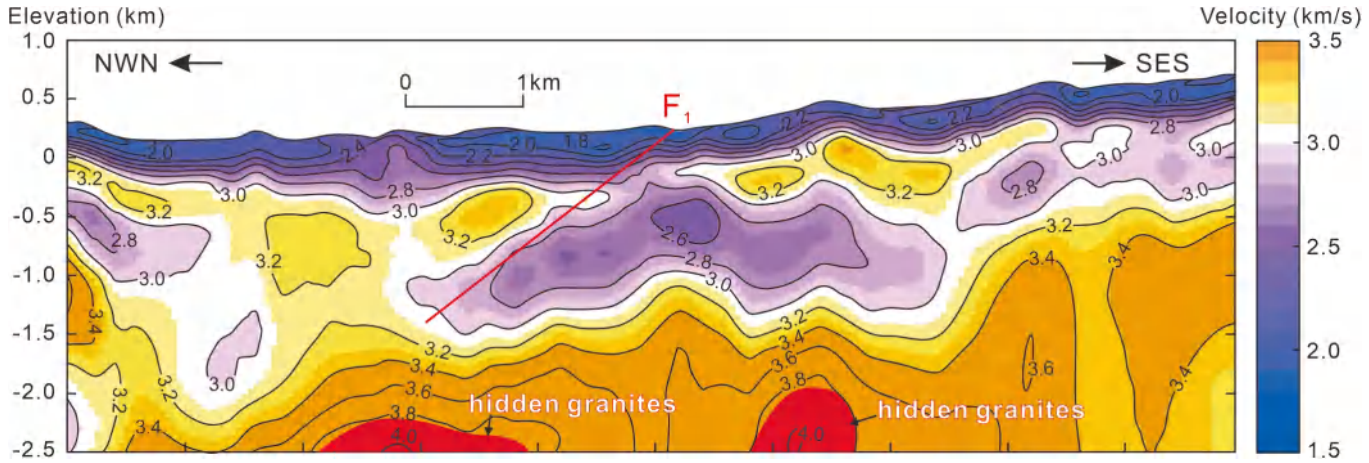

Fig. 3. Presents the vertical profile of the shear-wave velocity from the Woxi Au-Sb-W deposit (modified from Wang et al., 2022). The red areas indicate the presence of hidden granites inferred from shear-wave high-speed anomaly.

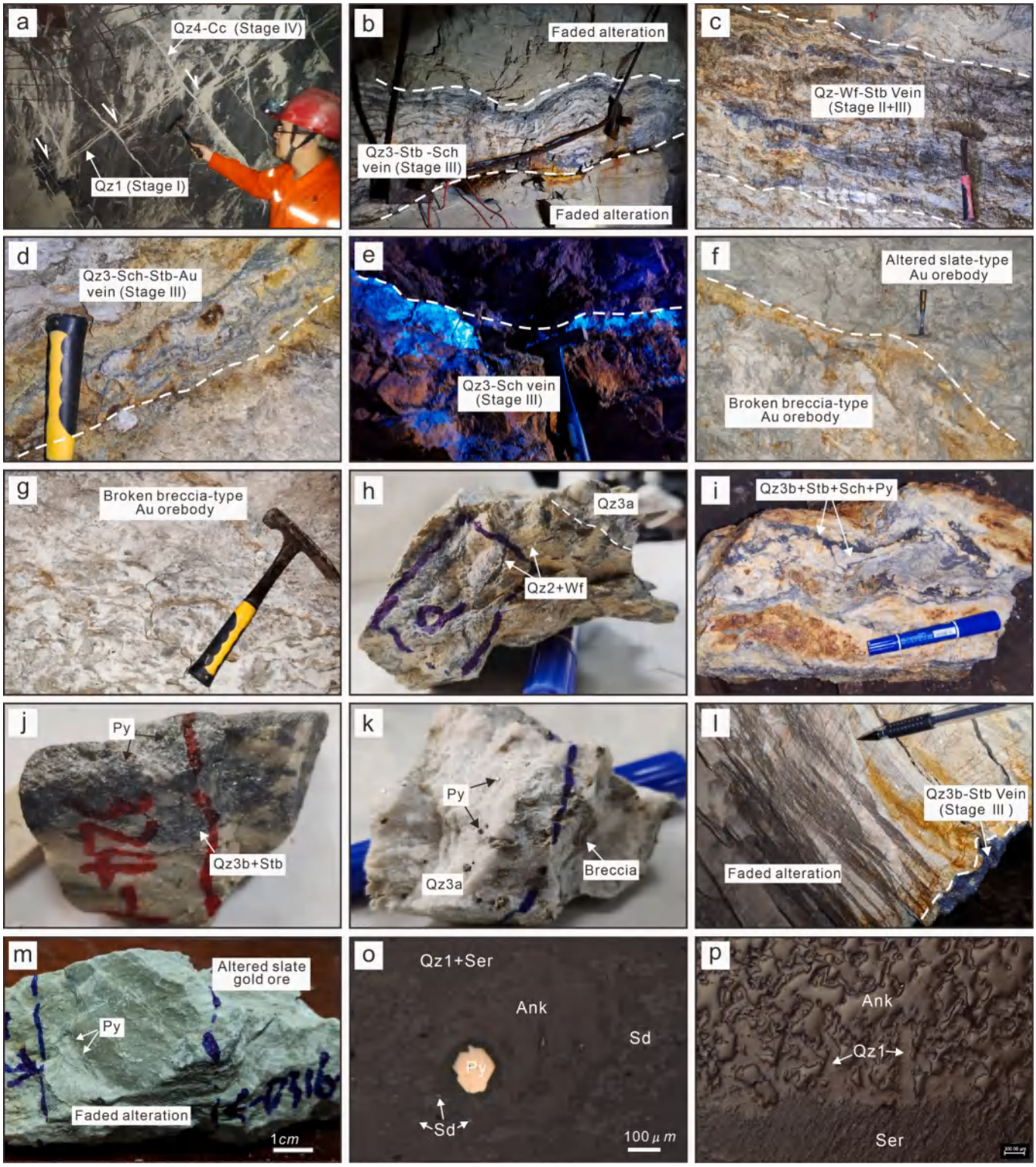

Fig. 4. Photographs showing the ore bodies and host rocks in the field, and hand specimens form the Woxi Au-Sb-W deposit.
(a) In the late stage of ore formation, the quartz vein of calcite crosses the early-stage quartz vein. (b-e) Veins controlled by interlayer shear fractures show different ore-forming stages and mineral assemblages. The surrounding rocks exhibit typical fading alteration. (f) Brecciated conglomerate and altered rock type gold mineralization. (j) Brecciated conglomerate gold mineralization, with coarse pyrite and milky white quartz development. (h) Altered slate ore, quartz-wolframite veins intersected by smoky gray quartz (Qz3). (i) Gold-antimony-tungsten ores. (j) Quartz-stibnite veins. (k) Quartz conglomerate gold ores. (l) Quartz-veined ore body with characteristic weathered surrounding rocks. (m-p) early stage carbonatization in the altered rock gold ores, and the pyrite in main ore-forming stage grows in the carbonate cavities (o). Stage-mineralization stage; Qz-quartz; Py-pyrite; Wf-wolframite; Sch-scheelite; Stb-stibnite; Au-gold; Ser-sericite; Ank-ankerite; Sd-Siderite.

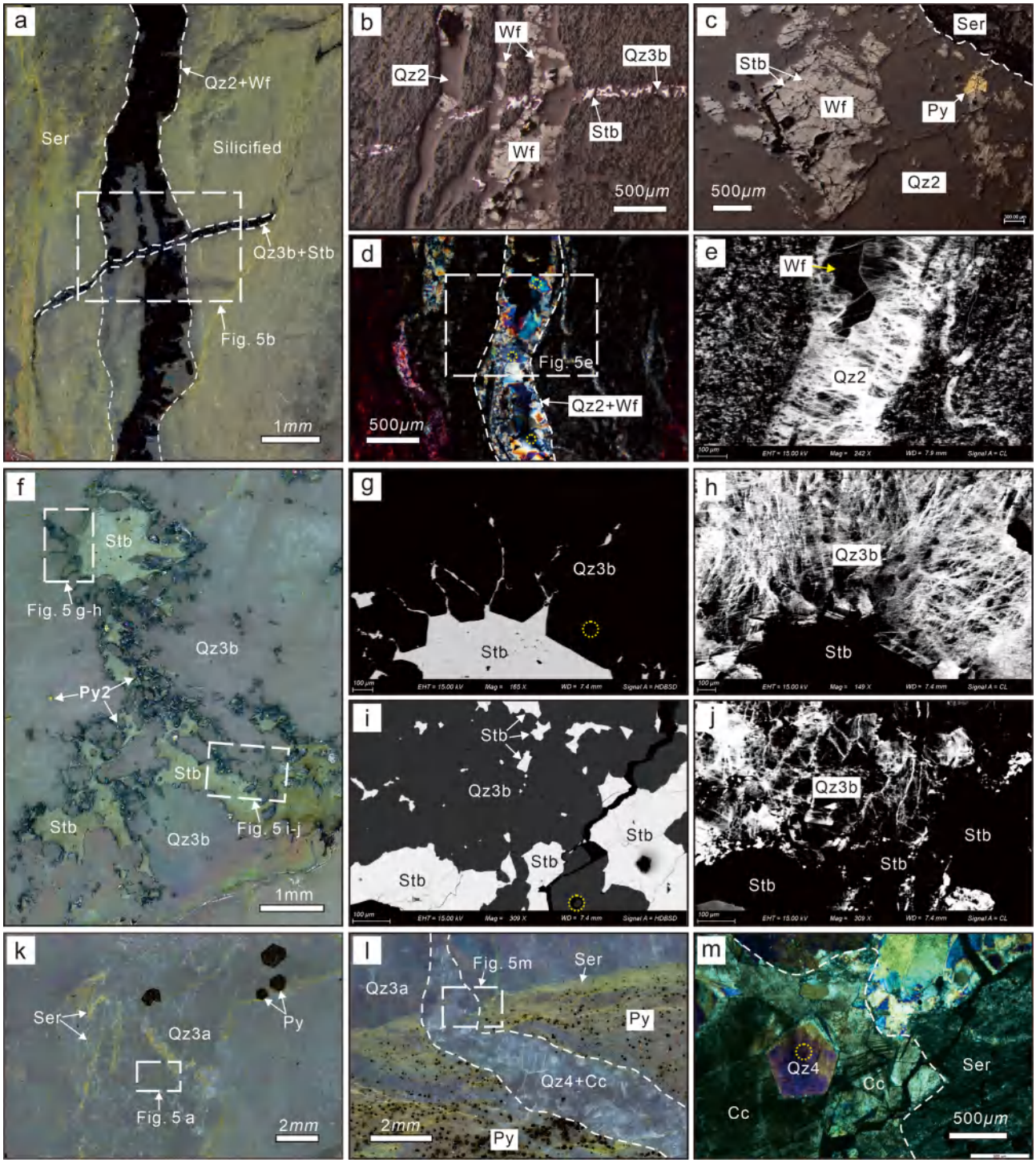

Fig. 5. Thin sections and microphotographs of quartz samples at different stages, including SEM and CL images, were used for LA-ICP-MS trace element and SIMS O isotope analysis. (a-b) Cross-cutting quartz veins with silicified sericitized alteration in quartz-scheelite veins. (c) Later quartz (Qz3a) enclosing early-stage scheelite (Stage II). The filling of late-stage stibnite (Stage III) within scheelite fractures is noticeable. (d-e) Early quartz-scheelite veins (Stage I). (f-j) Coexisting smoky quartz (Qz3a) is intimately associated with stibnite, showing finely disseminated pyrite (4j). Two different forms are observed in CL images: reticulate and fragmented. (k) Milky white quartz (4 k) with coarse pyrite development. (l) Late-stage quartz-calcite vein (Stage IV) crosscutting earlier veins (Stage III). (m) Quartz (Qz4) is closely associated with calcite in late-stage veins. Qz-quartz; Wf-wolframite; Py-pyrite; Stb-stibnite; Ser-sericite; Cc-calcite. Yellow dashed circles represent LA-ICP-MS analysis points.

4.2. Analytical methods

4.2.1. CL structure observation

In the State Key Laboratory of Nuclear Resources and Environmental of East China University of Science and Technology (SKLNRE, ECUT), detailed observations of the microscopic characteristics and natural gold occurrence of the minerals under analysis were conducted using an optical microscope. Subsequently, the samples were further observed and photographed using a Zeiss SIGMA 300 backscattered electron scanning electron microscope (BSE-SEM) equipped with an Oxford

Table 1
Sampling of hydrothermal quartzs from different generations in the Woxi deposit.

Sample no.	Stage	Vein/ Elevation(m)	Features
D311	II/III	V1/-25	Interlayered quartz vein deposit (329°∠25°), containing gold-antimony-tungsten-bearing ores, with deformation of early quartz-wolframite veins
D315	III	V1/-25	Deformed interlayer veins (30°∠40°), Qz-Au-Py ores, smoky quartz.
D316	III	V6/-475	Layered fractures in veins (5°∠60°), Qz-Py-Au, massive ores, milky white quartz and coarse-grained pyrite.
D321	III	V8/-1050	Thick interlayer veins (87°∠40°), Qz-Py-Au, breccia ores, milky white quartz, coarse-grained pyrite in quartz and fine-grained pyrite in surrounding rocks.
D323	III	V7/-1050	Interlayer veins (100°∠45°), Qz-Py-Au ores, milky white quartz, late-stage calcite intergrowth
D324	III	V3/-1050	Interlayer vein (160°∠50°), Qz-Py-Stb-Au ore, ivory quartz, banded pyrite or aggregate

IE380 energy-dispersive X-ray spectrometer (EDS). Special attention was focused on the development of fractures and rims to aid in selecting appropriate testing points. CL images were acquired using an acceleration voltage and beam current density of 15 kV and 10nA, respectively, for a duration of 80 s.

4.2.2. LA-ICP-MS in-situ trace element analysis

The in-situ LA-ICP-MS analysis of trace elements in uranium-multi-metal centers was completed at the State Key Laboratory of Nuclear Resources and Environment at East China University of Science and Technology. The analysis utilized the PerkinElmer NexION 1000 quadrupole ICP-MS and the ESI NWR 193 He excimer laser ablation system. The laser ablation energy density was 4.6 J/cm^2, with a pulse rate of 6 Hz and an ablation diameter of 44 μm. Helium gas was used as the carrier gas for ablation. During the testing process, NIST610 glass and NIST612 were utilized as external and calibration standards respectively, with two sets of NIST610 glass standards inserted every 6 test points and one set of NIST612 standards inserted every 6 test points. ^{29}Si was used as the internal standard element. The quartz trace element data was processed using Iolite software (Paton et al., 2011).

4.2.3. Oxygen isotope analysis by SIMS

The quartz SIMS oxygen isotope analysis is carried out at the Beijing Research Institute of Uranium Geology (BRIUG) using the CAMECA IMS-1280HR SIMS. Thin rock sections that have undergone laser in-situ trace element testing are selected, and suitable areas are cut out and embedded in epoxy resin, primarily considering the paragenesis of different mineralization stages and characteristic zoning structures. Surface polishing is performed using an automated polishing machine and 0.25 μm diamond paste to achieve relief less than 3 μm. Subsequently, a 20-second cleaning is conducted in an ultrasonic cleaner with ethanol to remove any polishing residue from previous steps, ensuring high-quality SIMS oxygen isotope measurements (Li et al., 2021).

The sample is coated with a gold film of approximately 50 nm in thickness to ensure conductivity, and a vertical incidence electron beam gun is used to compensate for charge. Analysis is carried out using ~ 2–3nA Cs + as the primary beam, with an acceleration energy of + 10 kV. The acceleration voltage for secondary ions is set at −10 kV. The analysis spot is square in shape, with dimensions of 10 × 15 μm^2. Sputtering is performed for 20 s to remove the gold film and clean the sample surface. Nuclear magnetic resonance is used to stabilize the instrument's magnetic field, and mass scanning is conducted at the beginning of each analysis. Oxygen isotopes (^{16}O, ^{18}O) are simultaneously measured on two Faraday cups, with an intensity of 2–3 × 10^9 counts per second for ^{16}O$^-$. After 60 s of automatic beam centering, oxygen isotope measurement is achieved through a 64 s signal integration. The individual instrument uncertainty (i.e., internal precision) for individual analyses is typically better than 0.2–0.3 ‰ (2σ). For detailed experimental procedures, refer to (Li et al., 2021; He et al., 2021).

5. Results

5.1. Quartz installment and structural characteristics

Based on the mineral generation sequence of the Woxi deposit and observation of ore hand specimens, we conducted research on Qz2 (stage II), Qz3a, Qz3b (stage III), and Qz4 (stage IV). Among them cathodoluminescence studies were carried out on Qz2 and Qz3. Qz2 is derived from the quartz-wolframite vein in the second mineralization stage (Fig. 4h; Fig. 5a-d). On hand specimens, it appears as a smoky gray color and is associated with pyrite and wolframite. CL images show that Qz2 is generally brighter with localized darker areas, displaying a dense spiderweb-like texture (Fig. 5e), related to hydrothermal activity. Qz3 from the quartz-stibnite-gold vein of the third-stage mineralization is composed of the early milky white quartz Qz3a occurring in the quartz-gold ore (Fig. 4k; Fig. 5k), and the late milk-white quartz Qz3b coexisting with stibnite (Fig. 4j; Fig. 5f-j). Qz3a is widely present in angular vein breccias formed under fluid overpressure (Fig. 4g, k), locally with the gold grades of up to 30 g/t, indicating its significance as the main mineralization stage for gold. CL images reveal that Qz3a presents as well-formed crystal aggregates, overall darker,and occupies distinct growth zoning and remnants of early-stage quartz incorporated, which are cut by later-oriented fibrous quartz (Fig. 7a), possibly related to later hydrothermal activity. In contrast, Qz3b exhibits a spiderweb-like or mosaic textures coexisting with spiderweb-like textures (Fig. 5j). Qz4 represents the late-stage mineralization quartz, cross-cutting the earlier mineralized bodies (Fig. 5l, m).

5.2. In-situ trace element composition by LA-ICP-MS

Seventy in-situ LA-ICP-MS trace element analyses, with twenty, fourteen, nineteen, and seventeen for Qz2, Qz3a, Qz3b and Qz4, respectively, were conducted on quartz from the different stages of mineralization, and are listed in Appendix 1. The variations in trace element abundance are shown in Fig. 6. The test results indicate that quartz contains abundant trace elements such as Al, Li, Ge, P, K, and Ti, while other elements such as Be, Cu, Zn, and Pb are either close to or below the detection limit. Previous studies have shown that Ti, Li, Al, and Ge are primarily present in the structure of quartz, which can reflect the physical and chemical conditions during quartz formation (Götze et al., 2004; Larsen et al., 2004). There is uncertainty regarding the presence and quantification of other elements. For example, the quantification of B and P can be affected by polyatomic interferences (Müller et al., 2008; Audétat et al., 2014). Na, K, and Ca are susceptible to interference from fluids and mineral inclusions, while Fe, As, and Sb can be contaminated by pyrite, arsenopyrite, or stibnite (Yan et al., 2020; Li et al., 2020b). Therefore, this study focuses on the four elements: Ti, Li, Al, and Ge.

Qz2 of the second-stage mineralization in Woxi deposit has relatively high overall contents of Al, Li, and Ge, ranging from 538 to 4794 ppm (average 1974 ppm), from 4.2 to 117 ppm (average 56.3 ppm), and from 5.5 to 15.4 ppm (average 10 ppm) respectively. Qz3 of the third-stage mineralization is much lower in Al and Li contents, compared to those of Qz2. Nevertheless, Qz3a with growth rings is lower than the reticulated Qz3b. In Qz3a, the content of Al and Li ranges from 40 to 1063 ppm (average 244 ppm) and from 0.64 to 60 ppm (average 10.8 ppm) respectively, while in Qz3b, the contents of Al and Li span from 53 to 1120 ppm (average 391 ppm) and from 0.08 to 41.8 ppm (average 14.1

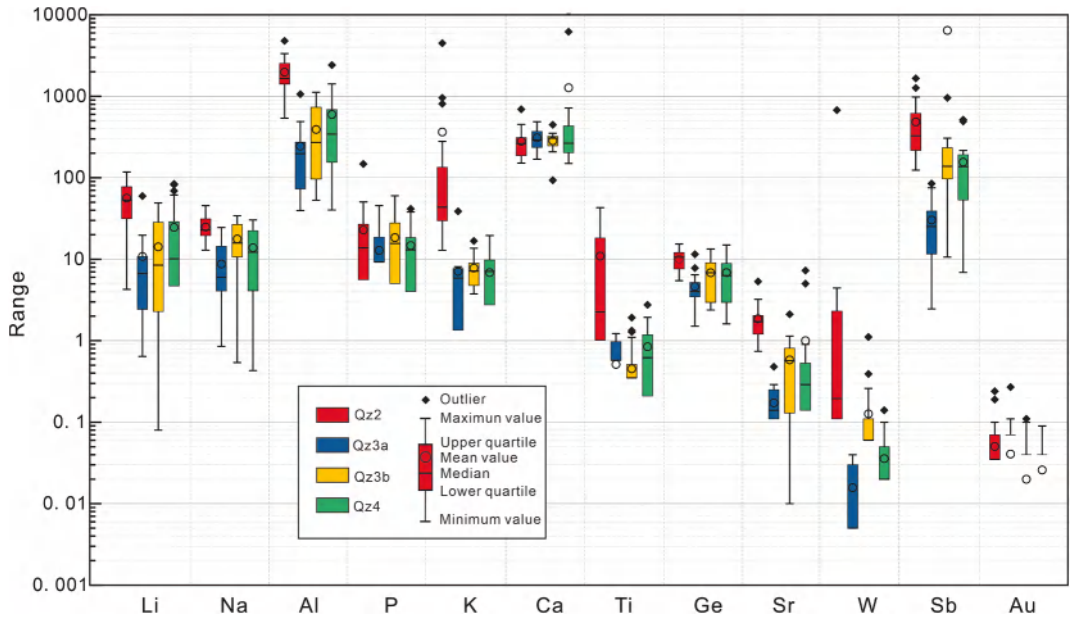

Fig. 6. LA-ICP-MS trace element compositions for the various generations of Woxi quartz.

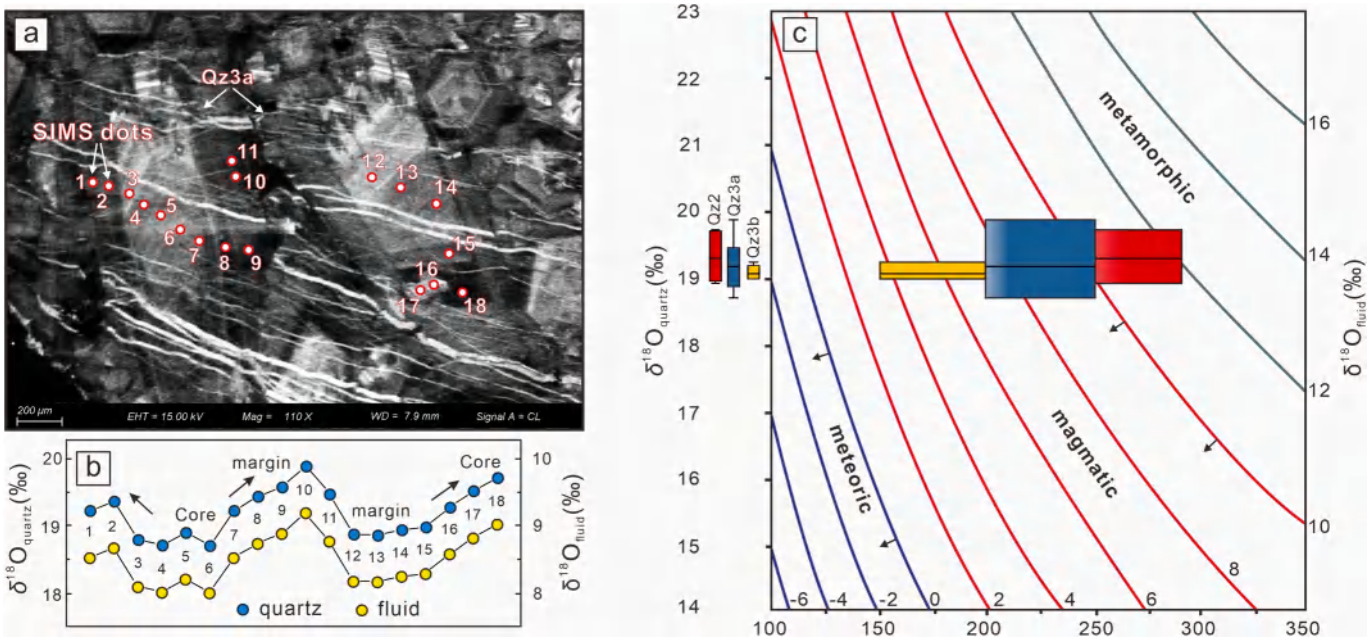

Fig. 7. (a) The CL image of phase Qz3a in the third stage shows a typical ring structure, with red dots representing SIMS O isotope positions; (b) shows the variation in SIMS O isotope test results from Fig. (a), demonstrating fluctuations in O isotopes during the mineralization process; (c) $\delta^{18}O$ range of quartz samples from the mineralization stages (II-III) (Qz2, n = 7; Qz3a, n = 18; Qz3b, n = 7). The left side shows a boxplot that encompasses the entire data range and corresponds to the quartz formation temperature range based on mineralogy and microthermometry (Yi, 2012). The line within the box represents the mean value. The fluid $\delta^{18}O$ value was calculated using the quartz-H_2O fractionation equation from Sharp et al. (2016).

ppm) respectively. The contents of Al and Li in Qz4 increases relative to Qz3, ranging from 40.3 to 2421 ppm (average 596 ppm) and from 1.94 to 84 ppm (average 24.6 ppm) respectively. In addition, the Ge contents are highest in Qz2, ranging from 5.5 to 15.4 ppm (average 10 ppm), lowest in Qz3a, ranging from 1.5 to 11.5 ppm (average 4.6 ppm), and low but similar in both the Qz3b and Qz4 (ranging from 2.5 to 13.4 ppm, with an average of 6.8 ppm, and from 1.6 to 15 ppm, with an average of 6.9 ppm, respectively). Furthermore, the Ti contents characterize a decreasing trend, with the highest values in Qz2 of the second-stage mineralizaion (an average of 10.9 ppm) and lowest but comparable among the early third-stage Qz3a, the late third-stage Qz3b, and the fourth-stage Qz4 (average values of 0.51 ppm, 0.45 ppm, and 0.84 ppm respectively). The significantly elevated Ti in Qz2 (large outliers of up to 42 ppm) is a characteristic indicator distinguishing Qz2 from both the Qz3 and Qz4.

5.3. *In-situ oxygen isotopic component by SIMS*

A total of thirty-two in situ O isotope analyses by SIMS are undertaken on the ore-forming stage quartz samples. Specifically, we analyzed mineral separates of Qz3a with typical zonation structures from core to rim, including seven, eighteen and seven analyzed dots for Qz2, Qz3a

and Qz3b, respectively. The SIMS O isotope data are listed in Appendix 2, and the variations of SIMS O isotope components for Qz2 and Qz3 can be seen in Fig. 7 and Fig. 8. The test results show that the oxygen isotopic values of the ore-forming quartz (stage II-III) exhibit very small variations ($\delta^{18}O_{quartz}$ = 18.5‰ – 19.9 ‰), with Qz2 (average $\delta^{18}O_{quartz}$ = 19.29‰) > Qz3a (average $\delta^{18}O_{quartz}$ = 19.2‰) > Qz3b (average $\delta^{18}O_{quartz}$ = 19.05‰). This is in contrast with the previously published conventional quartz single mineral analysis data showing a large variation ($\delta^{18}O_{quartz}$ = 15.3‰ – 26.1 ‰, Luo et al., 1984; Zhang, 1985; Ma and Liu, 1991; Zhu and Peng, 2015). Yi (2012) detailed the formation stages of the main minerals in the Woxi deposit (consistent with this study), and measured the average homogenization temperatures (AHT) of fluid inclusions at different stages: Qz2 average 269 °C (between 245 to 288 °C, stage 2: quartz-wolframite-scheelite), Qz3a average 216 °C (between 197 to 245 °C, early stage 3: quartz-pyrite-gold), Qz3b average 186 °C (between 147 to 197 °C, later stage 3: quartz-stibnite-pyrite-gold). The microthermometric data of this study can be well compared with related studies (Luo et al., 1984; Zhu and Peng, 2015), showing representative characteristics. Therefore, based on the microthermometric data of this study, the calculated oxygen isotope values ($\delta^{18}O_{fluid}$) of ore-forming fluids in equilibrium with quartz formed during the main second- and third- stage mineralization at Woxi range from 5.83‰ to 11.64‰ (Fig. 8a, b; Appendix 2), with the $\delta^{18}O_{fluid}$ values of Qz2, Qz3a, and Qz3b being 10.83‰ – 11.64‰, 8.01‰ – 9.19‰, and 5.82‰ – 6.56‰ respectively. Although the estimated AHT for each stage may not be highly accurate, the maximum range and trend of fluid oxygen isotope values were well constrained (Fig. 7c).

The Fig. 9 displays a comparison of the equilibrium $\delta^{18}O_{fluid}$ values calculated from in-situ O isotope analysis of quartz in this study, previous bulk quartz analyses, and the $\delta^{18}O_{fluid}$ values of typical gold-polymetallic deposits in the JOB, as well as different types of gold deposits in China and worldwide. The $\delta^{18}O_{fluid}$ values obtained from different stages of quartz have distinct sources, representing the most significant difference compared to the uncertainty in previous bulk analyses. Specifically, the $\delta^{18}O_{fluid}$ values of Qz2 range from 10.83‰ to 11.64‰, indicating a magmatic fluid source and falling within the range of traditional metamorphic fluids. This information has been overlooked in previous research and shares similarities with Phanerozoic orogenic gold deposits, orogenic gold deposits in China, Carlin-type gold deposits, and porphyry system gold-polymetallic deposits in terms of $\delta^{18}O_{fluid}$ values. This includes deposits such as Cenrro de Pasco, Daba, Yrieix, and Madrid. On the other hand, Qz3 (including Qz3a and Qz3b) primarily reflects the source of metasomatic lithospheric mantle, including deposits like Xichong and Xi'an near the Woxi deposit, as well as the typical Jiaodong gold province.

6. Discussion

6.1. The relationship between CL intensity and trace element variations

The CL intensity of hydrothermal quartz is related to the trace elements entering the lattice, with the content of Ti or Al being the main

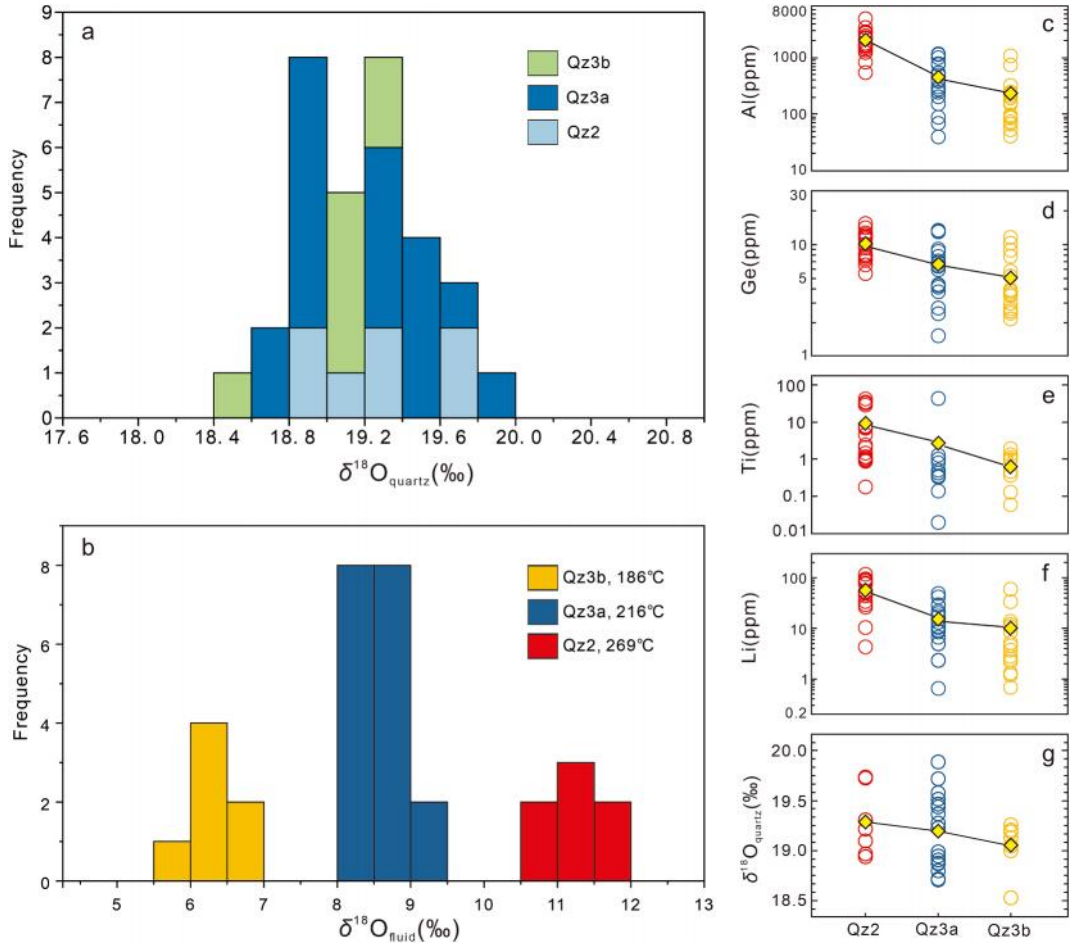

Fig. 8. (a-b) Shows the in-situ SIMS $\delta^{18}O$ values of mineralized quartz and fluids related to mineralization. It presents a narrow range of $\delta^{18}O$ values. The temperature used to calculate $\delta^{18}O_{fulid}$ is from the AHT of inclusions measured by Yi, (2012). (c-g) illustrate the variations in $\delta^{18}O$ values of mineralized quartz and concentrations of Li, Al, Ti, and Ge. Numerical values are represented by circles, while average values are indicated by squares connected by black lines. Fluid $\delta^{18}O$ values were calculated using the quartz-H_2O fractionation equation from Sharp et al., (2016).

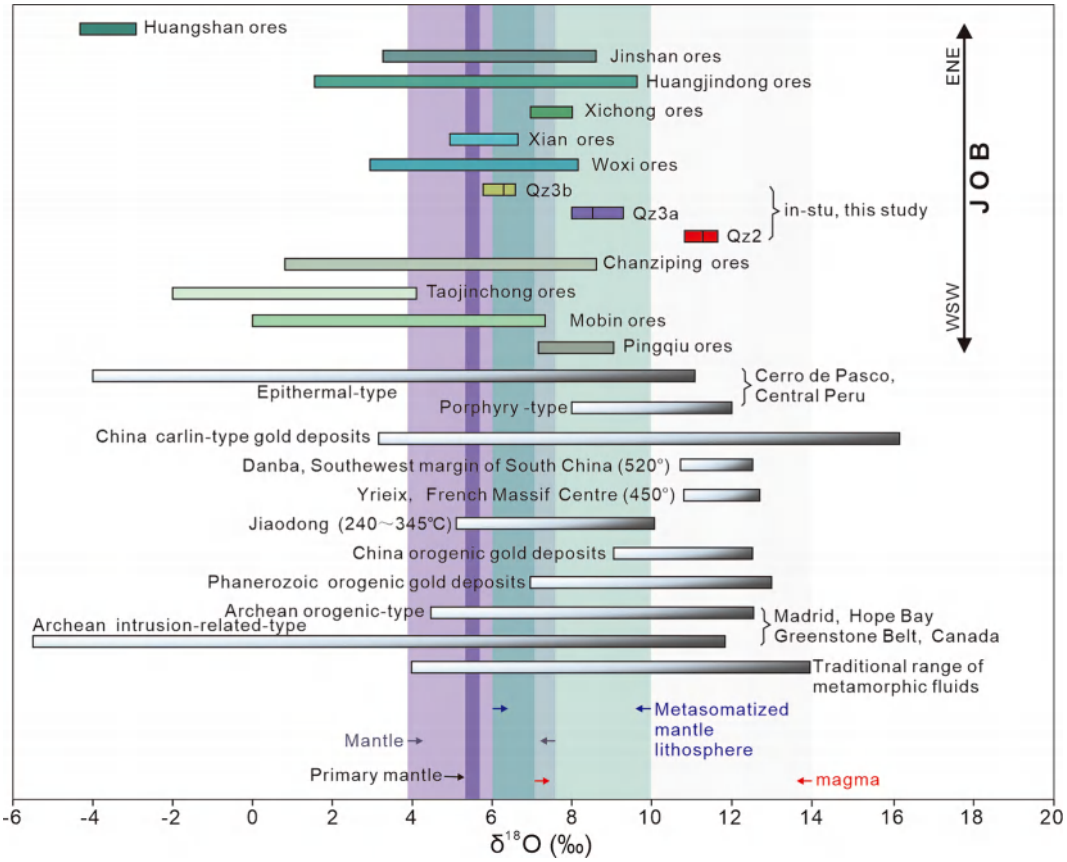

Fig. 9. Plot of $\delta^{18}O_{fluid}$ calculated from quartzs of ore-forming stage from Woxi (previous data come from Luo et al., 1984; Ma and Liu, 1991; Zhu and Peng, 2015). Also shown are calculated $\delta^{18}O_{fluid}$ values of JOB gold-polymetallic deposits (Xu et al., 2017 and its literature) including Pingqiu, Tangjinchong, Mobin, Chanziping, Xichong, Xian, Huangjindong, Jinshan, and Huangshan, Jiaodong gold deposits (Mao et al., 2008; Deng et al., 2015), Danba of Southwest margin of South China (Wang et al., 2020b), Yrieix of French Massif Central (Vallance et al., 2004), Cerro de Pasco of Central Peru (Rottier et al., 2021), Madrid of Hope Bay Greenstone Belt in Canada (Kerr et al., 2018), China carlin-type gold deposits (Yan et al., 2020; Li et al., 2020b), China orogenic gold deposits (Wang et al., 2022), wordwide traditional range of metamorphic fluids (Sheppard et al., 1986), and the typical range for Phanerozoic orogenic gold deposits (Goldfarb and Groves, 2015). The range for mantle, primary mantle, magma and metasomatized mantle lithosphere from Korolev et al. (2018), Goldfarb and Groves (2015) and Wang et al. (2022).The isotopic partition coefficients for quartz are from Sharp et al. (2016).

factor (Götze et al., 2004; Rusk et al., 2008; Raimbourg et al., 2022). In high-temperature ore deposits, the substitution of Ti^{4+} for Si^{4+} in the lattice of hydrothermal quartz is the main reason for the increase in CL intensity (Donovan et al., 2011), and there is a strong positive correlation between the CL intensity of hydrothermal quartz in porphyry deposits and Ti content (Mueller et al., 2003). In low-temperature ore deposits, the CL intensity of quartz is generally related to the content of Al and other monovalent cations (such as Li, K, P, and Fe) (Rusk et al., 2008).

The main mineralization temperature of the Woxi deposit is < 300° (Yi, 2012; Zhu and Peng, 2015), and the Ti content in hydrothermal quartz is generally low. The average value of Ti is Qz2 > Qz3 < Qz4 (Fig. 7), which is not related to the sequentially decreasing CL intensities (Fig. 5e; Fig. 6a; Fig. 5h, j). The Al content in Qz2 of the second stage is much higher than that in Qz3 of the third stage, and its luminescence intensity is also higher. The overall Al content in Qz3 of the second stage is low, and Qz3b is slightly lower than Qz3a, which is related to the decreased luminescence intensity of both phases. These characteristics indicate that the CL intensity of hydrothermal quartz in the area is generally positively correlated with the content of Al, but the differences in luminescence intensity caused by Al content are not particularly significant. The CL image of Qz3a shows a typical alternating bright and dark band structure, which may be related to the growth rate of quartz, changes in formation environment, or pulsating fluid flow (Goette et al., 2011; Li et al., 2023b).

6.2. *Variation of trace elements and properties of ore-forming fluids*

Ti, Li, Al, and Ge elements usually enter the quartz lattice of hydrothermal quartz by replacing Si^{4+} ions. The concentrations of these elements can reflect the physical and chemical conditions during quartz formation (Götze et al., 2004; Larsen et al., 2004; Goette et al., 2011; Audétat et al., 2014). The trace element contents of different generations at the Woxi deposit show that the contents of Al, Li, Ge, and Ti in Qz2 of the main ore-forming stage are much higher than those in Qz3, especially both the Al and Ti. When Al^{3+} replaces Si^{4+} in the quartz lattice, it occur together with monovalent cations (such as Li^{+} or K^{+}) to achieve charge balance ($Si^{4+} \rightarrow Al^{3+} + Li^{+}$) (Larsen et al., 2004; Audétat et al., 2014). There is a clear correlation between Al and Li in different stages of quartz at the Woxi deposit (Fig. 10a), especially in Qz3 and Qz4 ($R^2 = 0.92$), strongly supporting the coupled mechanism of ($Si^{4+} \rightarrow Al^{3+} + Li^{+}$). Previous studies have shown that Al in low-temperature (<350 °C) quartz has a strong positive correlation with monovalent cations (such as Li^{+}), while the positive correlation in high-temperature quartz (>400 °C) is weaker (Rusk, 2012). Qz2 exhibits a weaker correlation than Qz3 + Qz4 (Fig. 8a), primarily due to a few extreme values (Al > 3000 ppm). After removing these outliers, the $R^2 = 0.87$of Qz2, which is slightly different from Qz3 + Qz4. The findings suggest that the formation temperature of Qz2 is higher than that of Q3 + Q4, and they were generally formed in a low-temperature environment (< 350℃) (Yi, 2012; Zhu and Peng, 2015). However, Qz2 experienced ore-forming fluid pulses with high temperatures (>400 ℃). The Ti content in quartz

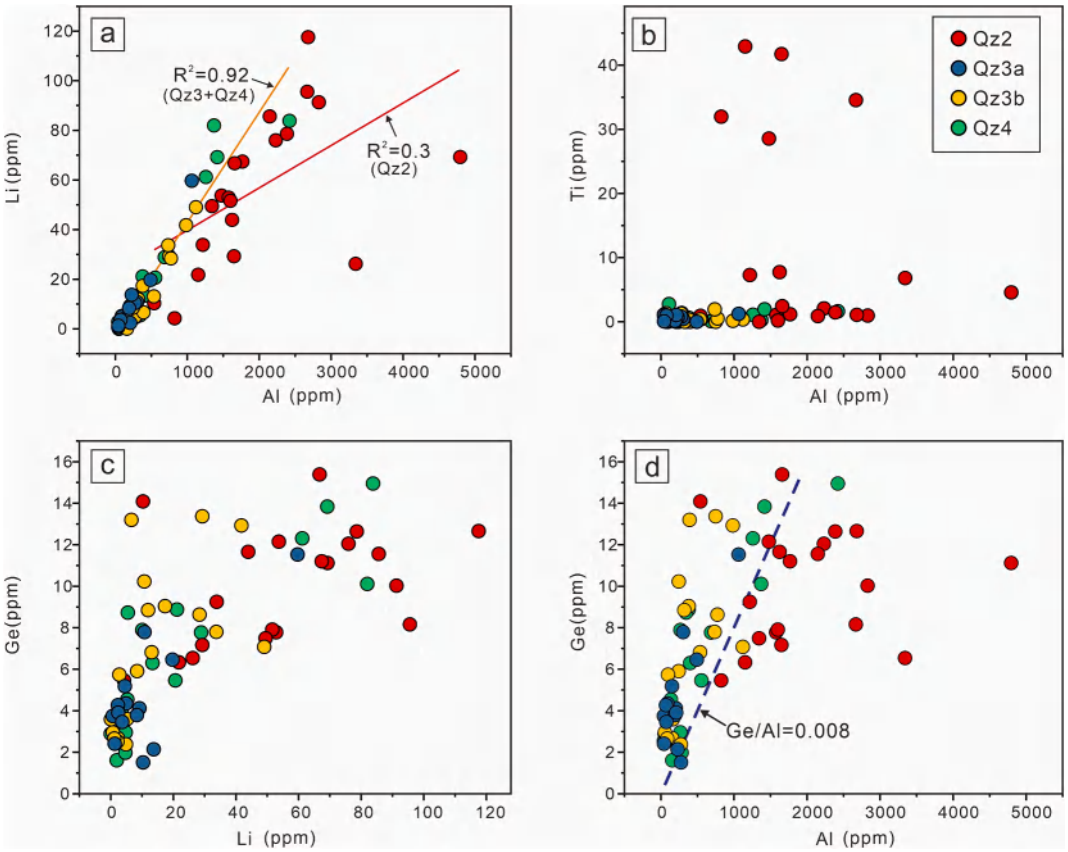

Fig. 10. Scatter plots of Al vs Li, Al vs Ti, Li vs Ge, and Al vs Ge for different generations of quartz in the Woxi deposit.

also supports these results (Fig. 6, Appendix 1). Overall, the Ti content in Qz2 is higher than that in Qz3 + Qz4; although most Ti contents in Qz2 are below 10 ppm, there are a few outliers (26–42 ppm). Although titanium may not be completely applicable to hydrothermal quartz (usually formed below 600℃, Huang and audetat, 2012), the Ti content results of quartz in the main metallogenic stage of Woxi deposit may still indicate that the formation temperature of Qz2 is significantly higher than that of Qz3 + Qz4, and there is high-temperature (>400℃) fluid pulse participating in mineralization in Qz2 stage (Zhang et al., 2019b; Li et al., 2020b), and this is brand new information.

It is notable that individual points with high Ti content (32 ppm) and exceptionally high K content (4482 ppm) in Qz2 indicate the possible presence of Ti-containing minerals (such as rutile) and K-containing minerals (such as kaolinite) micro-inclusions (Pi et al., 2017). Generally, the contents of trace elements such as Ti, Al, and K in ore-forming fluid decrease with temperature drop (Larsen et al., 2009). In the third ore-forming stage, the overall contents of Al, K, and Ti in Qz3a (quartz-gold ore) are higher than that in Qz3b (quartz-stibnite ore), indicating that stibnite mainly formed in the late stage at a lower ore-forming temperature.

The content of Al in hydrothermal quartz is strongly depends on the pH value of the fluid, and it is consistent with the content of Al in the fluid but not significantly related to temperature (Rusk et al., 2008; Lehmann et al., 2011). This is consistent with the lack of correlation between Ti and Al in the Woxi quartz (Fig. 10b). Studies have shown that (Rusk et al., 2008) at a temperature of 200 °C, the solubility of Al in a fluid with a pH of 1.5 is six times higher than that in a fluid with a pH of 3.5. At pH = 1.5, Al minerals are mainly kaolinite, while at pH = 3.5, muscovite begins to appear. Therefore, the concentration of Al in the fluid can indicate the evolution of fluid-rock interaction processes. The variation of Al values in Qz2 of the second stage is relatively small (mainly in the range of 538–3341 $\times$ 10^{-6}) and the average content is relatively high (average 1974 $\times$ 10^{-6}), indicating its formation in a acidic (pH is about 3) fluid environment, with silicified alteration dominantly (Rusk et al., 2008). The Al contents in Qz3 and Qz4 are at the same level, but they increase from Qz3a, via Qz3b to Qz4. The Al content in Qz3a is relatively low but largely variable (mainly in the range of 39.7–1063 $\times$ 10^{-6}, average 244 $\times$ 10^{-6}), indicating an increase in fluid pH compared to that of the second-stage Qz2, and thus requiring the occurrence of pH oscillations. Considering the zonal structure of quartz (Fig. 6a) and the angular ore minerals (Fig. 4g, k), this process may be related to periodic fluid depressurization (from lithostatic pressure to hydrostatic pressure) causing fluctuations in the physicochemical state (Zhang et al., 2019b; Chi et al., 2022). The Al content in Qz3b (mainly in the range of 53–1120 $\times$ 10^{-6}, average 391 $\times$ 10^{-6}) increases, indicating a decrease in pH value. The Al content in Qz4 (mainly in the range of 40–1471 $\times$ 10^{-6}, average 596 $\times$ 10^{-6}) increases again, higher than in Qz3, possibly due to intense fluid-rock reactions leading to alteration of the surrounding rocks and decomposition of Al-bearing minerals (such as kaolinite and illite), causing Al to reenter the fluid (Rusk et al., 2008; Yan et al., 2020). Overall, the pH value of the ore-forming fluid in the third-stage Qz3 (rich in Au-Sb-W) is between 3 - 5 (Rusk et al., 2008; Li et al., 2020b), while the pH value of the gold-forming fluid is higher than that of the Sb-W forming fluid. In addition, the content of CO_2 may be a more important factor affecting the Al content in the fluid compared to pH (Lehmann et al., 2011), the higher the CO_2 content in the fluid, the lower the solubility of Al. The Al content in the Qz2 stage is unusually high, indicating a very low CO_2 content in the ore-forming fluid. Conversely, the Al content in Qz3 is significantly lower, suggesting a higher CO_2 content in the ore-forming fluid. CO_2 serves as a crucial dissolution buffer that enhances the maximum solubility of Au complexes (Lu, 2008). This phenomenon can logically explain why the ore-forming fluid in the Qz2 stage is relatively deficient in gold, while the fluid in the Qz3 stage is comparatively rich in gold. Specifically, Qz3a in the quartz-

sulfide-gold stage exhibits the lowest Al content, indicating the highest CO_2 content and a fluid abundant in Au complexes. This characteristic also implies that the Al content in quartz could serve as a potential exploration indicator (Gao et al., 2022).

Due to compatibility, Ge^{4+} can directly substitute for Si^{4+} in the quartz lattice (Götze et al., 2004; Audétat et al., 2014), thus the content of Ge in hydrothermal quartz is mainly controlled by the concentration of Ge in the fluid (or melt). In the low-temperature isomorphic substitution process of quartz, only when enough Ge enters the lattice, Al atoms can be captured by the lattice catalyzed by Ge (Rakov, 2015). In the Woxi deposit, Ge, Al, and Li in different generations of quartz are positively correlated (Fig. 10 a, c), supporting this mechanism. The strong enrichment of Ge in Qz2 (average 10.2 ppm) indicates that the initial ore-forming fluid of the second-stage Qz2 stage is a Ge-rich solution, and it formed at a higher temperature (Müller et al., 2018). In Qz3 and Qz4, the content of Ge (average 6.7 ppm for Qz3a, average 5.02 ppm for Qz3b, average 6.87 ppm for Qz4) is also significantly higher than the Ge content in the upper crust (1.4 ppm, Rudnick and Gao 2004), but the Al value is lower and the correlation between Ge and Al is not obvious, indicating that the initial fluid of Qz3 and Qz4 may not be high in Ge, and Ge mainly comes from the decomposition or metasomatism of detrital quartz, feldspar, or other Ge-bearing minerals (such as mica or kaolinite) in the late surrounding rocks (Lehmann et al., 2011). It also indicates that there is a strong fluid-rock interaction during the third-stage mineralization. Of course, the high Ge content in Qz2 may also be contributed by later fluids. Müller et al. (2018) believed that the Ge/Al ratio can differentiate magmatic quartz (Ge/Al ratio < 0.008) from hydrothermal quartz (Ge/Al ratio > 0.008). In the Woxi deposit, the Ge/Al ratio can effectively distinguish different stages of quartz into two groups: Qz2 is shown as "magmatic quartz," while Qz3 + Qz4 is "hydrothermal quartz." This result may only indicate two different stages of hydrothermal mineralization, becuase, field observations show that Qz2 is not magmatic quartz (Fig. 3c, h; Fig. 4a-e), it occurs in the form of thin veins in strongly silicified altered ores.

In summary, the contents and changes of Al, Li, Ti and Ge elements in quartz at different stages in Woxi deposit show that Qz2 is significantly different from Qz3 + Qz4: Qz2 ore-forming fluid has relatively higher temperature and high-temperature ore-forming fluid pulse, higher trace element content and lower pH value, and is strongly rich in Al, Ge and poor in Au; Qz3 and Qz4 have relatively low trace element contents and higher pH values (Qz3a → Qz3b → Qz4 increase in turn), and Qz3a gold precipitation has the highest pH value.

6.3. Deposition mechanisms of ores and sources of ore-forming fluids

Previous studies on the origin of materials were mostly based on whole-rock analysis on S-Pb and C-H-O isotopes of the Woxi mineral ores. However, the mixing of some unrelated vein quartz or sulfides has led to the uncertainty of the fluid source area as a mixed signal and research results, such as deep-seated crustal fluids (Peng and Frei, 2004; Zhu and Peng, 2015), mixing of metamorphic fluids and atmospheric water (Yi, 2012; Zhang, 2017), and mixing of magmatic fluids and surrounding rock fluids (Peng et al., 2006), etc. In this study, O isotopes in quartz of the different stages of mineralization at Woxi were investigated using in-situ microanalysis technique, which revealed the episodic evolution and origin of ore-forming fluids. In Qz2, the content of Ti (Fig. 6, Appendix 1) shows a small amount of extremely high value (28–42 ppm) and a high Al content (average 1975 ppm) consistent with low-temperature quartz (Rusk, 2012). At the same time, $\delta\,^{18}O_{fluid}$ of Qz2 is mainly shown as the range of magmatic and metamorphic fluids (Fig. 5, Fig. 7, Fig. 11), which is more consistent with the gold polymetallic deposits of magmatic system, such as Cerro de Pasco (Fig. 11). The possible explanation is that the mineralization in Qz2 stage is an exsolution fluid of magma (generally $\delta^{18}O > 10$, Hoefs, 2021) formed by the melting of metamorphic rocks in the deep crust, and may be mixed with a small amount of metamorphic fluid (cooling). Because Qz2 is relatively rich in trace elements, especially high Al, indicating a rapid and low-pressure growth environment (Raimbourg et al., 2022), we speculate that its formation mechanism may be due to the instantaneous vaporization of ore-forming fluid and the rapid coprecipitation of a series of trace elements under the extremely low pressure generated by the expansion of ore-bearing structural cavity (Weatherley and Henley, 2013).

In the Qz3 of the third-stage mineralization, i.e. the quartz-iron sulfide-stibnite-scheelite-gold stage, the range of $\delta^{18}O_{fluid}$ values in the ore-forming fluids is small (Fig. 6c; Fig. 8), and is estimated to fall within the range of magma and metasomatic lithospheric mantle based on temperature. In the Qz3a stage (quartz-pyrite-gold), the Al content is an order of magnitude lower compared to Qz2, and exhibits a large variation range. However, the fluctuation of Ti content is not significant, indicating that the fluid in this period experienced pH fluctuations under relatively stable temperature conditions, possibly related to the

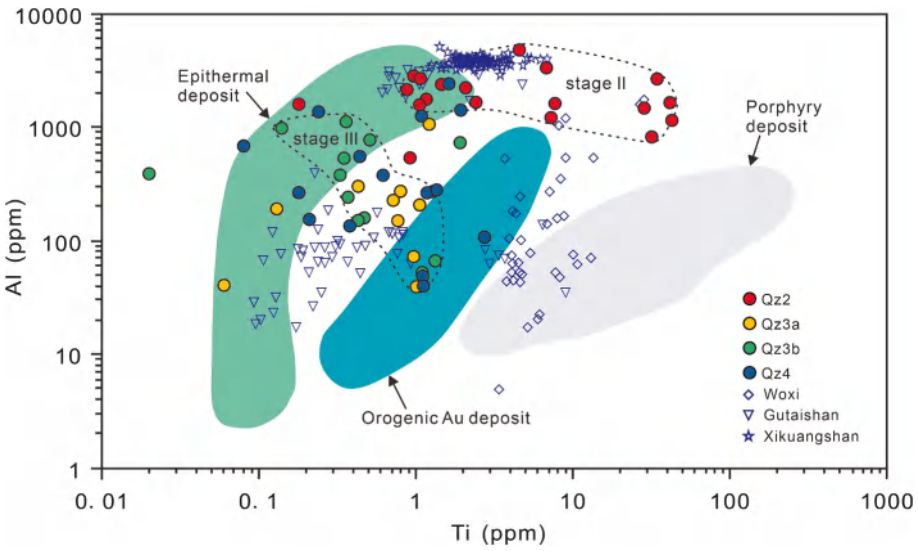

Fig. 11. Displays a logarithmic Ti versus Al plot of quartz from Woxi deposits, which is compared with data from (Rusk, 2012) including porphyry-type Cu-Mo-Au deposits, orogenic Au deposits, and epithermal Au deposits. The black dashed circles represent the main range of Qz2 and Qz3. Data sources: Woxi and Xikuangshan mining sites (Fu et al., 2020b), Gutaishan mining site (Feng et al., 2020).

aforementioned water–rock reactions (Rusk, 2012; Xu et al., 2022), which consistent with the widespread fading alteration in the surrounding rocks of the study area (Chen et al., 2008; Xu et al., 2017).The CL image of Qz3a reveals a banded structure with alternating light and dark bands (Fig. 6a), and the variation of in-situ SIMS O isotopes in the texture demonstrates fluctuations in the sources and intensity of ore-forming fluids (Fig. 6a, b). The $\delta^{18}O$ values from the core to the edge of Qz3a, there are two trends of increase and decrease, both within the range of magma and metasomatic lithospheric mantle activity, indicating mantle derived fluid dominated and limited metamorphic fluid participation, which may be caused by the participation of mantle derived fluid pulsation with different intensities in mineralization (Li et al., 2023b). Therefore, fluctuations in pH and periodic hydrothermal pulses leading to pressure changes may effectively promote gold precipitation. In the Qz3b stage, the Al content in quartz decreases, and the Ti content decreases significantly, indicating an increase in fluid pH and a decrease in temperature, which may be related to the mixing of atmospheric water (Li et al., 2018; Li et al., 2019b; Li et al., 2019c; Fu et al., 2020a). This is consistent with the decreasing trend of in-situ O isotopes in quartz from Qz3a to Qz3b stage (Fig. 6c; Fig. 8). Therefore, fluid mixing may be the main precipitation mechanism for Sb-Sch in this stage. The widespread development of hydraulic breccia and multi-stage open filling veins in the Qz3 stage also indicates periodic fluid activity, which may be controlled by deep fault valve mechanisms (Sibson et al., 1988; Peterson and Mavrogenes, 2014; Chi et al., 2022).

6.4. Genetic of ore deposits

The contents of Al and Ti in hydrothermal quartz can be used to indicate the genetic types of gold deposits (Rusk, 2012; Wang et al., 2021b). In the Al vs Ti diagram (Fig. 11), different generations of Al and Ti elements in the Woxi deposit exhibit two groups, including Qz2 with Qz3 and Qz4. The Al content in the ore-forming stage Qz2 (average 2102 ppm) is much higher than that in typical orogenic gold-bearing hydrothermal quartz (100–1000 ppm, Rusk, 2012). The data points mainly fall above the orogenic and porphyry gold deposits, partly overlapping with the upper margin of shallow low-temperature hydrothermal type, indicating early rich Al, Ge, and Ti, and poor Au in the quartz units. The data points of Qz3 span different types of gold deposits. Qz3a (quartz-gold) mainly falls in the region between shallow low-temperature and orogenic types, while Qz3b (quartz-stibnite-wolframite) spans three types of gold deposits (including Fu et al., 2020b data). It is similar to the quartz from the ancient Taishan gold deposit in the region, which is defined as related to the emplacement of the Bai Ma Shan S-type granite formed during the late Indosinian extensional background (Feng et al., 2020).

The covariation between the isotopes and trace elements of hydrothermal quartz may reflect the physical–chemical parameters of the fluid (Li et al., 2020b). In the research area, there is a covariant (decreasing) relationship between the $\delta^{18}O_{fluid}$ in the main ore-forming stage and the major trace elements Al, Ge, and Ti (Fig. 8c-g). This relationship seems to be attributed to a decrease in temperature (Müller et al., 2018; Li et al., 2020b). However, due to (1) the relatively high-temperature quartz-wolframite veins (Qz2) being located at the topmost part of the deposit (Chen et al., 2008; Li et al., 2022a), while the low-temperature Qz3 (quartz-stibnite-scheelite-gold) is developed from the shallow to deep parts of the deposit; (2) significant differences in fluid properties between the Qz2 stage and the Qz3-Qz4 stages, with an evolutionary trend from Qz3a to Qz3b to Qz4; (3) coexistence of interbedded brittle-ductile shear deformation and brittle domain fault gouges (Fig. 2d); and brittle-ductile deformation features in early wolframite veins, while brittle ore-bearing structures in late antimony veins. All of these observations suggest that early quartz-wolframite (with minor gold and scheelite) formed in deeper environments, and after a period of mineralization hiatus and crustal uplift, late-stage large-scale gold-antimony-tungsten (Qz3) superimposed mineralization occurred during subsequent tectonic-magmatic activities. Therefore, it is not a simple covariant relationship, but the combination of in-situ trace elements, oxygen isotopes, and geological features reflect the superimposition of two stages of mineralization processes.

Some scholars believe that the Woxi gold-antimony-tungsten deposit is a sedimentary-exhalative (SEDEX) type deposit (Gu et al., 2012). However, the host rocks of the deposit are Neoproterozoic rocks, while the main mineralization age is in the Late Mesozoic (Dai et al., 2022; Li et al., 2022a; Li et al., 2023a) or Paleozoic (Peng et al., 2003), which does not support this view. Some scholars classify it as an orogenic gold deposit of the Caledonian period (Zhu and Peng, 2015), mainly based on the Paleozoic mineralization age and similar fluid characteristics to orogenic gold deposits (such as medium–low temperature, low salinity, and a combination of CO_2-NaCl-H_2O) (Yi, 2012; Zhu and Peng, 2015). However, the new and more accurate LA-ICP-MS U-Pb mineralization ages range from 149 to 124 Ma (Tang et al., 2022; Dai et al., 2022; Li et al., 2022a; Zhu et al., 2023; Li et al., 2023a; Li et al., 2024), indicating an important connection between the mineralization dynamics and lithospheric extension caused by subduction and back-arc extension of the paleo-Pacific plate (Fig. 9c, f) (Li et al., 2014; Zhu and Xu, 2019), rather than a significant relationship with the Caledonian orogeny.

This research support a two-stage mineralization model of the Woxi deposit, which is related to the deep magma intrusion and the addition of mantle-derived fluids, consistent with the early inferences (Ma and Liu, 1991; Peng and Frei, 2004; Peng et al., 2006), and supported by the in-situ S isotope of pyrites in ore-forming stage (Dai et al., 2022; Li et al., 2024). Furthermore, the new geophysical exploration results reveal the presence of intrusive rocks at depths greater than 2 km (Wang et al., 2022), further supporting this finding. Importantly, the metallogenic age of the Woxi deposit spans about 25 Ma and shows two main metallogenic periods, namely, the average ages of the early wolframite (containing a small amount of gold and scheelite) and the late gold-antimony-scheelite are ~ 142 Ma and ~ 130 Ma, respectively (Tang et al., 2022; Li et al., 2024). For the Woxi deposit, which is driven by deep tectonic-magmatic activity, a magmatic intrusion event is difficult to explain the mineralization for such a long time, because in the middle and upper crust, it only takes nearly 10000 years for 1 km wide intrusions to condense to the solidus, and even larger intrusions can condense to the temperature conditions of the solidus as long as tens of thousands of years (Stimac et al., 2001). Therefore, there may be two stages of emplacement (remelting reactivation) in the deep part of Woxi, which is coupled with the tectonic setting of episodic subduction and roll-back of the paleo Pacific in Yanshanian (Chu et al., 2019; Zhu and Xu, 2019).

In summary, we have summarized the two-stage mineralization model of the Woxi super-large gold-antimony-tungsten deposit (Fig. 12). In the early stage of mineralization (ca. 142 Ma), under the tectonic setting of the westward subduction and rollback of the paleo-Pacific plate, mantle convection occurred in the distant back-arc region (Fig. 12 c), and magma formed by crustal (metamorphic rocks) decompression melting infiltrated into the upper crust along magma channels(Fig. 12 a). Subsequently, ore-bearing fluids evolved from the magma rapidly ascended through large-scale fault zones in the lithosphere (such as the HGF, Fig. 1c). In the ore-bearing structures, when the hydrostatic pressure is greater than the hydrostatic pressure, the ore bearing space expands rapidly and the ore-forming fluid flashing, resulting in the precipitation of quartz (Qz2) – wolframite (Fig. 12 a, b). The ore-forming fluid at this stage is a reductive magmatic fluid (with high-temperature fluid pulse) that is strongly rich in Ge and Al, relatively rich in Ti, and pH around 3. The water rock reaction ratio is low (Rusk et al., 2008). During the late mineralization stage (ca. 130 Ma), the paleo-Pacific plate subducted and retreated again, resulting in slab detachment and mantle upwelling (Fig. 12 f), along with large-scale lithospheric extension and magmatic activity (Griffin et al., 2013; Zhu and Xu, 2019). The upwelling asthenospheric mantle may carry metamorphic fluids from the subducting plate, causing the lithospheric

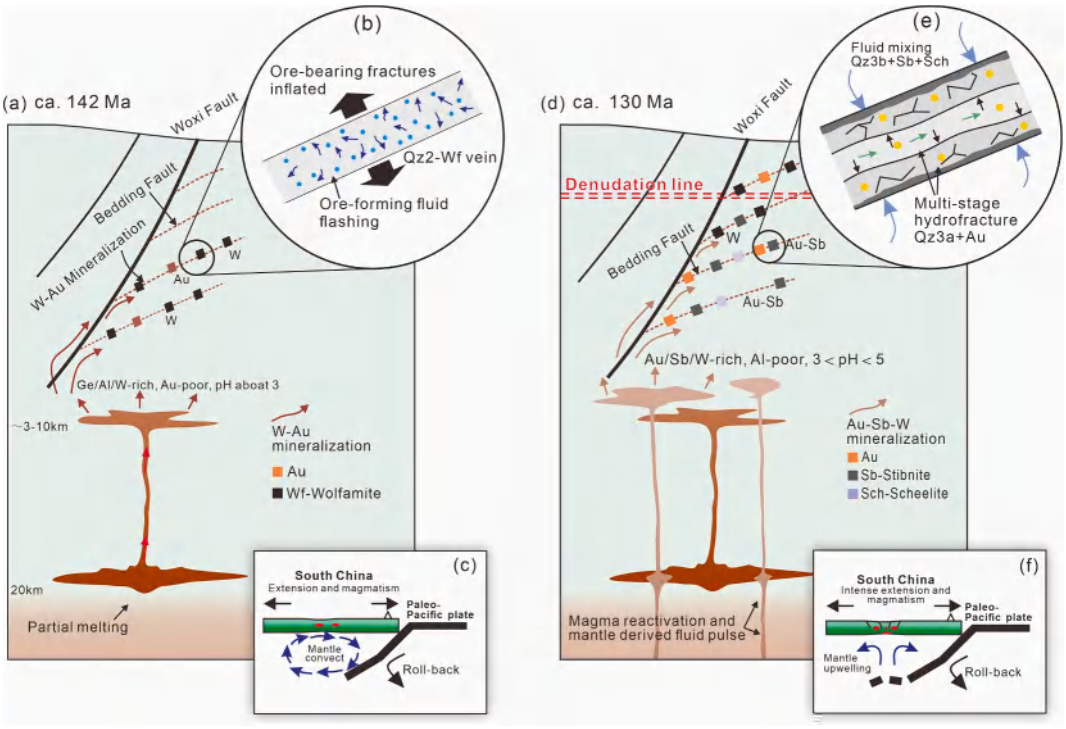

Fig. 12. Ore-controlling structural background, genetic model, and main metal precipitation mechanism of the Woxi deposit. The two-stage ore-forming model of the Woxi deposit is related to lithosphere extension and magmatism caused by subduction-rollback of the paleo-Pacific plate. The subduction model of the paleo-Pacific plate is based on (Zhu and Xu, 2019; Li et al., 2022a). The ages of the two ore-forming stages are the average values of the corresponding ore-forming stage ages obtained by previous researchers.

mantle in the back-arc area to undergo metasomatism rich in gold (Zhu and Sun, 2021). This process can also activate the early residual metasomatic lithospheric mantle (Deng et al., 2020; Dai et al., 2022), releasing fluid rich in gold ore formation (Fig. 12 d). The mantle derived Au rich fluid mixed with the fluid evolved from the crust mantle mixed magma to further form Au, Sb and W enriched ore-forming fluids (Fu et al., 2020b; Li et al., 2022b; Li et al., 2024), and then formed a large-scale gold-antimony-scheelite metallogenic superimposition in the lower order structure in the shallow crust through the structural conduction at different scales described in the early stage (Fig. 12e). The early (Qz3a) Au metallogenic period of this stage reflects the addition of periodic mantle derived fluids and the long metallogenic process, which may be related to the fault valve mechanism (Sibson et al., 1988; Chi et al., 2022). Water rock reaction and fluid pH fluctuation jointly promote the precipitation of gold. The mineralization has the highest pH value, the highest CO_2 and the lowest Al content. The late (Qz3b) antimony mineralization is related to the addition of low-temperature water (probably atmospheric water) (Li et al., 2019b; Li et al., 2020a; Fu et al., 2020b; Li et al., 2024), and the ore-forming fluid relatively rich in Al and pH between 3–5 originate from magma(Fig. 12 d, e). Additionally, based on the above study, we believe that the content of Al in quartz may be a potential exploration indicator at the regional (Gao et al., 2022).

The formation of large to super-large ore deposits is usually the result of the best combination of multiple special geological processes (Richards, 2013). Our research indicates that the Woxi gold (antimony-tungsten) deposit mainly formed in a stretching background related to the westward subduction of the ancient Pacific plate, coupled with deep-seated multiple intrusions of magma and early tectonic activation, as well as dual mineralization processes. Xu et al. (2017) proposed the concept of "intracontinental activation type" to summarize a type of mineral deposit located within the continent, which is related to tectonic-magmatic activation, especially stretching background. This study demonstrates that the Woxi deposit may be one of the best examples of this type of deposit. In the JOB within South China, the evolution of ore-forming fluids (such as changes in Al and CO_2 content) may be one of the factors contributing to the diversity of mineralization. For intracontinental mineralization in South China, post-arc lithospheric stretching caused by continental margin subduction is a key tectonic background for mineralization, controlling the formation of regional Yanshanian large to super-large gold-polymetallic deposits through tectonic-magmatic activation and possible overprinting mineralization.

7. Conclusions

This study suggestted a dual mineralization process in the Woxi gold-antimony-tungsten deposit, i. e., the late hypabyssal large-scale gold-antimony-scheelite mineralization is superimposed on the early wolframite mineralization (small amount Scheelite and Au):

1. The CL intensity of early stage quartz Qz2 (stage II) and late stage quartz Qz3 + Qz4 (stage III − stage IV) is mainly positively correlated with the content of Al, but the difference of luminous intensity caused by al content is not significant.
2. The early stage quartz wolframite (a small amount of pyrite scheelite gold) ore-forming fluid is rich in trace elements, strongly rich in Al, Ge and relatively rich in Ti, which is an acid reducing fluid with relatively high temperature (with high-temperature fluid pulse) and pH of about 3, while the late stage gold antimony tungsten ore-forming fluid is characterized by low temperature, no enrichment of trace elements, relatively rich in Ge, poor in Ti and pH of 3–5.
3. The ore-forming fluid in the early stage (Qz2) is mainly derived from the molten magmatic fluid of deep metasedimentary rocks, and the possible mechanism of quartz wolframite precipitation is fluid flash; in the late stage (Qz3), the ore-forming fluid was added by periodic mantle derived fluid. The gold precipitation in the early stage (Qz3a) was related to water rock reaction, pH and pressure fluctuation, and

the Sb precipitation in the late stage (Qz3b) was related to the mixing of atmospheric water.

Our research results combined with previous data show that the tectonic setting of Yanshanian intracontinental mineralization in South China, including the Woxi Au-Sb-W deposit, is the large-scale extension of the lithosphere in the back arc region caused by episodic subduction of the continental margin paleo-Pacific plate. The Woxi Au-Sb-W deposit, which is related to pre-tectonic activation and multi-stage magmatic intrusion, can be defined as "intracontinental activation type". Our work also shows that quartz is useful for identifying superimposed mineralization in intracontinental JOB.

Declaration of competing interest

The authors declare that they have no known competing financial interests or personal relationships that could have appeared to influence the work reported in this paper.

Data availability

Data will be made available on request.

Acknowledgments

This study was funded by the Science and Technology Program of the Geological Bureau of Hunan Province (HNGSTP202407, 201917, HNGSTP202306, HNGSTP202302), the Natural Science Foundation of Hunan Province (2024JJ8344), and the National Natural Science Foundation of China (41930428). We would like to thank Dr. Sheng He from the Beijing Research Institute of Uranium Geology (BRIUG), Dr. Jian Zhang and Yan Zhao from East China University of Technology (ECUT) for their assistance in experiments and writing, as well as Chenzhou Mining Co., Ltd. for its support of this study. We are very grateful to Professor Huan Li from Central South University (CSU), the other anonymous reviewer, and the responsible editor Professor Huayong Chen and editor Alla Dolgopolova for their valuable review and contributions to this article.

Appendix 1 The main trace element content of quartz in different mineralization stages of the Woxi deposit (LA-ICP-MS, ppm).

Sample no.	Stage	Li	Na	Al	P	K	Ca	Ti	Ge	Sr	Sb	W	Au	Pb
D311-1b-1	Qz2	33.87	16.44	1215.84	20.68	43.39	183.37	7.29	9.25	1.11	275.04	0.17	0.05	0.00
D311-1b-2	Qz2	95.57	20.57	2668.08	31.09	85.70	248.12	34.56	8.16	2.00	980.99	421989.03	0.07	0.62
D311-1b-3	Qz2	53.72	12.89	1476.92	18.10	27.25	269.27	28.57	12.15	1.18	368.26	168202.68	0.03	0.05
D311-1b-4	Qz2	75.98	25.30	2230.66	7.45	72.75	290.35	2.08	12.05	2.35	309.20	0.00	0.10	0.11
D311-1b-5	Qz2	69.27	25.34	4794.71	2.70	808.45	151.05	4.57	11.12	1.78	197.32	0.18	0.10	0.00
D311-1b-6	Qz2	85.63	21.44	2146.77	50.41	19.34	259.85	0.88	11.56	1.27	175.41	1.48	0.00	0.09
D311-1b-7	Qz2	10.33	21.66	538.41	18.95	16.53	169.17	0.92	14.09	1.78	342.85	0.05	0.03	0.06
D311-1b-8	Qz2	91.32	35.00	2828.39	22.64	36.83	174.66	0.97	10.03	1.94	140.23	0.06	0.00	0.06
D311-1d-1	Qz2	67.42	24.51	1766.84	34.75	31.63	318.68	1.17	11.20	1.26	1264.22	675.46	0.19	1.49
D311-1d-1-1	Qz2	52.88	19.39	1576.24	3.77	43.56	331.94	1.06	7.78	1.87	624.77	0.12	0.00	0.31
D311-1d-2	Qz2	78.62	38.55	2385.77	14.26	43.02	264.37	1.46	12.64	2.85	610.16	0.19	0.00	0.00
D311-1d-2-1	Qz2	51.63	23.96	1599.68	0.31	48.57	417.02	0.18	7.91	2.09	361.38	0.10	0.07	0.07
D311-1d-3	Qz2	117.55	35.95	2680.40	0.00	27.64	266.28	1.07	12.66	1.46	261.50	4.44	0.00	0.07
D311-1d-6	Qz2	49.48	20.28	1342.89	13.32	45.70	166.13	0.00	7.49	1.65	876.26	0.20	0.05	0.00
D311-1d-6-1	Qz2	4.26	32.81	822.91	148.08	4482.17	452.14	31.97	5.46	1.00	159.97	3.12	0.04	0.13
D311-1d-7	Qz2	29.26	19.68	1649.68	11.98	278.94	236.36	41.74	7.17	1.23	236.70	1.12	0.00	0.14
D311-1d-8	Qz2	43.95	45.40	1622.84	31.97	38.96	692.23	7.73	11.66	5.33	1655.62	0.16	0.24	0.12
D311-1d-8-1	Qz2	66.75	15.43	1659.18	12.82	12.82	238.46	2.42	15.39	0.74	124.10	0.00	0.00	0.00
D311-1d-9	Qz2	26.20	29.68	3341.33	0.00	958.38	190.15	6.81	6.54	3.23	254.76	0.51	0.04	0.27
D311-1d-4	Qz3a	2.29	11.58	151.64	2.86	8.96	336.37	0.43	2.68	0.78	224.94	0.00	0.11	0.07
D311-1d-4-1	Qz3a	21.81	14.12	1150.73	13.03	183.07	305.44	42.91	6.33	1.02	489.53	0.79	0.00	0.55
D311-1d-4-2	Qz3a	29.27	2.15	747.84	0.00	13.68	318.88	0.00	13.37	0.13	10.61	0.26	0.00	0.08
D311-1d-5	Qz3a	4.90	15.85	271.71	11.40	7.39	265.06	1.28	2.38	0.62	233.18	0.00	0.00	0.02
D311-1d-5-1	Qz3a	6.63	15.70	390.74	33.86	6.17	323.95	0.02	13.20	0.91	306.27	0.06	0.00	0.05
D311-1d-5-2	Qz3a	13.11	22.42	535.30	5.04	13.31	308.96	0.35	6.82	2.11	957.48	0.01	0.00	0.07
D315-1a-1	Qz3a	49.03	31.33	1119.79	20.04	16.80	305.65	0.36	7.08	1.07	138.21	0.01	0.00	0.09
D315-1a-3	Qz3a	8.45	14.45	242.99	15.61	12.57	246.49	0.00	5.91	0.57	192.41	0.00	0.00	0.00
D315-1a-3-1	Qz3a	28.38	26.75	773.23	10.39	3.75	207.88	0.51	8.63	0.72	56.12	0.00	0.04	0.05
D315-1a-4	Qz3a	17.36	34.13	380.08	24.71	7.17	265.28	0.33	9.04	0.66	137.93	0.11	0.00	0.21
D315-1a-6	Qz3a	41.78	28.84	983.86	5.03	4.35	251.25	0.14	12.93	0.53	70.42	0.08	0.00	0.00
D316-1a-3	Qz3a	19.73	14.96	489.37	11.45	3.04	370.14	0.00	6.46	0.29	22.44	0.00	0.03	0.02
D316-1a-4	Qz3a	9.16	5.33	202.05	3.51	7.54	236.04	0.00	4.12	0.11	43.76	0.03	0.00	0.00
D316-1a-5	Qz3a	10.80	7.49	302.35	3.86	6.74	271.36	0.43	7.79	0.20	84.78	0.00	0.00	0.02
D316-1a-6	Qz3a	0.64	1.64	39.69	0.00	1.35	244.14	1.01	3.75	0.00	2.46	0.00	0.11	0.02
D321-1a-2	Qz3a	10.36	6.66	274.17	21.50	7.99	487.42	0.80	1.51	0.13	11.63	0.03	0.00	0.00
D321-1a-4	Qz3a	4.94	19.36	88.08	0.00	0.00	222.37	0.00	4.35	0.15	24.05	0.00	0.27	0.00
D321-1a-5	Qz3a	2.32	24.47	68.54	0.00	3.79	233.16	0.00	4.27	0.19	38.39	0.04	0.00	0.12
D315-1a-2	Qz3b	33.72	28.68	733.91	32.32	7.47	237.26	1.92	7.80	1.14	117.16	0.06	0.00	0.05
D315-1a-5	Qz3b	11.95	25.69	318.61	13.02	8.74	93.11	0.00	8.85	0.81	138.31	0.10	0.08	0.17
D316-1a-1	Qz3b	59.70	4.08	1063.11	17.68	7.16	463.26	1.22	11.53	0.11	75.07	0.04	0.00	0.08
D316-1a-2	Qz3b	4.52	4.24	150.75	0.00	1.32	318.18	0.77	5.18	0.13	29.00	0.01	0.00	0.04
D316-1a-7	Qz3b	13.74	0.85	227.85	17.17	7.68	168.53	0.72	2.14	0.05	8.18	0.00	0.00	0.00
D316-1a-8	Qz3b	8.38	4.17	192.12	18.57	8.12	254.43	0.13	3.79	0.48	12.76	0.03	0.00	1.12
D321-1a-1	Qz3b	2.42	14.43	207.85	45.50	38.74	413.78	1.06	3.91	0.25	26.29	0.04	0.07	0.00
D321-1a-3	Qz3b	3.69	3.09	73.09	7.07	0.95	346.68	0.97	3.46	0.04	7.89	0.00	0.00	0.00
D321-1a-6	Qz3b	1.29	11.90	40.91	33.79	4.98	309.27	0.06	2.41	0.29	38.86	0.00	0.09	0.00
D324-1-1-1	Qz3b	2.77	24.25	96.19	22.81	4.75	447.10	0.00	5.74	0.39	96.58	0.39	0.05	0.15
D324-1-2	Qz3b	10.74	13.95	243.07	27.82	4.47	307.89	0.37	10.23	0.01	64393.11	0.07	0.00	56.43
D324-1-2-1	Qz3b	5.17	0.54	89.28	0.00	4.19	332.44	0.00	3.60	0.05	212.21	0.00	0.00	0.10

(*continued on next page*)

(*continued*)

Sample no.	Stage	Li	Na	Al	P	K	Ca	Ti	Ge	Sr	Sb	W	Au	Pb
D324-1-3	Qz3b	2.15	7.20	67.08	23.31	7.58	312.81	1.33	2.52	0.10	36.87	0.02	0.00	0.06
D324-1-4	Qz3b	0.67	10.67	52.90	0.00	5.39	225.13	1.10	2.96	0.13	103.29	0.13	0.00	0.00
D324-1-4-1	Qz3b	1.18	19.53	85.61	41.23	6.64	278.38	0.00	2.66	0.11	129.36	0.00	0.00	0.00
D324-1-5	Qz3b	0.08	2.82	160.18	60.23	5.04	351.38	0.47	3.59	0.25	54722.79	1.11	0.10	27.25
D316-2-1	Qz4	81.96	20.65	1371.19	0.00	7.47	327.69	0.24	10.11	0.27	160.31	0.02	0.03	0.06
D316-2-2	Qz4	2.79	0.46	40.27	17.92	7.08	10955.71	1.12	2.55	7.26	6.88	0.03	0.00	2.76
D316-2-3	Qz4	0.00	6.16	49.17	14.69	7.81	264.75	1.11	2.89	0.49	9.87	0.08	0.07	0.02
D316-2-4	Qz4	61.20	5.16	1258.61	11.36	0.03	158.88	1.09	12.31	0.08	130.91	0.00	0.00	0.00
D316-2-4-1	Qz4	69.20	7.58	1417.15	4.02	2.78	230.76	1.94	13.84	0.17	137.11	0.00	0.00	0.01
D316-2-5	Qz4	5.31	2.21	136.08	0.00	3.08	194.71	0.38	4.54	0.10	14.50	0.05	0.00	0.02
D316-2-5-1	Qz4	28.88	30.29	686.69	18.46	2.71	149.58	0.08	7.77	0.53	53.47	0.00	0.04	0.04
D316-2b-1	Qz4	83.82	21.74	2420.75	0.00	15.31	6200.99	1.63	14.95	5.01	491.77	0.04	0.00	1.69
D321-1a-7	Qz4	3.46	0.68	108.25	14.57	19.56	225.39	2.75	4.02	0.00	76.89	0.10	0.00	0.12
D321-1a-8	Qz4	1.94	4.11	154.98	28.46	0.55	192.10	0.21	1.61	0.04	11.34	0.10	0.00	8.75
D321-1a-9	Qz4	21.16	0.43	379.34	41.61	0.00	236.35	0.62	8.88	0.14	515.43	0.00	0.00	0.06
D323-1a-1	Qz4	10.11	12.20	266.42	0.00	7.44	452.56	0.18	7.89	0.26	204.20	0.00	0.09	0.02
D323-1a-2	Qz4	13.34	22.42	399.12	13.04	2.76	394.63	0.00	6.30	0.47	166.70	0.00	0.04	0.19
D323-1a-3	Qz4	20.65	15.92	553.73	34.24	14.38	431.55	0.44	5.46	0.29	91.23	0.00	0.00	0.00
D323-1a-4	Qz4	5.46	30.14	343.24	37.89	9.82	720.41	0.00	8.73	0.90	215.75	0.14	0.04	0.07
D323-1a-5	Qz4	4.71	30.16	281.35	4.52	4.29	203.47	1.36	1.98	0.62	191.95	0.05	0.09	0.00
D323-1a-6	Qz4	4.79	25.48	265.59	9.82	11.36	270.92	1.18	2.96	0.41	166.27	0.00	0.04	0.10

Appendix 2 The in-situ SIMS O isotopic composition of quartz in the main mineralization stage of the Woxi deposit

Sample no.	Stage	^{16}O count	±s	$^{18}O/^{16}O$	±s	$\delta 18O_{VSMOW}$(‰)	±s	AHT(°C)	$\delta^{18}O$Fluid(‰)
			%		%		abs(‰)		
L479@01	Qz2	1.73E+09	0.039	0.0020322	0.007	**18.94**	**0.07**	**269.00**	10.84
L479@2	Qz2	1.71E+09	0.045	0.002032523	0.008	**19.10**	**0.08**		11.00
L479@3	Qz2	1.71E+09	0.033	0.002032768	0.010	**19.22**	**0.10**		11.12
L479@4	Qz2	1.71E+09	0.031	0.002032937	0.011	**19.31**	**0.11**		11.21
L479@5	Qz2	1.71E+09	0.030	0.002032263	0.011	**18.97**	**0.11**		10.87
L479@6	Qz2	1.76E+09	0.037	0.002033814	0.009	**19.74**	**0.09**		11.64
L479@7	Qz2	1.74E+09	0.033	0.002033798	0.011	**19.73**	**0.11**		11.63
L480@01	Qz3a	1.78E+09	0.060	0.002032445	0.011	**19.23**	**0.11**	**216.00**	8.53
L480@02	Qz3a	1.78E+09	0.040	0.002032729	0.006	**19.37**	**0.06**		8.67
L480@03	Qz3a	1.78E+09	0.047	0.002031578	0.008	**18.80**	**0.08**		8.10
L480@04	Qz3a	1.79E+09	0.054	0.002031419	0.009	**18.72**	**0.09**		8.02
L480@05	Qz3a	1.78E+09	0.052	0.002031809	0.008	**18.91**	**0.08**		8.21
L480@06	Qz3a	1.78E+09	0.082	0.002031408	0.010	**18.71**	**0.10**		8.01
L480@07	Qz3a	1.78E+09	0.081	0.002032436	0.009	**19.23**	**0.09**		8.53
L480@08	Qz3a	1.78E+09	0.037	0.002032857	0.014	**19.44**	**0.14**		8.74
L480@09	Qz3a	1.78E+09	0.067	0.002033152	0.008	**19.58**	**0.08**		8.88
L480@10	Qz3a	1.77E+09	0.037	0.002033761	0.011	**19.89**	**0.11**		9.19
L480@11	Qz3a	1.78E+09	0.030	0.00203293	0.009	**19.47**	**0.09**		8.77
L480@12	Qz3a	1.77E+09	0.028	0.002031746	0.006	**18.88**	**0.06**		8.18
L480@13	Qz3a	1.78E+09	0.034	0.002031726	0.008	**18.87**	**0.08**		8.17
L480@14	Qz3a	1.76E+09	0.047	0.002031877	0.008	**18.95**	**0.08**		8.25
L480@15	Qz3a	1.78E+09	0.026	0.002031964	0.007	**18.99**	**0.07**		8.29
L480@16	Qz3a	1.78E+09	0.021	0.002032544	0.006	**19.28**	**0.06**		8.58
L480@17	Qz3a	1.77E+09	0.038	0.002033023	0.010	**19.52**	**0.10**		8.82
L480@18	Qz3a	1.77E+09	0.046	0.002033429	0.008	**19.72**	**0.08**		9.02
L477@01	Qz3b	1.99E+09	0.091	0.002032408	0.010	**19.26**	**0.10**	**186.00**	6.56
L477@2	Qz3b	1.99E+09	0.043	0.002031989	0.009	**19.05**	**0.09**		6.35
L477@3	Qz3b	2.00E+09	0.052	0.002032274	0.010	**19.19**	**0.10**		6.49
L477@4	Qz3b	2.00E+09	0.066	0.002031885	0.008	**19.00**	**0.08**		6.30
L477@5	Qz3b	2.00E+09	0.151	0.00203216	0.007	**19.13**	**0.07**		6.43
L477@6	Qz3b	1.98E+09	0.112	0.002032304	0.010	**19.21**	**0.10**		6.51
L477@7	Qz3b	2.00E+09	0.090	0.00203094	0.010	**18.53**	**0.10**		5.83

Note: The average homogenization temperatures (AHT) at different stages of ore formation are derived from the microthermometry conducted by Yi et al. (2012).

References

Audétat, A., Garbe-Schönberg, D., Kronz, A., Pettke, T., Rusk, B., Donovan, J.J., Lowers, H.A., 2014. Characterisation of a Natural Quartz Crystal as a Reference Material for Microanalytical Determination of Ti, Al, Li, Fe, Mn, Ga and Ge. Geostand. Geoanal. Res. 39 (2), 171–184.

Bai, D.Y., Li, B., Zhou, C., Sun, J., Wei, F.H., Zeng, G.Q., Jiang, W., Li, Y.M., Jiang, Q.S., 2021. Gold mineralization events of the Jiangnan Orogen in Hunan and their tectonic settings. Acta Petrol. Mineral. 40 (05), 897–922 in Chinese with English abstract.

Bai, D.Y., Li, B., Wu, M.J., Wang, Z.F., 2023. Deformation Sequences, Ore-forming Epoch and Attributes of Ore-bearing Structurals in the Zhazixi Sb-W Deposit, Hunan Province. Geotectonica et Metallogenia 47 (02), 260–283 in Chinese with English abstract.

Cao, X.Z., Flament, N., Li, S.Z., Müller, R.D., 2021. Spatio-temporal evolution and dynamic origin of Jurassic-Cretaceous magmatism in the South China Block. Earth Sci. Rev. 217, 103605.

Cernuschi, F., Dilles, J.H., Osorio, J., Proffett, J.M., Kouzmanov, A.K., 2023. A Reevaluation of the Timing and Temperature of Copper and Molybdenum Precipitation in Porphyry Deposits. Econ. Geol. 118 (5), 931–965.
Chen, M.H., Yang, H.C., Lou, Y.L., Bao, Z.X., Bao, J.M., 2008. Minerogenic particularity of Woxi W-Sb-Au deposit in west Hunan. Contributions to Geology and Mineral Resources Research, 23(01): 32-35+42(in Chinese with English abstract).
Cheval-Garabédian, F., Faure, M., Marcoux, E., Gouin, J., Picault, M., 2020. The La Bellière gold and antimony district (French Armorican Massif): A two-stage evolution model controlled by Variscan strike-slip tectonic. Ore Geol. Rev. 125, 103681.
Chi, G.X., Xu, D.R., Xue, C.J., Li, Z.H., Ledru, P., Deng, T., Wang, Y.M., Song, H., 2022. Hydrodynamic Links between Shallow and Deep Mineralization Systems and Implications for Deep Mineral Exploration. Acta Geologica Sinica (Beijing) 96 (1), 1–25.
Chu, Y., Lin, W., Michel, F., Xue, Z.H., Ji, W.B., Feng, Z.T., 2019. Cretaceous episodic extension in the South China Block, East Asia; evidence from the Yuechengling Massif of central South China. Tectonics 38 (10), 3675–3702.
Dai, J.F., Xu, D.R., Chi, G.X., Li, Z.H., Deng, T., Zhang, J., Li, B., 2022. Origin of the Woxi orogenic Au-Sb-W deposit in the west Jiangnan Orogen of South China: Constraints from apatite and wolframite U-Pb dating and pyrite in-situ S-Pb isotopic signatures. Ore Geol. Rev. 150, 105134.
Deng, J., Liu, X.F., Wang, Q.F., Pan, R.G., 2015. Origin of the Jiaodong-type Xinli gold deposit, Jiaodong Peninsula, China: Constraints from fluid inclusion and C-D–O–S–Sr isotope compositions. Ore Geol. Rev. 65, 674–686.
Deng, J., Wang, Q.F., Santosh, M., Liu, X.F., Liang, Y.Y., Yang, L.Q., Zhao, R., Yang, L., 2020a. Remobilization of metasomatized mantle lithosphere: a new model for the Jiaodong gold province, eastern China. Miner. Deposita 55 (2), 257–274.
Deng, T., Xu, D.R., Chi, G.X., Wang, Z.L., Chen, G.W., Zhou, Y.Q., Li, Z.H., Ye, T.W., Yu, D.S., 2020b. Caledonian (Early Paleozoic) veins overprinted by Yanshanian (Late Mesozoic) gold mineralization in the Jiangnan Orogen: A case study on gold deposits in northeastern Hunan, South China. Ore Geol. Rev. 124, 103586.
Dong, S.W., Zhang, Y.Q., Li, H.L., Shi, W., Xue, H.M., Li, J.H., Huang, S.Q., Wang, Y.C., 2018. The Yanshan orogeny and late Mesozoic multi-plate convergence in East Asia—Commemorating 90th years of the "Yanshan Orogeny". Sci. China-Earth Sci. 61 (12), 1888–1909.
Donovan, J.J., Lowers, H.A., Rusk, B.G., 2011. Improved electron probe microanalysis of trace elements in quartz. Am. Mineral. 96 (2–3).
Du, Y.S., Xu, Y.J., 2012. A Preliminary Study on Caledonian Event in South China. Geol. Sci. Technol. Inf. 31 (05), 43–49 in Chinese with English abstract.
Feng, Y.Z., Zhang, Y., Xie, Y.L., Shao, Y.J., Tan, H.J., Li, H.B., Lai, C.K., 2020. Ore-forming mechanism and physicochemical evolution of Gutaishan Au deposit, South China: Perspective from quartz geochemistry and fluid inclusions. Ore Geol. Rev. 119, 103382.
Fu, S.L., Hu, R.Z., Bi, X.W., Sullivan, N.A., Yan, J., 2020a. Trace element composition of stibnite: Substitution mechanism and implications for the genesis of Sb deposits in southern China. Appl. Geochem. 118, 104637.
Fu, S.L., Lan, Q., Yan, J., 2020b. Trace element chemistry of hydrothermal quartz and its genetic significance: A case study from the Xikuangshan and Woxi giant Sb deposits in southern China. Ore Geol. Rev. 126, 103732.
Gao, S., Zou, X.Y., Hofstra, A.H., Qin, K.Z., Marsh, E.E., Bennett, M.M., Li, G.M., Jiang, J. L., Su, S.Q., Zhao, J.X., Li, Z.Z., 2022. Trace elements in quartz: insights into source and fluid evolution in magmatic-hydrothermal systems. Econ. Geol. 117 (6), 1415–1728.
Goette, T., Pettke, T., Ramseyer, K., Koch-Mueller, M., Mullis, J., 2011. Cathodoluminescence properties and trace element signature of hydrothermal quartz; a fingerprint of growth dynamics. Am. Mineral. 96 (5–6), 802–813.
Goldfarb, R.J., Groves, D.I., 2015. Orogenic gold: Common or evolving fluid and metal sources through time. Lithos 233, 2–26.
Götze, J., Plötze, M., Graupner, T., Hallbauer, D.K., Bray, C.J., 2004. Trace element incorporation into quartz: A combined study by ICP-MS, electron spin resonance, cathodoluminescence, capillary ion analysis, and gas chromatography. Geochim. Cosmochim. Acta 68 (18), 3741–3759.
Griffin, W.L., Begg, G.C., O'Reilly, S.Y., 2013. Continental-root control on the genesis of magmatic ore deposits. Nat. Geosci. 6 (11), 905–910.
Gu, X.X., Zhang, Y.M., Schulz, O., Vavtar, F., Liu, J.M., Zheng, M.H., Zheng, L., 2012. The Woxi W-Sb–Au deposit in Hunan, South China: An example of Late Proterozoic sedimentary exhalative (SEDEX) mineralization. J. Asian Earth Sci. 57, 54–75.
He, S., Li, Y., Wu, L.G., Guo, D.F., Li, Z.Y., Li, X.H., 2021. High precision zircon SIMS Zr isotope analysis. J. Anal. At. Spectrom 36 (1), 263–273.
Hoefs, J., 2021. Stable Isotope Geochemistry. Springer Textbooks in Earth Sciences, Geography and Environment, Switzerland.
Hu, R.Z., Chen, W.T., Xu, D.R., Zhou, M.F., 2017. Reviews and new metallogenic models of mineral deposits in South China: An introduction. J. Asian Earth Sci. 137, 1–8.
Hu, R.Z., Gao, W., Fu, S.L., Su, W.C., Peng, J.T., Bi, X.W., 2024. Mesozoic intraplate metallogenesis in South China. Earth Sci. Front. 31 (1), 226–238 in Chinese with English abstract.
Huang, R.F., Audétat, A., 2012. The titanium-in-quartz (TitaniQ) thermobarometer: A critical examination and re-calibration. Geochim. Cosmochim. Acta 84, 75–89.
Jia, S.S., Wang, E.D., Fu, J.F., Wang, X.D., Li, W.Q., 2019. Geology, fluid inclusions and isotope geochemistry of the Herenping gold deposit in the southern margin of the Yangtze Craton, China: A sediment-hosted reduced intrusion-related gold deposit? Ore Geol. Rev. 107, 926–943.
Kerr, M.J., Hanley, J.J., Kontak, D.J., Morrison, G.G., Petrus, J., Fayek, M., Zajacz, Z., 2018. Evidence of upgrading of gold tenor in an orogenic quartz-carbonate vein system by late magmatic-hydrothermal fluids at the Madrid Deposit, Hope Bay greenstone belt, Nunavut, Canada. Geochim. Cosmochim. Acta 241, 180–218.
Korolev, N.M., Melnik, A.E., Li, X.H., Skublov, S.G., 2018. The oxygen isotope composition of mantle eclogites as a proxy of their origin and evolution: A review. Earth Sci. Rev. 185, 288–300.
Larsen, R.B., Henderson, I., Ihlen, P.M., Jacamon, F., 2004. Distribution and petrogenetic behaviour of trace elements in granitic pegmatite quartz from south Norway. Contrib. Miner. Petrol. 147 (5), 615–628.
Larsen, R.B., Jacamon, F., Kronz, A., Muller, A., Welch, M.D., 2009. Trace element chemistry and textures of quartz during the magmatic hydrothermal transition of Oslo Rift granites. Mineral. Mag. 73 (4), 691–707.
Lehmann, K., Pettke, T., Ramseyer, K., 2011. Significance of trace elements in syntaxial quartz cement, Haushi Group sandstones, Sultanate of Oman. Chem. Geol. 280 (1), 47–57.
Li, B, XU, D.R., Bai, D.Y., Zhong, X., Li, Y.M., Gao, C., Zeng, G.Q., Zou, G.J., Ling, Y.X., 2022. Characteristics of Structural Deformation and its Tectonic Setting in the Huishangang Area,Northern Xuefeng Orogen. Geotectonica et Metallogenia, 46(01): 1-21(in Chinese with English abstract).u.
Li, J.W., Hu, R.Z., Xiao, J.F., Zhuo, Y.Z., Yan, J., Oyebamiji, A., 2020b. Genesis of gold and antimony deposits in the Youjiang metallogenic province, SW China: Evidence from in situ oxygen isotopic and trace element compositions of quartz. Ore Geol. Rev. 116, 103257.
Li, H., Kong, H., Zhou, Z.K., Tindell, T., Tang, Y.Q., Wu, Q.H., Xi, X.S., 2019a. Genesis of the Banxi Sb deposit, South China: Constraints from wall-rock geochemistry, fluid inclusion microthermometry, Rb–Sr geochronology, and H-O–S isotopes. Ore Geol. Rev. 115, 103162.
Li, H., Danišík, M., Zhou, Z.K., Jiang, W.C., Wu, J.H., 2020a. Integrated U-Pb, Lu–Hf and (U–Th)/He analysis of zircon from the Banxi Sb deposit and its implications for the low-temperature mineralization in South China. Geosci. Front. 11 (4), 1323–1335.
Li, Z.X., Li, X.H., 2007. magmatic province in Mesozoic South China: A flat-slab subduction model Formation of the 1300-km-wide intracontinental orogen and postorogenic. Geology 35 (2), 179–182.
Li, Y., Li, X.H., 2023. Quartz for All Time. Nat. Geosci. 16, 112.
Li, Y., Tang, G.Q., Liu, Y., He, S., Chen, B., Li, Q.L., Li, X.H., 2021. Revisiting apatite SIMS oxygen isotope analysis and Qinghu-AP reference material. Chem. Geol. 582, 120445.
Li, Y., Pan, J.Y., Wu, L.G., He, S., Bachmann, O., Li, X.H., 2023b. Transient tin mineralization from cooling of magmatic fluids in a long-lived system. Geology 51, 305–309.
Li, H., Wu, Q.H., Evans, N.J., Zhou, Z.K., Kong, H., Xi, X.S., Lin, Z.W., 2018. Geochemistry and geochronology of the Banxi Sb deposit: Implications for fluid origin and the evolution of Sb mineralization in central-western Hunan, South China. Gondw. Res. 55, 112–134.
Li, W., Xie, G.Q., Mao, J.W., Cook, N.J., We, H.T., Ji, Y.H., Fu, B., 2023a. Precise age constraints for the Woxi Au-Sb-W deposit, South China. Econ. Geol. 118 (2), 509–518.
Li, B., Xu, D.R., Bai, D.Y., Chi, G.X., Dai, J.F., Gao, C., Deng, T., Zou, S.H., Ma, W., Wang, G.J., Ling, Y.X., Zeng, G.Q., Li, Y.M., 2022a. Structural deformation, metallogenic epoch and genetic mechanism of the Woxi Au-Sb-W deposit, Western Hunan Province, South China. Sci. China-Earth Sci. 65 (12), 2358–2384.
Li, B., Xu, D.R., Bai, D.Y., Chen, X., Zou, S.H., Dai, J.F., Ma, W., Zeng, G.Q., 2024. Episodic mineralization at Yanshannian in the Woxi Au-Sb-W deposit, western Hunan, South China: Constraints from in-situ scheelite LA-ICP-MS U-Pb geochronology and element-isotope of pyrite. Acta Petrol. Sin. 40 (1), 215–240 in Chinese with English abstract.
Li, S.Z., Zang, Y.B., Wang, P.C., Suo, Y.H., Li, X.Y., Liu, X., Zhou, Z.Z., Liu, X.G., Wang, Q., 2017. Mesozoic tectonic transition in South China and initiation of Palaeo-Pacific subduction. Earth Sci. Front. 24 (04), 213–225 in Chinese with English abstract.
Li, J.H., Zhang, Y.Q., Dong, S.W., Johnston, S.T., 2014. Cretaceous tectonic evolution of South China: A preliminary synthesis. Earth Sci. Rev. 134, 98–136.
Li, H., Zhou, Z.K., Algeo, T.J., Wu, J.H., Jiang, W.C., 2019b. Geochronology and geochemistry of tuffaceous rocks from the Banxi Group: Implications for Neoproterozoic tectonic evolution of the southeastern Yangtze Block, South China. J. Asian Earth Sci. 177, 152–176.
Li, H., Zhou, Z.K., Evans, N.J., Kong, H., Wu, Q.H., Xi, X.S., 2019c. Fluid-zircon interaction during low-temperature hydrothermal processes: Implications for the genesis of the Banxi antimony deposit, South China. Ore Geol. Rev. 114, 103137.
Li, H., Zhu, D.P., Shen, L.W., Algeo, T.J., Elatikpo, S.M., 2022b. A general ore formation model for metasediment-hosted Sb-(Au-W) mineralization of the Woxi and Banxi deposits in South China. Chem. Geol. 607, 121020.
Lu, H.Z., 2008. Role of CO_2 fluid in the formation of gold deposits: Fluid inclusion evidences. Geochimica 37 (04), 321–328 in Chinese with English abstract.
Luo, X.L., Yi, S.J., Liang, J.C., 1984. The genesis of Xiangxi Au-Sb-W-deposit. Geol. Prospect. 7, 1–10 in Chinese.
Ma, D.S., Liu, Y.J., 1991. Study on the geochemical characteristics of stratumcontrolled gold mines in Jiangnan gold metallogenic belt and its genesis. Sci. China (series b) 4, 424–433 in Chinese.
Mao, J.W., Wang, Y.T., Li, H.M., Pirajno, F., Zhang, C.Q., Wang, R.T., 2008. The relationship of mantle-derived fluids to gold metallogenesis in the Jiaodong Peninsula: Evidence from D-O-C-S isotope systematics. Ore Geol. Rev. 33 (3), 361–381.
Mao, J.W., Cheng, Y.B., Chen, M.H., Pirajno, F., 2013. Major types and time-space distribution of Mesozoic ore deposits in south China and their geodynamic settings. Miner. Deposita 48 (3), 267–294.
Mao, J.W., Xie, G.Q., Li., X.F., Zhang, Z.H., Wang, Y.T., 2005. Geodynamic process and metallogeny: History and present research trend, with a special discussion on

continental accretion and related metallogeny throughout geological history in South China, Mineral Deposits, 24(3):193-205(in Chinese with English abstract).
Mao, J.W., Li, H.Y., 1997. Research on genesis of the gold deposits in the Jiangnan terrain. Geochimica 26 (5), 71–81 in Chinese with English abstract.
Mao, J.W., Zheng, W., Xie, G.Q., Lehmann, B., Goldfarb, R., 2021. Recognition of a Middle-LateJurassic arc-related porphyry copper belt along the southeast China coast: Geological characteristics and metallogenic implications. Geology 49 (5), 592–596.
Monecke, T., Monecke, J., Reynolds, T.J., Tsuruoka, S., Bennett, M.M., Skewes, W.B., Palin, R.M., 2018. Quartz Solubility in the H2O-NaCl System: A Framework for Understanding Vein Formation in Porphyry Copper Deposits. Econ. Geol. 113 (5), 1007–1046.
Mueller, A., Wiedenbeck, M., van den Kerkhof, A.M., Kronz, A., Simon, K., 2003. Trace elements in quartz; a combined electron microprobe, secondary ion mass spectrometry, laser-ablation ICP-MS, and cathodoluminescence study. Eur. J. Mineral. (Stuttgart) 15 (4), 747–763.
Müller, A., Wiedenbeck, M., Flem, B., Schiellerup, H., 2008. Refinement of phosphorus determination in quartz by LA-ICP-MS through defining new reference material values. Geostand. Geoanal. Res. 32 (3), 361–376.
Müller, A., Herklotz, G., Giegling, H., 2018. Chemistry of quartz related to the Zinnwald/Cínovec Sn-W-Li greisen-type deposit, Eastern Erzgebirge, Germany. J. Geochem. Explor. 190, 357–373.
Paton, C., Hellstrom, J., Paul, B., Woodhead, J., Hergt, J., 2011. Iolite: Freeware for the visualisation and processing of mass spectrometric data. J. Anal. At. Spectrom 26 (12), 2508.
Peng, J.T., Hu, R.Z., Zhao, J.H., Fu, Y.Z., Lin, Y.X., 2003. Scheelite Sm-Nd dating and quartz Ar-Ar dating for Woxi Au-Sb-W deposit, western Hunan. Chin. Sci. Bull. 48, 2640–2646.
Peng, B., Robert, F., Tu, X.L., 2006. Nd-Sr-Pb Isotopic Geochemistry of Scheelite from the Woxi W-Sb-Au Deposit, Western Hunan: Implications for Sources and Evolution of Ore-forming Fluids. Acta Geol. Sin. 80 (4), 561–570 in Chinese with English abstract.
Peng, B., Liu, S.Y., Adam, P., Pieczonka, J., Tang, X.Y., Yu, C.X., Xie, S.R., 2008. Mineralogical characteristics and their implications for deep prospecting of the Woxi gold deposit in western Hunan, China. Geol. China 35 (6), 1286–1290 in Chinese with English abstract.
Peterson, E.C., Mavrogenes, J.A., 2014. Linking high-grade gold mineralization to earthquake-induced fault-valve processes in the Porgera gold deposit, Papua New Guinea. Geology 42 (5), 383–386.
Pi, Q.H., Hu, R.Z., Xiong, B., Li, Q.L., Zhong, R.C., 2017. In situ SIMS U/Pb dating of hydrothermal rutile; reliable age for the Zhesang carlin-type gold deposit in the Golden Triangle region, SW China. Mineralium Deposita 52 (8), 1179–1190.
Pirajno, F., Ernst, R.E., Borisenko, A.S., Fedoseev, G., Naumov, E.A., Pirajno, F., Seltmann, R., Cook, N.J., Borisenko, A.S., 2009. Intraplate magmatism in Central Asia and China and associated metallogeny. Ore Geol. Rev. 35 (2), 114–136.
Raimbourg, H., Famin, V., Canizarès, A., Le Trong, E., 2022. Fluid Pressure Changes Recorded by Trace Elements in Quartz. Geochem. Geophys. Geosyst., 23(10): e2022GC010346.
Raimondo, T., Hand, M., Collins, W.J., 2014. Compressional intracontinental orogens: Ancient and modern perspectives. Earth Sci. Rev. 130, 128–153.
Rakov, L.T., 2015. Role of germanium in isomorphic substitutions in quartz. Geochem. Int. 53 (2), 171–181.
Richards, J.P., 2013. Giant ore deposits formed by optimal alignments and combinations of geological processes. Nat. Geosci. 6 (11), 911–916.
Rottier, B., Kouzmanov, K., Casanova, V., Bouvier, A., Baumgartner, L.P., Wälle, M., Fontboté, L., 2021. Tracking fluid mixing in epithermal deposits-Insights from in-situ $\delta^{18}O$ and trace element composition of hydrothermal quartz from the giant Cerro de Pasco polymetallic deposit, Peru. Chem. Geol. 576, 120277.
Rudnick, R.L., Gao, S., 2004. Composition of the continental crust. Treatise Geochem 3. Elsevier, Amsterdam, 1-64.
Rusk, B.G., Lowers, H.A., Reed, M.H., 2008. Trace elements in hydrothermal quartz; relationships to cathodoluminescent textures and insights into vein formation. Geology 36 (7), 547–550.
Rusk, B.G., 2012. Cathodoluminescent Textures and Trace Elements in Hydrothermal Quartz. In: Götze, J., Möckel, R. (eds) Quartz: Deposits, Mineralogy and Analytics. Springer Geology. Springer, Berlin.
Sharp, Z.D., Gibbons, J.A., Maltsev, O., Atudorei, V., Pack, A., Sengupta, S., Shock, E.L., Knauth, L.P., 2016. A calibration of the triple oxygen isotope fractionation in the SiO_2-H_2O system and applications to natural samples. Geochim. Cosmochim. Acta 186, 105–119.
Sheppard, S.M.F., Valley, J.W., Taylor, H.P., O'Neil, J.R., 1986. Characterization and isotopic variations in natural waters. Rev. Mineral. 16, 165–183.
Shu, L.S., 2021. Principal features of intracontinental orogenic belt and discussions on its dynamics. Acta Geol. Sin. 95 (1), 98–106 in Chinese with English abstract.
Shu, L.S., Yao, J.L., Wang, B., Faure, M., Charvet, J., Chen, Y., 2021. Neoproterozoic plate tectonic process and Phanerozoic geodynamic evolution of the South China Block. Earth Sci. Rev. 216, 103596.
Sibson, R.H., Robert, F., Poulsen, K.H., 1988. High-angle reverse faults, fluid-pressure cycling, and mesothermal gold-quartz deposits. Geology 16 (6), 551–555.
Stimac, J.A., Goff, F., Wohletz, K., 2001. Thermal modeling of the Clear Lake magmatic-hydrothermal system, California, USA. Geothermics 30 (2), 349–390.
Tang, Y.W., Han, J.J., Lan, T.G., Gao, J.F., Liu, L., Xiao, C.H., Yang, J.H., 2022. Two reliable calibration methods for accurate in situ U-Pb dating of scheelite. J. Anal. At. Spectrom 37 (2), 358–368.
Vallance, J., Boiron, M., Cathelineau, M., Fourcade, S., Varlet, M., Marignac, C., 2004. The granite hosted gold deposit of Moulin de Cheni (Saint-Yrieix District, Massif Central, France); petrographic, structural, fluid inclusion and oxygen isotope constraints. Miner. Deposita 39 (3), 265–281.
Wang, X.L., Zhou, J.C., Chen, X., Zhang, F.F., Sun, Z.M., 2017. Formation and Evolution of the Jiangnan Orogen. Bulletin of Mineralogy, Petrology and Geochemistry, 36 (05): 714-735+696(in Chinese with English abstract).
Wang, Y.J., Fan, W.M., Zhang, G.W., Zhang, Y.H., 2013. Phanerozoic tectonics of the South China Block: Key observations and controversies. Gondw. Res. 23 (4), 1273–1305.
Wang, Y., Qiu, K.F., Müller, A., Hou, Z.L., Zhu, Z.H., Yu, H.C., 2021b. Machine Learning Prediction of Quartz Forming-Environments. J. Geophys. Res. Solid Earth 126 (8).
Wang, Y., Liu, J.S., Shen, C.M., Deng, B., Su, W.J.L., Chen, Q.F., Li, J.L., 2022b. Seismic Ambient Noise Tomography with Dense Linear Arrays and Its Application in the Exploration of the Woxi Au-Sb-W Deposit in Hunan. Geol. J. China Univ. 28 (3), 402–413 in Chinese with English abstract.
Wang, C., Shao, Y.J., Zhang, X., Lai, C., Liu, Z.F., Li, H., Ge, C., Liu, Q.Q., 2020a. Metallogenesis of the Hengjiangchong gold deposit in Jiangnan Orogen, South China. Ore Geol. Rev. 118, 103350.
Wang, Q.F., Yang, L., Zhao, H.S., Groves, D.I., Weng, W.J., Xue, S.C., Li, H.J., Dong, C.Y., Yang, L.Q., Li, D.P., Deng, J., 2022a. Towards a universal model for orogenic gold systems: A perspective based on Chinese examples with geodynamic, temporal, and deposit-scale structural and geochemical diversity. Earth Sci. Rev. 224, 103861.
Wang, K.X., Zhai, D.G., Liu, J.J., Wu, H., 2021a. LA-ICP-MS trace element analysis of pyrite from the Dafang gold deposit, South China: Implications for ore genesis. Ore Geol. Rev. 139, 104507.
Wang, Q.F., Zhao, H.S., Groves, D.I., Deng, J., Zhang, Q.W., Xue, S.C., 2020b. The Jurassic Danba hypozonal orogenic gold deposit, western China: indirect derivation from fertile mantle lithosphere metasomatized during Neoproterozoic subduction. Miner. Deposita 55 (2), 309–324.
Weatherley, D.K., Henley, R.W., 2013. Flash vaporization during earthquakes evidenced by gold deposits. Nat. Geosci. 6 (4), 294–298.
Xu, J.W., Chen, M.H., Zhou, X.L., Huang, W.J., 2015. Metallogenic characteristics and structure in deep part of W-Sb-Au polymetallic deposit and vertical variation of mineralization, Woxi in western Hunan. Mineral Resour. Geol. 29 (6), 708–713 in Chinese with English abstract.
Xu, D.R., Deng, T., Chi, G.X., Wang, Z.L., Zou, F.H., Zhang, J.L., Zou, S.H., 2017. Gold mineralization in the Jiangnan Orogenic Belt of South China: Geological, geochemical and geochronological characteristics, ore deposit-type and geodynamic setting. Ore Geol. Rev. 88, 565–618.
Xu, K., Xu, D., Deng, T., Li, Z.H., Zou, S.H., Wang, Z.L., Hai, Y., Zhang, S.W., Qian, Q., Guo, S.C., 2022. Genesis of altered slate type ores in the Huangjindong gold deposit, Jiangnan orogenic belt, south China. J. Geochem. Explor. 241, 107047.
Yan, J., Mavrogenes, J.A., Liu, S., Coulson, I.M., 2020. Fluid properties and origins of the Lannigou Carlin-type gold deposit, SW China: Evidence from SHRIMP oxygen isotopes and LA-ICP-MS trace element compositions of hydrothermal quartz. J. Geochem. Explor. 215, 106546.
Yang, S.X., Blum, N., 1999. A fossil hydrothermal system or a source-bed in the Madiyi Formation near the Xiangxi Au-Sb-W deposit, NW Hunan, PR China? Chem. Geol. 155 (1), 151–169.
Yang, M.Z., Jiang, S.Y., Zhao, K.D., Zhou, Y.Y., Zhang, D., 2021. Two episodic Au-Mo mineralization in the Laowan district from the Tongbai orogenic belt of China: Constraints from U-Pb dating of zircon, rutile, and REE phosphate, and Re-Os dating of molybdenite. Gondw. Res. 96, 142–162.
Yi, S.X., 2012. Researh on geological features, fluid inclusion and genesis of Woxi Au-Sb-W deposit in Hunan province. Central South University, Changsha(in Chinese with English abstract). Master Thesis.
Zeng, G.P., Gong, Y.J., Wang, Z.F., Hu, X.L., Xiong, S.F., 2017. Structures of the Zhazixi Sb–W deposit, South China: Implications for ore genesis and mineral exploration. J. Geochem. Explor. 182, 10–21.
Zeng, Y.S., Wang, Q.F., Groves, D.I., Santosh, M., Wang, Y.N., Wang, T.Y., Yang, L., Chen, W., Deng, J., 2023. Prolonged Mesozoic intracontinental gold mineralization in the South China Block controlled by lithosphere architecture and evolving Paleo-Pacific Plate subduction. Earth Sci. Rev. 240, 104387.
Zhai, M.G., Santosh, M., 2013. Metallogeny of the North China Craton: link with secular changes in the evolving Earth. Gondw. Res. 24 (1), 275–297.
Zhang, L.G., 1985. Stable isotopic geology of W-Sb-Au ore deposits developed along the Xuefeng uplift in western Hunan. Geol. Prospect. 21, 24–28 in Chinese.
Zhang, J.F., 2017. The study on ore-forming fluids in the Woxi Au-Sb-W deposit, Hunan province. Chengdu University of Technology, Chengdu(in Chinese with English abstract). Master Thesis.
Zhang, Y., Cheng, J.M., Tian, J., Pan, J., Sun, S.Q., Zhang, L.J., Zhang, S.T., Chu, G.B., Zhao, Y.J., Lai, C., 2019b. Texture and trace element geochemistry of quartz in skarn system: Perspective from Jiguanzui Cu-Au skarn deposit, Eastern China. Ore Geol. Rev. 109, 535–544.
Zhang, G.W., Guo, A.L., Wang, Y.J., Li, S.Z., Dong, Y.P., Liu, S.F., He, D.F., Cheng, S.Y., Lu, R.K., Yao, A.P., 2013. Tectonics of South China Continent and its implications. Sci. China-Earth Sci. 56 (11), 1804–1828.
Zhang, C.L., Santosh, M., Zhu, Q.B., Chen, X.Y., Huang, W.C., 2015. The Gondwana connection of South China: Evidence from monazite and zircon geochronology in the Cathaysia Block. Gondw. Res. 28 (3), 1137–1151.
Zhang, Y.Q., Xu, X.B., Jia, D., Shu, L.S., 2009. Deformation record of the change from Indosinian collision-related tectonic system to Yanshanian subduction-related tectonic system in South China during the Early Mesozoic. Earth Sci. Front. 16 (01), 234–247 in Chinese with English abstract.
Zhang, L., Yang, L.Q., Groves, D.I., Sun, S.C., Liu, Y., Wang, J.Y., Li, R.H., Wu, S.G., Gao, L., Guo, J.L., Chen, X.G., Chen, J.H., 2019a. An overview of timing and

structural geometry of gold, gold-antimony and antimony mineralization in the Jiangnan Orogen, southern China. Ore Geol. Rev. 115, 103173.
Zhou, Y.Q., Xu, D.R., Dong, G.J., Chi, G.X., Deng, T., Cai, J.X., Ning, J.T., Wang, Z.L., 2021. The role of structural reactivation for gold mineralization in northeastern Hunan Province, South China. J. Struct. Geol. 145, 104306.
Zhu, Y.N., Peng, J.T., 2015. Infrared microthermometric and noble gas isotope study of fluid inclusions in ore minerals at the Woxi orogenic Au-Sb-W deposit, western Hunan, South China. Ore Geol. Rev. 65, 55–69.
Zhu, Y.N., Peng, J.T., Xing, L.Z., Tang, Y.W., 2023. U-Pb dating of scheelite, wolframite and apatite from the Woxi Au-Sb-W deposit, western Hunan Province and their geological significance. Acta Petrol. Sin. 39 (06), 1829–1846 in Chinese with English abstract.
Zhu, R.X., Sun, W.D., 2021. The big mantle wedge and decratonic gold deposits. Sci. China-Earth Sci. 64 (9), 1451–1462.
Zhu, R.X., Xu, Y.G., 2019. The subduction of the west Pacific plate and the destruction of the North China Craton. Sci. China-Earth Sci. 62 (9), 1340–1350.

第40卷 第2期
2024年6月

华 南 地 质
South China Geology

Vol.40, No.2, 398–412
Jun., 2024

doi:10.3969/j.issn.2097–0013.2024.02.000

湘东北虎形山钨铍矿区隐伏花岗岩体地球化学特征及成因研究

徐军伟[1,2],王玉华[3*], 曾认宇[4],廖凤初[1,2],李素欣[1,2]

XU Jun-Wei[1,2], WANG Yu-Hua[3*], ZENG Ren-Yu[4], LIAO Feng-Chu[1,2], LI Su-Xin[1,2]

1.地球化学过程与资源环境效应湖南省重点实验室,湖南 长沙 410014;2.湖南省地球物理地球化学调查所,湖南 长沙 410014;3.中南大学有色金属成矿预测与地质环境监测教育部重点实验室,湖南 长沙 410083;
4.东华理工大学核资源与环境国家重点实验室,江西 南昌 330013

1. Provincial Key Laboratory of Geochemical Processes and Resource Environmental Effects, Central South University, Changsha 410014, Hunan, China; 2.Geophysical and Geochemical Survey Institute of Hunan Province, Changsha 410014, Hunan, China; 3. Key Laboratory of Metallogenic Prediction of Nonferrous Metals and Geological Environment Monitoring (Ministry of Education), Central South University, Changsha 410083, Hunan, China; 4.State Key Laboratory of Nuclear Resources and Environment, East China University of Technology, Nanchang 330013, Jiangxi, China

摘要:湘东北虎形山钨铍多金属矿床为一大型的石英、云英岩细脉带型白钨矿床和绿柱石铍矿床。本文通过对矿区内新发现的隐伏花岗岩体详细的岩石地球化学分析,探讨了该岩体的成因、物质来源和构造环境,以期为区域岩浆作用与成矿关系研究提供理论支撑。结果表明,虎形山花岗岩为富SiO_2(71.86%~73.22%)和Al_2O_3(13.99%~14.55%),贫TFe_2O_3(1.17%~1.63%)和MgO(0.28%~0.36%),且相对贫钠富钾(K_2O/Na_2O介于1.11~1.78之间)的高钾钙碱性、过铝质花岗岩,并具有强烈富集轻稀土元素(La_N/Yb_N=9.29~21.9)和大离子亲石元素(Rb、Ba、U、K)而相对亏损重稀土元素和高场强元素(Nb、Ti、P)的特征;虎形山花岗岩是在较低压力(<5 kbar)和初始温度为707℃~746℃环境中经高程度分离结晶作用(斜长石、钾长石、磷灰石等)形成的S型花岗岩,其地壳源区为泥质岩和砂屑岩组成的冷家溪群;结合区域构造演化,本文认为燕山期古太平洋板块的低角度俯冲造成湘东北地区地壳发生强烈的变形,随后区域应力的减弱使得增厚的岩石圈发生拆沉,在此情况下,地壳减薄或幔源物质底侵引起了该地区强烈的岩浆活动,进而形成了虎形山花岗岩。

关键词:虎形山隐伏花岗岩体;岩石成因;物质来源;构造环境;湘东北

中图分类号:P618.67;P618.72　　**文献标识码:**A　　**文章编号:**2097-0013(2024)02-0398-15

Xu J W, Wang Y H, Zeng R Y, Liao F C and Li S X. 2024. Geochemistry and Genesis of Concealed Granite in Huxingshan Tungsten–Beryllium Ore District, Northeastern Hunan Province. South China Geology, **40(2): 398–412**

Abstract: The tungsten-beryllium polymetallic deposit at Huxingshan in northeastern Hunan Province is a large-scale quartz and greisen vein-belt type scheelite and beryl beryllium deposit. To investigate its genesis, material source and tectonic environment, we carried out detailed rock geochemical analyses on the newly discovered concealed granite bodies in the Huxingshan mining area, so to provide the theory support for the

收稿日期:2024-2-20;**修回日期:**2024-4-8
基金项目:湖南省自然资源科技计划项目(20230134DZ)
第一作者:徐军伟(1982—),男,博士,从事矿产勘查与矿床地质研究工作,E-mail:108350600@qq.com
通讯作者:王玉华(1994—),男,博士,从事成矿地球化学研究,E-mail:yuhuawang2018@126.com

relationship between local magmatism and mineralization. The results show that the Huxingshan granite is a series of high-K calc-alkaline peraluminous granite rich in SiO_2 (71.86% ~73.22%) and Al_2O_3 (13.99% ~ 14.55%), poor in TFe_2O_3 (1.17%~1.63%) and MgO (0.28%~0.36%), and relatively poor in Na and rich in K (with the (K_2O /Na_2O) ration between 1.11 and 1.78). It is characterized by strong enrichment of light rare earth elements (La_N/Yb_N=9.29~21.9) and large ion lithophile elements (Rb, Ba, U, K), and relative depletion of heavy rare earth elements and high field strength elements (Nb, Ti, P). The geochemical characteristics show that Huxingshan granite is an S-type granite formed in an environment of lower pressure (< 5 kbar) and an initial temperature of 727℃~785℃. It was formed by a high degree of fractional crystallization (plagioclase, potash feldspar, apatite, etc.), and its crust source area is Lengjiaxi Group composed of mudstone and sandstone. Combined with the tectonic evolution history of the region, this study concluded that the low-angle subduction of the Paleo-Pacific Plate during the Yanshan Period caused strong deformation of the crust in the northeast Hunan region, and the subsequent weakening of regional stresses led to the detachment of the thickened lithosphere, in which case the crustal thinning or underplating of mantle source material had caused intense magmatism in the region, which resulted in the formation of the Huxingshan Granite.

Key words: concealed granite body in Huxingshan deposit; Petrogenesis; Material source; Tectonic setting; Northeast Hunan province

中生代华南板块处于特提斯构造域向古太平洋构造域转化阶段(Zhou X M et al.,2006;舒良树,2012;柏道远等,2024),该阶段形成了以印支期和燕山期为主的岩浆岩,其出露面积约占该区岩浆岩的 90%(Zhou X M et al.,2006;Li B et al.,2015;潘大鹏等,2017),且形成了大量的W、Sn、Bi、Mo等多金属矿床(Pirajno and Bagas,2002;Mao J R et al.,2011;吴福元等,2023)。因此,作为大陆地壳的重要组成部分,花岗岩不仅对研究区域构造演化及成岩成矿作用具有重要的指示意义,也是该地区开展战略性关键金属找矿勘查工作的重要对象(王德滋和沈渭洲,2003;舒良树,2012;王开朗等,2013;Zeng R Y et al.,2016)。

中生代是华南板块构造-岩浆-成矿作用的高峰期,其中又以白垩纪最为频繁(贾小辉等,2023)。我国江南造山带中的一系列钨矿床形成于这一时期,如大湖塘脉状浸染型钨矿、朱溪矽卡岩型钨矿、狮尾洞石英脉型钨矿等(Mao J R et al.,2011;徐斌等,2015;陆建军等,2022;吴福元等,2023)。湘东北地处江南造山带中段北侧,是一个极富特色的铜多金属成矿集中区,前人在该地区已发现虎形山钨铍多金属矿、桃林铅锌矿和崔家坳钨多金属矿等多处大中型矿床(张九龄,1989;李先富和余研,1991;沈萍,2010;唐朝永等,2013)。临湘虎形山矿区位于湘东北地区的北东侧,2010年至2020年期间,矿区先后开展了普查、详查工作,探获WO_3资源储量20.67万吨。通过对含矿石英脉中石英流体包裹体进行Rb-Sr同位素测年,获得矿床的成矿年龄分别为135 ± 5 Ma(王开朗等,2013)和134 ± 2 Ma(Xu J W et al.,2020),属燕山晚期。尽管成矿作用被认为与岩浆活动关系密切,但是研究区并未发现大规模的岩浆岩出露,结合区域航测异常,推测深部存在隐伏岩体。2011-2014年,湖南省有色地质勘查局在该矿区的勘探工作中首次发现了深部的隐伏花岗岩体,该隐伏岩体的发现为研究区域岩浆作用及与成矿的关系提供了新的思路(湖南省有色地质勘查局247队,2015)。因此,基于前期工作,本文选取虎形山隐伏花岗岩体开展了系统的主量、微量元素分析,并尝试讨论了虎形山花岗岩的岩石成因、源区性质及成岩构造环境,以期为区域岩浆作用与成矿关系研究提供理论支撑。

1 区域地质概况

华南板块是由北西侧的扬子地块和南东侧的华夏地块在新元古代早期碰撞拼接而成(Li X H et

al.,2009),板块内呈北东东向展布的江南造山带通常被认为是上述两个地块的过渡边界(图1a)。湘东北地区主要经历了武陵、雪峰、加里东、印支、燕山等多期次构造运动,并形成了区内断层走向及褶皱轴向近东西向与北东向两组构造形迹相互交错的构造格局(Xu J W et al.,2020)。东西向的构造特征以压性为主,北东向的构造特征则以压扭性为主,且后者切割前者,这说明近东西向构造为早期,北东向构造为相对晚期(Xu J W et al.,2020)。

湘东北地区出露的地层主要为元古宙冷家溪群和板溪群,其次是寒武系、白垩系和第四系(图1b)。作为区域上的基底地层,冷家溪群为一套低绿片岩相浊积复理石和火山岩建造(许德如等,2009),岩性主要为泥质板岩、砂质板岩、粉砂岩和杂砂岩及相关的火山岩系(李鹏春等,2005);板溪群主要由新元古代(约820 ~ 750 Ma)变质沉积物组成,其与下伏地层(冷家溪群)之间的不整合接触关系记录了新元古代扬子地块和华夏地块之间的碰撞信息(Zhao G C,2015)。寒武系主要由炭泥质沉积物组成,白垩系主要为块状砾岩,并呈角度不整合覆于早期地层之上,第四系主要为黏土、粉砂及砂砾石层,多含铁锰结核及薄膜(Xu J W et al.,2020)。研究区岩浆岩出露广泛,以花岗岩为主,基性岩多呈脉状零星出露,岩浆活动表现为多期次的特征,在晋宁期、加里东期、海西-印支期和燕山期均有发生(湖南省地质矿产局,1988),其中,以燕山期岩浆活动最为活跃,形成了如连云山、金井、望湘、桃花山-小墨山、幕阜山、蕉溪岭等众多岩体。

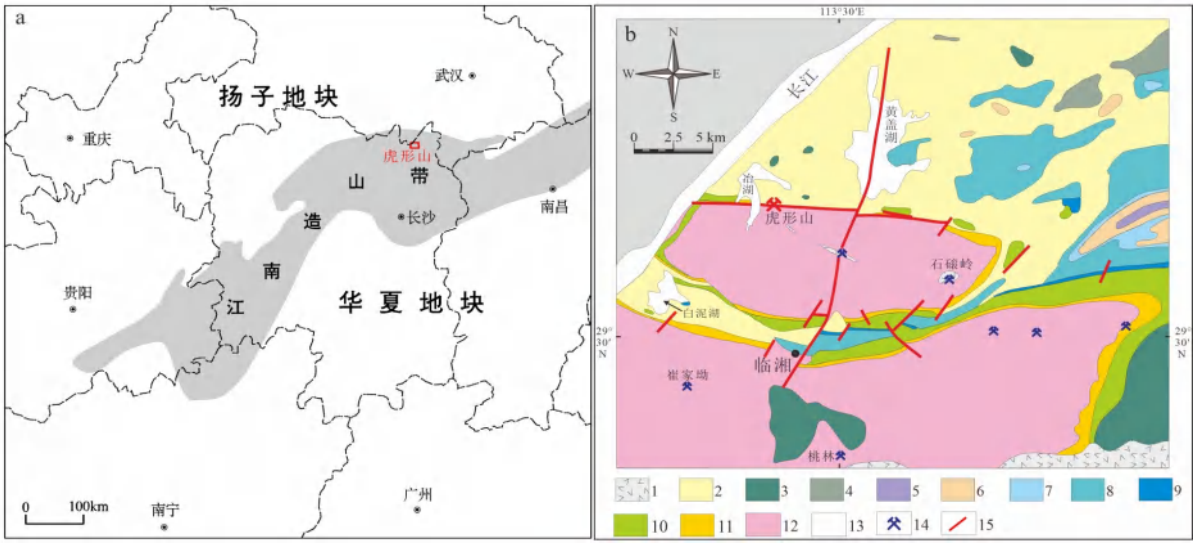

图1 湘东北区域位置图(a)及幕阜山西缘区域地质图(b)

Fig. 1 Regional geological map (a) and Regional geological map (b) of the western margin of the Mufushan area in northeastern Hunan Province

图a底图据唐朝永等(2013);图b据1∶5万区域地质图修改

1.幕阜山花岗岩;2.第四系;3.白垩系;4.侏罗系;5.三叠系;6.二叠系;7.石炭系;8.志留系;9.奥陶系;10.寒武系;11.新元古代板溪群;12.新元古代冷家溪群;13.河流和湖泊;14.矿床;15.断裂

2 矿床地质

虎形山大型钨铍多金属矿床位于湖南省北部临湘市(图1b)。新元古代冷家溪群和寒武系牛蹄塘组是矿区南部的主要地层,矿床的北部被第四系覆盖(图2a)。虎形山含钨铍矿体主要赋存于F1断裂北部的牛蹄塘组中,与冷家溪群呈不整合接触(图2a、2b)。冷家溪群主要由板岩、千枚岩和变质凝灰质砂岩组成,构成东西向逆冲断层(F1)的上盘;

牛蹄塘组厚度达1000 m,主要由碳质板岩和泥灰岩组成,构成F1的下盘。二者共同组成了虎形山钨矿体的围岩,并经历了强烈的硅化、云英岩化、黄铁矿化和绢云母化蚀变,同时伴随着强烈的韧性变形和褶皱。

虎形山钨铍多金属矿床为石英、云英岩细脉带型白钨矿床和绿柱石铍矿床。其矿体呈脉状产出,主要受F1断裂带及其下盘寒武系牛蹄塘组地层控制,矿体走向与F1断裂带近于平行,为近EW向,倾向S,倾角50°~80°,已圈定钨矿体共计37条,其中探明矿体22条(图2,唐朝永等,2013)。

矿区地表出露的侵入岩主要为花岗岩脉,宽度小于1 m,侵入到牛蹄塘组,并伴有强烈的围岩或花岗岩蚀变。在ZK3304钻孔中发现了一个深层花岗岩体,位于距地表1324 m以下,钻孔揭露46 m,未见底,其顶板地层为冷家溪群易家桥组的灰绿色硅质板岩,并经历了不同程度的绢云母蚀变,该岩体侵入到牛蹄塘组底部,为虎形山大型钨铍多金属矿床深部的隐伏岩体(图2b)。

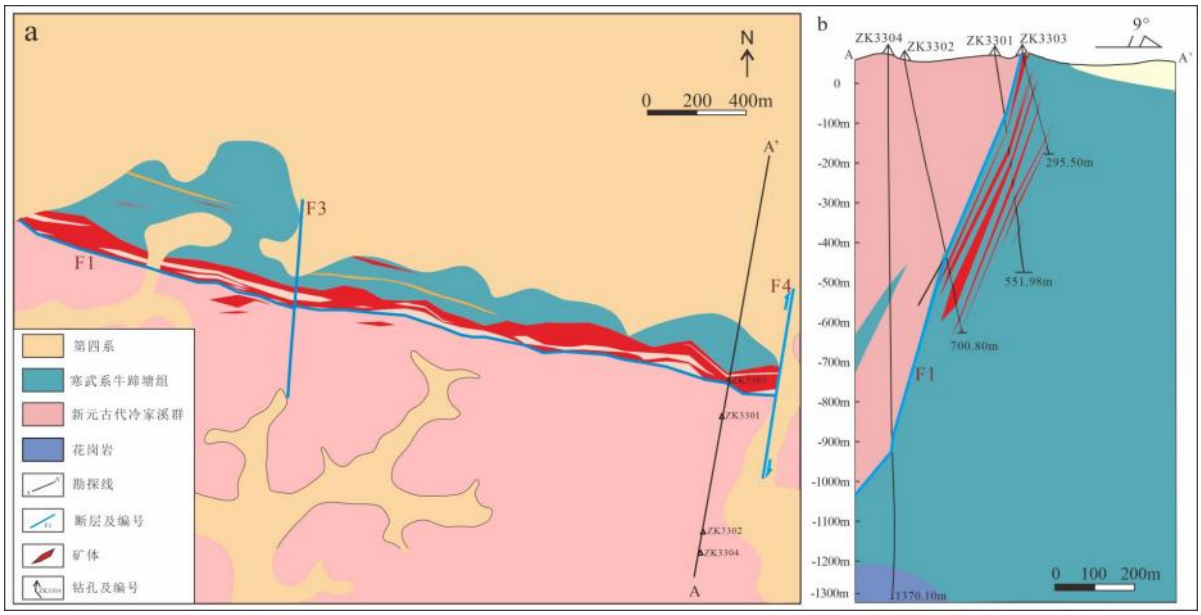

图2　虎形山钨铍矿区地质图(a)和33勘探线(A-A')地质剖面图(b)

Fig. 2　Geological map of the Huxingshan W-Be mining area and (b) Geological cross-section through the Huxingshan W-Be mining area along exploration lines 33(A-A')

a图修改自湖南省有色金属地质勘查局247探矿队(2015)

3 样品特征、采集和测试方法

虎形山隐伏花岗岩整体呈灰白色,中-细粒结构,块状构造(图3a)。岩石主要由石英(~44 %)、钾长石(~28 %)、斜长石(~12 %)、黑云母(~6 %)和少量白云母(~4 %)组成(图3)。石英呈他形粒状、连晶集合体状,交代、包含、熔蚀长石、云母等;钾长石呈他形-半自形,见格子双晶和微纹结构,表面泥化显混浊状;斜长石为半自形板条状,发育聚片双晶,边缘多被石英交代、熔蚀(图3b);黑云母具鲜艳的干涉色,呈片状、细片状,交代长石、石英等(图3c、d)。岩石定名为中细粒黑云母花岗岩。

本次研究的8件虎形山花岗岩样品均采集于钻孔ZK3304,样品均避开围岩捕掳体和各种脉岩。

样品的主量元素和微量元素地球化学分析均由澳实分析检测(广州)有限公司完成。在冷冻温度条件下,将岩石样品粉末化至200目,并置于90°C王水中2~3 h,使其溶解,在1025°C下点燃1 g研磨样品后,测定点火损失(LOI)值。主量元素采用硼酸锂溶解(S<10wt%)或偏硼酸锂-焦硼酸锂-硝酸钠熔融(S>10wt%)后进行X-射线荧光光谱分析

(XRF),仪器为荷兰 PANalytical Axios Max 型 X 射线荧光光谱仪,X 光管工作电压为 40 kV,工作电流为 70 mA,分析误差优于 5%。样品微量元素含量使用美国 Agilent 5110 电感耦合等离子体质谱仪(ICPMS)进行测试,精度为 10^{-6} 级,当元素含量大于 10×10^{-6} 时,误差小于 5%,而当元素含量小于 10×10^{-6} 时,误差小于 10%。测试过程中使用美国地质调查局(USGS)标准(玄武岩 BCR-2、玄武岩 BHVO-1 和 AGV-1)作为参考标样来监测分析过程,详细的分析方法和流程参考 Liu Q Q et al.(2017)。

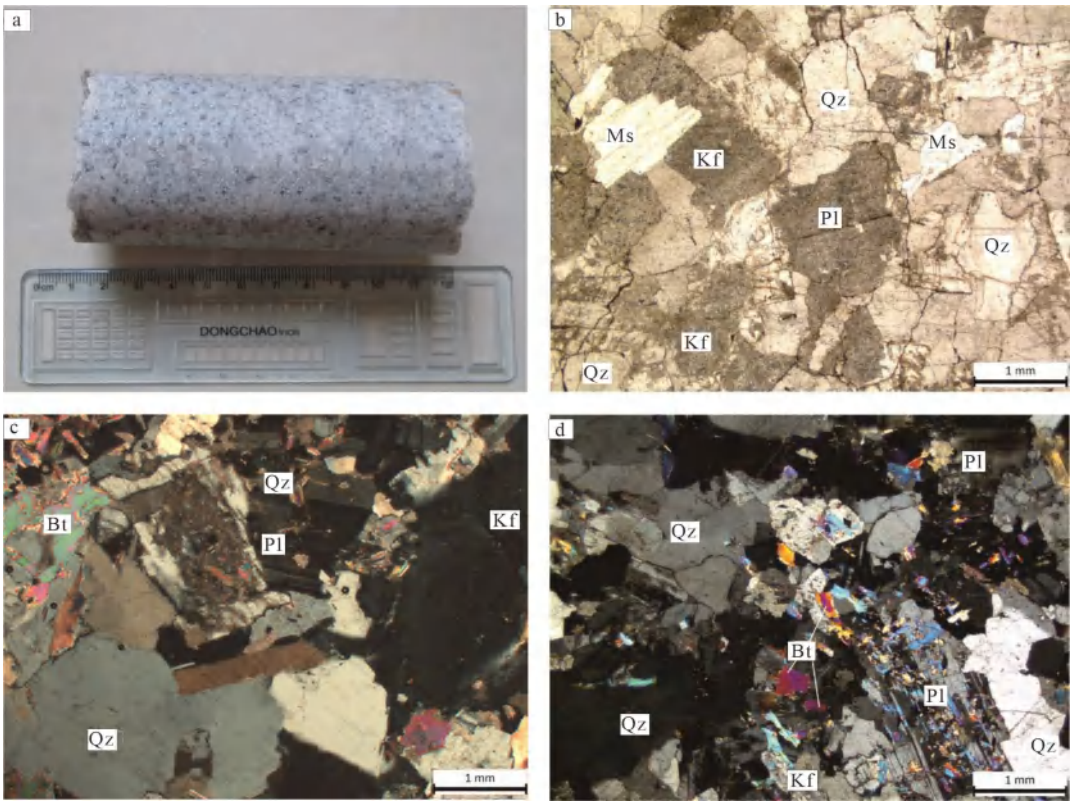

图 3 虎形山花岗岩 ZK3304 岩芯样品(a)及显微结构照片(b-单偏光,c、d-正交偏光)

Fig. 3 Core drilling and typical microstructure photos of Huxingshan granite (b-single polarization, c, d-orthogonal polarization)

Qz-石英;Kf-钾长石;Pl-斜长石;Bt-黑云母;Ms-白云母

4 岩石地球化学特征

样品主量元素测试结果(表 1)显示,虎形山花岗岩的 SiO_2 含量较高,介于 71.86% ~ 73.22%之间,平均为 72.52%;Na_2O 含量介于 2.74% ~ 3.70%之间,平均为 3.42%,K_2O 含量介于 4.05% ~ 4.87%之间,平均为 4.35%,K_2O/Na_2O 比值介于 1.11 ~ 1.78 之间,平均值为 1.28,整体上具有高钾特征。根据路远发和李文霞(2021)提供的 CIPW 标准矿物计算程序对虎形山花岗岩样品进行了 CIPW 计算,结果(表 2)表明:石英、斜长石和钾长石为虎形山花岗岩的主要矿物(三种矿物占总含量的 95%以上),其次为紫苏辉石(2.00% ~ 2.66%)、刚玉(1.15% ~ 2.72%)以及少量的磁铁矿和磷灰石。上述特征与显微镜下(图 3)的观察结果一致。在全碱-硅(TAS)分类图(图 4a)中,样品点均落入花岗岩的区域;在 SiO_2-K_2O 图解上落入高钾钙碱性系列(图 4b)区域;Al_2O_3 介于 13.99% ~ 14.55%之间,平均为 14.23%,铝饱和指数(A/CNK)介于 1.08 ~ 1.21 间,平均值为 1.12,总体上表现为过铝质特征(图 4 c);TFe_2O_3(1.17% ~ 1.63 %)和 MgO(0.28% ~ 0.36 %)含量较低(表 1),在 SiO_2- $FeO_T/(FeO_T+MgO)$ 图解中,样品点均落入镁质区(图 4 d)。

表 1　虎形山钨铍矿区隐伏花岗岩主量元素分析结果（%）

Table 1　Result of major element analyses of concealed granite in the Huxingshan W–Be mining area（%）

样品号	ZK3304-12	ZK3304-13	ZK3304-14	ZK3304-15	ZK3304-17	ZK3304-18	ZK3304-21
SiO_2	72.96	71.91	72.53	71.86	72.72	72.10	73.22
TiO_2	0.11	0.13	0.13	0.16	0.16	0.17	0.16
Al_2O_3	14.09	14.55	13.99	14.19	14.08	14.02	14.36
TFe_2O_3	1.17	1.23	1.25	1.54	1.54	1.63	1.44
MnO	0.03	0.04	0.05	0.05	0.05	0.05	0.04
MgO	0.28	0.32	0.31	0.36	0.33	0.35	0.28
CaO	1.01	1.24	1.57	1.35	1.35	1.47	1.23
Na_2O	2.74	3.29	3.29	3.66	3.62	3.39	3.70
K_2O	4.87	4.42	4.31	4.05	4.17	4.15	4.26
P_2O_5	0.09	0.06	0.05	0.04	0.05	0.05	0.04
LOI	1.66	1.79	2.03	2.68	1.51	1.92	1.37
Total	99.07	99.06	99.59	100.02	99.65	99.37	100.18
A/CNK	1.20	1.15	1.07	1.09	1.08	1.09	1.10
$Mg^{\#}$	32.16	34.01	32.95	31.65	29.07	29.80	29.84
A/NK	1.74	1.98	1.96	2.12	2.04	2.04	2.04
K_2O/Na_2O	1.78	1.34	1.31	1.11	1.15	1.22	1.15

注:A/CNK=n(Al)/ n(Ca+Na+K);A/NK=n(Al)/ n(Na+K);$Mg^{\#}$=100×n(Mg)/n(Mg+TFe^{2+}).

表 2　虎形山钨铍矿区隐伏花岗岩　CIPW 标准矿物分子计算结果(%)

Table 2　The calculation results of the CIPW standard mineral molecular of concealed granite in the Huxingshan W–Be mining area(%)

样品号	ZK3304-12	ZK3304-13	ZK3304-14	ZK3304-15	ZK3304-17	ZK3304-18	ZK3304-21
石英(Qz)	36.35	33.06	33.28	31.71	32.21	32.93	32.04
斜长石(Pl)	28.40	34.62	36.27	38.55	37.81	36.69	37.69
钾长石(Kf)	29.74	27.12	26.36	24.86	25.33	25.38	25.71
刚玉(C)	2.72	2.25	1.15	1.41	1.25	1.39	1.49
紫苏辉石(Hy)	2.00	2.16	2.17	2.60	2.50	2.66	2.22
钛铁矿(Tl)	0.21	0.25	0.25	0.31	0.31	0.33	0.31
磁铁矿(Nag)	0.35	0.37	0.37	0.46	0.46	0.49	0.42
磷灰石(Ap)	0.21	0.14	0.12	0.10	0.12	0.12	0.09
锆石(Zr)	0.01	0.01	0.01	0.02	0.02	0.02	0.02
铬铁矿(Chr)	0	0	0	0	0.01	0	0
合计	100	100	100	100	100	100	100
分异指数(DI)	94.49	94.80	95.91	95.12	95.35	95	95.44

虎形山花岗岩样品的稀土总量ΣREE介于62.3×10^{-6} ~ 124×10^{-6}之间,平均值为101×10^{-6},La_N/Yb_N比值介于9.29 ~ 21.9之间,平均值为17.3,Gd_N/Yb_N比值介于1.77~3.11之间,平均值为2.27,Sm_N/Yb_N比值介于2.71 ~ 5.26之间,平均值为3.91(表3),在稀土元素球粒陨石标准化配分模式图上表现为轻重稀土分异明显,轻稀土相对富集、重稀土相对亏损(图5 a);样品的δEu介于0.51 ~ 0.63之间,平均值为0.56,具有明显的负Eu异常;而δCe介于3.10 ~ 3.22之间,反映样品具有微弱的正Ce异常。8件样品中Ba和Rb元素含

量分别为391×10⁻⁶～572×10⁻⁶和281×10⁻⁶～337×10⁻⁶，其次，Zr含量为42×10⁻⁶～92×10⁻⁶，Th和Nb含量相对较低，分别为7.15×10⁻⁶～14.9×10⁻⁶和9.6×10⁻⁶～11.8×10⁻⁶，Sr含量为95×10⁻⁶～202×10⁻⁶，Eu的含量更低，在0.38×10⁻⁶～0.64×10⁻⁶之间（表3）。在微量元素原始地幔标准化蛛网图（图5 b）中，样品整体显示为右倾型曲线，富集大离子亲石元素Rb、Th、U、K、Ta、La、Ce等，亏损Ba、Nb、P、Ti、Sr、Nd略有亏损。

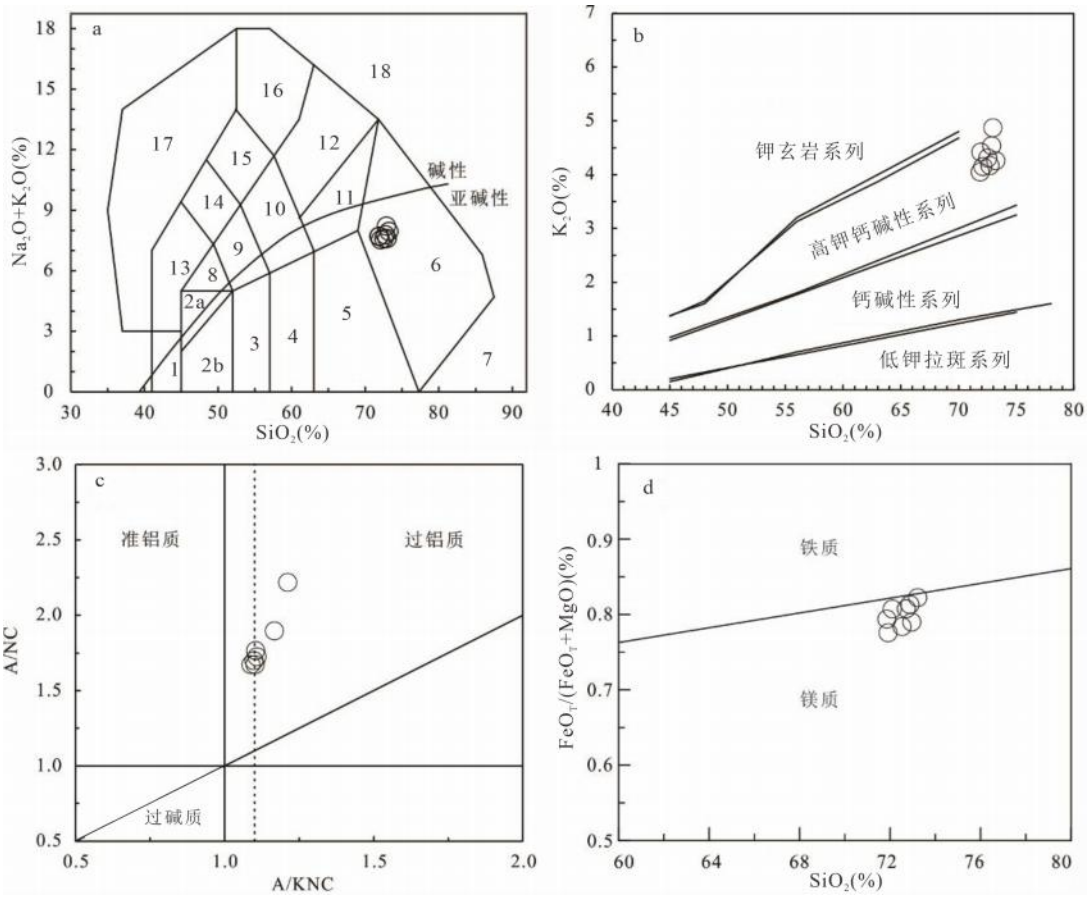

图4 虎形山钨铍矿区隐伏花岗岩相关判别图解

Fig. 4 Related discrimination diagram of concealed granite in the Huxingshan W-Be mining area

a.侵入岩TAS分类图解（底图据Middlemost，1994）；b. K_2O-SiO_2图解（底图据Rickwood，1989）；c. A/KNC-A/NC图解（底图据Maniar and Piccoli，1989）；d. SiO_2- FeO_T/（FeO_T+MgO）图解（底图据Ronald Frost et al.，2001）

图a中：1.橄榄辉长岩；2a.碱性辉长岩；2b.亚碱性辉长岩；3.辉长闪长岩；4.闪长岩；5.花岗闪长岩；6.花岗岩；7.硅英岩；8.二长辉长岩；9.二长闪长岩；10.二长岩；11.石英二长岩；12.正长岩；13.副长石辉长岩；14.副长石二长闪长岩；15.副长石二长正长岩；16.副长正长岩；17.副长深成岩；18.霓方钠岩/磷霞岩/粗白榴岩

5 讨论

5.1 岩浆源区的温度、压力

花岗岩作为地壳的重要组成部分，在大陆区域构造和岩浆演化过程中起着重要的作用（王德滋和沈渭洲，2003；王开朗等，2013；吴福元等，2023）。花岗岩结晶时的温度、压力、氧逸度、挥发分含量、含水量等物理化学条件的变化直接影响成矿元素在熔体相和流体相之间的分配、运移，从而制约成矿作用的进行（张德会，2020）。通过花岗岩中重要矿物（如锆石、黑云母等）的化学成分特征能够反映岩浆的源区性质、成因类型、构造环境以及成岩时的物理化学条件等信息（Wones and Eugster，1965；Patiño Douce，1993；周新民，2007；王晓霞等，2024），对揭示成岩、成矿作用过程有重要的指示意义。

表 3　虎形山钨铍矿区隐伏花岗岩微量、稀土元素分析结果(×10⁻⁶)

Table 3　Results of trace and rare earth element analyses of concealed granite in the Huxingshan W–Be mining area (×10⁻⁶)

样品号	ZK3304-12	ZK3304-13	ZK3304-14	ZK3304-15	ZK3304-16	ZK3304-17	ZK3304-18	ZK3304-21
Li	0.66	2.36	0.17	0.84	0.40	0.29	0.19	0.17
Be	41.8	7.07	17.0	8.36	6.56	6.53	5.20	7.19
V	13.0	12.0	11.0	13.0	13.0	14.0	15.0	14.0
Cr	20.0	20.0	20.0	20.0	10.0	30.0	20.0	30.0
Cu	343	1474	23.4	28.7	26.6	25.0	19.8	47.4
Zn	84.3	507	48.6	57.5	53.5	57.1	50.3	50.6
Ga	26.4	26.4	25.4	27.5	25.7	25.0	26.1	23.9
Rb	337	330	297	290	303	287	337	281
Sr	95.0	125	148	202	162	160	151	140
Y	10.5	8.60	9.20	13.0	9.30	11.8	11.8	11.5
Zr	42.0	63.0	70.0	92.0	78.0	88.0	91.0	87.0
Nb	10.6	10.6	10.6	11.8	10.5	9.90	10.4	9.60
Mo	202	62.7	3.81	2.52	3.57	1.38	4.43	41.7
Sn	11.2	17.4	5.12	12.3	11.2	6.95	4.49	4.49
Cs	17.8	19.4	23.0	12.9	15.3	17.0	19.0	16.3
Ba	391	572	539	570	566	448	432	490
La	13.4	21.9	20.8	29.0	21.9	26.4	28.4	27.3
Ce	26.2	42.2	39.5	55.7	42.0	49.7	53.5	50.4
Pr	2.85	4.50	4.17	5.86	4.43	5.09	5.39	5.20
Nd	9.90	15.5	14.5	19.9	14.9	17.4	18.3	17.0
Sm	2.44	3.29	3.04	4.09	3.14	3.35	3.61	3.54
Eu	0.38	0.53	0.56	0.64	0.57	0.52	0.53	0.54
Gd	2.14	2.61	2.46	3.10	2.50	2.60	2.60	2.55
Tb	0.34	0.35	0.37	0.48	0.35	0.42	0.44	0.40
Dy	1.99	1.72	1.99	2.58	1.88	2.17	2.21	2.14
Ho	0.37	0.29	0.35	0.45	0.34	0.43	0.44	0.41
Er	1.00	0.75	0.82	1.19	0.91	1.18	1.20	1.09
Tm	0.15	0.11	0.11	0.18	0.13	0.17	0.17	0.16
Yb	0.98	0.68	0.69	1.08	0.90	1.14	1.09	1.02
Lu	0.15	0.10	0.10	0.14	0.14	0.17	0.16	0.15
Hf	1.80	2.40	2.70	3.10	3.00	3.00	3.20	2.90
Ta	2.10	1.90	2.10	2.00	1.70	1.90	2.10	1.90
W	39.0	5.00	6.00	8.00	2.00	4.00	5.00	6.00
Pb	32.3	37.4	39.3	35.5	32.9	41.1	40.3	34.0
Bi	1.93	10.4	1.77	1.50	0.90	0.52	7.74	0.98
Th	7.15	10.9	10.8	14.0	10.9	12.9	14.9	13.4
U	8.21	10.2	8.71	12.4	9.06	9.59	16.9	9.98
∑REE	62.3	94.5	89.5	124	94.1	111	118	112
Th/U	0.87	1.07	1.24	1.13	1.20	1.35	0.88	1.34
U/Th	1.15	0.94	0.81	0.89	0.84	0.74	1.14	0.74
La_N/Yb_N	9.29	21.9	20.5	18.2	16.5	15.7	17.7	18.2
Gd_N/Yb_N	1.77	3.11	2.88	2.32	2.25	1.85	1.93	2.02
Sm_N/Yb_N	2.71	5.26	4.79	4.12	3.80	3.20	3.60	3.78
δEu	0.51	0.55	0.63	0.55	0.62	0.54	0.53	0.55
δCe	3.22	3.20	3.16	3.20	3.19	3.16	3.17	3.10
TZr(°C)	742	707	736	734	727	746	741	734

注:下标 N 表示该元素经过球粒陨石标准化,据 McDonough and Sun (1995);$\delta Eu = Eu/Eu^* = 2Eu_N/(Sm_N \times Gd_N)$;δCe=2Ce/(La+Pr);TZr(°C)的计算据 Watson and Harrison (1983)

锆石是花岗质岩浆中较早结晶的副矿物，具有相对稳定且对温度敏感的特征，因此锆石饱和温度被认为近似代表花岗质岩石近液相线的温度（King et al.，1997）。本文采用 Watson and Harrison（1983）的模拟公式来计算花岗岩的锆石饱和温度：

T_{Zr}（℃）= 12900/[2.95 + 0.85 M + ln(496000/Zr_{melt})]-273

式中，令全岩 n(Si)+n(Al)+n(Fe)+n(Mg)+n(Ca)+n(Na)+n(K)+n(P)=1，则 M = n(Na + K + 2Ca)/n(Al × Si)。

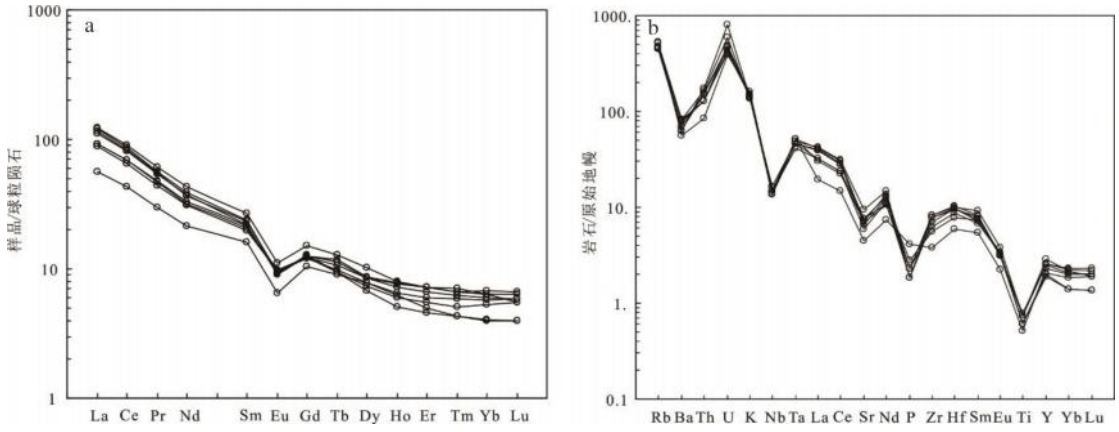

图 5 虎形山钨铍矿区隐伏花岗岩稀土元素球粒陨石标准化配分模式图（a）及微量元素原始地幔标准化蛛网图（b）

Fig. 5 Normalized distribution pattern of rare-earth element chondrites（a）and normalized diagram of trace elements in primitive mantle of the concealed granite（b）in the Huxingshan W-Be mining area

标准化值据 Sun and McDonough（1989）

在没有进行全岩锆石矿物 Zr、Hf 校正时，纯锆石中 Zr = 497626×10^{-6}，同时，用全岩的 Zr 含量近似代表熔体中的 Zr 含量（王楠等，2017），计算出虎形山花岗岩样品的锆石饱和温度在 707 ~ 746℃之间（表 3），接近但略低于 A 型花岗岩形成的平均温度（764℃，King et al.，1997），显然，虎形山花岗岩体受到了结晶分异作用的影响。

当前有很多方法来计算花岗岩的压力，如角闪石全铝压力计、黑云母全铝压力计和通过拉曼光谱获得流体包裹体内压等，李小伟等（2011）系统总结了这些压力计的应用限制条件和误差。相比于其他方法，在不考虑花岗岩结构的情况下，Q-Ab-Or 图解既可以反映花岗岩矿物（组合）的结晶演化顺序，也可以反映两种长石和石英共结时的压力条件和水活度等信息（黄凡等，2009；李小伟等，2011）。考虑到虎形山花岗岩不存在典型的斑状结构，因此可直接将 CIPW 计算得到的长石、石英含量（表 2）投影于 Q-Ab-Or 图解中来推测其源区的压力条件。在图 6a 中，虎形山花岗岩样品普遍投影于 1 ~ 5 kbar 之间，反映较低的源区压力条件和较浅的源区深度。该结论与（$CaO+Al_2O_3$）-CaO/Al_2O_3 图解（图 6b）中样品点位于低压线以下区域的指示意义一致。

5.2 成因分析

虎形山花岗岩富 SiO_2、Al_2O_3，贫 CaO，CIPW 刚玉分子>1%（1.15% ~ 2.72%），A/CNK 介于 1.07 ~ 1.20 之间（表 1、表 2），并富集云母等过铝质矿物，显示出 S 型花岗岩的特征（Chappell and White，1992；Zeng R Y et al.，2016）。对于 S 型花岗岩而言，随着结晶分异程度的加强，P_2O_5 含量将会上升，Th 和 Y 含量将会下降。在图 7 中，P_2O_5 与 Th 和 Y 主要呈负相关，也显示了 S 型花岗岩的特征。虽然虎形山花岗岩的 10000Ga/Al 值（3.14 ~ 3.66）均大于 2.6，显示为 A 型花岗岩的特征，但是其具有一系列明显区别于 A 型花岗岩的特征，如：（1）高场强元素 Zr、Nb、Ce 和 Y 值之和介于 89.3×10^{-6} ~ 172.5×10^{-6}，远低于 A 型花岗岩的该值下限值（350×10^{-6}）；（2）其 AKI 值介于 0.69 ~ 0.76 之间，低于 A 型花岗岩的平均值（0.95）；（3）其锆石饱和温度为 707 ~ 746℃，明显低于澳大利亚 Lachlan 褶皱带铝质 A 型花岗岩 839℃的平均锆石饱和温度（King et al.，1997），接

近但略低于典型S型花岗岩的平均锆石饱和温度(764℃,King et al.,1997)。研究认为,高分异的I型或者S型花岗岩与部分典型的A型花岗岩的主、微量元素特征接近(Whalen et al.,1987;Chappell et al.,2012)。虎形山花岗岩具有较低的Fe、Mg、Ti含量,同时其较低的$Mg^{\#}$(27.81 ~ 32.95)、Zr/Hf、Rb/Sr和Th/U值以及较高的分异指数(DI=94.49~95.91),均显示出较高程度的分异演化(王连训等,2008)。Ba、Sr、Eu的负异常用来揭示斜长石和钾长石的结晶分离;P和Ti的负异常则与磷灰石和钛铁矿的分离结晶有关。此外,在Sr-Ba图解(图8a)和La-$(La/Yb)_N$图解(图8b)中,显示虎形山花岗岩经历了斜长石、钾长石、磷灰石、独居石和褐帘石的结晶分异过程。因此,虎形山花岗岩部分A型花岗岩的特征是由其较高的分异程度造成的。综上,虎形山花岗岩应为高分异的S型花岗岩。

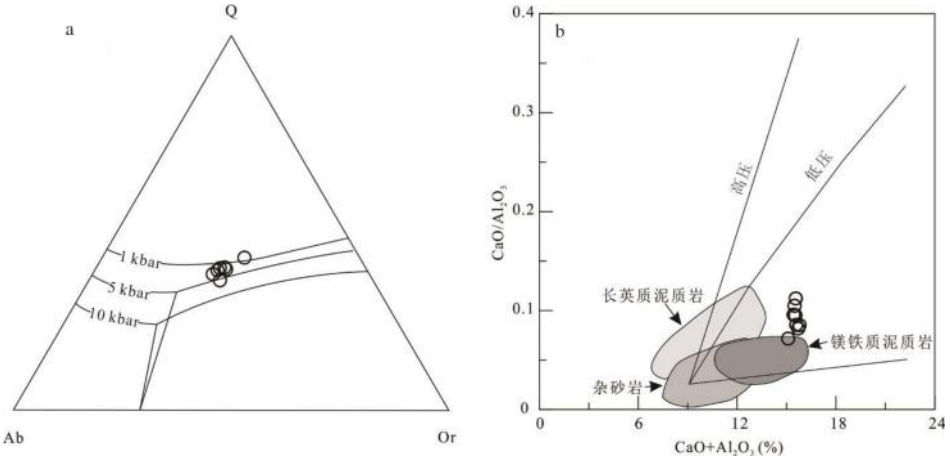

图6　虎形山钨铍矿区隐伏花岗岩CIPW标准化Q-Ab-Or图解(a)及($CaO+Al_2O_3$)-CaO/Al_2O_3图解(b)

Fig. 6　Diagram of CIPW standardized Q-Ab-Or (a)and CaO / Al_2O_3 - ($CaO + Al_2O_3$) (b)diagram of the concealed granite in the Huxingshan W-Be mining area

a图底图据Johannes and Holtz(1996);b图底图据Patiño Douce(1999)

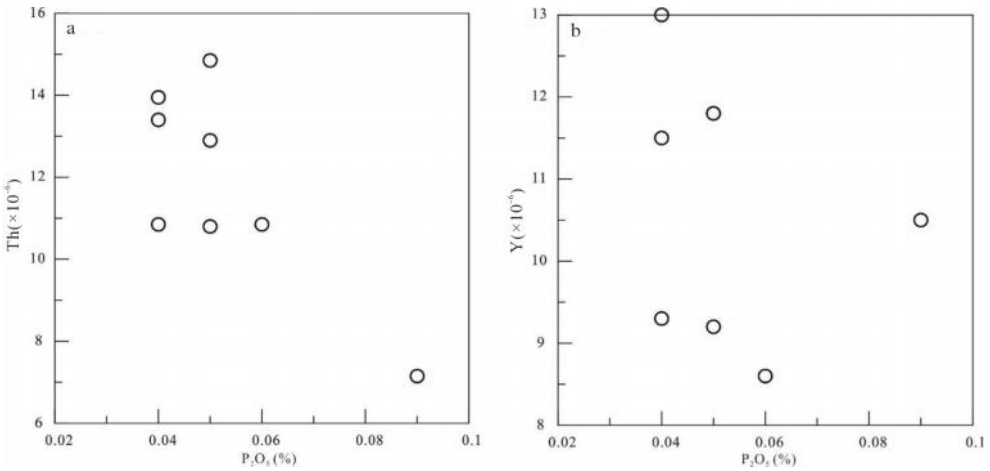

图7　虎形山钨铍矿区隐伏花岗岩P_2O_5-Th(a)及P_2O_5-Y(b)图解

Fig. 7　Illustration of P_2O_5-Th (a) and P_2O_5-Y(b) in the concealed granite of the Huxingshan W-Be mining area

5.3 源区特征

在Rb/Sr-Rb/Ba图解(图9a)中,虎形山花岗岩样品投影点趋势与实验中的杂砂岩、泥质岩、砂屑岩等脱水熔融的投影点均不重合,而与杂砂岩和泥质岩的混合趋势相符。我们之前通过对虎形山花岗岩中单颗粒锆石的Hf同位素研究显示,ε_{Hf}

K_2O、Rb、Cs 和 TiO_2 含量,且具有较低的 Na_2O/K_2O(均小于 1)和 Al_2O_3/TiO_2 值(均小于 200),高的 Rb/Sr 值(均大于 1),显示云母矿物脱水熔融的特征(Miller, 1985; Castro et al., 1999)。Wang Y J et al. (2003)认为 Rb/Sr>5 是岩浆源区白云母脱水熔融的标志,而 Rb/Sr<5 则反映主要与黑云母的脱水熔融有关。虎形山花岗岩的 Rb/Sr 值均小于 5,显示该花岗岩源区主要受黑云母的脱水熔融控制。此外,虎形山花岗岩较低的 CaO(1.01% ~ 1.57%)含量指示角闪石的脱水熔融作用受限或者没有(Masberg et al., 2005)。综上,黑云母的脱水熔融在虎形山花岗岩碎屑岩的混合源区部分熔融中起主导作用。

中元古界的冷家溪群为湘东北地区的基底地层。虎形山花岗岩具有 Rb、Th、U、K 等 LILE 富集,Ba、Sr、Nb、Ta、P 相对亏损的特征(图 5b),与冷家溪群的微量元素特征(许德如等,2006)相似。此外,前期的研究表明虎形山花岗岩锆石 $\varepsilon_{Hf}(t)$ 的最低值为-9.64,可以近似代表其源区古老地壳的 $\varepsilon_{Hf}(t)$ 值(Xu J W et al., 2020),而该值对应的 T_{DM2}(1806 Ma)与冷家溪群碎屑锆石的 T_{DM2} 峰值相同(1.8 Ga,孟庆秀等, 2013),因此,本文推测冷家溪群为虎形山花岗岩的地壳物质源区。

5.4 大地构造意义

在早-中三叠世,由于古特提斯洋的关闭,在华南地区发生了强烈的构造-岩浆作用,形成了大量的同期花岗岩(250 ~ 220 Ma)。此后,华南地区发生了从特提斯构造域向太平洋构造域的转换。众多学者通过对华南众多沉积盆地及岩浆岩的研究,190 ~ 160 Ma 被认为是该构造体制的转换期(邓平等, 2003; Shu L S et al., 2009; 舒良树, 2012)。在太平洋构造域中,华南地区晚中生代强烈的岩浆活动主要与古太平洋板块向华南板块低角度的平俯冲有关(Zhou X M et al., 2006; Li Z X and Li X H, 2007),在东南沿海地区形成了大量的早白垩世花岗岩,普遍认为它们是被俯冲扰动的地幔物质上涌而导致的地壳物质部分熔融形成的(Zhou X M and Li W X, 2000; 周新民, 2007)。

唐朝永等(2013)对虎形山矿化石英脉进行了 Rb-Sr 同位素测年,结果为 135 ~131Ma,表明它们是燕山晚期的产物。Xu J W et al. (2020) 对虎形山白云母-石英脉流体包裹体进行 Rb-Sr 等时线测年,结果为 134±2 Ma,与其花岗岩的锆石 U-Pb 年龄(137.8±0.5 Ma)在误差范围内一致,这些均表明虎形山矿床及矿区内的花岗岩形成时代均为白垩纪。虽然在构造判别图(图 10)中,虎形山花岗岩样品均投影于同碰撞的区域,然而,如前文所述,华南地区的同碰撞造山作用发生于三叠纪,早白垩世湘东北已经完成了由陆内碰撞向陆内拉伸的转变(李鹏春等, 2005; 王连训等, 2008)。在临近的赣北地区发育大量拉伸环境下的板内 A 型花岗岩,其形成时期为 140 ~ 90 Ma, (Li X H, 2000; Jiang Y H et al., 2011; 黄兰椿和蒋少涌, 2012; Yang S Y et al., 2012),这表明白垩纪的虎形山花岗岩不可能形成于同碰撞环境。因此,虎形山花岗岩的同碰撞地球

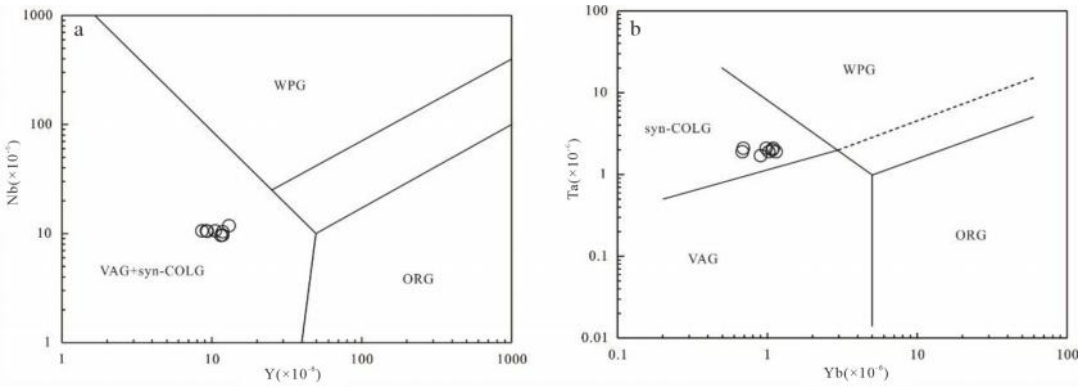

图 10　虎形山钨铍矿区隐伏花岗岩构造环境判别图解

Fig. 10　Discrimination map of the tectonic environment of the concealed granite in the Huxingshan W-Be mining area

底图据 Pearce et a1. 1984;WPG-板内花岗岩;ORG-洋脊花岗岩;VAG-火山弧花岗岩;syn-COLG-同碰撞花岗岩

初探[J].矿产与地质,27(5):353-362.

王 楠,吴才来,秦海鹏.2017.川西义敦岛弧中生代典型花岗岩体矿物学、地球化学特征及岩浆来源探讨[J].地质论评,63(4):981-1000.

王德滋,沈渭洲.2003.中国东南部花岗岩成因与地壳演化[J].地学前缘,10(3):209-220.

王开朗,游先军,张强录,刘利生,唐朝永,陈云华,晏月平,任杰.2013.湖南省临湘市虎形山地区铷锶同位素年代学研究[J].矿产与地质,27(2):151-157.

王连训,马昌前,张金阳,陈 玲,张 超.2008.湘东北早白垩世桃花山—小墨山花岗岩体岩石地球化学特征及成因[J].高校地质学报,14(3):334-349.

王晓霞,王 涛,陈小丹,柯昌辉,杨 阳.2024.花岗质岩石中黑云母成分区域性变化对深部物质示踪及成矿的约束:以秦岭地区为例[J].岩石学报,40(3):811-826.

吴福元,郭春丽,胡方泱,刘小驰,赵俊兴,李晓峰,秦克章.2023.南岭高分异花岗岩成岩与成矿[J].岩石学报,39(1):1-36.

徐 斌,蒋少涌,罗 兰.2015.江西彭山锡多金属矿集区尖峰坡锡矿床 LA-MC-ICP-MS 锡石 U-Pb 测年及其地质意义[J].岩石学报,31(3):701-708.

许德如,贺转利,李鹏春,陈广浩,夏 斌,符巩固.2006.湘东北地区晚燕山期细碧质玄武岩的发现及地质意义[J].地质科学,41(2):311-332.

许德如,王 力,李鹏春,陈广浩,贺转利,符巩固,吴 俊.2009.湘东北地区连云山花岗岩的成因及地球动力学暗示[J].岩石学报,25(5):1056-1078.

张德会.2020.成矿作用地球化学(第二版)[M].北京:地质出版社,1-481.

张九龄.1989.湖南桃林铅锌矿床控矿条件及成矿预测[J].地质与勘探,25(4):1-7.

周新民.2007.南岭地区晚中生代花岗岩成因与岩石圈动力学演化[M].北京:科学出版社.

Cai K D, Sun M, Yuan C, Zhao G C, Xiao W J, Long X P, Wu F Y. 2011. Geochronology, petrogenesis and tectonic significance of peraluminous granites from the Chinese Altai, NW China[J]. Lithos, 127(1-2): 261-281.

Castro A, Patiño Douce A E, Gurllermo Corretgé L, De la Rosa J D, El-Biad M, El-Hmidi H. 1999. Origin of peraluminous granites and granodiorites, Iberian massif, Spain: an experimental test of granite petrogenesis[J]. Contributions to Mineralogy and Petrology, 135(2-3): 255-276.

Chappell B W, Bryant C J, Wyborn D. 2012. Peraluminous I-type granites[J]. Lithos, 153: 142-153.

Chappell B W, White A J R. 1992. I-and S-type granites in the Lachlan Fold Belt[J]. Transactions of the Royal Society of Edinburgh: Earth Sciences, 83(1-2): 1-26.

Frost B R, Barnes C G, Collins W J, Arculus R J, Ellis D J, Frost C D. 2001. A Geochemical Classification for Granitic Rocks[J]. Journal of petrology, 42(11): 2033-2048.

Jiang Y H, Zhao P, Zhou Q, Liao S Y, Jin G D. 2011. Petrogenesis and tectonic implications of Early Cretaceous S-and A-type granites in the northwest of the Gan-Hang rift, SE China[J]. Lithos, 121(1-4): 55-73.

Johannes W, Holtz F. 1996. Petrogenesis and Experimental Petrology of Granitic Rocks[M]. Springer, Berlin, 1-335.

King P L, White A J R, Chappell B W, Allen C M. 1997. Characterization and origin of Aluminous A-type Granites from the Lachlan Fold Belt, Southeastern Australia[J]. Journal of Petrology, 38(3): 371-391.

Li B, Jiang S Y, Zhang Q, Zhao H X, Zhao K D. 2015. Cretaceous crust-mantle interaction and tectonic evolution of Cathaysia Block in South China: Evidence from pulsed mafic rocks and related magmatism[J]. Tectonophysics, 661: 136-155.

Li X H. 2000. Cretaceous magmatism and lithospheric extension in Southeast China[J]. Journal of Asian Earth Sciences, 18(3): 293-305.

Li X H., Li W X, Li Z X, Lo C H, Wang J, Ye M F, Yang Y H. 2009. Amalgamation between the Yangtze and Cathaysia Blocks in South China: constraints from SHRIMP U-Pb zircon ages, geochemistry and Nd-Hf isotopes of the Shuangxiwu volcanic rocks[J]. Precambrian Research, 174 (1-2): 117-128.

Li Z X, Li X H. 2007. Formation of the 1300-km-wide intracontinental orogen and postorogenic magmatic province in Mesozoic South China: A flat-slab subduction model[J]. Geology, 35(2): 179-182

Liu Q Q, Li B, Shao Y J, Lu A H, Lai J Q, Li Y F, Luo Z Z. 2017. Molybdenum mineralization related to the Yangtze's lower crust and differentiation in the Dabie Orogen: Evidence from the geochemical features of the Yaochong porphyry Mo deposit[J]. Lithos, 282: 111-127.

Maniar P D, Piccoli P M. 1989. Tectonic discrimination of granitoids[J]. Geological Society of America Bulletin, 101(5): 635-643.

Mao J R, Takahashi Y, Kee W S, Li Z L, Ye H M, Zhao X L, Liu K, Zhou J. 2011. Characteristics and geodynamic evolution of Indosinian magmatism in South China: a case

agronomy

MDPI

Article

Synergistic Remediation of Cd-Contaminated Soil with Pure Natural Adsorption Material and Hyperaccumulator Plant

Jun Guo [1,2,3], Honggen Xu [2,3]*, Fengxiang Yin [4,5], Jian Cao [4,5], Xuesheng Xu [1], Cong Li [2,3], Fengcun Huang [2,3], Fangwei Chen [2,3], Xiong Mao [2,3] and Qi Liao [2,3]

1 Hunan Provincial Key Laboratory of Geochemical Processes and Resource Environmental Effects, Geophysical and Geochemical Survey Institute of Hunan, Changsha 410014, China; wkyxxs@126.com
2 Changsha General Survey of Natural Resources Centre, China Geological Survey, Changsha 410600, China; xiafeng8093@163.com (J.G.); licong@mail.cgs.gov.cn (C.L.); huangfengcun@mail.cgs.gov.cn (F.H.); chenfangwei@mail.cgs.gov.cn (F.C.); maoxiong@mail.cgs.gov.cn (X.M.); liaoqi@mail.cgs.gov.cn (Q.L.)
3 Huangshan Observation and Research Station for Land-Water Resources, Huangshan 245000, China
4 School of Minerals Processing and Bioengineering, Central South University, Changsha 410083, China; 225612132@csu.edu.cn (F.Y.); caojianlzu@163.com (J.C.)
5 Key Laboratory of Hunan Province for Clean and Efficient Utilization of Strategic Calcium-Containing Mineral Resources, Central South University, Changsha 410083, China
* Correspondence: xuhonggen@mail.cgs.gov.cn

Abstract: In recent years, cadmium (Cd) contamination in agricultural soil has emerged as a significant global environmental issue, posing irreversible harm to crops and human health. As a result, efficient soil remediation techniques are urgently needed. For this issue, synergistic remediation by material and plant is an effective approach. In this study, a natural and green adsorption material (starch/montmorillonite composite, SMC) of Cd was prepared, which was further employed in synergistic remediation toward soil Cd contamination with the cadmium hyperaccumulator plant *Bidens bipinnata*. The results of the pot experiment demonstrated that an available Cd removal rate of 77.92 could be obtained, and the results of the field experiments demonstrate that the concentrations of Cd in contaminated soil could be reduced below the risk-screening values for agricultural land. Further analyses, including a microbial community diversity study, changes in soil BCR fraction components, and a TCLP toxicity leaching experiment, unequivocally elucidated that the synergy of SMC and *Bidens bipinnata* enhanced the remediation efficiency of Cd in contaminated soil. This study confirmed the application potential of the synergy of SMC and *Bidens bipinnata* toward Cd-contaminated soil.

Keywords: Cd contamination; available Cd; starch/montmorillonite composites; *Bidens bipinnata*; collaborative remediation

Citation: Guo, J.; Xu, H.; Yin, F.; Cao, J.; Xu, X.; Li, C.; Huang, F.; Chen, F.; Mao, X.; Liao, Q. Synergistic Remediation of Cd-Contaminated Soil with Pure Natural Adsorption Material and Hyperaccumulator Plant. *Agronomy* **2024**, *14*, 1299. https://doi.org/10.3390/agronomy14061299

Received: 8 May 2024
Revised: 7 June 2024
Accepted: 11 June 2024
Published: 15 June 2024

1. Introduction

Synergistic remediation techniques are an efficient and safe approach to addressing heavy metal pollution in agricultural soil [1], which includes microbial–plant synergy, electrokinetic–plant synergy, and chemical or adsorption material–plant synergy [2]. Among various synergistic remediation techniques, the synergy of adsorption material and plants promotes the transfer of the total heavy metal content in soil from large aggregates to small aggregates through passivation control and reduces the available heavy metal content in large aggregates [3]. Furthermore, the synergy of adsorption material and plants could also transform heavy metals in the soil from an unstable state to a stable state, which enhances the vital activity of plants and the tolerance and stability of plants to heavy metals. As a consequence, the synergy of adsorption material and plants occupies a dominant position among all the synergistic remediation techniques [4].

For the synergistic remediation techniques using adsorption material–plant synergy, the adsorption material plays the role of solidification or passivation, which is greatly conducive to the remediation of heavy metals in soil. However, on the other hand, adsorption materials are often synthetic materials, which have adverse effects on soil properties and the surrounding environment after long-term use. Fly ash material and *Jatropha curcas* are used for the synergistic remediation of heavy metal-contaminated soil [5]. Iron oxides in fly ash materials (FeO, Fe_3O_4) can form coordination compounds with heavy metals in the soil, reducing their activity. However, simultaneous use introduces new metal ions (Fe^{3+}), which may lead to other safety issues in the long term. Limestone, red mud composite material, and lettuce are used for the synergistic remediation of As, Cd, Pb, and Zn contamination [6]. The alkalinity of limestone affects the growth and activity of soil microorganisms, thereby influencing the balance of the soil ecosystem [7]. At present, green adsorption materials are urgently needed for the further development of material–plant synergistic remediation techniques.

Montmorillonite is a widely used and inexpensive natural clay mineral. Due to the layered silicate structure, montmorillonite possesses an interlayer space capable of cation exchange and a large specific surface area (up to 800 m^2/g) [8,9]. As a result, montmorillonite has been increasingly employed as a green and cost-effective adsorption material for heavy metal contaminants [10,11]. In recent years, various organic compounds have been utilized in the modification of montmorillonite to obtain highly efficient montmorillonite passivators. Until now, montmorillonite has been modified with different types of organics, including anionic compounds (such as sodium dodecyl sulfate [12]), cationic compounds (such as quaternary ammonium salt [13]), and neutral compounds (polyacrylamide [14]). However, over time, these compounds will be degraded, resulting in organic or inorganic sulfides and nitrides, which could severely impact the soil property, microbiota, and other ecological factors. In previous studies, we noticed that starch is particularly suitable as an environment remediation material. Starch is a natural polymer and there are almost no heteroatoms except oxygen atoms in the starch molecule. After degradation, the degradation products of starch have little impact on the soil environment. Based on these factors, a natural and green adsorption material (starch/montmorillonite composite, SMC) was proposed to be efficient towards heavy metal contaminants in soil, which was also a perfect adsorption material candidate used in material–plant synergistic remediation techniques.

The use of adsorption material against heavy metals in soil is usually hindered by the interface reactions between the adsorption material and soil, which affects the inherent adsorption capacity of the adsorption material for heavy metals [12]. Therefore, it is difficult for the adsorption material to completely adsorb the heavy metals firmly bound to the soil. In this regard, the material–plant synergistic remediation technique could promote the upper limit of the adsorption material towards heavy metals. The heavy metals in soil (including the parts that are difficult to adsorb) could be gradually released by beneficial microorganisms and organic substances produced by plant growth. Moreover, through mild biological processes, the toxicity of the heavy metals released was reduced. Both aspects are beneficial to the remediation of heavy metals in soil [15]. In this work, the SMC-*Bidens bipinnata* synergistic remediation technique was developed, and the remediation effect was confirmed by pot experiments (in a greenhouse) and field experiments (in a location on the eastern edge of Dongting Lake, Hunan Province, China). In addition, detailed mechanism studies have also been conducted. This study offers insights into the synergy of material–plant synergistic remediation of Cd-contaminated soil and also provides a soil remediation technical for Cd-contaminated sites.

2. Materials and Methods

2.1. Characteristics of Contaminated Soil

The soil samples were collected from a location on the eastern edge of Dongting Lake in Yueyang County, Hunan Province, which is an area with heavy metal pollution in agriculture. The eastern edge of Dongting Lake was divided into nine grids, an area of 10 cm × 10 cm was selected as a representative of each grid, and the depth of soil sampling was 0–18 cm [16]. Soil samples in this interval are representative of heavy metal pollution remediation, and the weight of the samples taken out was approximately 25 kg. These nine samples were mixed well, and 100 g was taken out for testing (Table 1), while the others were evenly divided into three 8 kg portions of soil for subsequent experiments. It is situated in the southwest part of Yueyang County, at 113°02′ east longitude and 29°07′ north latitude (Figure 1). The sampling site is situated in the Zhongzhou levee area on the banks of Dongting Lake. It has a subtropical monsoon climate characterized by hot summers, mild winters, and abundant and concentrated rainfall. Soil sampling revealed severe Cd contamination in the area. Despite heavy metal contamination, the affected area continues to support a diverse range of wild plant species. For the purpose of phytoremediation screening, fifteen representative native plants, noted for their substantial biomass and widespread distribution, were selected. These species include *Chinese brake herb*, *ramie*, *Equisetum hyemale*, *Imperata cylindrica*, *Dandelion*, *Coleseed*, *Bermuda grass*, *Petroselinum crispum*, *Symphyotrichum subulatum*, *Ficus benjamina*, *Aster indicus*, *Wormwood*, *Bidens bipinnata*, *Peacock grass*, and *Black nightshade*.

Figure 1. Heavy metal-polluted agricultural area at sampling site.

Table 1. Heavy metal content and pollution level of soil in affected area (mg/kg).

Items	Cu	Pb	Zn	Cd	Cr	As	Ni
Total heavy metal (mg/kg)	52.2	90	126	1.91	98.6	53.9	36.3
Agricultural Soil Risk Screening Standard Value (mg/kg)	150	120	200	0.3	250	30	60
Agricultural Soil Risk Control Standard Value (mg/kg)	-	500	-	1.5	800	200	-
Pi value	0.348	0.75	0.73	6.36	0.394	1.79	0.605
Pollution Level [17]	Clean	Relatively clean	Clean	Heavy pollution	Clean	Slight pollution	Clean

Determination of total Cd content in soil: Roots, stones, and other foreign objects were removed from the soil, which was then air-dried and ground to below 0.15 mm. A 0.1 g soil sample was weighed into a 100 mL conical flask, and 6 mL of aqua regia was added. After ensuring sufficient contact between the soil sample and aqua regia, a glass funnel was placed at the top of the conical flask to facilitate the reflux of aqua regia vapor. The conical flask was heated to a slight boil and maintained for two hours. Once digestion was complete, the conical flask was cooled to room temperature, and the extract was filtered to a fixed volume. The soil Cd content was then measured using ICP-MS (NexION 300X, PerkinElmer, Waltham, MA, USA).

Determination of the available Cd content in soil: After drying, soil samples were crushed to below 2 mm. A 10 g soil sample and 20 mL of DTPA-$CaCl_2$-TEA buffer solution were added to a 100 mL conical flask. The conical flask was shaken at room temperature for 2 h, followed by centrifugation and filtration. The supernatant was then taken for ICP measurement of the available Cd in the soil.

TCLP (Toxicity Characteristic Leaching Procedure)-extractable Cd content: Processed and dried soil samples were crushed to below 0.85 mm, and 1 g of the soil sample and 20 mL of the extraction solution were weighed and placed in a centrifuge tube, subjected to constant-temperature shaking for 18 h, centrifuged, and filtered, while the Cd toxicity leaching amount in the soil was detected by ICP-MS (the 1 L extraction solution was prepared with acetic acid (17.5 mol/L) and sodium hydroxide (1 mol/L), pH = 2.88 ± 0.5).

Determination of soil pH: 10 g of the air-dried soil sample was weighed into a 50 mL beaker. Twenty-five milliliters of deionized water was added, and the container was sealed with plastic wrap. The mixture was stirred for 2 min on a magnetic stirrer and allowed to stand for 30 min, and the pH was measured within 1 h using a pH meter.

Soil Cd fractionation was determined using the European Community Bureau of Reference (BCR) sequential extraction method, consisting of three steps. The specific steps are as follows:

The bioaccumulation factor (BF) of a plant for a certain element is defined as the ratio of the element's concentration in the plant (C_{Plant}, mg/kg) to its concentration in the soil (C_{Soil}, mg/kg). The translocation factor (TF) represents the ratio of the element's concentration in the aboveground parts of the plant (C_{shoot}, mg/kg) to that in the belowground parts (C_{Root}, mg·kg^{-1}). These formulas are defined as follows:

$$BF = C_{Plant}/C_{Soil}$$

$$TF = C_{Shoot}/C_{root}$$

The removal rate is one of the key indicators for evaluating the effectiveness of remediation materials. The removal rate is defined as the ratio of the amount of heavy metals removed during remediation to the initial concentration of heavy metals before remediation.

$$\text{Removal rate} = C_{Before} - C_{After}/C_{Before}$$

2.6. Total DNA Extraction, 16S rRNA Amplification and High-Throughput Sequencing

Soil microbial quantification: DNA extraction was conducted on soil samples before and after synergistic remediation. After extraction, 0.8% agarose gel electrophoresis was used for molecular size determination, and a UV spectrophotometer (NanoDrop NC2000, Thermo Fisher Scientific, Waltham, MA, USA) was used for DNA quantification [18]. Bacterial 16S rDNA genes in the V3-V4 region were amplified using genomic DNA as a template, employing the forward primer 338F (5′-ACTCCTACGGGAGGCAGCA-3′) and the reverse primer 806R. PCR was initiated with denaturation at 98 °C for 30 s, followed by amplification cycles consisting of denaturation at 98 °C for 15 s, annealing at 50 °C for 30 s, and extension at 72 °C for 30 s, for a total of 26 cycles to accumulate ample DNA

fragments with a final extension step at 72 °C for 5 min to ensure complete product extension. Amplified fragments were screened via 2% agarose gel electrophoresis and stored at 4 °C. The quantification of PCR products was performed using the Quant-iT Pico Green dsDNA Assay Kit on a Microplate reader (BioTek, FLx800, Vermont, US), followed by pooling according to the required data volume for each sample. After pooling, libraries were constructed using the TruSeq Nano DNA LT Library Prep Kit (Illumina, California, US), followed by quality control and quantification of libraries. Qualified libraries underwent paired-end sequencing on the Illumina NovaSeq platform using the NovaSeq 6000 SP Reagent Kit (500 cycles, Illumina, California, US). Data analysis was performed using QIIME2 2019.4 [19].

2.7. Statistical Analysis Methods

To eliminate interference from unrelated factors (such as seed germination failure or pest damage), all experiments were conducted with three pots of plants, and each analysis was repeated three times to ensure data reliability. Statistical analysis was performed using IBM SPSS Statistics 26. One-way ANOVA was used to compare intergroup differences in various parameters, with significance set at $p < 0.05$. Post hoc analysis was conducted using Duncan's test, and the results are displayed in figures and tables using letter notation. [20]

3. Results

3.1. Characterization of Materials

Following the synthesis of SMC, surface morphology was determined to confirm the deposition of starch onto the montmorillonite surface and investigate the adsorption mechanism between starch and montmorillonite. Experiments performed in aqueous phase systems provided robust evidence that starch modification significantly enhanced the capacity of montmorillonite to adsorb heavy metal cations.

3.1.1. Surface Morphology Characterization of SMC

The morphology of starch, montmorillonite, and SMC is shown in Figure 2. In Figure 2A, starch exhibits a granular or aggregated structure, with loosely arranged particles. Starch particles are circular, elliptical, or irregular in shape, with a smooth and uniform surface and an average particle size of 10 µm. Figure 2B displays the platy or layered structure of montmorillonite, with clear interlayer spacing and well-defined crystal edges, arranged closely. Figure 2C,D depicts the particles of SMC, where it is observed that the starch particles open up into smaller granules and adhere to the surface of montmorillonite, resulting in a smoother and more rounded surface. Figure 2D reveals that the montmorillonite surface has adsorbed numerous starch molecules, indicating the significant adsorption capacity of montmorillonite. Additionally, the elemental analysis of SMC is shown in Figure 2E, where an increase in C, O on the modified montmorillonite surface is evident. The main components include C, O, Si, Al, Fe, K, and Ca, accounting for 46.2 wt%, 31.8 wt%, and 17.2 wt%, respectively.

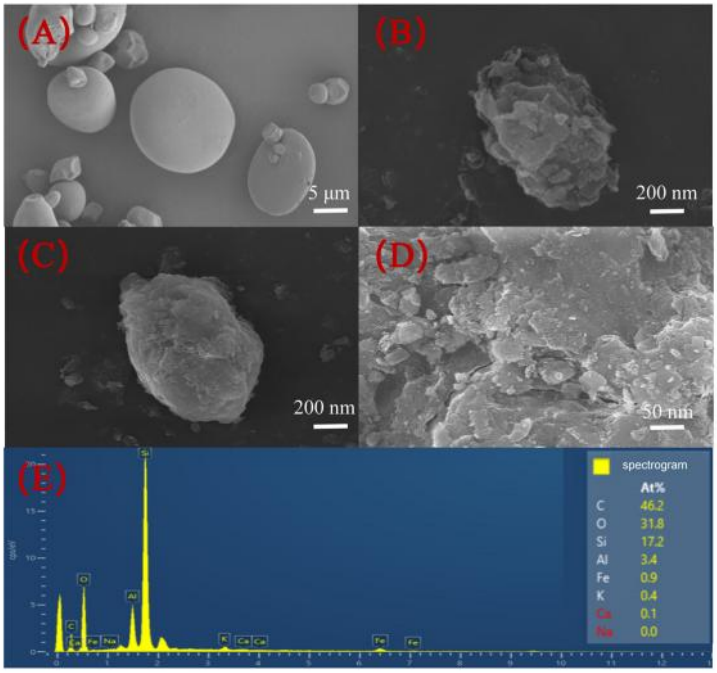

Figure 2. SEM images of unmodified starch (**A**), montmorillonite (**B**), modified montmorillonite (**C**), and magnified view of modified montmorillonite (**D**). EDS elemental mapping of the modified montmorillonite (**E**).

3.1.2. Adsorption Efficiency of SMC towards Heavy Metals in Solution

Water is the primary transport medium of heavy metals in soil. Therefore, the adsorption capacity of SMC for heavy metals was first detected in the water phase. Table 2 shows the adsorption capacity of montmorillonite and SMC towards heavy metal ions. Compared to montmorillonite, the adsorption capacity was significantly improved after modification. For Cd^{2+}, Pb^{2+}, and Cu^{2+}, the removal rates of natural montmorillonite were 50.45%, 64.37%, and 74.33%, while the removal rates of SMC increased to 95.31%, 94.12%, and 87.92%. The modification resulted in an increase of 44.86, 29.75, and 13.59 percentage points, respectively. For natural montmorillonite, the comprehensive adsorption capacity for seven heavy metals is due to the cation exchange capacity. For modified montmorillonite SMC, the improved adsorption capacity for seven heavy metals is due to the reserved cation exchange capacity of montmorillonite and the additional chelation capacity of starch [21].

Table 2. Removal rate (%) of heavy metal ions in aqueous phase by montmorillonite and SMC.

Material	Cu	Pb	Zn	Cd	Cr	As	Ni
Montmorillonite (%)	74.33	64.37	50.31	50.45	33.45	28.07	39.66
SMC (%)	87.92	94.12	73.22	95.31	48.23	48.23	51.37

3.2. Screening of Indigenous Hyperaccumulating Plants

In order to develop a candidate remediation plant that is suitable for the eastern edge of Dongting Lake, 15 native plants were collected with the standard of relatively large biomass from the vicinity of the contaminated site, including Peacock grass, Dandelion, Bermuda grass, Bidens bipinnate, and other plants (as shown in Figure 3). The plants were divided into shoot and root parts, and the heavy metal content in the plants was determined. The bioaccumulation factor (BF) and translocation factor (TF) of the plants were calculated as the screening criteria (Table 3).

Different plants exhibit varying degrees of tolerance and response to heavy metals. The aboveground and underground parts of these 15 plants contain different concentrations of heavy metals, indicating their varying abilities to accumulate Cd. Plants 5, 6, 7, and 13 exhibited strong Cd enrichment capacity, with BF values greater than 0.5 for both shoot and root parts. Among them, plant 13, *Bidens bipinnata*, exhibits the highest accumulation capacity, with Cd contents of 2.2833 mg/kg in the aboveground part and 3.2704 mg/kg in the underground part. Apart from these four plants, plants 2, 3, 4, 12, 14, and 15 show relatively high translocation factors, which are conducive to long-term extraction in plant remediation and represent potential remediation plants.

Generally, plants with higher BF and TF values are considered more suitable for remediation, as they can effectively absorb heavy metals from the soil and transfer them to the aboveground parts, thereby reducing the heavy metal content in the soil [22]. By evaluating the BF and TF of 15 native plants, it was determined that plants 2, 3, 4, 5, 6, 7, 12, 13, 14, and 15 have stronger abilities to absorb and transport heavy metals, playing a more significant role in the remediation process. Therefore, these 10 plants were selected for subsequent pot experiments.

Figure 3. Fifteen Indigenous hyperaccumulating plants of the Eastern Margin of Dongting Lake (1. *Chinese brake herb*, 2. *ramie*, 3. *Equisetum hyemale*, 4. *Imperata cylindrica*, 5. *Dandelion*, 6. *Coleseed*, 7. *Bermuda grass*, 8. *Petroselinum crispum*, 9. *Symphyotrichum subulatum*, 10. *Ficus benjamina*, 11. *Aster indicus*, 12. *Wormwood*, 13. *Bidens bipinnata*, 14. *Peacock grass*, and 15. *Black nightshade*).

Table 3. Cd content, Bioaccumulation Factor (BF), and Transfer Factor (TF) in 15 indigenous hyperaccumulating.

Plant	Cd Content (mg/kg)	BF	TF	Plant	Cd Content (mg/kg)	BF	TF
1 shoot	0.0145	0.0076	0.3713	9 shoot	0.0998	0.0522	0.2791
1 root	0.0391	0.0205		9 root	0.3575	0.1872	
2 shoot	0.0529	0.0277	0.6451	10 shoot	0.0945	0.0495	0.1755
2 root	0.0820	0.0430		10 root	0.5385	0.2819	
3 shoot	0.1729	0.0905	0.6725	11 shoot	0.1885	0.0987	0.2622
3 root	0.2570	0.1346		11 root	0.7189	0.3764	

4 shoot	0.1541	0.0807	0.9862	12 shoot	0.1003	0.0525	0.6524
4 root	0.1563	0.0818		12 root	0.1537	0.0805	
5 shoot	1.1768	0.6161	0.8376	13 shoot	2.2833	1.1954	0.6982
5 root	1.4049	0.7356		13 root	3.2704	1.7123	
6 shoot	1.8418	0.9643	0.7760	14 shoot	0.5077	0.2658	0.6873
6 root	2.3735	1.2427		14 root	0.7386	0.3867	
7 shoot	1.6964	0.8881	1.3830	15 shoot	0.2916	0.1527	0.9119
7 root	1.2266	0.6422		15 root	0.3197	0.1674	
8 shoot	0.3021	0.1581	0.4652				
8 root	0.6493	0.3399					

3.3. Remediation Effect of SMC in Cd Contaminated Soil

The dosage of adsorption material plays a decisive role in the synergistic remediation process. Therefore, the remediation effect of using different dosages of SMC was tested in contaminated soil with high Cd concentrations (Cd = 10 mg/kg) and low Cd concentrations (Cd = 3 mg/kg). From Figure 4, it can be seen that at high or low Cd concentrations, the optimized dosage of SMC is 2%, and the corresponding reduction rates of available Cd are 37.75% and 21.76%, which is much higher than the previously reported reduction rate obtained by clay mineral passivators (9.54%, 13.9%) [23,24]. Experimental results indicated high remediation efficiency of SMC in soils with varying cadmium concentrations. The optimal dosage is determined to be 2%, while the optimal remediation concentration of Cd^{2+} is 3 mg/kg. Subsequent pot experiments will be conducted based on these conditions for synergistic remediation.

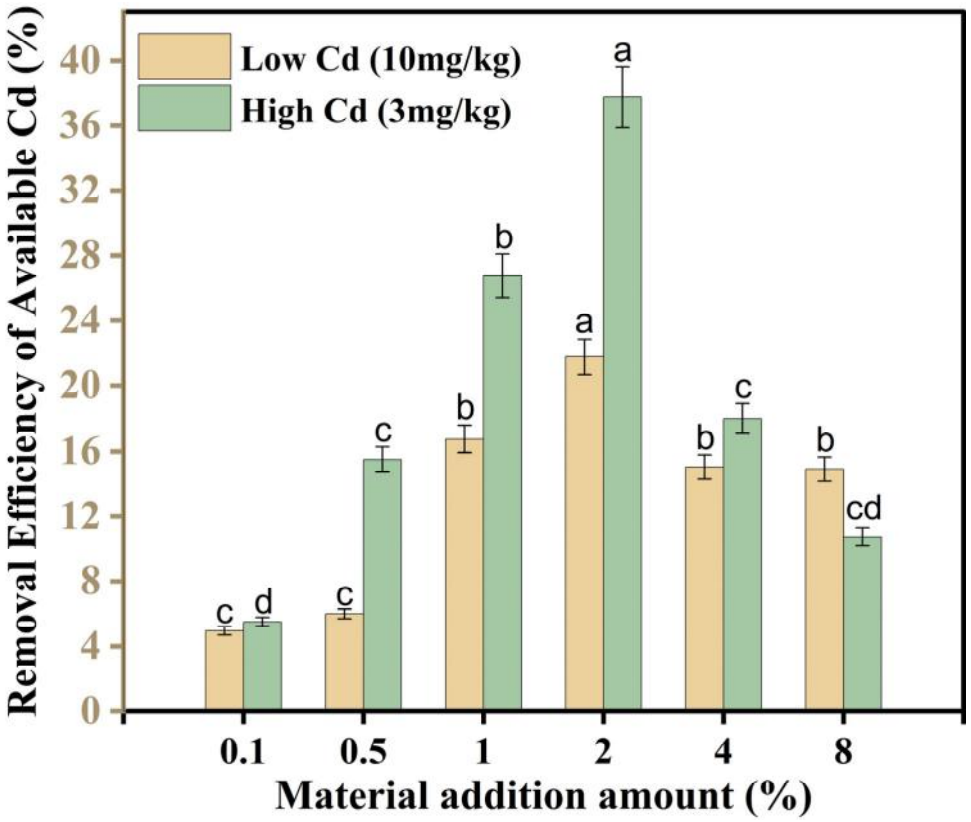

Figure 4. Remediation effect of SMC for Cd in soil with high and low concentrations (different letters above the bars in the bar chart indicate significant differences at the $p < 0.05$ level between different treatments. Error bars represent the standard deviation of the mean, $n = 3$).

3.4. Screening of Remediation Plants by Potted Experiment

Pot experiments were conducted using ten selected remediation plants with higher TF and BF values out of the 15 plant species screened in the remediation site, in artificial synthetic Cd-contaminated soil. The ten plant species were subjected to three treatments: (a) natural conditions without any treatment, (b) the addition of 3 mg/kg Cd^{2+}, and (c) the addition of SMC after Cd^{2+} addition. After 90 days of greenhouse cultivation, photographs were taken and are shown in Figure 5. It was observed that all ten seed species were able to germinate and survive in uncontaminated soil (Figure 5A), while under Cd^{2+} stress (Figure 5B), only seven plant species germinated, with stunted growth and significantly reduced biomass. However, upon the addition of SMC material (Figure 5C), the growth of the plants improved markedly, alleviating the heavy metal stress. Nevertheless, ramie exhibited excessively slow growth and was deemed unsuitable as a remediation plant. Conversely, the other six plant species, namely *Peacock grass*, *Bidens bipinnata*, *Coleseed*, *Bermuda grass*, *Black nightshade*, and *Dandelion*, exhibited robust growth with higher biomass.

Specific measurements of biomass, plant height, and water content were conducted for these six plants (Figure 6). The results indicate that the addition of Cd significantly stressed the growth of all plants. However, with the addition of SMC, toxic Cd in the soil was immobilized, which alleviated growth inhibition caused by the toxicity of Cd and promoted a significant increase in biomass. This is similar to findings from other studies on heavy metal-contaminated soils [25]. Among them, *Bidens bipinnata* had the highest biomass under natural conditions. However, it decreased significantly under heavy metal stress and then recovered to the highest biomass after the addition of SMC. Trends in water content, plant height, and biomass were generally consistent, indicating that heavy metals have a significant impact on plant metabolism. Under metal stress, changes occur in the physiological characteristics and cell structure of plants, such as increased cell wall thickness and vacuole volume, the disruption of internal chloroplast tissues, increased number of plastids, and the disintegration of primary cell wall fibers [26]. The addition of SMC eliminated these effects, promoting the absorption and transport of substances within plants, thereby establishing tolerance to heavy metals.

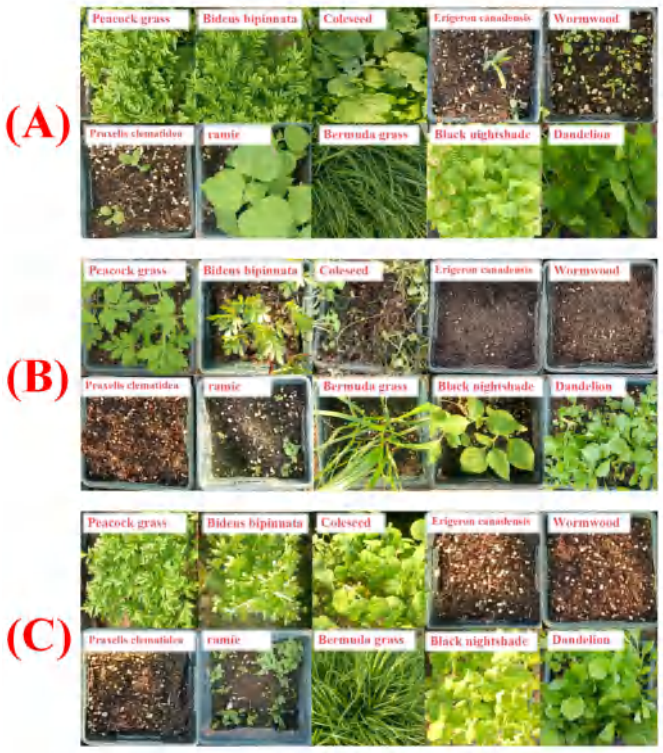

Figure 5. Comparison of growth conditions of 10 plant species before and after material remediation ((**A**): control group (plant growth status under natural conditions), (**B**): single premeditation group, (**C**): SMC–plant synergistic repair group).

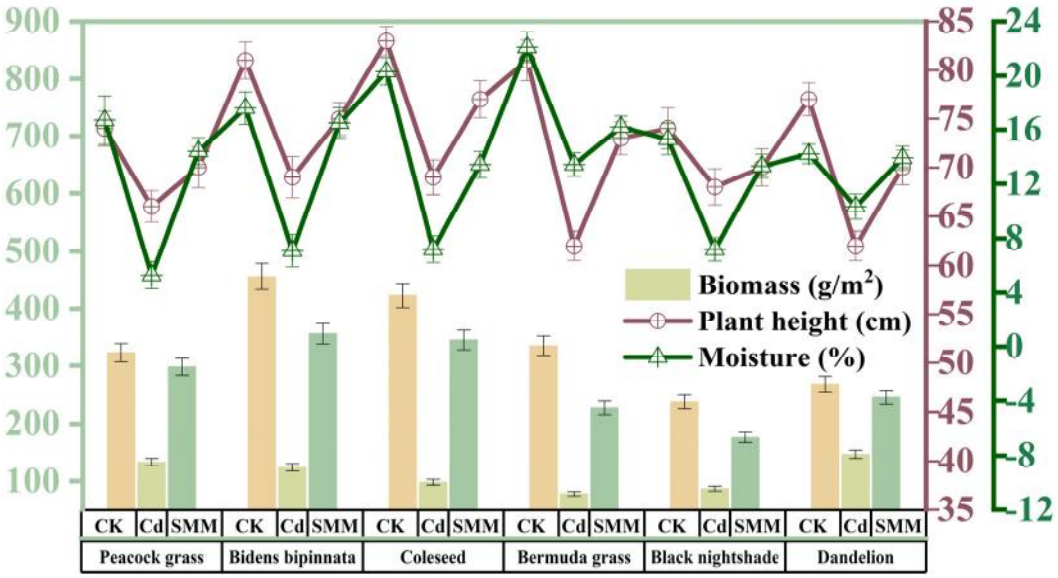

Figure 6. Biomass, plant height, and water content changes in the six selected plants from Figure 5 under natural conditions (CK), Cd ion stress (Cd), and Cd ion stress with the addition of SMC chemical material (SMC).

Figure 7 depicts the heavy metal content in the tissues of six plant species from Figure 6. It can be observed that all six plants exhibit a certain adsorption capacity to Cd. Under Cd stress, plants secrete organic acids, which could chelate with Cd^{2+} in the soil to reduce the toxicity of Cd^{2+}, and as a result, the damage to various enzymes inside the plant via free Cd^{2+} could be reduced [27]. The sequence of Cd content in the plant tissues in plant remediation without the material is *Bidens bipinnata* > *Peacock grass* > *Coleseed* > *Bermuda grass* > *Dandelion* > *Black nightshade*. For material–plant synergistic remediation, the sequence is similar (*Bidens bipinnata* > *Peacock grass* > *Bermuda grass* > *Black nightshade* > *Coleseed* > *Dandelion*). Furthermore, the amount of heavy metals absorbed by the plants obtained from material–plant synergistic remediation is significantly lower than that from plant remediation, similar to the results of previous research by Li [28]. The largest difference in these two different remediation processes is obtained in *Bidens bipinnata* (1.89 mg/kg), while the smallest difference is in *Black nightshade* (1.42 mg/kg). The responsible reason is that during material–plant synergistic remediation, the Cd that is difficult to dissolve from the soil could be released in the form of chelates by various secretions (such as small organic acids) from the plant roots, and the cadmium complex is further solidified by SMC. In this way, the solubility, transferability, and toxicity of Cd in the soil was substantially inhibited, thereby the bioavailability of Cd in the soil was significantly reduced after material–plant synergistic remediation (the extraction rate of Cd by plants was also reduced). Moreover, there is a significant difference in the adsorption amount of Cd by plants under the same material, indicating that the interaction between plants and materials is not entirely consistent, possibly related to plant secretions. Based on the screening results, *Bidens bipinnata* and *Peacock grass* exhibit relatively high extraction amounts under both conditions, while *Coleseed* performs well in single-plant remediation but is not as effective as Bermuda grass after the addition of the material. Combining the results of Figures 6 and 7, three plants were suitable for synergistic remediation (*Bidens bipinnata*, *Peacock grass*, and *Bermuda grass*).

The removal efficiency of available Cd of *Bidens bipinnata* in plant remediation and synergistic remediation is 11% and 77.33%, respectively. *Bermuda grass* activates Cd during plant remediation and passivates Cd during synergistic remediation, with the removal efficiency of available Cd of −30.67% and 38%, respectively. The passivation effects of *Peacock Grass* during both plant and synergistic remediation are not significant, at 2.67% and 11%, respectively, both lower than the removal efficiency of available Cd in soil treated with *Bidens bipinnata*. The available Cd content of heavy metals is related to the physical and chemical properties of the soil, such as the pH value, texture, and dissolved organic matter [29]. The pH of *Bermuda grass* and *Peacock grass* is significantly lower than that of *Bidens bipinnata*, and the activation of Cd in the soil may be influenced by both pH and the action of rhizosphere microorganisms. After the addition of the material, the pH of the three tested plants increases to some extent. This may be attributed to the weak alkalinity of the modified montmorillonite itself. As the pH value increases, the adsorption and fixation of Cd by the soil gradually increase, weakening the activation effect of plant secretions on Cd and reducing the available Cd content [30]. *Bidens bipinnata* exhibits the highest removal rate, possibly due to its high enzyme activity in the soil (i.e., alkaline phosphatase, dehydrogenase, and urease) [31], which reduces oxidative damage to plants under heavy metals.

3.5. Screening of SMC Dosage by Potted Experiments

It can be observed in Figure 9 that the addition of SMC improves the remediation effect of Cd and the extraction efficiency of heavy metals by *Bidens bipinnata* is greatly enhanced. With the SMC dosage increased, the reduction rate of available Cd in the soil first increased and then decreased. When the SMC dosage was 2%, the available Cd removal efficiency of the synergistic remediation was the highest, reaching 77.92%. However, after the SMC dosage exceeded 2%, there was a significant decrease in the reduction rate of available Cd. The reason for this is that excessive SMC changes the pH value of the soil, which affects the solubility of Cd and the absorption capacity of plants. Cd^{2+} is less soluble under alkaline conditions, thereby the extraction rate of Cd by *Bidens bipinnata* was reduced [32,33]. On the other hand, excess SMC may alter the soil structure and aeration, thereby affecting the growth and development of plant roots. If the soil structure becomes too dense, roots may not be able to fully extend and absorb nutrients, leading to restricted plant growth.

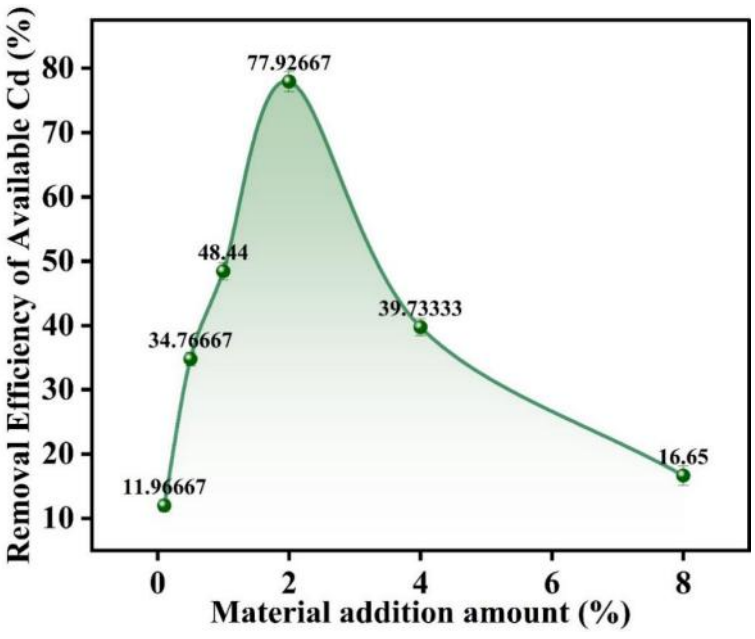

Figure 9. The removal efficiency of available Cd in soil during the synergistic remediation of SMC-*Bidens bipinnata* under different material dosages.

3.6. Application of SMC-Bidens bipinnata Synergistic Remediation Technology in Field

In practical field applications, the efficacy of synergistic remediation technology was evaluated. The optimized plant *Bidens bipinnata*, along with the optimal dosage (2%) of SMC, was implemented in contaminated soils located on the eastern edge of Dongting Lake, Yueyang City. Initial soil assessments revealed that the Cd content in the soil of the appointed field was 1.91 mg/kg, which was categorized as "heavy pollution", while that of the As content was 53.9 mg/kg, which was categorized as "slight pollution". Other heavy metal concentrations were within acceptable limits ("Relatively clean" range).

Therefore, the object of field experiments was focused on the reduction in total Cd and As in field soil (Figure 10). The results in Figure 10 indicated that synergistic remediation exhibited a notable passivation effect on both Cd and As, with the passivation effect increasing gradually over time. After 60 days, the concentration of Cd in remediated soil decreased to 0.29 mg/kg (Table 4), which was lower than the agricultural soil pollution risk screening value of 0.3 mg/kg (stipulated in GB15618-2018 [34]). Similarly, the concentration of As in remediated soil dropped to 28.4 mg/kg, which was also lower than the screening value of 30 (stipulated in GB15618-2018 [34]. For synergistic remediation with an extended period (60–120 days), the variations in the concentration of Cd and As in the soil became relatively minor, possibly attributed to the saturation of coordination between the oxygen-containing functional groups in the passivator with Cd and As ions [35]. In summary, Cd and As in the contaminated soil of the eastern edge of Dongting Lake were effectively inhibited below the screening value for agricultural land risk by the application of synergistic remediation.

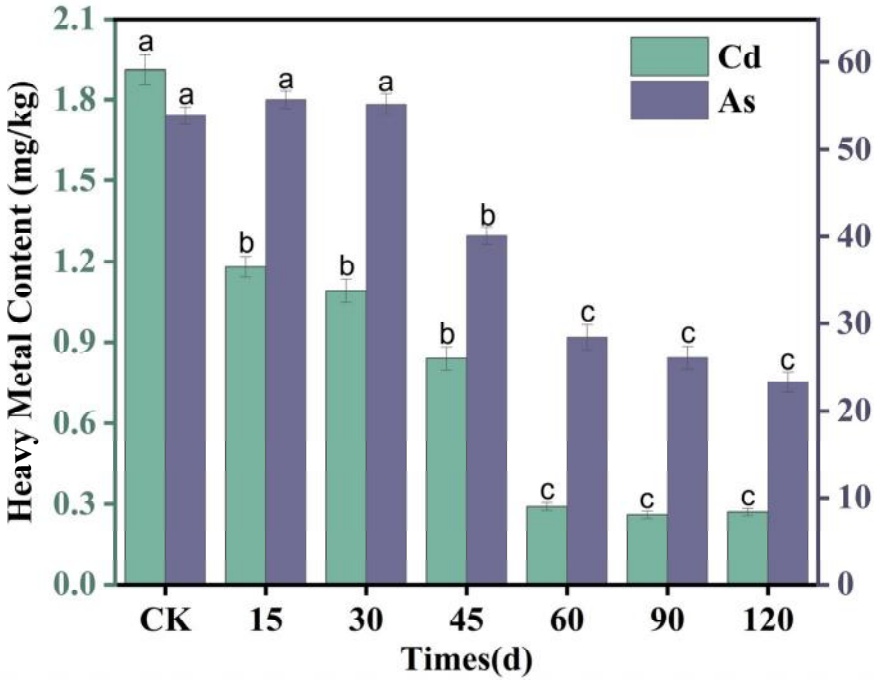

Figure 10. Influence of synergistic remediation on Total Cd and As contents in soil in the field conditions (different letters above the bars in the bar chart indicate significant differences at the $p < 0.05$ level between different treatments. Error bars represent the standard deviation of the mean, $n = 3$).

Table 4. Heavy metal content and pollution level in soil after remediation (mg/kg).

Items	Cd	As
Total heavy metal (mg/kg)	0.29	28.4
Agricultural Soil Risk Screening Standard Value (mg/kg)	0.3	30
Pi value	0.94	0.94
Pollution Level	Relatively clean	Relatively clean

In the process of synergistic remediation with materials and plants, microorganisms play a crucial role in the restoration of soil ecosystems and the remediation of heavy metal pollution. A deeper understanding of the changes in local microbial communities could elucidate the synergistic effects of SMC-*Bidens bipinnata* [36]. Therefore, high-throughput sequencing analysis of microbial DNA (16s V3V4) extracted from the soil was conducted to investigate the changes in microbial population diversity before and after remediation. Figure 11 illustrates the relative abundance of species at the genus level in soil obtained from potting and field experiments before and after synergistic remediation.

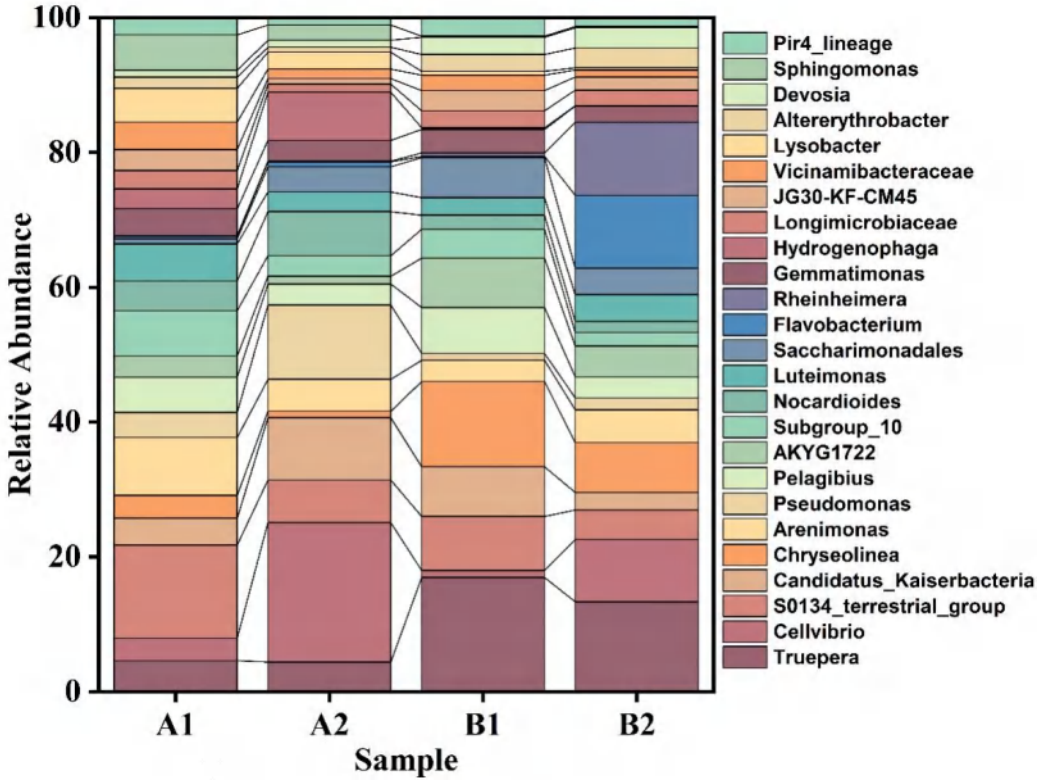

Figure 11. Genus-level species abundance composition stacked bar chart. A1: soil before pot experiment remediation; A2: soil after pot experiment remediation; B1: soil before field experiment remediation; B2: soil after field experiment remediation.

A1 and A2 represent soil samples from the potting experiment. There were significant differences in dominant bacterial communities before and after remediation. In sample A1, the dominant bacterial taxa were Subgroup_10, Arenimonas, and S0134_terrestrial_group. Among these, only Arenimonas exhibited certain environmental remediation capabilities. In sample A2, dominant bacterial taxa included S0134_terrestrial_group, *Nocardioides*, *Hydrogenophaga*, Candidatus_Kaiserbacteria, *Pseudomonas*, and *Bacillus subtilis*. Notably, the relative abundance of Candidatus_Kaiserbacteria increased from 4% to 9%, indicating its role in promoting plant growth and soil nutrient cycling [37,38]. *Bacillus subtilis*, with its relative abundance increasing from 3% to 21%, secretes β-galactosidase, which can be used to assess heavy metal biotoxicity. *Bacillus subtilis* cultured in high-

concentration Cd environments secretes extracellular polymeric substances (EPSs) and cell enzyme proteins, enhancing its resistance to heavy metals [39]. Furthermore, *Bacillus subtilis* produces auxins, promoting plant growth and enhancing the synergistic effects of synergistic remediation.

B1 and B2 represent soil samples from the actual field. Before remediation, the dominant bacterial taxa in B1 included *Saccharimonadales*, *Pelagibius*, AKYG1722, Candidatus_Kaiserbacteria, S0134_terrestrial_group, *Chryseolinea*, and *Truepera*. After remediation, the dominant taxa were *Chryseolinea*, *Cellvibrio*, *Flavobacterium*, *Hafnia alvei*, and *Truepera*. *Flavobacterium* and *Hafnia alvei* were virtually absent in other soils. *Hafnia alvei* contains dipeptidase, conferring Cd resistance [40]. The Devosia genus secretes organic compounds that chelate heavy metals, converting them into more stable organic forms [41]. Overall, the addition of materials enhances the robustness of soil microbial communities and selects for microorganisms with stronger resistance to heavy metals. Through the combined adsorption of materials, plants, and microorganisms, more heavy metal ions in the effective state are chelated.

There are significant differences between the microorganisms in the soil obtained from potting and field experiments, possibly due to the effects of soil composition and properties. The pH value of the potting soil was 6.2, while that of the actual soil was 5.21. The higher acidity of actual soil inhibits bacterial nutrient uptake and reduces bacterial activity. H^+ ions react with extracellular bacterial secretions, competing for heavy metal ion binding sites, reducing microbial adsorption of heavy metals. Additionally, H^+ ions increase the activity of heavy metals, leading to an increase in the effective state of Cd. This may be one of the reasons why the available Cd removal rate of *Bidens bipinnata* is higher than that of other plants. The addition of materials promotes a pH increase, mitigating the effects of H^+ ions on microorganisms, facilitating better synergy between microorganisms and plants, and thereby significantly improving the efficacy of synergistic remediation.

3.7. Changes in Soil BCR Fraction Components

Due to the close relationship between the available content of heavy metals and their distribution and binding states in the soil, sequential extraction experiments were conducted to assess the changes in the forms of Cd in the soil after synergistic remediation. As shown in Figure 12, all six plants facilitated the transformation of oxidizable and reducible forms into residual forms. In CK, the residual form in soil accounted for 40%, which could reach up to 63% after synergistic remediation. The oxidizable and reducible forms decreased to 4% and 5%, respectively, while the weak acid-soluble form remained relatively unchanged. Among all metal components, the residual form was almost impossible to extract from the soil, while the reducible and weak acid-soluble forms were more easily absorbed by plants. All six plants could transform Cd from forms available for plant uptake and utilization into stable residual forms, reducing its activity. Among them, *Bidens bipinnata* transformed the most residual forms, resulting in the lowest bioavailability of Cd in the soil. This may be attributed to the combined effects of its secretions and enzymatic degradation, as well as the cooperative metabolism and degradation of rhizospheric microorganisms.

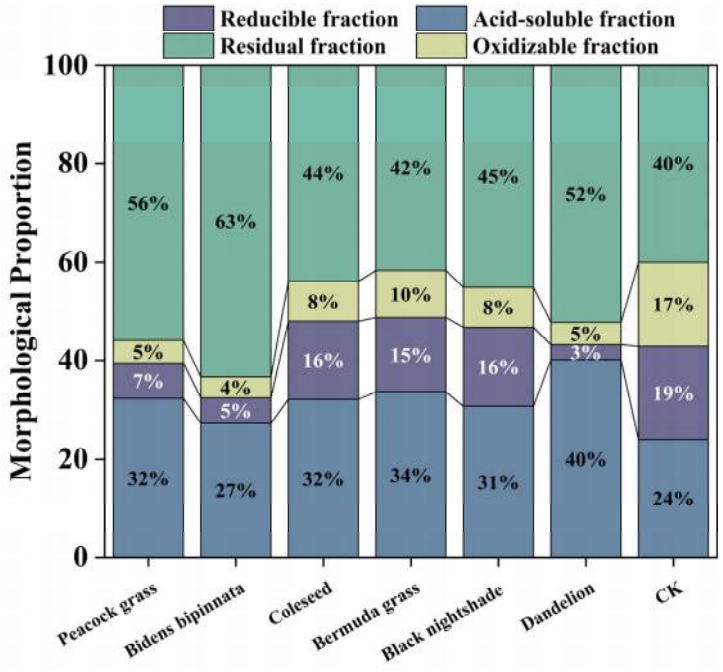

Figure 12. BCR fraction components of Cd in synergistic remediation soil.

3.8. TCLP Toxicity Leaching Experiment

Figure 13 presents the results of the TCLP leaching test for Cd after synergistic remediation with materials and plants. As depicted in Figure 13a, all treatments effectively reduce the migration of Cd, and except for the blank control CK, all values are below the threshold of 1 mg/L set by the US Environmental Protection Agency [42]. When the amount of material added is low, the concentration of Cd decreases with increasing addition, similar to the trend observed in the effective removal rate mentioned earlier. When the material addition reaches 2%, the release of Cd is minimal at 0.229 mg/L, representing an 83% reduction compared to the control group. However, when the material addition exceeds 2%, excessive material may potentially affect plant growth and soil fertility. It could also inhibit the activity and diversity of soil microorganisms, leading to deterioration of the soil ecosystem and a loss of biodiversity, thereby reducing the adsorption of heavy metals by microorganisms and plants and increasing the migration and desorption of heavy metals in the soil. As shown in Figure 13b, Cd toxicity leaching gradually decreases with time, reaching a stable level around 60 days, indicating that the Cd^{2+} adsorbed by the remediation material has reached saturation. Since the remediation material is green and non-polluting, the concentration of TCLP toxicity leaching in the soil changes relatively little over time, indicating that the remediation effect is well-maintained.

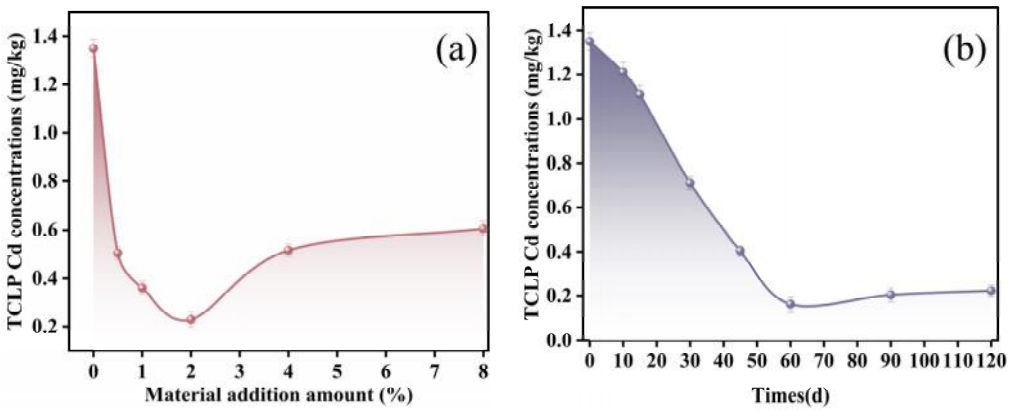

2. Kang, J.W. Removing environmental organic pollutants with bioremediation and phytoremediation. *Biotechnol. Lett.* **2014**, *36*, 1129–1139. https://doi.org/10.1007/s10529-014-1466-9.
3. Cristaldi, A.; Conti, G.O.; Jho, E.H.; Zuccarello, P.; Grasso, A.; Copat, C.; Ferrante, M. Phytoremediation of contaminated soils by heavy metals and PAHs. A brief review. *Environ. Technol. Innov.* **2017**, *8*, 309–326. https://doi.org/10.1016/j.eti.2017.08.002.
4. Katoh, M.; Hashimoto, K.; Sato, T. Lead and Antimony Removal from Contaminated Soil by Phytoremediation Combined with an Immobilization Material. *Clean-Soil Air Water* **2016**, *44*, 1717–1724. https://doi.org/10.1002/clen.201500162.
5. Jain, S.; Tembhurkar, A.R. Growth, remediation, and yield assessment of *Jatropha curcas*, *Millettia pinnata*, and *Helianthus annus* on fly ash amended soil: A comparative study. *Acta Physiol. Plant.* **2023**, *45*, 35. https://doi.org/10.1007/s11738-023-03516-9.
6. Lee, S.H.; Kim, E.Y.; Park, H.; Yun, J.; Kim, J.G. In situ stabilization of arsenic and metal-contaminated agricultural soil using industrial by-products. *Geoderma* **2011**, *161*, 1–7. https://doi.org/10.1016/j.geoderma.2010.11.008.
7. Wang, S.; Chen, N.; Liu, X.; Fu, Y.; Liu, H. Utilization of municipal sludge passivated by coal ash on yellow garden soil. *Fujian J. Agric. Sci.* **2018**, *33*, 1097–1103.
8. Jiang, K.; Xiang, A.H.; Liu, K.; Peng, Q. Potential of montmorillonite and humus-like substances modified montmorillonite for remediation of Pb and Zn-contaminated soils. *Appl. Clay Sci.* **2023**, *234*, 106853. https://doi.org/10.1016/j.clay.2023.106853.
9. Zhao, C.; Yao, J.; Knudsen, T.S.; Liu, J.; Zhu, X.; Ma, B.; Li, H.; Cao, Y.; Liu, B. Performance and mechanisms for Cd(II) and As(III) simultaneous adsorption by goethite-loaded montmorillonite in aqueous solution and soil. *J. Environ. Manag.* **2023**, *330*, 117163. https://doi.org/10.1016/j.jenvman.2022.117163.
10. Yu, K.; Xu, J.; Jiang, X.; Liu, C.; McCall, W.; Lu, J. Stabilization of heavy metals in soil using two organo-bentonites. *Chemosphere* **2017**, *184*, 884–891. https://doi.org/10.1016/j.chemosphere.2017.06.040.
11. Xu, Y.; Liang, X.; Xu, Y.; Qin, X.; Huang, Q.; Wang, L.; Sun, Y. Remediation of Heavy Metal-Polluted Agricultural Soils Using Clay Minerals: A Review. *Pedosphere* **2017**, *27*, 193–204. https://doi.org/10.1016/s1002-0160(17)60310-2.
12. Yang, J.; Yu, K.; Liu, C. Chromium immobilization in soil using quaternary ammonium cations modified montmorillonite: Characterization and mechanism. *J. Hazard. Mater.* **2017**, *321*, 73–80.
13. Fan, J.; Cai, C.; Chi, H.; Reid, B.J.; Coulon, F.; Zhang, Y.; Hou, Y. Remediation of cadmium and lead polluted soil using thiol-modified biochar. *J. Hazard. Mater.* **2020**, *388*, 122037. https://doi.org/10.1016/j.jhazmat.2020.122037.
14. Sarkar, B.; Naidu, R.; Rahman, M.M.; Megharaj, M.; Xi, Y. Organoclays reduce arsenic bioavailability and bioaccessibility in contaminated soils. *J. Soils Sediments* **2012**, *12*, 704–712. https://doi.org/10.1007/s11368-012-0487-z.
15. Liu, X.; Laipan, M.; Zhang, C.; Zhang, M.; Wang, Z.; Yuan, M.; Guo, J. Microbial weathering of montmorillonite and its implication for Cd(II) immobilization. *Chemosphere* **2024**, *349*, 140850. https://doi.org/10.1016/j.chemosphere.2023.140850.
16. Yost, J.L.; Hartemink, A.E. How deep is the soil studied–an analysis of four soil science journals. *Plant Soil* **2020**, *452*, 5–18.
17. El Fadili, H.; Ali, M.B.; Touach, N.; El Mahi, M. Ecotoxicological and pre-remedial risk assessment of heavy metals in municipal solid wastes dumpsite impacted soil in Morocco. *Environ. Nanotechnol. Monit. Manag.* **2022**, *17*, 100640.
18. Yu, G.; Ullah, H.; Lin, H.; Sunahara, G.I.; Zhang, X.; Chen, B.; Yu, H.; Shahab, A.; Liu, L.; Liu, J. Long-term phytoextraction potential and mechanism of *Celosia argentea* on soils with different levels of Cd and Mn co-contamination. *J. Environ. Chem. Eng.* **2024**, *12*, 112125. https://doi.org/10.1016/j.jece.2024.112125.
19. Shi, G.; Hu, J.; Zhang, S.; Ni, G.; Shi, W.; Hu, C.; Zhao, X. The application of exogenous Se improved the remediation efficiency of *Lolium multiflorum Lam* grown in nonylphenol-Cd Co-contaminated soil. *J. Environ. Chem. Eng.* **2022**, *10*, 108962. https://doi.org/10.1016/j.jece.2022.108962.
20. Brunetti, G.; Kodešová, R.; Švecová, H.; Fér, M.; Nikodem, A.; Klement, A.; Grabic, R.; Šimůnek, J. On the use of mechanistic soil–plant uptake models: A comprehensive experimental and numerical analysis on the translocation of carbamazepine in green pea plants. *Environ. Sci. Technol.* **2021**, *55*, 2991–3000.
21. Yao, K.; Cai, J.; Liu, M.; Yu, Y.; Xiong, H.; Tang, S.; Ding, S. Structure and properties of starch/PVA/nano-SiO_2 hybrid films. *Carbohydr. Polym.* **2011**, *86*, 1784–1789. https://doi.org/10.1016/j.carbpol.2011.07.008.
22. Eid, E.M.; Shaltout, K.H.; Moghanm, F.S.; Youssef, M.S.; El-Mohsnawy, E.; Haroun, S.A. Bioaccumulation and translocation of nine heavy metals by *Eichhornia crassipes* in Nile Delta, Egypt: Perspectives for phytoremediation. *Int. J. Phytoremediation* **2019**, *21*, 821–830.
23. Huang, S.; Rao, G.; Ashraf, U.; He, L.; Zhang, Z.; Zhang, H.; Mo, Z.; Pan, S.; Tang, X. Application of inorganic passivators reduced Cd contents in brown rice in oilseed rape-rice rotation under Cd contaminated soil. *Chemosphere* **2020**, *259*, 127404. https://doi.org/10.1016/j.chemosphere.2020.127404.
24. Li, X.Y.; Mu, L.; Zhang, C.; Fu, T.L.; He, T.B. Effect of amendments on bioavailability of cadmium in soil-rice system: A field experiment study. *Environ. Sci. Pollut. Res.* **2023**, *30*, 37659–37668. https://doi.org/10.1007/s11356-022-24875-9.
25. Cheng, J.; Sun, Z.; Yu, Y.; Li, X.; Li, T. Effects of modified carbon black nanoparticles on plant-microbe remediation of petroleum and heavy metal co-contaminated soils. *Int. J. Phytoremediation* **2019**, *21*, 634–642. https://doi.org/10.1080/15226514.2018.1556581.
26. Cheng, J.; Sun, Z.; Li, X.; Yu, Y. Effects of modified nanoscale carbon black on plant growth, root cellular morphogenesis, and microbial community in cadmium-contaminated soil. *Environ. Sci. Pollut. Res.* **2020**, *27*, 18423–18433.
27. Zou, J.; Song, F.; Lu, Y.; Zhuge, Y.; Niu, Y.; Lou, Y.; Pan, H.; Zhang, P.; Pang, L. Phytoremediation potential of wheat intercropped with different densities of *Sedum plumbizincicola* in soil contaminated with cadmium and zinc. *Chemosphere* **2021**, *276*, 130223. https://doi.org/10.1016/j.chemosphere.2021.130223.

28. Li, H.; Liu, Y.; Luo, Z.; Zhou, Y.; Hou, D.; Mao, Q.; Zhi, D.; Zhang, J.; Yang, Y.; Luo, L. Effect of RM-based-passivator for the remediation of two kinds of Cd polluted paddy soils and mechanism of Cd(II) adsorption. *Environ. Technol.* **2021**, *42*, 1623–1633. https://doi.org/10.1080/09593330.2019.1675772.
29. Shrivastava, A.; Ghosh, D.; Dash, A.; Bose, S. Arsenic Contamination in Soil and Sediment in India: Sources, Effects, and Remediation. *Curr. Pollut. Rep.* **2015**, *1*, 35–46. https://doi.org/10.1007/s40726-015-0004-2.
30. Tang, X.; Li, Q.; Wu, M.; Lin, L.; Scholz, M. Review of remediation practices regarding cadmium-enriched farmland soil with particular reference to China. *J. Environ. Manag.* **2016**, *181*, 646–662. https://doi.org/10.1016/j.jenvman.2016.08.043.
31. Shah, V.; Dani, P.; Daverey, A. Phytoremediation of Heavy Metal Contaminated Soil Using *Bidens pilosa*: Effect of Varying Concentrations of Sophorolipids. *Appl. Biochem. Biotechnol.* **2023**, *196*, 2399–2413. https://doi.org/10.1007/s12010-023-04684-7.
32. Zhu, R.; Chen, Q.; Zhou, Q.; Xi, Y.; Zhu, J.; He, H. Adsorbents based on montmorillonite for contaminant removal from water: A review. *Appl. Clay Sci.* **2016**, *123*, 239–258. https://doi.org/10.1016/j.clay.2015.12.024.
33. Fang, L.; Hong, R.; Gao, J.; Gu, C. Degradation of bisphenol A by nano-sized manganese dioxide synthesized using montmorillonite as templates. *Appl. Clay Sci.* **2016**, *132*, 155–160. https://doi.org/10.1016/j.clay.2016.05.028.
34. *GB 15618-2018*; Soil Environmental Quality: Agricultural Land Soil Pollution Risk Control Standards. Ministry of Ecology and Environment of the People's Republic of China: Beijing, China, 2018.
35. Bashir, S.; Ali, U.; Shaaban, M.; Gulshan, A.B.; Iqbal, J.; Khan, S.; Husain, A.; Ahmed, N.; Mehmood, S.; Kamran, M.; et al. Role of sepiolite for cadmium (Cd) polluted soil restoration and spinach growth in wastewater irrigated agricultural soil. *J. Environ. Manag.* **2020**, *258*, 110020. https://doi.org/10.1016/j.jenvman.2019.110020.
36. Xun, W.; Li, W.; Xiong, W.; Ren, Y.; Liu, Y.; Miao, Y.; Xu, Z.; Zhang, N.; Shen, Q.; Zhang, R. Diversity-triggered deterministic bacterial assembly constrains community functions. *Nat. Commun.* **2019**, *10*, 3833.
37. Lei, C.; Lu, T.; Qian, H.; Liu, Y. Machine learning models reveal how biochar amendment affects soil microbial communities. *Biochar* **2023**, *5*, 89. https://doi.org/10.1007/s42773-023-00291-1.
38. Diao, Y.; Zhou, L.; Ji, M.; Wang, X.; Dan, Y.; Sang, W. Immobilization of Cd and Pb in soil facilitated by magnetic biochar: Metal speciation and microbial community evolution. *Environ. Sci. Pollut. Res.* **2022**, *29*, 71871–71881. https://doi.org/10.1007/s11356-022-20750-9.
39. Shi, H.; Fan, Q.; Wang, S.; Zhang, J.; Zhang, G.; Zheng, H.; Zhao, Y.; Chang, S.; Hou, F. *Bacillus subtilis* field spray on alpine meadows promotes digestibility in Tibetan sheep via increasing the nutrient quality of herbage and enhancing rumen bacterial populations. *Anim. Feed Sci. Technol.* **2024**, *310*, 115920. https://doi.org/10.1016/j.anifeedsci.2024.115920.
40. Awolope, O.K.; O'Driscoll, N.H.; Di Salvo, A.; Lamb, A.J. The complete genome sequence of *Hafnia alvei* A23BA; a potential antibiotic-producing rhizobacterium. *BMC Res. Notes* **2021**, *14*, 8. https://doi.org/10.1186/s13104-020-05418-2.
41. Boros-Lajszner, E.; Wyszkowska, J.; Borowik, A.; Kucharski, J. Energetic value of *Elymus elongatus* L. and *Zea mays* L. grown on soil polluted with Ni^{2+}, Co^{2+}, Cd^{2+}, and sensitivity of rhizospheric bacteria to heavy metals. *Energies* **2021**, *14*, 4903.
42. Kede, M.L.F.; Correia, F.V.; Conceição, P.F.; Salles Junior, S.F.; Marques, M.; Moreira, J.C.; Pérez, D.V. Evaluation of mobility, bioavailability and toxicity of Pb and Cd in contaminated soil using TCLP, BCR and earthworms. *Int. J. Environ. Res. Public Health* **2014**, *11*, 11528–11540.

2024年4月 矿 床 地 质 第43卷 第2期
April，2024 MINERAL DEPOSITS 43（2）：289~303

文章编号：0258-7106（2024）02-0289-15 Doi: 10. 16111/j. 0258-7106. 2024. 02. 004

湘南地区东湘桥沉积型锰矿床地球化学特征及成矿机理

廖凤初[1,2]，刘湘华[1,2,3**]，徐军伟[1]，熊伊曲[3]，李 斌[3]，赖健清[3]，骆检兰[1]，陈雨林[1]，罗益周[1]，王 勇[4]

（1 湖南省地球物理地球化学调查所，湖南 长沙 410014；2 广西民族大学建筑工程学院，广西 南宁 530006；3 中南大学地球科学与信息物理学院，湖南 长沙 410083；4 湖南省地质调查所，湖南 长沙 410014）

摘 要 湘南地区广泛发育二叠纪海相沉积型锰矿，为揭示其成矿过程及机理，文章以湖南永州东湘桥锰矿床沉积剖面为研究对象，对其开展主、微量元素和碳-氧同位素分析。结果表明，富锰岩层富Cr、Ni、Co等元素的地球化学特征，其Co/Zn、Mn/Fe、Y/Ho比值和多判别图解共同指示该矿床为热液沉积，表明成矿物质Mn主要来源于海底热液。Mo和U元素富集因子（Mo_{EF}和U_{EF}）、U/Th和V/(V+Ni)比值等沉积氧化还原指标分析结果表明，高品位锰矿石层产于氧化向缺氧转变的背景下，而低品位含锰岩层则主要产于氧化或强烈缺氧环境下。富锰岩层的$\delta^{13}C_{PDB}$（−0.2‰~1.9‰）和$\delta^{18}O_{SOMW}$（18.1‰~23.1‰）与海相碳酸盐岩相似，表明成矿物质的C和O主要来源于海水。基于上述结果，笔者认为东湘桥锰矿床成矿过程受海水CO_3^{2-}浓度和沉积氧化还原条件的双重控制，其成矿过程可以概况为2个阶段： 深水盆地的热液Mn在还原条件下以可溶Mn^{2+}向近岸CO_3^{2-}过饱和的浅水台地迁移； 当沉积环境由氧化向缺氧转变时，锰氧化物在沉积/水界面还原释放Mn^{2+}，显著提高水柱中溶解Mn浓度，促进富锰碳酸盐矿物析出，形成高品位锰矿石。

关键词 二叠纪；孤峰组；沉积型锰矿；地球化学；祁零盆地

中图分类号：P618.32 **文献标志码**：A

(FPDIFNJDBM DIBSBDUFSJTUJDT BOE NFUBMMPHFOJ
TFEJNFOUBSZ NBOHBOFTF EFQPTJU JO TPVUIFS

LIAO FengChu[1,2], LIU XiangHua[1,2,3], XU JunWei[1], XIONG YiQu[3], LI Bin[3], LAI JianQing[3], LUO JianLan[1], CHEN YuLin[1], LUO YiZhou[1] and WANG Yong[4]

（1 Geophysical and Geochemical Survey Institute of Hunan, Changsha 410000, Hunan, China; 2 School of Civil Engineering and Architecture, Guangxi Minzu University, Nanning 530006, Guangxi, China; 3 School of Geosciences and Info-Physics, Central South University, Changsha 410083, Hunan, China; 4 Geological Survey Institute of Hunan Province, Changsha 410014, Hunan, China）

"CTUSBDU

The Permian marine sedimentary manganese deposits are widely developed in the southern Hunan region. In order to reveal the ore-forming processes and mechanisms, this study focuses on the sedimentary profile of the Dongxiangqiao manganese deposit in Yongzhou, Hunan Province. Major and trace elements, as well as carbon-oxygen isotopes, were analyzed. The results indicate that the manganese-rich rock layers enrich in elements such as Cr, Ni, Co. The ratios of Co/Zn, Mn/Fe, and Y/Ho, along with interpretations from multiple discriminant diagrams, collectively indicate that the ore deposit is a hydrothermal deposit, suggesting that the ore-forming materi-

* 本文得到湖南省地质院科研项目（编号：HNGSTP202402）和国家自然科学基金项目（编号：42073001、42372105）联合资助
第一作者简介 廖凤初，男，1969年生，教授级高级工程师，主要从事矿床学研究。Email：171382971@qq.com
** 通讯作者 刘湘华，男，1986年生，讲师/工程师，从事岩石学、矿床学研究。Email：xianghua_geology@163.com
收稿日期 2023-12-17；改回日期 2024-03-15。秦思婷编辑。

al, manganese (Mn), primarily derived from seafloor hydrothermal fluid. The analysis results of sedimentary redox indicators, such as the enrichment factor of Mo and U (Mo_{EF} and U_{EF}), as well as U/Th and V/(V+Ni) ratios, indicate that the layers of high-grade manganese ores were formed in the context of the transition from oxic to anoxic conditions. In contrast, low-grade manganese-bearing rock layers were mainly formed in oxic or strongly anoxic conditions. The $\delta^{13}C_{PDB}$ (−0.2‰~1.9‰) and $\delta^{18}O_{SOMW}$ (18.1‰~23.1‰) values of the manganese-rich rock layers, similar to marine carbonate rocks, suggest that the sources of ore-forming materials C and O are primarily derived from seawater. Based on these results, this study proposes that the ore-forming process of the Dongxiangqiao manganese deposit is controlled by both seawater CO_3^{2-} concentration and sedimentary redox conditions. The ore-forming process can be summarized infollowing two stages: Hydrothermal Mn in deep-water basins migrates towards nearshore CO_3^{2-} supersaturated shallow-water platforms under reducing conditions; When the sedimentary environment transitions from oxic to anoxic conditions, manganese oxides at the sediment/water interface are reduced to release Mn^{2+}, significantly increasing the dissolved Mn concentration in the water column, promoting the precipitation of manganese-rich carbonate minerals, and forming high-grade manganese ores.

, F Z X P SPEErian, Gufeng Formation, sedimentary-type manganese deposit, geochemistry, Qiling basin

锰是一种重要的金属元素,广泛应用于钢铁、化学、建材和新能源等诸多领域,因此,锰矿是中国国民经济建设的战略性关键金属矿产之一(王登红, 2019; 鞠建华等, 2022)。中国锰矿床以海相沉积型和表生型为主(付勇等, 2014)。其中,海相沉积型锰矿在中国锰资源总量中占比超过70%,是中国目前勘探开发重点关注的矿床类型(丛源等, 2018)。二叠纪是华南沉积型锰矿发育的重要时期之一,在贵州、安徽和湖南等地形成了一系列碳酸锰矿床(许卫等, 2005; 杨瑞东等, 2009; 廖凤初等, 2016; 石少华等, 2016; 柏道远等, 2020)。以往的研究显示,华南二叠纪海相沉积型锰矿总体具有品位低,单矿体资源量少,矿床数量多的特点(付勇等, 2014)。然而,在局部地区,该时期的锰资源异常丰富,显示出极好的成矿潜力,如贵州遵义铜锣井等大型锰矿床(刘平等, 2008; 汪洋等, 2020)。从成矿预测与找矿潜力评价方面而言,空间上显著的Mn富集差异强调了对该时期锰矿床成矿机理认识的必要性和重要性。

湖南是二叠纪海相沉积型锰矿资源大省,发育典型矿床包括湘南地区的东湘桥锰矿床和水埠头锰矿床等(刘磊等, 2015; 廖凤初等, 2016)。这些矿床的锰矿石主要产于二叠系孤峰组中(石少华等, 2016),与华南其他地区二叠纪锰矿石层位(孤峰组或茅口组)基本一致(谢建成等, 2006; 刘志臣等, 2019)。尽管这些矿床的锰矿石品位通常相对较低(w(MnO)<10%),但其在近地表风化后形成的氧化锰资源可以达到工业开采标准。湘南地区拥有45个锰矿床和195个找矿远景区,是中国重要的锰矿开采区(姚敬劬等, 1998)。近年来,湘南地区锰矿床的地质勘查发现,这些矿床中局部存在高品位(w(MnO)>20%)的碳酸锰矿石层,表明该地区具有较好的沉积型锰矿资源找矿潜力。然而,以往对该地区锰矿床的研究多聚焦于母岩风化后形成的表生型矿床(张林等, 2015; Deng et al., 2017),很少关注原生沉积型锰矿床的成因。

本文选取湖南永州东湘桥沉积型锰矿床为研究对象,通过系统的元素和同位素地球化学分析,重点解析锰矿成矿物质来源和沉积氧化还原条件,探讨Mn富集机理及主控因素,建立成矿模式,以期为该地区锰矿资源的进一步找矿勘查与开发提供科学建议,同时也为华南地区二叠纪海洋锰循环与成矿过程提供新的认识。

1 地质背景

东湘桥锰矿床位于湖南省永州市西南约40 km处的珠山镇一带,地处华南准地台的桂湘赣褶皱带中的祁零盆地。该地区岩石地层除缺失志留系和新近系外,寒武系—第四系均有发育。其中,古生代滨浅海相碳酸盐岩和硅质碎屑岩在区内广泛出露,中生代—新生代陆相碎屑沉积零星出露(图1a)。受加里东期、印支期和燕山期多期次造山运动影响,区内发育一系列轴向近南北向和北东向的

褶皱和断层(图 1a)。东湘桥锰矿在构造上受北东向向斜控制,该向斜核部由二叠系浅海碳酸盐岩和硅质碎屑岩组成,向两翼过渡到石炭系和泥盆系碳酸盐岩夹碎屑沉积,东西两翼地层基本对称发育(图 1b)。锰矿主要赋存于二叠系小江边组和孤峰组碳酸盐岩中,通常呈层状、似层状及透镜状产出,富锰矿物主要由菱锰矿和锰方解石组成,含少量锰白云石。矿区富锰岩系空间上的厚度变化较大,沿向斜轴线,以向斜中部最厚,南北两端较薄,向斜轴线东侧较西侧薄。此外,随着华南地区在中新世晚期—上新世的快速抬升,富锰岩系在地表经风化作用形成了大量高品位氧化锰矿(图 1b),是该地区锰矿开采的重要矿床类型之一(Deng et al., 2017)。

此次选取的研究剖面(ZK4306)是东湘桥锰矿床 T43 勘探线上的钻孔剖面(图 1b),位于向斜东翼(图 2a)。该钻孔垂直深度为 188 m,自下而上地层依次为二叠系栖霞组、小江边组、孤峰组和龙潭组,以及上覆第四系。其中,栖霞组顶部由灰黑色碳质灰岩组成;小江边组底部为青灰色钙质泥岩,向上变为砖红色和青灰色含铁-锰灰岩,在顶部发育锰矿石层;孤峰组下部为浅灰黑色含锰灰岩,上部为锰矿石层,顶部为钙质泥岩;龙潭组下部为灰黑色泥岩,向上逐渐过渡为粉砂质泥岩(图 2b)。

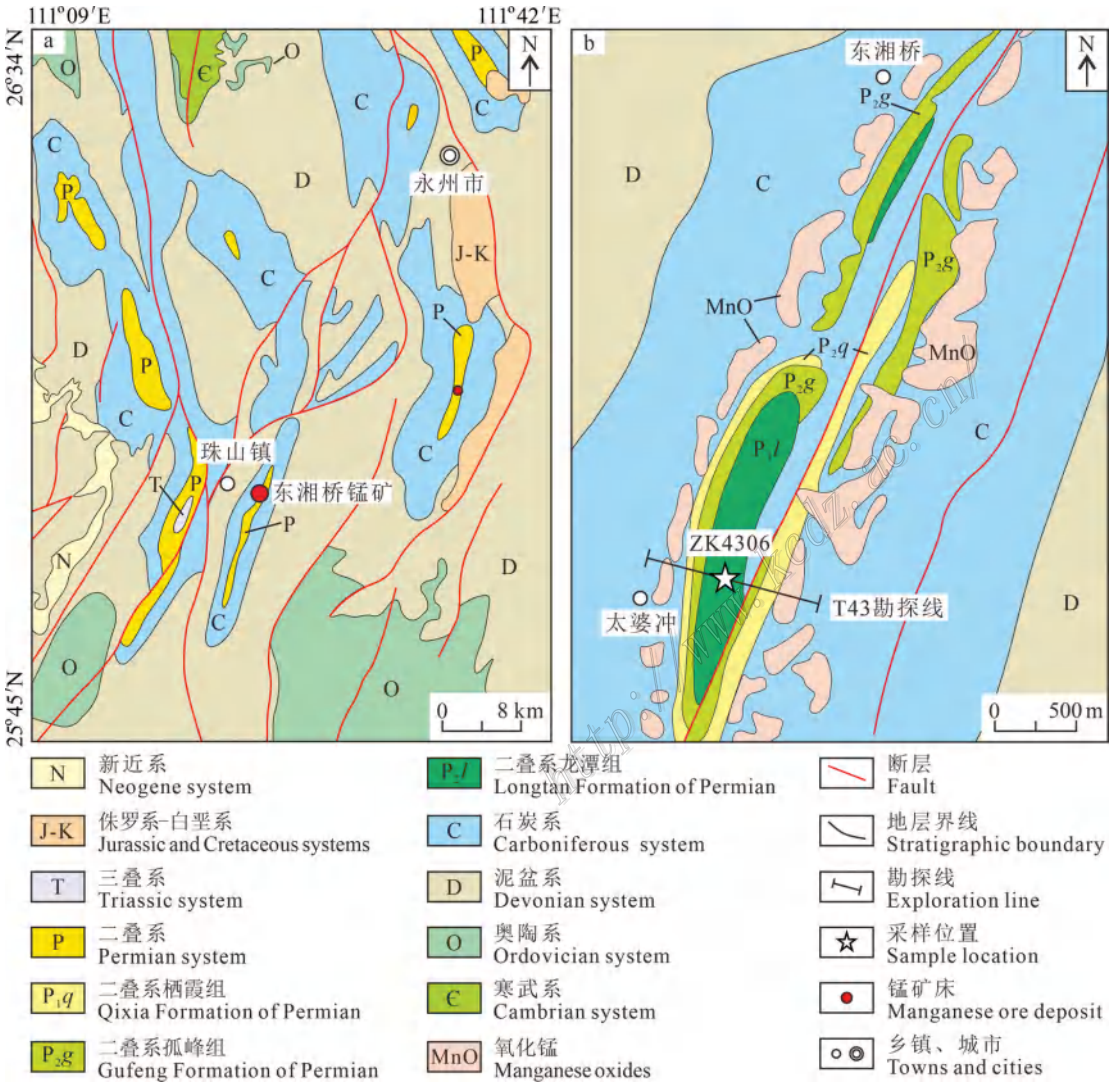

图 1　祁零盆地区域地质图(a)及东湘桥锰矿矿区地质简图(b)(据 Deng et al., 2017 修改)

Fig. 1　Regional geological map of Qiling basin (a) and simplified geologic map (b) of the Dongxiangqiao manganese deposit (modified from Deng et al., 2017)

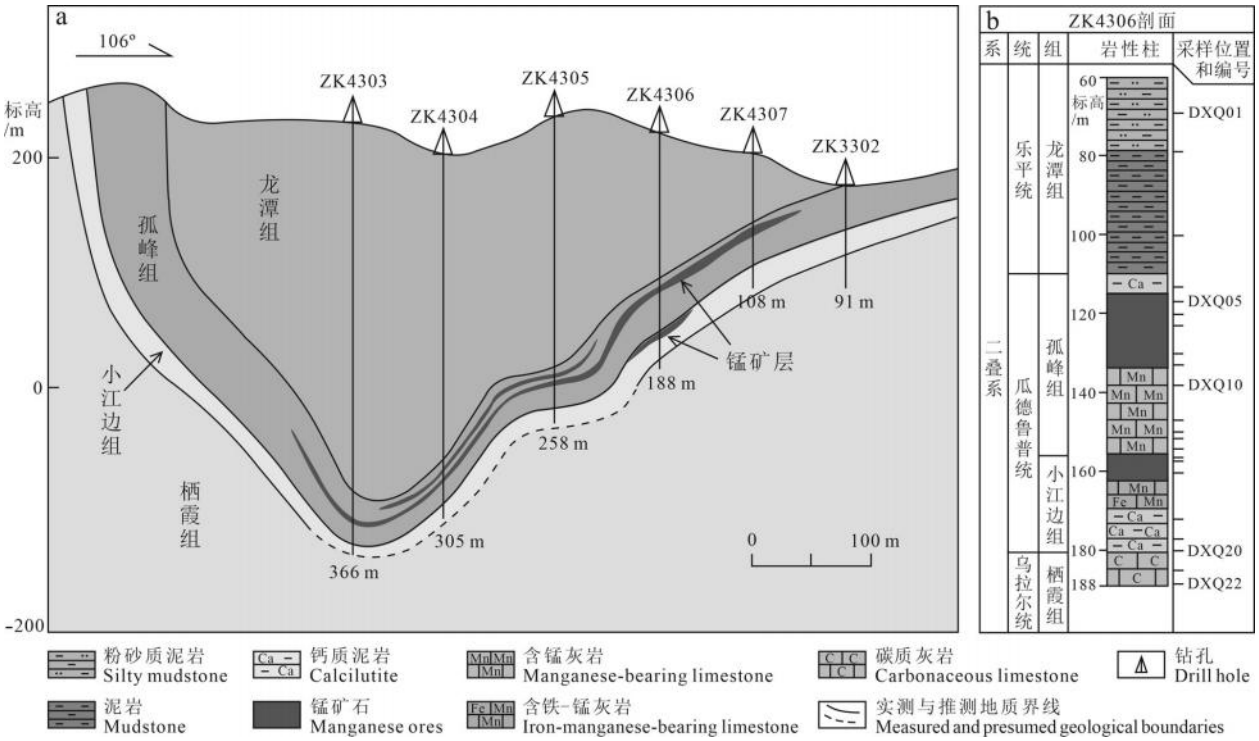

图2 东湘桥矿区T43勘探线剖面地质简图(a)与ZKT4306钻孔岩性柱状图(b)

Fig. 2 Schematic geologic section at T43 exploration line through the Dongxiangqiao ore deposit(a) and lithostratigraphic column of the ZKT4306 borehole(b)

2 样品采集及分析方法

样品采集

为了揭示东湘桥锰矿成矿机理及沉积时期海洋沉积环境变化,本文对研究剖面(ZK4306)连续采集了22件岩石样品用于地球化学分析,并对其中2件样品进行了矿物学分析,样品采集位置详见图2b和表1。

所有样品的采集均选取新鲜、无明显蚀变的岩芯区域,以保证地球化学数据的可靠性。岩石样品在玛瑙坩埚中研磨至粉末(小于200目),用于地球化学分析。

分析方法

(1) 全岩主、微量元素分析

全岩主、微量元素分析在北京安美科创石油科技有限公司完成。

全岩主量元素测定由两部分组成: 采用重量法测定岩石烧失量,本次实验参照国标(GB/T 14506.34-2019)完成; 熔样制片和上机测试,该部分实验参照国标(GB/T 14506.28-2010)完成。主量元素含量测定采用荷兰帕纳科(PANalytical)生产的Axios mAX波长色散X射线荧光光谱仪(XRF)完成。通过重复样和国家标准物质(GSR-4、GSR-5、GSR-6)的测定评估数据的准确性,主量元素分析不确定性小于5%。

微量元素分析首先采用HNO_3+HF混合酸对全岩粉末样品进行消解,制备待测溶液,之后上机测试,该部分实验参照国标(GB/T 14506.30-2010)完成。溶液样品微量元素在赛默飞公司(Thermo Fisher)生产的Element XR高分辨率等离子体质谱仪(HR-ICP-MS)上进行测定。通过重复样和国际标准物质(BHVO-2、BCR-2、RGM-2)的测定评估数据质量,微量元素分析精度优于5%。

(2) 总有机碳含量分析

总有机碳(TOC)含量分析在中南大学有色金属成矿预测与地质环境监测教育部重点实验室的碳硫分析仪(Leco CS744)上完成。称取~100 mg粉末样品置于渗水坩埚中,加入过量稀盐酸以保证完全去除无机碳,淋洗至中性,并干燥,之后上机测试。重复样和有证参考物质(CRM:Leco 502-899,碳=3.19±

表 东湘桥锰矿；，岩石样品主量元素分析结果 *w* # %

5 B C M F. B K P S F M F N F O U T B O B M #Z4U JPDGBSMPSDFLTTVBMNUQTM F T G S P N F S JUMFM%PMOFH;,J B O H R J B P N B O H B O F T F E F Q P T J U

样品号	TOC	MnO	TFe_2O_3	CaO	MgO	K_2O	Na_2O	SiO_2	Al_2O_3	TiO_2	P_2O_5
DXQ01	0.71	0.34	4.16	1.26	1.44	2.39	0.59	69.09	12.62	0.63	0.14
DXQ02	0.98	0.06	5.25	0.73	1.58	3.51	0.78	57.67	21.33	0.73	0.10
DXQ03	1.18	0.21	7.25	0.78	1.36	2.52	0.94	51.60	21.06	0.59	0.10
DXQ04	9.83	2.18	4.14	9.97	1.07	1.75	0.30	44.81	9.51	0.78	0.54
DXQ05	1.75	14.71	3.85	27.11	2.73	0.34	0.13	18.14	2.02	0.14	0.18
DXQ06	0.93	17.01	2.58	31.06	2.76	0.28	0.12	11.00	1.53	0.10	0.26
DXQ07	1.11	14.77	4.16	26.57	2.91	0.39	0.12	18.56	2.16	0.09	0.20
DXQ08	1.89	11.76	7.71	23.32	2.40	0.18	0.08	24.61	1.64	0.07	0.13
DXQ09	2.10	13.94	6.59	20.69	2.10	0.52	0.08	26.90	2.14	0.07	0.11
DXQ10	0.60	8.33	4.93	20.25	2.15	0.29	0.09	37.27	1.34	0.08	0.20
DXQ11	1.21	7.95	6.45	13.91	2.87	0.52	0.10	43.45	3.38	0.16	0.15
DXQ12	0.65	8.49	4.07	16.76	1.30	0.10	0.07	46.60	0.60	0.04	0.28
DXQ13	1.57	4.89	11.02	12.83	2.56	0.40	0.07	43.62	3.70	0.13	0.13
DXQ14	0.32	8.97	8.79	13.50	2.70	0.13	0.09	41.84	2.28	0.08	0.44
DXQ15	0.33	15.39	5.98	18.58	2.55	0.11	0.09	30.16	1.40	0.06	0.58
DXQ16	0.30	14.47	6.02	14.69	2.16	0.35	0.11	36.78	2.64	0.10	0.36
DXQ17	0.26	28.78	3.57	20.13	1.61	0.36	0.08	14.84	1.60	0.08	0.31
DXQ18	0.31	3.85	8.63	7.24	3.29	2.71	0.10	55.32	6.50	0.27	0.14
DXQ19	0.29	1.23	5.27	2.78	1.86	0.60	0.14	77.47	4.15	0.12	0.06
DXQ20	0.35	1.73	1.74	7.62	1.17	0.33	0.09	74.91	2.87	0.10	0.03
DXQ21	6.74	0.25	1.17	17.32	1.27	1.17	0.09	49.95	3.96	0.12	0.48
DXQ22	2.57	0.24	0.94	31.30	7.18	0.64	0.08	19.81	2.61	0.12	0.28

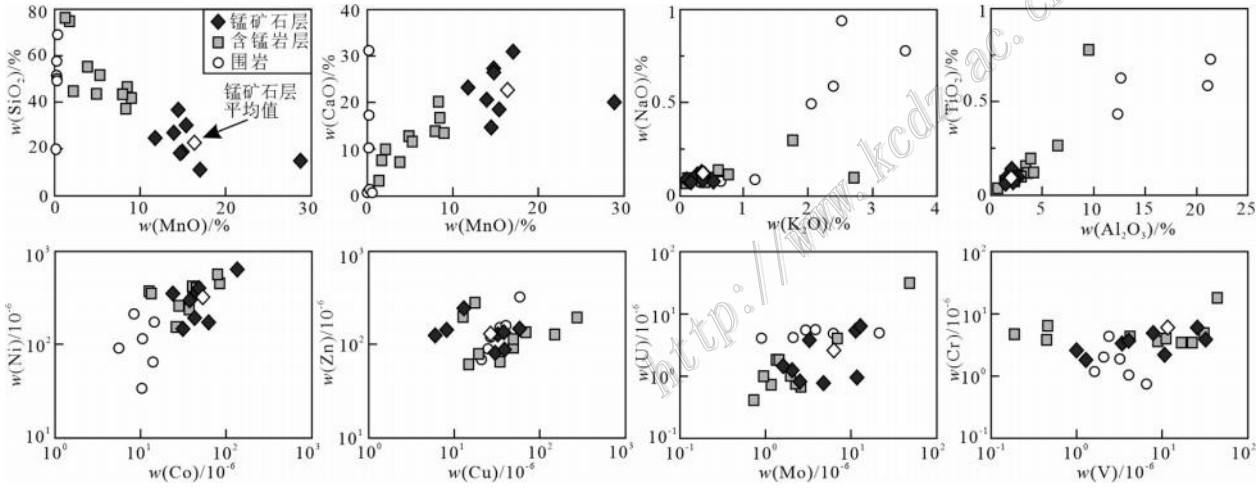

图3 东湘桥锰矿床中富锰岩石与围岩主、微量元素相关性图

Fig. 3 Correlation diagrams of major and trace elements in Mn-rich rocks and country rocks from the Dongxiangqiao manganese deposit

碳-氧同位素特征

对含碳酸盐矿物的19件样品进行碳-氧同位素测试，分析结果列于表3。其中，8件锰矿石层样品的$\delta^{13}C_{PDB}$和$\delta^{18}O_{SOMW}$值变化范围较窄，分别为−0.2‰~1.4‰（平均值0.6‰）和19.2‰~21.8‰（平均值20.7‰）。9件含锰岩层样品的$\delta^{13}C_{PDB}$和$\delta^{18}O_{SOMW}$值分别为0.7‰~1.9‰（平均值1.2‰）和18.1‰~23.1‰（平均值20.3‰）。在围岩样品中，2件

表　东湘桥锰矿;,　岩石样品微量元素 w #　和碳-氧同位素 w # ‰ 分析结果

5BCMF'OBMZUJDBM SFTVMUw #G U,SDBEDSFCFPMOFBNCFED Y ZwH # ‰ JFTUSPQIE TBNQMFT GSPN ESJ

;,　PG UIF %POHYJBOHRJBP NBOHBOFTF EFQPTJU

样品编号	Co	Ni	Cu	Zn	Mo	V	Cr	U	Th	Y	Ho	$(Y/Ho)_{PAAS}$	U_{EF}	Mo_{EF}	V/(V+Ni)	U/Th	$\delta^{13}C_{PDB}$	$\delta^{18}O_{SMOW}$
DXQ01	14.5	175.0	26.5	119.0	0.9	63.3	121.0	4.1	16.3	32.5	1.1	1.1	1.8	0.7	0.3	0.3	*	*
DXQ02	14.0	65.1	24.6	89.0	2.1	118.0	106.0	4.2	20.3	33.9	1.1	1.2	1.1	1.0	0.6	0.2	*	*
DXQ03	10.4	33.8	20.7	68.2	20.9	162.0	76.2	5.0	18.4	30.8	1.1	1.1	1.3	10.0	0.8	0.3	*	*
DXQ04	26.3	161.0	272.0	193.0	46.3	575.0	1811.0	30.9	8.6	74.5	2.0	1.4	17.6	49.3	0.8	3.6	1.1	19.0
DXQ05	42.9	194.0	57.8	146.0	3.2	178.0	486.0	3.8	2.5	39.8	1.0	1.4	10.2	16.1	0.5	1.6	1.0	20.8
DXQ06	31.3	148.0	29.9	80.6	12.6	105.0	352.0	6.4	1.1	35.5	0.9	1.5	22.7	83.4	0.4	5.6	0.7	21.8
DXQ07	62.5	174.0	38.5	87.3	11.1	219.0	229.0	5.4	2.5	46.2	1.1	1.5	13.6	52.0	0.6	2.2	1.4	19.6
DXQ08	23.9	356.0	30.3	127.0	2.0	404.0	606.0	1.3	1.6	29.0	0.8	1.4	4.1	12.5	0.5	0.8	0.7	21.5
DXQ09	37.6	301.0	37.8	134.0	1.6	467.0	392.0	1.5	2.4	35.1	1.0	1.3	3.7	7.5	0.6	0.6	0.4	21.1
DXQ10	28.8	269.0	19.2	79.6	1.2	120.0	437.0	0.7	1.0	29.7	0.8	1.3	3.0	8.7	0.3	0.7	0.9	19.0
DXQ11	44.4	401.0	34.1	64.7	1.4	301.0	364.0	1.8	3.1	37.8	1.0	1.4	2.9	4.3	0.4	0.6	1.1	20.6
DXQ12	37.0	251.0	14.7	60.6	1.0	233.0	397.0	1.0	1.0	29.3	0.8	1.4	9.0	16.0	0.5	1.0	1.9	23.0
DXQ13	42.3	405.0	48.0	114.0	2.0	451.0	504.0	1.1	4.8	40.4	1.2	1.2	1.6	5.3	0.5	0.2	1.8	21.1
DXQ14	84.1	459.0	17.4	278.0	2.5	27.5	388.0	0.7	3.7	39.0	1.0	1.4	1.7	11.1	0.1	0.2	1.0	21.0
DXQ15	46.3	385.0	8.1	142.0	2.5	55.0	184.0	0.8	3.6	55.6	1.5	1.4	3.2	18.0	0.1	0.2	0.3	20.5
DXQ16	135.0	647.0	12.9	242.0	11.5	118.0	375.0	1.0	2.8	57.4	1.5	1.4	2.0	44.1	0.2	0.3	-0.2	20.7
DXQ17	47.9	397.0	6.0	124.0	5.0	46.7	261.0	0.7	1.6	39.0	1.0	1.4	2.5	31.4	0.1	0.5	0.5	19.2
DXQ18	79.6	573.0	12.6	196.0	1.3	368.0	347.0	1.8	6.9	42.0	1.1	1.4	1.5	2.1	0.4	0.3	0.7	18.1
DXQ19	14.0	355.0	149.0	127.0	2.2	27.8	650.0	0.8	2.6	20.5	0.6	1.3	1.0	5.3	0.1	0.3	0.8	19.0
DXQ20	13.3	369.0	48.2	92.8	0.7	15.3	477.0	0.4	1.8	21.5	0.5	1.5	0.8	2.5	0.0	0.2	1.2	18.4
DXQ21	8.4	215.0	58.1	320.0	2.9	75.6	205.0	5.5	1.7	22.2	0.5	1.6	7.6	7.4	0.3	3.2	2.2	19.3
DXQ22	5.6	91.7	40.0	158.0	3.8	82.9	442.0	5.6	1.5	11.9	0.3	1.7	11.6	14.6	0.5	3.7	1.6	22.6

注:*代表无数据;Mo和U元素富集因子(Mo_{EF}和U_{EF})计算公式参考Algeo等(2020),标准物质为平均上地壳,取值来自McLennan, 2001;$(Y/Ho)_{PAAS}$代表相对后太古代澳大利亚页岩(PASS)标准化,PAAS取值来自Taylor等(1985)。

来自于栖霞组灰岩的$\delta^{13}C_{PDB}$和$\delta^{18}O_{SOMW}$值分别为1.6‰~2.2‰(平均值1.9‰)和19.3‰~22.6‰(平均值20.9‰)。总体而言,锰矿石层、含锰灰岩和围岩样品具有相似的碳、氧同位素组成。

富锰矿物特征

对东湘桥矿区孤峰组和小江边组2件锰矿石层样品的原位富锰矿物观测结果显示,二者具有显著的富锰矿物学差异。

其中,孤峰组锰矿石层样品(DXQ06)中富锰矿物主要为锰方解石,多呈椭球状,为岩石的主要矿物组成(图4a),其内部和边缘可见纯方解石组分,锰方解石孔隙间发育草莓状黄铁矿(图4b)。小江边组锰矿石层样品(DXQ17)主要由方解石组成,富锰矿物为菱锰矿,扫描电镜观测视域内未见其他类型含锰矿物,这些菱锰矿以集合体形式嵌于方解石之间(图4c),菱锰矿内部和边缘可见晶型较好、颗粒较大的方解石,以及半自形黄铁矿发育(图4d)。

4　讨　论

成矿物质 .O来源

海水中的Mn主要来源于地表风化经河流输入或海底热液输入(Von Damm, 1990; Post, 1999),在特定的条件下富集于沉积物中形成海相沉积型锰矿床(Maynard, 2010)。在地质历史上,众多海相沉积型锰矿床形成过程中都伴随着强烈的海底热液活动,解释为海底热液活动为成矿输送锰质(谢建成等,2006; 刘平等, 2008; Yu et al., 2016; Zhang et al., 2022)。矿石中元素比例和浓度可用于甄别成矿物质Mn的来源(Nath et al., 1992; Hein et al., 2008)。与热液相关的锰矿床,其Co/Zn比值通常较低,约为0.15,而水成沉积的锰矿的Co/Zn比值通常大于2.5

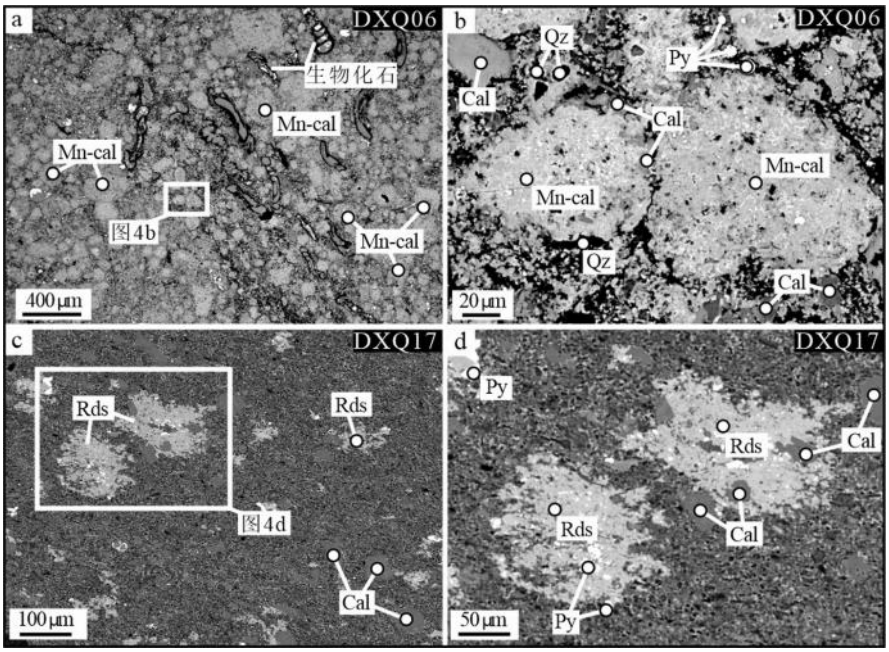

图4 东湘桥锰矿床中富锰矿物扫描电镜照片

a、b. 孤峰组锰矿石层样品；c、d. 小江边组锰矿石层样品

Rds—菱锰矿；Mn-cal—锰方解石；Cal—方解石；Qz—石英；Py—黄铁矿

Fig. 4 Scanning electron microscopy images of manganese rich minerals from the Dongxiangqiao manganese deposit

a, b. The sample of manganese ores from Gufeng Formation; c, d. The sample of manganese ores from Xiaojiangbian Formation

Rds—Rhodochrosite; Mn-cal—Manganocalcite; Cal—Calcite; Qz—Quartz; Py—pyrite

(Toth, 1980)。东湘桥锰矿的Co/Zn比值为0.1~0.7，平均值为0.4(表3)，明显低于水成沉积，接近热液沉积，表明其受到热液流体的影响。通常来说，在与热液相关的海底喷流沉积型锰矿床中，由于铁和锰的分馏，通常会产生高或低的Mn/Fe比值(0.1<Mn/Fe<10)，而在水成沉积的锰矿床中这一比值接近于1(Nicholson et al., 1997)。在东湘桥锰矿床中，含锰岩层和锰矿石层样品的Mn/Fe比值表现出较大的变化范围(0.5~8.9，平均值2.8，表2)，与喷流沉积型矿床的Mn/Fe比值相当。在海底喷溢口附近，由于热液流体中Y的化学行为保守而不与海水完全混合，导致该环境下形成的锰矿具有高的Y/Ho比值(Bau et al., 1999)。东湘桥锰矿样品Y/Ho比值相对于后太古代黑色页岩(PAAS)标准化后为1.2~1.5(表3)，大于1，与典型热液流体输入Mn沉积的锰矿床一致(Bau et al., 2014; Josso et al., 2017)。与热液相关的锰矿通常也会富集Cr、Ni和Co等元素，这主要是由于海底喷发的基性-超基性岩滤出所致(Hein et al., 2008; Sasmaz et al., 2014)。在东湘桥锰矿床中，相对于含锰层上下的围岩，含锰层普遍具有高的Cr、Ni、Co含量(图5)。

在Co-Ni-Zn和Mn-Fe-(Co+Ni+Cu)×10三元图解(图6a、b)中，东湘桥含锰岩层与锰矿石层样品大多落入热液区域。然而，在(Fe+Mn)/4-(Cu+Ni)×15-(Zr+Y+Ce)×100图解(图6c)中，大多样品显示落入热液与水成混合曲线上，这表明热液来源的Mn可能在热液口与海水进行了一定程度的混合后在靠近热液口附近沉积，或是这些热液Mn在海洋中经历了远距离的迁移，在热液口远端沉积。Al/(Al+Fe+Mn)-Fe/Ti的判别图解(图6d)更倾向支持后一种观点，表现为大多数含锰和锰矿石样品位于热液端员与水成端员的混合曲线之下，暗示了热液Mn被大比例海水稀释。综上所述，东湘桥锰矿床具有热液沉积地球化学特征，成矿物质Mn主要来源于海底热液流体。

沉积氧化还原条件

锰是一种多价态金属元素，其在海洋中的循环过程严格受到氧化还原条件的控制。在氧化条件下，Mn^{2+}在热力学上不稳定，易形成高价态的锰氧化物或氢氧化物而缓慢沉淀，导致氧化水体中通常具有低的Mn^{2+}浓度(Calvert et al., 1993; 1996)。在还

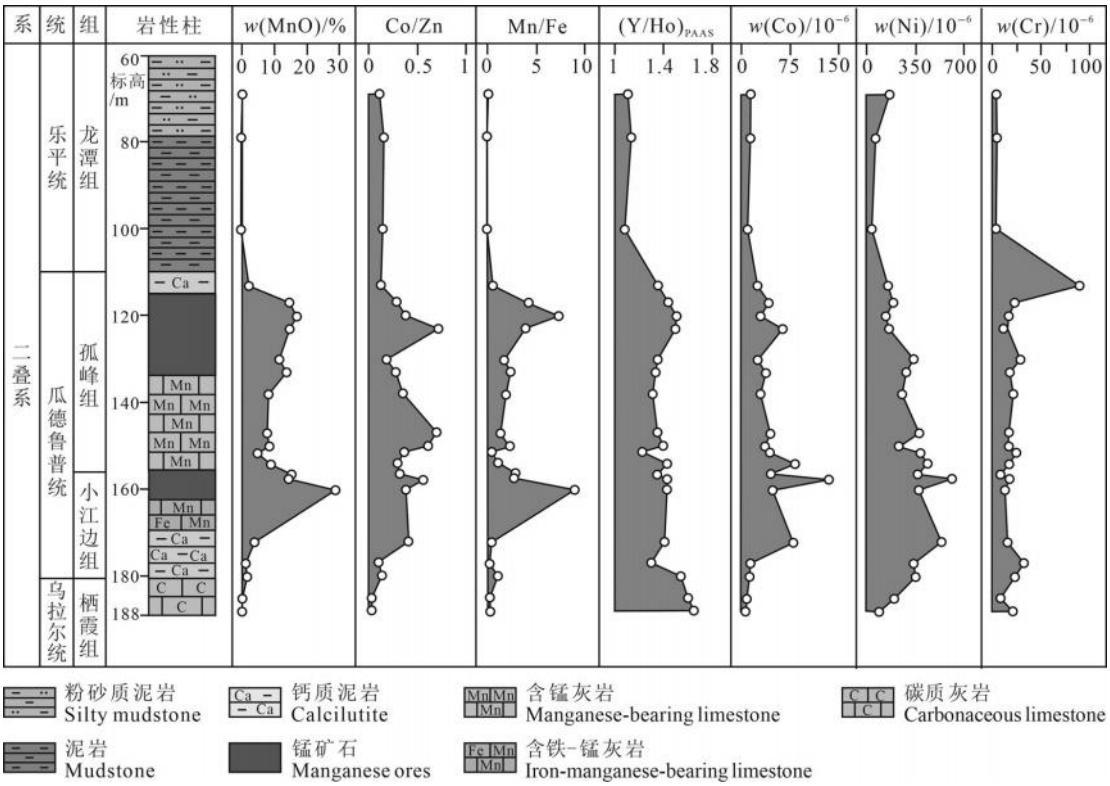

图5　东湘桥锰矿床ZK4306剖面典型元素化学地层

Fig. 5　Chemostratigraphic column of drill hole ZK4306 of the Dongxiangqiao manganese deposit

原条件下,锰氧化物或氢氧化物被还原形成可溶的Mn^{2+},其通常不会与有机质结合,也很难形成稳定的锰硫化物,这使得缺氧水体中通常具有相对高的Mn^{2+}浓度(Glasby et al., 1999; Algeo et al., 2004)。在氧化/还原化学界面附近,锰(氢)氧化物还原溶解释放的Mn^{2+}部分向上扩散进入到上覆氧化水体,部分向下进入到下伏缺氧水体中,使得该化学界面附近具有高的溶解态Mn^{2+}浓度(Calvert et al., 1993)。在氧化还原化学分层的海洋中,当碱度较高时,缺氧水体中溶解态Mn^{2+}可以通过交代碳酸盐矿物形成富锰碳酸盐岩矿物,如锰方解石、锰白云石和菱锰矿等(Pedersen et al., 1982; Morford et al., 2001; Herndon et al., 2018; Wittkop et al., 2020)。因此,识别锰矿的沉积氧化还原条件对于理解海相沉积物中锰富集过程至关重要。

海相沉积物中的氧化还原敏感元素富集因子和元素比值是判别沉积氧化还原条件的重要指标(Algeo et al., 2020)。沉积物的Mo和U元素富集因子(Mo_{EF}和U_{EF})小于10和大于10分别代表其沉积于氧化-次氧化和缺氧条件下(Tribovillard et al., 2012)。U/Th比值小于0.75、0.75~1.25和大于1.25分别代表了氧化、贫氧和次氧化-缺氧沉积环境(Jones et al., 1994)。V/(V+Ni)比值小于0.6、0.6~0.84和大于0.84分别代表氧化-贫氧、次氧化和缺氧沉积环境(Hatch et al., 1992)。在研究剖面中,尽管基于各氧化还原指标阈值所指示的沉积环境有所差异,但它们沉积序列上的变化趋势相对一致,具体表现为栖霞组沉积晚期,水体缺氧程度相对较高;小江边组至孤峰组沉积时期,水体逐渐由氧化向缺氧转变;龙潭组沉积早期,水体则逐渐由缺氧向氧化转变(图7)。

小江边组中下部低品位含锰岩层普遍具有低的TOC含量,以及低的Mo_{EF}、U_{EF}、U/Th和V/(V+Ni)比值,反映其沉积时氧化还原界面位于沉积水界面之下,水柱以含氧为特征。而顶部的高品位锰矿石层具有高Mo_{EF}和Mo/U比值(图7),表明其沉积时存在"Fe-Mn梭效应"(Fe-Mn particulate shuttle effect)(Algeo et al., 2009)。其背后的机制是Fe-Mn(氢)氧化物在沉积/水界面附近被还原,将吸附的Mo释放出来,并被沉积物捕获,造成沉积物中Mo相对于U的额外富集。这一效应的产生需要氧化/还原界面

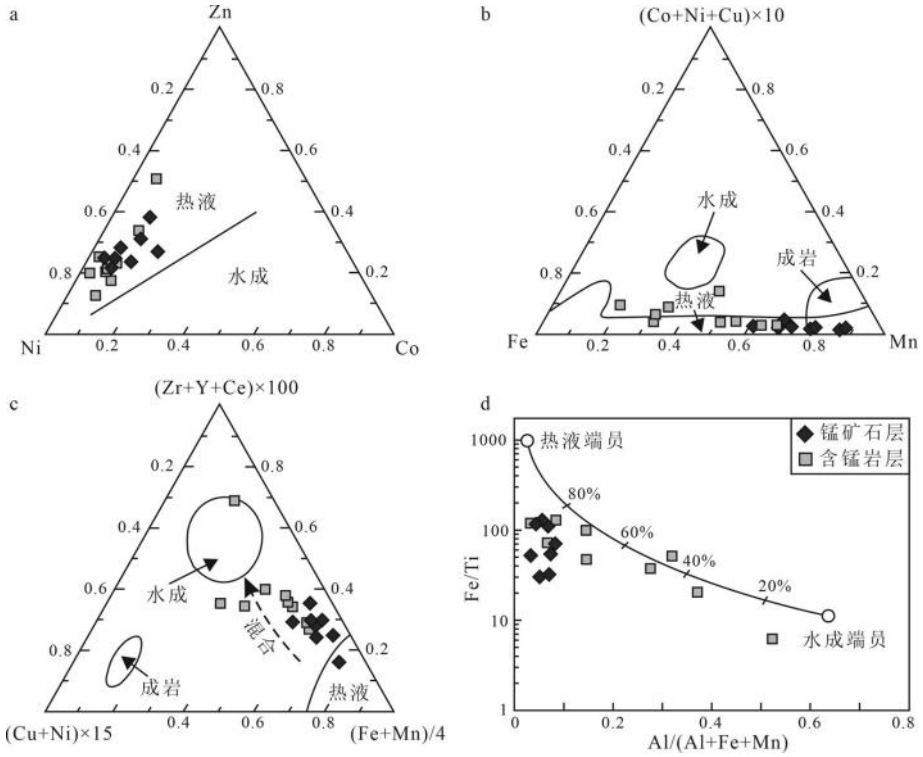

图6 东湘桥锰矿床Mn来源综合判别图

a. Co-Ni-Zn判别图(底图据Choi et al., 1992修改);b. Mn-Fe-(Co+Ni+Cu)×10判别图(底图据Toth, 1980修改);c. (Fe+Mn)/4-(Cu+Ni)×15-(Zr+Y+Ce)×100判别图(底图据Josso et al., 2017修改);d. Al/(Al+Fe+Mn)-Fe/Ti判别图(底图据Marchig et al., 1982修改)

Fig. 6 Comprehensive discriminant diagrams of Mn source of the Dongxiangqiao manganese deposit

a. Ternary discriminant diagram of Co-Ni-Zn (base map modified after Choi et al., 1992); b. Ternary discriminant diagram of Mn-Fe-(Co+Ni+Cu)×10 (base map modified after Toth, 1980); c. Ternary discriminant diagram of (Fe+Mn)/4-(Cu+Ni)×15-(Zr+Y+Ce)×100 (base map modified after Josso et al., 2017); d. Al/(Al+Fe+Mn)-Fe/Ti discriminant diagram (base map modified after Marchig et al., 1982)

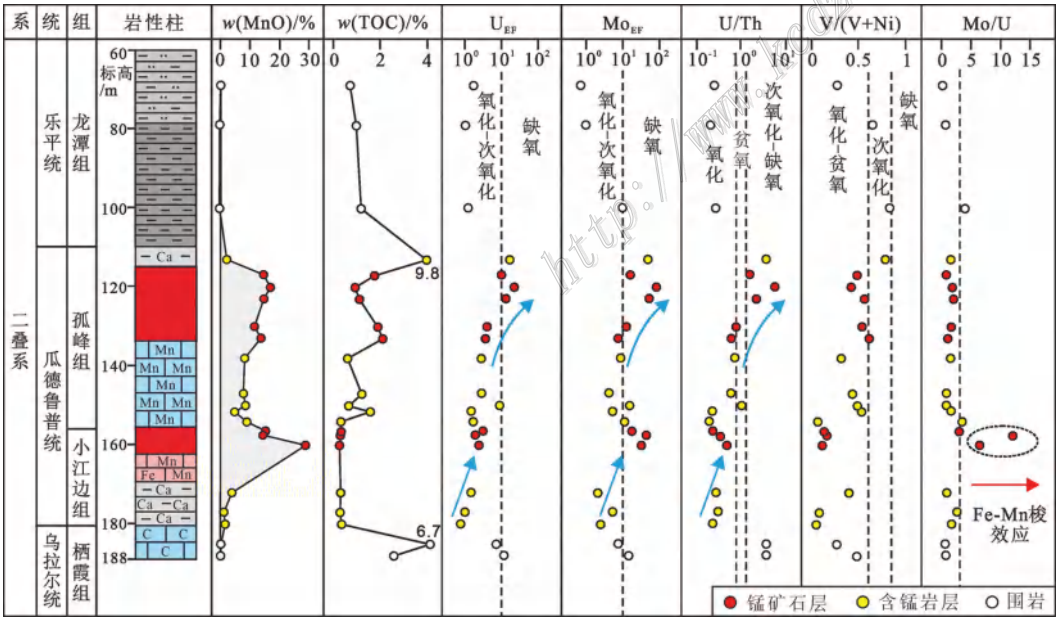

图7 东湘桥锰矿床ZK4306剖面氧化还原化学地层(图例参照图5)

Fig. 7 Redox chemostratigraphy of section ZK4306 in the Dongxiangqiao manganese deposit (legends refer to Fig. 5)

靠近沉积/水界面,通常指示氧化/还原界面在沉积/水界面附近频繁波动的沉积环境(Algeo et al., 2009)。孤峰组下部含锰岩层同样具有相对低的Mo_{EF}、U_{EF}、U/Th和V/(V+Ni)比值,与小江边含锰岩层相似,指示其沉积于氧化环境。相比之下,孤峰组高品位锰矿石层较小江边组具有更高的Mo_{EF}、U_{EF}、U/Th和V/(V+Ni)比值,且不存在"Fe-Mn梭效应"(图7),表明其形成于氧化/还原界面位于略高于沉积/水界面的弱缺氧环境。在孤峰组顶部的含锰钙质泥岩层显示出有机质(TOC=9.8%)和氧化敏感元素高度富集的地球化学特征(图7),这与栖霞组顶部灰岩相似,指示它们沉积于氧化还原界面位于水柱中,且远离沉积/水界面的强缺氧环境。值得强调的是,强缺氧沉积环境下沉积的栖霞组灰岩和孤峰组钙质泥岩均具有低的MnO含量。以上结果表明:在东湘桥锰矿床中,高品位锰矿石均形成氧化向缺氧转变的背景下;而低品位含锰岩层则形成于氧化或强缺氧环境(图7)。

成矿机理与成矿预测

主流观点认为,大多数海相沉积型锰矿最初以锰氧化物形式沉淀,并在早期成岩过程中与有机质反应形成碳酸锰(Maynard, 2010; Yan et al., 2022)。然而,在东湘桥锰矿床中,含锰岩层和锰矿石的无机碳同位素($\delta^{13}C$)和氧同位素($\delta^{18}O$)特征与围岩(栖霞组灰岩)和典型海相碳酸盐岩相似,明显不同于有机质,且不位于有机质降解演化趋势线上(图8),表明这些富锰碳酸盐矿物的C和O主要来自于海水中的

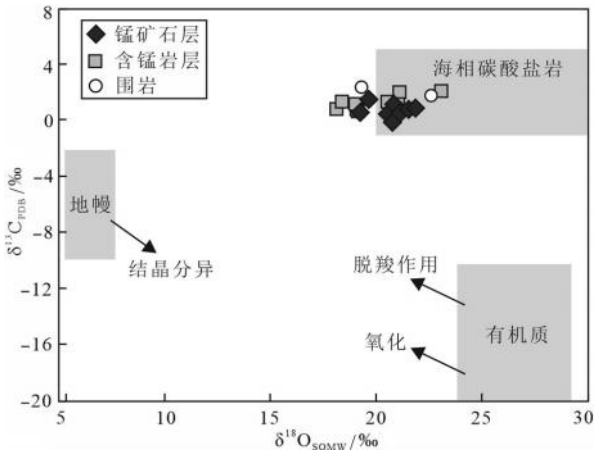

图8　东湘桥锰矿床$\delta^{13}C_{PDB}$-$\delta^{18}O_{SOMW}$同位素组成(底图据Xu et al., 2020修改)

Fig. 8　$\delta^{13}C_{PDB}$-$\delta^{18}O_{SOM}$ composition of the Dongxiangqiao manganese deposit (base map modified after Xu et al., 2020)

HCO_3^{2-}或CO_3^{2-}。虽然富锰碳酸盐矿物在灰岩中的占比较低可能会导致其碳-氧同位素信号被其他碳酸盐矿物均一化,但富锰层位中普遍低的TOC含量难以支持锰氧化物与有机质反应形成碳酸锰的成矿模式,因为该类型锰矿通常与黑色页岩伴生,具有高的TOC含量(余文超等, 2020)。此外,在有机质参与反应形成碳酸锰的矿床中,高品位锰矿石层通常形成于沉积环境由缺氧向氧化转变的阶段,这主要是因为缺氧水体中高度富集的可溶Mn^{2+}在氧化环境下可以形成锰氧化物的沉淀(余文超等, 2020; Dong et al., 2023),这一特征与东湘桥锰矿中高品位锰矿石形成于氧化向缺氧转变的背景相悖。

由于东湘桥锰矿与灰岩伴生,其成矿机理更可能是高碱度(富HCO_3^{2-}和CO_3^{2-})水体环境条件下,受沉积氧化还原条件调控Mn^{2+}浓度的锰富集成矿过程:　在氧化条件下(即氧化/还原界面位于沉积/水界面之下),锰(氢)氧化物的沉淀降低水柱中溶解Mn^{2+}浓度,Ca^{2+}和Mg^{2+}的竞争优势使得Mn^{2+}难以形成菱锰矿,取而代之的生成富锰碳酸盐矿物,如锰方解石和锰白云石(图9a)。尽管锰(氢)氧化物在早期成岩过程中通过还原作用可以释放Mn^{2+}进入沉积物孔隙水中(Glasby et al., 1999),但平衡溶解度计算表明,孔隙水中溶解锰浓度至少要比氧化环境高5个数量级才能形成锰碳酸盐矿物(Pedersen et al., 1982)。这共同导致氧化环境下形成低品位含锰灰岩;　在弱缺氧条件下(即氧化还原界面位于沉积/水界面附近),锰(氢)氧化物在沉积/水界面附近被还原,导致沉积/水界面附近的溶解Mn^{2+}浓度显著提高,形成大量Mn-Ca混合相的富锰碳酸盐矿物(图9b),例如孤峰组锰矿石层中出现的大量锰方解石(图4a、b)。化学界面附近异常高的溶解Mn^{2+}浓度甚至允许纯的菱锰矿沉淀,例如小江边组锰矿石层中观察的菱锰矿富集(图4c、d);　在强缺氧环境下(氧化/还原界面位于水柱中,且远离沉积/水界面),锰(氢)氧化物在氧化/还原界面附近被还原成Mn^{2+}释放回水柱,大部分被重新氧化,仅有少量的Mn^{2+}可以结合到碳酸盐矿物中。即使缺氧水柱中积累了大量溶解Mn^{2+},其浓度也通常很难达到菱锰矿沉淀的水平(Calvert et al., 1993),更多是形成富锰沉积物(Herndon et al., 2018; Wittkop et al., 2020),难以达到矿床级别(图9c)。在这种水体CO_3^{2-}过饱和的模式下,沉积环境由氧化向缺氧转变所导致的锰氧化物在沉积/水界面溶解释放Mn^{2+}是Mn富集成矿的关键性

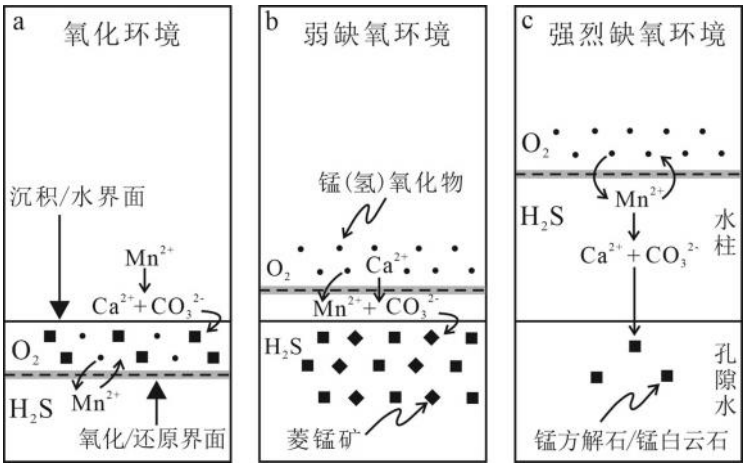

图9 东湘桥锰矿床Mn富集机理示意图

Fig. 9 Schematic diagram of Mn enrichment mechanism of the Dongxiangqiao Manganese deposit

因素。特别是,当氧化/还原界面在沉积水界面附近波动时,Fe-Mn(氢)氧化物还原形成的“Fe-Mn梭效应”会极大地提高Mn^{2+}供给,形成高品位锰矿,这也是东湘桥锰矿床中小江边组顶部Mn高度富集的原因。

从沉积相来说,东湘桥锰矿赋存于灰岩中,表明其沉积于浅水台地环境。正如前文所述,锰矿中的Mn主要来源于海底热液流体,且与海水经历了一定程度的混合,东湘桥锰矿床可能位于热液口远端的位置,这与沉积相所指示浅水台地相沉积一致。因此,东湘桥锰矿床成矿模式可以概况为以下过程:深水盆地的含Mn热液在还原条件下以可溶的Mn^{2+}形式向近岸浅水环境迁移,在CO_3^{2-}过饱和的浅水台地区,沉积氧化还原条件变化影响水柱中溶解Mn^{2+}浓度,进而形成富锰碳酸盐矿物(图10)。在这种成矿模式中,台地环境下海水中过饱和CO_3^{2-}是Mn富集成矿重要前提,沉积氧化还原条件则决定了矿石的品位高低,沉积环境由氧化向缺氧转变的时期是有利成矿期。在成矿预测方面,优质靶区可以进一步向深水盆地探索,这主要基于以下几方面考虑:一是东湘桥锰矿床远离热液口,更浅水区域Mn的供给有限,难以形成高品位矿石;二是东湘桥锰矿中低品位含锰岩层厚度大,且多形成于氧化环境下,由于水体中溶解氧由浅水向深水区存在浓度梯度,理论上在深水区会存在更有利于Mn富集的由氧化向缺氧转变的过渡带;三是深水区域缺氧水体富集Mn^{2+},且具有高的有机碳埋藏,在底水出现氧化时可以形成锰

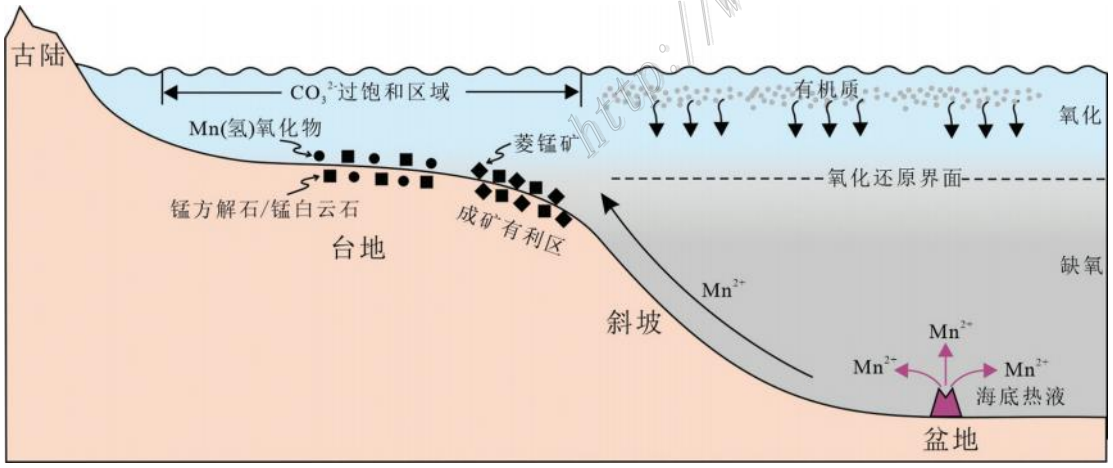

图10 湘南地区东湘桥沉积型锰矿床成矿模式图

Fig. 10 Model for deposition of the Dongxiangqiao sedimentary-type manganese deposit in the southern Hunan region

氧化物沉淀,并在成岩过程中与有机质反应形成碳酸锰,这类海相锰矿床在地质历史时期十分常见,且锰矿石品位和资源储量均较好。

5 结　论

(1) 东湘桥锰矿床的成矿物质 Mn 主要来源于海底热液,Mn^{2+}经历了远距离迁移。在远离深水盆地热液口的浅水台地,海水 CO_3^{2-} 过饱和的地区是 Mn 富集成矿的有利场所。

(2) 沉积氧化还原条件控制了东湘桥矿区锰矿石的品位。在氧化条件下,锰(氢)氧化物的沉积降低水柱中溶解 Mn^{2+}浓度,限制富锰碳酸盐矿物的大量沉淀,形成低品位含锰灰岩。在弱缺氧环境下,锰(氢)氧化物在沉积/水界面附近还原释放 Mn^{2+},提高水柱中溶解 Mn 浓度,导致大量富锰碳酸盐矿物沉淀,甚至生成纯的菱锰矿,形成高品位锰矿石层。在强缺氧环境下,由于氧化/还原界面远离沉积/水界面,水柱中的溶解 Mn^{2+}浓度不足以支持大量富锰碳酸盐矿物沉淀,最终形成富锰沉积物,达不到矿床级别。

(3) 东湘桥锰矿成矿机理不同于成岩过程中锰氧化物与有机质反应形成碳酸锰的典型海相锰矿,是一种成因较为特殊的锰矿床。基于东湘桥锰矿床成矿机理,笔者认为该地区高品位锰矿找矿靶区应向斜坡-盆地深水相沉积进一步探索。

致　谢　感谢湖南省地球物理地球化学调查所伍德娣、李睿在野外调查采样过程中的无私帮助!感谢北京安美科创石油科技有限公司在室内测试分析过程中的大力支持!感谢南方科技大学地球与空间科学系陈晓东博士后在岩矿鉴定方面提供的帮助!最后,感谢两位匿名审稿专家提出的宝贵建议!

3FGFSFODFT

Algeo T J and Maynard J B. 2004. Trace-element behavior and redox facies in core shales of Upper Pennsylvanian Kansas-type cyclothems[J]. Chemical Geology, 206: 289-318.

Algeo T J and Tribovillard N. 2009. Environmental analysis of Paleoceanographic systems based on molybdenum-uranium covariation[J]. Chemical Geology, 268: 211-225.

Algeo T J and Li C. 2020. Redox classification and calibration of redox thresholds in sedimentary systems[J]. Geochimica et Cosmochimica Acta, 287: 8-26.

Bai D Y, Tang F P, Li B, Zeng G Q, Li Y M and Jiang W. 2020. Summary of main mineralization events in Hunan Province[J]. Geology in China, 49(1): 151-180(in Chinese with English abstract).

Bau M and Dulski P. 1999. Comparing yttrium and rare earths in hydrothermal fluids from the Mid-Atlantic Ridge: Implications for Y and REE behaviour during near-vent mixing and for the Y/Ho ratio of Proterozoic seawater[J]. Chemical Geology, 155: 77-90.

Bau M, Schmidt K, Koschinsky A, Hein J, Kuhn T and Usui A. 2014. Discriminating between different genetic types of marine ferromanganese crusts and nodules based on rare earth elements and yttrium[J]. Chemical Geology, 381: 1-9.

Calvert S E and Pedersen T F. 1993. Geochemistry of recent oxic and anoxic sediments: Implications for the geological record[J]. Marine Geology, 113: 67-88.

Calvert S E and Pedersen T F. 1996. Sedimentary geochemistry of manganese: Implications for the environment of formation of manganiferous black shales[J]. Economic Geology, 91: 36-47.

Choi J H and Hariya Y. 1992. Geochemistry and depositional environment of Mn oxide deposits in the Tokoro Belt, northeastern Hokkaido, Japan[J]. Economic Geology, 87: 1265-1274.

Cong Y, Dong Q J, Xiao K Y, Chen J P, Gao Y B and Yin J N. 2018. Characteristics and predicted of Mn resources in China[J]. Earth Science Frontiers, 25(3): 118-137(in Chinese with English abstract).

Coplen T B, Kendall C and Hopple J. 1983. Comparison of stable isotope reference samples[J]. Nature, 302: 236-238.

Deng X D and Li J W. 2017. Mineralogy and $^{40}Ar/^{39}Ar$ geochronology of supergene Mn-oxides in the Dongxiangqiao deposit, Hunan Province, South China[J]. Mineralogy and Petrology, 111: 253-265.

Dong Z G, Peng Z D, Robbins L J, Konhauser K O, Zhang B L, Zhang L C, Li J, Li W J, Zhang L and Wang C L. 2023. Episodic ventilation of euxinic bottom waters triggers the formation of black shale-hosted Mn carbonate deposits[J]. Geochimica et Cosmochimica Acta, 341: 132-149.

Fu Y, Xu Z G, Pei H X and Jiang R. 2014. Study on metallogenic regularity of manganese ore deposits in China[J]. Acta Geologica Sinica, 488(12): 2192-2207(in Chinese with English abstract).

Glasby G P and Schulz H D. 1999. E_h, pH diagrams for Mn, Fe, Co, Ni, Cu and As under seawater conditions: Application of two new types of E_h, pH diagrams to the study of specific problems in marine geochemistry[J]. Aquatic Geochemistry, 5: 227-248.

Hatch J R and Leventhal J S. 1992. Relationship between inferred redox potential of the depositional environment and geochemistry of the Upper Pennsylvanian (Missourian) stark shale member of the Dennis Limestone, Wabaunsee County, Kansas, U. S. A[J]. Chemical Geology, 99: 65-82.

Hein J R, Schulz M S, Dunham R E, Stern R J and Bloomer S H. 2008. Diffuse flow hydrothermal manganese mineralization along the active Mariana and southern Izu-Bonin arc system, western Pacific[J]. Journal of Geophysical Research: Solid Earth, 113: 1-29.

Herndon E M, Havig J R, Singer D M, McCormick M L and Kump L R. 2018. Manganese and iron geochemistry in sediments underlying the redoxstratified Fayetteville Green Lake[J]. Geochimica et Cosmochimica Acta, 231: 50-63.

Jones B and Manning D A. 1994. Comparison of geochemical indices used for the interpretation of Palaeoredox conditions in ancient mudstones[J]. Chemical Geology, 111: 111-129.

Josso P, Pelleter E, Pourret O, Fouquet Y, Etoubleau J, Cheron S and Bollinger C. 2017. A new discrimination scheme for oceanic ferromanganese deposits using high field strength and rare earth elements[J]. Ore Geology Reviews, 87: 3-15.

Ju J H, Zhang Z Z, Pan Z S, Che D and Li H M. 2022. Determination of mineral resources in China's strategic emerging industries and analysis of the demand of the "14th five year plan"[J]. China Mining Magazine, 31(9): 1-11(in Chinese with English abstract).

Liao F C and Luo Y Z. 2016. Genesis and prospecting direction of manganese carbonate ore in Qiling basin[J]. Modern Mining, 564 (4): 146-150(in Chinese).

Liu L, Liu M and Hu X T. 2015. Geological characteristics and metallogenic analysis of Shuibutou Manganese deposit in Hunan Province[J]. Acta Mineralogica Sinica, 35(Supp.): 898-899: 151-180 (in Chinese).

Liu P, Liao Y C, Yin K H, Ye D S, Zhu H, Han Z H and Yang G L. 2008. Hydrothermal sedimentary manganese deposits associated to volcanic activities-Permian manganese deposit in Guizhou[J]. Geology in China, 35(5): 992-1006(in Chinese with English abstract).

Liu Z C, Zhou Q, Yan J X, Wang Y, Chen D, Zhong Y L and Qin X J. 2019. Structure of Zunyi rift basin in Guizhou Province during the Permian and its controlling on manganese deposits[J]. Journal of Palaeogeography(Chinese Edition), 21(3): 517-526(in Chinese with English abstract).

Marchig V, Gundlach H, Möller P and Schley F. 1982. Some geochemical indicators for discrimination between diagenetic and hydrothermal metalliferous sediments[J]. Marine Geology, 50: 241-256.

Maynard J B. 2010. The chemistry of manganese ores through time: A signal of increasing diversity of Earth-surface environments[J]. Economic Geology, 105: 535-552.

McLennan S M. 2001. Relationships between the trace element composition of sedimentary rocks and upper continental crust[J]. Geochemistry, Geophysics, Geosystems, 2: 1-24.

Morford J L, Russell A D and Emerson S. 2001. Trace metal evidence for changes in the redox environment associated with the transition from terrigenous clay to diatomaceous sediments, Saanich Inlet, BC[J]. Marine Geology, 174: 355-369.

Nath B N, Balaram V, Sudhakar M and Plüger W L. 1992. Rare earth element geochemistry of ferromanganese deposits from the Indian Ocean[J]. Marine Chemistry, 38:185-208.

Nicholson K, Nayak V K and Nanda J K. 1997. Manganese ores of the Ghoriajhor-Monmunda area, Sundergarh district, Orissa, India: Geochemical evidence for a mixed Mn source[J]. Geological Society London Special Publications, 119:117-121.

Pedersen T F and Price N B. 1982. The geochemistry of manganese carbonate in Panama Basin sediments[J]. Geochimica et Cosmochimica Acta, 46: 59-68.

Post J E. 1999. Manganese oxide minerals: Crystal structures and economic and environmental significance[J]. Proceedings of the National Academy of Sciences, 96: 3447-3454.

Sasmaz A, Türkyilmaz B, Öztürk N, Yavuz F and Kumral M. 2014. Geology and geochemistry of Middle Eocene Maden complex ferromanganese deposits from the Elazığ - Malatya region, eastern Turkey[J]. Ore Geology Reviews, 56: 352-372.

Shi S H, Tang F P, Luo X Y and Chen J F. 2016. Geological environment and mineralization of sedimentary manganese deposit in Hunan Province[J]. Geology and Exploration, 52(2): 209-219(in Chinese with English abstract).

Taylor S R and Mclennan S M. 1985. The continental crust: Its composition and evolution: An examination of the geochemical record preserved in sedimentary rocks[M]. Oxford: Blackwell Scientific Publishing. 1-312.

Toth J R. 1980. Deposition of submarine crusts rich in manganese and iron[J]. Geological Society of America Bulletin, 91: 44-54.

Tribovillard N, Algeo T J, Baudin F and Riboulleau A. 2012. Analysis of marine environmental conditions based on molybdenum-uranium covariation-applications to Mesozoic paleoceanography[J]. Chemical Geology, 324: 46-58.

Von Damm K L. 1990. Seafloor hydrothermal activity: Black smoker chemistry and chimneys[J]. Annual Review of Earth and Planetary Sciences, 18: 173-204.

Wang D H. 2019. Study on critical mineral resources: Significance of research, determination of types, attributes of resources, progress of prospecting, problems of utilization, and direction of exploitation[J]. Acta Geologica Sinica, 93(6): 1189-1209(in Chinese with English abstract).

Wang Y, Liu Z C, Chen D, Xiao L and Xiao L. 2020. Characteristics of metallogenic formation, basin prototype and manganese facies belt of the Permian Maokou Formation in Zunyi area, Guizhou Province[J]. Journal of Palaeogeography, 22(5): 989-1000(in Chinese with English abstract).

Wittkop C, Swanner E D, Grengs A, Lambrecht N and Katsev S. 2020. Evaluating a primary carbonate pathway for manganese enrichments in reducing environments[J]. Earth and Planetary Science Letters, 538: 116-201.

Xu H, Gao J, Yang R, Du L J, Liu Z, Chen J, Feng K and Yang G. 2020. Genesis for rare earth elements enrichment in the Permian manganese deposits in Zunyi, Guizhou Province, SW China[J]. Acta Geologica Sinica, 94: 90-102.

Xu J C, Du J G, Xu W and Yang X Y. 2006. The geological and geochemical characteristics of manganese-bearing sequences of Guichi, Anhui Province, East China[J]. Geological Review, 52(3): 396-408(in Chinese with English abstract).

Xu W, Yue S C, Du J G, Wu L B, Sun C Y, Wang Y S and Tao Q Y.

2005. Stable isotope characteristics of the manganese-bearing rock series of the Permian Gufeng Formation in the Guichi area, Anhui, China[J]. Geological Bulletin of China, 24(8): 778-782(in Chinese with English abstract).

Yan H, Pi D H, Jiang S Y, Mao J W, Xu L G, Yang X Q, Hao W D, Mänd K, Li L, Konhauser K O and Robbins L J. 2022. Mineral paragenesis in Paleozoic manganese ore deposits: Depositional versus post-depositional formation processes[J]. Geochimica et Cosmochimica Acta, 325: 65-86.

Yang R D, Cheng M L and Wei H R. 2009. Geochemical characteristics and origin of a manganese deposit in the Middle Permian Maokou Formation in Shuicheng, Guizhou, China[J]. Geotectonica et Metallogenia, 33(4): 613-619(in Chinese with English abstract).

Yao J Q, Su C G and Peng S G. 1998. The paleo-structural manganese basin and manganese ore prospecting in central and southern Hunan[M]. Beijing: Metallurgical Industry Press. 193-203(in Chinese).

Yu W C, Algeo T J, Du Y S, Maynard B, Guo H, Zhou Q, Peng T, Wang P and Yuan L J. 2016. Genesis of Cryogenian Datangpo manganese deposit: Hydrothermal influence and episodic post-glacial ventilation of Nanhua Basin, South China[J]. Palaeogeography, Palaeoclimatology, Palaeoecology, 459: 321-337.

Yu W C, Du Y S, Zhou Q, Wang P, Qi L, Xu Y, Jin S, Pan W, Yuan L J, Xie X F and Yang B N. 2020. Coupling between metallogenesis of the Cryogenian Datangpo-type manganese deposit in South China and major geological events[J]. Journal of Palaeogeography (Chinese Edition), 22(5): 855-871(in Chinese with English abstract).

Zhang B L, Lü Z C, Dong Z G, Zhang X, Yu X F, Li Y S, Zhen S M and Wang C L. 2022. Source characteristics of the Carboniferous Ortokarnash Manganese deposit in the western Kunlun Mountains[J]. Minerals, 12: 1-24.

Zhang L, Peng Y and Xing X D. 2015. Geological and geochemical characteristics and geological implication of Shuibutou manganese deposit, Qiyang-Lingling basin[J]. Land & Resources Herald, 12(1): 9-14(in Chinese with English abstract).

附中文参考文献

柏道远, 唐分配, 李彬, 曾广乾, 李银敏, 姜文. 2020. 湖南省成矿地质事件纲要[J]. 中国地质, 49(1): 151-180.

丛源, 董庆吉, 肖克炎, 陈建平, 高永宝, 阴江宁. 2018. 中国锰矿资源特征及潜力预测[J]. 地学前缘, 25(3):118-137.

付勇, 徐志刚, 裴浩翔, 江冉. 2014. 中国锰矿成矿规律初探[J]. 地质学报, 88(12): 2192-2207.

鞠建华, 张照志, 潘昭帅, 车东, 李厚民. 2022. 我国战略性新兴产业矿产厘定与“十四五”需求分析[J]. 中国矿业, 31(9): 1-11.

廖凤初, 罗益周. 2016. 祁零盆地碳酸锰矿成因及找矿方向[J]. 现代矿业, 564(4): 146-150.

刘磊, 刘明, 胡雪涛. 2015. 湖南水埠头锰矿地质特征及成矿分析[J]. 矿物学报, 35(增): 898-899.

刘平, 廖友常, 殷科华, 叶德书, 朱华, 韩忠华, 杨光龙. 2008. 与火山活动有关的热水沉积锰矿——以贵州二叠纪锰矿为例[J]. 中国地质, 35(5): 992-1006.

刘志臣, 周琦, 颜佳新, 汪洋, 陈登, 钟月丽, 秦先进. 2019. 二叠纪贵州遵义次级裂谷盆地结构及其对锰矿的控制作用[J]. 古地理学报, 21(3): 517-526.

石少华, 唐分配, 罗小亚, 陈剑锋. 2016. 湖南省沉积型锰矿地质环境及成矿作用[J]. 地质与勘探, 52(2): 209-219.

汪洋, 刘志臣, 陈登, 肖林, 肖亮. 2020. 贵州遵义二叠系茅口组锰矿成矿建造、盆地原型及锰矿相带特征[J]. 古地理学报, 22(5): 989-1000.

王登红, 2019. 关键矿产的研究意义、矿种厘定、资源属性、找矿进展、存在问题及主攻方向[J]. 地质学报, 93(6): 1189-1209.

谢建成, 杜建国, 许卫, 杨晓勇. 2006. 安徽贵池地区含锰岩系地质地球化学特征[J]. 地质论评, 52(3): 396-408.

许卫, 岳书仓, 杜建国, 吴礼彬, 孙乘云, 王有生, 陶启云. 2005. 安徽贵池地区二叠纪孤峰组含锰岩系稳定同位素特征[J]. 地质通报, 24(8): 778-782.

杨瑞东, 程玛莉, 魏怀瑞. 2009. 贵州水城二叠系茅口组含锰岩系地质地球化学特征与锰矿成因分析[J]. 大地构造与成矿学, 33(4): 613-619.

姚敬劬, 苏长国, 彭三国. 1998. 湘中湘南古构造成锰盆地及锰矿找矿[M]. 北京:冶金工业出版社. 193-203.

余文超, 杜远生, 周琦, 王萍, 齐靓, 徐源, 靳松, 潘文, 袁良军, 谢小峰, 杨炳南. 2020. 华南成冰纪“大塘坡式”锰矿沉积成矿作用与重大地质事件的耦合关系[J]. 古地理学报, 22(5): 855-871.

张林, 彭昱, 邢旭东. 2015. 祁零盆地水埠头锰矿床的地质地球化学特征及意义[J]. 国土资源导刊, 12(1): 9-14.

煤田地质与勘探
Coal Geology & Exploration

doi: 10.12363/issn.1001-1986.23.10.0631

湖南省热水圩地热田干热岩形成的热源机制与成因模式

杜　江[1,2]，蔡宁波[1,2,3]，张保建[4,*]，王克营[1,2]，何立宏[1]，廖凤初[1]

(1. 湖南省地球物理地球化学调查所，湖南 长沙 410014；2. 湖南省地质新能源勘探开发工程技术研究中心，湖南 长沙 410014；3. 中国地质大学(武汉) 高等研究院，湖北 武汉 430074；4. 中国地质科学院，北京 100037)

摘要：湖南省热水圩地热田90℃以上的高温温泉指示该地热田具备良好的地热地质条件，是潜在的干热岩勘查有利地段。为合理评价热水圩干热岩的储层温度与勘查开发前景，对汝城地区热水圩地热田的深部地质构造、地球化学和重、磁、电、震地球物理特征、地温场特征等进行综合分析，自深至浅揭示热水圩地热田深部热结构，探讨干热岩形成的热源机制与地球动力学过程。结果表明：(1) 利用 SiO_2 地热温标估算的热水圩地热田深部热储温度为 79.4~143.9℃；(2) 热水圩附近中棚岩体、鱼王岩体等花岗岩体平均生热率为 7.07~8.44 μW/m^3，明显大于中国大陆主要地质构造单元的地壳平均生热率；(3) 重、磁特征反映出热水圩地区岩石圈厚度相对较薄，大地电磁与地震波速解释的区域内壳内高导低速体与深大断裂带相吻合，指示这些深大断裂有可能构成深部热物质上侵的通道。在此基础上，总结归纳了湖南省热水圩地热田干热岩的成因模式：太平洋板块俯冲与回撤，导致板块前缘形成强烈的热扰动，造成软流圈的隆起和幔源热物质的上侵，形成相对较高的幔源热源；生热率较高的花岗岩体与铀矿体放射性产热形成了良好的地壳热源；深大断裂构成深部热物质上侵的通道，同时为浅部干热岩的形成提供重要热源。有利的热源条件及沿深大断裂的深部热物质上侵，使湖南省东南部形成以热水圩周边岩体为代表的干热岩有利靶区。根据综合确定的地温梯度推算，热水圩地热田呈隐伏状态的、致密的、裂隙不发育的埋深在 4 000~6 000 m 的花岗岩体温度可达 176.80~256.60℃，是良好的、近期可勘查开发的干热岩体。

关　键　词：干热岩；地球化学；重、磁、电、震联合；热源机制；成因模式；热水圩

中图分类号：P542+.5；P545　　**文献标志码：**A

Heat source-related mechanisms and genetic modes for the formation of hot dry rocks in the Reshuiwei geothermal field, Hunan Province

DU Jiang[1,2], CAI Ningbo[1,2,3], ZHANG Baojian[4,*], WANG Keying[1,2], HE Lihong[1], LIAO Fengchu[1]

(1. *Geophysical and Geochemical Survey Institute of Hunan*, *Changsha* 410014, *China*; 2. *Hunan Geological New Energy Exploration and Development Engineering Technology Research Center*, *Changsha* 410014, *China*; 3. *Institute of Advanced Studies*, *China University of Geosciences*, *Wuhan* 430074, *China*; 4. *Chinese Academy of Geological Sciences*, *Beijing* 100037, *China*)

Abstract: Thermal springs with temperatures exceeding 90°C indicate that the Reshuiwei geothermal field in Hainan Province enjoys sound geothermal geological conditions, making this geothermal field a potential favorable area for hot dry rock (HDR) exploration. To carry out a reasonable evaluation of the geothermal reservoir and prospects for exploration and exploitation of HDRs in the Reshuiwei geothermal field in the Rucheng area, this study comprehensively analyzed the deep geological structures, geochemical characteristics, geophysical characteristics including gravity, magnetic, electrical, and seismic properties, and geothermal field characteristics of the geothermal field. Furthermore, it revealed the deep thermal structures of the geothermal field from deep to shallow and explored the heat source-related mechanisms and geodynamic process for the formation of HDRs in the the geothermal field. Primary results are as follows: (1) The Reshuiwei geothermal field exhibits deep reservoir temperatures ranging from 79.4 to 143.9°C, as estimated using a silica geothermometer; (2) The Zhongpeng and Yuwang granite plutons near the Reshuiwei area display average heat production rates between 7.07 and 8.44 μW/m^3, which are significantly higher than the average heat production rates of the crust in the major geological units in Chinese continent; (3) The gravity and magnetic characteristics reveal relatively thin lithosphere in the Reshuiwei area. Furthermore, the interpretations of the magnetotelluric sounding and seismic wave velocities reveal that the crust hosts geobodies with high conductivity and low velocity, which coincide with deep-seated fault zones. This indicates that these faults might serve as pathways for the upward intrusion of deep thermal materials. Based on these results, this study summarized the genetic mode of HDRs in the Reshuiwei geothermal field. Specifically, the subduction and retreat of the Pacific Plate led to intensive thermal disturbances to the plate front, further resulting in the uplift of the asthenosphere and the intrusion of mantle-derived thermal materials. As a result, a relatively highly located mantle-derived heat source was formed. Granite

收稿日期：2023-10-11；**接收日期：**2024-01-01
基金项目：湖南省地质院科研项目（HNGSTP-202102，HNGSTP-202330）
第一作者：杜江，1988 年生，男，四川南充人，硕士，高级工程师，研究方向为能源地质. E-mail: 1025774576@qq.com
***通信作者：**张保建，1972 年生，男，山东临邑人，博士，正高级工程师，研究方向为地热地质、水文地质、环境地质. E-mail: zbjsddk@126.com

plutons with high heat production rates and uranium deposits featuring radioactive heat production form a favorable crustal heat source. Furthermore, deep-seated faults serve as pathways for the upward intrusion of deep thermal materials while supplying heat sources for the formation of shallow HDRs. The favorable thermal source conditions and the upward intrusion of deep thermal materials along deep-seated faults jointly lead to the formation of a favorable HDR target area represented by plutons around Reshuiwei in southeastern Hunan. As inferred from the comprehensively determined geothermal gradients, the concealed and tight granite plutons with scarce fractures and burial depths ranging from 4000 to 6000 m in the Reshuiwei geothermal field exhibit temperatures reaching 176.80–256.60°C, serving as favorable HDRs to be explored and exploited in the near future.

Keywords: hot dry rock; geochemistry; gravity, magnetic, electricity, and seismic combination; heat source-related mechanism; genetic mode; Reshuiwei

干热岩资源主要是指埋深较浅(目前一般在3 000~5 000 m)、温度较高、能被人类所开发利用的地下高温岩体[1]。国际上干热岩开采的研究已有将近 50 年历史，干热岩资源以远超其他能源的资源规模以及绿色、低碳的资源品质而广受关注[2]。1974 年，美国洛斯 阿拉莫斯(Los Alamos)国家实验室在新墨西哥州的 Fenton Hill 首先开展了干热岩勘查开发研究。迄今为止，全球共建立了 39 个干热岩开发的增强型地热系统(Enhanced Geothermal Systems，EGS)工程，总装机容量 12.2 MW，其中法国苏尔茨项目于 2013 年实现了商业性发电，发电功率 1.5 MW[3]。

我国对干热岩的勘查研究相对较晚，研究成果主要集中于近十年内。在干热岩的成因机制方面，王贵玲研究团队[4-7]通过综合分析国内外干热岩资源特征，将我国干热岩资源类型划分为高放射性产热型、沉积盆地型、近代火山型和强烈构造活动带型，并分析了其成因机制。并对未来我国干热岩资源重点勘查方向及靶区进行了论述，建立干热岩选区指标体系，圈定有利靶区。张保建等[1,8]研究了河北唐山马头营与共和盆地干热岩的成因机制，阐述深部热物质的上涌过程及地球内外力地质作用对地球浅部地热场的塑造与热异常制约过程。在干热岩的热源机制方面，张超等[9]指出花岗岩放射性生热、附加岩浆热与深部地幔热是干热岩常见的热源。在干热岩资源的评价指标方面，刘德民等[10-11]指出干热岩勘查评价的主要指标为岩石圈厚度和莫霍面埋深、居里等温面埋深、地温梯度、大地热流、新构造运动、高温温泉与气田等；论述了控热构造对干热岩热能的传输与聚敛具有很重要的作用，将控热构造划分为生热、导热、储热和释热构造。在干热岩的勘查方向方面，饶松等[12]通过分析对比国内外典型干热岩系统成因机制，综合考虑全球高温地热带分布和中国陆区板块构造背景、现今大地热流分布格局、岩石圈热结构、莫霍面深度及壳内热源、新生代火山活动、温泉分布、深大断裂分布与活动性，以及现有干热岩勘查结果，圈定了中国陆区最具潜力的干热岩勘探靶区。在干热岩的开发利用方面，李奉翠等[13]研究了中深层地热井下同轴换热器长期换热性能。孙致学等[14]基于离散裂缝模型开展了 CO_2 增强型地热系统传热-渗流-应力(THM)耦合数值模拟。汪集暘等[15]系统总结了煤田区地热资源开发利用与储能技术。上述研究为我国干热岩的热源机制、勘查方向、靶区优选、开发技术等方面提供了较好的研究基础。

湖南省处于中国中部岩石圈厚度较大的地区，迄今为止尚无已探明的干热岩资源，被认为是大地热流值偏低的区域，但湖南省却发现有热水圩和灰汤两处90℃以上的高温天然温泉，特别是汝城地区热水圩温泉曾记录到 98℃的水温，这说明湖南省局部地区也具有良好的地热地质条件。与汝城地区邻近的广东惠州黄沙洞惠热 1 井深度 3 009 m，测温温度高达 127.5℃，甘浩男等[16]指出黄沙洞地区地壳热流与地幔热流值相近，构造活动相关热流也占有相当比例。孙明行等[17]研究了广西干热型地热资源成因机制与赋存模式，指出钦州盆地以壳、幔物质上涌所形成的传导型热为主要热源，归属于强烈构造活动带—沉积盆地型干热型地热资源区；合浦盆地以“低速高导”局部熔融层为主要热源，以次级幔枝或热点为热源补给，归属于近代火山—沉积盆地型干热型地热资源区。说明包括湖南省在内的华南地区局部也具有良好的干热岩勘查前景。湖南省特别是汝城地区高放射性花岗岩布广泛，放射性铀、钍、钾含量丰富，生热率高。汝城地区经历多次构造运动，构造格局复杂多样，构造形迹纵横交错，深大断裂广泛发育，构造运动具有长期性、复杂性和明显的阶段性和继承性。龙西亭等[18]、杨汉元[19]、叶见玲等[20]根据汝城地区的地质构造、地温场特征、高放射性花岗岩体等地热地质条件，推测汝城地区热水圩一带具有良好的干热岩赋存条件与干热岩资源潜力。欧健等[21]采用地热温标、管道模型及基于生热率的深部地温反推法等地温梯度估算方法，综合确定了湖南省现今的地温梯度，其中热水圩及周边地温梯度达 3.0~4.0℃/hm，据此推断热水圩一带 4 000 m 深度温度为 176.80℃，5 000 m 深度温度为 216.70℃。

综上所述，湖南省局部地区可能具有较好的干热岩赋存条件。笔者在前人研究基础上，综合分析汝城地区热水圩一带的深部地质与构造、地球化学和地球物理特征、地温场特征等，探讨热水圩地热田干热岩形成的热源机制与地球动力学过程，以期为下一步的湖南省干热岩勘查提供理论基础与勘查方向。

1 研究区地质背景

1.1 地质背景

研究区位于华夏地块与扬子地块结合部位的华南多期复合造山带内，在两地块拼合增生以前属于华夏古陆北西缘斜坡带，在两地块碰撞后，构成了万洋山-诸广山走滑岩浆带的重要组成部分。两地块的会聚走滑和离散走滑，奠定了区域的基本构造型式，造成了构造形迹纵横交错、组合较为复杂的格局，反映了区域构造运动不但具有长期性、复杂性，而且具有明显的阶段性和继承性。特别是其邻近的 NNE 向郴州-临武深大断裂与 NW 向常德-安仁深大断裂，均是具有多期活动的深大走滑断裂，在不同方向深大断裂的交汇部位容易形成岩浆活动及上侵的主要空间。热水圩地区位于 NE 向遂川-热水大断裂与 NW 向塘湾大断裂交汇处北侧，强烈的燕山运动使断裂交汇处下部物质熔融，并沿断裂多次脉(涌)动上侵而形成中棚复式岩体(图 1)。沿遂川-热水断裂有大量温泉出露，如上堡、丰州、热水、城口等温泉，这表明热水断裂是一条高热异常带，且现今仍在活动，为热流体的深循环与上涌提供了条件。

热水圩地热田位于华南地区复式岩体-诸广山岩体的北侧，该岩体规模宏大，由印支期和燕山期花岗岩与花岗闪长岩组成，呈岩基产出[22]。岩体周缘是新元古界和古生界变质岩。区域断裂纵横交错发育，规模最大的断裂呈 NNE 向、NW 向和 NEE 向，其中 NNE 向走滑断裂规模最大，控制着区域温泉的分布，在整个华南地区形成数个温泉带[23-24]。区域上经过多期造山隆升作用，高山峻岭发育，高程 500~1 200 m。区域地形南高北低，地表水系向北排泄，热田产出在山间洼地中，最低高程 347 m。

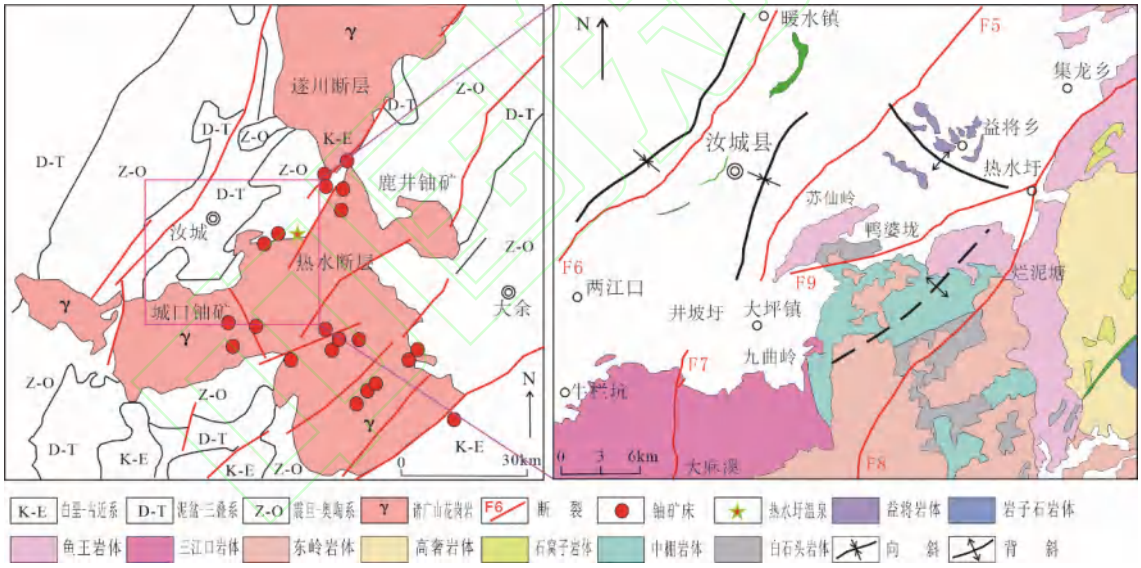

图 1 热水圩区域地质及岩体分布

Fig.1 Regional geology and rock mass distribution map of the Reshuiwei Area

1.2 地热田概况

热水圩地热田位于印支晚期花岗岩体与变质岩接触带上，地表被第四系覆盖，平均厚度 2.3m。东部为印支晚期中粒斑状黑云母花岗岩，西部地层由老到新依次为新元古代岭秀组砂岩、粉砂质板岩和板岩，震旦系砂岩、硅质岩和板岩，以及寒武系炭质板岩、砂岩夹板岩。热田面积 4 km^2，有地热勘探钻井 21 口，钻探深度 200~380m，其中高温井(终孔温度 70~92℃)6 口，中温井(终孔温度 40~70℃)9 口，低温井(终孔温度小于 40℃)6 口。钻井基本覆盖了整个热田，温度最高的 2 口井温度达到 90~92℃，单井流量 2 000 t/d。

1.3 水文地质条件

研究区基岩为变质砂岩、板岩和花岗岩，岩性致密且完整、不透水，主要地下水类型为构造裂隙潜水或构造裂隙承压水。由于研究区经历了多期构造运动和多次岩浆侵入，断裂交叉发育，断裂破碎带控制了

地下水分布及循环。

地下水富集程度由断裂破碎带规模及性质决定，研究区河谷深切多呈“V”形，峡谷多陡崖，裂隙交横密集成网，地下水类型为 HCO_3-Na·Mg 型和 HCO_3-Mg·Ca 型。洼陷地区是地下水和地表水共同的排泄区，热水圩地热田产出在最大的山间洼地，热水河流经地热田表面，深大断裂经过地热田下方，温泉在河谷边缘呈线性出露。

1.4 热储分布及特征

热水圩地热田热储构造由断裂破碎带及裂隙构成，主要断裂有 2 组，一组为早期共轭断裂，走向相互垂直；另一组为后期形成的新断裂，控制了现今河流的走向，地表温泉在新断裂边出露。中高温温泉水在断裂交汇带排泄，断裂倾角大，挤压和张性裂隙均有发育。张裂隙是地下水排泄的主要通道，周边多数张性裂隙被结晶充填，远离张性裂隙中心则裂隙封闭，现有的有效热储被限制在洼陷区的有限空间内[25]。

热水圩地热田温泉最高温度达 98℃，周边有多眼钻孔(孔深 200~350 m)揭露到了 90℃的热储，揭露的热储层位之上的地温梯度达 20.90~60.6℃/hm[26](表 1)，且多数钻孔在揭露热水后地温梯度急剧降低或变为负值，指示出热水圩地热田具有显著的对流型地热的特点，因此，地热田钻孔实测的地温梯度不能直接用来推算深部热储的温度。

表 1 热水圩地热田主要钻孔地温梯度实测结果

Table 1 Measured geothermal gradients of major boreholes in the Reshuiwei geothermal field

孔号	地面高程/m	初见热水孔深/m	孔内最高温度/℃	换算后静置水位高程/m	最大单位涌水量/(L s^{-1} m^{-1})	岩性	地温梯度/(℃ hm^{-1})
ZK1	341.905	16.20	92.2	342.528	6.519	花岗闪长岩	35.3
ZK4	341.734	11.00	91.2	342.504	6.626	花岗闪长岩	20.9
ZK16	345.516	146.80	88.3	343.206	0.085	花岗闪长岩	60.6
ZK15	369.594	219.12	83.5	345.774	0.135	花岗闪长岩	25.6
ZK21	375.084	249.70	84.6	346.564	0.095	花岗闪长岩	26.0
ZK19	372.372	161.22	88.9	340.772	0.029	花岗闪长岩	26.3
SK5	369.245	139.50	87.5	340.945	0.261	花岗闪长岩	24.5

2 研究方法

本文在前人研究基础上，通过地球化学和地球物理手段以及其反映的深部地质结构，来推测热水圩地区深部热物质的上侵过程及有利的聚热、成热条件与干热岩成因机制。

2.1 地热温标

依据温泉或热水孔的水化学资料，利用各类地热温标公式估算热储温度，是确定深部热储温度和地温梯度的一种简单实用的方法。SiO_2 地热温标是应用最早也是最常用的地热温标，其理论依据是地热流体中 SiO_2 的含量主要取决于不同温度、压力下石英在水中的溶解度。试验表明，水中 SiO_2 的析出量与温度呈函数关系[27]。

一般来说 SiO_2 温标包括石英和玉髓温标两种，前者适用于中-高温热储(大于 110℃)温度计算，玉髓温标用于小于 110℃温度条件。由于用 SiO_2 地热温标估算热储温度在湖南省及周边取得了较好的估算效果[26,28-29]，且从地热地质条件分析，热水圩地热田深部热储温度一般大于 110℃，为全面掌握湖南省地热资源热储温度及深部地热潜能，选取热水圩地热田近年来所采取的 11 处温泉或地热井的水化学数据，运用 SiO_2 地热温标法估算其热储温度。计算公式如下：

$$t = \frac{1309}{5.19 - \lg W} - 273.15 \quad (1)$$

2.2 放射性元素放热

由于地球仍然含有很多长半衰期的放射性元素，地壳浅表的放射性元素以 ^{238}U、^{232}Th、^{40}K 为主。研究表明[30-32]，温泉与铀矿在空间分布上有一致性分布规律，形成的地质构造条件上有相似性，温泉水化学成分与铀矿化特征及其围岩蚀变之间有一定的相关性。

放射性元素放热是地壳浅表形成地热异常的重要原因之一。岩石放射性生热率 A 是指单位体积岩石中所含放射性元素在单位时间内由放射性衰变所产生的能量，μW/m^3。岩石生热率可由实测的岩石中铀、钍、钾 3 种放射性元素质量分数计算获得：

$$A = 10^{-2} \times \rho \times (9.52 \times C_U + 2.56 \times C_{Th} + 3.48 \times C_K) \quad (2)$$

2.3 重、磁异常反演

B. H. Arney 等[33]利用重力与地震资料对爱达荷州 Mountain Home 地区进行了干热岩潜力评估。W. J. Hinze 等[34]在美国中部大陆利用重、磁异常圈定了干热岩有利区。A. Rimi 等[35]利用摩洛哥地热田的重、磁异常数据计算出居里面的深度为 10~40 km，为后续

评估提供依据。上述研究成果表明，重、磁异常可用来圈定干热岩有利区段。

结合研究区以往地质构造研究成果，利用重、磁异常特征，进一步揭示研究区深部地质结构及其反映的深部热物质活动状态。基于收集的湖南省航磁数据，通过磁异常反演，利用下延 20 km 和 30 km 叠加重新推断中酸性岩体。同时，基于磁异常反演的居里面深度与岩体、深大断裂相叠加，来判断居里面深度对地热异常的影响。

2.4 电法与地震勘探

S. Thiel 等[36]对干热岩进行三维大地电磁正演模拟，并在澳大利亚南部 Paralana 验证，结果能够很好地反映盖层、热储层的电性信息。K. Suzuki 等[37]利用地震反射波法和可控源音频大地电磁法(Controlled Source Audio-frequency Magneto Tellurics，CSAMT)联合反演对日本 Ogachi 干热岩实验区进行探测，很好地反映地下储层信息。Gao Ji 等[38]利用三维大地电磁成像结果首次表征了共和盆地干热岩地热系统的三维分布特征。

通过收集“深部探测技术与实验研究”专项课题(SinoProbe-02-04)开展的大井-泉州超长大地电磁测深剖面数据，及其反演的华南壳、幔电性结构模型[39]，来了解横穿湖南省南部凤凰-热水圩一线的电性结构及其反映的深部地质结构(图 2)。

地震波是研究岩石圈内部结构构造的主要参数，可用来辅助判断有无深部幔源热物质上侵及其通道。根据台湾-黑水地学断面的其中湖南省凤凰-茶陵段地震探测资料[40-41]，建立凤凰-茶陵段的速度、密度模型，为研究湖南东南部深部地质结构提供地震学方面的证据。

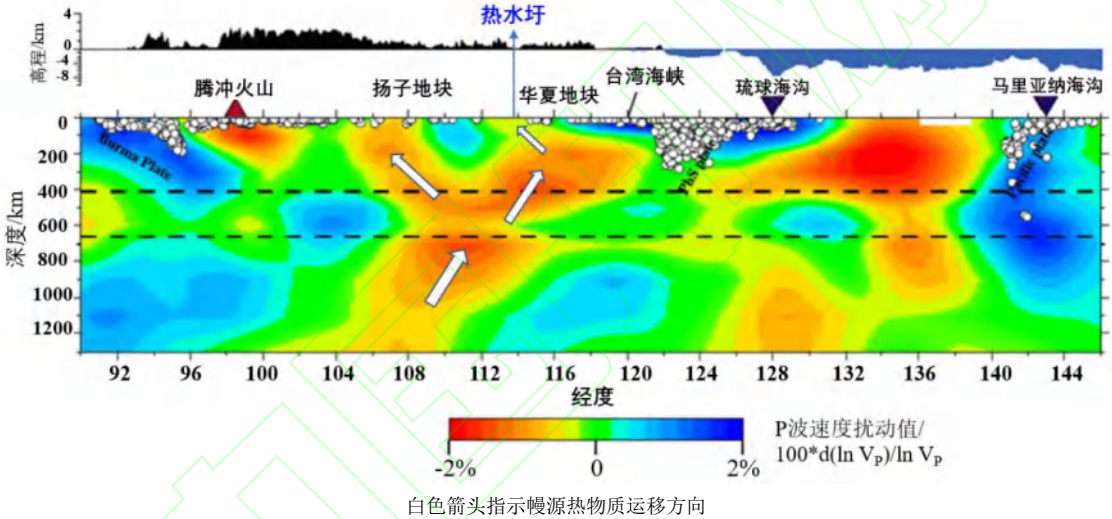

图 2　沿中国南部北纬 25 °剖面 P 波速度扰动的垂直横截面[48]

Fig.2　Vertical cross section showing disturbances to the P-wave velocity along the 25 °N seismic section of southern China

3　结果与讨论

3.1　热储温度

根据式(1)计算得出了热水圩地热田的热储温度，从表 2 看出，热水圩地热田深部热储的温度为 79.4~143.9℃，其中位于地热田中心部位(泉 1、泉 2、ZK1、ZK4)的深部热储温度为 135.8~143.9℃。由于采取的井泉水样多是深部地热水与浅层冷水的混合水，因此用地热温标法估算的热储温度一般偏小。推断在热水圩地热田深部很可能赋存有 150℃以上的高温岩体，具有良好的干热岩赋存潜力。

表 2　热水圩地热田热储温度 SiO_2 温标法计算结果

Table 2　Geothermal reservoir temperatures of the Reshuiwei geothermal field calculated using SiO_2 geothermometry

热泉及钻孔编号	SiO_2 质量浓度/(mg·L^{-1})	SiO_2 温标计算的热储温度/℃	热泉及钻孔编号	SiO_2 质量浓度/(mg·L^{-1})	SiO_2 温标计算的热储温度/℃
泉 1	112	143.6	ZK19	30	79.4
泉 2	112	143.6	ZK21	60	110.5
ZK1	112.5	143.9	SK5	75	121.7
ZK4	97.5	135.8	城口	44	95.9
ZK15	46	98.0	汤湖	62	112.1
ZK16	88	130.2	——	——	——

3.2 放射性生热及对地热异常的影响

热水圩地区所在的花岗岩岩体铀丰度一般达 20×10^{-6}，最高达 50×10^{-6}；铀浸出率一般达 20%以上；震旦系、寒武系岩石铀丰度较高，一般达$(8\sim40)\times10^{-6}$，且铀浸出率高达 30%~42%[42]。根据湖南省地质队近年来对热水圩地区及周边不同花岗岩岩体的 U、Th、K 含量测试结果[19]，计算了热水圩地区及周边不同花岗岩岩体的岩石生热率[43](表 3)，热水圩地区花岗岩的岩石生热率为 3.13~14.84 μW/m^3，生热率平均值为 7.11 μW/m^3。其中中棚岩体岩石生热率为 5.86~14.72 μW/m^3，生热率平均值为 8.44 μW/m^3；鱼王岩体岩石生热率为 3.72~14.86 μW/m^3，生热率平均值为 7.07 μW/m^3，均远远超过中国大陆主要地质构造单元的地壳平均生热率 1.9 μW/m^3[44]，这两个岩体均以黑云母花岗岩为主，U、Th、K 含量相对较高，是区内岩石生热率最高的两个岩体，均位于热水圩温泉附近(图 1)，指示放射性热源是本区的重要热源之一。钻孔取得的花岗岩样品生热率与地表样品测得岩石生热率相近，反映了该区岩体放射性生热率较稳定。

章邦桐等[45]研究认为，深部传导热的热能有限，放射性元素成矿期在岩浆岩成岩之后 10 Ma 至数 Ga 之后(岩矿时差)，岩浆余热在铀矿成矿期已经缓慢冷却，区域铀矿床成矿热能主要由放射性元素产生的热源长期积累形成。岩石圈伸展作用引发的深部热物质上侵及地热流体大规模循环，在不断演化为富铀热液流体形成热液型铀矿的同时，也形成地壳浅表的重要热源。因此，放射性元素热源是本区的重要热源，在 4 000 m 以浅具有较好的干热岩资源远景。

通过研究区中心的遂川-热水断裂带呈 NE 向展布，受遂川-热水断裂带的遂川断裂与热水断裂的叠接区控制[46]。在断裂带北东部是著名的鹿井铀矿田，其中丰州铀矿与温泉共伴生；在断裂带南部的城口铀矿，与城口镇 6 处温泉共伴生，其中锦城温泉水温 75℃，流量 72 m^3/h。热水圩温泉及其附近的温泉均与铀矿床(点)具有密切的空间联系，其中鹿井铀矿田地壳的放射性生热量至少为 72.66 mW/m^2，远高于全球平均地壳放射性生热量 40 mW/m^2[47]。这是热水圩地区高热异常的主要影响因素之一。

表 3 热水圩地区花岗岩样放射性元素测试及生热率计算结果

Table 3 Results of the radioactive element tests and heat production rate calculation of granite samples from the Reshuiwei area

岩体	岩性	元素质量分数			密度/(10^3 kg m^{-3})	生热率/(μW·m^{-3})
		U/10^{-6}	Th/10^{-6}	K/%		
益将岩体	石英闪长岩	6.33(1)	18.70(1)	3.15(1)	2.63(1)	3.13(1)
鱼王岩体	黑云母花岗岩	5.34~45.30 17.39(28)	14.50~52.70 34.18(28)	2.37~5.24 4.16(28)	2.58~2.69 2.64(28)	3.72~14.86 7.07(28)
三江口岩体	黑云母二长花岗岩	8.87~27.20 16.71(20)	13.00~47.60 35.27(20)	3.14~5.20 4.15(20)	2.61~2.69 2.65(20)	4.14~9.51 6.99(20)
东岭岩体	黑云母花岗岩	7.49~38.90 17.86(8)	12.20~49.90 27.86(8)	3.13~4.51 3.79(8)	2.56~2.66 2.62(8)	3.25~11.37 6.66(8)
石窝子岩体	石英闪长岩	9.05(1)	26.70(1)	4.35(1)	2.64(1)	4.48(1)
中棚岩体	黑云母花岗岩	15.40~49.80 24.80(10)	12.20~45.50 28.14(10)	3.20~5.35 3.98(10)	2.58~2.68 2.62(10)	5.86~14.72 8.44(10)
总计		5.34~49.80 18.05(68)	12.20~52.70 32 .53(68)	2.37~5.35 4.08(68)	2.56~2.69 2.64(68)	3.13~14.86 7.11(68)

注：表中数据 5.34~45.30/17.39(28)为最小值~最大值/平均值（样品数）。

3.3 重、磁、电、震反映的深部地质结构及聚热分析

3.3.1 低速高导体指示的幔源热物质上侵趋势

Huang 等[48]通过 P 波层析成像结果显示中国中东部地区 200 km 以上深度范围内为大范围的地震波速高速异常(图 3)，在 600 km 深度处，扬子地块的东西两端均为地震波速高速异常，推测东侧的高速异常体为西太平洋板块的俯冲体。扬子地块上方局部位置被来自华夏地块的低速异常所取代，扬子克拉通浅部的低速异常被解释为南部华夏地块的软流圈热物质沿着地层薄弱区以及断裂带上涌；而在地壳与上地幔顶

部的区域内呈现为高速异常，表明该区域的高速体并未被取代，推测来自软流圈的热物质上涌至上地幔顶部后侵蚀岩石圈，从而导致板块拆沉并产生了 50~200 km 深度范围内的高速异常，因此该高速异常体大致为分离的岩石圈。这与“深部探测技术与实验研究”专项课题(SinoProbe-02-04)所做的大井-泉州超长大地电磁测深剖面高导体特征是基本一致的[39](图 4)，都反映了在华夏地块边缘的深大断裂等岩石圈薄弱带，有幔源热物质的明显上侵趋势。说明除了地幔热流传导外，局部岩石圈脆弱带，还存在幔源热物质的上侵(图 2、图 3 中低速高导体，白色箭头反映了幔源热物质运移方向)，这是形成局部带状(点状)热异常的主要原因之一。

根据湖南省三维地球结构模型地壳速度基础数据，汇编成扬子、华南板块及两板块结合带岩石圈三维结构的密度、速度柱数据模型，如图 4 所示。邵阳以东中地壳低速体最明显，低速体 P 波速度为 5.8~6.2 km/s，主要见于 10~15 km 深度，厚度 4.0~5.2 km(图 5)。区域低速一般都在 12~15 km 的壳内韧性剪切滑动面产生，该低速异常体可能位于构造-岩浆作用、构造滑脱作用的部位，这个构造部位也被很多研究者认为是地震的多发部位和深部幔源、壳源流体的活跃部位。壳内低速体多在板块边缘或微地块结合带、深大断裂带及其次级断裂附近出现，说明这些深大断裂有可能构成深部热物质上侵的通道，为浅部干热岩的形成提供重要热源。

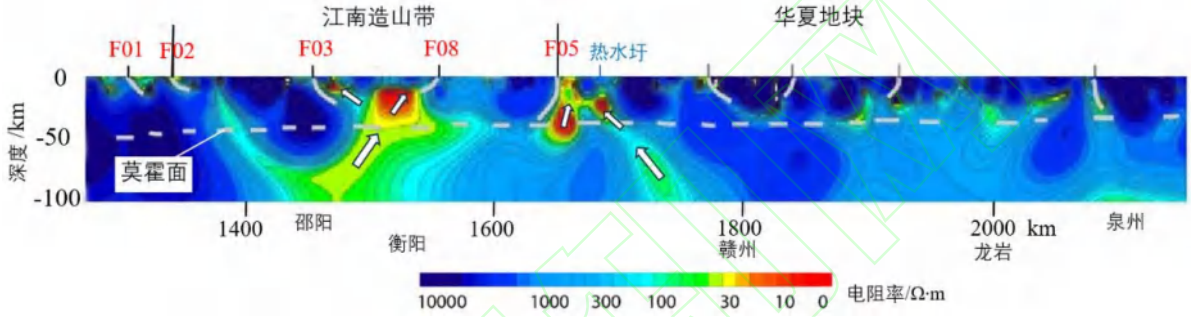

图 3　大井-泉州大地电磁测深剖面南段江南构造带和华夏地块电性结构模型

Fig.3　Electrical structure model of the Jiangnan Orogen and Cathaysia Block in the southern section of the Dajing-Quanzhou magnetotelluric sounding profile

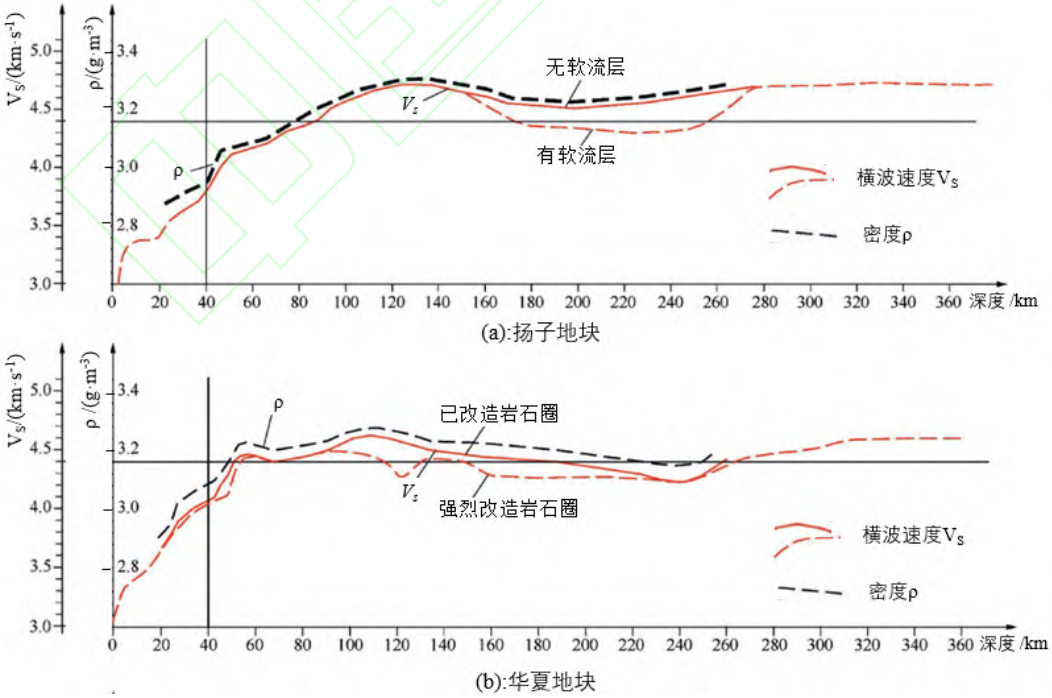

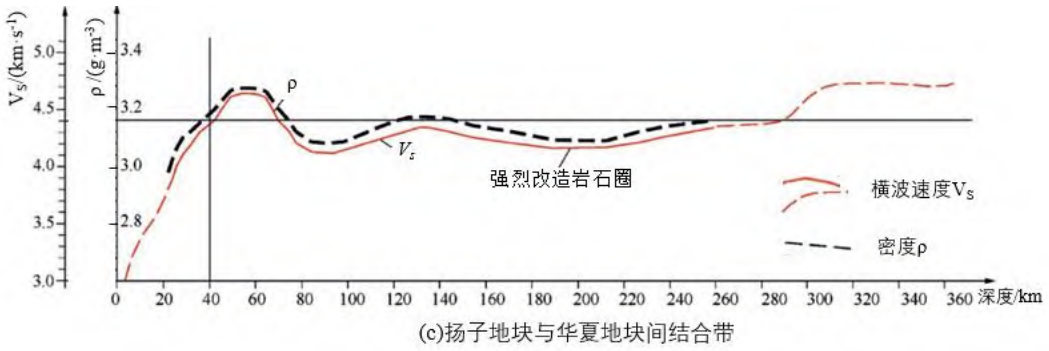

图 4　扬子地块、华南地块及两地块结合带岩石圈三维结构数据柱模型曲线

Fig.4　Curves of the data column models of the 3D lithospheric structure in the Yangtze and South China plates and their suture zone

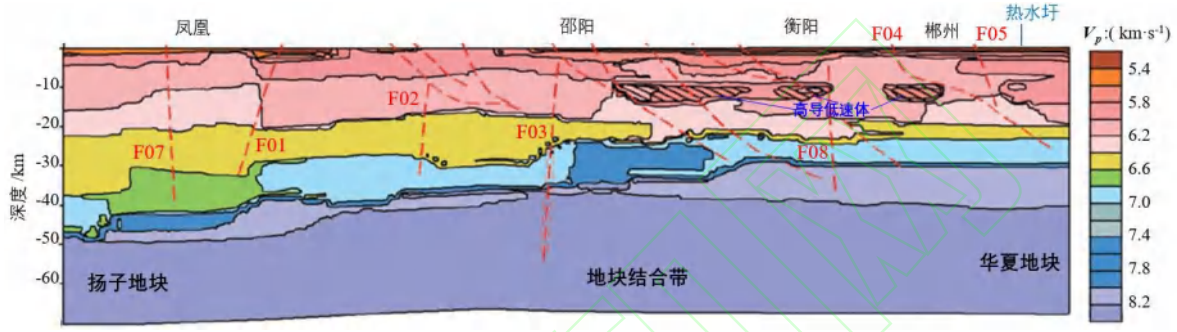

F01：麻阳-澧县断层; F02：通道-安化断层; F03：桃江-城步断层; F04：文家市- 双牌断层;
F05：郴州-临武断层; F07：花垣-慈利断层; F08：界牌-祁阳断层

图 5　凤凰-茶陵地壳 P 波速度剖面

Fig.5　Crustal P-wave velocity profile of the Fenghuang-Chaling section

3.3.2　重、磁特征反映的深部热结构特征

从图 6 看出，汝城-桂东一线呈现 NE 向重力负异常梯度带(图 6a)，长度超过 250 km，宽约 20 km，重力值为-35~-60 mGal，水平梯度为 1.25 mGal /km，这主要是对断裂构造和岩浆岩带的综合反映。NE 向串珠状重力负异常带主要为低密度隐伏-半隐伏花岗岩带和下古生界地层的综合反映。与重力低值相间分布的重力高值主要与上古生界碳酸盐地层分布有关。温泉沿断裂带密集分布，反映了 NE 向断裂对地热资源具有明显控制作用。汝城盆地也呈现重力负异常，这是因为该区域虽然地壳厚度相对较大，但岩石圈厚度却相对较薄所致。岩石圈厚度的局部减薄，可能与软流圈的上侵有关。

研究区磁异常曲线起伏较大，但幅值变化不大(图 6b)，这可能与区内大量不同时代、不同类型的浅表层中酸性岩体相关。根据磁异常反演结果，汝城干热岩研究区一带居里面为 23~26 km(图 7)，相对周边地区偏浅。特别是位于莫霍面、居里面的陡变带(图 6c)，这也是深浅物质交替循环的有利地带，利于深部热物质的上侵。

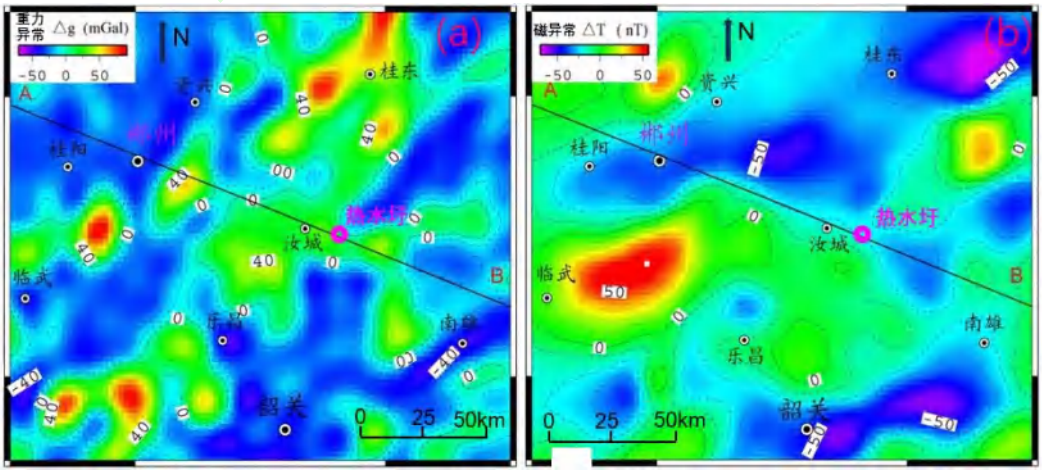

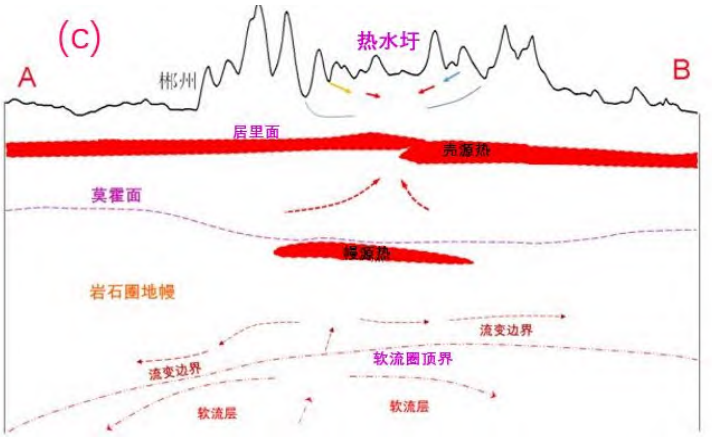

(a):重力异常；(b):磁异常；(c):深部热结构

图 6　热水圩地区重、磁特征及其反映的深部热结构模式

Fig.6　Gravity and magnetic characteristics of the Reshuiwei area and the deep thermal structures they reflected

重、磁特征表明，热水圩地区相对较薄的岩石圈厚度，软流圈热物质沿深大断裂的上侵，特别是 NE 向深大断裂与 NW 向大断裂的交汇部位多呈现相对开启的应力状态，为深部热物质的上侵(图 6c)提供了有利条件，使其深部保持了相对高热的地质背景。

3.4　干热岩形成的其他有利因素

除上述干热岩形成的有利因素外，热水圩地区干热岩形成的其他有利因素还有：

1) 地块结合带与深大断裂控热

研究区位于华夏地块与扬子地块结合部位的华南多期复合造山带内，在两地块拼合增生以前属于华夏古陆北西缘斜坡带，在两地块碰撞后，构成了万洋山-诸广山走滑岩浆带的重要组成部分。两地块结合带的走滑和离散走滑，奠定了区域的基本构造形式，造成了构造形迹纵横交错、组合较为复杂的格局，反映了区域构造运动不但具有长期性、复杂性，而且具有明显的阶段性和继承性。特别是其邻近的 NE 向茶陵-郴州深大断裂与 NW 向常德-安仁深大断裂，均是具有多期活动的深大走滑断裂，在两条断裂的交汇部位是岩浆活动及上侵的主要空间。根据大地电磁测深剖面(图 3)，在郴州-临武深大断裂及其东侧较大次级断裂的深部均有高导低速体自下而上分布的特征，是深部热物质上侵的有利通道。

区域内温泉群主要沿 NE 向遂川-热水大断裂展布，表明 NE 向大断裂是主要的控热断裂。就某个单独泉群来说，地热井(泉)主要沿 NW 向构造形迹展布，表明区域内 NW 向断裂是主要的开启性控水断裂。因此，NE 向大型控热断裂与 NW 向开启断裂的交汇部位，也是现今深部热物质上涌的有利通道，继承了中生代以来的岩浆活动规律，此交汇部位也是干热岩赋存的有利部位。

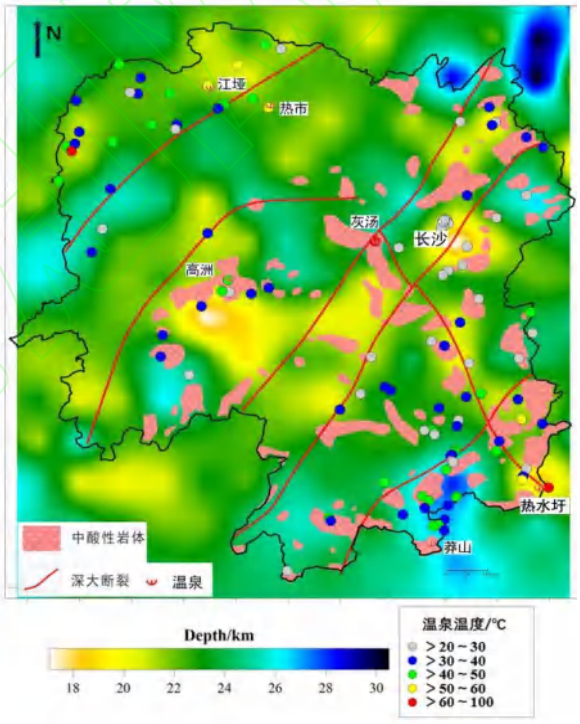

图 7　基于磁异常反演的居里面深度、岩体、深大断裂及温泉点的叠加

Fig.7　Map showing the superposition of the Curie depth derived from magnetic anomaly inversion, plutons, deep faults, and thermal spring outcrops

2) 地球动力学机制

湖南省东南部地处西太平洋俯冲板片的前缘。大洋板块的俯冲会导致地壳岩石圈的破碎变形，并形成一系列 NNE 向深大断裂。深部热对流的加剧促使了软流圈的强烈隆起，俯冲进入软流圈的大洋板块使深部热扰动变得更加剧烈，并且随着大洋岩石圈和拆沉的大陆岩石圈等“冷”物质的下沉，需要一个上升流来

平衡，于是上升的软流圈高温物质开始不断的加热和底侵深部岩石圈，在岩石圈破裂的区域上侵得最快，当底侵程度逐渐加剧的时候，本来已经裂解的岩石圈底部开始发生拆沉作用或者使已经变得可塑的岩石圈向四周流动，从而导致岩石圈减薄，当上侵动力不足的时候，高温物质便存在于上侵能达到的最大高度，开始对周围围岩进行加热，一部分热量通过热传导的方式经薄地壳或断裂带传导到近地表，软流圈剧烈隆起的地区由于深部持续的热源供应必然形成浅部的高温热田和地表的高大地热流值。

新构造运动时期 (距今 10~8 Ma)，中国大陆地壳受到西南侧印度板块向北低角度俯冲碰撞和东侧西太平洋板块向西高角度俯冲双重动力体系的控制。受到东、西两大动力体系的影响，湖南地区应力场以近东西向的水平挤压为主，这就导致该区的古老构造形迹在新构造期间发生了不同程度的复活，出现了许多规模和活动性不等的活动断裂及断块隆起区、裂陷区[49]。因此，自中新世以来，深大断裂的局部活化与新构造运动形成的活动断裂，使深部幔源热物质继续沿各级断裂自深部向浅部上侵。

3) 热储与盖层

研究区呈隐伏状态的花岗岩岩体是良好的热储，其中在构造破碎处形成地热水储层，致密且裂隙不发育的埋深在 4 000~6 000 m 的花岗岩岩体温度可达 176.80~256.60℃[21]，形成良好的、近期可勘查开发的干热岩体。汝城盆地内热导率较低的震旦系至古近系地层，热导率一般在 1.86~2.14 W/m•k，明显低于花岗岩岩体 2.6~2.7 W/m•k 的热导率，构成了深部热储的良好保温盖层。

4 干热岩成因模式

综上所述，热水圩一带地热资源(干热岩)的成因模式可归纳为：太平洋板块俯冲与回撤，导致板块前缘形成强烈的热扰动，造成软流圈的隆起和幔源热物质的上侵，形成相对较高的幔源热源。同时，生热率较高的地壳岩体与铀矿体放射性产热形成了温度较高的地壳热源(图 8)。有利的热源条件及沿深大断裂的深部热物质上侵，使湖南省东南部形成以热水圩花岗岩体为代表的干热岩有利靶区。郴州-临武、遂川-热水等深大断裂导水、导热，浅部低温地下水通过断裂流向深部热源，经加热后对流上升与其他浅部地下水混合，至山间沟谷或山前平原低洼处出露地面，形成温泉。

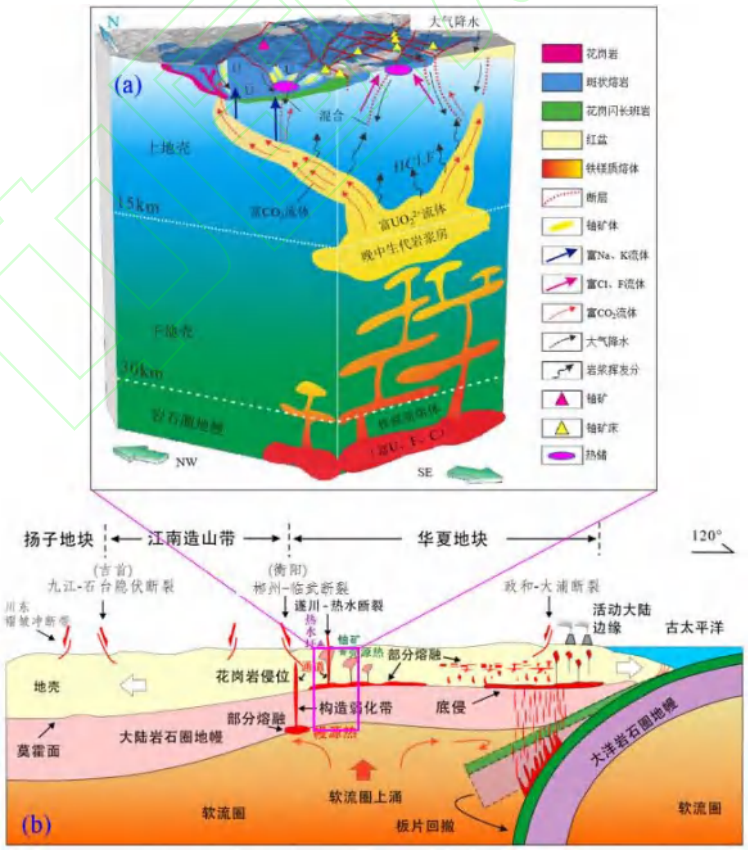

(a) 干热岩形成模式，修改自余辉[50]；(b) 地球动力学机制与热源机制，修改自陈昌昕等[51]

图 8　湖南省热水圩地热田干热岩形成机制模式

Fig.8　Formation mechanism and mode of hot dry rocks in the Reshuiwei geothermal field, Hunan Province

5　结 论

a. 湖南省热水圩位于西太平洋板块俯冲与回撤的前缘，中生代以来岩石圈伸展-减薄作用明显；扬子、华夏地块结合带附近的深大断裂一般均切穿地壳甚至岩石圈。中新世以来，深大断裂的局部活化与新构造运动形成的活动断裂，使 NE 向、NW 向深大断裂的交汇部位多呈开启性良好的构造环境。高导低速体与深大断裂带的吻合指示这些深大断裂有可能构成深部热物质上侵的通道，有利于深部幔源热物质的上侵和热流侧向向上传导，为浅部干热岩的形成提供重要热源。

b. 热水圩周边岩体的放射性生热率较高，周边鹿井、城口等铀矿床、矿点密布，为放射性生热率高值区，形成壳源异常热源，在不同级次断裂网络的导通作用下，对干热岩的形成具有重要意义。

c. 根据综合确定的地温梯度推算，热水圩地热田呈隐伏状态的、致密的、裂隙不发育的埋深在 4 000~6 000 m 的花岗岩体温度可达 176.8~256.60℃，是良好的、近期可勘查开发的干热岩体。

符号注释：

A 为岩石生热率，μW/m^3；t 为热储温度，℃；W 为热水中溶解的 H_4SiO_4 形式的 SiO_2 含量，mg/L；C_U、C_{Th} 分别为岩石中的 U、Th 质量分数，10^{-6} %；C_K 为 K 质量分数，%；ρ 为岩石密度，1 000 kg/m^3。

参考文献(References)

[1] 张保建，雷玉德，赵振，等. 共和盆地干热岩形成的地球动力学过程与成因机制[J]. 地学前缘，2023，30(5)：384–401.
ZHANG Baojian，LEI Yude，ZHAO Zhen，et al. Geodynamic processes and mechanisms of the formation of hot dry rock in the Gonghe Basin[J]. Earth Science Frontiers，2023，30(5)：384–401.

[2] 张英，冯建赟，罗军，等. 渤海湾盆地中南部干热岩选区方向[J]. 地学前缘，2020，27(1)：35–47.
ZHANG Ying，FENG Jianyun，LUO Jun，et al. Screening of hot dry rock in the south–central part of the Bohai Bay Basin[J]. Earth Science Frontiers，2020，27(1)：35–47.

[3] 毛翔，国殿斌，罗璐，等. 世界干热岩地热资源开发进展与地质背景分析[J]. 地质论评，2019，65(6)：1462–1472.
MAO Xiang，GUO Dianbin，LUO Lu，et al. The global development process of hot dry rock (enhanced geothermal system) and its geological background[J]. Geological Review，2019，65(6)：1462–1472.

[4] 甘浩男，王贵玲，蔺文静，等. 中国干热岩资源主要赋存类型与成因模式[J]. 科技导报，2015，33(19)：22–27.
GAN Haonan，WANG Guiling，LIN Wenjing，et al. Research on the occurrence types and genetic models of hot dry rock resources in China[J]. Science & Technology Review，2015，33(19)：22–27.

[5] 马峰，孙红丽，蔺文静，等. 中国 EGS 示范工程靶区选址与指标矩阵评价[J]. 科技导报，2015，33(8)：41–47.
MA Feng，SUN Hongli，LIN Wenjing，et al. Target site selection and index matrix evaluation of EGS trial project in China[J]. Science & Technology Review，2015，33(8)：41–47.

[6] 蔺文静，甘浩男，王贵玲，等. 我国东南沿海干热岩赋存前景及与靶区选址研究[J]. 地质学报，2016，90(8)：2043–2058.
LIN Wenjing，GAN Haonan，WANG Guiling，et al. Occurrence prospect of HDR and target site selection study in southeastern of China[J]. Acta Geologica Sinica，2016，90(8)：2043–2058.

[7] 蔺文静，王贵玲，邵景力，等. 我国干热岩资源分布及勘探：进展与启示[J]. 地质学报，2021，95(5)：1366–1381.
LIN Wenjing，WANG Guiling，SHAO Jingli，et al. Distribution and exploration of hot dry rock resources in China：Progress and inspiration[J]. Acta Geologica Sinica，2021，95(5)：1366–1381.

[8] 张保建，李燕燕，高俊，等. 河北省马头营干热岩的成因机制及其示范意义[J]. 地质学报，2020，94(7)：2036–2051.
ZHANG Baojian，LI Yanyan，GAO Jun，et al. Genesis and indicative significance of hot dry rock in Matouying，Hebei Province[J]. Acta Geologica Sinica，2020，94(7)：2036–2051.

[9] 张超，胡圣标，黄荣华，等. 干热岩地热资源热源机制研究现状及其对成因机制研究的启示[J]. 地球物理学进展，2022，37(5)：1907–1919.
ZHANG Chao，HU Shengbiao，HUANG Ronghua，et al. Research status of heat source mechanism of the hot dry rock geothermal resources and its implications to the studies of genetic mechanism[J]. Progress in Geophysics，2022，37(5)：1907–1919.

[10] 刘德民，张昌生，孙明行，等. 干热岩勘查评价指标与形成条件[J]. 地质科技通报，2021，40(3)：1–11.
LIU Demin，ZHANG Changsheng，SUN Minghang，et al. Evaluation indexes and formation conditions of hot dry rock exploration[J]. Bulletin of Geological Science and Technology，2021，40(3)：1–11.

[11] 刘德民，韦梅华，孙明行，等. 干热岩控热构造系统厘定与类型划分[J]. 地球科学，2022，47(10)：3723–3735.
LIU Demin，WEI Meihua，SUN Minghang，et al. Classification and determination of thermal control structural system of hot dry rock[J]. Earth Science，2022，47(10)：3723–3735.

[12] 饶松，黄顺德，胡圣标，等. 中国陆区干热岩勘探靶区优选：来自国内外干热岩系统成因机制的启示[J]. 地球科学，2023，48(3)：857–877.
RAO Song，HUANG Shunde，HU Shengbiao，et al. Exploration target selection of hot dry rock in Chinese continent：Enlightenment from genesis mechanism of global hot dry rock system[J]. Earth Science，2023，48(3)：857–877.

[13] 李奉翠，韩二帅，梁磊，等. 中深层地热井下同轴换热器长期换热性能研究[J]. 煤田地质与勘探，2021，49(2)：194–201.
LI Fengcui，HAN Ershuai，LIANG Lei，et al. Long–term heat transfer performance of underground coaxial heat exchanger for medium–deep geothermal[J]. Coal Geology & Exploration，2021，49(2)：194–201.

[14] 孙致学，姜传胤，张凯，等. 基于离散裂缝模型的 CO_2 增强型地热系统 THM 耦合数值模拟[J]. 中国石油大学学报(自然科学版)，2020，44(6)：79–87.
SUN Zhixue，JIANG Chuanyin，ZHANG Kai，et al. Numerical simulation for heat extraction of CO_2–EGS with thermal–hydraulic–mechanical coupling method based on discrete fracture models[J]. Journal of China University of Petroleum(Edition of Natural Science)，2020，44(6)：79–87.

[15] 汪集暘，孔彦龙，段忠丰，等. “双碳”目标下煤田区地热资源开发利用与储能技术[J]. 煤田地质与勘探，2023，51(2)：1–11.
WANG Jiyang，KONG Yanlong，DUAN Zhongfeng，et al.

Geothermal energy exploitation and storage in coal field under the dual carbon goal[J]. Coal Geology & Exploration，2023，51(2)：1–11.

[16] 甘浩男，蔺文静，王贵玲，等. 广东惠州黄沙洞地区岩石圈热–流变结构及其热源启示[J]. 水文地质工程地质，2023，50(4)：26–38.
GAN Haonan，LIN Wenjing，WANG Guiling，et al. Lithospheric thermo–rheological structure of the Huangshadong geothermal field in Huizhou of Guangdong and its heat–sources implications[J]. Hydrogeology & Engineering Geology，2023，50(4)：26–38.

[17] 孙明行，张起钻，刘德民，等. 广西干热型地热资源成因机制与赋存模式[J]. 地质科技通报，2022，41(3)：330–340.
SUN Minghang，ZHANG Qizuan，LIU Demin，et al. Genesis and occurrence models of hot–dry geothermal resources in Guangxi[J]. Bulletin of Geological Science and Technology，2022，41(3)：330–340.

[18] 龙西亭，袁瑞强，邓新平，等. 汝城干热岩地热资源研究[J]. 科技导报，2015，33(19)：68–73.
LONG Xiting，YUAN Ruiqiang，DENG Xinping，et al. Hot dry rock geothermal resources in Ru County[J]. Science & Technology Review，2015，33(19)：68–73.

[19] 杨汉元. 湖南汝城地区干热岩资源前景及参数孔选址研究[J]. 中国煤炭地质，2020，32(6)：41–47.
YANG Hanyuan. Study on hot dry rock resources prospect and stratigraphic well siting in Rucheng area，Hunan[J]. Coal Geology of China，2020，32(6)：41–47.

[20] 叶见玲，杨汉元，何大芳，等. 湖南省干热岩资源潜力及有利区分析[J]. 煤炭技术，2019，38(3)：70–72.
YE Jianling，YANG Hanyuan，HE Dafang，et al. Resource potential and favorable area analysis of hot dry rock in Hunan Province[J]. Coal Technology，2019，38(3)：70–72.

[21] 欧健，皮建高，张保建，等. 基于多种估算方法的湖南省现今地温梯度综合确定[J]. 地球学报，2023，44(3)：543–557.
OU Jian，PI Jiangao，ZHANG Baojian，et al. Comprehensive determination of present geothermal gradient in Hunan Province based on multiple estimation methods[J]. Acta Geoscientica Sinica，2023，44(3)：543–557.

[22] 邓平，任纪舜，凌洪飞，等. 诸广山南体印支期花岗岩的 SHRIMP 锆石 U–Pb 年龄及其构造意义[J]. 科学通报，2012，57(14)：1231–1241.
DENG Ping，REN Jishun，LING Hongfei，et al. SHRIMP zircon U–Pb ages and tectonic implications for Indosinian granitoids of southern Zhuguangshan granitic composite，south China[J]. Chinese Science Bulletin，2012，57(14)：1231–1241.

[23] 李建威，李先福，李紫金，等. 走滑变形过程中的流体包裹体研究：以湘东地区为例[J]. 大地构造与成矿学，1999，23(3)：240–247.
LI Jianwei，LI Xianfu，LI Zijin，et al. Fluid inclusions study in the process of strike slip faulting：A case study in eastern Hunan Province[J]. Geotectonica et Metallogenia，1999，23(3)：240–247.

[24] 傅昭仁，李紫金，郑大瑜. 湘赣边区 NNE 向走滑造山带构造发展样式[J]. 地学前缘，1999，6(4)：263–272.
FU Zhaoren，LI Zijin，ZHENG Dayu. Structural pattern and tectonic evolution of NNE–trending strike–slip orogenic belt in the border region of Hunan and Jiangxi Provinces[J]. Earth Science Frontiers，1999，6(4)：263–272.

[25] 赵宝峰，汪启年，官大维，等. 带状热储地热田温度场特征及控热因素：以湖南省汝城县热水圩地热田为例[J]. 地质通报，2022，41(11)：2035–2046.
ZHAO Baofeng，WANG Qinian，GUAN Dawei，et al. Temperature field characteristics and thermal control factors of banded reservoirs geothermal field：An example of Reshui–town geothermal field，Hunan Province[J]. Geological Bulletin of China，2022，41(11)：2035–2046.

[26] 杨支援，叶见玲. 湖南汝城干热岩赋存条件及资源类型分析[J]. 湘潭大学学报(自然科学版)，2021，43(6)：107–116.
YANG Zhiyuan，YE Jianling. Analysis on occurrence conditions and resource types of hot dry rock in Rucheng，Hunan Province[J]. Journal of Xiangtan University(Natural Science Edition)，2021，43(6)：107–116.

[27] FOURNIER R O. Chemical geothermometers and mixing models for geothermal systems[J]. Geothermics，1977，5(1–4)：41–50.

[28] 王莹，周训，于湲，等. 应用地热温标估算地下热储温度[J]. 现代地质，2007，21(4)：605–612.
WANG Ying，ZHOU Xun，YU Yuan，et al. Application of geothermometers to calculation of temperature of geothermal reservoirs[J]. Geoscience，2007，21(4)：605–612.

[29] 甘浩男，蔺文静，闫晓雪，等. 粤中隐伏岩体区地热赋存特征及热异常成因分析[J]. 地质学报，2020，94(7)：2096–2106.
GAN Haonan，LIN Wenjing，YAN Xiaoxue，et al. Analysis of geothermal occurrence characteristics and origin of the thermal anomalies in the hidden igneous rock area in the central Guangdong[J]. Acta Geologica Sinica，2020，94(7)：2096–2106.

[30] 李学礼. 江西温泉成因与铀矿化关系研究[J]. 华东地质学院学报，1992，15(3)：201–220.
LI Xueli. Study on the relationship between Jiangxi hot–spring genesis and uranium mineralization[J]. Journal of East China Geological Institute，1992，15(3)：201–220.

[31] 钟小平. 湖南省深断裂构造及其与铀成矿的关系[J]. 湖南科技学院学报，2007，28(9)：55–58.
ZHONG Xiaoping. Deep fault structures in Hunan Province and their relationship with uranium mineralization[J]. Journal of Hunan University of Science and Engineering，2007，28(9)：55–58.

[32] 李庆阳，蔡惠蓉，陈彦. 地热场与深部铀矿的关系研究及应用[J]. 中国地质，2010，37(1)：198–203.
LI Qingyang，CAI Huirong，CHEN Yan. The study and application of the relationship between the geothermal field and the deep uranium ore deposit[J]. Geology in China，2010，37(1)：198–203.

[33] ARNEY B H，GOFF F. Evaluation of the hot–dry–rock geothermal potential of an area near Mountain Home，Idaho[R]. Los Alamos：Los Alamos National Laboratory，1982.

[34] HINZE W J，BRAILE L W，VON FRESE R R B，et al. Exploration for hot dry rock geothermal resources in the Midcontinent USA：Hot dry rock conceptual models for exploration，HDR test site investigations，and the Illinois Deep Drill Hole Project[R]. Los Alamos：Los Alamos National Laboratory，1986.

[35] RIMI A，FERNANDEZ M，MANAR A，et al. Geothermal anomalies and analysis of gravity，fracturing and magnetic features in Morocco[J]. International Journal of Medical Robotics + Computer Assisted Surgery Mrcas，2005，10(4)：432–438.

[36] THIEL S，PEACOCK J，HEINSON G S，et al. Electromagnetic monitoring of stimulated hot dry rock systems–modelling and examples from South Australia[C]// AGU Fall Meeting，AGU Fall Meeting Abstracts，2011：S39–44.

[37] SUZUKI K，KAIEDA H，OHTA Y，et al. Seismic reflection method and CSAMT method at Ogachi Hot Dry Rock site[C]//1998：275–279.

[38] GAO Ji，ZHANG Haijiang，ZHANG Senqi，et al. Three–dimensional magnetotelluric imaging of the geothermal system beneath the Gonghe Basin，Northeast Tibetan Plateau[J]. Geothermics，2018，76：15–25.

[39] 张帆. 青藏高原东北缘(大井)–华南(泉州)壳幔电性结构特征及其构造涵义[D]. 北京：中国地质大学(北京)，2013.
ZHANG Fan. The characteristics and tectonic implications of electrical structure in the crust and mantle from the northeastern margin of the Tibetan Plateau (Dajing) to south China

(Quanzhou)[D]. Beijing : China University of Geosciences(Beijing)，2013.

[40] 袁学诚，宋宝春，寿嘉华，等. 台湾–黑水地学断面：1990 年中国地球物理学会第六届学术年会论文集[C]. 武汉：地球物理学会，1990.

[41] 饶家荣，王纪恒，曹一中. 湖南深部构造[J]. 湖南地质，1993(A08)：1–101.
RAO Jiarong，WANG Jiheng，CAO Yizhong. Deep structure in Hunan[J]. Hunan Geology，1993(A08)：1–101.

[42] 陈小东，黄如松，应西荣，等. 湘南桂北地区铀矿地质–水文地球化学找矿标志及找矿模式[J]. 铀矿地质，2002，18(4)：229–234.
CHEN Xiaodong，HUANG Rusong，YING Xirong，et al. Geologic–hydrogeochemical prospecting criteria and prospecting model for uranium deposits in southern Hunan and northern Guangxi[J]. Uranium Geology，2002，18(4)：229–234.

[43] 周立坚. 汝城地热田地热井非线性增温成因浅析[J]. 华南地质与矿产，2016，32(3)：218–223.
ZHOU Lijian. The cause of nonlinear temperature increase of geothermal well in Rucheng geothermal field[J]. Geology and Mineral Resources of South China，2016，32(3)：218–223.

[44] 汪洋，汪集旸，邓晋福，等. 中国大陆地壳和岩石圈铀、钍、钾丰度的大地热流约束[J]. 地球物理学进展，2001，16(3)：21–30.
WANG Yang，WANG Jiyang，DENG Jinfu，et al. Heat flow constraint on the abundance of uranium，thorium and potassium in crust and lithosphere of the continental area of China[J]. Progress in Geophysics，2001，16(3)：21–30.

[45] 章邦桐，谢炳荣，戴永善. 华南花岗岩型铀矿床成矿热源的分析和计算[J]. 矿床地质，1990，9(3)：270–278.
ZHANG Bangtong，XIE Bingrong，DAI Yongshan. The analysis and calculation of metallogenic heat source for granite–type uranium deposits in south China[J]. Mineral Deposits，1990，9(3)：270–278.

[46] 李先福，李建威，傅昭仁，等. 湘赣边区鹿井矿田走滑构造特征分析[J]. 大地构造与成矿学，1999，23(2)：123–129.
LI Xianfu，LI Jianwei，FU Zhaoren，et al. Analysis of strike–slip tectonics in the Lujing Orefield at the border between Hunan and Jiangxi Provinces，China[J]. Geotectonica et Metallogenia，1999，23(2)：123–129.

[47] 李建威，李紫金，傅昭仁，等. 遂川–热水走滑断裂带热异常与热液铀成矿作用[J]. 地质科技情报，2000，19(3)：39–43.
LI Jianwei，LI Zijin，FU Zhaoren，et al. Heat sources and hydrothermal uranlum mineralization in the Suichuan–Reshui strike–slip fault zone[J]. Geological Science and Technology Information，2000，19(3)：39–43.

[48] HUANG Jinli，ZHAO Dapeng. High–resolution mantle tomography of China and surrounding regions[J]. Journal of Geophysical Research，2006，111(B9)：B09305.

[49] 李浩民，吴中海，王浩男，等. 长江中游湖南、湖北地区主要活动断裂及地震地质特征[J]. 地质力学学报，2016，22(3)：478–499.
LI Haomin，WU Zhonghai，WANG Haonan，et al. Geological characteristics of the main active faults and earthquakes in Hunan and Hubei areas，the middle reaches of the Yangtze River[J]. Journal of Geomechanics，2016，22(3)：478–499.

[50] 余辉. 相山火山盆地穿地壳岩浆系统的三维精细结构及动力学背景[D]. 南昌：东华理工大学，2021.
YU Hui. Three–dimensional fine structure and geodynamics setting of transcrustal magmatic system beneath the Xiangshan Volcanic Basin[D]. Nanchang : East China University of Technology，2021.

[51] 陈昌昕，吕庆田，陈凌，等. 华南陆块地壳厚度与物质组成：基于天然地震接收函数研究[J]. 中国科学：地球科学，2022，52(4)：760–776.
CHEN Changxin，LYU Qingtian，CHEN Ling，et al. Crustal thickness and composition in the south China Block : Constraints from earthquake receiver function[J]. Science China Earth Sciences，2022，52(4)：760–776.

doi:10.13301/j.cnki.ct.2024.04.023

湘中冷水江矿区煤s 气地C 条%分析 *

杜 江[1,2], 蔡宁波[1,2], 张良平[1]

(1. 湖南省地球物理地球化学调查所, 长沙 410014; 2. 湖南省地质新能源勘探开发工程技术研究中心, 长沙 410014)

摘 要: 基于勘探资料和实验数据,分析了冷水江矿区煤层含气性和储层特征,估算了煤层气资源量。研究表明: 研究区 3、5 煤层累计厚度 3.5 m。3、5 煤层含气量一般大于 8 m^3/t, 最高可达 20.37 m^3/t。3、5 煤层煤体结构较破碎,孔隙、裂隙发育,渗透性差,吸附性好,储层压力适中。研究区煤层气地质资源量 28.37 亿 m^3,资源丰度 0.61 亿 m^3/km^2,资源前景较好。

关键词: 含气性; 储层特征; 资源量; 冷水江矿区; 煤层气

中图分类号: P618.11 **文献标志码**: A **文章编号**: 1008 – 8725(2024)04 – 114 – 05

Analysis of CBM Geological Conditions in Lengshuijiang Mining Area in Central Hunan Province

DU Jiang[1,2], CAI Ningbo[1,2], ZHANG Liangping[1]

(1. Geophysical and Geochemical Survey Institute of Hunan, Changsha 410014, China; 2. Hunan Geological New Energy Exploration and Development Engineering Technology Research Center, Changsha 410014, China)

Abstract: Based on exploration data and experimental data, analyzes the coal seam gas –bearing property and reservoir characteristics of Lengshuijiang mining area, and estimates the amount of CBM resources. Research shows that the cumulative thickness of the 3rd and the 5th coal seams in the study area is 3.5 m. The gas content of the 3rd and the 5th coal seams are generally greater than 8 m^3/t, up to 20.37 m^3/t. The 3rd and the 5th coal seams have a more broken coal body structure, more developed pores and fissures, poor permeability, good adsorption, and moderate reservoir pressure.The geological resources of CBM in the study area is 28.37×10^8 m^3, and the resource abundance is 0.61×10^8 m^3/km^2, which has good resource prospects.

Key words: gas–bearing property; reservoir characteristics; resources; Lengshuijiang mining area; CBM

0 引言

近年来,我国煤层气产业取得了实质性进展,在山西沁水盆地、内蒙古鄂尔多斯盆地等地基本实现了规模化开发;在南方安徽、贵州、四川等地也取得了重大突破。

湖南省煤层气资源较丰富,地质资源量约 810 亿 m^3,其中湘中地区涟源凹陷的渣渡、金竹山、冷水江等矿区煤层气资源量较大, 地质资源量均超过了 25 亿 m^3,具有较好的勘探开发前景。但是,由于地质条件、勘探投入等因素,湖南省煤层气工作程度较低,各含煤层气矿区基本处于勘查初期阶段,煤矿区煤层含气性、储层物性等参数严重匮乏,因此在湘中地区开展煤层气研究十分有意义。本文主要介绍湘中冷水江矿区煤层气地质条件, 分析该区煤层含气性和储层特征,为该区煤层气勘探开发提供依据。

1 矿区地CAB

冷水江矿区位于涟邵煤田北段中部,行政上隶属于湖南省新化县、冷水江市管辖。矿区南起化溪、北至坪溪,东自中连、西至桑梓,含化溪、大跃、晓云、坝塘、中连、塘冲 6 个井田。地理坐标:北纬 27°38′42″~27°47′30″;东经:113°20′55″~113°29′01″,南北长约 16.3 km,东西宽约 13.3 km。

冷水江矿区北端为受断层切割的不对称向斜盆地构造,在化溪以南,主要构造线为 10°~20°,化溪以北为 45°,延长至笋山以北逐渐近南北走向,呈一向东突起的弧形。南东翼宽阔平缓,一般倾角 15°~30°,具小型波状起伏,西北翼倾角较陡,一般在 50°~70°,局部地段直立或倒转。向斜在资江以南急剧变窄,收敛仰起,在中连一带向斜颇为宽阔,如图 1 所示。东翼北端短轴小褶、断裂极为发育,煤层破坏严重。矿区次级褶曲及断层较发育,构造复杂程度为中等类型。矿区出露的地层由老至新依次为泥盆系上统孟公坳组(D_3m),石炭系下统石磴子组(C_1s)、测水组(C_1c)、梓门桥组(C_1z),石炭系上统壶天群(C_2h)(见图 1)。

* 湖南省自然资源标准项目(2022B02)

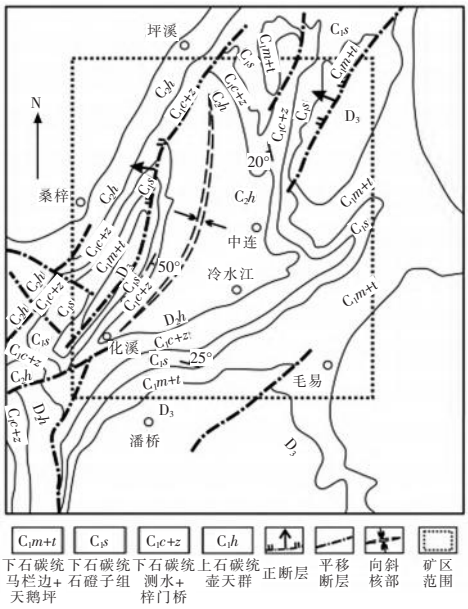

图 1　冷水江矿区地C* 图

2　含煤地s 与煤s

矿区含煤地层为石炭系下统测水组下段(C_1c^1)，全组厚 102~170 m，一般厚约 130 m，主要发育粉砂岩、细砂岩、泥质砂岩和砂质泥岩。含煤 7 层，自上而下命名为 1、2、3、4、5、6、7 煤层，具工业价值煤层 4 层，其中 2、4 煤层局部可采，3、5 煤层为全区主要可采煤层，如图 2 所示。

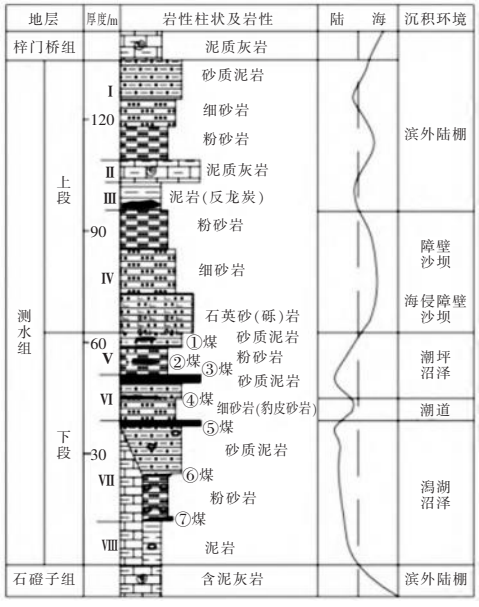

图 2　冷水江矿区5 合DE 图

3 煤层位于测水组下段(C_1c^1)中部或中下部，上距 2 煤层约 15 m，厚 0~15.87 m，一般厚 1.5 m，煤层结构较复杂，夹矸 1~8 层，矿区内最大埋藏深度约 1 050 m。5 煤层位于测水组下段(C_1c^1)中部，厚 0~11.44 m，一般 2.0 m，结构复杂，夹矸 1~10 层，矿区内最大埋藏深度约 1 100 m。

3　煤s 含气性特征

冷水江矿区主采煤层为 3、5 煤层，总体上煤层气含量较大，中浅部 3 煤层含气量 1.07~20.37 m^3/t，浓度 18.3%~92.41%，晓云、中连井田含气量一般大于 8 m^3/t；中浅部 5 煤层含气量 0.69~20.10 m^3/t，浓度 21.5%~93.33%，晓云、中连井田含气量一般大于 8 m^3/t，如表 1、图 3 所示。冷水江矿区煤层埋深与含气量关系图如图 4 所示。冷水江矿区煤层厚度与含气量关系图如图 5 所示。

表 1　冷水江矿区煤s 气含R 统计表

井田	煤层	含气量/$m \cdot t^{-1}$	浓度/%
化溪	3	4.71~5.58	53.7~79.74
	5	6.20~9.79	85.8~90.24
晓云	3	7.95~20.37	86.41~92.41
	5	7.32~17.4	89.09~93.33
中连	3	2.63~14.50	18.53~85.53
	5	4.20~20.10	69.41~98.17
塘冲	3	1.07~3.48	29.0~48.07
	5	1.48~4.37	21.5~72.95
大跃	3	2.46~6.24	24.59~79.10
	5	0.69~7.8	25.31~90.98
坝塘	3	2.53~7.9	26.57~78.21
	5	3.16~8.98	78.32~83.39

煤层气富集规律：(1)南段比北段高，东翼比西翼高，具体为化溪、晓云、中连井田煤层气含量较高，大跃、坝塘、唐冲井田埋深较浅，煤层气含量较低(见表 1、图 3)。(2)一般认为煤层气含量随埋深逐渐增大，将矿区内煤层埋深与含气量进行拟合，两者呈正相关；且 5 煤层含气量一般高于 3 煤层含气量(见表 1、图 4)。(3)煤层气含量与煤层厚度密切相关，一般煤层厚度大则煤层气含量高，将矿区内煤层厚度与含气量进行拟合，两者呈正相关(见图 5)。此外，井下观察瓦斯突出部位常出现在煤包和煤层厚度变化地段。(4)煤层气含量与煤层本身的结构有关，绝大部分糜棱煤、粒状煤、鳞片状，煤层气含量较高。

4　煤储s 特征

4.1　宏观煤岩特征与煤体结构

冷水江矿区 3 煤、5 煤，煤岩特征近似，颜色一般为黑色或灰黑色，条痕淡黑色或褐灰色，玻璃或金属光泽；细–中条带状结构，局部为线理状、鳞片状结构；参差状、阶梯状或贝壳状断口。宏观煤岩类型以半亮型煤和半暗型煤为主，次为暗淡型煤，光亮型煤不常见。

3 煤多为粒状、少数块状、线理状、透镜状，机械强度低，受力易碎小块、薄片及粉状，裂隙为薄膜状方解石充填，局部见构造镜面，多为碎粒煤，少量为碎裂煤、糜棱煤。5 煤多为粒状，局部块状，用手捏易碎，滑动面发育，镜下见揉皱褶曲，多为碎粒煤，少量为碎裂煤、糜棱煤。

4.2　显微煤岩特征

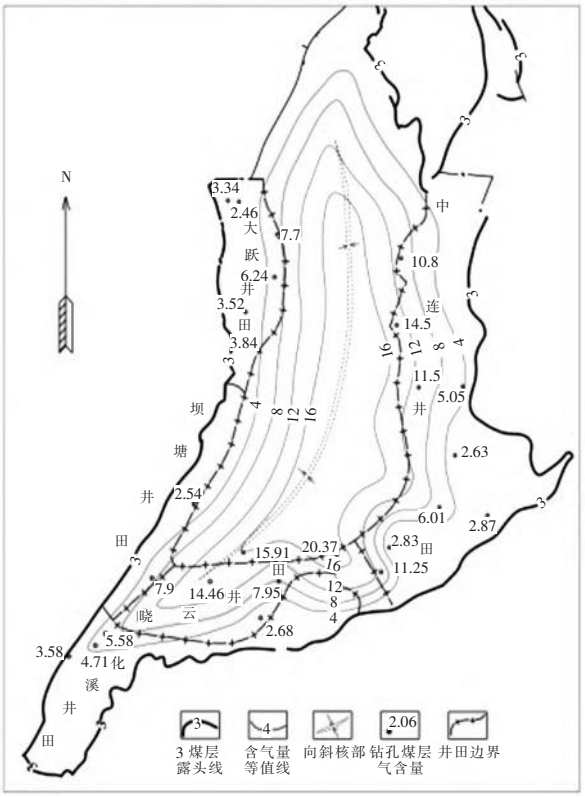

(a)3 煤层含气量等值线图

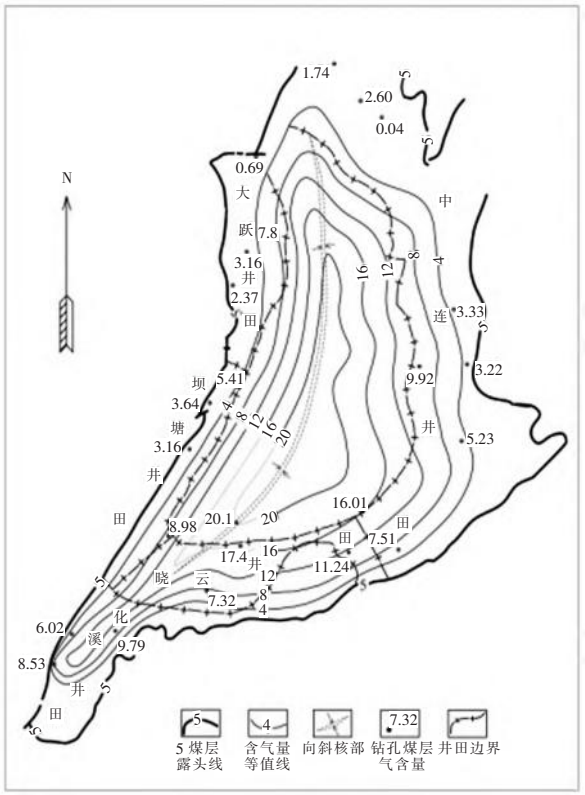

(b)5 煤层含气量等值线图

图 3　冷水江矿区煤s 含气R 等值线图

3、5 煤层显微组分以镜质组为主,次为惰质组,几乎不含壳质组。镜质组主要由均质镜质体和基质镜质体组成,次为结构镜质体,其余组分少量。惰质组由丝质体或半丝质体组成,或主要由粗粒体组成。无机组分主要为石英、黏土矿物,次为方解石和微量黄铁矿、赤铁矿。煤的最大镜质组反射率 $R_{o,max}$= 2.37%~3.51%,平均 2.95%,为无烟煤二号,高变质程度的煤孔裂隙较发育,提高了煤的渗透性和基质孔隙连通性。

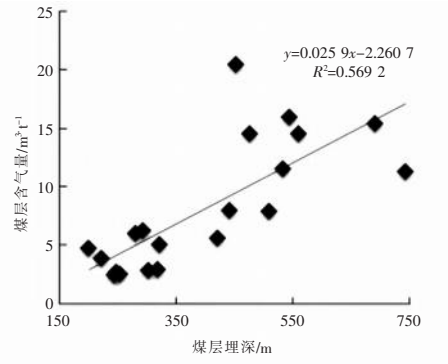

(a)3 煤层

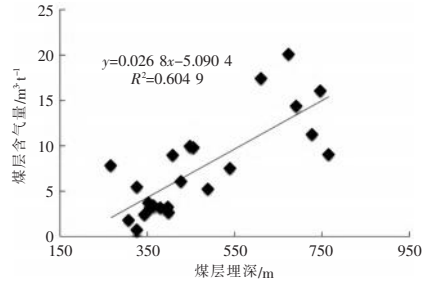

(b)5 煤层

图 4　冷水江矿区煤s2a　与含气R 关系图

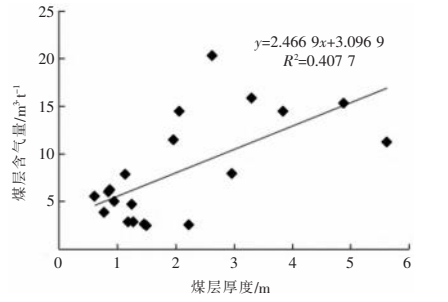

(a)3 煤层

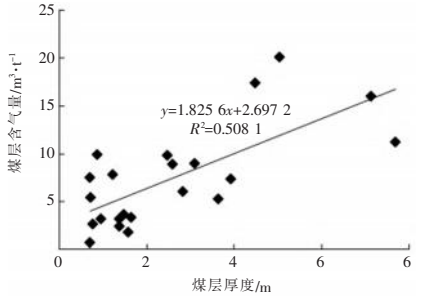

(b)5 煤层

图 5　冷水江矿区煤s 厚度与含气R 关系图

4.3　孔裂隙特征

(1)孔隙特征

煤是一种多孔隙的物质，利用扫描电镜观察和研究煤储层中的微孔隙和微裂隙是一种行之有效的方法。冷水江矿区 3 煤层显微组分以镜质组为主，其次为丝质体，矿物质有伊利石和高岭石。孔隙为残留胞腔孔，发育静压裂隙、层间裂隙、层面裂隙，剪性裂隙(X 形)，如图 6(a)、图 6(b)所示。煤体显微构造有的原生结构完整，有的煤体已变形，角砾，碎粒，糜棱质多见。5 煤组分以镜质组为主，沥青质体较多，含矿物质，孔隙特征与 3 煤相差不大，局部可见裂隙，组分间隙，如图 6(c)、图 6(d)所示。3 煤层孔隙度 8.62%，5 煤层孔隙度 11.04%。

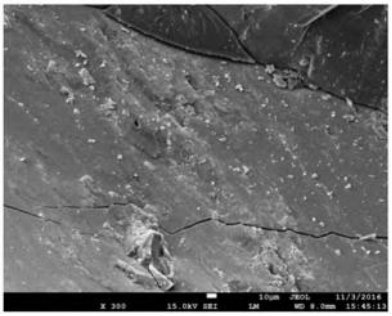

(a)层面、层间裂隙，镜质组为主(3 煤)

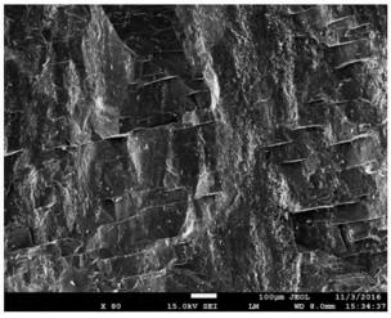

(b)垂直层理静压裂隙，原生结构(3 煤)

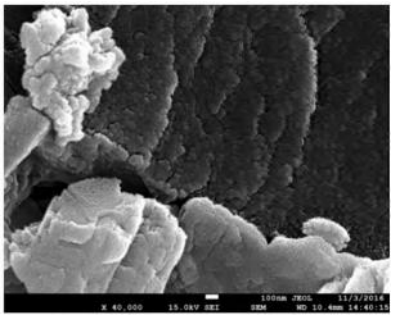

(c)沥青质体的球粒结构(5 煤)

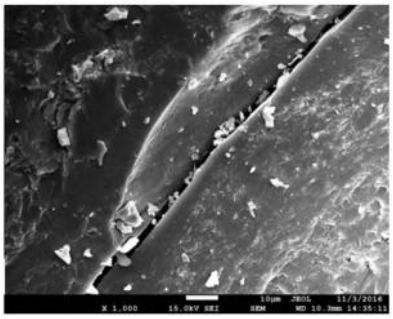

(d)局部裂隙，有充填物(5 煤)

图 6　煤s.　观w 裂隙特征图

(2)比表面积与孔隙类型

3 煤层比表面积 0.532 m^2/g，BJH 最大孔径 4.048 nm，总孔体积 1.436×10^{-3} cm^3/g，液氮吸脱附曲线如图 7(a)所示。煤低温液氮吸附曲线呈倒 S 形，属于 IUPAC 分类方案中的 IV 型曲线。表明孔隙类型以两端开口的孔和墨水瓶孔为主。5 煤层比表面积 24.987 m^2/g，BJH 最大孔径 4.074 nm，总孔体积 20.99×10^3 cm^3/g，液氮吸脱附曲线如图 7(b)所示。煤低温液氮吸附曲线呈倒 S 形，属于 BET 分类方案中的 IV 型曲线。孔隙类型以两端开口的孔和墨水瓶孔为主，同时含有少量的一端开口的孔，大孔不发育。总的来说，5 煤具有更大的比表面积和孔体积，有利于吸附更多的甲烷气体。二者孔隙类型相同，以两端开口的孔和墨水瓶孔为主。

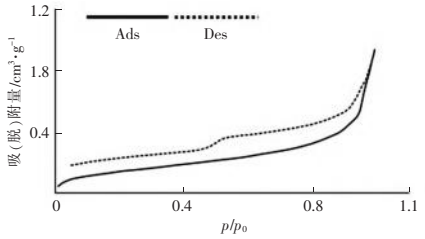

(a)3 煤层

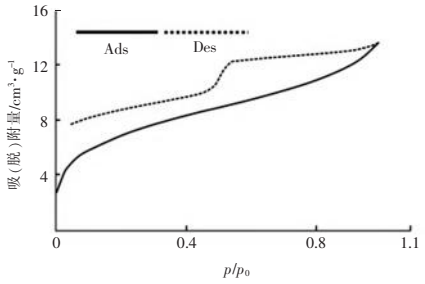

(b)5 煤层

图 7　煤s 吸附脱附曲线图

p. 脱附压力　p_0. 吸附压力

(3)渗透性特征

冷水江矿区 3、5 煤层煤体结构破碎，3 煤层为碎粒煤，局部为糜棱煤，5 煤层多为糜棱煤；渗透率低，3 煤层渗透率 0.005~0.02 mD，5 煤层渗透率 0.001~0.01 mD。

4.4　吸附性特征

依据《煤的甲烷吸附量测定方法(高压容量法)》(MT/T 752—1997)，测试得到 2 组压力和吸附量的数据对，根据数据对拟合得到兰氏体积 V_L 和兰氏压力 p_L。3 煤层兰氏体积为 30.82 mL/g，总体较大，表明 3 煤层具有较强的吸附能力，如表 2 所示。5 煤层吸附性与 3 煤层相当。

4.5　储层压力

相邻涟参一井测水组 3、5 煤层的储层压力分别为 3.74、4.38 MPa，储层压力梯度分别为 9.1 kPa/m

表2　等温吸附试验结果表(空气干燥基)

煤层	煤阶	温度/℃	V_L/mL·g^{-1}	p_L/MPa
3	WY	25	30.82	1.78
		50	26.06	2.34
5	WY	25	30.62	1.86
		50	26.89	2.85

和9.2 kPa/m,属常压储层,如表3所示。

表3　涟参一井煤储s 压力参数表

钻井	煤层	埋深/m	储层压力/MPa	储层压力梯度/kPa·m^{-1}	压力类型
涟参一井	3	409.63	3.74	9.1	正常
	5	478.35	4.38	9.2	正常

5　资源R 估算

运用体积法,分别估算3、5煤层煤层气地质资源量,预测过程中要求:(1)以地质边界或人为技术边界划分估算块段;(2)煤层厚度大于0.6 m,含气量大于4 m³/t;(3)预测深度为风化带边界(或采空区边界)~埋深600 m、600~1 000 m、1 000~1 500 m这3个区间。估算结果,冷水江矿区煤层气地质资源可达28.37亿m³,如表4所示,资源丰度0.61亿m³/km²,资源前景可观。煤层气地质资源量

$$G=\sum_{i=1}^{n}0.01A_iH_iD_iC_i$$

式中　A_i——块段i含气面积,km²;

H_i——块段i煤层平均净厚度,m;

D_i——块段i煤的空气干燥基平均质量密度,t/m³;

C_i——块段i煤的空气干燥基平均含气量,m³/t。

6　结'

(1)冷水江矿区位于测水组涟源沉积中心,3、5煤层为主采煤层,3煤层一般厚度1.5 m,5煤层一般厚度2.0 m,累计平均厚度3.5 m。

表4　冷水江矿区煤s 气地C 资源估算表

煤层	深度/m	块段面积/km²	煤炭资源量/万t	煤层含气量/m³·t^{-1}	煤层气资源量/亿m³	资源类别
3	<600	11.34	3 488	12.3	4.29	预测
	600~1 000	32.56	7 614	14.3	10.91	预测
	1 000~1 500	2.72	532	24.0	1.28	预测
	合计	46.62	11 634		16.47	预测
5	<600	14.13	3 409	9.1	3.10	预测
	600~1 000	23.01	3 623	15.7	5.70	预测
	1 000~1 500	8.31	1 288	24.0	3.10	预测
	合计	45.45	8 320		11.90	预测
总计		46.62	19 954		28.37	预测

(2)3、5煤层含气量较大,中浅部3煤层含气量为1.07~20.37 m³/t,5煤层含气量为0.69~20.10 m³/t,晓云、中连井田含气量一般大于8 m³/t;中深部煤层含气量逐渐变大,与埋深呈正相关。

(3)3、5煤层显微组分以镜质组为主,宏观煤岩类型以半亮型煤和半暗型煤为主,变质程度高,均为无烟煤;煤体结构较破碎、孔裂隙较发育、渗透性差、吸附性好,煤储层压力适中,煤储层特征一般。

(4)冷水江矿区煤层气地质资源28.37亿m³,资源丰度0.61亿m³/km²,资源前景较好。

参(　文献:

[1]天工. 我国3个煤层气产业化基地启动建设[J]. 天然气工业,2018,38(10):89.

[2]门相勇,娄钰,王一兵,等. 中国煤层气产业"十三五"以来发展成效与建议[J]. 天然气工业,2022,42(6):173-178.

[3]王小清,龙新良,赵训林. 湘中石炭系测水组煤系特征及煤炭资源预测[J]. 煤田地质与勘探,2012,40(6):8-12.

[4]芮昀,刘成,王建君. 川南地区筠连区块乐平组煤层气成藏条件与成藏模式研究[J]. 煤炭技术,2019,38(7):87-89.

[5]杜志强,吴艳. 六盘水杨梅树向斜煤层气地质条件及开发潜力评价[J]. 中国煤炭地质,2019,31(7):27-31.

[6]何金坪,汪小勇,骈红野. 贵州省织金县中寨井田煤层气分布特征及资源潜力[J]. 现代矿业,2018,34(9):65-69.

作)*+　:杜江(1988-),四川南充人,高级工程师,硕士,研究方向:非常规天然气地质,电子信箱:1025774576@qq.com.

,　任编辑:李富文　-　稿日期:2023-04-25

Acta Geologica Sinica (English Edition), 2024, 98(4): 992–1006

The Geology, Fluid Inclusions, and O-S Isotopes of the Mibei Gold Deposit, Hunan Province, Southern China

XUE Wenhao[1], LIANG Yayun[1, *], LI Xiaofeng[2, 3], LI Mingyi[4], XIE Wenbo[2, 3], PENG Xue[2, 3], XIA Rui[4, 5], HE Hongsheng[2, 3] and XIAO Jincheng[2, 3]

[1] *School of Civil and Resource Engineering, University of Science and Technology Beijing, Beijing 100083, China*
[2] *Geophysical and Geochemical Survey Institute of Hunan, Changsha 410116, China*
[3] *New Geological Energy Exploration and Development Engineering Technology Research Center of Hunan, Changsha 410116, China*
[4] *State Key Laboratory of Geological Processes and Mineral Resources, China University of Geosciences (Beijing), Beijing 100083, China*
[5] *Comprehensive Survey Command Center for Natural Resources, China Geological Survey, Beijing 100055, China*

Abstract: The Mibei gold deposit, located in the southwestern part of the Xuefengshan uplift zone, the middle section of the Jiangnan orogenic belt in southern China, has estimated gold resources of approximately seven tons. This deposit is primarily a quartz vein-type gold deposit, with ore bodies occurring mainly within Neoproterozoic metasediments. The main metallic minerals in the ore are pyrite, chalcopyrite, and arsenopyrite. In this study, the petrography and microthermometry of ore-forming fluid inclusions, oxygen isotopes of gold-bearing quartz, and sulfur isotopes of gold-bearing sulfides and arsenopyrite were analyzed. Three types of fluid inclusions were identified: type Ia three-phase inclusions comprising vapor and two phases of liquids (V_{CO2} + L_{CO2} + L_{H2O}), type Ib two-phase liquids (L_{CO2} + L_{H2O}), type II two-phase vapor-rich inclusions (V/V + L > 50%), and type III pure liquid inclusions. Type I inclusions were heated uniformly to the liquid phase, type II inclusions were heated uniformly to the gas phase, and type III inclusions were heated without change. In general, the temperature range of homogenization to liquid phase of fluid inclusions in the Mibei gold deposit is 204–227℃. The salinity of the inclusion ranges from 4.6 to 12.2 wt% NaCl equiv. The $\delta^{18}O_{SMOW}$ of gold-bearing quartz varies from 16.9‰ to 17.5‰. The $\delta^{18}O_{H2O}$ of gold-bearing quartz are varied from 6.5‰ to 7.5‰. The $\delta^{34}S$ values of gold-bearing pyrite range from 1.7‰ to 6.8‰. The $\delta^{34}S$ values of gold-bearing arsenopyrite range from 5.6‰ to 5.9‰. The $\delta^{34}S$ values of pyrite from wall rocks slate range from 6.4‰ to 11.6‰. This evidence implies that the ore-forming fluids of the Mibei gold deposit originated from magmatic-hydrothermal processes, mixing with minor S from the surrounding metasediments. Combined with the evolution of the Jiangnan orogenic belt, due to the magmatic and tectonic activities of the Xuefengshan uplift during the Caledonian period, the fault seal mechanism controlled the ore-forming process. Overall, the Mibei gold deposit is more akin to a magmatic-hydrothermal gold deposit.

Key words: ore-forming fluid, ore genesis, Mibei gold deposit, Xuefengshan uplift zone, Jiangnan orogenic belt

Citation: Xue et al., 2024. The Geology, Fluid Inclusions, and O-S Isotopes of the Mibei Gold Deposit, Hunan Province, Southern China. Acta Geologica Sinica (English Edition), 98(4): 992–1006. DOI: 10.1111/1755-6724.15184

1 Introduction

The Jiangnan orogenic belt is rich in mineral resources, including gold (Lu et al., 2020; Zhang L et al., 2020; Han et al., 2021; Li W et al., 2021), antimony (Li H et al., 2018), chromite (Liu et al., 2021), manganese (Pei et al., 2017; Yang et al., 2022), tungsten (Chen et al., 2012; Zhang Y et al., 2020) and more. Geochronology has proven that gold mineralization of the Jiangnan orogenic belt mainly occurred during the Caledonian period (Peng et al., 2003) and the Indosinian–Yanshanian period (Deng et al., 2017; Li W et al., 2021). However, there is significant controversy regarding the genesis of ore deposits (Hu et al., 2017; Xu et al., 2017; Zhang et al., 2018). In the Jiangnan Orogen, Au and Au-Sb deposits are classified into several types, including orogenic deposits (Zhang et al., 2018; Zhang Y et al., 2020), magmatic-hydrothermal deposits (Hu et al., 2017; Li W et al., 2018), stratiform hydrothermal deposits (Gu et al., 2005), and intracontinental tectonic reactivation-type deposits (Xu et al., 2017). The Hunan polymetallic mineralization province, located in the middle section of the Jiangnan orogenic belt, is rich in gold deposits. Within its borders, 58 large- to small-scale gold deposits have been discovered, with a cumulative confirmed gold reserve of 600 t (Huang et al., 2020). The Xuefengshan uplift zone is one of the most important structural units in this region and hosts several significant gold deposits, such as the Woxi, Yuhengtang, Xingfengshan, Mobin, and Taojinchong gold deposits (Yan et al., 1994; Ding and

* Corresponding author. E-mail: yayunl@yeah.net

Wang, 2009; Bai et al., 2021; Li W et al., 2021; Dai et al., 2022). Thus, the different ages and genetic types of gold deposits developed in the Xuefengshan uplift zone could provide effective information for tracing the genesis of gold mineralization in the Jiangnan orogenic belt.

The Mibei gold deposit, along with the Mobin, Xiaojia, and Taojinchong gold deposits, is located in the southwestern part of the Xuefengshan uplift zone. Mineralization in the Mibei gold deposit consists of gold-bearing quartz veins hosted within the second section of the Wuqiangxi Formation of the Neoproterozoic Banxi Group. Although basic geological research has been conducted on the Mibei gold deposit, such as the distribution of ore bodies and the occurrence of gold (Xie, 2014; Yang, 2019), the fluid source and ore genesis still need to be discussed. The petrography and microthermometry of fluid inclusions, oxygen isotopes of quartz, and sulfur isotopes of pyrite in the Mibei gold deposit were analyzed in this study, providing a new perspective of the characteristics and sources of ore-forming fluids. Additionally, this study combines the regional geological context to elucidate the ore-forming mechanisms and deposit types of the Mibei gold deposit. This study serves as a crucial foundation for a deeper understanding of ore-forming mechanisms during the Caledonian period in the Xuefengshan uplift belt, Hunan polymetallic mineralization province. Finally, the genetic type of the gold deposits was determined, referring to the significant magmatic activity in the Jiangnan orogenic belt.

2 Geological Setting

The study area is situated in the southwestern segment of the Xuefengshan metallogenic belt (Fig. 1b), which is located along the eastern margin of the Yangtze Block and adjacent to the Yangtze Block and the South China fold belt junction zone (Fig. 1a; Wang et al., 2005; Zhang et al., 2009; Zheng et al., 2022). The exposed strata in the region primarily consist of the Neoproterozoic, Cambrian, Cretaceous, and Quaternary strata (BGMRHN, 1988). The Neoproterozoic strata consist of a lower segment comprised of slates of the Lengjiaxi Group and its equivalents, an intermediate segment comprised of slates and metasedimentary rocks of the Banxi Group, and an upper segment of Ediacaran formations. The Cambrian strata are well developed in the study area, primarily in the southern part (Chu et al., 2012). The dominant rock type is carbonaceous shale, followed by siliceous rock (Liu et al., 2022). The lower Cambrian segment conformably overlies the Ediacaran Formations. From bottom to top, it is divided into the Aoxi and Huaqiao formations (Wang C S et al., 2013). The Aoxi Formation is primarily composed of carbonaceous shale, with limestone as the secondary lithology, whereas the Huaqiao Formation consists of limestone interbedded with carbonaceous shale. The upper segment of the Cambrian strata can be divided from bottom to top into the Chefu, Bitiao, and

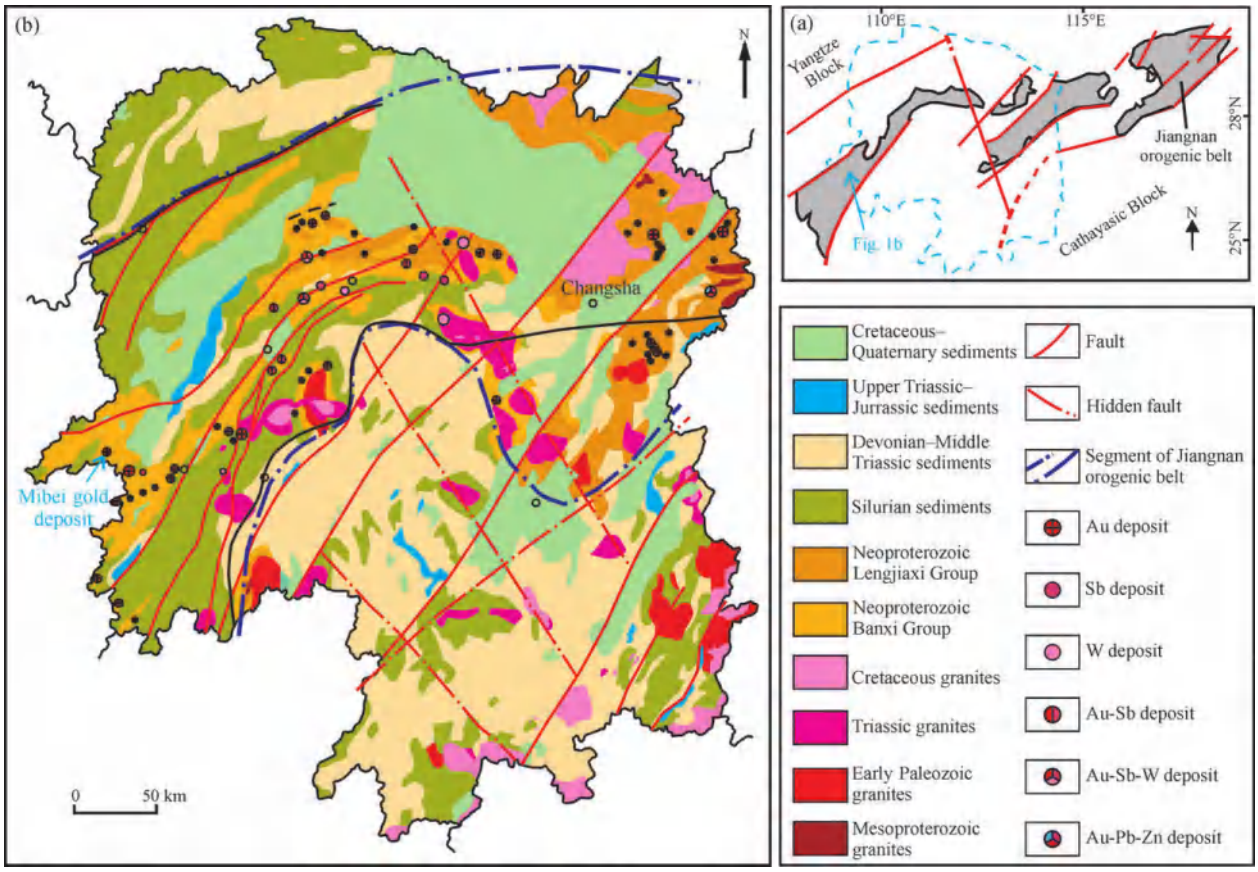

Fig. 1. (a) Sketch map showing tectonic units of the middle of Jiangnan orogenic belt (modified after Mao et al., 1997), (b) simplified geological map of Hunan Province (modified after Hunan Institute of Geology Survey, 2017; Bai et al., 2021).

Tianjiaping formations. These formations consist of marlstone and argillaceous limestone from bottom to top. The Permian strata are limestone, exposed in the southern Lishan–Kezhai area, and are unconformably overlain by the Banxi Group (Zhang et al., 2010). Cretaceous strata of the DongJing Formation are present on the northern edge of the area and around Xinhuang County. The lower part of this formation consists of a conglomerate overlain by light purple-red sandstone, showing an angular unconformity with the underlying strata (Wang et al., 2022). The Quaternary strata are mainly distributed on terraces along riverbanks and gully valleys. They consist of sandy clay, sub-clay, and gravel-sand layers, among others.

The region has experienced a complex tectonic history since the Paleoproterozoic, including the Caledonian, Yanshan, and Indosinian movements, resulting in an intricate structural pattern (Li and Li, 2007; Chu et al., 2015; Wang et al., 2020). The main framework of this area is composed of northeast-northeast to east-northeast-trending fold and fault structures (Chu et al., 2012). The northeast-trending structures primarily consist of a series of northeast-trending fold axes, and compressional and compressional-shear faults. These northeast-trending structures are most widely distributed within the territory of Xinhuang County and include features such as the Mawang anticline, Tiantang–Hetan syncline, Jinchangxi anticline, and Xiashenzhu syncline. The major compressional reverse faults in the northeast direction include the Dalong thrust, Fulu thrust, Huashan reverse, Yanjia, Mibei, and Luoyan reverse faults. The NE-trending folds and faults developed during the Caledonian period, and the NNE-trending folds dominated the thrust nappe-fold belt during the Yanshanian period (Fang et al., 2002). Additionally, there are a few small-scale northwest to north-northwest trending fault structures in the area, likely associated with compressional shear faults, with predominant characteristics of extension and extension-shear (Hunan Metallurgy Team 245 et al., 1975).

The Jiangnan orogenic belt, an accretionary orogenic belt, is located along the suture zone between the Yangtze Craton and the Cathaysia Block; its development occurred between 870 and 805 million years ago (Zhao and Cawood, 1999; Yao et al., 2019; Mao et al., 2022). The magmatic and tectonic activities that occurred between 830 and 770 million years ago in the Jiangnan orogenic belt are thought to represent a transition from subduction to collision with the orogenic belt (Chen et al., 2018; Huang et al., 2019; Yan et al., 2021), which is primarily characterized by ductile shear deformation (Yao et al., 2021). Gold mineralization in the Jiangnan Orogen occurred primarily during the Caledonian (~420 Ma) and Yanshan periods (~200 Ma) (Peng et al., 2003; Deng et al., 2017; Bai et al., 2021; Du et al., 2022; Zhu et al., 2023). The Xuefengshan uplift, located in the central part of the Jiangnan Orogen, contains gold and gold-antimony deposits primarily associated with the magmatic-tectonic activities during the Caledonian and Indosinian–Yanshan periods (Huang et al., 2020). During the Caledonian and Indosinian–Yanshan periods, the southern section of Xuefengshan underwent significant compressional deformation, resulting in NE-NNE trending folds and reverse faults (Bai et al., 2014), playing a crucial role in gold mineralization within the uplifted zone (Peng, 1999; Lu et al., 2005).

The region is rich in mineral resources, with the discovery of over 20 different minerals including gold, lead-zinc, copper, potassium, vanadium, scheelite, cadmium, refractory clay, quartz crystals, phosphorus, iron, mercury, antimony, cobalt, molybdenum, nickel, manganese, silver, rare earth elements, rare metals, limestone, and dolomite (Li Y H et al., 2021; Lü et al., 2021; Bai et al., 2022). Gold deposits are primarily located in the Mibei area, whereas scheelite, lead-zinc, vanadium-molybdenum, and phosphorus deposits are predominantly found in the Gongxi area of Xinhuang County.

3 Ore Geology

The main exposed rock formations in the Mibei gold mine area are the second unit (Pt*bnw*^{2}) of Wuqiangxi Formation of the Neoproterozoic Banxi Group, along with a small amount of Quaternary deposits (Fig. 2a). Pt*bnw*^{2} comprises grayish-green and bluish-gray thinly to thickly bedded fine-grained sandstone containing tuffaceous and banded fine-grained sandstone. It exhibits ribbon-like and banded structures with alternating sandstone and mudstone layers. The Quaternary consists mainly of clay, sub-clay, and weathered rock fragments that are predominantly distributed on both sides of the streams as alluvial deposits. The main structural feature of the area is the Jinchangxi anticline, which is part of a regional anticline with an overall trend of approximately 38 °–43 °. The Jinchangxi anticline serves as the primary ore-controlling structure in the mining area, and gold ore bodies are located within the fractured zones in the core and on both flanks of the anticline. Magmatic rocks are not well developed in the area, with only limited occurrences of sodium-rich silicified rocks and a few hydrothermal calcite and quartz veins found in clastic rocks.

The Mibei gold deposit in Xinhuang County, Hunan, has an estimated gold resource of approximately seven tons (BGMRHN, 2013). This deposit is primarily a quartz vein-type gold deposit, with orebodies occurring mainly within the Pt*bnw*^{2}. The orebodies consist of discontinuous, layer-like veins composed of a network of vein-like and vein-shaped quartz (Fig. 2b). The boundaries between the surrounding rocks and orebodies are visible, with the orebodies primarily occurring at the intersection of the lower part of the fractured zones and joint fractures. The orientation of the orebodies is predominantly north-northeast. The thickness of the orebodies varies, with the thickest being approximately 1 meter and the thinnest ranging from a few centimeters to over 10 cm, generally averaging about 50–60 cm. In the mining area, a total of 6 gold-bearing quartz veins have been discovered, all trending north-northeast, which were formed in the Caledonian period (Bai et al., 2014), with lengths ranging from 130 to 1000 m and widths extending more than 50 m (Fig. 3). The main ore minerals are pyrite, chalcopyrite, and arsenopyrite. The gangue minerals primarily consist of

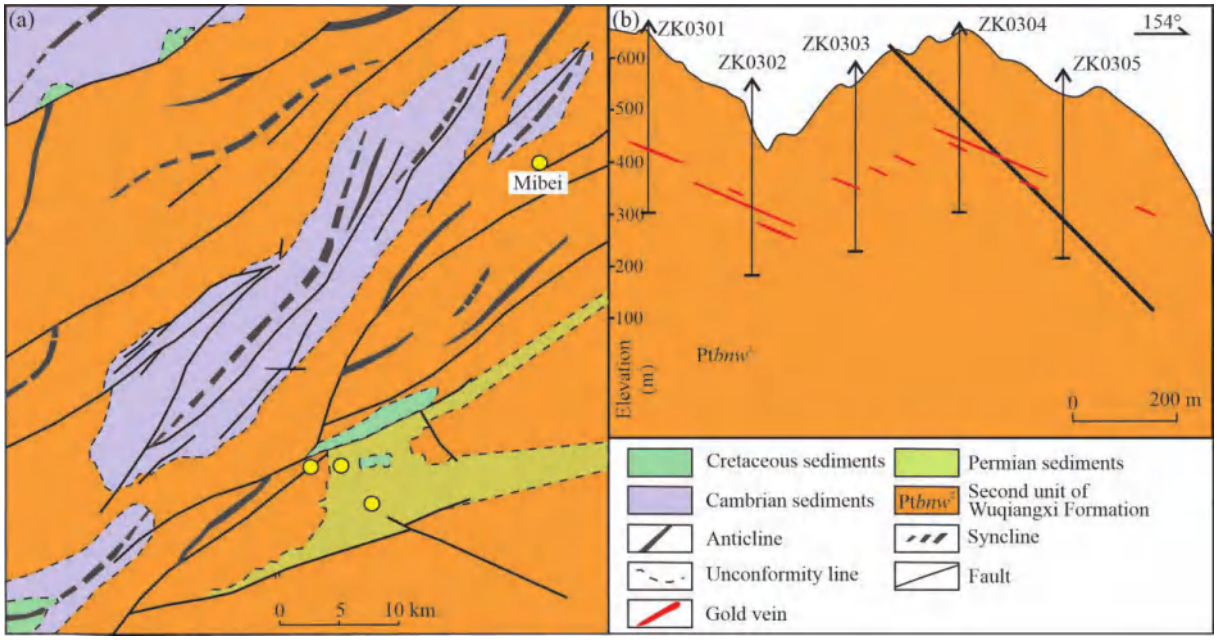

Fig. 2. (a) Geological map of the Mibei gold deposit (modified after Li and Yu, 1991; Xie, 2014); (b) Mibei gold mine exploration profile line chart.

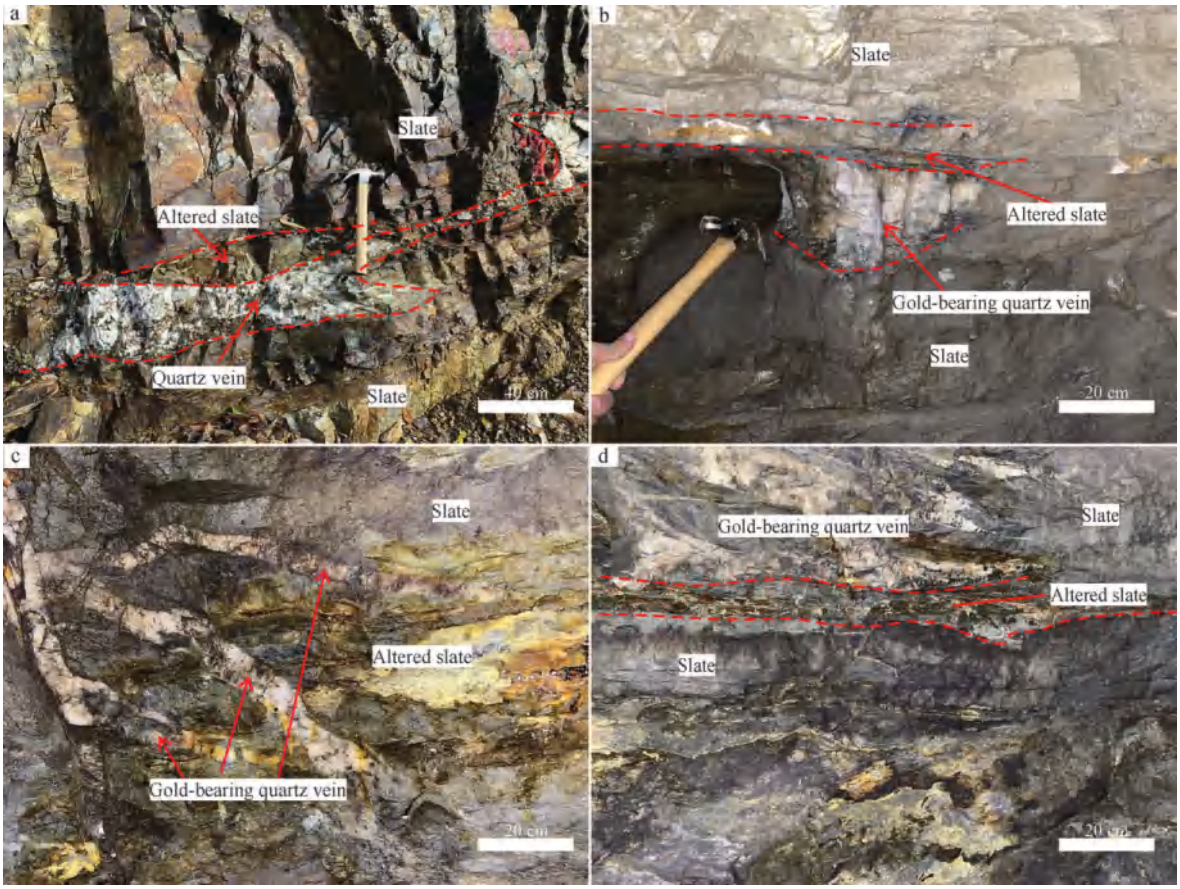

Fig. 3. The distribution characteristics of ore bodies in the Mibei mining area.
(a) The boundary between the surrounding rock and the quartz vein can be seen in the outcrop of the Mibei Township; (b) the ore bodies in the Mibei mining area are formed between slate and quartz veins; (c) Mibei gold-bearing quartz vein; (d) the ore body between quartz vein and surrounding rock is produced along the layer.

quartz, calcite, and plagioclase (Fig. 4). The ore structures are mainly composed of inclusions, replacement, fracturing, and star-like structures. Depend on the mineral assemblages and the crosscut relationship, the mineralization of the Mibei gold deposit is mainly divided into three stages: the quartz-pyrite stage (Stage I), the early stage of gold mineralization, is characterized by the emergence of a small amount of pyrite and a large amount of quartz (Fig. 4a); the pyrite-arsenopyrite-chalcopyrite-gold-quartz-sericite stage (Stage II), the main metallogenic stage of gold mineralization, are characterized by the appearance of more pyrite, arsenopyrite, and chalcopyrite in the quartz veins (Fig. 4b–d); pyrite-quartz-calcite stage (Stage III), the late stage of mineralization, developed the pyrite, calcite, chlorite (Fig. 4e, f). Within approximately 1 meter of either side of the ore veins, there are observable alterations in the rock formations, including sericitization, carbonate alteration, arsenopyrite alteration, chloritization, and epidotization (Fig. 5).

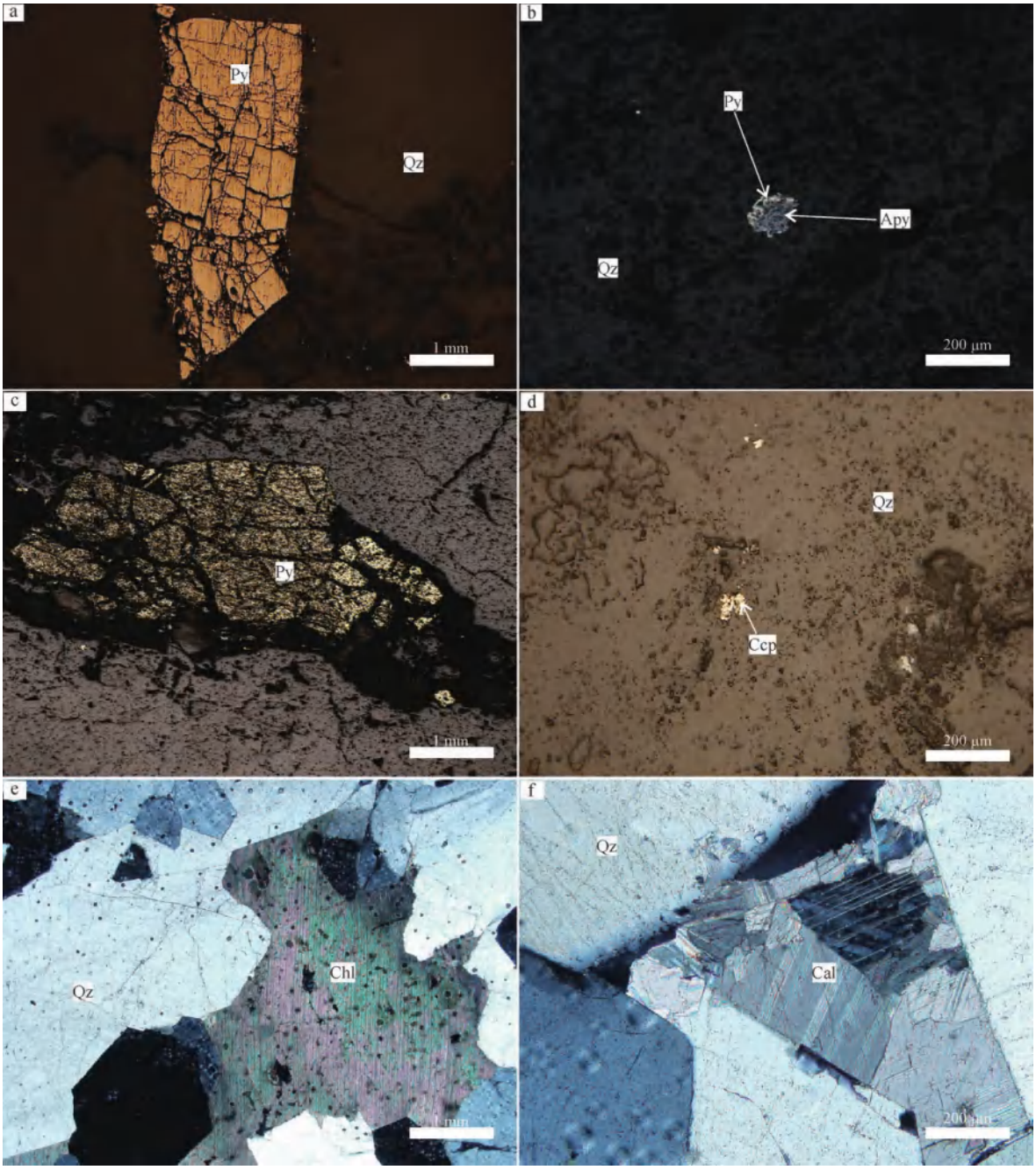

Fig. 4. Mineral composition and structural characteristics of the Mibei gold deposit under microscope.
(a) Visible quartz with pyrite (reflected light); (b) quartz arsenopyrite is embedded by pyrite (reflected light); (c) disseminated pyrite in quartz (reflected light); (d) a small amount of chalcopyrite can be seen in quartz (reflected light); (e) plagioclase is metasomatized into chlorite; (f) visible lattice twin plagioclase. Apy: arsenopyrite; Cal: calcite; Ccp: chalcopyrite; Chl: chlorite; Py: pyrite; Qz: quartz.

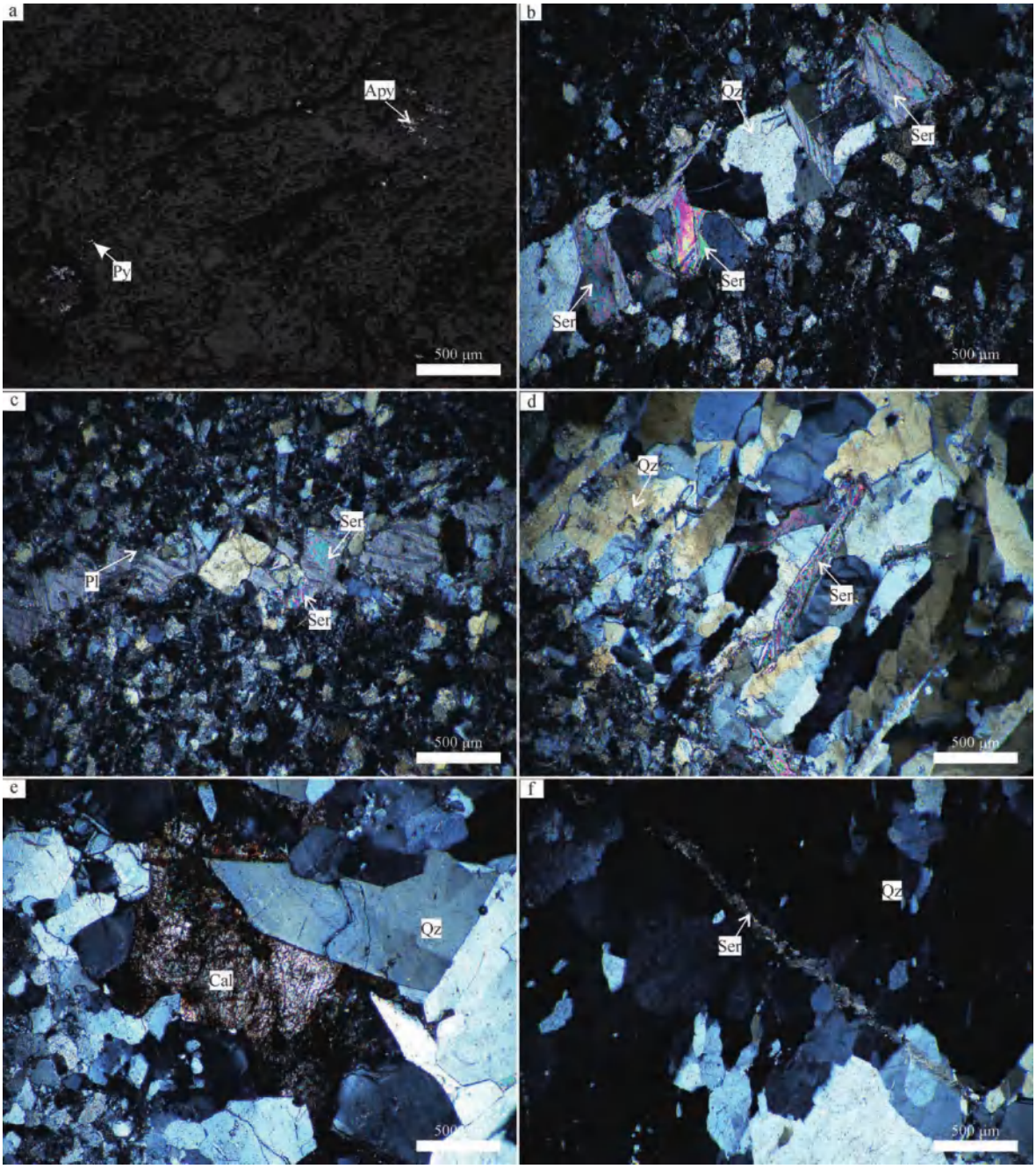

Fig. 5. Alteration characteristics of the Mibei gold deposit.
(a) Quartz arsenopyrite and pyrite are spotted (reflected light); (b) quartz vein alteration zone in ore-bearing surrounding rock, plagioclase metasomatism sericitization to form sericite; (c) plagioclase and a small amount of sericite coexist in the surrounding rock of the ore-hosting rock, and the plagioclase sericite metasomatizes to form sericite (transmitted light); (d) plagioclase sericitization (transmitted light) in quartz; (e) calcite chloritization-propylitization (transmitted light); (f) sericite veins (transmitted light) occur in quartz . Apy: arsenopyrite; Py: pyrite; Qz: quartz; Ser: sericite; Pl: plagioclase; Cal: calcite.

4 Sampling and Analytical Methods

Two unweathered slate wall rocks and three mineralized slates were collected from the regional surface of the gold deposit. Eighteen samples from the main mineralization stages were collected from underground workings (with elevation of +25 m) in the Mibei gold deposit. Doubly polished thin sections were prepared for the fluid inclusion study, and typical samples were crushed to 40–80 meshes for mineral separation. Pyrite, arsenopyrite, and quartz were handpicked using a binocular microscope. All mineral separates were cleaned in an ultrasonic bath before being powdered using an agate mortar. Pyrite and arsenopyrite were analyzed for S isotopes and quartz for O isotopes.

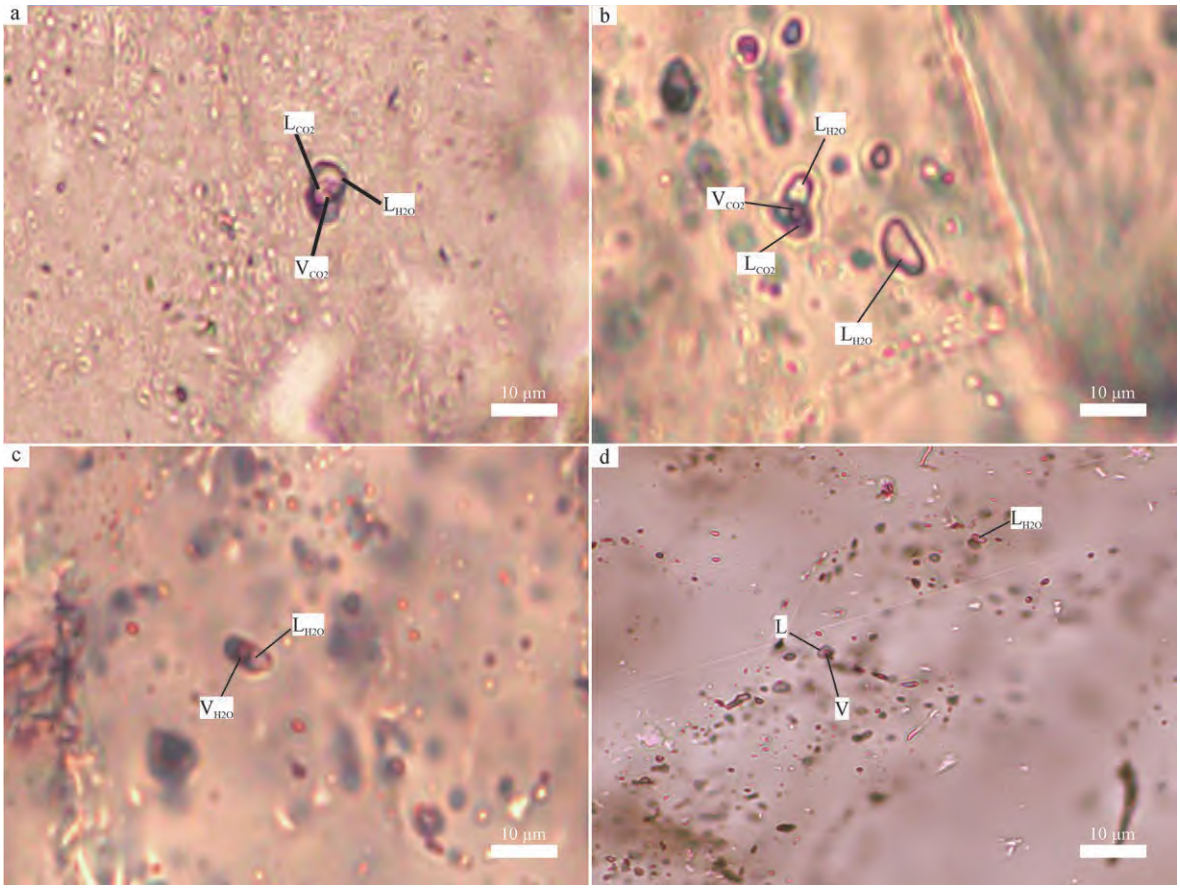

Fig. 6. Microscopic photos of fluid inclusions in the Mibei gold deposit.
(a) Oval V_{CO2} + L_{CO2} + L_{H2O} two-phase inclusions (type Ia) in quartz at room temperature; (b) irregular V_{CO2} + L_{CO2} + L_{H2O} two-phase inclusions (type Ia) in quartz at room temperature; (c) L_{CO2} + L_{H2O} two-phase inclusions (type Ib) and pure liquid H_2O inclusions (type III) in quartz at room temperature; (d) two-phase, vapor-rich fluid inclusions (type II) in quartz at room temperature.

Table 1 Microthermometric data for fluid inclusions in the Mibei gold deposit, Hunan

Sample	Stage	Type	Minerals	T_{ice} (℃)	$T_{h\text{-}total}$ (℃)	Salinity (%)
XH-2	I	Ib	Quartz	−9.2 to −2.4	205.8 to 273.2	4.0 to 13.1
	II	Ia	Quartz	−4.7 to −3.3	191.2 to 208.0	5.4 to 7.4
MB-2	II	Ib	Quartz	−8.4 to −5.2	181.2 to 232.6	8.1 to 12.1
	II	II	Quartz	−7.3 to −2.8	222.1 to 259.6	4.6 to 10.8
	II	Ia	Quartz	−6.3 to −5.2	205.3 to 213.6	8.1 to 9.6
MB-3	II	Ib	Quartz	−8.2 to −4.8	183.0 to 247.3	7.6 to 11.1
	II	II	Quartz	−5.3 to −4.4	219.8 to 225.3	6.9 to 8.3
XH-3	III	Ib	Quartz	−7.8 to −3.8	177.8 to 242.3	6.2 to 11.5

equiv.; Type Ib fluid inclusions have freezing point temperatures varied from −8.2°C to −4.8°C, homogenization temperatures varied from 183.0 ℃ to 247.3 ℃, and salinity varied from 7.6 to 11.1 wt% NaCl equiv.; Type II fluid inclusions show freezing point temperatures varied from −5.3°C to −4.4°C, homogenization temperatures varied from 219.8 ℃ to 225.3 ℃, and salinity varied from 6.9 to 8.3 wt% NaCl equiv.

In sample XH-3, Type Ib fluid inclusions have freezing point temperatures varied from −7.8°C to −3.8°C, homogenization temperatures varied from 177.8 ℃ to 242.3 ℃, and salinity varied from 6.2 to 11.5 wt% NaCl equiv.

6 Isotope Geochemistry

6.1 Oxygen isotope composition

The $\delta^{18}O_{mineral\text{-}SMOW}$ of quartz from the main mineralization stages was analyzed (Table 2; Fig. 9). The $\delta^{18}O_{SMOW}$ are varied from 16.9‰ to 17.5‰. The $\delta^{18}O_{H2O}$ are varied from 6.5‰ to 7.5‰.

6.2 Sulfur isotope composition

Sulfur isotope compositions of pyrite and arsenopyrite from the ores are listed in Table 3 and graphically shown in Fig. 10. The $\delta^{34}S_{CDT}$ values of pyrite from slate range from 6.4‰ to 11.6‰. The $\delta^{34}S_{CDT}$ values of pyrite from ore range from 1.7‰ to 6.8‰. The $\delta^{34}S_{CDT}$ values of arsenopyrite from ore range from 5.6‰ to 5.9‰.

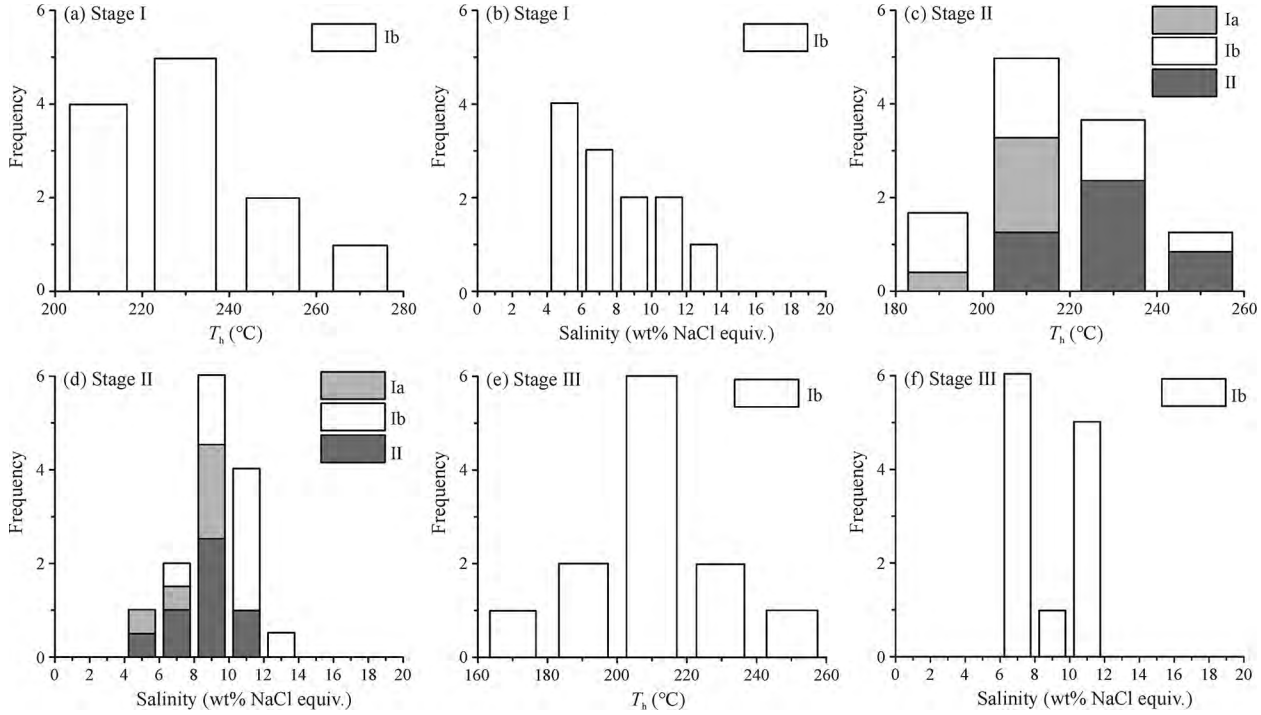

Fig. 7. Homogenization temperature and salinity histogram of quartz fluid inclusions in the Mibei gold deposit.

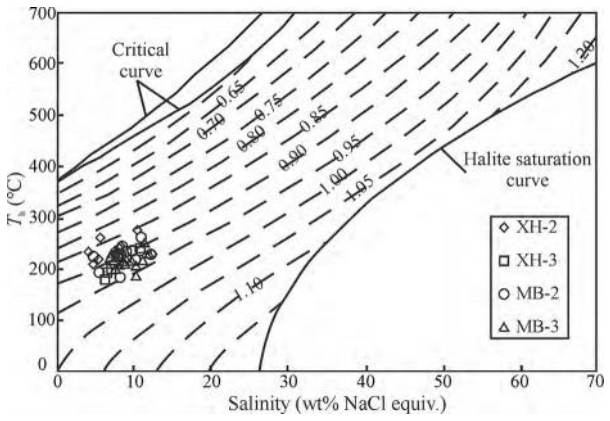

Fig. 8. Homogeneity temperature-salinity diagram of fluid inclusions in the Mibei gold deposit.
Dashed line denotes isodensity line (based on Bodnar, 1983).

Table 2 O isotope values of quartz in the Mibei gold deposit, Hunan

Sample	$\delta^{18}O_{V\text{-}SMOW}$ (‰)	$\delta^{18}O_{H2O}$ (‰)	$T_{h\text{-}total}$ (°C)
20MB-2-1	17.5	7.1	222.2
20MB-2-2	16.9	6.5	222.2
20MB-3-1	17.3	6.9	222.2
20MB-3-2	17.1	6.7	222.2

7 Discussion

7.1 Features and sources of the ore fluids

The fluid inclusions in the Mibei gold deposit are primarily composed of aqueous and CO_2-bearing inclusions (Fig. 6). The ore-forming temperature falls within the 177.8°C to 259.6°C range, with salinity less than 12 wt% NaCl equiv. The ore-forming fluids exhibit medium-to low-temperature and low-salinity characteristics. This is consistent with the fluid characteristics of other coeval gold deposits in the same region, such as the Pincha gold deposit in the southern part of the Mibei gold deposit (Peng and Hu, 1999), the Mobin gold deposit southeast of the Mibei gold deposit (Ding and Wang, 2009), and the Taojinchong gold deposit in the eastern part of the Mobin gold deposit (Yan et al., 1994). The ore-forming pressure in the Mibei gold deposit ranges from 1.50 to 3.46 MPa, indicating a shallow, low-temperature ore-forming environment.

The $\delta^{18}O_{SMOW}$ of quartz ranging from 16.9‰ to 17.5‰ reflects a low temperature alteration and/or contamination process (Deng et al., 2011). The $\delta^{18}O$ values of water in fluid inclusions within the quartz veins, calculated using the equation ($1000\ln\alpha_{quartz\text{-}H2O} = 3.38 \times 10^6 \times T^{-2} - 3.40$; Clayton et al., 1972), range from 6.5‰ to 7.1‰, which resemble those of magmatic water (5.5‰–9.5‰; Sheppard, 1986; Cui et al., 2021). This evidence implies the presence of magma-derived fluid. Many gold deposits at the southwest part of Xuefengshan uplift show similar oxygen isotopes in quartz, such as Pingcha ($3.3‰ \leq \delta^{18}O_{H2O} \leq 5.3‰$; Peng and Dai, 1998); Mobin ($-0.4‰ \leq \delta^{18}O_{H2O} \leq 5.1‰$; Ding and Wang, 2009); Taojinchong ($-2.0‰ \leq \delta^{18}O_{H2O} \leq 8.9‰$; Yan et al., 1994), and Woxi gold deposit at the northwest end of Xuefengshan uplift zone ($4.3‰ \leq \delta^{18}O_{H2O} \leq 8.2‰$; Luo et al., 1984; Peng and Frei, 2004).

The pyrite in the Mibei gold deposit exhibits low $\delta^{34}S$ values ranging from 1.7‰ to 6.8‰, which is consisted with the $\delta^{34}S_{CDT}$ values of arsenopyrite of ore, which ranged

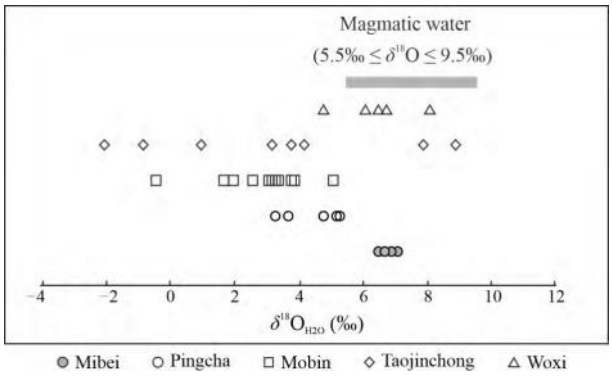

Fig. 9. The comparison diagram of quartz oxygen isotope in the metallogenic period of gold deposits, in the Xuefengshan uplift zone.
Data from Luo et al., 1984; Yan et al., 1994; Peng and Hu, 1999; Ding and Wang, 2009.

Table 3 Sulfur isotope values of sulfides in the Mibei gold deposit, Hunan

Sample	Mineral	$\delta^{34}S_{V\text{-}CDT}$ (‰)
20XH-1	Py	6.4
2XH-2		11.6
20XH-3		5.8
20MB-2-1		5.7
20MB-2-2		6.8
20MB-3-2		1.7
20XH-3-1	Apy	5.9
20XH-3-1		5.6

from 5.6 to 5.9‰. The $\delta^{34}S$ values of gold-bearing sulfides are close to the values of magmatic sulfur ($\delta^{34}S = 0 \pm 5‰$; Ohmoto, 1986). Many gold deposits in the Xuefengshan uplift belt, confirmed to have magmatic-hydrothermal characteristics in their ore-forming fluids, show similar $\delta^{34}S$ values of gol sulfides, such as the Woxi gold-antimony deposit ($-5.8‰ \le \delta^{34}S_{W\text{-}Py} \le 0.4‰$; Dai et al., 2022), the Yuhengtang gold deposit ($-5.0‰ \le \delta^{34}S \le 5.3‰$; Li W et al., 2021), and the Daping gold deposit ($0.23‰ \le \delta^{34}S_{W\text{-}Py} \le 1.98‰$; Kong et al., 2022). Besides, in this study, the $\delta^{34}S_{CDT}$ values of pyrite from the surrounding slate of the Wuqiangxi Formation were also analyzed, ranging from 6.4 to 11.6‰, which overlap with $\delta^{34}S$ values of pyrite of the Mibei gold deposit ($5.8‰ \le \delta^{34}S_{W\text{-}Py} \le 11.6‰$, $n = 3$; $5.6‰ \le \delta^{34}S_{W\text{-}Apy} \le 5.9‰$, $n = 2$; Fig. 10). This suggests that the minor sulfur in the Mibei gold deposit originated from the surrounding rock. Therefore, the ore-forming fluids of the Mibei gold deposit originated from magmatic-hydrothermal processes and were mixed with minor sulfur from the metasedimentary wall rock.

7.2 Genetic type of the Mibei gold deposit

The Mibei gold deposit occurred in the form of a gold-bearing quartz vein hosted by Precambrian metasedimentary deposits on an orogenic belt; it shows medium to low temperature and low salinity of the ore-forming fluid, which is similar to the orogenic gold deposit (Groves et al., 1998; Goldfarb and Groves, 2015). The ore-forming fluids of orogenic gold deposits are metamorphic hydrothermal fluids, and the release of gold-rich fluids is caused by metamorphism from

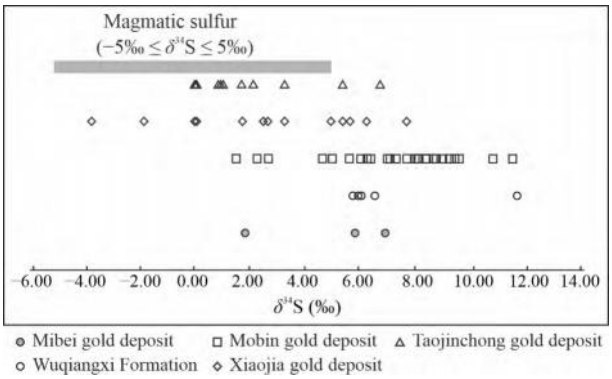

Fig. 10. Comparison diagram of metal sulfide $\delta^{34}S$ of gold deposits in the southwest section of Xuefeng Mountain.
Data from Yu, 1987; Ohmoto, 1986; Liu et al., 1997; Liu S F et al., 2017; Peng et al., 2023.

greenschist facies to amphibolite facies in the upper crust (Goldfarb et al., 2005; Large et al., 2011; Steadman and Large, 2016; Deng et al., 2022). However, the $\delta^{18}O$ values of gold-bearing quartz veins and $\delta^{34}S$ values of gold-bearing pyrite and arsenopyrite at Mibei in this study implied magmatic source of ore-forming fluids. Although $\delta^{34}S$ values of sulfides at Mibei show the mixing of minor sulfur originated from the surrounding rock, the surrounding slate have low contents of Au (The whole-rock Au contents of slate <1 ppb; Li W et al. 2021). Therefore, the surrounding metamorphic slate could not have provided gold-rich fluid to the Mibei gold deposit. Alternatively, magmatism could have released ore-forming fluids for the Mibei gold deposit, which is similar to the Carlin-type Au deposits in Nevada, USA (Barker et al., 2009) and metasedimentary-hosting lode gold deposits in the Jiaodong Peninsula, eastern North China Craton (Deng et al., 2023). These features are indicative of a magmatic-hydrothermal ore deposit in the Mibei gold deposit. In the Xuefengshan uplift, a previous study also demonstrated some magmatic-hydrothermal ore deposits, such as the Yuhengtang gold deposit (Li W et al., 2021) and the Wangu gold deposit (Deng et al., 2017).

7.3 Possible metallogenic process of the Mibei gold deposit

Research indicates that the deposits formed during the Caledonian period in the Jiangnan Orogen are related to regional metamorphism that occurred between 465 and 445 million years ago (Peng et al., 2003; Wang et al., 2011; Ni et al., 2015). However, gold mineralization is believed to have occurred during the later stages of the Caledonian movement (Liu A L et al., 2017) and is associated with magmatic activity in the region between 445 million and 390 million years ago (Wang Y J et al., 2013; Tang et al., 2022; Fig. 11).

Wang (1999) reported a K-Ar age of 404 Ma by the ore-related K-feldspar within the interlayer veins of the Mobin gold deposit in the eastern part of the Mibei gold deposit. Peng (1998) obtained an Rb-Sr age of 435 ± 9 Ma by the gold-bearing quartz from the Pingcha gold deposit located in the southern part of the Mibei gold deposit. Li Y H et al

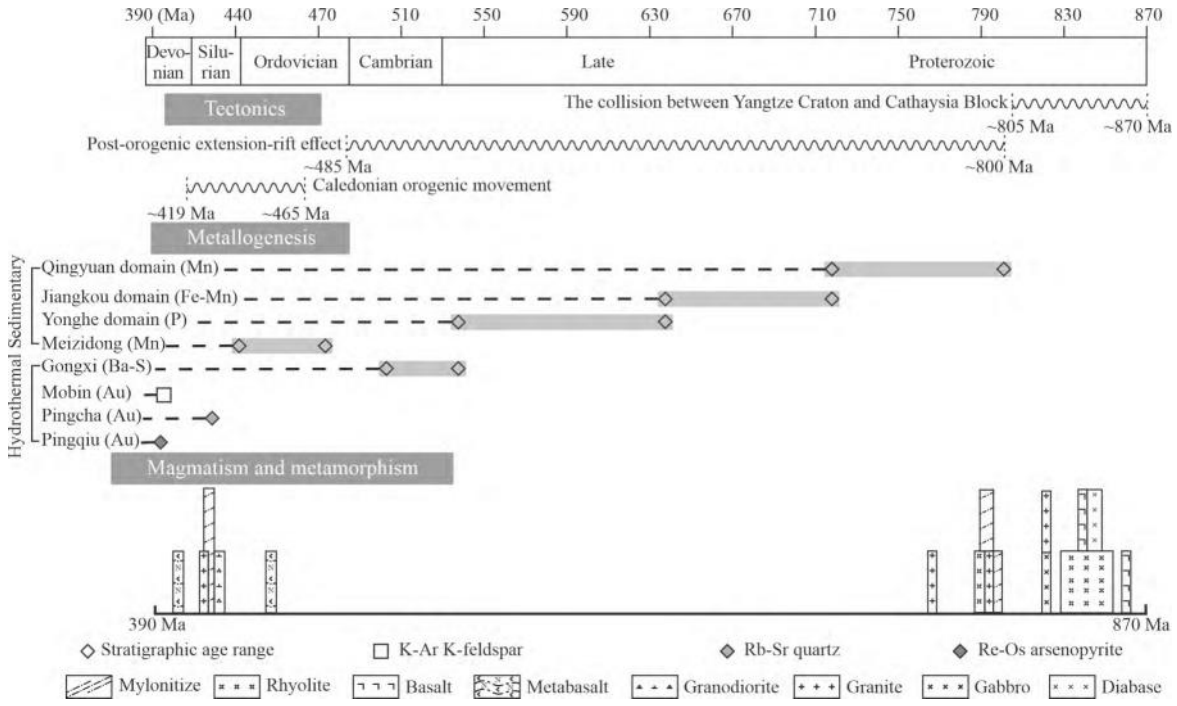

Fig. 11. Structure-magma-mineralization event diagram in Xuefengshan uplift zone.
Data from Hu et al., 1992; Xu et al., 1992; Zhao et al., 1997; Lu et al., 2006; Li et al., 2008; Shu et al., 2008; Dong et al., 2010; Wang et al., 2010; Zhang et al., 2011; Wang et al., 2012; Zhang C L et al., 2013; Zhang Y Z et al., 2013; Xu et al., 2014; Wang et al., 2014; Du et al., 2021; Bai et al., 2022; Tang et al., 2022.

(2021) reported a Re-Os isochron age of 400 ± 24 Ma by the gold-carrying arsenopyrite from the Pingqiu gold deposit in the southern part of the Mibei gold deposit. Gold deposits with similar geological conditions near the Mibei gold deposit have ages ranging from 435 Ma to 400 Ma (Fig. 11). Therefore, it is inferred that the age of gold mineralization in the Mibei gold deposit is approximately 400 Ma.

Gold mineralization in the Hunan polymetallic mineralization province, located in the middle section of the Jiangnan orogenic belt, is closely associated with the magmatic and tectonic activities of the Xuefengshan uplift during the Caledonian period (Wang et al., 2021; Tang et al., 2022). The Woxi syncline, Huangtuao syncline, and Yuezhai NE-trending faults served as channels for ore-forming fluids. Gold was primarily transported in the form of gold-sulfur complexes. Owing to the overthrust of the Lengjiaxi Group caused by a reverse fault at the base of the Lengjiaxi Group, which uplifted the Baxi Group, the fault seal mechanism controlled the ore-forming process (Bai et al., 2014; Liu et al., 2022). This led to increased fractures, reduced pressure, fluid oxidation, and rapid gold deposition (Li et al., 2022).

The mineralization process at the Mibei gold deposit can be summarized as follows:

First, during the later stages of the Caledonian movement, as the Jiangnan Orogen transitioned from a collisional to an extensional regime, large-scale magmatism carrying ore-forming fluid occurred and was uploaded into the shallow regions of the crust.

Second, the magma released heat and hydrothermal fluids that migrated and mixed with minor amounts of S from the surrounding slate when the hydrothermal fluids passed through the metamorphic strata.

Third, as the western segment of the Xuefengshan uplift gradually rose, a fault valve mechanism was triggered. In areas with interbedded sliding surfaces and fractured zones, the pressure of gold-bearing hydrothermal fluids decreased. This reduction in pressure caused fluid oxidation, leading to the destabilization of gold-sulfide complexes and subsequent precipitation of gold.

8 Conclusions

(1) The ore-forming fluids of the Mibei gold deposit originated from magmatic hydrothermal processes and were mixed with minor sulfur from the metasedimentary wall rock.

(2) The Mibei gold deposit is more akin to a magmatic-hydrothermal gold deposit.

(3) Because the magmatic and tectonic activities of the Xuefengshan uplift during the Caledonian uplift of the Baxi Group, the fault seal mechanism controlled the ore-forming process.

Acknowledgments

This research was financially supported by National Natural Science Foundation of China (Grant No. 42273063), the Young Elite Scientists Sponsorship (YESS) Program of the China Association for Science and Technology (Grant No. YESS20220661).

Manuscript received Feb. 07, 2024
accepted Apr. 24, 2024
associate EIC: FEI Hongcai
edited by GUO Xianqing

References

Bai, D.Y., Li, B., Zhou, C., Sun, J., Wei, F.H., Zeng, G.Q., Jiang, W., Li, Y.M., and Jiang, Q.S., 2021. Gold mineralization events of the Jiangnan Orogen in Hunan and their tectonic settings. Acta Petrologica et Mineralogica, 40: 897–922 (in Chinese with English abstract).

Bai, D.Y., Tang, F.P., Li, B., Zeng, G.Q., Li, Y.M., and Jiang, W., 2022. Summary of main mineralization events in Hunan Province. Geology in China, 49: 151–180 (in Chinese with English abstract).

Bai, D.Y., Zhong, X., Jia, P.Y., and Xiong, X., 2014. Study on the deformation in the southern Xuefeng orogenic belt. Geotectonica et Metallogenia, 38: 512–529 (in Chinese with English abstract).

Barker, S.L.L., Hickey, K.A., Cline, J.S., Dipple, G.M., Kilburn, M.R., Vaughan, J.R., and Longo, A.A., 2009. Uncloaking invisible gold: Use of Nanosims to evaluate gold, trace elements, and sulfur isotopes in pyrite from Carlin-type gold deposits. Economic Geology, 104: 897–904.

Bodnar, R.J., 1983. A method of calculating fluid inclusion volumes based on vapor bubble diameters and PVTX properties of inclusion fluids. Economic Geology, 78: 535–542.

Bureau of Geology and Mineral Resource of Hunan Province (BGMRHN), 1988. Regional Geology of Hunan Province. Beijing: Geological Publishing House, 1–719 (in Chinese with English abstract).

Bureau of Geology and Mineral Resource of Hunan Province (BGMRHN), 2013. The Resource Reserve Verification Report of Mibei Gold Mine in Mibei Mining Area, Xinhuang Dong Autonomous County, Hunan Province (in Chinese with English abstract).

Chen, G.H., Wan, H.Z., Shu, L.S., Zhang, C., and Kang, C., 2012. An analysis on ore-controlling conditions and geological features of the Cu-W polymetallic ore deposit in the Zhuxi area of Jingdezhen, Jiangxi Province. Acta Petrologica Sinica, 28: 3901–3914 (in Chinese with English abstract).

Chen, X., Wang, X.L., Wang, D., and Shu, X.J., 2018. Contrasting mantle-crust melting processes within orogenic belts: Implications from two episodes of mafic magmatism in the western segment of the Neoproterozoic Jiangnan Orogen in South China. Precambrian Research, 309: 123–137.

Chu, Y., Faure, M., Lin, W., and Wang, Q.C., 2012. Early Mesozoic tectonics of the South China block: Insights from the Xuefengshan intracontinental orogen. Journal of Asian Earth Sciences, 61: 199–220.

Chu, Y., Lin, W., Michel, F., and Wang, Q.C., 2015. Early Mesozoic intracontinental orogeny: Example of the Xuefengshan–Jiuling belt. Acta Petrologica Sinica, 31: 2145–2155 (in Chinese with English abstract).

Clayton, R.N., O'Neil, J.R., and Mayeda, T.K., 1972. Oxygen isotope exchange between quartz and water. Journal of Geophysical Research, 77: 3057–3067.

Cui, H., Zhong, R., Xie, Y., Wang, X., and Chen, H., 2021. Melt–fluid and fluid–fluid immiscibility in Na_2SO_4–SiO_2–H_2O system and its implications for the formation of rare earth deposits. Acta Geologica Sinica (English Edition), 95(5): 1604–1610.

Dai, J.F., Xu, D.R., Chi, G.X., Li, Z.H., Deng, T., Zhang, J., and Li, B., 2022. Origin of the Woxi orogenic Au-Sb-W deposit in the west Jiangnan Orogen of South China: Constraints from apatite and wolframite U-Pb dating and pyrite in-situ S-Pb isotopic signatures. Ore Geology Reviews, 150: 105124.

Deng, J., Wang, Q.F., Liu, X.F., Zhang, L., Yang, L.Q., Yang, L., Qiu, K.F., Guo, L.N., Liang, Y.Y., and Ma, Y., 2022. The formation of the Jiaodong gold province. Acta Geologica Sinica (English Edition), 96(6): 1801–1820.

Deng, J., Wang, Q.F., Wan, L., Liu, H., Yang, L.Q., and Zhang, J., 2011. A multifractal analysis of mineralization characteristics of the Dayingezhuang disseminated-veinlet gold deposit in the Jiaodong gold province of China. Ore Geology Reviews, 40: 54–64.

Deng, J., Wang, Q.F., Zhang, L., Xue, S.C., Liu, X.F., Yang, L., Yang, L.Q., Qiu, K.F., and Liang, Y.Y., 2023. Metallogenetic model of Jiaodong-type gold deposits, eastern China. Science China Earth Sciences, 66: 2287–2310 (in Chinese with English abstract).

Deng, T., Xu, D.R., Chi, G.X., Wang, Z.L., Jiao, Q.Q., Ning, J.T., Dong, G.J., and Zou, F.H., 2017. Geology, geochronology, geochemistry and ore genesis of the Wangu gold deposit in northeastern Hunan Province, Jiangnan Orogen, South China. Ore Geology Reviews, 88: 619–637.

Ding, Q.F., and Wang, G., 2009. Study on fluid inclusion and genesis of Mobin gold deposit in Hunan Province. Global Geology, 28: 467–475 (in Chinese with English abstract).

Dong, S.W., Xue, H.M., Xiang, X.K., and Ma, L.C., 2010. The discovery of Neoproterozoic pillow lava in spilite-ceratophyre of Lushan area, northern Jiangxi Province, and its geological significance. Geology in China, 37: 1021–1033 (in Chinese with English abstract).

Du, Y., Guo, A.M., Lu, Y.Y., Luo, X.Y., Tian, L., Wang, J.Y., Zhou, L.T., and Fan, H., 2021. Petrogenesis of the Caledonian granites in the northern part of Miaoershan pluton, southwestern Hunan Province: Evidence from petrology, geochemistry and zircon U-Pb age. Geology in China, 48: 1540–1561 (in Chinese with English abstract).

Du, Y., Tian, L., Zheng, Z.F., Chen, J.F., Zhang, X.Q., Wang, J.Y., Zhou, L.T., Fan, H., and Li, C., 2022. Sm-Nd dating of scheelite in Luojiachong W-Sn deposit, Miaoershan area, southwestern Hunan Province: Implications for polycyclic tectonic-magmatic activities and metallogenesis in South China. Geological Bulletin of China, 41: 886–902 (in Chinese with English abstract).

Fang, W.X., Hu, R.Z., Su, W.C., Qi, L., Xiao, J.F., and Jiang, G.H., 2002. Geochemical characteristics of Dahebian–Gongxi superlarge barite deposits and analysis on its background of tectonic geology, China. Acta Petrologica Sinica, 247–256 (in Chinese with English abstract).

Goldfarb, R.J., and Groves, D.I., 2015. Orogenic gold: Common or evolving fluid and metal sources through time. Lithos, 233: 2–26.

Goldfarb, R.J., Baker, T., Dubé, B., Groves, D.I., Hart, C.J.R., and Gosselin, P., 2005. Distribution, character, and genesis of gold deposits in metamorphic terran. One Hundredth Anniversary Volume: Society of Economic Geologists.

Groves, D.I., Goldfarb, R.J., Gebre-Mariam, M., Hagemann, S.G., and Robert, F.,1998. Orogenic gold deposits: A proposed classification in the context of their crustal distribution and relationship to other gold deposit types. Ore Geology Reviews, 13: 7–27.

Gu, X.X., Liu, J.M., Schulz, O., Vavtar, F., and Fu, S.H., 2005. REE geochemical evidence for the genesis of the Woxi Au-Sb-W deposit, Hunan Province. Geochemica, 34: 428–442 (in Chinese with English abstract).

Han, L., Ding, J.Y., Fan, M.S., Bao, T., and Pan, J.Y., 2021. Genesis of the Zhengchong gold deposit in the central part of the Jiangnan orogenic belt: Evidences from fluid inclusions and trace elements of pyrite. Bulletin of Mineralogy Petrology and Geochemistry, 40: 382–399 (in Chinese with English abstract).

Hu, R.Z., Fu, S.L., Huang, Y., Zhou, M.F., Fu, S.H., Zhao, C.H., Wang, Y.J., Bi, X.W., and Xiao, J.F., 2017. The giant South China Mesozoic low-temperature metallogenic domain: Reviews and a new geodynamic model. Journal of Asian Earth Sciences, 137: 9–34.

Hu, S.L., Zou, H.B., and Zhou, X.M., 1992. Two $^{40}Ar/^{39}Ar$ ages of the Proterozoic Jiangnan orogenic belt. Science Bulletin, 37: 286–286 (in Chinese with English abstract).

Huang, J.Z., Sun, J., Zhou, C., Lu, W., Xiao, R., Guo, A.M., Huang, G.F., Tan, S.M., and Wei, H.T., 2020. Metallogenic regularity and resource potential of gold deposits of Hunan area in the Jiangnan orogenic belt, South China. Acta Geoscientica Sinica, 41: 230–252 (in Chinese with English

China Geology, 39(2): 363–375 (in Chinese with English abstract).
Roedder, E., 1984. Fluid Inclusions. Washington, D.C.: Mineralogical Society of America, 12: 79–108.
Roedder, E., 1992. Fluid inclusion evidence for immiscibility in magmatic differentiation. Geochimica et Cosmochimica Acta, 56(1): 5–20.
Sheppard, S.M.F., 1986. Characterization and isotopic variations in natural waters. Reviews in Mineralogy and Geochemistry 16(1): 165–183.
Shu, L.S., Faure, M., Wang, B., Zhou, X.L., and Song, B., 2008. Late Palaeozoic–Early Mesozoic geological features of South China: Response to the indosinian collision events in southeast Asia. Comptes Rendus Geoscience, 340(2–3): 151–165.
Steadman, J.A., and Large, R.R., 2016. Synsedimentary, diagenetic, and metamorphic pyrite, pyrrhotite, and marcasite at the Homestake BIF-Hosted gold deposit, South Dakota, USA: Insights on Au-As ore genesis from textural and LA-ICP-MS trace element studies. Economic Geology, 111: 1731–1752.
Studley, S.A., Ripley, E.M., Elswick, E.R., Dorais, M.J., Fong, J., Finkelstein, D., and Pratt, L.M., 2002. Analysis of sulfides in whole rock matrices by elemental analyzer-continuous flow isotope ratio mass spectrometry. Chemical Geology, 192(1–2): 141–148.
Tang, Y., Wang, Q., Yang, Y.L., Zhou, Y.l., Cui, X.D., and Zou, H., 2022. Petrogenesis and geodynamic implications of the Baimashan granitic complex in central Hunan, South China. Geological Journal, 57(11): 4718–4745.
Wang, C., Peng, J.T., Xu, J.B., Yang. J.H., Hu, A.X., and Chen, X.J., 2021. Petrogenesis and metallogenic effect of the Baimashan granitic complex in central Hunan, South China. Acta Petrologica Sinica, 37(3): 805–829 (in Chinese with English abstract).
Wang, C., Shao, Y.j., Evans, N.J., Li, H., Zhou, H.D., Huang, K.X., Liu, Z.F., Chen, Y., Lai, C.K., and Liu, Q.Q., 2020. Genesis of Zixi gold deposit in Xuefengshan, Jiangnan Orogen (South China): Age, geology and isotopic constraints. Ore Geology Reviews, 117: 103301.
Wang, C.S., Zeng, X.W., Li, X.B., Liu, A., and Bai, Y.S., 2013. The classification and correlation of the Cambrian strata in western Xuefeng Mountain area. Geology in China, 40(2): 439–448 (in Chinese with English abstract).
Wang, C.X, Tong, Y.B., Yang, Z.Y., Yang, X.D., and Sun, X.X., 2022. Early Cretaceous paleomagnetic characteristics of Yuanma Basin, western Hunan and the indications to the structural deformation of eastern Sichuan fold belt. Chinese J. Geophys, 65(1): 280–300 (in Chinese with English abstract).
Wang, J.G., Yu, S.Q., Hu, Y.H., Zhao, X.D., Wu, M., and Gu, M.G., 2014. The discovery, petrology and geochronology of the retrograde eclogite in Jiangshan–Shaoxing suture zone. Geology in China, 41(4): 1356–1363 (in Chinese with English abstract).
Wang, J.S., Wen, H.J., Li, C., Ding, W., and Zhang, J.R., 2011. Re-Os isotope dating of arsenopyrite from the quartz vein-type gold deposit, southeastern Guizhou Province, and its geological implications. Acta Geologica Sinica, 85(06): 955–964 (in Chinese with English abstract).
Wang, Q., Wyman, D.A., Li, Z.X., Bao, Z.W., Zhao, Z.H., Wang, Y.X., Jian, P., Yang, Y.H., and Chen, L.L., 2010. Petrology, geochronology and geochemistry of ca. 780 Ma A-type granites in South China: Petrogenesis and implications for crustal growth during the breakup of the supercontinent Rodinia. Precambrian Research, 178(1–4): 185–208.
Wang, X.L., Shu, L.S., Xing, G.F., Zhou, J.C., Tang, M., Shu, X.J., Qi, L., and Hu, Y.H., 2012. Post-orogenic extension in the eastern part of the Jiangnan orogen: Evidence from ca. 800–760 Ma volcanic rocks. Precambrian Research, 222: 404–423.
Wang, X.Z., Liang, H.Y., Shan, Q., Cheng, J.P., and Xia, P., 1999. Metallogenic age of the Jinshan gold deposit and Caledonian gold mineralization in South China. Geological Review, 45(1): 19–25 (in Chinese with English abstract).
Wang, Y.J., Fan, W.M., Zhang, G.W., and Zhang, Y., 2013. Phanerozoic tectonics of the South China Block: Key observations and controversies. Gondwana Research, 23(4): 1273–1305.
Wang, Y.J., Zhang, Y.H., Fan, W.M., and Peng, T.P., 2005. Structural signatures and $^{40}Ar/^{39}Ar$ geochronology of the Indosinian Xuefengshan tectonic belt, South China Block. Journal of Structural Geology, 27(6): 985–998.
Xie, M.C., 2014. Analysis of geological characteristics of gold deposits in Mibei mining area, Hunan Province. Earth, 89–91 (in Chinese with English abstract).
Xu, B., Guo, L.Z., and Shi, Y.S., 1992. Proterozoic Terranes and Multiphase Collision Orogensin Anhui—Zhejiang—Jiangxi Area. Beijing: Geological Publishing House, 1–112 (in Chinese with English abstract).
Xu, D.R., Deng, T., Chi, G.X., Wang, Z.L., Zou, F.H., Zhang, J.L., and Zou, S.H., 2017. Gold mineralization in the Jiangnan orogenic belt of South China: Geological, geochemical and geochronological characteristics, ore deposit-type and geodynamic setting. Ore Geology Reviews, 88: 565–618.
Xu, X.B., Xue, D.J., Li, Y., Hu, P., and Chen, N.S., 2014. Neoproterozoic sequences along the Dexing–Huangshan fault zone in the eastern Jiangnan orogen, South China: Geochronological and geochemical constraints. Gondwana Research, 25(1): 368–382.
Yan, C.L., Shu, L.S., Chen, Y., Faure, M., Feng, Z.H., and Zhai, M.G., 2021. The construction mechanism of the Neoproterozoic S-type Sanfang–Yuanbaoshan granitic plutons in the Jiangnan Orogenic Belt, South China: Insights from geological observation, geochronology, AMS and Bouguer gravity modeling. Precambrian Research, 354: 106054.
Yan, M., Ma, D.S., and Liu, Y.J., 1994. Ore-forming fluid geochemistry and genesis of the Taojinchong gold deposit. Mineral Deposits, 156–162 (in Chinese with English abstract).
Yang, H.S., 2019. Mineralization of Mibei gold deposit in southwest Hunan. World Nonferrous Metals, 81–82 (in Chinese with English abstract).
Yang, R.D., Gao, J.B., Xu, H., Luo, C.K., Gao, L., Ni, X.R., and Xue, Z.X., 2022. Ore-forming source analysis of huge manganese deposits in the Neoproterozoic Datangpo stage, Guizhou Province, China. Acta Geologica Sinica, 96: 1815–1826 (in Chinese with English abstract).
Yao, J.L., Cawood, P.A., Shu, L.S., and Zhao, G.C., 2019. Jiangnan Orogen, South China: A ~970–820 Ma Rodinia margin accretionary belt. Earth-Science Reviews, 196: 102872.
Yao, J.L., Shu, L.S., Zhao, G.C., Han, Y.G., and Liu, Q., 2021. Ca. 835–823 Ma doming extensional tectonics in the west Jiangnan accretionary orogenic belt, South China: Implication for a slab roll-back event. Journal of Geodynamics, 148: 101879.
Yu, D.L., 1987. The study of the stable isotope of the gold deposit at Mobin Hunan. Journal of Guizhou University of Technology (Natural Science Edition), 99–110 (in Chinese with English abstract).
Zhang, C.L., Santosh, M., Zou, H.B., Li, H.K., and Huang, W.C., 2013. The Fuchuan ophiolite in Jiangnan Orogen: Geochemistry, zircon U-Pb geochronology, Hf isotope and implications for the Neoproterozoic assembly of South China. Lithos, 179: 263–274.
Zhang, F.F., Wang, Y.J., Fan, W.M., Zhang, A.M., and Zhang, Y.Z., 2011. Zircon U-Pb Geochronology and Hf Isotopes of the Neoproterozoic Granites in the Central of Jiangnan Uplift. Geotectonica et Metallogenia, 35(1): 73–84 (in Chinese with English abstract).
Zhang, J., Ma, Z.J., Chen, B.H., Wang, Z.X., and Li, T., 2010. Paleozoic deformational characteristics of the central Xuefeng Mt. and implication-A case study on the Suining–Jingzhou–Tianzhu–Xinhuang section, China. Geoloical Bulletin of China, 29(1): 44–57 (in Chinese with English abstract).
Zhang, L., Groves, D.I., Yang, L.Q., Sun, S.C., Weinberg, R.F., Wang, J.Y., Wu, S.G., Gao, L., Yuan, L.L., and Li, R.H., 2020. Utilization of pre-existing competent and barren quartz veins as hosts to later orogenic gold ores at Huangjindong gold deposit, Jiangnan Orogen, southern China. Mineralium Deposita, 55: 363–380.
Zhang, L., Yang, L.Q., Groves, D.I., Liu, Y., Sun, S.C., Qi, P.,

#(Í ¹ !T C-r +±&‘- Õ CP #VP ¸ N ËO¹

陈高健· ,曹代勇 ,王安民 ,魏迎春 ,刘志飞 ,赵萌

中国矿业大学 北京 地球科学与测绘工程学院 北京
地球化学过程与资源环境效应湖南省重点实验室 湖南长沙

… >®¸ g-A/£7 &cŽ # 8 ¹ !T C-r -, '– &&‘- Õ C ‰ŠU+±ž ú , 3 ¹ !T C-r #(Í o ; 3E6; +±&‘ ZJ%BU3ñ(’ 7 Z * >¬„ F Bb ,. i , Â-, g) r 3#$5 ; , - , ËO¹Ž # g 、 +±P #VP ¸ N ËO¹, &&‘2(- Õ• =(Ü ° E =y ú $A。EGÐô 1 3ì =z 1 、ö) v A^¹ P 3 DQ‘ E<1 *bJ%&- Õ C Ô'– E =y 3 ½,-A/£ ¹ !T C-r &&‘+±- Õ CDð8 +±ž ú 。-A/£ þ (Ý , ¹ !T C-r UP #VP ¸ (Ü ° 8 …UKh-º - Õ C ‰ŠU+± u É , ¾ c &‘- Õ C/8 Ó+± ËJ¬。E - 4 É g 7 &cŽ # 8 ± EMg %õ] g &‘- Õ C/8 ÓD° { +±(ÝAŽý È - .ú ? F÷。

J[@ú&‘2(- Õ;P #VP ¸ ; ¹ !T C-r #(Í o ;- Õ C

Z + 3 1¨ $: ´ ([4 -. : ´ 0 4C$:

High-temperature and high-pressure simulation of coal graphitization with SiO_2 additive

Abstract

Key words

---

c /l L : L :

' FþM¦, :国家自然科学基金

%&520- ø : 陈高健 男 黑龙江哈尔滨人 硕士研究生 主要从事煤与煤系石墨方面的研究工作

EG %&52: 曹代勇 男 重庆人 博士 教授 主要从事煤与煤系石墨方面的教学和科研工作

煤系石墨是煤变质作用进入石墨化阶段的产物 属于隐晶质石墨 也是煤系非金属矿产的一种 受石墨烯研究热潮的驱动 煤系石墨的研究及开发逐渐受到了关注和重视

煤系石墨成矿控制因素可以分为内因 煤岩组分 及外因 温度 压力 两类 温度和压力是石墨化作用的主要控制因素 其中温度可为原子排列重结晶和结构转化提供所需的活化能 促进石墨微晶结构发育及晶格缺陷愈合过程 压力同样可为石墨化作用提供能量 降低石墨化起始温度 并促进碳层定向排列及秩理化 加快石墨化进程 我国已发现的大型煤系石墨矿多位于南方地区 如湖南鲁塘矿区 江西崇义矿区等 在地质历史上均受到强烈且复杂的构造 岩浆活动 证明煤系石墨矿产的形成离不开温度及压力的协同作用

随着煤石墨化研究的深入 无机矿物对石墨演化的影响逐渐受到重视 前人研究发现 硫 铁 钙等元素及其化合物可降低煤石墨化所需的条件 加快石墨化进程 等 发现含铝黏土矿物在高温下存在对煤石墨化的阻碍延缓作用 证明矿物在煤石墨化过程中并非单纯表现出催化效果

煤中常见矿物为石英 黏土类 碳酸盐及硫化物等 二氧化硅 广泛存在于石英及高岭土中 是煤中重要的无机组分之一 部分学者围绕 对煤石墨化的影响开展了一系列研究

等 通过对宾夕法尼亚无烟煤进行持续升温实验 发现 存在对石墨化进程起催化作用 邱钿 等 在此基础上提出高温环境下 催化石墨化的机理 在高温下与煤中的碳发生反应形成中间物 随温度进一步升高 受热分解形成石墨结晶 进而提升煤的石墨化程度

尽管围绕 对煤石墨化的影响已经开展了大量工作并取得了许多成果 但仍存在不足之处 自然界中煤系石墨矿床形成是岩浆接触变质作用和构造应力共同作用的结果 而已有研究大多基于高温热模拟实验 将煤系石墨形成的控制因素简化为单纯的温度 并得出 具有促进煤石墨化能力的结论 却忽视了自然条件下构造应力的存在 难以对天然煤系石墨的形成环境及演化过程进行还原 且应力的增大也可能阻碍部分反应的进行 部分矿物在温压协同作用下对煤石墨化的影响 可能与纯高温环境下截然不同 因此 对煤石墨化的影响不能简单运用纯高温模拟实验的结论 而应进行高温高压模拟实验 对自然环境温压协同作用下 影响煤石墨化过程进行正演 为自然条件下煤系石墨形成过程中 矿物的影响提供理论依据

1 ËO¹d î ÷ æ''

选取贵州格目底矿区的瘦煤为研究对象 经组分分离获得对模拟条件响应更为灵敏的富镜质组组分 进行酸洗脱矿处理排除煤中矿物可能存在的影响 以高温高压模拟实验为手段 选择 粉末作为添加剂 进行高温高压添加剂对比实验 对温压协同作用下 对石墨化作用的影响进行研究

1.1 ËO¹d î E6 ÷ 1)3

实验用原煤样采自贵州格目底矿区 为粒度 的粉末样 为排除煤中显微组分对实验产生影响 对样品镜煤 镜质组富集 条带进行手选分离 得到富镜质组样品 依照 烟煤组分分类 和 煤的显微组分组和矿物测定方法 对分离后的镜质组组分进行显微煤组分定量统计 将富集纯度达到 以上的样品作为模拟实验前驱物 其工业分析 煤的工业分析方法 和元素分析 煤的元素分析方法 结果见表

为尽可能排除煤中原有矿物对实验的影响 设置酸洗脱矿环节 将样品破碎并经过 目标准筛 称取 煤粉样放入塑料烧杯中与 的 质量分数 溶液混合 在 的恒温水浴条件下搅拌 然后滤掉 溶液 再向煤样中加入 溶液 质量分数 重复操作 直至滤液用 溶液检测无沉淀出现 将酸洗煤样用滤纸滤出 放入烘箱 真空干燥

=• **1** ï , ÂJ%BU3ñ+± G 3 ½ ÷ p 2M3 ½ • ›

Table 1 Industrial and elemental analyses data of vitrinite in Gemudi

采集地	*R*	显微组分体积分数			工业分析				元素分析			
		镜质组	惰质组	壳质组	*M*	*A*	*V*	*FC*	*C*	*H*	*N*	*O*
贵州格目底												

1.2 P #VP ¸ N ËO¹

本次实验采用六面顶压机 可以模拟最高 的温压条件 图

+1 P #VP ¸ ËO¹@ë4 —— š L•M£¸ g

Fig. 1 High-temperature and high-pressure experimental equipment (six-sided press)

实验条件参考国内外相关研究确定 实验温压 下限为 上限为 通过高温高压对自然条件下煤系石墨形成过程中的时间因素进行补偿 设置一组添加 样品 及一组无添加剂样品 为使得 达到最佳的影响石墨化能力 将镜质组与 按 的比例进行配比 高温高压模拟实验方案见表

=•2 P #VP ¸ N ËO¹æu

Table 2 Scheme of high-temperature and high-pressure simulation experiment

样品编号		实验条件	
无添加剂	添加	温度	压力

对实验后的样品开展 射线衍射 拉曼光谱及高分辨率透射电镜测试 进而对样品的石墨结构 晶格发育情况进行观察与定量分析

射线衍射( )分析

仪器选择 铜靶 加速电压 电流 扫描范围 θ 为 扫描速率为 射线波长为 图谱上两个衍射峰 θ 范围分别是 和 与标准石墨 衍射中的 峰和 峰位置相当 使用 软件对图谱进行处理 根据 方程和 公式计算其相关晶格参数 碳层间距 d 堆砌高度 L 和延展度 L

是研究煤中微晶结构常用的方法 可按照下述方法从谱图中求出 d L 和 L

d 为微晶的平均层间距 可根据 方程求得 计算公式为

$$d = \lambda / \theta$$

式中 λ 为 射线的波长 λ θ 为 峰对应的衍射角

L 为 c 轴方向微晶的平均堆积高度 计算公式为

$$L_c = \lambda/\beta \quad \theta$$

式中 β 为 峰的半峰宽

L 为微晶的平均大小尺寸 可根据 微晶公式求得

$$L_a = \lambda/\beta \quad \theta$$

式中 β 为 峰的半峰宽 θ 为 峰对应的衍射角

拉曼光谱分析

拉曼光谱常被用于有机物分析 测试仪器选择 原位共聚焦显微拉曼光谱仪 采用 激光器作为激发光源 激光功率为 扫描范围为 曝光时间为 使用 软件中的洛伦兹函数对获得的拉曼光谱进行拟合和数据处理分析

测得的拉曼光谱分布分为一级拉曼和二级拉曼 一级拉曼光谱位于 范围内可分为四个缺陷峰 至 峰 和一个有序石墨峰 峰 二级拉曼光谱位于 范围内 在低变质阶段只有两个峰 和 峰 随着石墨化程度增加 峰逐渐分裂 峰消失

峰为石墨内部的晶格缺陷和无序碳结构引起的缺陷峰 峰位于 位置 代表层面缺陷 峰位于 位置 代表层间缺陷 峰 峰分别位于 位置 代表内部无序结构的缺陷 多出现于石墨化程度较低的情况下

二级拉曼发育程度与石墨三维晶格的结构有序程度呈正相关

本次研究中使用参数 R 和 R 来表征样品中的结构缺陷程度 这两个参数多被用来定量评价晶格内部缺陷程度或碳材料的有序度

R 被称为 面内缺陷参数 用以表征石墨片层面内缺陷 的占比 适用于评价缺陷较少或

以　型缺陷峰为主的高石墨化程度样品　其计算公式为

$$R = A / A$$

式中 A 为对应峰面积

R 被称为 全缺陷参数　用以表征所有类型缺陷的百分比 适用于评价缺陷较多的低石墨化程度样品　其计算公式为

$$R = A / A$$

高分辨率透射电镜分析

采用　场发射透射电镜主机 加速电压　点分辨率　线分辨率　信息分辨率　使用放大倍数　倍

具体测试方法 将实验后样品研磨至粒径　在乙醇中超声分散后滴在微栅铜网 寻找架空在微栅铜网孔洞上的样品 选取样品内有代表性的微粒 进行多尺度观察 并拍摄高分辨图像

2　ËO¼ É=• ®

为避免残余　添加剂对后续测试分析造成干扰 将高温高压处理后的　样品分为两组 其中一组进行二次酸洗脱矿 另一组不作处理　对两组样品分别开展　对比测试 图

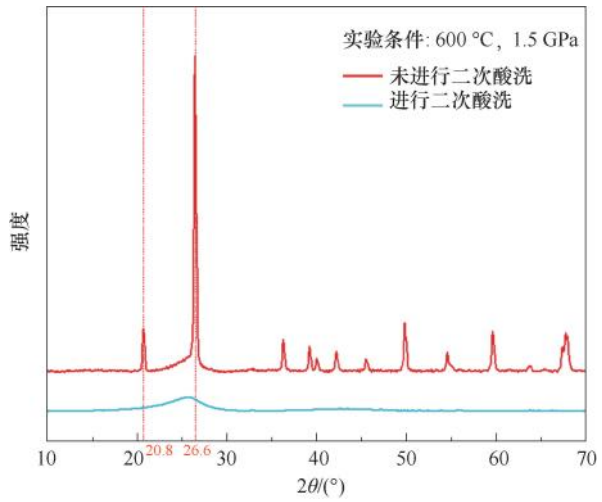

+ 2　¹ NF¥'D6^-, ËO¹d î **XRD** 4 É &!

Fig. 2　Comparative XRD patterns of secondary acid-washed and demineralized experimental samples

2.1　4 É

结果表明 二次酸洗脱矿后的样品仅在 θ　附近存在一宽缓石墨峰 未见其他明显杂峰 未进行二次酸洗脱矿的样品则在　附近存在尖锐明显的衍射峰 经查阅　卡片 其为　晶体特征峰

测试结果证明 高温高压实验后样品中仍存在较多的残余　添加剂 且　特征峰会与石墨特征峰叠合 进而造成后续分析误判　因此 对　测试及拉曼测试所需样品均进行二次酸洗脱矿 避免残余　产生影响 而对高分辨率透射电镜测试样品则不需进行二次脱矿

模拟实验样品经二次酸洗脱矿后开展　测试 得到的衍射图像如图　所示　通过计算 得到反映石墨化程度的微晶参数 碳层间距 d　以及代表石墨微晶结构发育程度的参数 延展度 L 和堆砌度 L　表

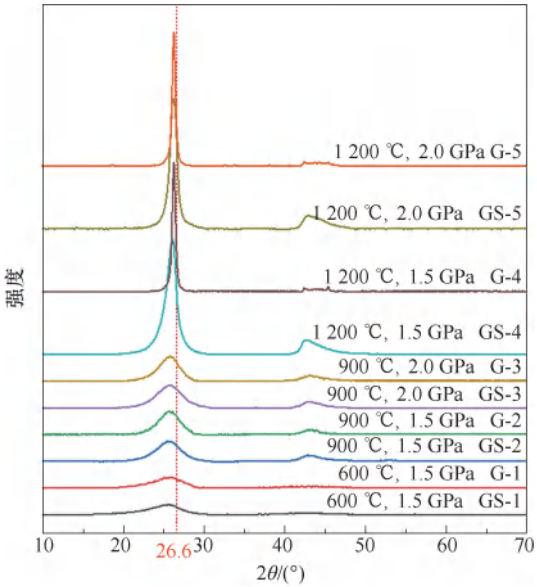

+ 3　N　ËO¹d î **XRD** +

Fig. 3　XRD patterns of the experimental samples

=• 3　N　ËO¹d î **XRD** ï •

Table 3　XRD parameters of the experimental samples

编号	温度	压力	θ	L	L	d

随着模拟实验温压的提升 无添加剂样品　添加　样品　中位于 θ　附近的　峰 皆向着标准石墨峰 θ　位置靠

拢 峰强不断提升 半高宽逐渐减小

条件下 所有样品的 峰整体宽缓 对称性较低 位于 附近的 峰几乎不发育 与 样品的石墨化程度均较差

条件下 所有样品的 峰峰强明显提升 半高宽减小 峰开始发育 石墨结构初步形成

条件下 在 压力的协同作用下 样品的 峰已发育至尖锐 对称形状 峰分裂为 及 两个峰 呈现石墨结构衍射峰型特征 代表完美石墨晶体的形成 样品的 峰相比于同条件 样品的半高宽更大 而且即使将压力升至 其 峰也未开始分裂

2.2 ö) v A^

对二次酸洗脱矿后实验样品的拉曼光谱进行分峰拟合 图 计算得到样品的结构表征参数 表

=• **4** ËO¹d î ö) ï •

Table 4 Raman parameters of the experimental samples

编号	温度	压力	R	R	R

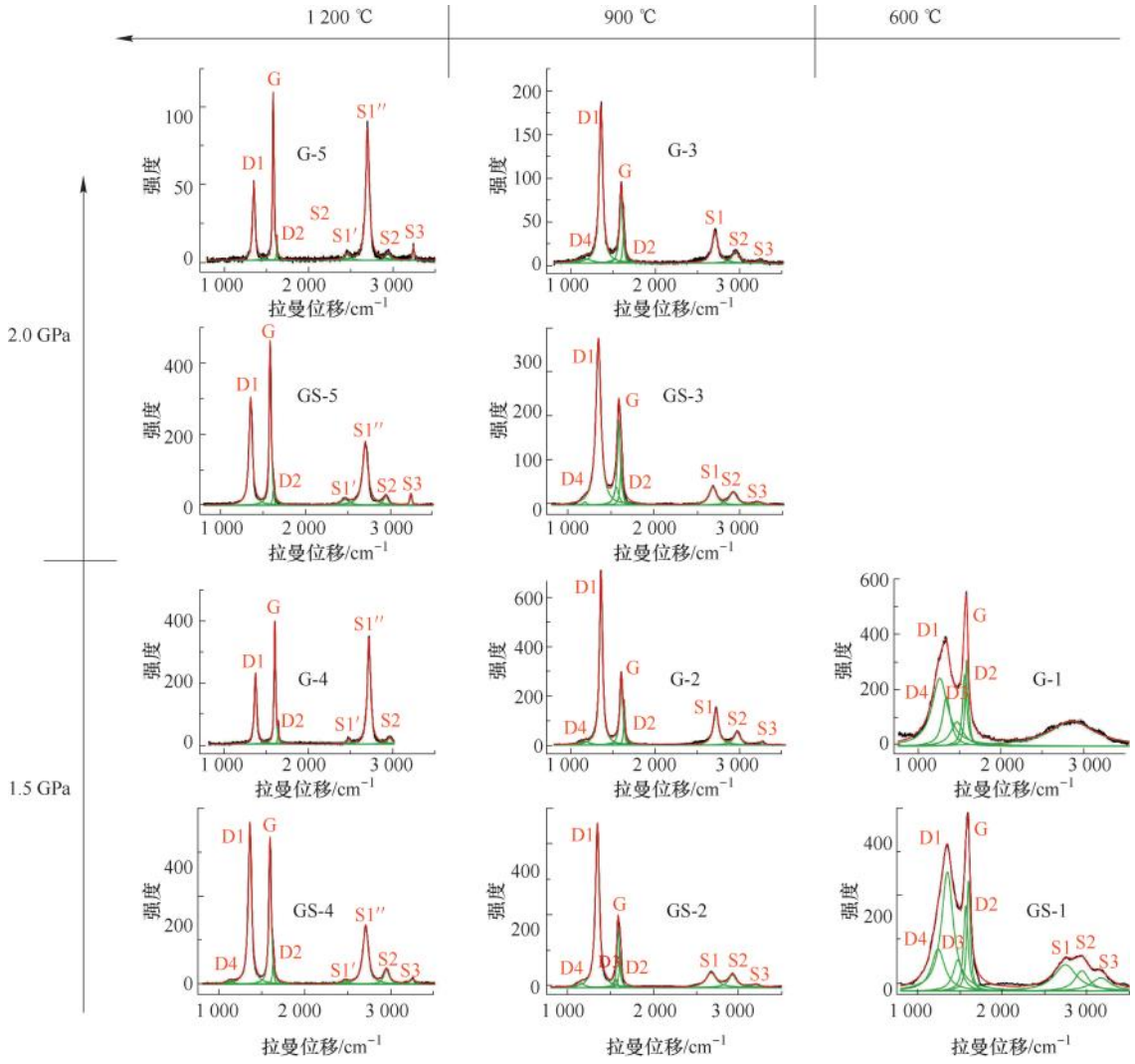

+ **4** N ËO¹d î ö) v A^

Fig. 4 Raman spectra of the experimental samples

可见 随着温压的升高 表征有序石墨结构的　峰强度逐渐增大 并向着　　位置靠近 表征无序结构的　峰强度不断减弱

实验样品的缺陷峰多以代表面内缺陷的　峰为主 而代表其他杂环缺陷峰的　　峰随温压升高而逐渐消失

在　　条件下　峰与　峰尚未完全分离 样品的石墨化程度均较低　而当温度达到　　后　　峰与　峰分裂并形成两个独立的　峰 出现明显的二级拉曼峰 表明三维有序石墨结构开始发育

当实验温度达到　　时　与　样品的一级拉曼出现明显差异 不同压力环境下的　样品的　峰均比同条件　样品的峰强更低 反映其内部晶格缺陷更少

观察二级拉曼峰形成情况可发现 不同温压条件下　样品的　峰均高于　样品的 说明其内部三维石墨结构发育程度更优

2.3　P 3DQ E<1*bJ‰

高分辨率透射电镜　　是研究纳米级微观结构特征的重要手段 能够更直观地观察到煤中大分子结构的空间排列特征和结构缺陷特征 是研究煤石墨化过程的重要方法　　运用　　手段可对未进行二次脱矿处理实验样品的石墨微晶形成情况进行观察 同时研究高温高压环境下　　影响煤石墨化作用的过程及机理 图　图

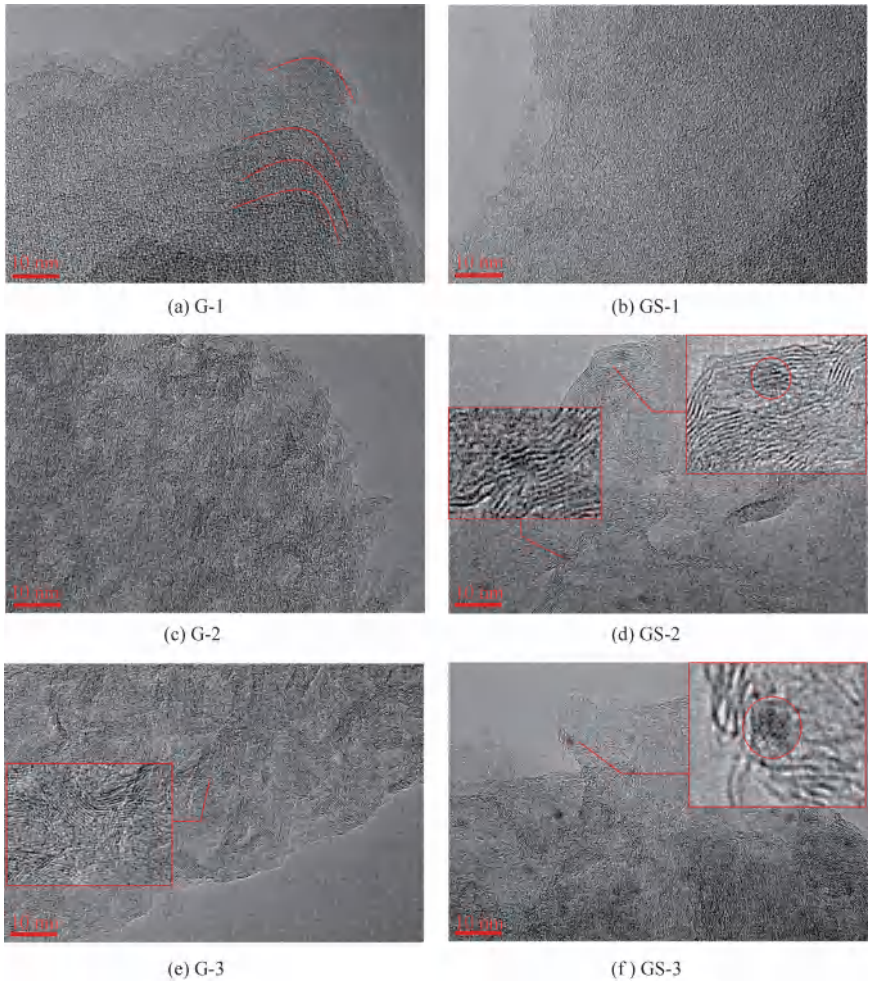

+5　600～900 ℃ Ž # 8 G、GS d î +±HRTEM ¦ ®

Fig. 5　High-resolution transmission electron microscopic images of G/GS at 600～900 ℃

条件下 在　样品中可则观察到条纹阶梯状堆叠结构形成 如图　　所示 说明样品内部石墨结构已具备发育雏形 而在　样品中未观察到明显石墨结构出现 碳层尚未开始堆叠 整体特征杂乱无序 如图　　所示 说明整体结构有序度和结晶程度较低

条件下　样品内部碳层开始自发有序的进行堆叠 碳层堆叠约　　层 延展长度可达几十纳米 如图　　所示 石墨结构逐渐形成　样品中碳层同样开始延展并相互堆叠 但发育规模低于同条件的　样品 内部仍存在大量无序碳结构 并可观察到许多深色颗粒状物质 部分已形成的碳层在与深色颗粒接触的位置处出现中断 如图　　所示

条件下 样品的石墨结构随压力升高得到进一步发育 碳层继续堆叠后以 小半圆 形状的柔皱石墨结构存在 如图 所示 而在 样品中仍可观察到深色颗粒的存在 放大后发现 该深色颗粒为多孔状结构 其存在阻碍了碳层的发育和堆叠 使得与其左侧接触的碳层发生弯曲 上下两端接触的碳层则发生中断 如图 所示

当温度升至 在 压力的协同作用下 与 样品中均形成了大片的石墨层片结构 碳层堆叠量可达数十层 样品中的石墨层片内部碳层整体呈现平整堆叠的形态 具有明显走向但边缘处的部分碳层发生位错缺陷 如图 所示 样品内部大型片状石墨层片与规模较小的柱状石墨层片共存 与 样品相比 其形成的石墨层片规模较小 内部碳层仍表现出一定的弯曲性 且在层片边缘拐角处碳层弯曲程度更高 如图 所示 证明 样品内部石墨微晶结构形成情况较差

条件下 随着压力的升高 样品中石墨层片规模进一步扩大 与 样品中的石墨层片均沿一定方向进行有序堆叠 形成三维石墨结构 样品中组成石墨结构的层片相比于 样品更为平直有序 堆叠更整齐 如图 所示

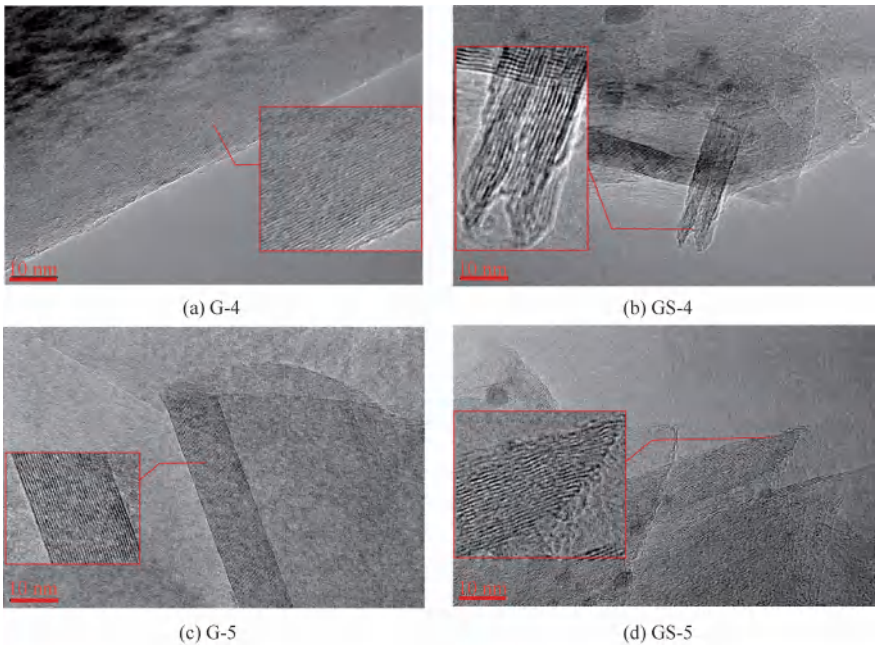

+ 6 1 200 ℃ Ž # 8 G/GS d î +±HRTEM ¦ ®

Fig. 6 High-resolution transmission electron microscopic images of G/GS at 1 200 ℃

3 3 ½; @@ç

3.1 - ÕÛ£4 ±K¼#V¸ Ž #$AC

以 d 作为评价石墨化程度的指标 绘制与 样品的 d 参数随温压变化的三维柱状图 图 可以看出 相同实验条件下 添加 的 样品的 d 值均高于无添加剂 样品 这表明 的参与降低了镜质组的石墨化程度 表现出对石墨化作用的阻碍效果

对不同温压条件下 与 样品的 d 之差的绝对值 d 进行分析发现 图 在 条件下 d 值处于实验中较低位置 此时 与 样品的 d 值较大 d 值均大于 尚未进入半石墨阶段 反应仍处于以芳构化作用和环缩合作用为主的煤化阶段 在此阶段影响微弱 随温度提升到 d 值升至实验中最高点 样品已进入半石墨阶段 而 样品的 d 值仍大于 的抑制效果也在该温度点达到最强 条件下 d 值逐渐

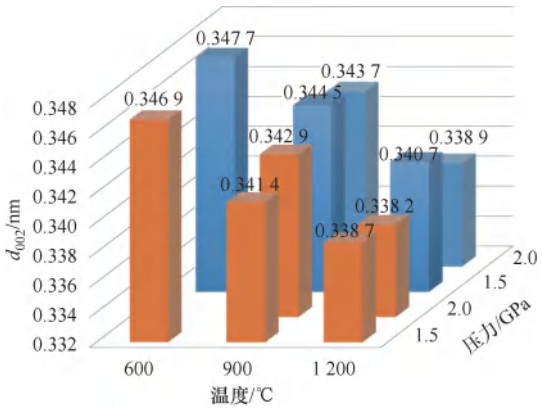

+ 7 G、GS d î d_{002} K¼#V¸ C 'ã +

Fig. 7 The d_{002} parameters of G and GS samples with temperature and pressure

减小 温度的升高减缓了　　对石墨化的阻碍作用 当压力由　　升至　　不同温度下的 d 值均在一定程度上减小 压力同样表现出对　　阻碍煤石墨化的减缓能力 且压力条件具有比温度由　　升至　　更好的减缓效果

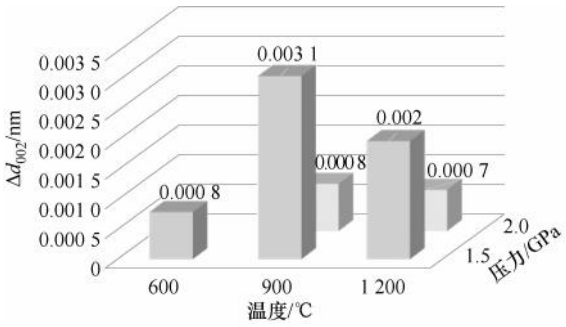

+ 8　Δd_{002} i K¼#V¸　C　'ã +

Fig. 8　The Δd_{002} parameters with temperature and pressure

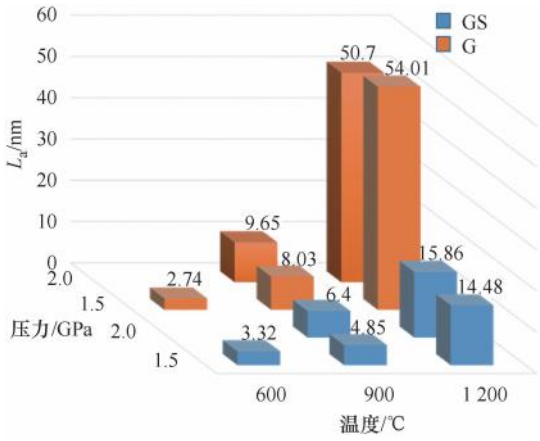

(a) L_a值随温压变化柱状图

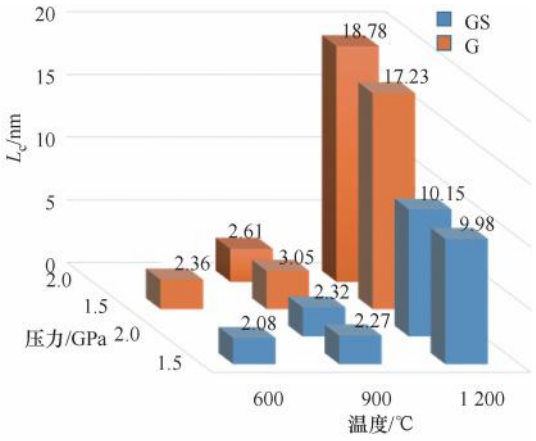

(b) L_c值随温压变化柱状图

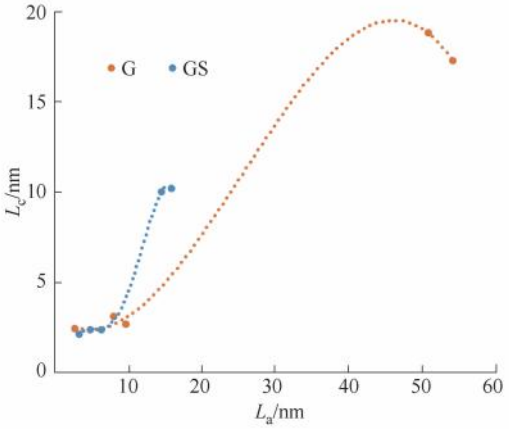

(c) L_a-L_c关系

+ 9　G、GS d î Û£4 ± ï •（L_a、L_c）

Fig. 9　Microcrystalline structure parameters（L_a, L_c）of G and GS samples

3.2　- Õ£ i 4gK¤K¼#V¸ Ž #$AC

构建实验样品 R　R 值随温压变化的三维柱状图 图　　以此研究高温高压条件下　　对石墨晶格缺陷愈合过程的影响

尽管　　阻碍了煤石墨化进程 使得添加样品的 d　值比无添加剂样品更高 但其并未改变样品的石墨化趋势 随温压升高 样品 d　值逐渐减小 向着高石墨化程度继续演化

通过计算实验样品的延展度 L　和堆砌度 L　绘制三维柱状图及 L　L 关系图 图　　可以发现　　样品石墨微晶结构的发育过程同样受到了　　的阻碍效果 其具有比同条件下　样品更低的 L　L 值

结合 L　L 关系图可发现　　与　　样品具有相似的微晶结构参数发育规律 均为抛物线型曲线　　并未改变样品的石墨微晶结构演化轨迹

样品的微晶结构发育受到明显抑制 其 L 值最高为　　是同条件下　样品的　　而对于在无添加剂情况下发育良好的延展度则受到更严重的抑制效果　　样品 L 值最高为　　仅为同条件下　样品的

样品的　　与　　样品的 R 值均呈现出减小的趋势 样品的晶格缺陷在温压协

同作用下逐渐愈合 石墨晶格趋于完善 但 样品的 R R 值均高于相同条件下的 样品 其内部晶格缺陷特别是面内缺陷 具有更高的占比

的存在阻碍了晶格缺陷随着温度 压力提升而消亡的过程 但并未改变石墨晶格缺陷在温压协同作用下逐渐愈合的演化轨迹

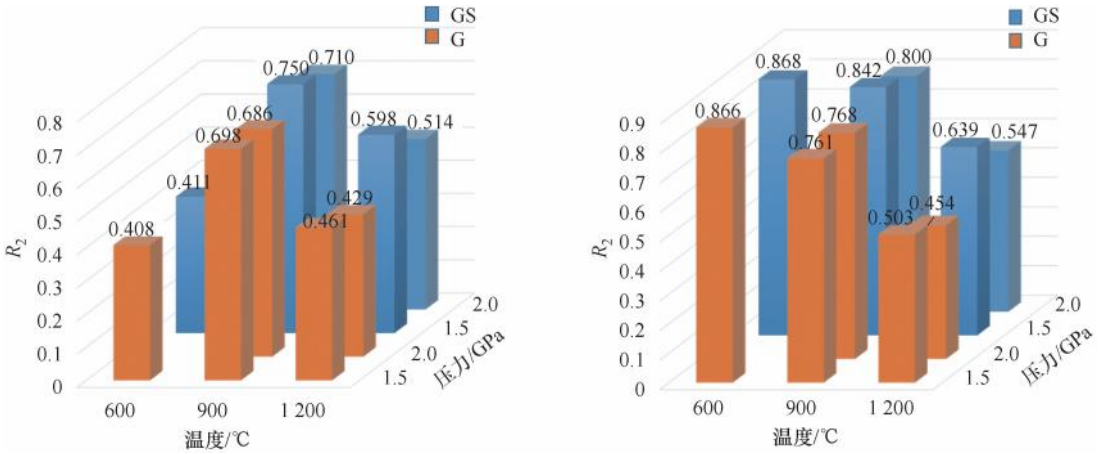

+ 10 G、GS d î ö) ï • K¼#V¸ C 'ã +

Fig. 10 Raman parameters with temperature and pressure of G and GS samples

通过构造 d R R 关系图 图 可对碳层间距与拉曼参数之间的关联进行分析 由图 可以看出 与 样品的晶格缺陷演化趋势相似 均为上凹曲线 的存在未改变样品缺陷消亡的规律 但 样品的 d R 曲线明显位于 样品上方 表明在相同碳层间距的情况下 样品的 R 值更高 面内缺陷占比更大 的存在阻碍了面内缺陷峰 消亡的过程 而通过 d R 关系图可发现 样品的曲线相比于 样品更靠近左侧 其在演化过程中可达到较 样品更低的缺陷度以及更小的晶格间距

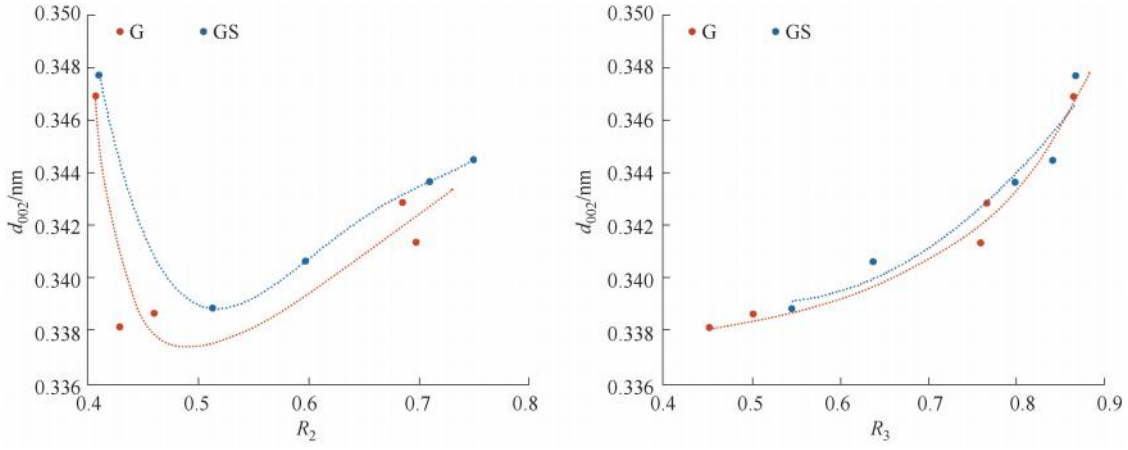

+ 11 d_{002}–R_2/R_3 2(+

Fig. 11 Relationship between d_{002}–R_2 and R_3

3.3 ₂ ž ú - Õ C ‰ƌU g)3

在高温高压模拟实验中 以 d 作为衡量石墨化程度的指标 发现 表现出对石墨化作用的阻碍效果 这与前人通过纯高温模拟实验得到的 可催化石墨化作用的结论截然相反 基于实验结果及学者研究成果 提出两种 在温压协同作用下阻碍煤石墨化作用的机理

化学抑制机理 学者已发现 在高温下可与煤中的碳发生反应形成中间物 中间物在更高的温度下分解并形成石墨晶体 而在高温高压实验体系内 压力的引入可以为化学反应提供活化能 弥补温度条件的不足 温压协同的环境可能降低了 的反应起始温度 使得 在较低温度下可与碳发生反应生成中间物 但压力增大的同时 也阻碍了中间物的分解 且实验温度不足以达到中间物分解所需温度 使得实验所提供的能量在中间

与重点方向 地学前缘

王路 董业绩 张鹤 等 煤成石墨化作用的影响因素及其实验验证 矿业科学学报

代世峰 任德贻 唐跃刚 煤中常量元素的赋存特征与研究意义 煤田地质与勘探

邱钿 煤的石墨化过程及煤系矿物变迁规律研究 徐州 中国矿业大学

曹代勇 王路 刘志飞 等 我国煤系石墨研究及资源开发利用前景 煤田地质与勘探

王路 煤系石墨的构造 热成矿机制研究 北京 中国矿业大学 北京

姜波 秦勇 金法礼　煤变形的高温高压实验研究　煤炭学报

于昭仪 谢卫宁 邱钿 等　添加剂对煤基石墨微观结构的影响　煤炭科学技术

相建华 曾凡桂 梁虎珍 等　不同变质程度煤的碳结构特征及其演化机制　煤炭学报

李焕同 曹代勇 邹晓艳 等　不同堆砌层数煤系石墨的拉曼光谱表征及其表面石墨化均匀程度　光谱学与光谱分析

曹代勇 魏迎春 李阳 等　煤系石墨鉴别指标厘定及分类分级体系构建　煤炭学报

秦勇　再论煤中大分子基本结构单元演化的拼叠作用　地学前缘

马翰明　高温高压下纳米碳化硅的分解　长春 吉林大学

刘志飞　基于模拟实验的煤岩显微组分石墨化差异性机制研究　北京 中国矿业大学 北京

Ń

（BP(4Œ³¼KuBbî ）

DOI:10.19856/j.cnki.issn.1001-5663.2024.01.008

思茅盆地页岩气地质条件及资源潜力分析

杜 江[1,2]

(1.湖南省地球物理地球化学调查所,湖南 长沙 410014;
2.湖南省地质新能源勘探开发工程技术研究中心,湖南 长沙 410014)

摘 要:根据野外调查及样品测试,从富有机质页岩的地化特征、物性特征及保存条件等分析了思茅盆地页岩气地质条件。研究表明:思茅盆地发育下密地组、羊八寨组、挖鲁八组及和平乡组四套暗色页岩;其中,羊八寨组页岩累计厚度普遍大于 100 m,TOC 平均为 1.06%~2.54%,R_o平均为 1.81%~3.47%,有机质类型主要为Ⅱ$_2$—Ⅲ型,脆性矿物含量平均为 49.5%,为思茅盆地页岩气有利层段。景谷洼陷南部和普文洼陷受深大断裂、地层抬升剥蚀、岩浆岩和变质岩带影响较小,盖层厚度大,页岩气保存条件相对较好。思茅盆地与相邻呵叻盆地具有相似的油气地质条件,具有一定的页岩气资源潜力,值得开展进一步的勘探研究工作。最后,综合考虑页岩分布、有机地化条件和保存条件,预测页岩气有利靶区主要位于勐班—德化及普文—象明一带。

关键词:页岩气;地质条件;资源潜力;有利靶区;思茅盆地
中图分类号:P618.1 **文献标识码**:A **文章编号**:1001-5663(2024)01-0061-11

0 引言

页岩气是一种自生自储于页岩层系中的游离态、吸附态非常规天然气[1-2]。页岩气勘探具有近 200 年的历史,尤其是近 10 年来,北美页岩气开发取得了快速的发展[3-4]。借鉴北美页岩气勘探开发经验,我国页岩气开发已经实现了局部地区突破,涪陵、长宁、威远等地相继建成工业化生产示范区[5-7]。

思茅盆地是云南省主要的含油气盆地之一[8],与泰国呵叻盆地相邻,后者自 1982 年投入开发以来,已经建成 13 亿方天然气、2.5 万吨原油的年产能,是泰国最大油气基地。上世纪末,思茅盆地发现了景谷地区陆相新近系小油田,并实现了小规模开发外,但是古生界、中生界(呵叻盆地油气藏目的层位)油气勘探仍未取得实质性的突破[9-10]。20 世纪中至 21 世纪初,国内学者研究了思茅盆地构造沉积演化背景[11-13]、岩性组合及有机地化特征,提出了上石炭统下密地组、上二叠统羊八寨组、上三叠统挖鲁八组及中侏罗统和平乡组等几套烃源岩,其中挖鲁八组、和平乡组富有机质页岩厚度小,有机碳含量低,下密地组分布有限,出露较少,都不是有效的、优质的页岩气目的层位;另一方面,羊八寨组富有机质页岩分布广泛,厚度较大,有机碳含量较高,成熟度适中,是思茅盆地最优质的页岩气目的层位[8,14]。所以,本文在总结前人研究成果的基础上,利用野外调查及测试数据,从富有机质页岩的地化特征、物性特征及保存条件等方面,重点分析了思茅盆地上二叠统羊八寨组页岩气地质条件和页岩气保存条件,进而分析资源潜力,优选有利区,为该区页岩气勘探开发提供基础资料和科学依据。

1 地质概况

思茅盆地位于滇西哀牢山、澜沧江之间,构造位置属于三江褶皱系北部,处在扬子地台、华南褶皱系、保山掸那地块之间[11-12],与南部的呵叻盆地相邻,盆地内发育“三凸两凹”二级构造单元(图 1)。该区受多期构造运动影响,构造演化极为复杂,具有陆壳裂解、多陆块相互作用、多岛弧一盆演化、陆内碰撞造山、

收稿日期:2023-07-18; **修回日期**:2023-10-05
第一作者:杜江(1988—),男,硕士,高级工程师,主要从事煤层气、页岩气地质研究。E-mail:1025774576@qq.com
引文格式:杜江. 思茅盆地页岩气地质条件及资源潜力分析[J].矿产与地质,2024,38(1):61-71.

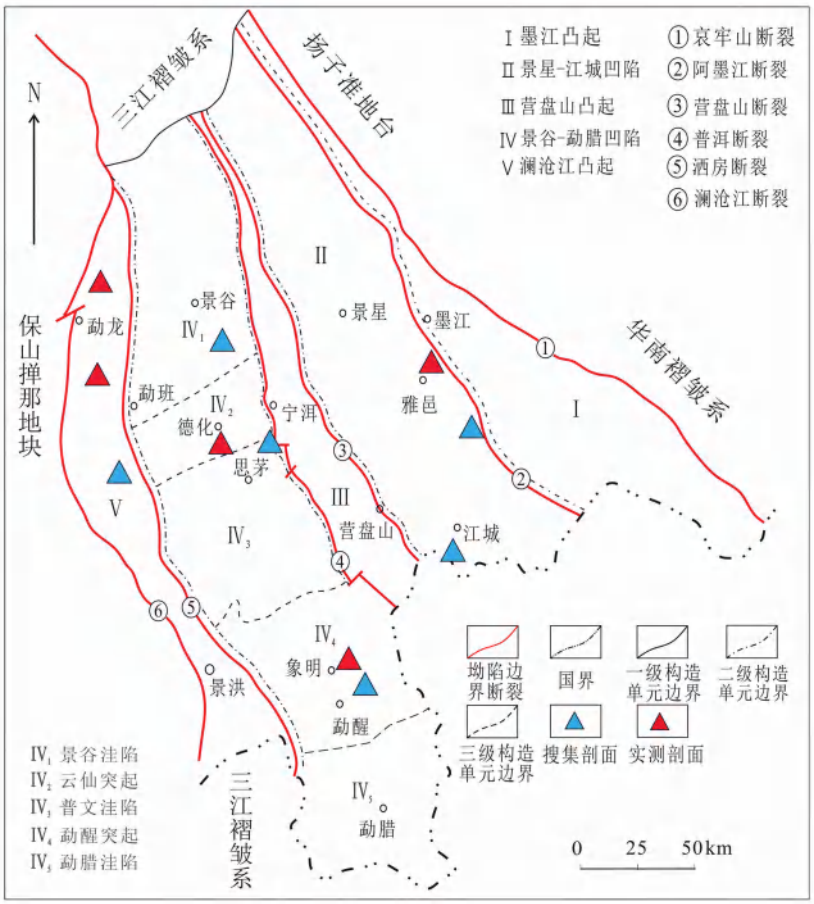

图 1 思茅盆地构造单元分布图

Fig.1 Distribution map of structural units in Simao Basin

挤压走滑等特征[12-13]。由于多期构造运动的影响，盆地内发育了一系列的性质复杂的断裂、褶皱。断裂走向为近 SN 向，相互切割，东部墨江—江城地区地层较为破碎，西部景谷—宁洱、勐腊地区相对完整。

思茅盆地发育泥盆系至新近系，缺失下三叠统、下侏罗统。地史时期伴随始—新特提斯洋的开启与闭合，形成了多套烃源岩。晚石炭世早期海侵规模达到高峰，形成了上石炭统灰色粉砂岩、粉砂质泥岩为主的下密地组，为该区第一套主力烃源岩（较厚，出露面积小）。早二叠世早期，随着古特提斯洋重新开启，发生规模海侵，至晚二叠世形成了一套暗色页岩、砂泥岩为主的羊八寨组，为该区第二套主力烃源岩（有机质丰度高，烃源岩厚度大）。中三叠世，中特提斯洋打开，晚三叠世继续扩张，形成了以灰色泥质粉砂岩与粉砂质泥岩互层为主的挖鲁八组，为该区第三套主力烃源岩（单层薄，有机质丰度低）。中侏罗世初期，新特提斯洋重新开启，盆地内普遍接受沉积，中侏罗统发育杂色泥页岩、泥灰岩、粉砂岩夹细砂岩，局部地区为灰色—灰黑色泥岩、页岩夹粉砂岩的和平乡组，为该区第四套主力烃源岩（厚度较小，有机质丰度低）（图 2）[15]。总体上，羊八寨组富有机质页岩分布广泛，厚度较大，有机碳含量较高，成熟度适中，是该区海相页岩气勘探首要目的层位[8,14]。

2 富有机质页岩特征

富有机质页岩厚度是生烃的物质保障，也有利于页岩气的富集和保存[16]。有机质是页岩生烃的母质，也是页岩气吸附的主要介质，所以有机质类型、丰度和成熟度是评价页岩生烃潜力的重要指标[16-18]。页岩矿物组成与含量往往会影响页岩气开采和压裂效果，页岩的脆性是评价储层岩石力学特征的重要指标，决定着页岩气储层的可压裂性，对页岩气的勘探开发影响重大[19]。

国内外成功开发页岩气的实践来看：商业性开发的页岩厚度一般大于 30 m，有机质类型多为 $Ⅱ_2$—Ⅲ，丰度 TOC 一般大于 2.0%，热演化程度 R_o 一般为 1.1%～3.5%，脆性矿物含量一般为 50%左右[16-19]。

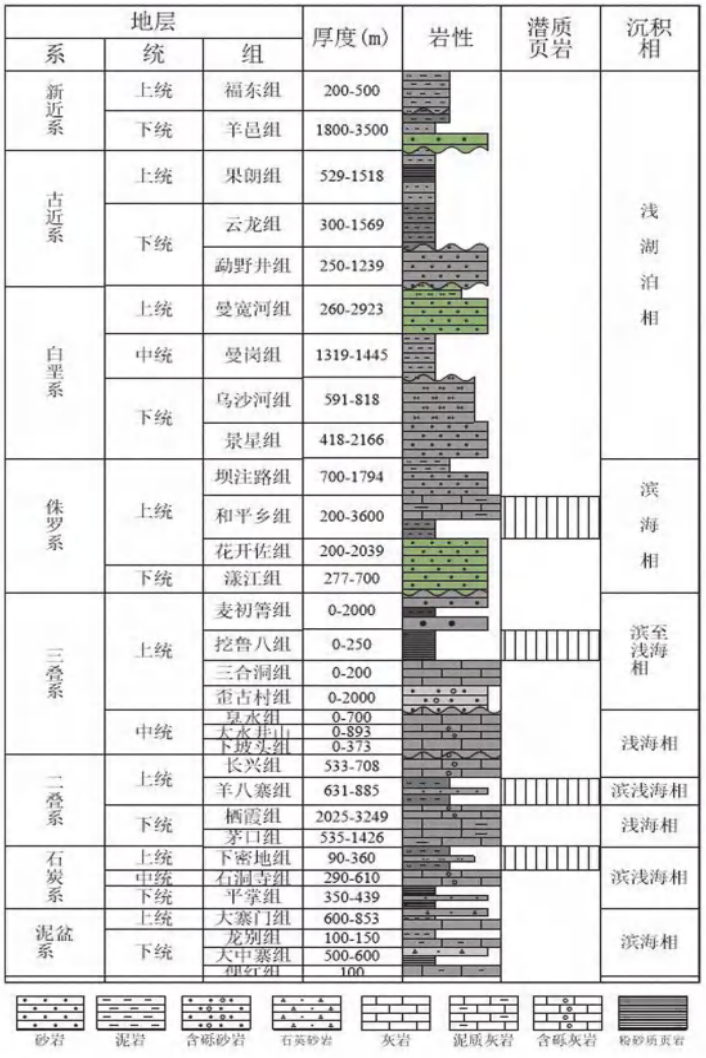

图 2　思茅盆地地层综合柱状图(据文献[15]修改)

Fig.2　Comprehensive stratigraphic column diagram of Simao Basin[15]

2.1　羊八寨组富有机质页岩厚度

思茅盆地上二叠统羊八寨组(P_3y)沉积环境为滨海相、浅海陆棚相[8,13],多发育砂岩、泥岩、页岩、砂泥互层,局部夹劣质薄煤层,具有交错层理、水平层理、缓波状交错层理。实测羊八寨组剖面富有机质页岩累计厚度为 80.14～187.6 m(表 1、图 3)。平面上,北部在镇沅以南、宁洱以北,景谷至墨江一带暗色页岩厚度最大,累计厚度一般大于 140 m,向周围逐渐减小。南部象明至雅邑狭长地带的暗色页岩厚度较大,累计厚度一般大于 120 m,并向东、西、南方向逐渐减小(图 4)。

表 1　思茅盆地页岩气形成条件地质参数对比

Table 1　Comparison of geological parameters of shale gas generation condition in Simao Basin

层位	剖面名称或采样点	累计厚度/m	TOC/%		R_o/%		备注
			范围值	平均值	范围值	平均值	
P_3y	宁洱德化	85.3	0.90～1.20	1.06	1.79～1.86	1.81	未见顶
	景谷小石岩	107.4	0.56～3.43	1.83	2.70～2.90	2.83	未见顶
	景谷勐龙	187.6	0.26～1.60	0.55	3.06～3.20	3.13	未见底
	墨江雅邑	126.8	1.31～4.72	2.54	3.27～3.38	3.33	未见底
	墨江羊八寨	—	2.44～2.67	2.25	3.35～3.54	3.47	采样点
	勐腊象明	80.14	0.82～6.78	1.99	3.04～3.94	3.40	未见底
	江城嘉禾	—	0.70～1.47	1.11	3.05～3.52	3.29	采样点

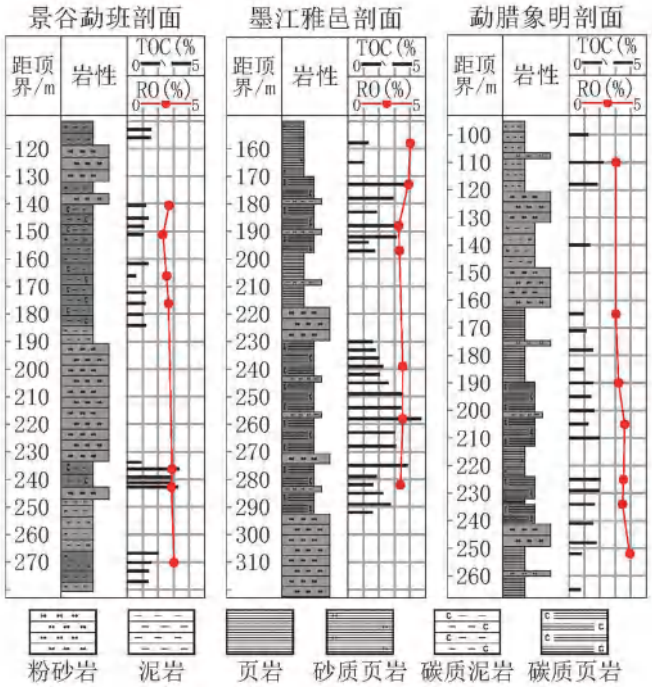

图 3 思茅盆地羊八寨组暗色页岩段典型剖面综合柱状图

Fig.3 Comprehensive column diagram of the typical profile of Yangbazhai Formation dark shale in Simao Basin

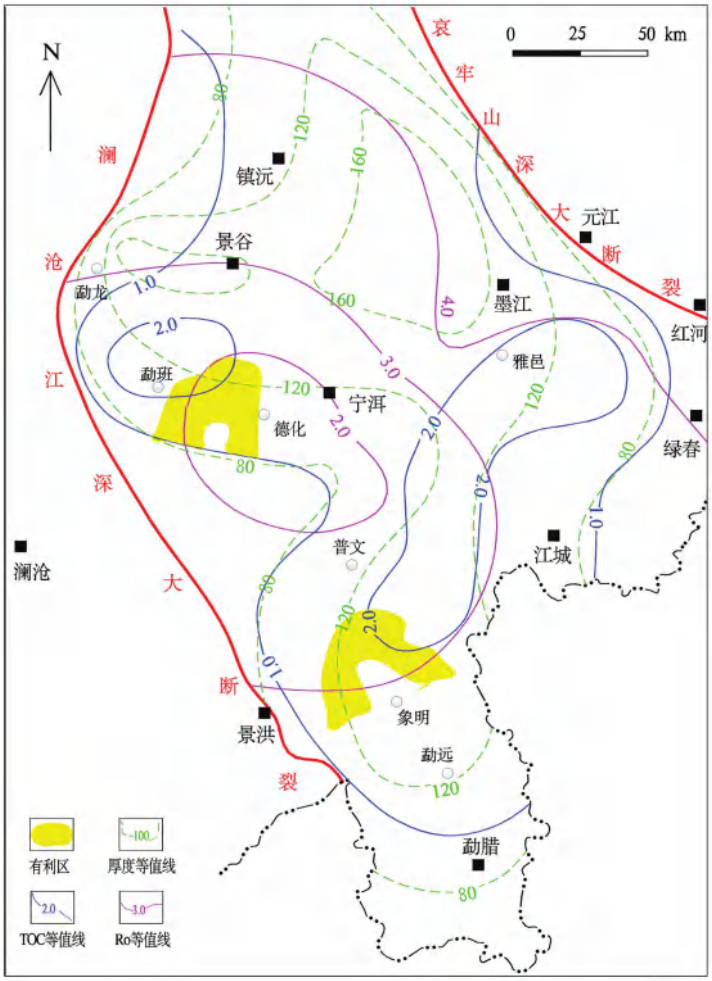

图 4 思茅盆地羊八寨组黑色页岩综合评价图

Fig.4 Comprehensive evaluation diagram of Yangbazhai Formation dark shale in Simao Basin

2.2　羊八寨组富有机质页岩地化特征

2.2.1　有机质类型

岩石热解分析表明,羊八寨组暗色泥页岩有机质类型以Ⅲ型为主;有机质显微组分壳质组为主,其次为镜质组,腐泥组含量一般较低,一般小于 20%,TI 指数一般为 0～40,少量大于 40 或小于 0,有机质类型多为$Ⅱ_2$型,少量为$Ⅱ_1$型、Ⅲ型。

2.2.2　有机质丰度与成熟度

思茅盆地景谷—宁洱地区羊八寨组暗色泥页岩 TOC 值为 0.23%～3.43%,一般小于 1.5%,平均仅为 0.90%;R_o为 1.31%～3.2%,一般小于 3.0%,平均为 2.40%,为过成熟早期阶段。墨江—江城地区羊八寨组暗色泥页岩样品 TOC 为 0.70%～4.72%,一般大于 1.5%,平均高达 2.49%;R_o为 3.27%～4.42%,平均为 3.69%,为过成熟晚期阶段。勐腊地区羊八寨组暗色泥页岩样品 TOC 为 0.27%～6.78%,一般为 1.0%～3.0%,平均为 1.68%;R_o为 3.04%～3.94%,平均值为 3.35%,为过成熟晚期阶段(表 1、图 4)。羊八寨组富有机质页岩有机质类型多为$Ⅱ_2$—Ⅲ型。

平面上,TOC 高值区主要位于景谷勐班、墨江雅邑、勐腊象明一带,TOC 平均值一般大于 2.0%,并向四周逐渐减小。R_o高值区主要位于盆地边缘深大断裂附近,R_o值一般大于 3.0%,局部可达 4.0%,具有向盆地中部逐渐减小的趋势,低值区位于宁洱、德化地区,R_o一般为 1.5%～2.0%(图 4)。

2.3　羊八寨组富有机质页岩物性特征

2.3.1　矿物组分

羊八寨组页岩矿物组分中石英含量最高,一般为 31.8%～57.2%,平均为 47.7%,其次为黏土矿物,含量一般为 33.7%～55.5%,平均为 45.9%,此外还含有少量的长石、方解石、白云石、菱铁矿和黄铁矿(图 5、图 6)。羊八寨组页岩脆性矿物含量一般为 31.8%～64.4%,平均为 49.5%,表明羊八寨组页岩具有较好的可压性。

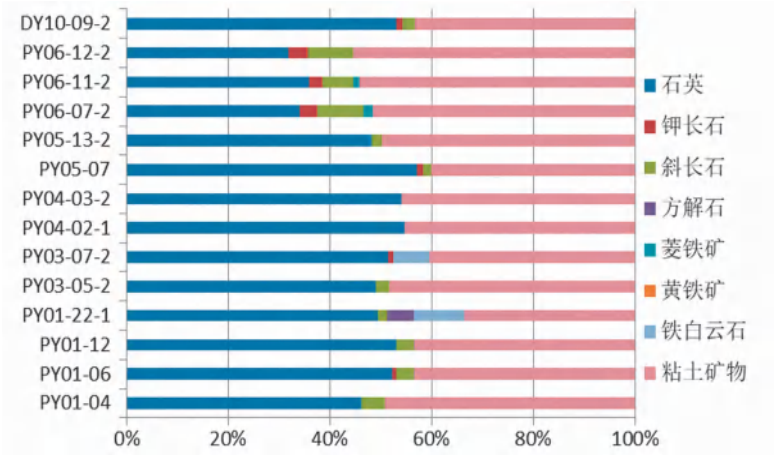

图 5　思茅盆地羊八寨组泥页岩矿物组成条形图

Fig.5　Bar graph of mineral composition of Yangbazhai Formation mudshale in Simao Basin

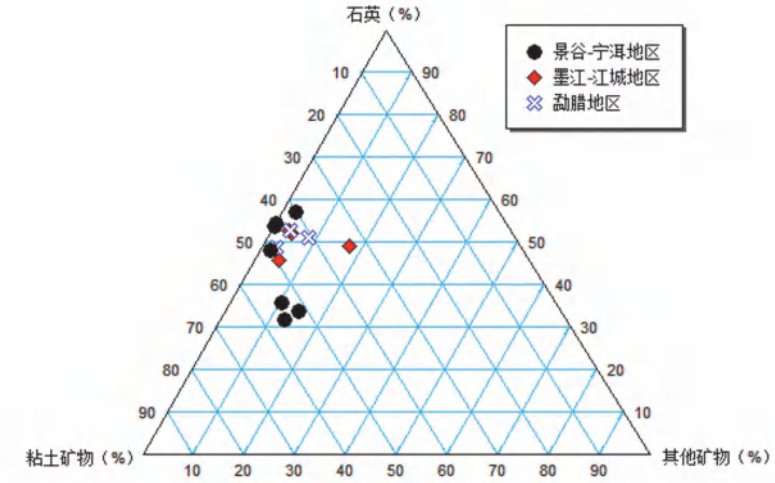

图 6　思茅盆地羊八寨组泥页岩矿物组成三元图

Fig.6　Ternary diagram of mineral composition of Yangbazhai Formation mudshale in Simao Basin

黏土矿物中又以伊蒙混层与伊利石与为主，含少量绿泥石与高岭石；伊蒙混层占 0%～79%，平均为 55%，伊利石占黏土矿物总量的 11%～67%，平均 39%；伊蒙混层和伊利石之和为 67%～90%；伊蒙间层比平均在 15%左右。

2.3.2 孔裂隙特征

(1)孔隙类型

羊八寨组页岩发育有机孔、粒间孔、晶间孔、溶蚀孔和微裂缝，以粒间孔、晶间孔和微裂缝为主，总体来看，孔隙裂隙不发育，岩石致密(图 7)。

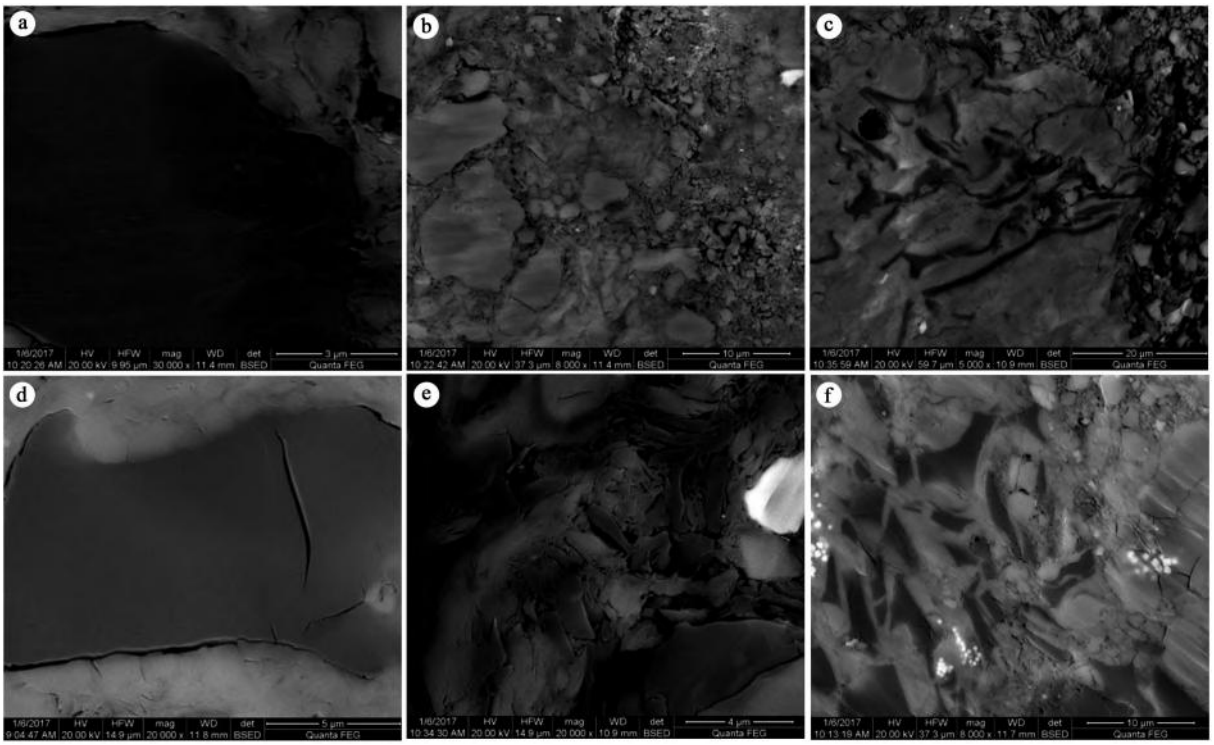

图 7 思茅盆地羊八寨组页岩孔裂隙类型照片

Fig.7 Microphotos of pore fracture types of Yangbazhai Formation shale in Simao Basin

(a) 有机质及其内部，未见孔隙；(b) 碎粒及粒间孔；(c) 壳质组碎屑，溶蚀孔，碎粒孔，黏土矿物；(d)有机质内及有机质与黏土矿物之间微裂缝；(e) 泥粒与泥粒孔，碎屑状有机质；(f) 壳质组碎屑，溶蚀孔，碎粒孔，黏土矿物。

(2)孔隙形态特征

根据国际纯粹与应用化学联合会(IUPAC)的分类，页岩样品的吸附等温线属于Ⅳ型。在较高压力(P/P_0>0.4，其中 P 为当前压力，MPa；Po 为 −196.15℃下的氮气饱和蒸汽压，约为 0.101 MPa)处，页岩样品的吸附曲线与解吸曲线不重合，产生吸附滞后。滞后环的形状则反映了吸附剂(页岩样品)中所存在孔隙结构的情况。页岩样品的Ⅳ型等温线和滞后回线说明页岩主体孔隙为中孔。IUPAC 在 de Boer 滞后环分类的基础上推荐了一种新的分类标准，将滞后环分为 4 类：H_1 型、H_2 型、H_3 型和 H_4 型。勐腊象明地区、景谷勐龙地区羊八寨组(P_3y)页岩样品滞回环属于 H_3 型(图 8)，反映羊八寨组对应样品是四周开放的平行板孔，从微孔到大孔各个孔径段的孔隙均较发育，孔隙的连通性较好，这种孔隙结构对页岩气体的运移有利。

(3)孔径分布特征

比表面积计算采用 Brunauer、Emmett 和 Teller 推导出的 BET 方程，孔径分布采用 BJH 法计算。羊八寨组页岩孔径分布相对较简单，孔径分布曲线峰值相对集中。页岩平均孔径为 4.8～8.8 nm，其平均值为 6.53 nm。根据 IUPAC 的分类，孔直径小于 2 nm 的孔隙称为微孔，孔直径在 2～50 nm 的孔隙为中孔，大于 50 nm 的孔隙为大孔，所以羊八寨组页岩样品孔径分布在中孔范围。

(4)孔隙比表面积和体积

思茅盆地羊八寨组组泥页岩比表面积在 2.708～26.611 m^2/g，平均为 15.736 m^2/g。孔体积在 0.006～0.032 22 mL/g 范围内，平均为 0.027 84 mL/g。其中下密地组比表面积为 17.927 m^2/g，总孔体积平均值同样为 0.031 24 mL/g；羊八寨组比表面积平均为 21.40 m^2/g，总孔体积平均在 0.014 85 mL/g。整体羊八寨组比表面积和总孔体积一般。

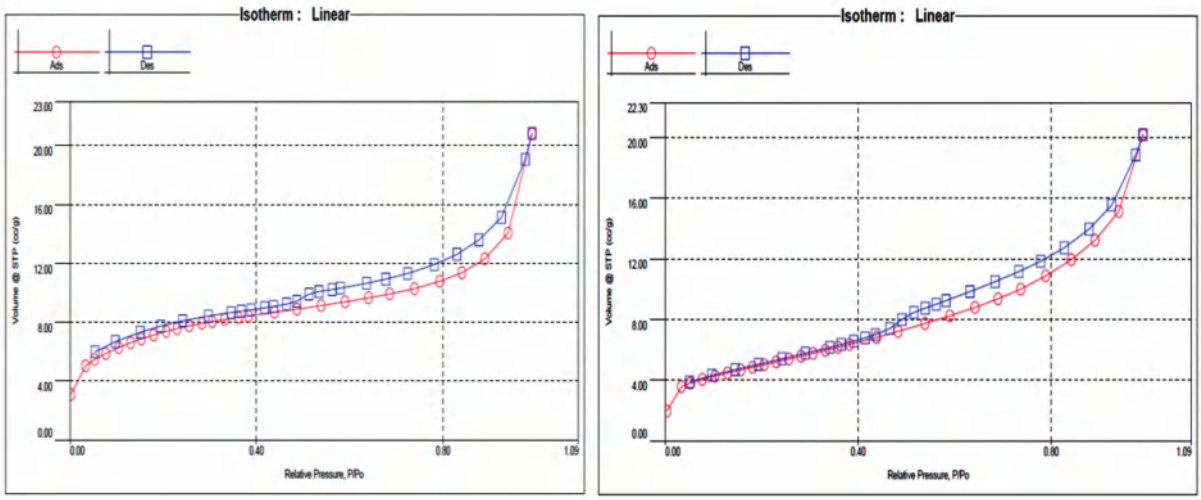

图 8　羊八寨组页岩样品吸-脱附曲线

Fig.8　Adsorption desorption curve of shale samples from Yangbazhai Formation

(a)勐腊象明　(b)景谷勐龙

2.3.3　吸附性特征

羊八寨组暗色泥页岩饱和吸附量主要在 1.18～6.52 m^3/t,平均值为 2.92 m^3/t,可见区内羊八寨组暗色泥页岩吸附性较好,具有相对较好的储集性能(图 9)。平面上泥页岩吸附性能变化较大,景谷—宁洱地区碧安附近泥页岩吸附性最好,而勐龙附近受区域断裂及岩浆岩影响,泥页岩局部变质为板岩,吸附性变差;墨江五素、江城象明地区羊八寨组泥页岩吸附性能一般。

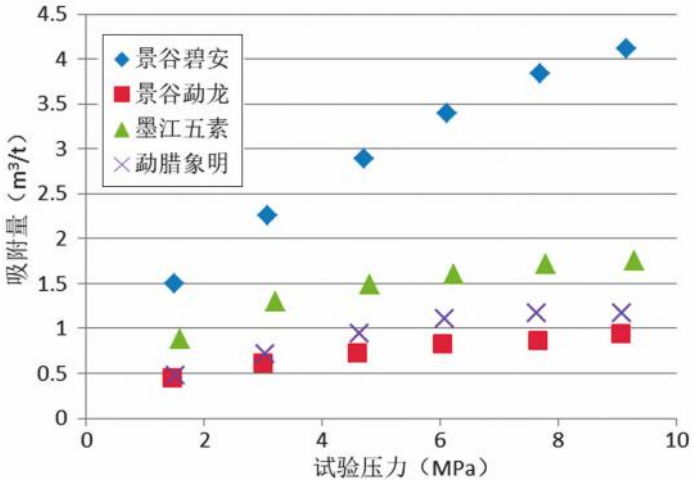

图 9　思茅盆地羊八寨组富有机质页岩等温吸附曲线

Fig.9　Isothermal adsorption curve of organic rich shale of Yangbazhai Formation in Simao Basin

2.4　其他层位富有机质页岩特征

2.4.1　上石炭统下密地组(C_3x)

密地组仅在墨江下密地、江城鲁凸等地零星出露。本次调查在墨江下密地附近测得剖面一条,岩性多为灰黄色粉砂、泥岩和深灰—灰黑色的页岩、泥岩,局部夹劣质薄煤层,该条剖面富有机质页岩累计厚度为 52.4 m,富有机质页岩 TOC 值为 0.65%～9.54%,平均为 3.77%,R_o为 2.5%～2.81%,平均为 2.67%。下密地组富有机质页岩有机质类型为Ⅱ$_1$—Ⅲ$_2$型。由于下密地组出露较少,样品数量有限,其地化特征有待进一步研究。下密地组石英含量为 37.5%～62.2%,平均为 48.7%;黏土矿物含量为 36.5%～60.7%,平均为 49.8%。

2.4.2　上三叠统挖鲁八组(T_3wl)

思茅盆地上三叠统挖鲁八组分布较为局限,在墨江—江城地区出露。本次调查在墨江一碗水测得典

型剖面一条，岩性多为深灰色页岩、粉砂质页岩，发育水平层理，富有机质页岩累计厚度为49.8 m。一碗水剖面富有机质页岩TOC为0.55%～1.05%，平均值为0.84%，R_o为2.43%～3.06%，平均为2.79%，为过成熟早期阶段；碧溪一带鲁八组泥页岩TOC为0.51%～1.53%，平均值为0.92%，R_o为3.31%～4.15%，平均为3.88%，为过成熟晚期阶段。挖鲁八组富有机质页岩有机质类型为Ⅱ型。暂不作为有效的、优质的页岩气目的层位。

挖鲁八组(T_3wl)暗色泥页岩石英含量最高，一般为42.8%～51.6%，平均47.3%，其次为黏土矿物，一般为43.2%～49.8%，平均为46.5%；此外还含有少量的长石、方解石、白云石和黄铁矿。

2.4.3 中侏罗统和平乡组(J_2h)

思茅盆地中侏罗统和平乡组出露极为广泛，整个盆地皆有出露，本次调查在景谷、思茅、景洪等地见暗色泥岩、钙质泥岩及泥灰岩出露，富有机质页岩厚度一般为10～26.5 m。TOC为0.05%～2.67%，一般小于0.6%，平均为0.39%。R_o为1.18%～2.26%，平均值为1.69%，一般小于2.0%，总体上富有机质页岩成熟度相对较低，属于高成熟阶段和平乡组泥页岩有机质类型为$Ⅱ_2$型为主，少量$Ⅱ_1$和Ⅲ型。暂不作为有效的、优质的页岩气目的层位。

和平乡组暗色泥页岩石英含量最高，一般为17.6%～58.8%，平均42.5%，黏土矿物一般为22.4%～49.1%，平均为34.4%，此外还含有少量的长石、方解石、白云石和黄铁矿。脆性矿物含量一般为41.9%～64.1%，平均为54.65%。

3 页岩气保存条件简析

三江褶皱系思茅盆地具有复杂的构造演化历史，多旋回、多期次的构造叠加对页岩气藏影响较大，这也决定了保存条件为页岩气富集的关键因素。因此，针对主要页岩层位，分析了断裂发育情况、盖层发育、抬升剥蚀、岩浆活动和变质岩带等对页岩气保存的影响。

3.1 断层发育情况

断裂对于页岩气保存具有二重性，适当规模的断裂体系，有利于页岩气的富集保存和产出，但是规模较大的张性断层极不利于页岩气的保存[13,20-21]。思茅盆地断层发育、分布广泛，断层性质复杂，具有多期活动的特点，大多具压扭性—逆冲—走滑性质。从形成时间分析，断裂的形成时间应为早三叠世、早侏罗世、晚白垩世、中—晚始新世、渐新世—早更新世五个强烈构造活动时期，其中渐新世、中新世形成的走滑断裂具有张性性质，开启性强，属于通天断裂，对页岩气的保存破坏作用极大。从平面上分析，墨江凸起、营盘山凸起、澜沧江凸起及景星—江城凹陷受通天断裂影响较大，页岩气保存条件差，而景谷—勐腊凹陷的景谷洼陷、普文洼陷受通天断裂影响较小，页岩气保存条件相对较好(图10)。

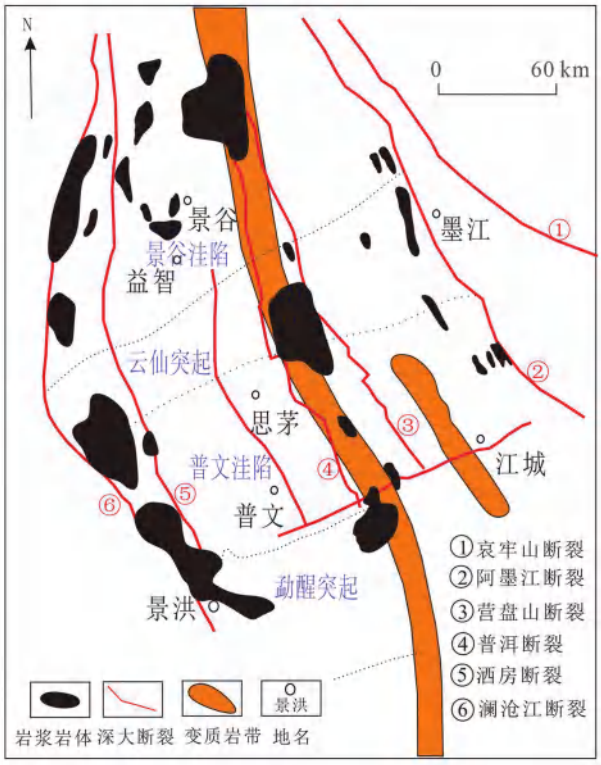

图10 思茅盆地深大断裂、岩浆岩和变质岩分布图

(据文献[13]修改)

Fig.10 Distribution map of deep faults, magmatic and metamorphic rocks in Simao Basin [13]

3.2 盖层条件

页岩气藏集生储盖为一体，部分学者认为页岩储层自身为一个封闭的系统，对盖层的研究相对较弱，但随着国内外页岩气勘探研究理论进步，越来越多的学者意识到盖层条件的重要性，尤其是复杂地质条件下盖层对页岩气的富集保存起到了至关重要的作用[13,21-23]。思茅盆地侏罗系到二叠系发育9套泥质岩，累计厚度可达1 996 m。羊八寨组烃源岩的直接盖层为羊八寨组、长兴组泥质岩，厚度100～600 m，但泥岩成岩程度较高，已达到晚成岩阶段，可塑性变差而封盖性降低，封盖性能一般。

3.3 抬升剥蚀

地壳抬升剥蚀会破坏区域盖层，降低断层封闭

性[13,22-23]。思茅盆地生烃演化史表明,该区经历了早三叠世、早侏罗世、晚白垩世、中—晚始新世、渐新世—早更新世五次强烈的抬升剥蚀作用,其中以晚白垩世的抬升剥蚀最为剧烈,直接导致烃源岩埋深减小,盖层厚度变薄,以及大气水下渗加剧,页岩气运移散失,极大程度上破坏了页岩气的富集保存(图 11)。盆地边缘墨江凸起、澜沧江凸起及勐醒突起抬升剥蚀与大气水下渗程度相对较大,其对页岩气藏的破坏较严重;景谷洼陷、普文洼陷由于上覆地层较厚,受抬升剥蚀与大气水下渗影响较小。

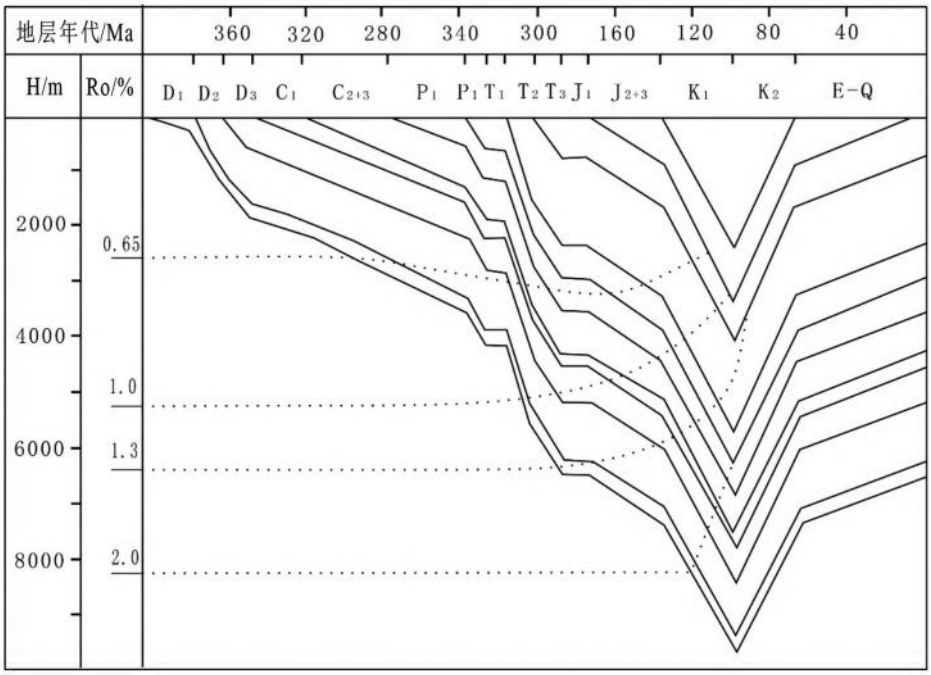

图 11　思茅盆地地层埋藏史(据文献[13])

Fig.11　Burial history of the strata in Simao Basin [13]

3.4　岩浆活动与变质作用

岩浆活动对具有促进泥页岩成熟及页岩气生成的积极作用,但如果页岩气成藏后遭到侵入岩体穿刺和烘烤,将对页岩气保存产生严重破坏[13,24]。思茅盆地发育多期次岩浆活动,三叠纪的岩浆活动对盆地西部古生界页岩气保存具有破坏作用,新生代的岩浆活动对盆地中部的古生界、中生界页岩气保存具有较大的破坏作用。

思茅盆地内存在两条中新生代接触变质带,其中沿中部断裂带分布的低压变质带,延伸较长,变质岩带内二叠系、三叠系、侏罗系已浅变质,对页岩气的保存具有不利影响(图 10)。

平面上,思茅盆地墨江凸起、营盘山凸起、澜沧江凸起受岩浆岩或变质岩带影响明显。如墨江、景谷勐龙等地羊八寨组页岩 R_o 多大于 3.0%,局部接近 4.0%,再如墨江碧溪挖鲁八组页岩 R_o 最大可达 4.15%,都表明上述区域受深大断裂附近的岩浆岩影响,导致泥页岩变质程度急剧增高,不同程度破坏页岩气保存条件。景谷洼陷南部益智—宁洱一带及普文洼陷羊八寨组页岩 R_o 多小于 3.0%,其中宁洱德化羊八寨组页岩 R_o 平均值仅为 1.81%,说明岩浆活动及变质岩带对页岩气保存条件破坏较弱,为相对有利区(图 10)。

4　页岩气资源潜力分析

上文已述,思茅盆地主要烃源岩层位为上二叠统羊八寨组,故本节重点分析羊八寨组页岩气资源潜力。上石炭统下密地组、上三叠统挖鲁八组、中侏罗统和平乡组等次要烃源岩层暂不论述。

在系统分析羊八寨组富有机质页岩厚度、有机地化特征、矿物组分及油气保存条件的基础上,对比相邻呵叻盆地油气地质条件。表明,两者具有相似的构造格架和地层层序、相似的构造演化史、相似的构造形态、相似烃源岩有机地化条件,但思茅盆地后期构造改造较强烈,保存条件较差(表 2)。总体上,思茅盆地具有一定的页岩气资源潜力,值得开展进一步的勘探研究工作。

表2 思茅盆地与呵叻盆地油气地质条件对比

Table 2 Comparison of oil and gas geological condition between Simao Basin and Khorat Basin

对比条件	思茅盆地	呵叻盆地
构造格架与地层层序	“北窄南宽,人字形断裂夹持盆地”,“三隆夹两凹”构造格局,以T、J、K为盖层	“北窄南宽,人字形断裂夹持盆地”,“三隆夹两凹”构造格局,以T、J、K为盖层
构造演化史	喜山:挤压抬升褶皱、走滑 印支—燕山:抬升剥蚀,海相转陆相 华力西:海陆交互转海相、特提斯域	喜山:改造相对较弱 印支—燕山:抬升剥蚀,海相转陆相 华力西期:海相、特提斯域
构造形态	发育永安构造,南北向隆起构造	发育普温气田,南北向隆起构造
烃源岩条件	烃源岩:上二叠统羊八寨组(P_3y) TOC:0.26%～6.78%,平均约为1.5% 干酪根:Ⅱ$_2$～Ⅲ型为主 R_o:1.79%～3.94%	烃源岩:上二叠统(P_3) TOC:0.11%～6.83%,平均1.01% 干酪根:Ⅱ型为主 R_o:1.75%～5.01%
成藏模式	构造、不整合面有关的复合圈闭	古潜山式油气藏,构造、不整合面复合圈闭
保存条件	(1)三叠—白垩系盖层 (2)侏罗系膏盐膏盐分布范围零星 (3)后期构造改造强	普温气田:(1)三叠—白垩系盖层 (2)白垩系膏盐广布 (3)后期构造改造弱

5 有利区优选

参考中国地调查局2015年制定的《页岩气基础地质调查工作指南》中对于页岩气有利区划分标准,考虑构造发育情况及富有机质页岩厚度、有机碳含量、成熟度及保存条件,预测了羊八寨组富有机质页岩有利区两处:勐班—德化有利区和普文-象明有利区(图4)。勐班—德化有利区富有机质页岩累计厚度80～120 m,有机碳含量平均为1.83%,镜质体反射率1.81%～2.83%;普文—象明有利区富有机质页岩累计厚度大于100 m,TOC平均为1.99%,R_o为3.40%;两处有利区内构造相对简单,盖层厚度大,受岩浆活动和变质作用影响小,保存条件较好(图10)。

6 结论

(1)思茅盆地发育上石炭统下密地组、上二叠统羊八寨组、上三叠统挖鲁八组及中侏罗统和平乡组4套烃源岩。羊八寨组富有机质页岩厚度最大(>100m),有机质丰度高(TOC平均为1.06%～2.54%),成熟度适中(R_o平均为1.81%～3.47%);羊八寨组页岩矿物组分以石英、黏土矿物为主,含少量长石、方解石、白云石、菱铁矿和黄铁矿,脆性矿物含量高(平均大于49.5%);页岩主要发育粒间孔、晶间孔和微裂缝,孔径3～5 nm,主要为中孔。羊八寨组为思茅盆地最优质的页岩气目的层位。

(2)景谷洼陷、普文洼陷远离深大断裂,受新生代的走滑断裂、地层抬升剥蚀、岩浆活动、接触变质作用影响较小,盖层稳定且厚度较大,保存条件相对较好。

(3)思茅盆地与呵叻盆地具有相似的构造格架、地层层序、构造演化史、构造形态、烃源岩有机地化条件,具有一定的页岩气资源潜力,但后期构造改造较强烈,保存条件较差,也具有较大的风险。

(4)思茅盆地页岩气有利区位于勐班—德化和普文—象明一带,该区羊八寨组富有机质页岩累计厚度大(80～120 m),有机碳含量较高(TOC平均为1.83%～1.99%),热演化程度适中(R_o为1.81%～3.40%),保存条件较好,是下一步勘探研究重点方向。

参考文献:

[1] 张金川,金之钧,袁明生. 页岩气成藏机理和分布[J]. 天然气工业,2004,24(7):15-18.

[2] 冷济高,龚大建,李飞,等. 黔东北地区牛蹄塘组页岩气勘探前景分析[J]. 地学前缘,2016,23(2):29-38.

[3] 董大忠,高世葵,黄金亮,等. 论四川盆地页岩气资源勘探开发前景[J]. 天然气工业,2014,34(12): 1-15.

[4] U.S. Energy information administration(EIA). Annual energy outlook 2014 with projects to 2040 [EB/OL].

[5] 郭彤楼. 中国是关键地质问题与成藏富集主控因素[J]. 石油勘探与开发,2016,43(3):317-325.

[6] 郭彤楼. 涪陵页岩气田发现的启示与思考[J]. 地学前缘,2016,23(1):29-30.

[7] 邹才能,董大忠,王玉满,等. 中国页岩气特征、挑战及前景(一)[J]. 石油勘探与开发,2015,42(6):689-701.

[8] 梁兴,叶舟,徐克定,等. 思茅坳陷油气地质特征与勘探远景展望[J]. 天然气工业,2005,25(6):1-6.

[9] 沈平,徐永昌,郑建京. 景谷盆地低演化油气的同位素地球化学特征[J]. 沉积学报,2002,20(1):151-154.

[10] 王大锐,高建昆,罗怀章,等. 云南景谷盆地低熟石油地球化学特征与意义[J]. 石油学报,2001,22(5):11-15.
[11] 谭富文. 云南思茅三叠纪弧后前陆盆地的沉积特征[J]. 沉积学报,2002,20(4):560-567.
[12] 史鹏亮,杨天南,梁明娟,等. 三江构造带新生代变形构造的时-空变化:研究综述及新数据[J]. 岩石学报,2015,31(11):3331-3352.
[13] 陈跃昆,廖宗廷,陈军. 滇西兰坪—思茅盆地 TSM 分析[M]. 武汉:中国地质大学出版社,2009.
[14] 卢齐军. 云南思茅坳陷油气勘探潜力分析[J]. 四川地质学报,2015,35(1):34-37.
[15] 梁兴,叶舟,徐克定,等. 思茅坳陷油气地质特征与勘探远景展望[J]. 天然气工业,2005,25(6):1-6.
[16] 涂乙,邹海燕,孟海平,等. 页岩气评价标准与储层分类[J]. 石油与天然气科学,2014,35(1):153-158.
[17] 王丽波,久凯,曾维特,等. 上扬子黔北地区下寒武统海相黑色泥页岩特征及页岩气远景区评价[J]. 岩石学报,2013,29(9):3263-3278.
[18] 单长安,张廷山,郭军杰,等. 中扬子北部上震旦统陡山沱组地质特征及页岩气资源潜力分析[J]. 中国地质,2015,42(6):1944-1958.
[19] 袁俊亮,邓金根,张定宇,等. 页岩气储层可压裂性评价技术[J]. 石油学报,2013,34(3):523-527.
[20] 李建青,高玉巧,花彩霞,等. 北美页岩气勘探经验对建立中国南方海相页岩气选区评价体系的启示[J]. 气地质与采收率,2014,21(4):23-27,32.
[21] 李海,白云山,王宝忠,等. 湘鄂西地区下古生界页岩气保存条件[J]. 油气地质与采收率,2014,21(6):22-25.
[22] 潘仁芳,唐小玲,孟江辉,等. 桂中坳陷上古生界页岩气保存条件[J]. 石油与天然气地质,2014,35(4):534-541.
[23] 魏祥峰,李宇平,魏志红,等. 保存条件对四川盆地及周缘海相页岩气富集高产的影响机制[J]. 石油实验地质,2017,39(2):147-153.
[24] 万丛礼,李钜源,金强,等. 断陷盆地岩浆侵入对页岩气的富集作用[J]. 天然气地球科学,2011,22(6):1088-1093.
[25] 孟江辉,潘仁芳,陈浩,等. 滇黔桂盆地泥盆系页岩气成藏条件及资源潜力分析[J]. 现代地质,2016,30(1):181-193.

Analysis of shale gas geological condition and resource potential in Simao Basin

DU Jiang[1,2]

(1. *Geophysical and Geochemical Survey Institute of Hunan*, *Changsha* 410014, *Hunan*, *China*;
2. *Hunan Geological New Energy Exploration and Development Engineering Technology Research Center*, *Changsha* 410014, *Hunan*, *China*)

Abstract: Based on field investigation and sample testing, the geological condition of shale gas in Simao Basin is analyzed from the geochemical characteristics, physical properties and preservation condition of organic rich shale. The study result shows that there are developed for four sets of dark shale in Simao Basin, Xiamidi Formation, Yangbazhai Formation, Waluba Formation and Hepingxiang Formation. Among them, because the cumulative thickness of shale in Yangbazhai Formation is generally greater than 100 meters, with an average TOC of 1.06% - 2.54% and an average Ro of 1.81% - 3.47%, and the organic matter type is mainly II2-3 type, with an average brittle mineral content of 49.5%, Yangbazhai Formation is a favorable shale gas layer in Simao Basin. The south part of Jinggu Depression and Puwen Depression are less affected by deep faults, stratigraphic uplift and erosion, magmatic rocks and metamorphic rock belts, and there is a thick cover rock layer, resulting in relatively good condition for shale gas preservation. Simao Basin has a similar oil and gas geological condition to the adjacent Khorat Basin, and there is a certain shale gas resource potential, which is worth further exploration and research work. Finally, for the comprehensive consideration of shale distribution, organic geochemical condition, and preservation condition, it is predicted that the favorable target area for shale gas is mainly located in the Mengban-Dehua and Puwen-Xiangming areas.

Keywords: shale gas, geological condition, resource potential, favorable target area, Simao Basin

中扬子地台宜昌地区寒武系水井沱组优质页岩储层发育特征及天然气富集机理研究

蔡宁波[*1,2]，王琳霖[3]，鲍一遥[4]，李怡普[4]，万泽鑫[4]，康志梅[4]，罗胜元[5]

（1.中国地质大学（武汉）高等研究院，湖北 武汉 430070；2.湖南省地质新能源勘探开发工程技术研究中心，湖南 长沙 410014；3.中国石化石油勘探开发研究院，北京 100083；4.长江大学油气资源与勘探技术教育部重点实验室，湖北 武汉 430100；5.中国地质调查局武汉地质调查中心，湖北 武汉 430205）

摘　要：本文针对宜昌地区最新的钻孔资料，利用多学科交叉手段，查明该地区水井沱组优质页岩储层的特征以及油气富集规律，建立页岩气保存模型，旨在为该地区页岩气勘探提供参考。研究结果表明，水井沱组页岩有机质丰度高，有机碳含量（TOC）主要分布在0.56%~8.42%，干酪根以II1型和I型为主，Ro等效值分布在2.4%~3.2%。水井沱组页岩储层孔隙度主要分布在0.5%~9.1%，渗透率主要分布在0.019～0.540×10^{-3} μm^2，其页岩的储集空间主要包括有机孔隙、无机孔隙以及裂缝等类型。储集空间的发育程度主要与有机质富集程度、黏土矿物含量以及页理缝的发育程度有关。天然气主要以吸附气（45.21%~81.44%）和游离气（18.56%~54.79%）的状态附存于水井沱组页岩储层中，溶解气的比例相对较小。水井沱组页岩储层的含气性主要受有机碳含量、脆性矿物比例以及裂缝发育程度有关。有机碳比例、脆性矿物比例和裂缝发育程度越高，储层含气性越好。综合地球化学、岩石物理和现场实测数据，本研究认为宜昌地区水井沱组页岩气极具商业价值，是我国南方理想的页岩气勘探开发目标之一。

关键词：页岩储层；页岩油气；控制因素；中扬子地台；成藏机理；油气勘查工程

1 前言

湖北宜昌地区构造格局稳定，页岩气保存条件好，地层底部的花岗岩刚性基底具有隔热作用，有利于区域内地层在构造运动中免遭断裂和褶皱的破坏，烃源岩既未因过度深埋，有机质热演化过度而使页岩气储层遭受破坏，也未因过度抬升剥蚀使气藏遭受破坏，页岩气的富集受控于总有机碳含量和黄陵隆起及其演化。由于中扬子地区寒武系页岩热成熟度高，构造演化经历复杂，成藏条件复杂，研究区的页岩储层特征、页岩气富集规律及影响因素尚未得到精细的综合性评价，主控因素不明确，页岩气保存模型也未明确，制约了勘探的深入开展。

2 地质概况

扬子地台水井沱组在寒武纪早期沉积环境为缺氧—硫化的水体条件，广泛、快速的海侵导致深水陆棚大面积覆盖，在早期陆棚斜坡地带发育厚度较大的黑色页岩层系有利于有机质保存，且厚度变化较大。黄陵背斜周缘的水井沱组与黔东南地区牛蹄塘组和四川盆地的筇竹寺

*文章来源：蔡宁波,王琳霖,鲍一遥,李怡普,万泽鑫,康志梅,罗胜元.中扬子地台宜昌地区寒武系水井沱组优质页岩储层发育特征及天然气富集机理研究[J].中国地质,2023,网络首发。

*第一作者简介：蔡宁波（1985—），男，博士，高级工程师；从事石油地质方面的研究工作；Email：626251285@qq.com。

*基金项目：中扬子高演化页岩气赋存机理与富集规律研究（编号2016ZX05034001-002）。

*参考文献详见原文。

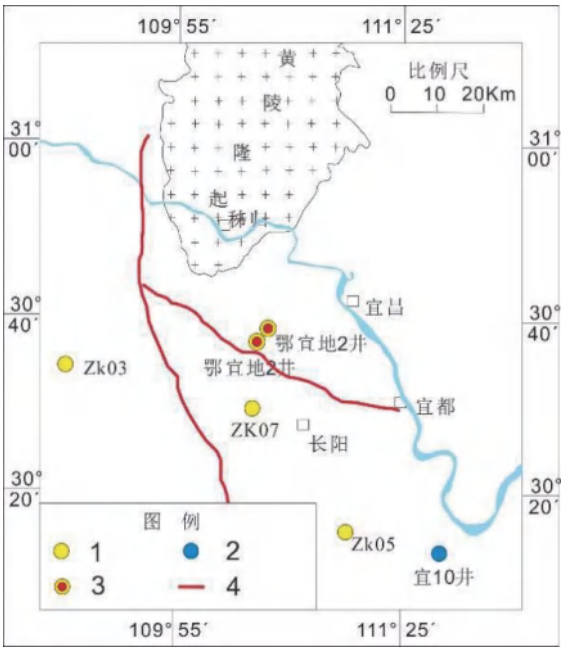

图 1 钻井及钻孔位置分布图

1–取样浅钻；2–地质调查井；3–参数井；4–区域断层

组大体相当。根据岩性，水井沱组可以划分为上、下段：上段为深灰色中—薄层状泥质条带灰岩，夹少量黑色灰质页岩，水平层理发育；下段为黑色含灰质页岩、含炭质页岩，见星点状黄铁矿，黄铁矿条带，发育水平层理；厚度横向变化大，宜昌北部地区呈由西向东变薄趋势。宜昌地区寒武系水井沱组与下伏岩家河组或灯影组呈假整合接触。

3 样品与分析方法

本次研究精选了鄂宜页 1 井、鄂宜地 2 井、ZK03 井、ZK05 井、长阳鸭子口白竹岭剖面以及南阳剖面等，系统采集了页岩岩石样品。研究完成的实验包括矿物组成以及黏土矿物的组成分析，烃源岩有机碳含量和干酪根碳同位素组成测定以及孔隙度、渗透率测定。有机碳含量利用岩石热解仪（Rock-Eval 6）测定，干酪根碳同位素（$\delta^{13}C_{org}$）组成利用稳定同位素比质谱仪（DELTA V Advantage）测试分析。样品的矿物组成以及黏土矿物组成利用 XRD 分析仪（X·Pert^3 Powder 型 X 射线粉末衍射仪）分析，此外还使用到 IB-09010CP 型离子截面抛光仪和 Helios NanoLab 660 型双束扫描电子显微镜，样品孔隙度和渗透率的测定利用页岩氦气法孔隙度和脉冲衰减法渗透率的测试方法（GB/T 34533-2017），分别使用 PHI-220 型自动孔隙度测定仪和 pdpl-200 型脉冲衰减法液体渗透率仪。

4 结果与讨论

4.1 宜昌地区寒武系页岩有机质富集特征

通过鄂宜页 1 井和鄂宜地 2 井的对比分析，水井沱组上段深灰色页岩的有机碳值整体偏低，分布在 0.56%~2.04%，平均值为 1.17%；水井沱组下段灰黑色—黑色页岩的有机碳值较高，在靠近底部位置达到最大，分布在 1.32%~8.42%，平均值为 3.49%（图 2）。水井沱组页岩有机碳大于 2.0% 的区间段绝大部分位于水井沱组下段，其中鄂宜页 1 井中 TOC 值大于 2.0% 的样品占比为 51.2%，水井沱组下段页岩的 TOC 值主要分布在 2.1%~6.4%，平均值为 3.65%；鄂宜地 2 井中页岩 TOC 值大于 2.0% 的样品占比为 36.9%，水井沱组下段页岩的 TOC 值分布主要在 1.45%~5.96%，平均值为 3.42%。宜昌地区的水井沱组页岩具有大规模生烃的能力。

干酪根的碳同位素组成也可用于判识页岩的有机质类型。长阳鸭子口剖面中仅 2 个样品的 $\delta^{13}C_{org}$ 值在 −30‰~−28‰，其余样品的 $\delta^{13}C_{org}$ 都小于 −30‰。在宜昌土城钻探的鄂宜地 2 井中，大部分泥页岩样品的 $\delta^{13}C_{org}$ 值都小于 −28‰，其中 $\delta^{13}C_{org}$ 值在 −30‰~ −28‰ 的样品占比为 44.45%，为 II_1 型干酪根；$\delta^{13}C_{org}$ 值小于 −30‰ 的样品占比为 22.22%，为 I 型干酪根；有 2 个样品的 $\delta^{13}C_{org}$ 值在 −28‰~−26‰，为 II_2 型干酪根；仅有一个样品检测为 III 型干酪根，分析判断可能为实验测试误差所致（图 3）。整体而言，水井沱组页岩的干酪根以 II_1 和 I 型有机质为主，表明水生低等藻类是其主要的有机质前驱物。

根据实测的反射率值（R_b 或 R_G）与镜质体反射率（R_o）之间的经验公式，计算得出等效的镜质体反射率来表征有机质的热演化程度，宜昌地

表 1 鄂宜地 2 井、宜 10 井水井沱组全岩 X 衍射组分统计表

井号	小层	样品个数	全岩 X 衍射分析结果/%				
			石英	长石	碳酸盐矿物	黄铁矿	黏土
鄂宜地 2 井	水四段	13	2.0~18.7	0~3.7	62.5~95.2	0~1.5	1.3~13.8
			6.4	2	86.9	0.2	4.5
	水三段	16	3.9~28.6	0~3.7	6.4~87.9	0~5.8	7.0~61.3
			14.5	1.9	52.1	3.3	27.3
	水二段	21	8.1~33.2	0.7~6.0	11.8~84.0	0~6.2	8.3~54.7
			21.4	2.8	35.8	3.7	37.6
	水一段	23	16.5~39.1	1.7~11.2	13.1~86.9	2.0~14.9	2.7~46.0
			29.2	4.4	29.6	5	32.7
宜 10 井	水四段	7	9.8~40.4	5.0~15.1	31.8~82.1	0	1.9~12.8
			17.6	7.8	70.7		3.9
	水三段	1	50.9	13	13.5	0	22.6
	水二段	3	34.9~45.6	8.3~14.2	28.3~39.7	0~1.9	12.0~15.1
			41.6	10.3	33.3	1	13.8
	水一段	5	31.2~49.2	4.8~9.5	41.0~58.0	0.5~1.8	8.0~11.5
			39.3	7.5	49.34	1.2	9.6

说明：数据格式为--最小值~最大值/平均值

表 2 鄂宜地 2 井、宜 10 井水井沱组黏土 X 衍射组分统计表

井号	小层	样品个数	黏土 X 衍射分析结果/%			
			黏土总含量	伊蒙混层	伊利石	绿泥石
鄂宜地 2 井	水四段	3	9.6~13.8	5.7~6.6	3.6~5.1	0~2.8
			11.2	6.1	4.2	0.9
	水三段	16	7.0~61.3	2.5~26.4	2.1~14.8	2.5~20.8
			27.3	11.8	7.5	7.9
	水二段	21	8.3~54.7	3.6~33.3	1.7~12.6	2.4~11.9
			37.6	20.6	8.9	8.3
	水一段	23	2.7~46.0	7.6~25.8	3.6~20.1	0.4~8.1
			32.7	19.3	11.8	3.2
鄂宜 10 井	水四段	7	1.9~12.8	0.8~4.5	1.0~5.6	0.1~2.7
			3.9	1.5	1.9	0.5
	水三段	1	22.6	5.4	12.4	4.7
	水二段	3	12.0~15.1	3.7~4.5	5.5~7.7	2.5~4.1
			13.8	4.1	6.5	3.2
	水一段	5	8.0~11.5	3.2~4.7	3.0~6.0	0.8~2.1
			9.6	3.8	4.4	1.4

说明：数据格式为--最小值~最大值/平均值

μm^2之间；水四段渗透率值为0.016~0.039×10^{-3} μm^2，平均值为0.023×10^{-3} μm^2，所有样品渗透率值均在0.01~0.05×10^{-3} μm^2之间。渗透率分布特征在整体上与孔隙度分布特征相似，水井沱组渗透率值略高于岩家河组，且水井沱组下部的渗透率值高于上部（图4D）。

4.2.3. 水井沱组页岩储集空间类型

有机孔隙。利用离子截面抛光仪和双束扫描电子显微镜观测鄂宜地2井水井沱组泥页岩孔隙特征：鄂宜地2井有机质孔隙较为发育（图5），孔隙形态多样，主要发育有圆形、椭圆形、不规则形状、弯月形等形态，空间上形成管柱状、洞穴状等复杂内部结构，管状孔隙吼道连接纳米级孔隙。有机质孔隙孔径变化范围较大，从纳米级到微米级，且以纳米级孔隙为主，一般镜下多见数十到几十纳米，同时部分有机质与无机矿物颗粒接触边缘可见孔径在数百个纳米左右的有机质孔。

无机孔隙。扫描电镜观察发现，鄂宜地2井和ZK05井中水井沱组泥页岩发育一定量的无机孔隙，主要包括粒间孔、黏土矿物晶间孔和微裂隙三种类型。其中，粒间溶孔主要为不稳定的矿物（如长石、碳酸盐矿物等）的溶蚀而形成，孔径多在数十纳米~数微米之间，并以纳米级孔隙为主。黏土矿物间发育一定数量的晶间孔隙，孔径较小，多为纳米级。泥页岩中也见开放型微裂隙，这些孔隙一般与微沉积构造纹理伴生，同时也可见黏土矿物层间发育的收缩缝（图5）。

裂缝。鄂宜地2井岩心中可见微观裂缝和宏观裂缝两种类型，这里主要介绍宏观裂缝。根据岩心观察结果显示，鄂宜地2井水井沱组下段的黑色页岩中裂缝总体不发育，上段碳酸盐岩含量较高的地层中构造裂缝较发育（图6）。为详细研究水井组中裂缝的纵向分布特征，对鄂宜页1井进行了地层微电阻率扫描成像测井（FMI），测量井段所见到的裂缝类型包括高导缝、高阻缝及微断层。其中，高导缝属于以构造作用为主形成的天然裂缝，在FMI动态图像上往往表现为褐黑色正弦曲线，该类裂缝也具备一定的渗透性，属于有效缝（图6）；高阻缝属于以

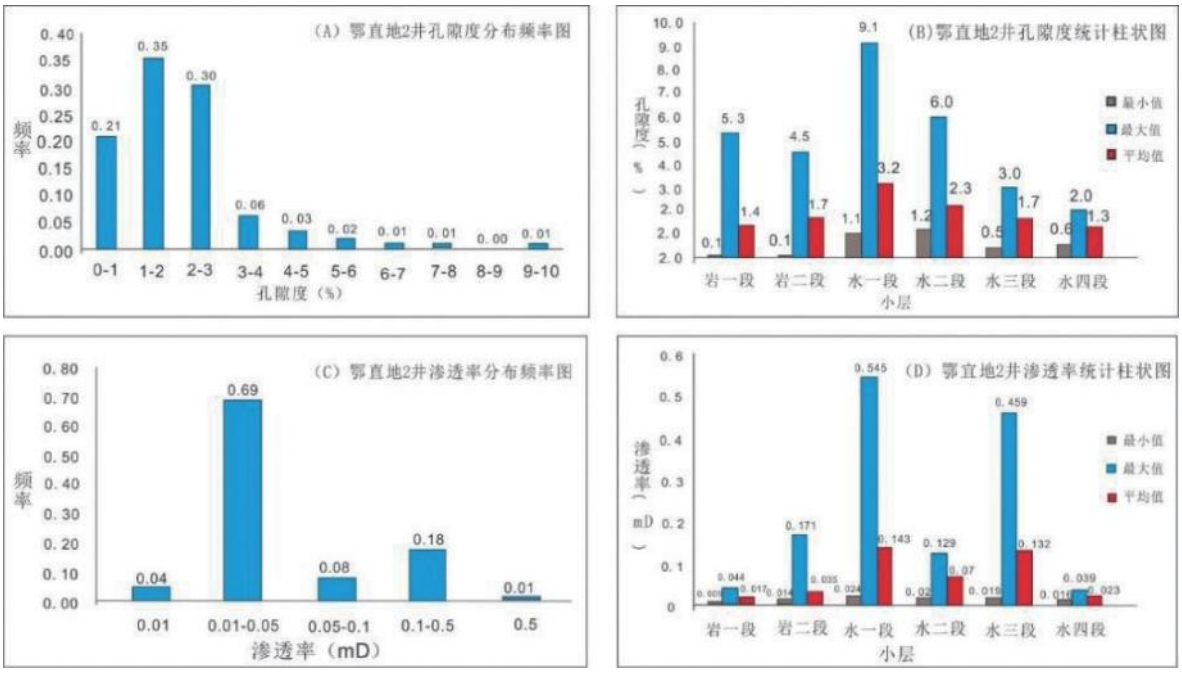

图4 鄂宜地2井岩家河—水井沱组相关柱状图

（A）孔隙度分布频率图；（B）各小层孔隙度统计图；（C）渗透率分布频率图；（D）各小层渗透率统计图.

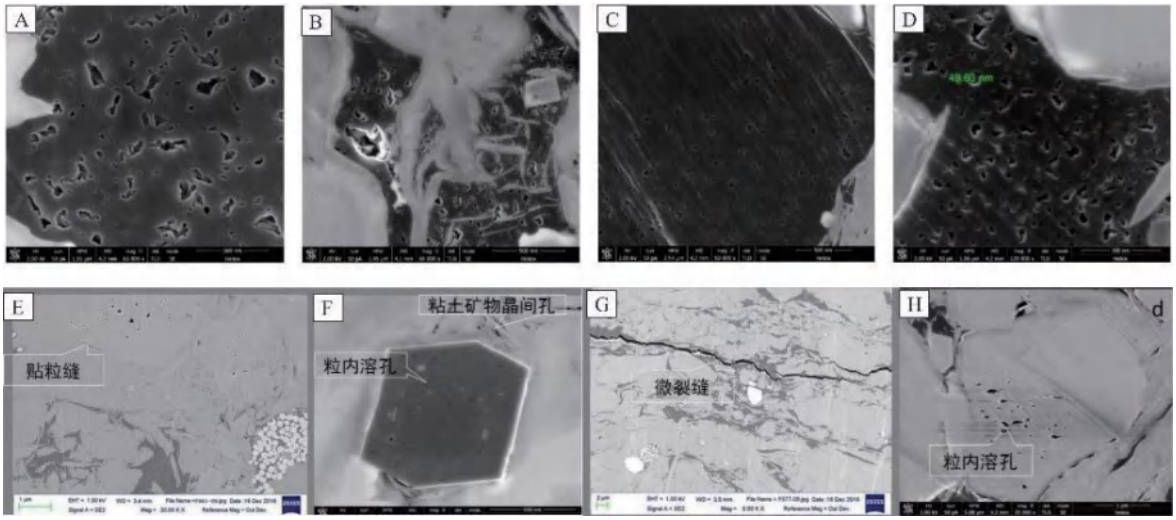

图5 宜昌地区水井沱组页岩典型有机孔与无机孔扫描电镜照片

A、B、C、D-有机孔;E、F、G、H-无机孔

构造作用为主形成的天然裂缝,但裂缝间隙被高阻矿物全部充填,也可能为闭合缝,裂缝有效性差,图像特征表现为亮黄色—白色的正弦曲线色晕(图6);高分辨率FMI成像测井显示断面上下盘明显位移特征,呈现正断层特征(图6)。

4.3. 宜昌地区寒武系页岩储层发育控制因素

4.3.1. 有机质富集程度

对鄂宜地2井水井沱组TOC与孔隙度之间相互拟合关系发现,水井沱组页岩储层TOC与孔隙度之间相关性不明显,但总体上随着TOC含量的增加孔隙度有略微增大的趋势(图7(A)),同时孔隙度大于2%的样品TOC含量大多

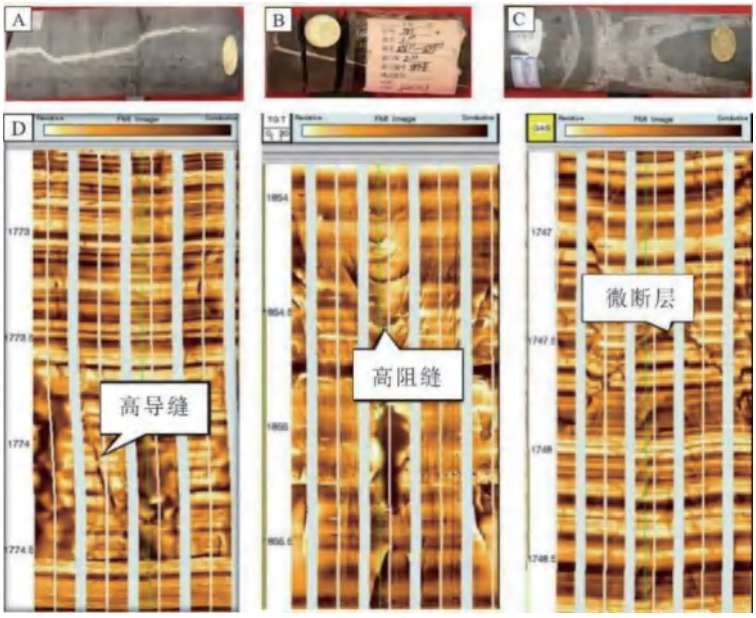

图6 鄂宜地2井水井沱组岩心裂缝照片

A—1660.76~1662.21m垂直缝,方解石全充填;B—1699.68~1701.34高角度裂缝,全充填;C—1724.2~1724.5m高角度直劈缝,方解石全充填). 裂缝FMI动态图像特征(D):(左)高导缝;(中)高阻缝;(右)微断层.

876.9~1 938.4 m深度段，其岩性主要是深灰色钙质泥岩、硅质泥岩、泥质灰岩等。

有机碳含量越高，页岩吸附能力越强，两者存在很好的正相关关系。利用建立的线性关系式可以对已知TOC的页岩含气量进行初步预测，当页岩TOC为2%时，吸附气含量为0.92 m^3/t；TOC为5%时，吸附气含量为2.38 m^3/t。高TOC含量的页岩中气体赋存主要与有机质颗粒有关，原因主要是有机碳含量越高，页岩的生气潜力就越大，单位体积页岩的含气量就越高；泥页岩微

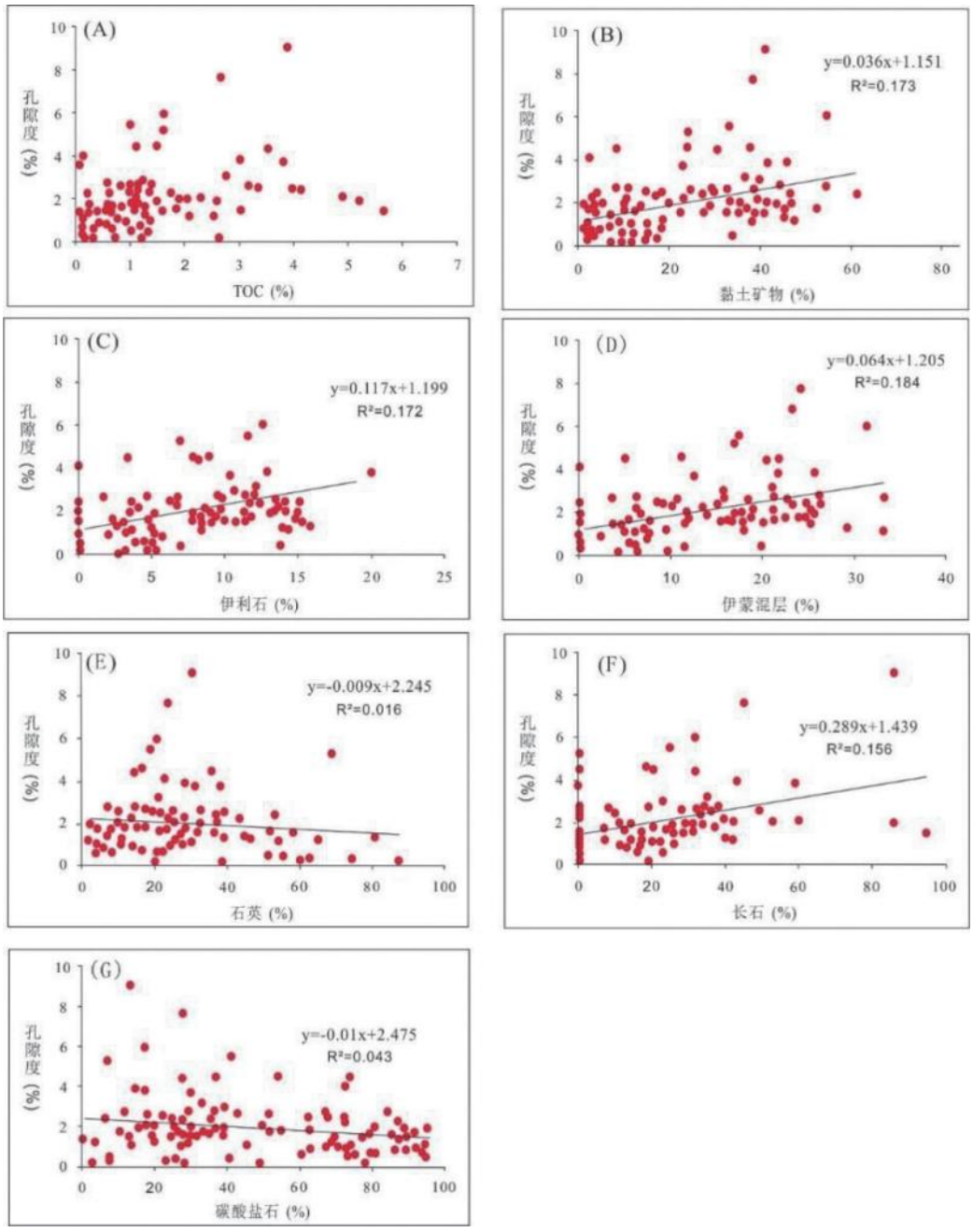

图7 鄂宜地2井水井沱组页岩孔隙度与不同物质含量的关系

(A)TOC；(B)黏土矿物；(C)伊利石孔；(D)伊蒙混层；(E)石英；(F)长石；(G)碳酸盐矿物.

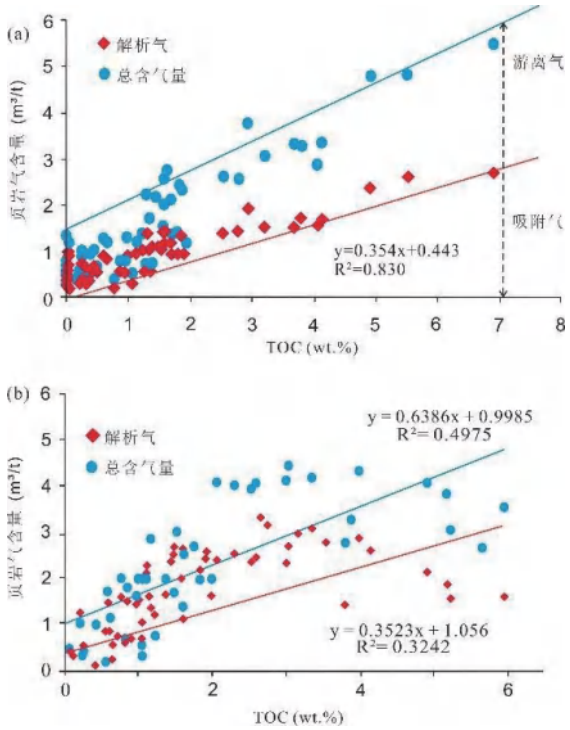

图 8　现场解析含气量与 TOC 关系图

(a)鄂宜页 1 井,(b)宜地 2 井

孔、中孔的表面积随着 TOC 含量的增加而增大，且有机质表面具亲油性，对气态烃有较强的吸附能力。

(2)脆性矿物比例。在宜昌地区，寒武系水井沱组下部黑色页岩可见大量生物结构石英，含气页岩层石英含量在 12.5%~44.4%，平均为 26.63%，页岩含气量、TOC 含量与石英含量呈明显正相关性(图 9)，两者相关系数 R^2 可达 0.67~0.71，表明整体上寒武系水井沱组页岩硅质的富集与有机质密切相关，硅质来源可能与生物作用有关。

此外脆性矿物黄铁矿的普遍存在，斯伦贝谢 ELANPLUS 测井解释含气页岩层黄铁矿重量百分比在 0.2%~6.22%，平均为 2.55%，黄铁矿与有机质呈同步正向变化(图 9)，同时黄铁矿含量和页岩含气量呈正相关关系(图 9)，相关系数 R^2 可达 0.82，表明页岩原始沉积时的还原环境有利于有机质的保存。岩芯观察表明，黄铁矿多呈毫米级的显微星点状散布于页岩中，高海洋生物生产力造成大量的有机碳输入的同时

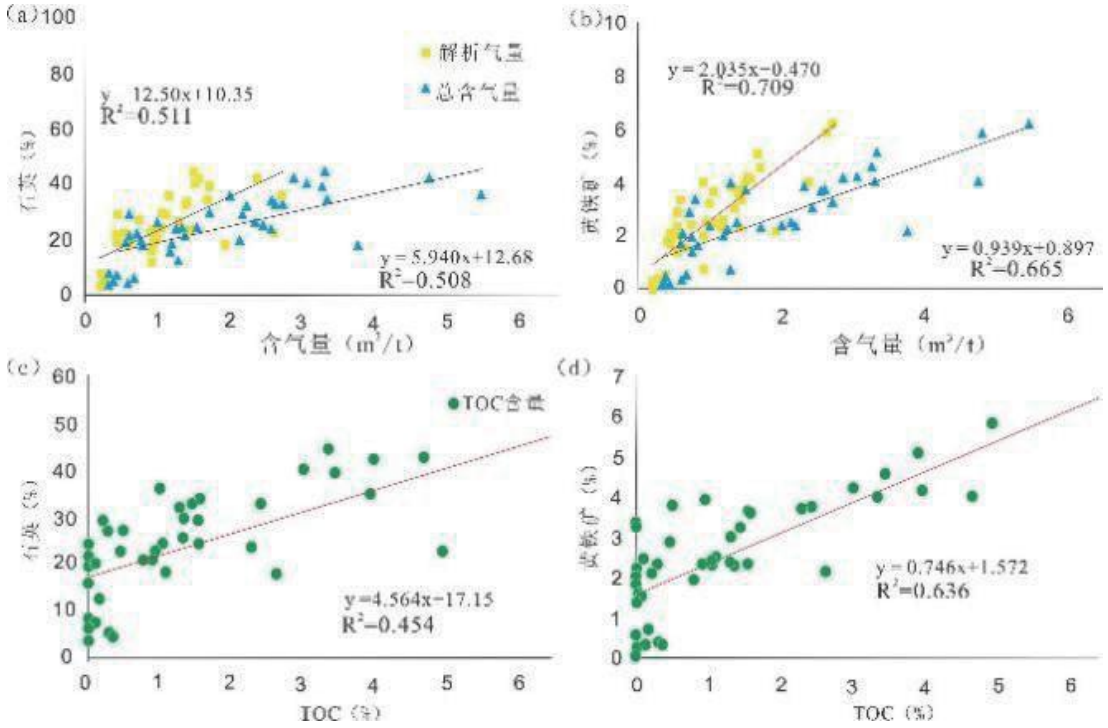

图 9　鄂宜页 1 井脆性矿物含量与含气性相关性分析图

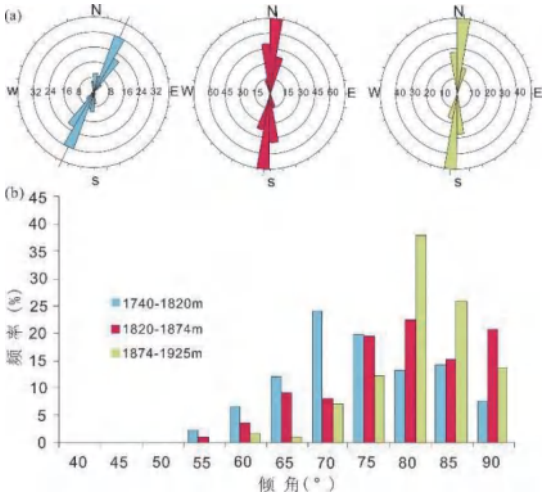

图10 鄂宜页1井水井沱组裂缝分布特征图
a.裂缝倾向玫瑰花图,b.裂缝倾角概率分布图

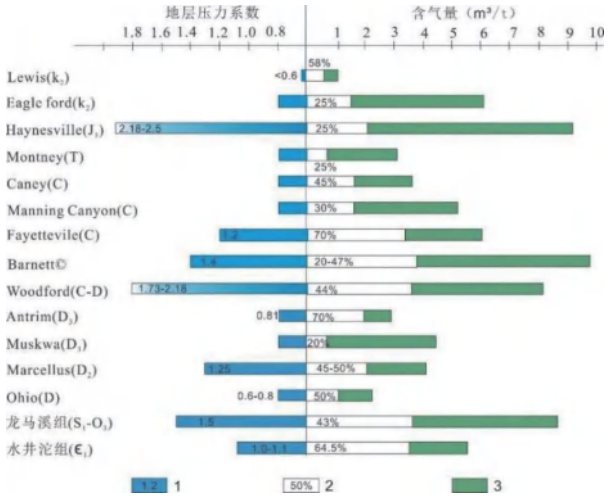

图11 典型区块页岩含气性、赋存状态及与地层压力间关系
1-地层压力系数;2-吸附气及含量;3-游离气

产生高强度的硫酸盐还原环境,水体或孔隙水中的S^{2-}以铁的硫化物形式和有机质同时埋藏起来,这类沉积的原生黄铁矿大量发育是强还原环境的体现。

(3)储层裂缝分布。裂缝发育带不但提供了游离态页岩气赋存的空间,而且为页岩气的运移、聚集提供了输导通道,对页岩气的开发十分有利。

鄂宜页1井水井沱组页岩天然裂缝发育(图10)。利用FMI成像测井资料对水井沱组裂缝统计表明,页岩层发育大量构造成因的天然裂缝,裂缝间隙多被方解石等高阻矿物全部或部分充填。目地层1 820~1 874 m深度段范围内发育高阻缝222条,裂缝主频为65°~75°;1 740~1 820 m发育高阻缝91条,裂缝主频为80°~90°;裂缝走向受区域构造应力的控制,与其西南部的天阳坪断层走向接近。含气量与裂缝发育密度有很好的对应关系。

鄂宜页1井页岩气中游离气占比大小与储层裂缝发育直接相关。1 854.35~1 870.84 m深度段含气量高,页岩储层致密,TOC含量和成熟度十分接近,随着页岩储层裂缝发育程度的增加,总含气量增大。岩心同样揭示该段发育水平缝、垂直缝和高角度斜裂缝,部分被方解石充填,部分未充填。

(4)地层压力。依据现场实测解析气含量,考虑钻探、取芯过程中损失时间,通过回归方程计算了损失的游离气含量。研究表明鄂宜页1井游离气含量占总含气量的18.57%~50.46%,平均为35.52%。当含气量大于2 m^3/t时,游离气含量占比接近38.64%,表明水井沱组页岩中吸附气含量占主要地位,页岩气大多数以吸附态赋存在矿物颗粒、干酪根和孔隙表面,少部分以游离态存在于页岩各种孔隙中。

宜昌地区寒武系页岩中较低的游离气占比与地层常压状态有关。现场解析获得的游离气含量占56%~65%,产气段地层压力系数为1.4;北美页岩中游离气含量在40%~80%之间,其中Antrim为生物气,含气量1.13~2.83 m^3/t,地层为常压;Lewis为热解气,低压,两套页岩均以吸附气为主,含气量较低(小于2 m^3/t);Barnett、Marcellus、Haynesville等典型页岩气藏超压特征明显,含气性较高(2~9.9 m^3/t),游离气量比例大,吸附气含量不超过50%。超压气藏游离气含量高的机理在于生烃增压产生微裂缝,大幅增强储层渗流性能。同时压力增大提高了页岩气含量,更有利于增强页岩气的封存。

4.4.3. 水井沱组页岩气成藏模式

黄陵刚性基底及其较早的隆升时间和持续的缓慢隆升方式直接制约着寒武系水井沱组页岩气的形成与保存，也是宜昌地区区分南方其他地区寒武系页岩气保存富集的关键。因此，从保存条件来看，宜昌寒武系水井沱组页岩气应属基底控藏类型。据此，联系控盆的继承性古隆起同样受控基底断裂构造影响，这里将宜昌地区寒武系页岩气保存模式确定为“基底控藏型”保存模式（图 12）。

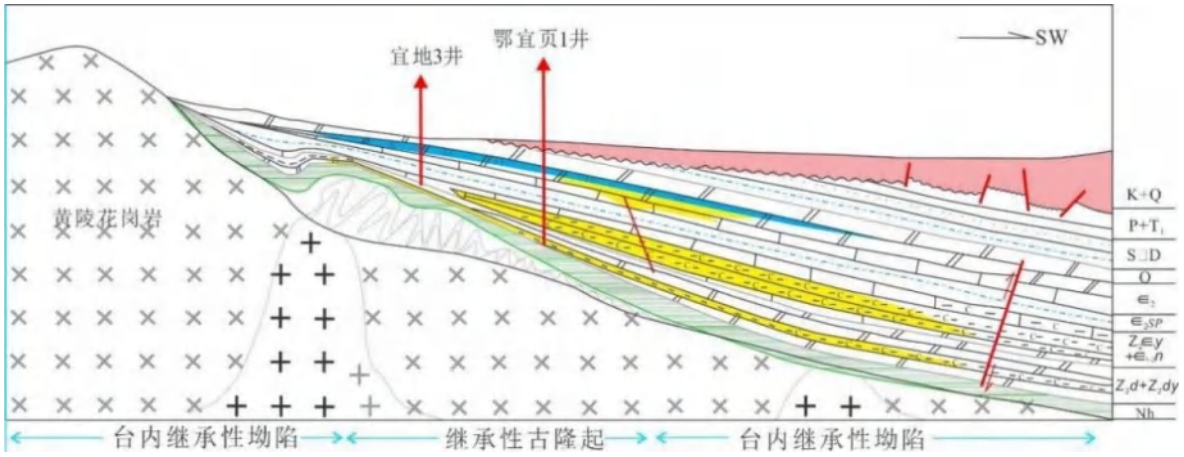

图 12　宜页 1 井寒武系页岩气“基底控藏型”保存模式

水井沱组自下而上石英含量减少，碳酸盐岩含量增加，黏土含量先增加再减少；黏土矿物中伊蒙混层相对含量增加、绿泥石相对含量减少、伊利石相对含量先减少再增加。

（2）水井沱组页岩孔隙度主要分布在 0.5%~9.1%，渗透率主要分布在 0.019~0.540×10^{-3} μm^2。水井沱组页岩储集空间的发育程度主要与有机质富集程度、黏土矿物含量以及页理缝的发育程度有关。有机质内部微孔较多，其含量的增加可以提高页岩的孔隙度。黏土矿物多具有层状结构，其晶间孔隙相对较多。此外，成岩过程中不同类型黏土矿物的转换（如蒙脱石的伊利石化）也可以有效增加孔隙度。尽管页理缝本身对储集性能的影响相对较小，但页理缝的发育可以连通更多的无机孔隙和有机孔隙，从而使得总的有效孔隙体积增加，这对于页岩气的赋存和开发起到积极作用。

5. 结论

本文查明了水井沱组的优质页岩储层特征和油气成藏规律，取得了如下认识：

（1）水井沱组页岩有机质丰度高，有机碳含量（TOC）随埋深有机碳含量逐渐增大。水井沱组页岩中干酪根以 II_1 型和 I 型为主，Ro 等效值分布在 2.4%~3.2%，表明水生低等藻类是主要的有机质前驱物，主要处于过成熟晚期干气阶段。

（3）天然气主要以吸附气（45.21%~81.44%）和游离气（18.56%~54.79%）的状态附存于水井沱组页岩储层中，溶解气的比例相对较小。水井沱组页岩的含气性主要受有机质含量、脆性矿物比例、储层裂缝分布以及地层压力影响，有机碳含量越高页岩吸附能力越强，两者存在很好的正相关关系。脆性矿物（如石英等）在机械和化学性质方面相对稳定，页岩埋藏过程中脆性矿物可起支撑作用，减小压实应力对颗粒之间孔隙的影响。此外，页岩的总含气量与储层裂缝的发育程度呈正相关关系。游离气在页岩储层中的比例与地层压力有关，由于宜昌地区超压相对不发育，因此，游离气的比例相对较低。联系控盆的继承性古隆起同样受控基底断裂构造影响，本文将宜昌地区寒武系页岩气保存模式确定为“基底控藏型”保存模式。

doi: 10.19388/j.zgdzdc.2023.06.**
引用格式：郭军,苑坤,郭经纬,等.桂中—南盘江地区黔水地1井打屋坝组页岩储层含气性及可压性评价[J].中国地质调查,2023,10(6): ** - **.(Guo J, Yuan K, Guo J W, et al. Gas bearing and complessibility evaluation of shale reservoir in Dawuba Formation of Qianshuidi 1 Well in Guizhong - Nanpanjiang area [J]. Geological Survey of China, 2023, 10(6): 00 - 00.)

桂中—南盘江地区黔水地1井打屋坝组页岩储层含气性及可压性评价

郭 军[1], 苑 坤[2,3], 郭经纬[1], 陈相霖[3], 李 岩[1]
(1. 湖南省地球物理地球化学调查所,湖南 长沙 410000; 2. 中国地质大学(北京),北京 100083;
3. 中国地质调查局油气资源调查中心,北京 10083)

摘要： 桂中—南盘江地区的黔水地1井在直井钻探过程中获得了稳定的页岩气流,取得了石炭系打屋坝组良好的海相页岩气发现。基于钻井、录井、测井、分析测试资料,通过对打屋坝组页岩储层岩相、有机地球化学、物性、裂缝发育程度和含气性等开展综合研究,解释了研究区页岩储层的含气性及可压性。研究发现：①打屋坝组为一套从碳酸盐斜坡相的下斜坡亚相过渡至台盆相的巨厚泥页岩层系,其中打屋坝组一段上部—三段中下部发育好—优质烃源岩,天然裂缝发育,气测全烃最大值63.41%,解吸气量平均值1.08 m^3/t,具备良好的页岩气生成条件和资源潜力；②主要含气层段的脆性矿物总含量在31% ~94%之间,泊松比为0.31,体积弹性模量为27.2 GPa,破裂压力处于29.7 ~48.5 MPa之间。综合评价显示该套地层具备较好的破裂潜力和裂缝保持能力,大规模体积压裂容易形成复杂裂缝网络,该套地层压力较高,具备压裂形成工业产能的条件,可作为下一步勘探开发的目标层段。

关键词： 黔水地1井；打屋坝组；页岩气；含气性；可压性
中图分类号： P618.13；TE132.2 **文献标志码：** A **文章编号：** 2095 - 8706(2023)06 - 0000 - 06

0 引言

近年来,随着我国加大了页岩气勘探开发力度,国内学者针对页岩气地层的生烃条件、储集特征、成藏规律等方面开展了大量研究[1-4],在四川盆地及其周缘地区的涪陵、富顺—永川、长宁—威远等地均获得了页岩气勘探的重大突破,并形成了工业化开发[5-6]。石炭系打屋坝组是四川盆地周缘海相沉积中发育富有机质泥页岩的层位之一,同时也是桂中—南盘江地区页岩气勘探的目标地层[7-9],但目前针对打屋坝组储层的认识和勘探实践还较少。黔水地1井位于贵州省六盘水市市郊,是一口以探明打屋坝组页岩气地质形成条件及含气性,获取资源评价关键参数为目的页岩气调查井,在钻探过程中获得了良好的页岩气发现[10]。本文结合实钻数据与室内解释,系统研究了该井的页岩储层含气性及其可压性特征,对该地区的下一步勘探方向可起到引导作用,有助于准确寻找页岩气产能建设的目标区。

1 地质背景

桂中—南盘江地区位于上扬子地块的六盘水断陷区,“垭都—紫云—罗甸”裂陷槽西部,黔西南坳陷与黔中滇东隆起交接处(图1)。根据区域调查和野外露头资料,研究区及周缘地区在早石炭世呈现北东高、南西低的构造格局,早石炭世晚期—早二叠世,研究区主要受垭都—紫云断裂带和区内NEE向的隐伏断裂共同控制,同沉积断裂对研究区内的古地理演化起到了控盆控相作用。

收稿日期： 2023 - 03 - 21；**修订日期：** 2023 - 10 - 30。
基金项目： 中国地质调查局“桂中—南盘江页岩气地质调查(编号：DD20190088)”项目资助。
第一作者简介： 郭军(1983—),男,高级工程师,主要从事页岩气地质调查与钻探等工作。Email：603178746@qq.com。
通信作者简介： 苑坤(1985—),男,高级工程师,主要从事页岩气地质调查及储层评价等工作。Email：cheerlist@qq.com。

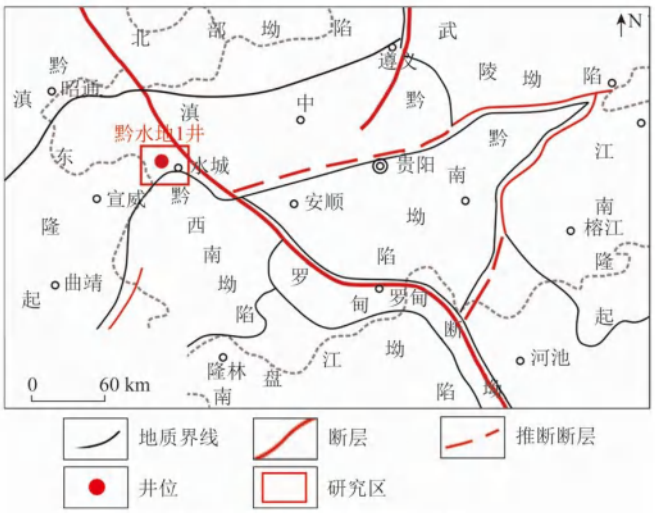

图 1　研究区构造位置图

Fig. 1　Structural location of the study area

黔水地 1 井位于桂中—南盘江地区的中北部，钻遇地层自上而下依次为：第四系（Q_4），厚 21 m，主要发育黄色、棕黄色含砾、泥砾黏土层；下石炭下统南丹组（C_1n），厚 1 426 m，主要发育浅灰色泥晶－中细粒生屑灰岩，底部碳质泥岩增多；下石碳统打屋坝组（C_1dw），四段层厚 66 m，主要发育灰色灰质泥页岩；三段厚 288 m，主要发育深灰色灰质泥岩、灰质页岩、灰色泥晶灰岩；二段层厚 122 m，主要发育深灰色灰质页岩夹灰黑色炭质泥岩；一段层厚 533 m，主要发育深灰色硅质泥岩、泥岩、灰质泥岩，性软、吸水性好，见少量黄铁矿颗粒；下石碳统睦化组（C_1n）主要发育深灰色黏土岩（图 2），估算目的层打屋坝组地层压力系数约 1.30，属于高压储层。黔水地 1 井打屋坝组地质录井综合柱状图见图 2。

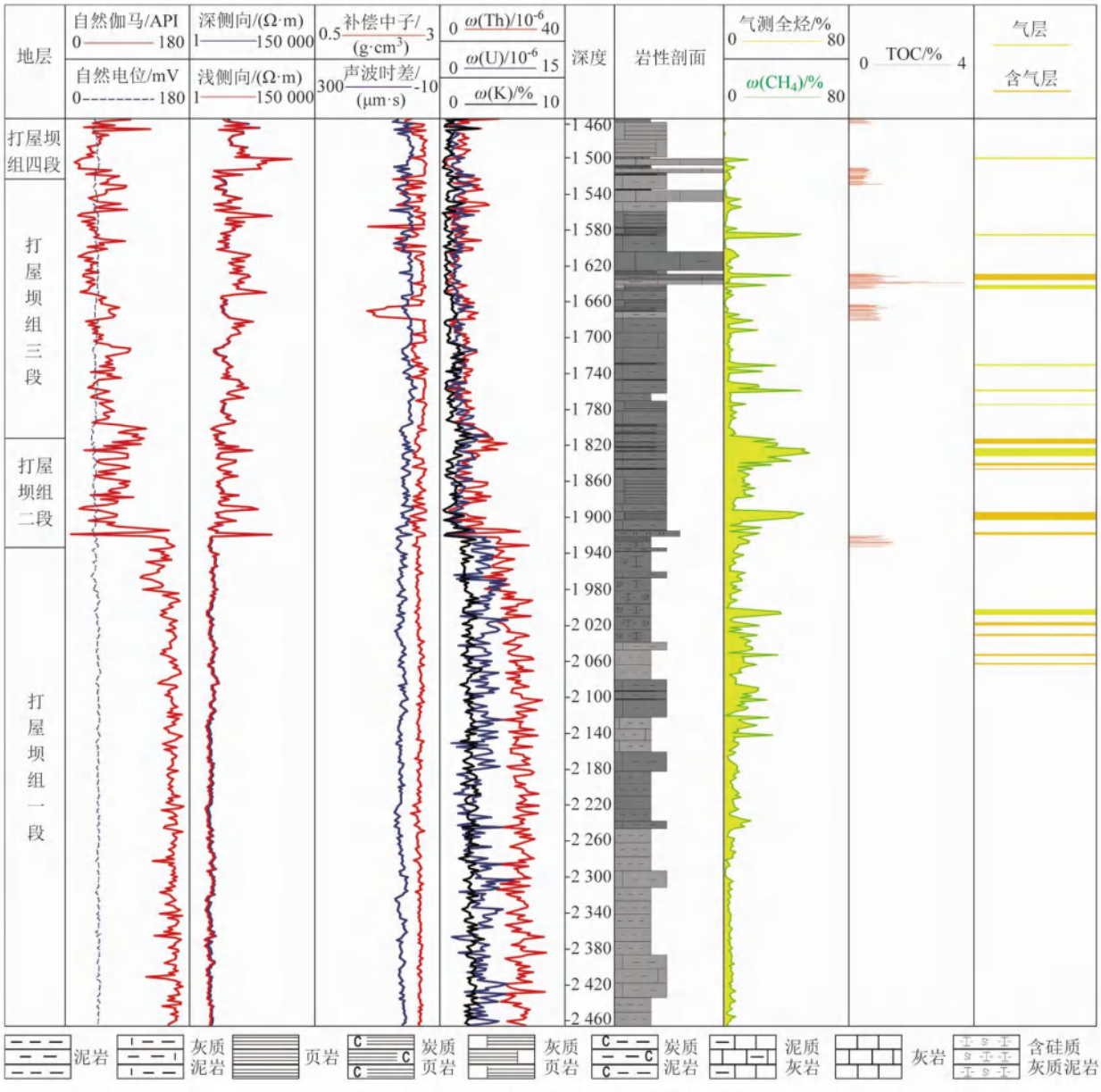

图 2　黔水地 1 井打屋坝组地质录井综合柱状图

Fig. 2　Comprehensive histogram of geological logging in Dawuba Formation of Qianshuidi 1 Well

2　页岩储层含气性

2.1　岩相组合特征

根据实钻资料，黔水地 1 井的全井地层具有灰质泥页岩 - 泥晶灰岩 - 灰质泥岩、灰质页岩 - 泥岩岩相组合特征，属于由碳酸盐斜坡相的下斜坡亚相过渡至台盆相，其环境闭塞、能量较低，是发育页岩气层的有利相带。

2.2　有机地球化学特征

全井采用美国 Leco CS230 碳硫分析仪完成 103 项次的岩心样品测试，分析精度优于 0.5%。测试结果表明：打屋坝组总有机碳（total organic carbon，TOC）含量在 0.33% ~3.67% 之间，平均 0.92%。其中打屋坝组三段中下部完成测试样品 47 件，岩性主要为深灰色、灰黑色泥页岩，TOC 在 0.33% ~3.67% 之间，平均 1.05%；二段完成测试样品 4 件，岩性为灰黑色泥岩，TOC 在 0.88% ~1.13% 之间，平均 1.01%；一段上部完成测试样品 10 件，岩性为灰黑色泥岩、灰质泥岩，TOC 在 0.48% ~1.42% 之间，平均 1.13%。整体上，打屋坝组一段—三段中下部上部达到了好—优质烃源岩的标准，具有较好的生烃潜力。

2.3　孔渗特征

页岩的孔渗性是评价页岩气储层的重要参数，可直接决定页岩含气量的多少以及页岩气在储层中运移的难易程度[11-12]。根据地球物理测井解释，黔水地 1 井打屋坝组页岩储层段的声波曲线数值多分布在 70 ~92.0 μs/ft 之间，补偿中子数值主要分布在 11.0% ~35.0% 之间，密度测井值主要分布在 2.2 ~2.6 g/cm^3 之间。综合解释孔隙度分布在 0.05% ~2.5% 之间，主要集中在 1% ~1.5% 之间；渗透率分布在 (0 ~0.1) ×10^{-3} μm^2 之间，大部分低于 0.028 ×10^{-3} μm^2，属于低孔超低渗储层。

2.4　含气特征

根据气测录井结果，黔水地 1 井全井气显示好的地层主要集中在 TOC 值较高的打屋坝组一段上部—三段中下部井段 1 540 ~2 070 m，其气测全烃最大值为 63.41%，甲烷最大值为 63.40%。现场解吸 68 件样品，气量在 0 ~1.18 m^3/t 之间，总含气量最高达 2.58 m^3/t，平均含气量为 1.08 m^3/t。多回次岩心出筒后的浸水实验显示岩心均冒泡强烈，呈密集串珠状（图 3）。多次关井点火，火焰最高达 3.0 m，最长持续 60 min 火焰高度未降，火焰呈黄色。打屋坝组在未压裂的情况下已能形成稳定的页岩气流，具备良好的勘探开发潜力。

图 3　黔水地 1 井浸水实验照片

Fig. 3　Water immersion experiment photo of Qianshuidi 1 Well

3　可压性主要评价指标

3.1　岩石矿物学特征

全井采用可读最小步长 0.000 1°的 Bruker D8 advance X 射线衍射仪对 47 件岩心样品进行全岩测试，分析显示打屋坝组的矿物成分以方解石、黏土矿物为主，其次为石英、白云石，少量黄铁矿、菱铁矿等，脆性矿物含量（长英质矿物与碳酸盐岩矿物之和所占矿物总量的百分比）在 31% ~100% 之间（图 4）；垂向上，脆性矿物的总含量随着泥质含量的增加而减少，受岩性岩相控制明显。其中，主要含气层段打屋坝组一段上部—三段中下部的脆性矿物总含量在 31% ~94% 之间，平均 73.5%。

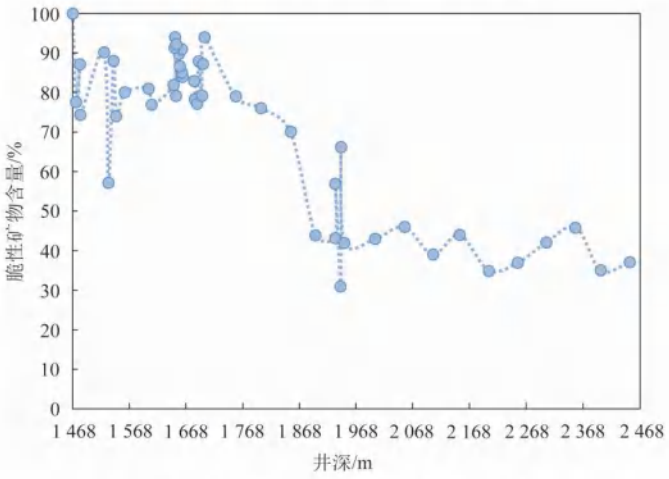

图 4　黔水地 1 井打屋坝组脆性矿物含量统计

Fig. 4　Content statistics of brittle minerals in Dawuba Formation of Qianshuidi 1 Well

3.2　裂缝发育特征

根据岩心观察，打屋坝组裂缝较发育，主要为

水平裂缝和斜裂缝(图 5),缝宽 0.1 ~ 10 mm,多呈现为半充填或未充填状态,部分全充填。充填物质多为方解石、泥质等,镜下观察显示裂缝,主要为构造微裂缝和成岩微裂缝。其中,构造微裂缝呈现切穿矿物颗粒、方解石脉及缝合线现象,具有一定的开启度并未被充填,大多数为有效裂缝;成岩微裂缝缝宽多在 0.02 ~ 0.1 mm 之间,充填物主要是有机质、方解石、黄铁矿。

图 5　斜裂缝岩心照片

Fig. 5　Core photo of diagonal cracks

通过采用哈里伯顿公司 LOG - IQ 测井系列的 XRMI 电成像测井和 Geoframe 解释系统,得出黔水地 1 井高导缝参数定量计算结果为:井段 1 400 ~ 1 650 m,裂缝长度 <11.812 m/m^2,平均 2.520 m/m^2;裂缝密度 <8.202 条/m,平均 2.464 条/m;裂缝孔隙度 < 0.668%,平均 0.084%;井段 1 650 ~ 2 400 m,裂缝长度 <8.193 m/m^2,平均 2.096 5 m/m^2;裂缝密度 <6.562 条/m,平均 2.084 条/m;裂缝孔隙度 <0.227%,平均 0.028%。

综上可知,打屋坝组天然裂缝发育,其为页岩气的保存成藏提供了储集空间,也为后期压裂改造并形成复杂裂缝网络提供了良好条件。

3.3　岩石力学特征

采用 ECLIPS - 5700 测井系统和 eXpress 解释系统开展交叉偶极子阵列声波测井采集数据进行处理,结果显示黔水地 1 井以页岩为主的地层纵波时差主要分布在 70 ~ 102 μs/ft 之间,横波时差主要分布在130 ~ 190 μs/ft 之间,纵横波速度比主要分布在 1.6 ~ 2.1 之间;主要含气层段 1 540 ~ 2 070 m 的泊松比处于 0.25 ~ 0.35 之间,平均 0.31;体积弹性模量处于 18.8 ~ 46.1 GPa 之间,平均 27.2 GPa;破裂压力处于 29.7 ~ 48.5 MPa 之间。

3.4　地应力方向特征

地应力方向与井眼崩落及诱导缝的方向的关系密切。在直井中,从图像上分析井眼崩落及钻井诱导缝的发育方向可以确定最大或最小水平主应力的方向[13-15]。根据微电阻率扫描成像测井数据,黔水地 1 井的井段 1 415 ~ 1 445 m、2 050 ~ 2 052 m 诱导缝发育。下部由于泥质含量高,地层塑性强,诱导缝发育较少;井段 1 400 ~ 1 650 m 井眼崩落特征不明显,井段1 650 ~ 2 400 m 井眼崩落局部发育。两者揭示的最大水平主应力方向均为 NW—SE 向。

4　储层可压性评价

黔水地 1 井的储层可压性评价分为 3 个方面。

(1)具备易形成复杂裂缝网络的能力。黔水地 1 井地区处于拉张、挤压、剪切等多种应力的作用之下,天然裂缝发育,且具有与 NW 向的最大主应力方向相近的高角度裂缝,使得页岩内的拉张应力得到了有效释放,导致主应力差减小,有利于储层的压裂改造;上部高应力差的灰岩岩层的存在可有效控制压裂缝的纵向延伸高度,有助于泥页岩井段的压裂效果。而黔水地 1 井中走向、倾向均杂乱分布的高阻缝,也为天然裂缝和压裂缝在体积改造过程中形成复杂裂缝网络提供了便利条件。

(2)具备较好的破裂潜力的脆性矿物可以反映页岩的脆性程度,其含量在一定程度上决定了页岩的可压裂性。脆性矿物含量的统计结果(图 4)显示黔水地 1 井主要含气层段打屋坝组一段上部—三段中下部的脆性矿物总含量在 31% ~ 94% 之间,在外力作用下易发生破碎,后期压裂改造中可产生较多诱导缝,故重点井段具备较好的破裂潜力。

(3)具备较好的裂缝保持能力。弹性模量和泊松比是反映岩石脆性的主要力学参数,弹性模量反映了页岩被压裂后保持裂缝的能力,泊松比反映了页岩在压力下破裂的能力[16]。一般认为岩石的弹性模量越大,泊松比越小,其脆性越高[17-18]。当弹性模量大于 24 GPa,泊松比小于 0.25 时,页岩的脆性指数高,可压裂性好[19]。依据岩石力学特征,黔水地 1 井主要含气层段的体积弹性模量(27.2 GPa)和泊松比(0.31)均大于标准值,表明该段地层保持裂缝能力较好,但需要的破裂压力相对较大。

5　结论

(1)黔水地 1 井打屋坝组由碳酸盐斜坡相的下

斜坡亚相过渡至台盆相，泥页岩发育，打屋坝组一段上部—三段中下部地层达到了好—优质烃源岩的标准，现场气测全烃最大值 63.41%，解吸气量平均值1.08 m^3/t，多次关井点火，在未压裂的情况下已能形成稳定的页岩气流。

（2）打屋坝组地层脆性矿物含量在 31% ~ 100% 之间，天然裂缝发育，最大水平主应力方向为 NW—SE 向；主要含气层段泊松比 0.31，体积弹性模量 27.2 GPa，破裂压力处于 29.7 ~ 48.5 MPa 之间。

（3）打屋坝组主要含气层段具备较好的破裂潜力、裂缝保持能力、大规模体积压裂形成复杂裂缝网络的便利条件等，再加上良好的气显示和较大的地层压力，揭示了该套地层具备压裂形成工业产能的可能，可作为下一步勘探开发的目标层段。

参考文献（References）：

[1] 何利，宋春彦，谭钦银，等. 川东南武隆地区五峰组—龙马溪组页岩气形成条件及富集区分析[J]. 海相油气地质，2017，22(3)：47 - 56.
He L，Song C Y，Tan Q Y，et al. Accumulation conditions and enrichment zones of shale gas in Wufeng - Longmaxi Formation in Wulong area of southeast Sichuan basin[J]. Marine Origin Petroleum Geology，2017，22(3)：47 - 56.

[2] 黄仁春，魏祥峰，王强. 四川盆地东南缘丁山地区页岩气成藏富集的关键控制因素[J]. 海相油气地质，2017，22(2)：25 - 30.
Huang R C，Wei X F，Wang Q. Key factors of shale gas accumulation in Dingshan area of southeastern Sichuan Basin[J]. Marine Origin Petroleum Geology，2017，22(2)：25 - 30.

[3] 姜振学，宋岩，唐相路，等. 中国南方海相页岩气差异富集的控制因素[J]. 石油勘探与开发，2020，47(3)：617 - 628.
Jiang Z X，Song Y，Tang X L，et al. Controlling factors of marine shale gas differential enrichment in southern China[J]. Petroleum Exploration and Development，2020，47(3)：617 - 628.

[4] 邱楠生，冯乾乾，腾格尔，等. 川东南丁山地区燕山期—喜马拉雅期差异构造 - 热演化与页岩气保存[J]. 石油学报，2020，41(12)：1610 - 1622.
Qiu N S，Feng Q Q，Borjigin T，et al. Yanshanian - Himalayan differential tectono - thermal evolution and shale gas preservation in Dingshan area，southeastern Sichuan Basin[J]. Acta Petrolei Sinica，2020，41(12)：1610 - 1622.

[5] 郭旭升，胡东风，李宇平，等. 涪陵页岩气田富集高产主控地质因素[J]. 石油勘探与开发，2017，44(4)：481 - 491.
Guo X S，Hu D F，Li Y P，et al. Geological factors controlling shale gas enrichment and high production in Fuling shale gas field[J]. Petroleum Exploration and Development，2017，44(4)：481 - 491.

[6] 易积正，王超. 四川盆地焦石坝地区龙马溪组海相页岩储层非均质性特征[J]. 石油实验地质，2018，40(1)：13 - 19.
Yi J Z，Wang C. Differential pore development characteristics in various shale lithofacies of Longmaxi Formation in Jiaoshiba area，Sichuan Basin[J]. Petroleum Geology & Experiment，2018，40(1)：13 - 19.

[7] 卢树藩，何犇，杜胜江. 黔南代页 1 井下石炭统打屋坝组页岩气地质条件及勘探前景[J]. 中国地质调查，2016，3(4)：6 - 11.
Lu S F，He B，Du S J. Geological conditions and exploration prospect of shale gas in Dawuba Formation of Lower Carboniferous of Daiye - 1 well in southern Guizhou Province[J]. Geological Survey of China，2016，3(4)：6 - 11.

[8] 苑坤，方欣欣，王婷，等. 黔南坳陷下石炭统打屋坝组页岩气地质条件及勘探前景[J]. 地质论评，2020，66(S1)：115 - 116.
Yuan K，Fang X X，Wang T，et al. Accumulation conditions and exploration potential of shale gas of Dawuba Formation，Southern Guizhou depression[J]. Geological Review，2020，66(S1)：115 - 116.

[9] 郭军，陈相霖，赵训林，等. 桂中—南盘江地区黔水地 1 井钻井关键技术[J]. 断块油气田，2021，28(3)：423 - 427.
Guo J，Chen X L，Zhao X L，et al. Key drilling technologies for well Qianshuidi 1 in Guizhong - Nanpanjiang area[J]. Fault - Block Oil & Gas Field，2021，28(3)：423 - 427.

[10] 陈相霖，苑坤，林拓，等. 四川垭紫罗裂陷槽西北缘（黔水地 1 井）发现上古生界海相页岩气[J]. 中国地质，2021，48(2)：661 - 662.
Chen X L，Yuan K，Lin T，et al. Discovery of shale gas within Upper Paleozoic marine facies by Qian Shuidi - 1 well in the northwest of Yaziluo rift trough，Sichuan Province[J]. Geology in China，2021，48(2)：661 - 662.

[11] 余川，聂海宽，曾春林，程礼军，邵晓州. 四川盆地东部下古生界页岩储集空间特征及其对含气性的影响[J]. 地质学报，2014，88(7)：1311 - 1320.
Yu C，Nie H K，Zeng C L，et al. Shale reservoir space characteristics and the effect on gas content in Lower Palaeozoic erathem of the eastern Sichuan Basin[J]. Acta Geologica Sinica，2014，88(7)：1311 - 1320.

[12] 张晓明，石万忠，徐清海，等. 四川盆地焦石坝地区页岩气储层特征及控制因素[J]. 石油学报，2015，36(8)：926 - 939，953.
Zhang X M，Shi W Z，Xu Q H，et al. Reservoir characteristics and controlling factors of shale gas in Jiaoshiba area，Sichuan Basin[J]. Acta Petrolei Sinica，2015，36(8)：926 - 939，953.

[13] 李玉坤，林俊丞，张广杰，等. 地应力变化与油井套管挤毁规律研究[J]. 石油机械，2017，45(8)：54 - 60.
Li Y K，Lin J C，Zhang G J，et al. Research on collapse of oil well casing under the variation of ground stress[J]. China Petroleum Machinery，2017，45(8)：54 - 60.

[14] 王璞，王成虎，王洪，等. 利用孔壁竖向裂缝方位数据分析沂沭断裂带的地应力场特征[J]. 地震地质，2020，42(6)：1316 -

1334.
Wang P, Wang C H, Wang H, et al. Analysis of in - situ stress parameters of Yishu fault zone based on orientation of ditf in BHTV image[J]. Seismology and Geology, 2020, 42(6): 1316 - 1334.
[15] 商恩俊. 昆北油田基岩储层裂缝特征及其对开发的影响[D]. 唐山: 华北理工大学, 2020.
SHANG E J. Fracture Characteristics of Bedrock Reservoir in Kunbei Oilfield and Its Influence on Development[D]. Tangshan: North China University of Science and Technology, 2020.
[16] 苗凤彬, 彭中勤, 王传尚, 等. 雪峰隆起西缘湘张地 1 井牛蹄塘组页岩含气性特征及控制因素[J]. 地球科学, 2019, 44(11): 3662 - 3677.
Miao F B, Peng Z Q, Wang C S, et al. Gas - bearing capacity and controlling factors of Niutitang formation shale in well XZD - 1, Western Margin of Xuefeng uplift [J]. Earth Science, 2019, 44(11): 3662 - 3677.
[17] 何建华, 丁文龙, 王哲, 等. 页岩储层体积压裂缝网形成的主控因素及评价方法[J]. 地质科技情报, 2015, 34(4): 108 - 118.
He J H, Ding W L, Wang Z, et al. Main controlling factors of fracture network formation of volume fracturing in shale reservoirs and its evaluation method[J]. Geological Science and Technology Information, 2015, 34(4): 108 - 118.
[18] 吴晶晶, 张绍和, 曹函, 等. 湘西北下寒武统牛蹄塘组页岩气储层可压裂性评价[J]. 中南大学学报: 自然科学版, 2018, 49(5): 1160 - 1168.
Wu J J, Zhang S H, Cao H, et al. Fracability evaluation of shale gas reservoir in Lower Cambrian Niutitang formation, northwestern Hunan[J]. Journal of Central South University: Science and Technology, 2018, 49(5): 1160 - 1168.
[19] Sondergeld C H, Newsham K E, Comisky J T, et al. Petrophysical considerations in evaluating and producing shale gas resources[C]// Proceedings of SPE Unconventional Gas Conference. Pittsburg: SPE, 2010.

Gas bearing and compressibility evaluation of shale reservoir in Dawuba Formation of Qianshuidi 1 Well in Guizhong - Nanpanjiang area

GUO Jun[1], YUAN Kun[2,3], GUO Jingwei[1], CHEN Xianglin[3], LI Yan[1]
(1. *Hunan Institute of Geophysics and Geochemistry, Changsha Hunan* 410014, *China*; 2. *China University of Geosciences (Beijing), Beijing* 100083, *China*; 3. *Oil and Gas Survey, China Geological Survey, Beijing* 100083, *China*)

Abstract: The stable shale gas flow was obtained during vertical well drilling of Qianshuidi 1 Well in Guizhong - Nanpanjiang area, meaning the good marine shale gas was discovered in Carboniferous Dawuba Formation. Based on the drilling, logging, well logging, analysis and testing data, the authors in this paper comprehensively studied the lithofacies, organic geochemistry, physical properties, fracture development and gas bearing of Dawuba Formation shale reservoir, and explained the gas bearing and compressibility of shale reservoir in the study area. The results show that: ① Dawuba Formation consists of a set of huge thick shale system which is from the lower slope subfacies of carbonate slope facies to the huge thick shale series of platform basin facies, and Good to high - quality source rock are well developed in the middle lower part of the third member and the upper part of the first member, with developed natural fractures. The maximum value of total hydrocarbon in gas logging is 63.41%, and the average value of desorption gas is 1.08 m^3/t, with good shale gas generation conditions and resource potential. ② The total content of brittle minerals in the main gas bearing intervals is 31% ~94%, and the Poisson's ratio is 0.31. The bulk modulus of elasticity is 27.2 GPa, and the fracture pressure is between 29.7 MPa and 48.5 MPa. This set of strata has good fracture potential and fracture retention ability, which means the complex fracture networks would be easily formed under large - scale volumetric fracture. Besides, the set of strata has high pressure and meets the conditions for fracturing to form industrial production capacity, making it a target layer for further exploration and development.

Keywords: Qianshuidi 1 well; Dawuba Formation; shale gas; gas bearing; compressibility

(责任编辑: 魏昊明)

doi: 10.19388/j.zgdzdc.2023.06.12
引用格式: 巩书华,李少青,王焕银,等.湖南张家界市永定区地质灾害发育规律及易发性评价研究[J].中国地质调查,2023,10(6): 101-110.(Gong S H,Li S Q,Wang H Y,et al. Research on the development law and susceptibility evaluation of geological disasters in Yongding District of Zhangjiajie City in Hunan Province [J]. Geological Survey of China,2023,10(6): 101-110.)

湖南张家界市永定区地质灾害发育规律及易发性评价研究

巩书华[1,2], 李少青[3], 王焕银[3], 王克营[1,2], 蔡宁波[1,2], 杜 江[1,2]
(1.湖南省地球物理地球化学调查所,湖南 长沙 410114; 2. 湖南省地质新能源勘探开发工程技术研究中心,湖南 长沙 410114; 3. 张家界市永定区自然资源局,湖南 张家界 427000)

摘要: 张家界市复杂的地质构造背景造就了独特的地貌景观,同时存在众多地质灾害隐患。通过分析张家界市永定区2014年至2022年详细的地质灾害调查资料,对区内地质灾害发育规律及易发性进行研究。结果表明: 区内地质灾害类型以滑坡为主,地质灾害空间分布以中部断层发育区与东北部页岩地层区最多,时间分布相对集中在5、6、7月雨季; 区内地质灾害与地形地貌、岩土体类型、构造活动密切相关,并受降雨及人类工程活动影响; 在碎屑岩丘陵地貌中灾害点密度最高; 在志留系砂质页岩岩组中地质灾害最易发; 受构造影响明显,断褶构造带处灾害点密集; 灾害高发期与雨季耦合,诱发因素主要是降雨; 不合理地切坡建房、道路建设等工程活动加剧地质灾害的发生。采用易发程度指数法,基于ArcGIS信息统计分析,将全区地质灾害易发程度划分为高易发区、中易发区与低易发区。研究可为永定区国土空间规划、地质灾害防治、旅游路线及重大工程建设规划提供指导。

关键词: 地质灾害; 孕灾条件; 发育规律; 易发性; 张家界
中图分类号: P694 **文献标志码**: A **文章编号**: 2095-8706(2023)06-0101-10

0 引言

地质灾害是由内因和外因共同作用影响下使地质环境恶化,并造成生命财产损失或资源环境破坏的灾害事件。内因主要包括地形地貌、岩土体类型、构造活动等; 外因包括降雨、地震等自然因素以及人类工程活动等诱发因素[1]。近年来。地质灾害发生频率与强度不断增大,严重威胁了人民生命财产安全,也制约了社会的可持续发展[2-3]。随着地质灾害危害性受到越来越多关注,各国学者对地质灾害发育规律及评价方法的研究工作也逐渐深入,针对不同地貌单元、不同地质灾害类型以及不同易发性及风险性评价模型与方法均有较多研究。如徐伟等[4]对西南红层地区地质灾害发育规律与成灾模式进行了总结分析; 张殿发等[5]分析了贵州喀斯特地貌地质灾害形成环境; 方琼等[6]研究了湖南省地貌与地质灾害影响关系。传统地质灾害易发性与风险性评价方法主要有信息量法[7]、逻辑回归法[8]、频率比和证据权法[9]、层次分析法[10]等。近年来,有学者提出不同方法模型组合评价,如确定性系数和逻辑回归的组合模型[11]、信息量法与遗传法融合模型[12]、模糊层次分析法与熵权法的主客观赋权模型[13],提升了易发性评价的精准度。

湘西北张家界市为著名的旅游城市,复杂的地质构造背景造就了绝美的地貌景观,但也存在着众多地质灾害隐患,加之新构造运动、澧水等河流侵蚀等内外地质作用影响,突发性地质灾害易发。以往研究多注重景区等特定范围的地质灾害发育规律分析[14-15],缺乏对全区的灾害发育特征研究。

收稿日期: 2022-11-07; **修订日期**: 2023-10-26。
基金项目: 湖南省自然资源厅"湖南省张家界市永定区1:10 000地质灾害调查和风险评价(编号: 湘地调[2022]67)"项目资助。
第一作者简介: 巩书华(1988—),男,高级工程师,主要从事水工环地质调查研究工作。Email: shuhua.gong@qq.com。

为此,本文根据近几年张家界市永定区地质灾害调查与评价工作,对区内地质灾害的孕灾地质条件和空间发育规律进行分析,划定全区地质灾害易发程度分区,旨在为相关部门国土空间规划、地质灾害防范与灾害趋势研判提供参考。

1 研究区概况

永定区地处武陵山脉腹地,位于扬子地台元第三隆起带的南端。地势整体呈西北高、东南低的特点,并由西向东倾斜,向沅水呈梯级递降,中部低洼,成半环状山丘盆地(图 1)。气候为中亚热带山原型季风湿润气候,年平均降雨天数为 154.7 天,年均降雨量约为 1 520.6 mm,平均气温为 16.8 ℃。春末夏初处于冷暖气流交替过渡期,是境内雨水最集中的时期。境内水系以熊壁岩—陈家湾—余家山—李家庄为分水岭,北部为澧水水系,南部为沅水水系。研究区地层出露较齐全,仅石炭系有缺失。

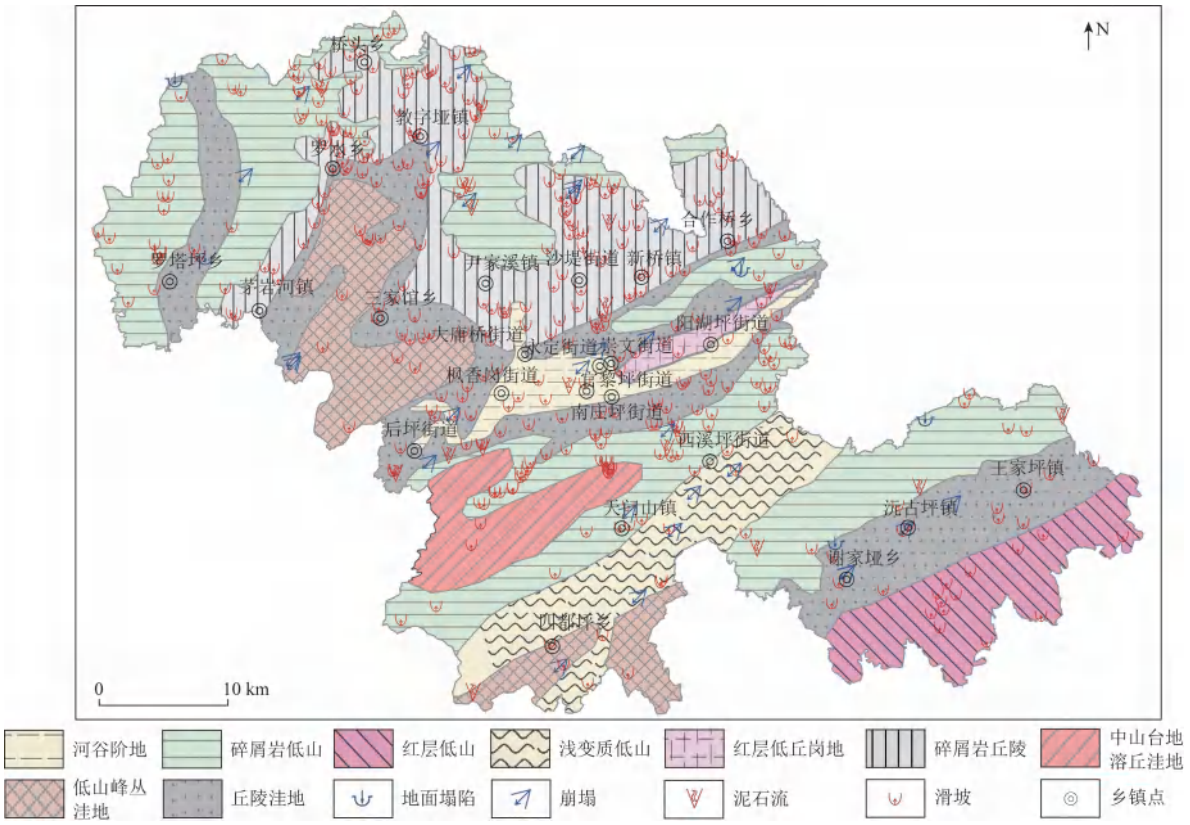

图 1 永定区地貌单元与地质灾害分布

Fig. 1 Distribution of landform division and geological hazards

2 地质灾害类型与分布特征

2.1 类型

通过查阅研究区 1∶5 万地质灾害调查资料以及最新风险普查和巡排查数据[16-17],统计区内地质灾害点共计 418 处,灾害类型以滑坡(含变形趋势为滑坡的隐患点)为主,崩塌(含变形趋势为崩塌的隐患点)、泥石流、地面塌陷等为次。其中:滑坡数量占灾害点总数的 88.04%;崩塌数量占灾害点总数的 7.17%;泥石流数量占灾害点总数的 3.59%;地面塌陷数量占灾害点总数的 1.20%。故滑坡是区内主要的地质灾害类型,其次为崩塌,最后为泥石流和地面塌陷等。

2.2 分布特征

(1)地质灾害分布受地层岩性制约明显。区内地质灾害在空间分布上总体是以中部断层发育区与东北部页岩地层区最多,西部及东南部相对较少。志留系分布区的灾害点数量最多,占灾害点总数的 30%;其次为寒武系中碎屑岩组分布区的灾害点数量,占灾害点总数的 12%;最后为奥陶系中碎屑岩组分布区的灾害点数量,占灾害点总数的 9.33%。

(2)时间分布相对集中在雨季。通过对研究区近 10 a 来各月发生的地质灾害的数量进行统计,并与区内各月份降雨特征对比发现,区内各类地质灾害月发生数量集中在 5、6、7 月,这 3 个月内发生的地

质灾害数量占灾害点总数的 89%(图 2)。这 3 个月是研究区每年降雨时间最长、累积降雨量最大的时期,说明降雨是本区地质灾害发生的关键诱发动力。降雨量达到一定量值后,会诱发大量的突发性地质灾害,暴雨来临时要注意区域性的群发地质灾害防治。

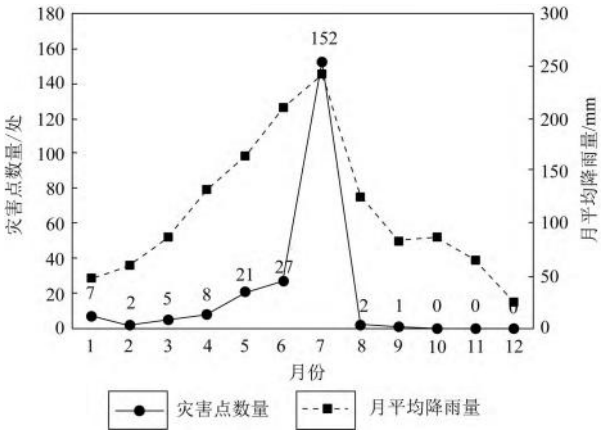

图 2　永定区各月份地质灾害频数

Fig. 2　Frequency of geological disasters in Yongding District by month

3　孕灾地质条件特征

3.1　地形地貌

研究区地貌单元,根据地貌成因、形态、海拔高度和相对切割深度,大体可划分为侵蚀堆积地貌、侵蚀构造地貌、剥蚀构造地貌以及溶蚀构造地貌 4 个大类 8 个亚类(表 1)。不同的地貌单元在斜坡类型、坡高、坡度等微地貌特征上有一定差别,发生的地质灾害类型、数量、规模也不同[18-19]。统计显示: 滑坡、崩塌及不稳定斜坡在各个地貌单元均有发育; 泥石流主要分布在具有宽阔的汇水区、丰富物源和合适地形因子(沟谷纵比降与坡度)的碎屑岩低山与丘陵洼地地貌中; 地面塌陷主要分布在溶蚀构造地貌中,基本为岩溶塌陷。区内地貌单元与灾害数量及密度的相关分析显示,地质灾害发育密度最高的为碎屑岩丘陵,达到 36.61 处/100 km^2,其次为丘陵洼地、碎屑岩低山和红层低丘岗地。

表 1　永定区地质灾害分布统计

Tab. 1　Statistics of geological hazard distribution in Yongding District

成因形态类型		地层岩性	分布面积		地质灾害		
			面积/km^2	百分比/%	数量/处	百分比/%	密度/(处·100 km^{-2})
侵蚀堆积地貌		第四系黏土、砂土、砂砾层等	87.25	4.27	12	2.88	13.75
侵蚀构造地貌	碎屑岩低山	下志留统—中志留统砂页岩	556.08	13.48	126	30.22	22.66
	红层低山	白垩系砂岩	141.90	3.97	14	3.36	9.87
	浅变质岩低山	五强溪组变质长石石英砂岩、板岩	174.51	5.09	13	3.12	7.45
剥蚀构造地貌	红层低丘岗地	白垩系砂岩、砾岩、砂砾岩等	23.01	0.71	5	1.20	21.73
	碎屑岩丘陵	奥陶系—志留系砂页岩	325.06	10.06	119	28.54	36.61
溶蚀构造地貌	中山台地溶丘洼地	寒武系—奥陶系中厚层状灰岩、白云岩	101.13	3.48	7	1.68	6.92
	低山峰丛洼地	寒武系—奥陶系灰岩、白云质灰岩、泥灰岩等	192.62	6.87	14	3.36	7.27
	丘陵洼地	石炭系—二叠系白云质灰岩、灰岩	443.16	16.96	107	25.66	24.14

地形坡度是影响地质灾害发生的重要因素[20],通过将研究区地形坡度按区间进行划分统计,发现区内 68% 以上的地质灾害分布在[25°,45°)之间,其中以[25°,35°)区间最多,占比为 41.67%(表 2)。针对单一灾种,滑坡、不稳定斜坡在各个坡度区间均有分布,在[20°,45°)地形坡度间数量较集中,此类土质滑坡的坡度集中区间在其他研究中也有证实[21]; 崩塌坡度范围为 60°以上,且发育较少,以岩质崩塌为主,集中在低山区; 泥石流集中在主沟纵坡坡度为[20°,60°)区间,这主要是因为区内泥石流大多是沟谷型,若沟谷纵坡坡度较小,则泥石流无势能到动能的转换,泥石流运动会停滞,反之,坡度较大,则泥石流能量转换大,运移速度快,在地形上,流程一般较短,汇水面积不大。

表 2　永定区地质灾害与坡度统计

Tab. 2　Geological hazard and slope statistics in Yongding District

坡度区间	灾害数量/处	比例/%	滑坡/处	崩塌/处	泥石流/处	地面塌陷/处
[0°,25°)	16	9.52	15	0	0	1
[25°,35°)	70	41.67	66	2	2	0
[35°,45°)	44	26.19	43	0	1	0
[45°,55°)	23	13.69	23	0	0	0
≥55°	15	8.93	11	4	0	0

3.2 岩土体类型

岩土体是各类地质灾害形成的物质基础,其类型特征关系着地质灾害的发生几率和发育时长[22]。通过分析研究区岩土体类型与地质灾害分布关系(图 3)发现:区内滑坡主要发生在碎屑岩类中,在志留系粉砂质页岩、页岩、粉砂岩半坚硬 – 坚硬岩组中分布最多,灾害点密度最大;崩塌在灰岩、白云岩夹泥质灰岩半坚硬 – 坚硬岩组中分布最多,灾害点密度最大;泥石流在粉砂质页岩、页岩、粉砂岩半坚硬 – 坚硬岩组中分布最多,灾害点密度最大。上述 3 个岩组为研究区主要易崩易滑工程地质岩组,其中以志留系砂质页岩岩组中地质灾害最易发,地面塌陷仅在区内碳酸盐岩岩组中有少量分布。

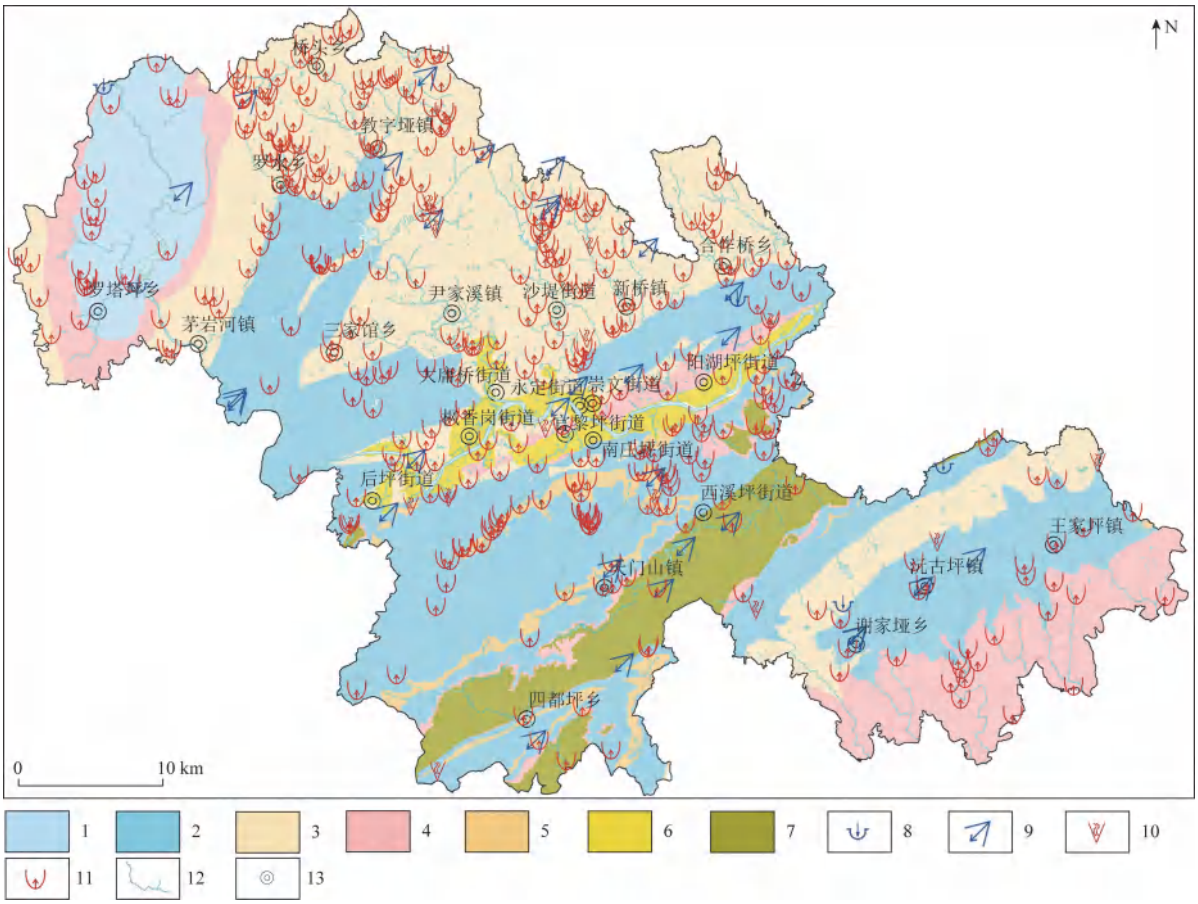

1. 灰岩夹泥质灰岩、砂岩半坚硬 – 坚硬岩组;2. 灰岩、白云岩夹泥质灰岩半坚硬 – 坚硬岩组;3. 粉砂质页岩、页岩、粉砂岩半坚硬 – 坚硬岩组;4. 红层砾岩、含砾砂岩、砂岩平坚硬 – 坚硬岩组;5. 硅质页岩、灰质页岩半坚硬 – 坚硬岩组;6. 第四系冲积物;7. 浅变质岩、砂岩坚硬岩组;8. 地面塌陷;9. 崩塌;10. 泥石流;11. 滑坡;12. 水系;13. 乡镇点

图 3 永定区岩土体类型与地质灾害分布关系

Fig. 3 Relationship between rock mass types and geological hazard distribution in Yongding District

3.3 构造活动

永定区经历多期构造运动,新构造运动也较为强烈,整体形成 NE—NNE 向断褶构造格局[23-24]。构造对区内地质灾害分布的影响表现为,邻近大型褶皱与断裂带,灾害点密度明显增大,距离断裂褶皱构造 1 km 范围以内的地质灾害点数量占总数的 55.98%,其中断裂构造附近灾害点数量占总数的 39.23%,褶皱构造附近灾害点数量占总数的 16.75%(图 4)。断裂周边分布较多的是滑坡和不稳定斜坡,灾害点沿断裂构造带两侧分布,这主要是由于断层沿走向易形成临空面及沟谷,可为滑坡等地质灾害的发生提供条件。褶皱附近同样以滑坡及不稳定斜坡最为发育,且在顺向坡易形成顺层滑坡,逆向坡则多形成崩塌。此外,由于背斜核部和两翼产生的节理裂隙较向斜多,岩石破碎程度较向斜大,导致背斜分布的地质灾害数量也比向斜略多(图 5)。

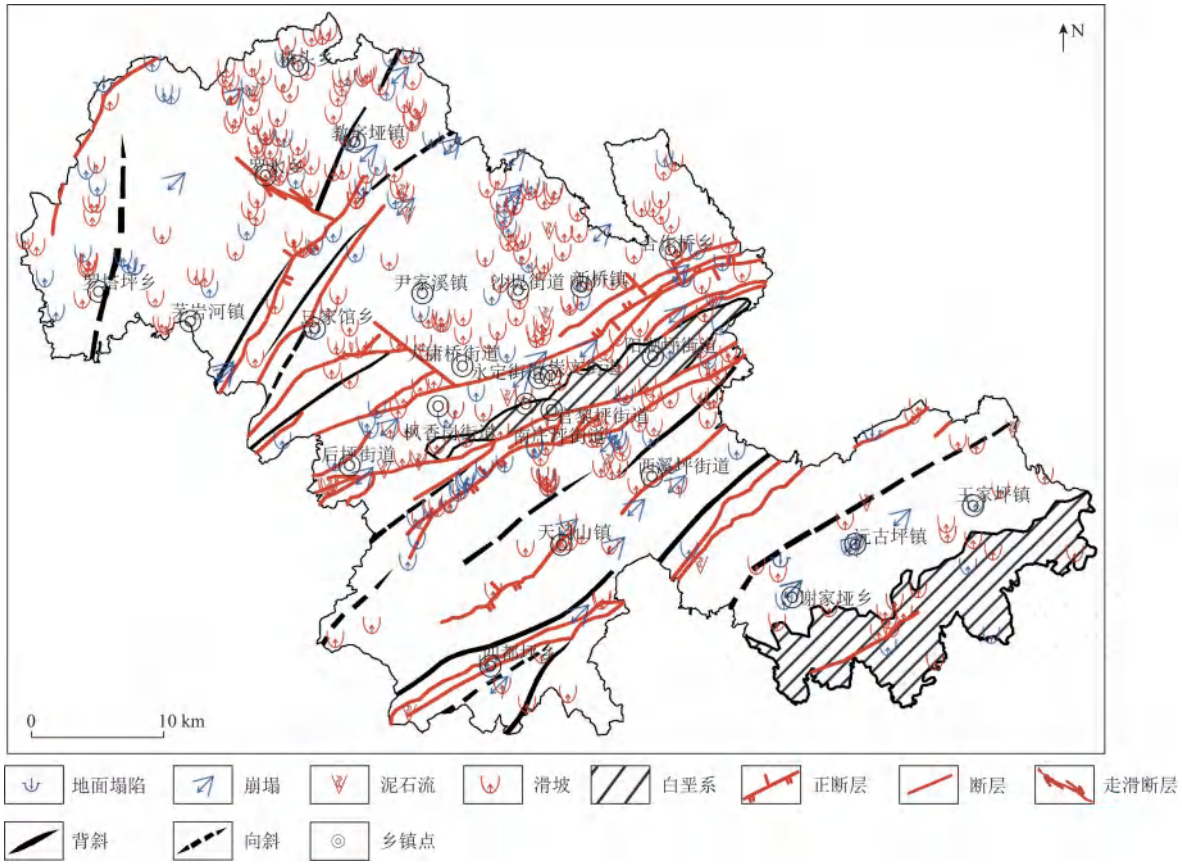

图 4　永定区地质构造与地质灾害分布关系

Fig. 4　Relationship between geological structures and geological disaster distribution

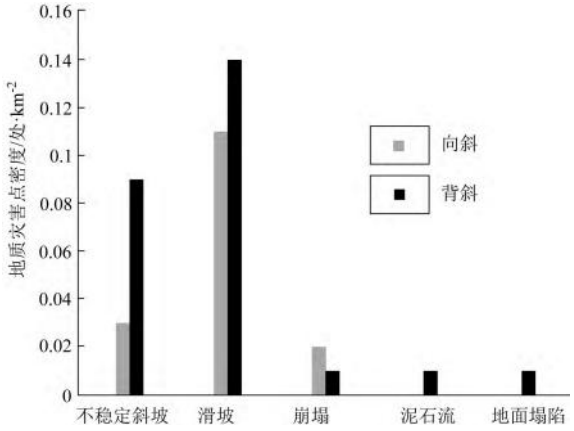

图 5　永定区不同褶皱构造与地质灾害分布关系

Fig. 5　Relationship between different fold structures and geological hazard distribution in Yongding District

4　诱发因素分析

4.1　降雨情况

研究区降雨丰沛且集中,常形成短时强降水,这种突发暴雨是区内地质灾害发生的主要诱发因素[25]。以 2003 年 7 月 7—9 日区内特大暴雨为例,其中 8 日的降雨量突破 417.3 mm,9 日降雨量达 110 mm,这次暴雨降水量占全年降雨量总和的 38.4%。期间全区发生地质灾害 66 处,占全年地质灾害总数的 52.8%。

永定区年均降水量平面分布大致有 2 个中心,分别为永定区南部地区四都坪和东南部谢家垭一带。区内年降水超过 1 500 mm,总体上向东北逐渐减小。在年均降雨量[1 000,1 200) mm 区间,地质灾害点数量最多,占灾害点总数的 51.4%；其次为降水量小于等于 1 000 mm 区间,灾害点数量占灾害点总数的 24.4%；大于 1 500 mm 降水区间内,灾害点发生数量最少,仅占灾害点总数的 3.1%。由此可见,研究区地质灾害的数量并不是单纯随年降水量增多而上升,以往研究也表明,灾害发生前 10 d 的有效降雨量对地质灾害影响更大[26-27]。

4.2　人类工程活动

永定区人为因素主导及参与诱发的地质灾害类型基本为滑坡和少量崩塌,统计有 97 处,占统计

总数量的 43.11%。通过对区内人口密度与地质灾害分布相关性分析(图 6),灾害点主要分布在人类活动程度较高的东北部地区以及澧水南岸 10 km 之内区域,这也说明人口较多的地区对自然环境的改造程度更多,人为增加了许多地质灾害风险。据调查,区内影响地质灾害发生的人类工程活动主要为不合理地切坡修路、建房,其次为矿山开采、地下水超采、植被破坏等活动。

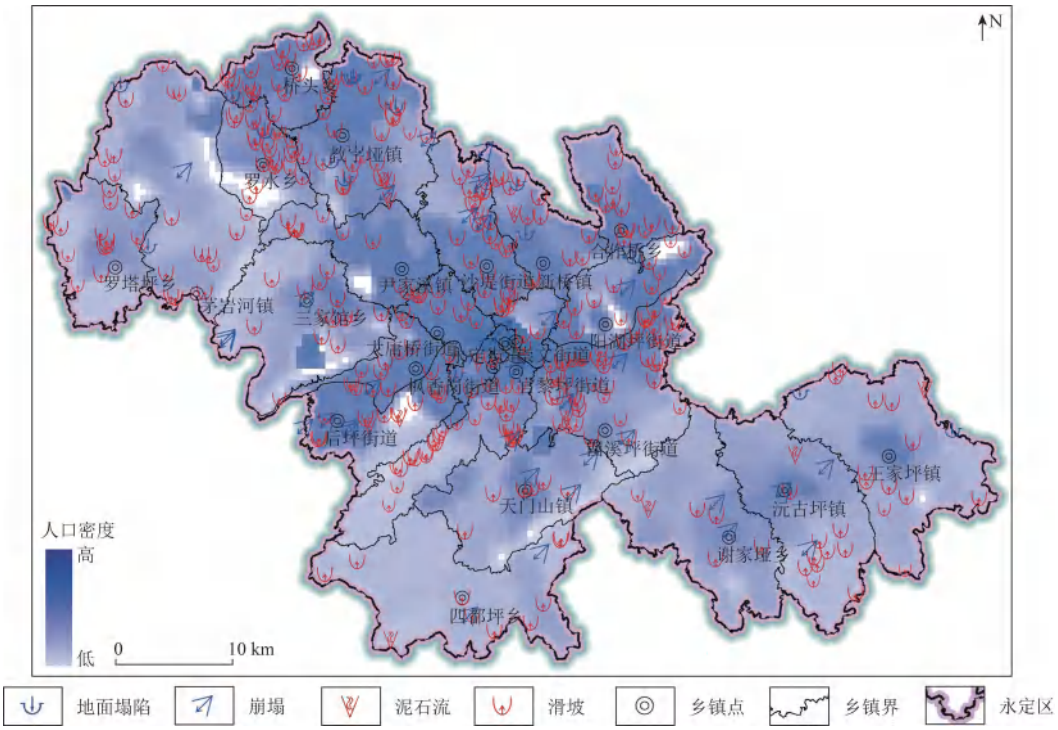

图 6 永定区人口密度与地质灾害分布关系

Fig. 6 Relationship between ropulation density and geological hazard distribution in Yongding District

5 地质灾害易发性分区评价

5.1 评价方法

本次评价方法采取易发程度指数法[28-30],在研究区选取地形地貌、地质构造、岩土体类型、植被覆盖情况、降雨量、人类工程活动及地质灾害点密度作为灾害易发性分区评价指标,将其与地质灾害发生的关系和权重系数建立地质灾害易发指数模型,对单灾害类型易发程度分区后再综合叠加分析。易发程度指数计算公式为

$$Z_p = \sum_{j=1}^{n} A_j \times q_j \quad 。 \tag{1}$$

式中:Z_p 为评价单元(1 km × 1 km)地质灾害易发程度指数;A_j 为各评价因子权重;q_j 为各评价因子分级值。

综合崩塌、滑坡、泥石流易发性指数和地面塌陷易发性指数,将两者易发性分区结果叠加分析,其中每个评价单元的信息叠加将满足如下逻辑运算公式[28]

$$Z = Z_{\mathrm{BHL}} \cup Z_{\mathrm{T}} \quad 。 \tag{2}$$

式中:Z 为评价单元地质灾害易发性综合指数;Z_{BHL} 为崩、滑、流地质灾害易发性指数;Z_{T} 为地面塌陷地质灾害易发性指数。

计算得到研究区所有地质灾害类型的易发性综合指数值,采用 ArcGIS 自然断点法数据统计,并结合前人经验,得到研究区易发程度分区阈值划分标准:当 $Z>6$ 时,为地质灾害高易发区;$3 \leqslant Z \leqslant 6$,为地质灾害中易发区;$1 \leqslant Z \leqslant 3$ 为地质灾害低易发区;$Z<1$ 时为地质灾害非易发区。

5.2 分区结果

根据易发程度指数评价方法,将全区地质灾害易发程度划分为高、中、低 3 类易发区(图 7)。

高易发区主要分布在区内东北部桥头乡至阳湖坪街道一带及东南端谢家垭乡至王家坪镇南部红层发育区,面积为 860.51 km^2。以低山丘陵地貌为主,局部地形切割深,山体坡度陡,断褶构造复杂,岩性以志留系页岩及白垩系砂页岩为主。人口

密度大,多切坡建房与公路修建等工程活动,地质环境较脆弱,灾害点密集。区内有地质灾害点 165 处,占全区灾害点总数的 73.33%,灾害点密度为 19.17 处/100 km^2。

中易发区主要分布在西北部罗塔坪乡、三家馆乡南部及四都坪至西溪坪街道一带,面积为 720.21 km^2。以中低山丘陵地貌为主,地形坡度较陡,构造发育,岩性以碳酸盐岩为主,人类工程活动多为矿山开采及公铁路施工。区内有地质灾害点 55 处,占全区灾害点总数的 24.44%,灾害点密度为 7.64 处/100 km^2。

低易发区主要分布在罗塔坪乡北部局部区域、茅岩河镇至三家馆乡一线、四都坪乡南部及谢家垭乡至王家坪镇北部一带,面积为 588.48 km^2。该区地貌包含低山丘陵、冲洪积阶地平原及中低山台地溶丘洼地,坡度变化大,地质构造相对简单。区内有地质灾害点 17 处,占全区灾害点总数的 2.22%,灾害点密度为 2.89 处/100 km^2。

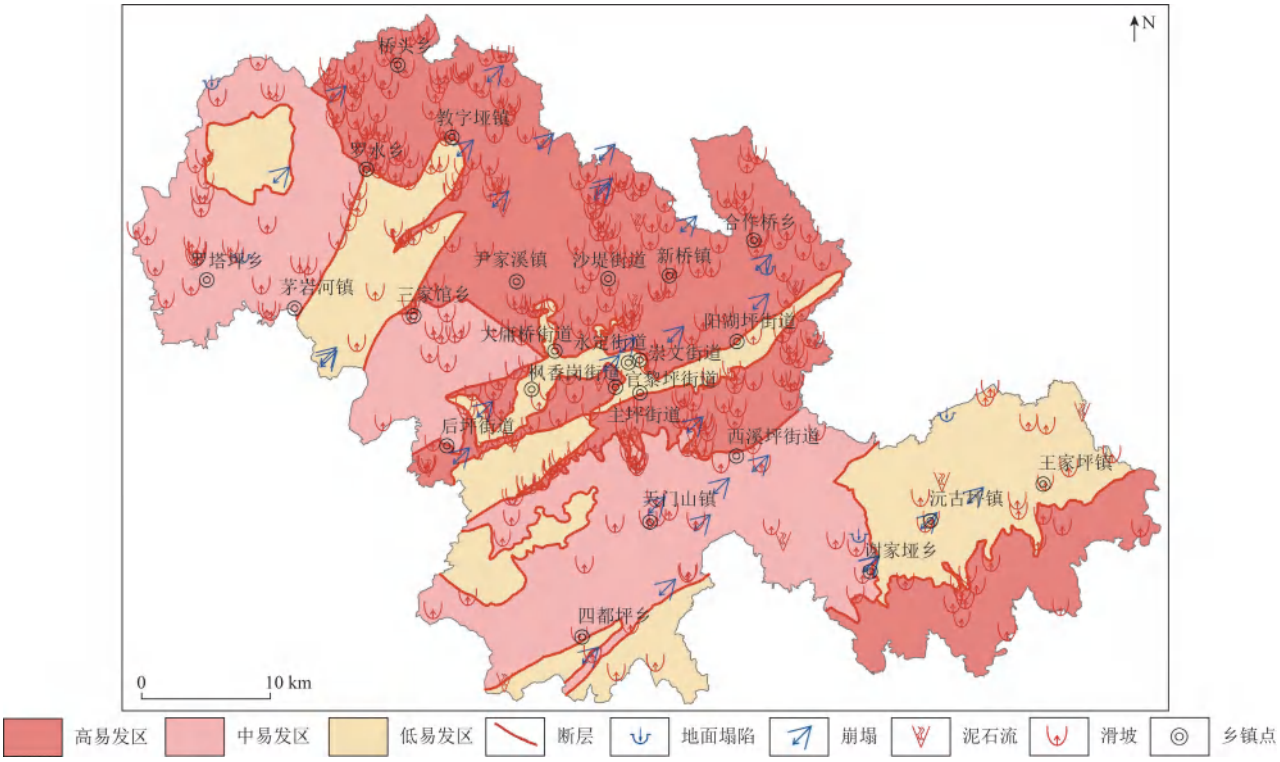

图 7　永定区地质灾害易发程度分区

Fig. 7　Geological disaster susceptibility zoning in Yongding District

6　结论

(1)张家界永定区地质灾害类型以滑坡为主,崩塌、泥石流、地面塌陷等为次。空间分布以中部断层发育区与东北部页岩地层区最多,受岩性控制,以志留系分布区的灾害点数量最多;时间分布相对集中在 5、6、7 月雨季。

(2)区内地质灾害与地形地貌、岩土体类型、构造活动密切相关,并受降雨及人类工程活动影响。主要规律为:在碎屑岩丘陵地貌中灾害点密度最高;在坡度范围[25°,45°)之间,发育 68% 以上的地质灾害,其中以[25°,35°)区间最集中;在志留系砂质页岩岩组中地质灾害最易发;受构造影响明显,断褶构造带处灾害点密集;灾害高发期与雨季耦合,突发性降雨诱发强烈;人口密集区切坡建房、道路建设等活动强烈,加剧地质灾害的发生。

(3)根据研究区地质灾害现状、孕灾条件要素、人类工程活动等诱发因子,采用易发程度指数法,基于 ArcGIS 信息统计分析,将全区地质灾害易发程度划分为高易发区(东北部桥头乡至阳湖坪街道一带及东南端谢家垭乡至王家坪镇南部红层发育区)、中易发区(西北部罗塔坪乡、三家馆乡南部及四都坪至西溪坪街道一带)与低易发区(罗塔坪乡北部局部区域、茅岩河镇至三家馆乡一线、四都坪乡南部及谢家垭乡至王家坪镇北部一带)。研究成

果可为永定区国土空间规划、地质灾害防治、旅游路线及重大工程建设规划提供指导。

参考文献(References):

[1] 王高峰,王爱军,田运涛,等. 基于图幅调查的六盘山镇孕灾地质条件分析[J]. 水土保持研究,2016,23(5):364 - 369.
Wang G F,Wang A J,Tian Y T,et al. Analysis on disaster - pregnant geological environment of Liupanshan town based on map sheet survey[J]. Research of Soil and Water Conservation,2016,23(5):364 - 369.

[2] Guzzetti F,Carrara A,Cardinali M,et al. Landslide hazard evaluation:A review of current techniques and their application in a multi - scale study, Central Italy[J]. Geomorphology, 1999,31(1 - 4):181 - 216.

[3] Uitto J I,Shaw R. Sustainable Development and Disaster Risk Reduction:Introduction[M]. Tokyo:Springer,2016.

[4] 徐伟,冉涛,田凯. 西南红层地区地质灾害发育规律与成灾模式——以云南彝良县为例[J]. 中国地质灾害与防治学报,2021,32(6):127 - 133.
Xu W,Ran T,Tian K. Developing law and disaster modes of geohazards in red bed region of southwestern China:A case study of Yiliang County of Yunnan Province[J]. The Chinese Journal of Geological Hazard and Control,2021,32(6):127 - 133.

[5] 张殿发,邹永廖. 喀斯特地质灾害的形成条件及其环境背景——以贵州省为例[J]. 矿物岩石地球化学通报,2002,21(1):39 - 42.
Zhang D F,Zou Y L. The contributory factors and environmental setting of karst Geohazards:A typical example in Guizhou Province[J]. Bulletin of Mineralogy Petrology and Geochemistry,2002,21(1):39 - 42.

[6] 方琼,段中满. 湖南省地形地貌与地质灾害分布关系分析[J]. 中国地质灾害与防治学报,2012,23(2):83 - 88.
Fang Q,Duan Z M. Distribution analysis of topography and geological hazards in Hunan province[J]. The Chinese Journal of Geological Hazard and Control,2012,23(2):83 - 88.

[7] 唐川,马国超. 基于地貌单元的小区域地质灾害易发性分区方法研究[J]. 地理科学,2015,35(1):91 - 98.
Tang C,Ma G C. Small regional geohazards susceptibility mapping based on geomorphic Unit[J]. Scientia Geographica Sinica,2015,35(1):91 - 98.

[8] Baharvand S,Rahnamarad J,Soori S,et al. Landslide susceptibility zoning in a catchment of Zagros Mountains using fuzzy logic and GIS[J]. Environmental Earth Sciences,2020,79(10):204.

[9] Chen W,Ding X,Zhao R X,et al. Application of frequency ratio and weights of evidence models in landslide susceptibility mapping for the Shangzhou district of Shangluo City,China[J]. Environmental Earth Sciences,2016,75(1):64.

[10] 江金进,赖波,江山,等. 珠海市横琴新区地质灾害分布特征及易发性评价[J]. 地质灾害与环境保护,2022,33(1):30 - 36.
Jiang J J,Lai B,Jiang S,et al. Distribution characteristics and susceptibility evaluation of geological hazards in Hengqin of Zhuhai city[J]. Journal of Geological Hazards and Environment Preservation,2022,33(1):30 - 36.

[11] 刘璐瑶,高惠瑛,李照. 基于 CF 与 Logistic 回归模型耦合的永嘉县滑坡易发性评价[J]. 中国海洋大学学报:自然科学版,2021,51(10):121 - 129.
Liu L Y,Gao H Y,Li Z. Landslide susceptibility assessment based on coupling of CF Model and logistic regression model in Yongjia County[J]. Periodical of Ocean University of China:Natural Science Edition,2021,51(10):121 - 129.

[12] 杨康,薛喜成,李识博. 信息量融入 GA 优化 SVM 模型下的地质灾害易发性评价[J]. 安全与环境工程,2022,29(3):109 - 118.
Yang K,Xue X C,Li S B. Geological hazard susceptibility assessment by incorporating information value into GA optimized SVM model[J]. Safety and Environmental Engineering,2022,29(3):109 - 118.

[13] 周苏华,付宇航,徐智文,等. 基于主客观赋权法的福建省地质灾害易发性评价[J]. 安全与环境学报,2023,23(9):3204 - 3214.
Zhou S H,Fu Y H,Xu Z W,et al. Geological disasters susceptibility mapping in Fujian Province based on subjective and objective weighting[J]. Journal of Safety and Environment,2023,23(9):3204 - 3214.

[14] 徐昊,朱鹏程,孟明超,等. 张家界黄龙洞景区危岩崩塌地质灾害评价及防治措施[J]. 国土资源导刊,2018,15(1):44 - 51.
Xu H,Zhu P C,Meng M C,et al. Geological hazard assessment and prevention measures of perilous rock collapse in Huanglong cave scenic area of Zhangjiajie[J]. Land & Resources Herald,2018,15(1):44 - 51.

[15] 李晋,覃事胜,刘新惠,等. 张家界大峡谷景区危岩体发育规律与防治建议[J]. 地质灾害与环境保护,2019,30(3):48 - 52.
Li J,Qin S S,Liu X H,et al. Development law and control suggestion of unstable rocks in Zhangjiajie grand canyon scenic area[J]. Journal of Geological Hazards and Environment Preservation,2019,30(3):48 - 52.

[16] 覃事胜,张弛,申旭辉,等. 湖南省张家界市永定区 1:5 万地质灾害详细调查报告[R]. 长沙,2016.
Tan S S,Zhang C,Shen X H,et al. Detailed Investigation Report of 1: 50 000 Geological Disasters in Yongding District,Zhangjiajie City,Hunan Province[R]. Changsha,2016.

[17] 王克营,巩书华,杜江,等. 湖南省张家界市永定区地质灾害风险普查报告[R]. 长沙,2022.
Wang K Y,Gong S H,Du J,et al. Geological Hazard Risk Survey Report of Yongding District,Zhangjiajie City,Hunan Province[R]. Changsha,2022.

[18] 阳岳龙,周群,林剑. 湖南主要地质灾害与地形地貌之关系[J]. 灾害学,2007,22(3):36 - 40.

Yang Y L,Zhou Q,Lin J. The relationship between main geological hazards and topography in Hunan[J]. Journal of Catastrophology,2007,22(3):36 - 40.

[19] 熊德清,崔笑烽. 喜马拉雅山脉地震带主要地质灾害与地形地貌关系——以西藏日喀则地区为例[J]. 地质通报,2021,40(11):1967 - 1980.
Xiong D Q,Cui X F. The relationship between main geological hazard and topography in the Himalayan seismic belt:A case study in the Xigaze area,Tibet[J]. Geological Bulletin of China,2021,40(11):1967 - 1980.

[20] 金福喜,罗滔,李杰. 湘东南某市地形地貌对地质灾害发育规律的控制作用分析[J]. 中国地质灾害与防治学报,2014,25(2):115 - 118.
Jin F X,Luo T,Li J. The analysis of the control action of geography of the development rule of geological hazard in a city of Southeastern of Hunan province[J]. The Chinese Journal of Geological Hazard and Control,2014,25(2):115 - 118.

[21] 郭果,陈筠,李明惠,等. 土质滑坡发育概率与坡度间关系研究[J]. 工程地质学报,2013,21(4):607 - 612.
Guo G,Chen J,Li M H,et al. Statistic relationship between slope gradient and landslide probability in soil slopes around reservoir[J]. Journal of Engineering Geology,2013,21(4):607 - 612.

[22] 杜国梁. 喜马拉雅东构造结地区滑坡发育特征及危险性评价[D]. 北京:中国地质科学院,2017.
Du G L. Development Characteristics and Hazard Assessment of Landslide in the Eastern Himalayan Syntaxis Region of Tibetan Plateau[D]. Beijing:Chinese Academy of Geological Sciences,2017.

[23] 巩书华,朱丽芬. 湘西北地质地貌特征对岩溶石漠化影响研究——以张家界市为例[J]. 中国岩溶,2021,40(3):504 - 512.
Gong S H,Zhu L F. Influence of geological and geomorphologic features on karst rocky desertification in northwestern Hunan Province:A case study of Zhangjiajie City[J]. Carsologica Sinica,2021,40(3):504 - 512.

[24] 姜端午,李大明,梅金华. 湘西北地区岩溶旋回及新构造遥感信息特征[J]. 湖南地质,2001,20(3):225 - 229.
Jiang D W,Li D M,Mei J H. Karst circle in westnorthern Hunan and its neotectonics remote sensing interpretation information[J]. Hunan Geology,2001,20(3):225 - 229.

[25] 陈静静,姚蓉,文强,等. 湖南省降雨型地质灾害致灾雨量阈值分析[J]. 灾害学,2014,29(2):42 - 47.
Chen J J,Yao R,Wen Q,et al. Hazard rainfall threshold analysis of rainfall - induced geological disasters in Hunan Province[J]. Journal of Catastrophology,2014,29(2):42 - 47.

[26] 宫清华,黄光庆,郭敏,等. 地质灾害预报预警的研究现状及发展趋势[J]. 世界地质,2006,25(3):296 - 302.
Gong Q H,Huang G Q,Guo M,et al. Present status of research and its developmental tendency on prediction and early warning of geologic hazards[J]. Global Geology,2006,25(3):296 - 302.

[27] 李明,杜继稳,高维英. 陕北黄土高原区地质灾害与降水关系[J]. 干旱区研究,2009,26(4):599 - 606.
Li M,Du J W,Gao W Y. Study on the relationship between geological disasters and precipitation in the Loess Plateau in North Shaanxi Province[J]. Arid Zone Research,2009,26(4):599 - 606.

[28] 中国地质灾害防治工程行业协会. T/CAGHP 017 - 2018 县(市)地质灾害调查与区划规范(试行)[S]. 武汉:中国地质大学出版社,2018.
China Geological Hazard Prevention Engineering Industry Association. T/CAGHP 017 - 2018 The Specification of Geological Disaster Investigation and Zonation for County[S]. Wuhan:China University of Geoscience Press,2018.

[29] 张刘柱,陈雪梅,郑立博,等. 易发程度指数法在宣州区地质灾害易发区划分中的应用研究[J]. 地质灾害与环境保护,2019,30(2):92 - 96.
Zhang L Z,Chen X M,Zheng L B,et al. Application of susceptibility index method in the division of geological hazard prone areas in Xuanzhou District[J]. Journal of Geological Hazards and Environment Preservation,2019,30(2):92 - 96.

[30] 许兆军,肖妮娜,刘志尧,等. 基于易发程度指数法的桂阳县地质灾害易发性分区研究[J]. 长春工程学院学报(自然科学版),2012,13(3):54 - 59.
Xu Z J,Xiao N N,Liu Z Y,et al. Research on geological disaster - prone area based on susceptibility index method in Guiyang County[J]. Journal of Changchun Institute of Technology (Natural Science Edition),2012,13(3):54 - 59.

Research on the development law and susceptibility evaluation of geological disasters in Yongding District of Zhangjiajie City in Hunan Province

GONG Shuhua[1,2], LI Shaoqing[3], WANG Huanyin[3], WANG Keying[1,2], CAI Ningbo[1,2], DU Jiang[1,2]

(1. *Hunan Institute of Geophysical and Geochemical Survey, Hunan Changsha* 410114, *China*; 2. *Geological New Energy Exploration and Development Engineering Technology Research Center of Hunan Province, Hunan Changsha* 410114, *China*; 3. *Yongding District Natural Resources Bureau of Zhangjiajie, Hunan Zhangjiajie* 427000, *China*)

Abstract: The complex geological structure in Zhangjiajie City has led to its unique landform landscape, meanwhice it has also posed numerous geological hazard risks. By analyzing detailed geological hazard investigation da-

ta of Yongding District from 2014 to 2022, the authors in this paper have studied its developmental patterns and susceptibility of geological hazards. The results indicate that landslide is the primary type of geological hazard in the area. Geological hazards are spatially most prevalent in the central fault zone and the northeastern shale formation zone, and they are temporally relatively concentrated during the rainy season in May, June and July. Geological hazards in this area are closely related to landform characteristics, lithology, and tectonic activities, and they are also influenced by rainfall and human engineering activities. The density of hazard points is highest in the debris hill landform, and the susceptibility of hazard points is highest in Silurian sandy shale formation. Besides, the geological hazards are significantly influenced by tectonics, with hazard points densely concentrated in fold and thrust structures. The high incidence period of hazards is coupled with the rainy season, and the main triggering factor is rainfall. And the unreasonable engineering activities, such as slope cutting for houses and roads construction, exacerbate the occurrence of geological hazards. By using the susceptibility index method and based on ArcGIS information statistics analysis, the authors in this paper have divided the susceptibility of geological hazards in the entire area into high, moderate, and low susceptibility zones. This study could provide guidance for land spatial planning, geological hazard prevention and control, and planning for tourism routes and major engineering construction in Yongding District.

Keywords: geological hazard; disaster pregnancy conditions; development law; susceptibility; Zhangjiajie City

(责任编辑: 刘丹)

2023年12月
December，2023

矿 床 地 质
MINERAL DEPOSITS

第42卷 第6期
42（6）：1101~1120

文章编号：0258-7106（2023）06-1101-20

Doi: 10. 16111/j. 0258-7106. 2023. 06. 002

湘东南东风岩体锆石U-Pb年代学、Hf同位素组成及稀土矿床特征*

张锦煦[1]，林碧海[1]，廖凤初[2]，孙 骥[1]，谭仕敏[1]，何艳林[2]，周 超[1]，朱继华[1]，熊 雄[1]，李 超[1]，陈剑锋[1, 2, 3**]

（1 湖南省地质调查所，湖南 长沙 410116；2 湖南省地球物理地球化学调查所，湖南 长沙 410116；3 中南大学有色金属成矿预测与地质环境监测教育部重点实验室，湖南 长沙 410083）

摘 要 文章对湘东南地区的东风岩体进行了锆石LA-ICPMS U-Pb年龄、Hf同位素以及岩石地球化学分析，以研究岩石成因及形成构造背景，并对东风风化壳离子吸附型重稀土矿的成因进行了探讨。东风岩体2件二长花岗岩的锆石U-Pb年龄为（433.5±2.6）Ma和（432.0±2.5）Ma，显示为加里东晚期。东风岩体锆石$\varepsilon_{Hf}(t)$值介于−5.12~−7.45，计算得到二阶段地幔亏损模式年龄（T_{DM2}）介于1714~1882 Ma，显示其成岩物质为壳源的特征。东风岩体的地球化学特征显示其为高钾钙碱性、强过铝质的花岗岩，在成因类型判别图解中显示为S型花岗岩，构造背景判别图解显示为后碰撞构造环境。综合东风岩体花岗岩的地球化学特征和Hf同位素特征，笔者认为，东风岩体形成于扬子板块与华夏板块陆内汇聚的后碰撞伸展环境，为增厚地壳减压熔融和软流圈地幔上涌诱发古老地壳物质重熔形成的S型花岗岩。东风稀土矿床为一个由富轻稀土元素的母岩经风化后形成的大型重稀土矿床，富含稀土元素的高Y型花岗岩母岩为矿床的形成提供了重要物质基础，气候及地形地貌条件为稀土元素发生淋滤迁移和吸附富集提供了重要保证。

关键词 东风花岗岩体；加里东期；锆石U-Pb定年和Hf同位素；离子吸附型稀土矿；矿床成因；湘东南

中图分类号：P618.7 **文献标志码**：A

Zircon U-Pb chronology, Hf isotopes and REE deposit characteristics of Dongfeng granitic pluton in southeastern Hunan Province

ZHANG JinXu[1], LIN BiHai[1], LIAO FengChu[2], SUN Ji[1], TAN ShiMin[1], HE YanLin[2], ZHOU Chao[1], ZHU JiHua[1], XIONG Xiong[1], LI Chao[1] and CHEN JianFeng[1, 2, 3]

(1 Geological Survey Institute of Hunan Peovince, Changsha 410116, Hunan, China; 2 Geophysical and Geochemical Survey Institute of Hunan, Changsha 410116, Hunan, China; 3 Key Laboratory of Metallogenic Prediction of Nonferrous Metals and Geological Environment Monitoring, Ministry of Education, Central South University, Changsha 410083, Hunan, China)

Abstracts

This paper presents new zircon LA-ICP-MS U-Pb ages, Lu-Hf isotope and geochemical data of the Dongfeng granitic pluton in southeastern part of Hunan Province, aiming to constrain its petrogenesis and tectonic implication, and to explore the metallogenic mechanism of the Dongfeng ion adsorption type heavy rare-earth deposit. The LA-ICP-MS zircon U-Pb analysis of two biotite monzogranite yielded $^{206}Pb/^{238}U$ ages of (433.5±2.6)Ma and

* 本文得到中国地质调查局二级项目(编号：DD20230055、12120115029301)、湖南省地质院科研项目(编号：HNGSTP202306)和湖南省自然资源厅科研项目(编号：2023-02)联合资助

第一作者简介 张锦煦，男，1982年生，硕士，高级工程师，从事地质找矿与研究工作。Email: 609126729@qq.com

** 通讯作者 陈剑锋，男，1985年生，博士，高级工程师，从事地质找矿与研究工作。Email: chenjianfeng021041@163.com

收稿日期 2023-05-11；改回日期 2023-10-25。秦思婷编辑。

(432.0±2.5)Ma, respectively, suggesting that the Dongfeng granitic pluton formed in Late Caledonian. The granites contain high K_2O and belong to calc-alkali, strongly peraluminous (A/CNK=1.12~1.43), and geochemically classified as S-type granite. The primitive mantle-normalized trace element spider diagram shows that the Dongfeng monzogranite is relatively depleted in Ba, Nb, Sr, P, Ti and relatively enriched in Rb, (Th+U), Nd, (Zr+Hf) as well as zircon $\varepsilon_{Hf}(t)$ (−5.12 to −7.45) and $^{176}Hf/^{177}Hf$ (0.282 300 to 0.282 374) values indicating that this pluton is mostly product of crust melting. Tectonic setting discrimination diagrams show characteristics of monzogranite produced in post-collisional extensional environment. Hf isotopic and geochemical analyses indicate that the Dongfeng monzogranite belongs to S-type granite, derived from the partial melting of old crustal materials, when asthenosphere mantle upwelling, causing remelting of crustal materials under the geodynamical background of extensional environment after intraplate convergence between Yangtze Plate and Cathaysia Plate. The Dongfeng deposit is a newly discovered, large-sized ion adsorption type heavy rare-earth deposit, with an averaging grade of 0.050%~0.099% of REO, which formed from weathering of biotite monzogranite enriched in LREE, the high content of Y in parent granite provides the major sources in the formation of the deposit. Topographic features and climatic characteristics in the Dongfeng area are the key conditions for eluviation and sorption inducing the formation of ion adsorption type rare-earth deposit.

Key words: Dongfeng granitic pluton, Caledonian, zircon U-Pb geochronology and Hf isotope, ion adsorption type rare-earth deposit, ore genesis, southeastern Hunan Province

湘东南地区地处南岭中段,位于华夏地块与扬子地块结合部位的东侧(图1a),区域NE向茶陵—郴州大断裂从区内通过(图1b)。区内多时代的花岗岩及其成矿作用长期以来为地质学者研究的重点,前人已对区内花岗岩地球化学特征及其侵位年龄、构造背景、成矿作用等进行了深入研究,特别是在年代学方面积累了较多的数据,如张文兰等(2011)获得彭公庙岩体的LA-ICP-MS锆石U-Pb年龄436.2~435.3 Ma,与程顺波等(2013)获得该岩体锆石SHRIMP U-Pb年龄(441.1±3.1)Ma比较吻合,证实其形成于加里东期;Wang等(2007a)获得五峰仙岩体的LA-ICP-MS锆石U-Pb年龄为(236.0±6)Ma,与陈迪等(2017)获得的(233.5±2.5)Ma的锆石SHRIMP U-Pb年龄在误差内一致,表明其形成于印支期;锡田岩体的锆石U-Pb年龄显示其有印支期和燕山期花岗岩,其中印支期花岗岩的侵位时限为225~220 Ma(陈迪等,2013;姚远等,2013;Liang et al., 2016; Wu et al., 2016),燕山期花岗岩为155~150 Ma(马铁球等,2005;陈迪等,2013;周云等,2013;牛睿等,2015;Zhou et al., 2015; Liang et al., 2016);万洋山岩体和诸广山北体均有加里东期、印支期和燕山期的花岗岩出露(伍光英等,2008;陈迪等,2016;郭爱民等,2017)。受多时代花岗岩浆活动的影响,该区发生了大规模多金属成矿作用。东风岩体位于该区茶陵—郴州大断裂东侧、彭公庙岩体与万洋山岩体之间(图1b),走向近南北,长约15 km,东西宽约3 km,出露面积43 km^2。岩体西侧侵入于寒武系—奥陶系浅变质砂岩、板岩中,东部与泥盆系跳马涧组石英砂岩呈沉积接触(图1c),据此可推断其应为加里东期岩体,但缺乏准确的年龄数据。

湘东南所在南岭地区不仅是中国钨锡等有色金属的富集地,也是中国离子吸附型稀土矿的矿集区(王登红等,2013),近年来湖南省地调院在该区开展了区域性找矿工作,在万洋山、彭公庙、东风岩体内陆续新发现了一批如青广坪、塘窝、白面石、牛头坳、东风等稀土矿床(点)(图1b),经初步调查评价,这些矿床(点)均具备寻找中大型离子吸附型稀土矿的潜力(湖南省地质调查院,2014;2018)。离子吸附型稀土矿床可分为轻稀土矿床和重稀土矿床,一般认为稀土矿的成矿作用对母岩的稀土元素成分具有明显的继承性(周美夫等,2020),表现为重稀土矿在相对富重稀土元素的母岩中富集,而轻稀土矿的母岩则具有相对富轻稀土元素的特征(Li et al., 2017)。而本文的研究显示,该区东风岩体内的东风稀土矿床则为一由富轻稀土元素的花岗岩作为母岩经风化后形成的重稀土矿床,其成矿作用研究对丰富稀土成矿理论及拓宽重稀土矿的找矿方向具有重要意义。

笔者在对东风岩体进行系统的岩石矿物学野外考察以及稀土矿含矿性调查基础上,获得2件花岗岩样品的锆石LA-ICPMS U-Pb年龄、Hf同位素数据

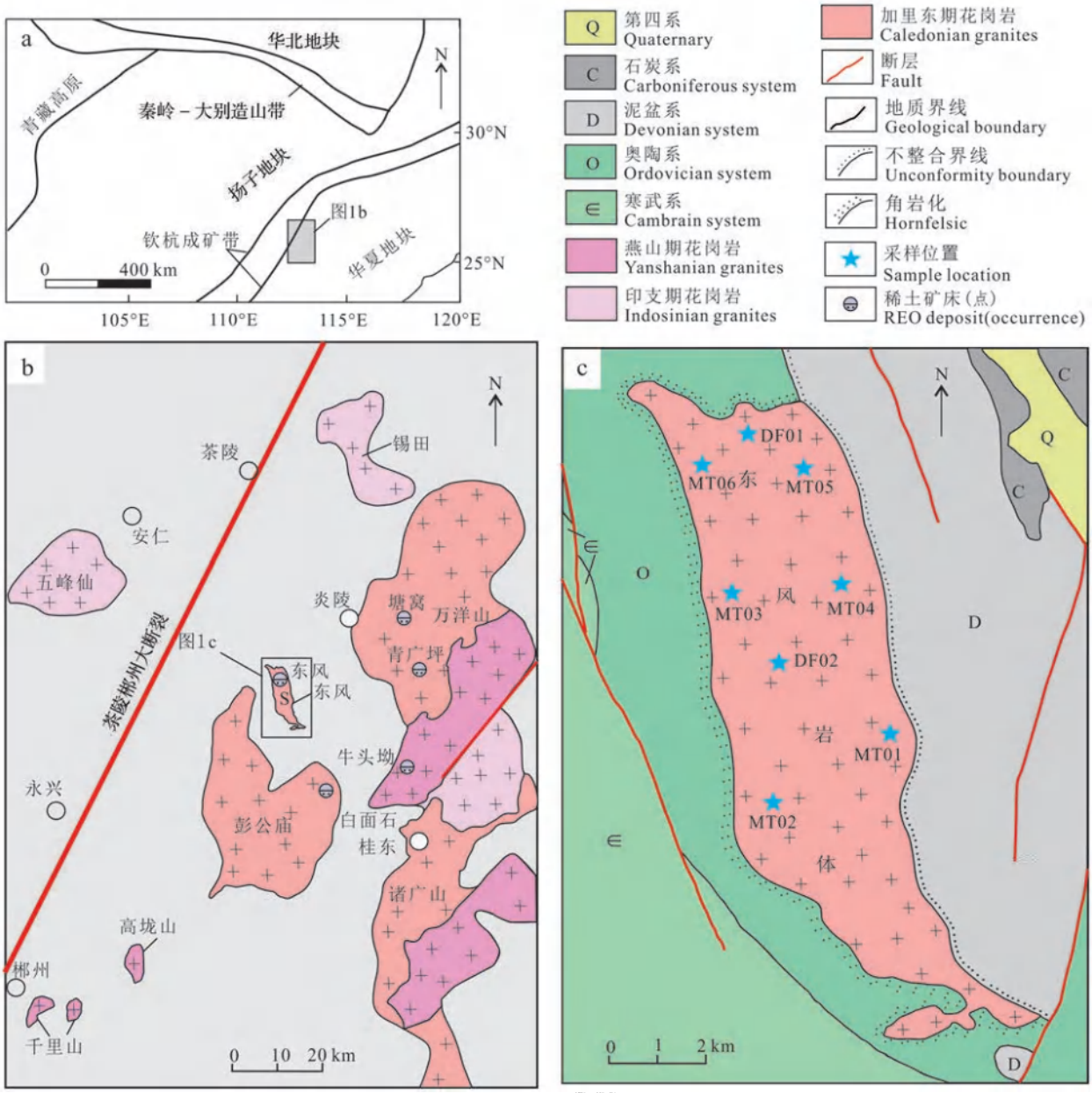

图 1　湘东南地区大地构造位置简图(a)、花岗岩分布图(b)和东风岩体地质简图(c)(据柏道远等,2006修改)

Fig. 1　Geotectonic location (a), distribution of granitic plutons (b) in southeastern Hunan Province and geologic sketch of the Dongfeng pluton (c) (modified after Bai et al., 2006)

及一批地球化学数据,据此对东风岩体侵位时限、岩石成因、构造背景,以及东风稀土矿床的成矿特征等问题进行探讨。

1　岩体地质特征及含矿性特征

由原湖南省地质调查院在该区所完成的1:1万地质测量成果显示,与相邻彭公庙岩体、万洋山岩体等大岩基内产出有大量晚期侵入的岩脉不同,东风岩体地表极少有石英脉和细晶岩脉出露,且岩体内未见有基性岩脉,其岩性单一,为粗中粒(少)斑状黑云母二长花岗岩。整个岩体地表风化严重(图2a),经浅井与浅钻工程揭露,其风化壳在垂向上可分为4层,即腐殖层、残坡积层、全风化层和半风化层(图3)。全风化层厚度基本大于10 m(山顶陡坎及河沟处除外),最厚部位约为38 m,呈土黄色或紫红色;腐

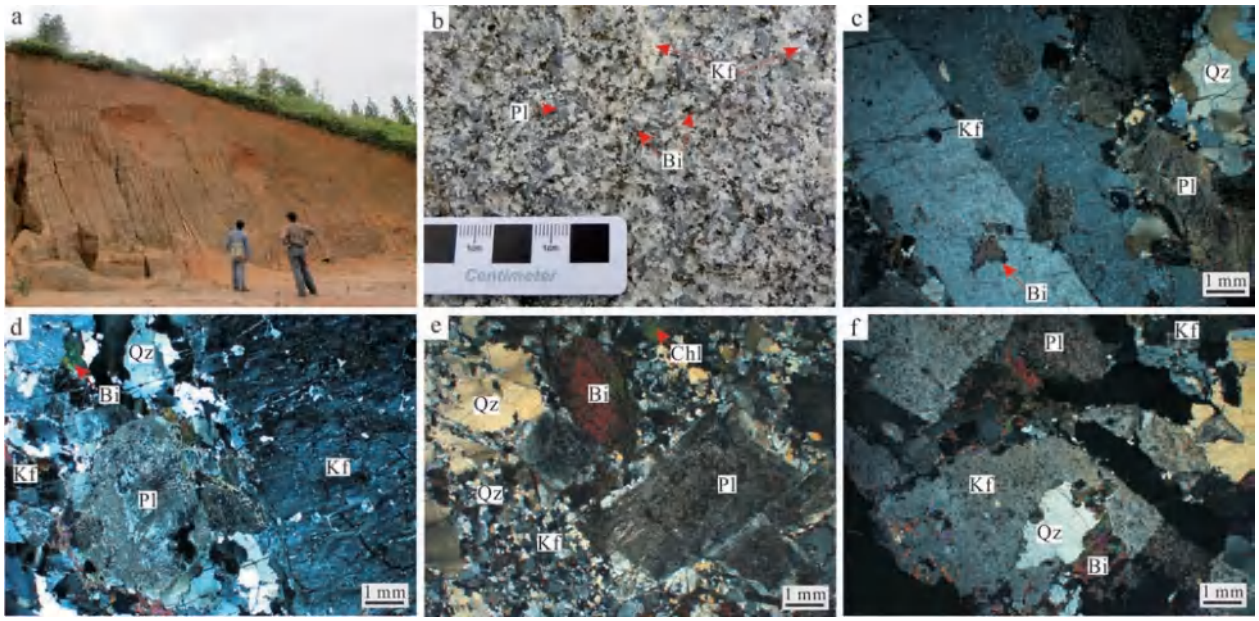

图2 东风岩体野外露头、岩石学特征和显微岩相学特征

a. 东风岩体野外露头;b. 花岗岩手标本照片;c. 钾长石斑晶具卡式双晶结构(+);d. 钾长石具条纹结构,斜长石绢云母化(+);e. 黑云母绿泥石化(+);f. 黑云母中的独居石和磷灰石(+)

Ap—磷灰石;Bi—黑云母;Chl—绿泥石;Kf—钾长石;Mnz—独居石;Pl—斜长石;Qz—石英;Ser—绢云母

Fig. 2 Photos of filed geology, petrological and micrograph of the Dongfeng pluton

a. Outcrop of the Dongfeng intrusive body; b. Hand specimen of granite; c. K-feldspar shows Carlsbad twin texture(+); d. K-feldspar shows stripe structure and plagioclase shows sericite-alteration(+); e. Chlorite altered biotite(+); f. Monazite and apatite coexisting with biotite(+)

Ap—Apatite; Bi—Biotite; Chl—Chlorite; Kf—Feldspar; Mnz—Monazite; Pl—Plagioclase; Qz—Quzrtz; Ser—Sericite

殖层和残坡积层厚度较小,一般在2~4 m左右,山顶部位不足2 m,甚至小于1 m;半风化层厚度不清。

在地表极少部位(河流中)见有未(弱)风化基岩,其岩性为粗中粒(少)斑状黑云母二长花岗岩,灰白色,粗中粒结构和似斑状结构,块状构造(图2b)。斑晶含量约占3%~8%,成分以钾长石为主,石英次之。基质矿物组成主要为钾长石(25%~35%)、斜长石(20%~35%)、石英(22%~30%)和黑云母(5%~10%),副矿物主要有独居石、磷灰石、榍石、锆石等。花岗岩蚀变十分普遍,多见有高岭土化、绿泥石化、钾长石化、绢云母化、硅化等。其中,钾长石化、高岭土化等与矿化关系密切。钾长石多呈半自形板状,具条纹结构,内部常包裹细粒石英、黑云母,斑晶常具有卡式双晶(图2c),基质见有格子双晶发育(图2d);斜长石多呈自形-半自形板状,多见聚片双晶,内部偶见有鳞片状绢云母化(图2d)等蚀变;石英为他形粒状,大者常具碎裂纹及波状消光(图2c~f),部分颗粒被长石侵蚀,具溶蚀港湾结构(图2e~f),另偶见细小(0.2~0.4 mm)等轴状石英呈锯齿状镶嵌集合体产出(图2e),可能为受重结晶作用而成;黑云母呈片状或细片状集合体,部分蚀变形成绿泥石(图2e),显示蚀变残余结构,见与副矿物独居石、磷灰石等共生(图2f)。

东风风化壳离子吸附型稀土矿产于东风岩体内部,原湖南省核工业地质局301队对东风稀土矿普查时实施了钻探工程,见矿厚度一般4.50~12.00 m,最厚达20.9 m,REO品位0.050%~0.248%。在东风岩体内部圈定的多个稀土矿体规模较大,形态较好,矿体均呈层状赋存于花岗岩全风化层中(图3),产状与全风化层产状及地形坡向基本一致,倾角较地形坡角略平缓,其中单个矿体的平均厚度最大可达15 m,一般为4~8 m,矿体平均品位(REO)为0.052%~0.099%。对矿体所采集的多件样品测试显示,Y_2O_3的配分含量最高可达53.8%,平均为40.7%,表明稀土矿的矿化以重稀土元素为主。经资源储量估算,在探矿权范围内获得333+334类稀土(REO)资源量10.87万t,表明东风稀土矿的稀土远景资源量达到大型(湖南省核工业地质局三〇一大队,2018)。

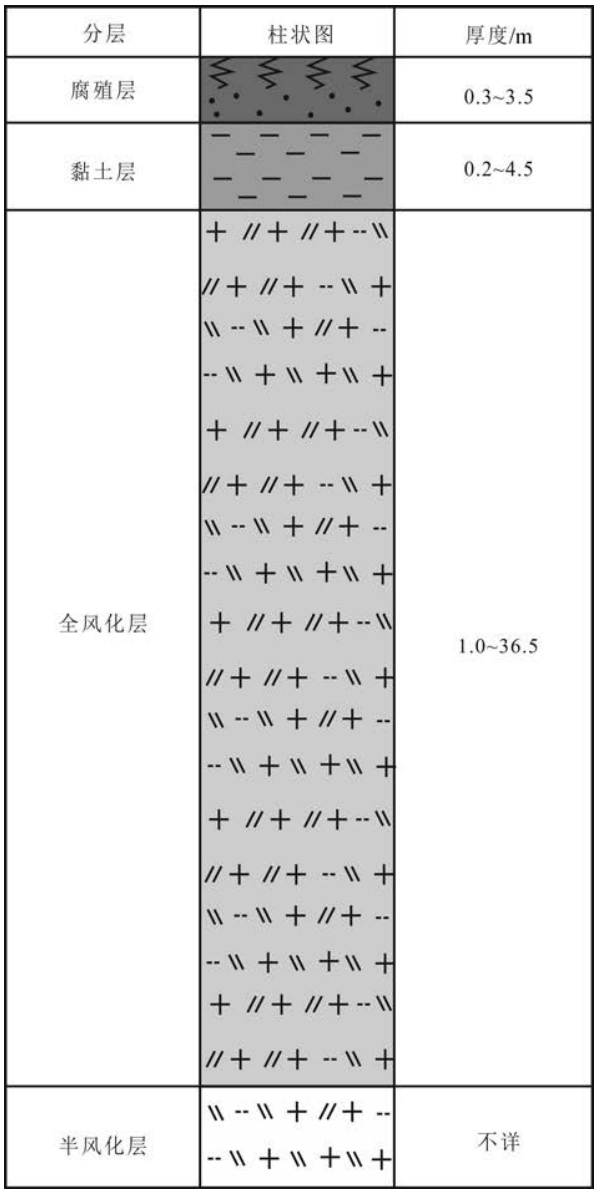

图 3　东风岩体风化壳柱状图

Fig. 3　Crust weathering profile of the Dongfeng pluton

2　样品分析测试

本次分析测试样品的采集位置见图 1b,用于挑选锆石的样品 DF01 和 DF02 采集于新开公路陡坎花岗岩全风化层,其中,样品 DF01 采集于岩体北部边缘,DF02 采集于岩体中部位置;用于主、微量元素分析的样品(MT01~06)为采集于切割较深河沟处的未遭受风化蚀变的新鲜花岗岩。

主、微量元素的分析测试在中国科学院地球化学研究所矿床国家重点实验室完成,主量元素在 Axios(PW4400)型 X 射线荧光光谱仪中完成,测试精度优于 3%;微量元素测试采用 Finnigan MAT 公司生产的 ELEMENT 型高分辨等离子质谱仪完成。

锆石单矿物是在无污染的环境下用人工重砂方法初选(包括手工碎样、水洗、磁选),然后在双目镜下挑选,选出晶形较好、具代表性的锆石用环氧树脂充分固定、抛光,制成样品靶。锆石的 CL 图像和 LA-ICPMS U-Pb 定年在中国科学院地球化学研究所矿床地球化学国家重点实验室完成。

锆石 U-Pb 测试分析仪器为 Perkinelmer 生产的 ELAN DRC-e 型等离子质谱仪,配套 GeoLasPro 193 nm 型准分子激光剥蚀系统,所用束斑直径为 32 μm。原始测试数据用 ICPMSDataCal 软件进行处理(Liu et al., 2008;2010)。普通 Pb 校正方法参照 Andersen(2002),^{206}Pb-^{238}U 加权平均年龄和协和图解由 ISOPLOT 软件获得(Ludwig et al., 2003)。单个数据点误差均为 1σ。

锆石 Hf 同位素分析在中国地质大学(武汉)GPMR 实验室 Neptune 多接收 MC-ICP-MS 仪器上进行。激光剥蚀所用斑束直径为 44 μm。详细仪器条件和数据获取详见 Hu 等(2012)。为了校正 ^{176}Lu 和 ^{176}Yb 对 ^{176}Hf 的干扰,取 $^{176}Lu/^{175}Hf$=0.026 56 和 $^{176}Yb/^{173}Yb$=0.793 81(Blichert et al., 1997; Segal et al., 2003)为定值。采用 $^{173}Yb/^{171}Yb$=1.130 17 和 $^{179}Hf/^{177}Hf$=0.7325 分别对 Yb 同位素和 Hf 同位素进行指数归一化质量歧视校正(Segal et al., 2003)。锆石标样 GJ-1 的 $^{176}Hf/^{177}Hf$ 标准值为 0.282 013±0.000 019(Hu et al., 2012)。

3　锆石 U-Pb 年龄及 Hf 同位素特征

3.1　锆石 U-Pb 年龄

东风岩体 2 件花岗岩样品 DF01 与 DF02 中的锆石均呈浅黄色至无色,绝大部分锆石晶型为自形-半自形;锆石为柱状,大小 150~400 μm,长轴与短轴之比多介于 2~4,锆石的阴极发光图像均显示出岩浆锆石所特有的韵律环带(Hoskin et al., 2003; 吴元保等, 2004)(图 4)。本次选择了环带清晰、无裂纹、锆石表面清晰的位置对其进行分析。

对样品 DF01 进行了共计 21 个点的测试(图 4,表 1),这些锆石的普通铅含量总体很低,其中,07、05 和 11 号测试点的年龄值明显高于其他测点,对应

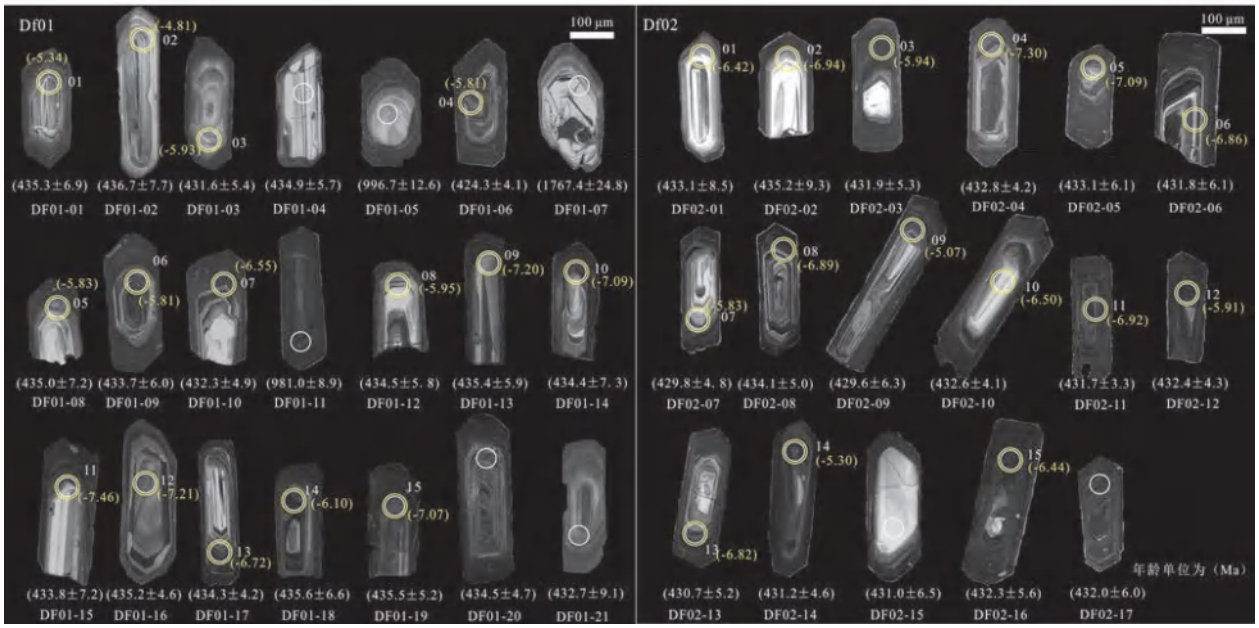

图4 东风花岗岩体的锆石阴极发光图像（白圈为U-Pb测试位置，黄圈为Hf同位素测试部位）

Fig. 4 CL images of zircon from the Dongfeng monzogranite (white and yellow circles indicating the laser spot of U-Pb dating and Hf isotope analysis, respectively)

的$^{206}Pb/^{238}U$年龄值分别为（1767.4±24.8）Ma、（996.7±12.6）Ma、（981.0±8.9）Ma，这些年龄值明显偏高的锆石为继承锆石。其余18个测点在U-Pb年龄曲线图（图5a）中的$^{206}Pb/^{238}U$年龄值相接近，其加权平均值为（433.5±2.6）Ma（MSWD=0.29）（图5b）。对样品DF02完成的17个点的分析测试（图4，表1）结果表明，锆石中的普通铅含量很低，这17个点的$^{206}Pb/^{238}U$年龄相近（图5c），其加权平均值为（432.0±2.5）Ma（MSWD=0.06）（图5d）。

3.2 Hf同位素特征

对样品DF01和DF02锆石U-Pb测年的打点部位分别进行了15个点的Hf同位素测试（图4）。

本次分析的2件样品共计30颗锆石的$^{176}Yb/^{177}Hf$和$^{176}Lu/^{177}Hf$比值范围分别为0.007 212~0.041 416和0.000 234~0.001 628（表2），$^{176}Lu/^{177}Hf$比值均小于0.002，表明这些锆石在形成以后，仅具有较少放射成因Hf的积累，因而可以用初始$^{176}Hf/^{177}Hf$比值来代表锆石形成时的$^{176}Hf/^{177}Hf$比值（吴福元等，2007）。考虑到2件样品的$f_{Lu/Hf}$的平均值为−0.97，明显小于铁镁质地壳的$f_{Lu/Hf}$（−0.34，Ameilin et al., 1999）和硅铝质地壳的$f_{Lu/Hf}$（−0.72，Vervoort et al., 1996），因此，其二阶段模式年龄更能反映其源区物质从亏损地幔抽取的时间（或其源区物质在地壳的平均存留年龄）。

其中，样品DF01共15颗锆石的$(^{176}Hf/^{177}Hf)_i$的变化范围在0.282 300~0.282 374（表2，图6b），Hf同位素成分比较均一，加权平均值0.282 332，对应的$\varepsilon_{Hf}(t)$变化范围为−4.74~−7.45，平均值−6.32（图6a、c）；地壳模式年龄（T_{DM2}）变化范围1714~1882 Ma，加权平均值1811 Ma（图6b）。

样品DF02共15颗锆石的$(^{176}Hf/^{177}Hf)_i$的变化范围0.282 305~0.282 369（表2，图6b），Hf同位素成分比较均一，加权平均值0.282 333，对应的$\varepsilon_{Hf}(t)$变化范围在−5.12~−7.28，平均值−4.42（图6a、c），地壳模式年龄（T_{DM2}）变化范围1733~1871 Ma，加权平均值1816 Ma（图6d）。

4 岩石地球化学特征

东风花岗岩体的主、微量元素分析结果见表3，结果显示花岗岩$w(SiO_2)$为68.48%~73.39%，平均70.34，稍低于中国花岗岩的平均含量（71.63%）（黎彤等，1998），从TAS图（图7a）可以看出，所有点均落入花岗岩与花岗闪长岩区域；$w(Al_2O_3)$较高，变化于

表 1　东风岩体花岗岩LA-ICP-MS的锆石U-Pb分析结果

Tabe 1　Zircon U-Pb dating results of the Dongfeng granitic pluton

样品点号	w(B)/10^{-6}		Th/U	同位素比值						年龄/Ma					
	^{232}Th	^{238}U		^{207}Pb/^{206}Pb	±1σ	^{207}Pb/^{235}U	±1σ	^{206}Pb/^{238}U	±1σ	^{207}Pb/^{206}Pb	±1σ	^{207}Pb/^{235}U	±1σ	^{206}Pb/^{238}U	±1σ
DF01-01	81	183	0.44	0.05447	0.00184	0.52602	0.01929	0.06986	0.00115	390.8	71.3	429.2	12.8	435.3	6.9
DF01-02	93	197	0.47	0.05456	0.00123	0.52645	0.01412	0.07008	0.00128	394.5	50.0	429.5	9.4	436.7	7.7
DF01-03	64	123	0.51	0.05394	0.00139	0.50964	0.01218	0.06924	0.00090	368.6	62.0	418.2	8.2	431.6	5.4
DF01-04	136	147	0.92	0.05316	0.00149	0.50856	0.01323	0.06979	0.00095	344.5	32.4	417.5	8.9	434.9	5.7
DF01-05	65	121	0.54	0.06619	0.00136	1.52293	0.03473	0.16720	0.00228	813.0	42.6	939.7	14.0	996.7	12.6
DF01-06	240	857	0.28	0.05080	0.00088	0.47728	0.00902	0.06804	0.00069	231.6	71.3	396.2	6.2	424.3	4.1
DF01-07	41	67	0.61	0.15644	0.00265	6.79408	0.14291	0.31543	0.00505	2417.6	28.7	2085	18.6	1767.4	24.8
DF01-08	95	141	0.67	0.05083	0.00198	0.48925	0.02044	0.06980	0.00119	231.6	90.7	404.4	13.9	435.0	7.2
DF01-09	229	939	0.24	0.04822	0.00090	0.45978	0.00897	0.06959	0.00099	109.4	44.4	384.1	6.2	433.7	6.0
DF01-10	172	575	0.30	0.04854	0.00090	0.46535	0.00969	0.06935	0.00082	124.2	42.6	388.0	6.7	432.3	4.9
DF01-11	188	432	0.43	0.06051	0.00106	1.37727	0.02644	0.16436	0.00160	620.4	37.8	879.3	11.3	981.0	8.9
DF01-12	67	135	0.49	0.04964	0.00206	0.47613	0.01956	0.06973	0.00096	189.0	96.3	395.4	13.5	434.5	5.8
DF01-13	137	463	0.30	0.04915	0.00122	0.47390	0.01284	0.06987	0.00097	153.8	59.3	393.9	8.8	435.4	5.9
DF01-14	109	453	0.24	0.05223	0.00133	0.50371	0.01450	0.06971	0.00121	294.5	59.3	414.2	9.8	434.4	7.3
DF01-15	63	136	0.46	0.05134	0.00195	0.49553	0.02045	0.06962	0.00120	257.5	88.9	408.7	13.9	433.8	7.2
DF01-16	79	304	0.26	0.05028	0.00127	0.48593	0.01255	0.06984	0.00077	209.3	57.4	402.1	8.6	435.2	4.6
DF01-17	141	277	0.51	0.05207	0.00136	0.50188	0.01297	0.06970	0.00070	287.1	59.3	413.0	8.8	434.3	4.2
DF01-18	143	434	0.33	0.05269	0.00138	0.51205	0.01575	0.06991	0.00110	322.3	59.3	419.8	10.6	435.6	6.6
DF01-19	115	376	0.30	0.05447	0.00121	0.52477	0.01174	0.06990	0.00086	390.8	50.0	428.3	7.8	435.5	5.2
DF01-20	175	430	0.41	0.05585	0.00119	0.54087	0.01251	0.06972	0.00078	455.6	48.1	439.0	8.2	434.5	4.7
DF01-21	93	279	0.33	0.05697	0.00164	0.55239	0.01754	0.07007	0.00114	494.5	51.8	438.8	9.3	432.7	9.1
DF02-01	19	94	0.60	0.05710	0.00136	0.54054	0.01411	0.06943	0.00150	427.8	57.4	431.3	9.9	433.1	8.5
DF02-02	16	68	0.50	0.05535	0.00144	0.52923	0.01496	0.06949	0.00141	509.3	31.5	447.2	7.8	435.2	9.3
DF02-03	109	291	0.24	0.05746	0.00083	0.55344	0.01191	0.06984	0.00155	387.1	42.6	427.0	7.2	431.9	5.3
DF02-04	25	95	0.39	0.05439	0.00102	0.52273	0.01085	0.06930	0.00088	344.5	37.0	419.4	5.6	432.8	4.2
DF02-05	49	159	0.30	0.05316	0.00088	0.51143	0.00841	0.06944	0.00069	405.6	38.9	430.3	6.9	433.1	6.1
DF02-06	51	158	0.29	0.05481	0.00094	0.52770	0.01032	0.06949	0.00101	298.2	48.1	410.9	7.4	431.8	6.1
DF02-07	24	92	0.40	0.05228	0.00109	0.49875	0.01096	0.06928	0.00101	376.0	77.8	422.3	12.1	429.8	4.8
DF02-08	33	115	0.34	0.05413	0.00186	0.51569	0.01808	0.06894	0.00080	316.7	35.2	417.7	6.2	434.1	5.0
DF02-09	65	188	0.26	0.05269	0.00084	0.50891	0.00926	0.06966	0.00082	435.2	134.2	432.3	16.8	429.6	6.3
DF02-10	48	259	0.68	0.05560	0.00252	0.53067	0.02528	0.06891	0.00105	542.6	33.3	452.2	5.9	432.6	4.1
DF02-11	79	211	0.26	0.05834	0.00085	0.56102	0.00906	0.06940	0.00067	588.9	29.6	457.5	5.4	431.7	3.3
DF02-12	123	277	0.20	0.05934	0.00082	0.56926	0.00836	0.06926	0.00055	388.9	37.0	424.9	6.1	432.4	4.3
DF02-13	32	102	0.30	0.05423	0.00088	0.51970	0.00913	0.06938	0.00072	390.8	61.1	423.2	9.7	430.7	5.2
DF02-14	16	83	0.60	0.05447	0.00147	0.51704	0.01455	0.06910	0.00086	416.7	54.6	428.1	9.0	431.2	4.6
DF02-15	19	97	0.68	0.05515	0.00144	0.52449	0.01352	0.06918	0.00077	388.9	40.7	425.0	8.1	431.0	6.5
DF02-16	59	182	0.27	0.05423	0.00097	0.51973	0.01211	0.06915	0.00107	300.1	48.1	410.5	7.4	432.3	5.6
DF02-17	31	102	0.31	0.05215	0.00108	0.49821	0.01096	0.06936	0.00093	300 .0	48.0	410 .0	7.0	432 .0	6.0

12.82%~15.09%,平均 14.15%,A/CNK 值为 1.12~1.43,A/NK 值 1.42~1.88,在 A/CNK-A/NK 图解(图 7b)中,均落入过铝质区域;w(K_2O + Na_2O)为 5.94%~8.42%,平均 7.03%;K_2O/Na_2O 值变化于 1.26~2.36,平均 1.79,表现为富 K 的特征;在 K_2O-SiO_2 图解(图 7c)中,样品均落在高钾钙碱性系列与钾玄岩系列。

东风岩体花岗岩具有与万洋山岩体、彭公庙岩体二长花岗岩相同的微量元素和稀土元素基本一致的特征(图 8)。东风岩体花岗岩的稀土元素总体含量中等(表 3),∑REE 为(140~186)×10^{-6},∑LREE/

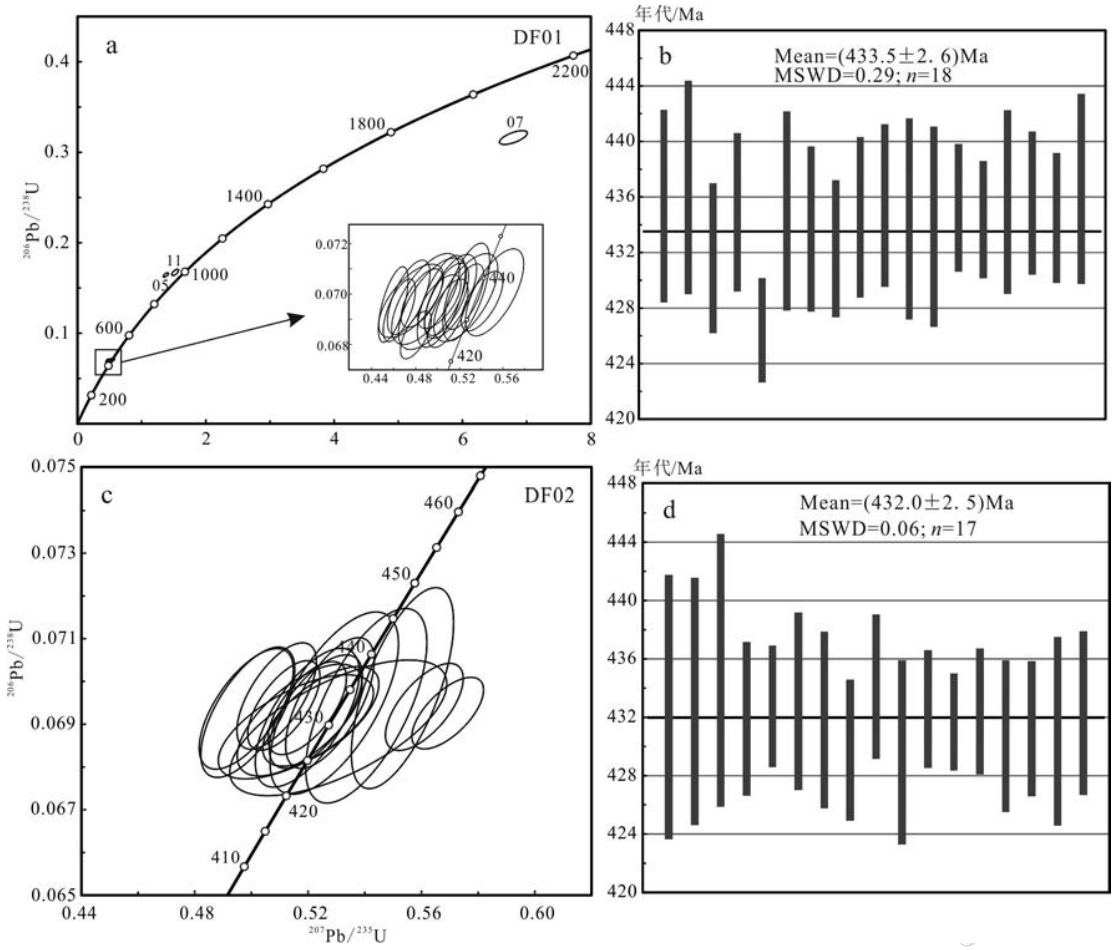

图5 东风花岗岩体的锆石U-Pb谐和曲线图(a,c)和加权平均年龄图(b,d)

Fig. 5 LA-ICPMS U-Pb Concordia age plots (a, c) and weighted average diagrams for zircons (b, d) from the Dongfeng monzogranite

∑HREE值为1.72~2.22,表明东风岩体花岗岩轻、重稀土元素分馏较明显,δEu值为0.41~0.75,平均值0.56。在稀土元素配分模式图(图8a)中,东风岩体花岗岩显示为一明显右倾的曲线,配分曲线具有较明显的Eu负异常,同时,LREE一侧相对较陡(分馏明显)、重稀土元素部分较为平坦(分馏不明显)的特征。HREE的相对亏损可能与锆石、磷灰石、独居石等的分离结晶有关,而Eu负异常明显则反映出岩浆结晶作用过程中斜长石、钾长石的分离结晶作用较明显。相较于花岗岩基岩,风化层花岗岩稀土矿体(湖南省核工业地质局301队,2018)中的稀土元素(除Ce外)均有明显富集,尤其是重稀土元素富集更加明显(图8b),Eu负异常也更加明显,配分曲线整体相对较平坦。

从以原始地幔对岩体微量元素进行标准化的微量元素蛛网图(图8c)中可以看出,东风岩体花岗岩不相容元素Rb、(Th+U)、Nd、(Zr+Hf)富集,而Ba、Nb、Sr、P、Ti明显亏损,显示出壳源花岗岩的特征(Chappell et al., 1992; Bea et al., 2011; Dong et al., 2013)。微量元素Ba、Sr亏损,说明岩石中存在有斜长石的熔融残留相或结晶分离相(Patino et al. 1991; 1995),P、Ti亏损可能与磷灰石、钛铁矿的分离结晶有关,而Nb可能由于富集到含钛的黑云母中而出现亏损(李昌年,1992),同时,Nb、Ta发生了较明显分馏,显示Nb相对亏损而Ta相对富集,也暗示花岗岩具有壳源花岗岩特征(陈小明等,2002)。

5 讨 论

5.1 东风岩体的侵位年龄

以往关于东风岩体的研究较少,仅在湖南省地质调查院(1972;2005)完成的1∶20万永兴幅区域地

表 2　东风花岗岩体的锆石 Hf 同位素组成

Table 2　Zircon Hf isotopic data of the Dongfeng granitic pluton

样品点号	年龄/Ma	$^{176}Yb/^{177}Hf$	$^{176}Lu/^{177}Hf$	$^{176}Hf/^{177}Hf$	2σ	$\varepsilon_{Hf}(0)$	$\varepsilon_{Hf}(t)$	T_{DM1}/Ma	T_{DM2}/Ma	$f_{Lu/Hf}$
DF01-01	435.3	0.024900	0.001015	0.282360	0.000016	−14.58	−5.30	1261	1748	−0.97
DF01-02	436.7	0.023967	0.000942	0.282374	0.000014	−14.08	−4.74	1238	1714	−0.97
DF01-03	431.6	0.023993	0.000972	0.282343	0.000016	−15.19	−5.97	1283	1788	−0.97
DF01-04	424.3	0.023736	0.000958	0.282346	0.000019	−15.07	−6.01	1278	1784	−0.97
DF01-05	435.0	0.021173	0.000863	0.282345	0.000019	−15.11	−5.79	1277	1779	−0.97
DF01-06	433.7	0.025003	0.000987	0.282346	0.000025	−15.06	−5.81	1279	1779	−0.97
DF01-07	432.3	0.029973	0.001036	0.282326	0.000030	−15.78	−6.57	1309	1826	−0.97
DF01-08	434.5	0.028634	0.001081	0.282343	0.000039	−15.17	−5.93	1286	1787	−0.97
DF01-09	435.4	0.037054	0.001417	0.282310	0.000038	−16.32	−7.16	1344	1865	−0.96
DF01-10	434.4	0.038118	0.001556	0.282314	0.000018	−16.18	−7.07	1343	1859	−0.95
DF01-11	433.8	0.027766	0.001031	0.282300	0.000025	−16.70	−7.45	1345	1882	−0.97
DF01-12	435.2	0.007212	0.000234	0.282301	0.000018	−16.67	−7.17	1316	1866	−0.99
DF01-13	434.3	0.034256	0.001364	0.282323	0.000024	−15.86	−6.70	1323	1836	−0.96
DF01-14	435.6	0.024174	0.000968	0.282338	0.000023	−15.35	−6.05	1290	1796	−0.97
DF01-15	435.5	0.025263	0.001001	0.282311	0.000021	−16.31	−7.02	1329	1857	−0.97
DF02-01	433.1	0.028238	0.001108	0.282331	0.000025	−15.60	−6.40	1304	1815	−0.97
DF02-02	435.2	0.028170	0.001098	0.282316	0.000018	−16.12	−6.87	1324	1847	−0.97
DF02-03	431.9	0.041416	0.001648	0.282349	0.000013	−14.97	−5.94	1298	1786	−0.95
DF02-04	432.8	0.026685	0.001039	0.282305	0.000025	−16.50	−7.28	1337	1871	−0.97
DF02-05	433.1	0.019290	0.000650	0.282308	0.000015	−16.41	−7.07	1320	1858	−0.98
DF02-06	431.8	0.028671	0.001122	0.282318	0.000016	−16.04	−6.86	1322	1844	−0.97
DF02-07	429.8	0.028706	0.001119	0.282347	0.000025	−15.01	−5.88	1281	1780	−0.97
DF02-08	434.1	0.010141	0.000343	0.282311	0.000015	−16.29	−6.85	1305	1845	−0.99
DF02-09	429.6	0.027864	0.001092	0.282369	0.000013	−14.26	−5.12	1251	1733	−0.97
DF02-10	432.6	0.029583	0.001157	0.282329	0.000032	−15.67	−6.49	1309	1821	−0.97
DF02-11	431.7	0.027559	0.001115	0.282317	0.000020	−16.10	−6.93	1324	1848	−0.97
DF02-12	432.4	0.019608	0.000781	0.282343	0.000017	−15.19	−5.90	1277	1784	−0.98
DF02-13	430.7	0.021711	0.000836	0.282317	0.000075	−16.08	−6.85	1314	1842	−0.97
DF02-14	431.2	0.037607	0.001520	0.282366	0.000029	−14.37	−5.32	1269	1746	−0.95
DF02-15	432.3	0.023397	0.000918	0.282329	0.000018	−15.68	−6.44	1301	1818	−0.97

注：$\varepsilon_{Hf}(t)=10\ 000\times\{[(^{176}Hf/^{177}Hf)_S-(^{176}Lu/^{177}Hf)_S\times(e^{\lambda t}-1)]/[(^{176}Hf/^{177}Hf)_{CHUR,0}-(^{176}Lu/^{177}Hf)_{CHUR}\times(e^{\lambda t}-1)]-1\}$；$T_{DM1}=1/\lambda\times\ln\{1+[(^{176}Hf/^{177}Hf)_S-(^{176}Hf/^{177}Hf)_{DM}]/[(^{176}Hf/^{177}Hf)_S-(^{176}Hf/^{177}Hf)_{DM}]\}$；$T_{DM2}=T_{DM1}-(T_{DM1}-t)\times[(f_{cc}-f_s)/(f_{cc}-f_{DM})]$；$f_{Lu/Hf}=(^{176}Lu/^{177}Hf)_S/(^{176}Lu/^{177}Hf)_{CHUR}-1$，其中，$\lambda=1.867\times10^{-11}$/a(Soderlund et al., 2004)；$(^{176}Lu/^{177}Hf)_S$ 和 $(^{176}Hf/^{177}Hf)_S$ 为样品同位素组成；$(^{176}Lu/^{177}Hf)_{CHUR}=0.0332$ and $(^{176}Hf/^{177}Hf)_{CHUR,0}=0.282\ 772$ (Blichert-Toft et al., 1997)；$(^{176}Lu/^{177}Hf)_{DM}=0.0384$，$(^{176}Hf/^{177}Hf)_{DM}=0.283\ 25$(Griffin et al., 2000)；$(^{176}Lu/^{177}Hf)_{mean\ crust}=0.015$；$f_{cc}=[(^{176}Lu/^{177}Hf)_{mean\ crust}/(^{176}Lu/^{177}Hf)_{CHUR}]-1$；$f_s=f_{Lu/Hf}$；$f_{DM}=[(^{176}Lu/^{177}Hf)_{DM}/(^{176}Lu/^{177}Hf)_{CHUR}]-1$；$t$=锆石结晶年龄。

质矿产调查与1∶25万衡阳幅区域地质矿产调查报告中提到将其形成年龄定为加里东期，但并未有准确的年代学数据作为支撑。

本次对东风岩体采集的2件粗中粒黑云母二长花岗岩锆石样品（DF01、DF02）的LA-ICP-MS U-Pb定年结果分别为（433.5±2.6）Ma和（432.0±2.5）Ma，两者在误差范围内非常一致，可以代表东风岩体的形成年龄。同时，2件样品的年龄与沈渭洲等（2008）利用LA-ICP-MS U-Pb定年获得的万洋山岩体黑云母二长花岗岩形成年龄（433.8±2.2）Ma一致，与张文兰等（2011）获得彭公庙岩体两件中粗粒黑云母花岗岩锆石LA-ICP-MS U-Pb的定年结果（435.3±2.7）Ma和（436.2±3.1）Ma在误差范围内也相同。东风岩体侵位年龄433 Ma左右，根据前人对华南加里东花岗岩早晚期岩浆活动的侵位时限划分标准（舒良树，2006；张芳荣等，2009），东风岩体的形成年龄对应于加里东晚期。这与野外所观察到岩体与奥陶系天马山组呈侵入接触关系、外接触带见有明显的角岩化

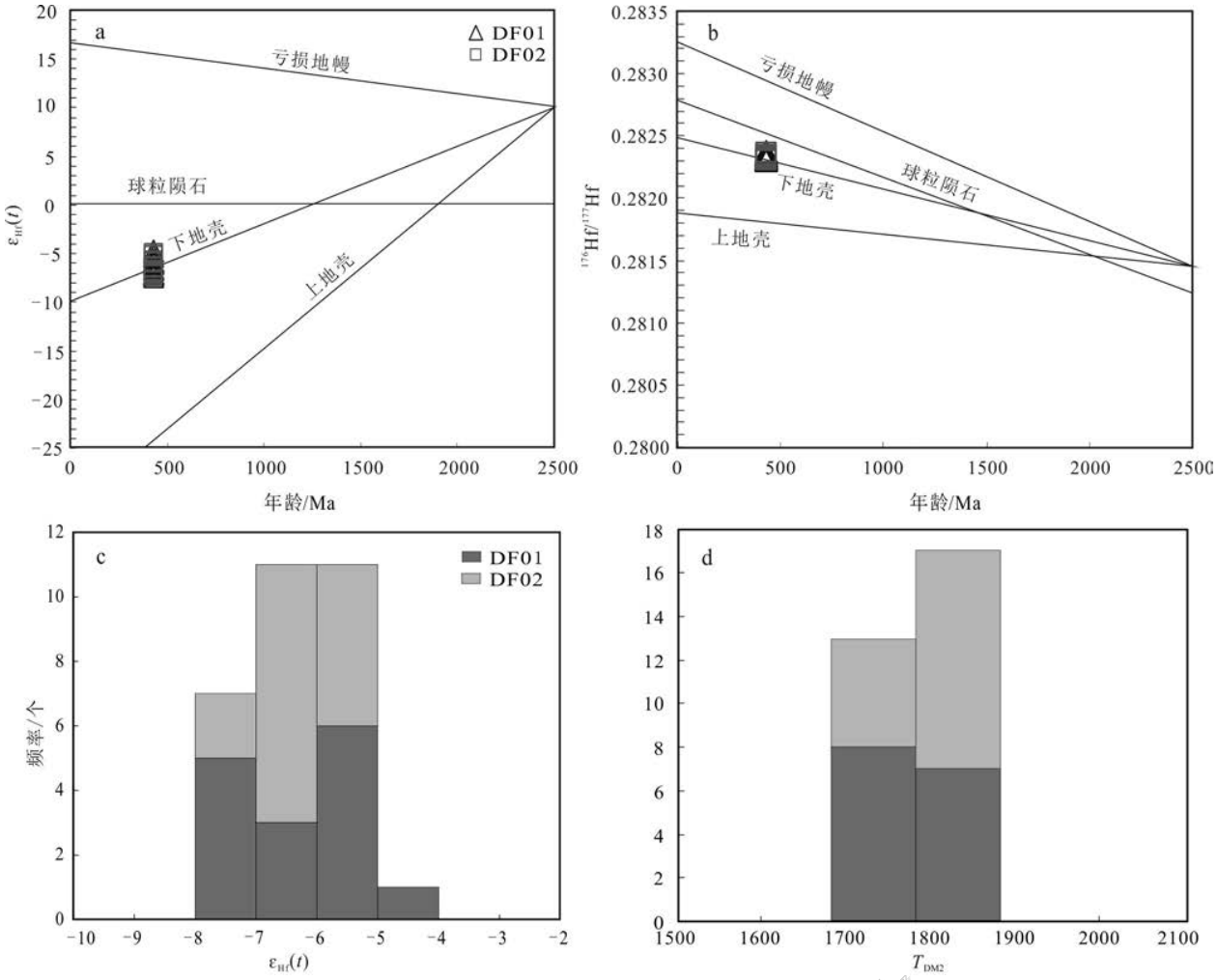

图6 东风岩体花岗岩锆石 $\varepsilon_{Hf}(t)$值图解(a)、$^{176}Hf/^{177}Hf$比值U-Pb年龄图解(b)、锆石 $\varepsilon_{Hf}(t)$值图解(c)和Hf同位素地壳模式年龄(T_{DM2})柱状图(d)

Fig. 6 $\varepsilon_{Hf}(t)$ ages diagram(a), $^{176}Hf/^{177}Hf$ U-Pb ages diagram(b), histogram of zircon $\varepsilon_{Hf}(t)$ ages(c) and histogram of zircon Hf-isotope crust model age (T_{DM2})(d) of the Dongfeng granitic pluton

等蚀变的地质现象相符。此外,东风岩体花岗岩与彭公庙岩体、万洋山岩体二长花岗岩具有相同的微量元素特征(图8),暗示这3个岩体的加里东期花岗岩有可能为起源于同一岩浆房的岩浆同时侵位形成,岩体在深部有可能相连。

5.2 岩体的成因类型及地质背景

东风花岗岩体黑云母二长花岗岩具有高钾钙碱性、强过铝质特征(图7b、c),铝饱和指数A/CNK值均大于1.1(1.12~1.43),经过标准矿物计算得到的刚玉分子含量为1.87%~4.82%;$10^4Ga/Al$值介于2.13~2.64,平均值(2.44)小于A型花岗岩的最低值(2.6)(Whalen et al., 1987),在岩石类型判别图解(图9a)中,测点均落入I&S型花岗岩区域或附近,在$w(K_2O)$-$w(Na_2O)$图解(图9b)中,样品落点较分散,但除个别点落入A型花岗岩区域内,大多数的点均落入S型花岗岩区域内或附近,这些特征均表明东风岩体花岗岩的岩石类型为S型花岗岩。

在稀土元素配分图(图8a)中,东风岩体花岗岩稀土元素显示一条明显右倾的曲线,其轻、重稀土元素比值LREE/HREE较高(5.32~6.86)。岩体具有较高的Yb含量、大离子亲石元素(LILE)含量以及相对较低的HREE、Sr和高场强元素(HFSE)含量,以及计算得到的分异系数(Di)为80.38~86.95(表3),这些特征均显示东风岩体花岗岩岩浆可能经历了一定程度的结晶分异作用,但其Nb/Ta值介于6.56~10.90(平均9.26),Zr/Hf值介于34.49~38.45(平均35.04),

表 3　东风岩体花岗岩样品的主量元素(w(B)/%)和微量元素(w(B)/10^{-6})分析结果

Table 3　Major and trace element compositions of the Dongfeng granitic pluton (w(B)/%) and trace elements w(B)/10^{-6}

组分	MT01	MT02	MT03	MT04	MT05	MT06	组分	MT01	MT02	MT03	MT04	MT05	MT06
SiO_2	68.48	71.42	73.39	70.18	69.64	68.91	Ce	75.9	77	56.4	69.2	79	54.6
TiO_2	0.55	0.48	0.34	0.43	0.52	0.45	Pr	8.55	7.5	6.87	7.08	10.4	6.45
Al_2O_3	14.93	13.01	12.82	14.35	14.71	15.09	Nd	33.3	29.2	26.2	26.0	39.2	24.9
TFe_2O_3	4.63	4.19	3.03	3.84	4.41	3.82	Sm	7.50	6.71	5.76	6.26	8.17	5.66
MnO	0.11	0.11	0.08	0.11	0.10	0.10	Eu	1.34	0.95	1.09	1.15	1.38	1.41
MgO	1.00	1.12	0.69	0.85	1.05	0.90	Gd	7.32	7.53	5.72	6.28	7.97	5.76
CaO	1.48	1.60	1.13	2.00	1.34	1.57	Tb	1.12	1.19	0.886	1.07	1.16	0.908
Na_2O	2.45	2.48	2.13	3.06	2.47	2.70	Dy	6.97	7.42	5.16	6.26	7.17	5.12
K_2O	5.19	3.62	5.02	3.86	3.47	5.72	Ho	1.37	1.55	0.96	1.20	1.30	1.01
P_2O_5	0.16	0.12	0.09	0.10	0.14	0.11	Er	3.95	4.8	3.11	3.67	3.96	3.17
SO_3	0.02	0.01	0.01	0.01	0.01	0.02	Tm	0.55	0.66	0.47	0.52	0.53	0.44
SrO	0.02	0.02	0.01	0.01	0.02	0.01	Yb	4.02	4.74	3.23	3.83	3.81	2.81
烧失量	1.26	1.46	0.85	0.84	1.85	0.61	Lu	0.53	0.68	0.43	0.51	0.48	0.39
总和	100.28	99.64	99.59	99.64	99.73	100.01	Hf	4.76	6.06	4.36	4.81	6.08	5.27
K_2O+Na_2O	7.64	6.10	7.15	6.92	5.94	8.42	Ta	1.33	1.41	0.91	1.82	1.57	0.95
K_2O/Na_2O	2.12	1.46	2.36	1.26	1.40	2.12	W	1.43	2.31	9.83	4.9	2.98	4.95
A/NCK	1.21	1.19	1.16	1.12	1.43	1.12	Pb	41.88	33.82	40.12	33.71	29.51	41.66
A/NK	1.55	1.62	1.43	1.56	1.88	1.42	Th	18.5	17.9	15.3	17.8	21.6	12.9
σ	2.27	1.3	1.67	1.75	1.31	2.72	U	3.60	4.68	2.71	3.48	4.24	3.95
Di	81.87	81.58	86.95	81.56	80.38	83.72	10^4Ga/Al	2.56	2.64	2.17	2.63	2.54	2.13
V	55.3	53.1	39.1	48.8	55.2	50	Zr/Hf	38.45	34.49	34.86	32.64	34.70	35.10
Cr	29.1	48.3	26.6	41.2	27.7	29.9	Nb/Ta	10.71	9.40	9.53	6.56	8.48	10.90
Ga	20.2	18.2	14.7	20	19.8	17	Th/U	5.14	3.82	5.65	5.11	5.09	3.27
Rb	212	177	188	236	171	212	∑REE	241.61	233.63	184.17	210.53	262.43	189.63
Sr	101	105	89.1	90.5	99.1	128	LREE	160.49	151.96	125.12	138.39	180.85	120.02
Y	55.3	53.1	39.1	48.8	55.2	50.0	HREE	81.13	81.68	59.05	72.14	81.58	69.61
Zr	183	209	152	157	211	185	L/H	1.98	1.86	2.12	1.92	2.22	1.72
Nb	14.21	13.22	8.70	11.95	13.29	10.39	$(La/Yb)_N$	6.05	4.63	6.40	5.38	8.04	6.89
Sn	6.98	6.35	5.22	14.00	3.22	4.98	Y/∑REE	0.23	0.23	0.21	0.23	0.21	0.26
Cs	11.80	11.30	8.52	30.50	11.50	8.27	δEu	0.54	0.41	0.57	0.55	0.52	0.75
Ba	731	455	719	298	438	917	δCe	1.06	1.21	0.95	1.16	0.89	0.98
La	33.9	30.6	28.8	28.7	42.7	27.0	TZr/°C	808.8	824.9	795.7	789.5	840.3	801.5

注:比值单位为1。

显示其远没有达到高分异花岗岩(Nb/Ta < 5, Zr/Hf < 26, Bau, 1996; Ballouard et al., 2016; 吴福元等, 2017)的程度。

从微量元素进行标准化的微量元素蛛网图(图8c)可以看出,样品均具有明显的Rb、(Th+U)、Nd、(Zr+Hf)富集,而Ba、Nb、Sr、P、Ti亏损,表明东风岩体花岗岩具有地壳物质熔融产物的特征(Chappell et al., 1992;凤永刚等, 2008;Bea et al., 2011;Dong et al., 2013)。

Hf同位素示踪研究已经广泛地应用于一些重要地球化学储库(如亏损地幔、球粒陨石和地壳等)的源区判别(吴福元等,2007)。东风岩体两件花岗岩样品单颗粒锆石的Hf同位素组成都比较均一,具有相似的$\varepsilon_{Hf}(t)$值变化范围(集中于−11~−5,表2,图6c),且Hf同位素二阶段模式年龄非常集中(变化于1.71~1.88 Ga,表3,图6d)。Hf同位素$\varepsilon_{Hf}(t) < 0$表明岩石为古老地壳部分熔融而形成(Vervoort et al., 1996; Griffin et al., 2002; 2006),东风岩体花岗岩$\varepsilon_{Hf}(t) < 0$,且在$\varepsilon_{Hf}(t)$-t图解(图6a)和$^{176}Hf/^{177}Hf$-t图解(图6b)中,样品点均集中分布于亏损地幔线及球粒

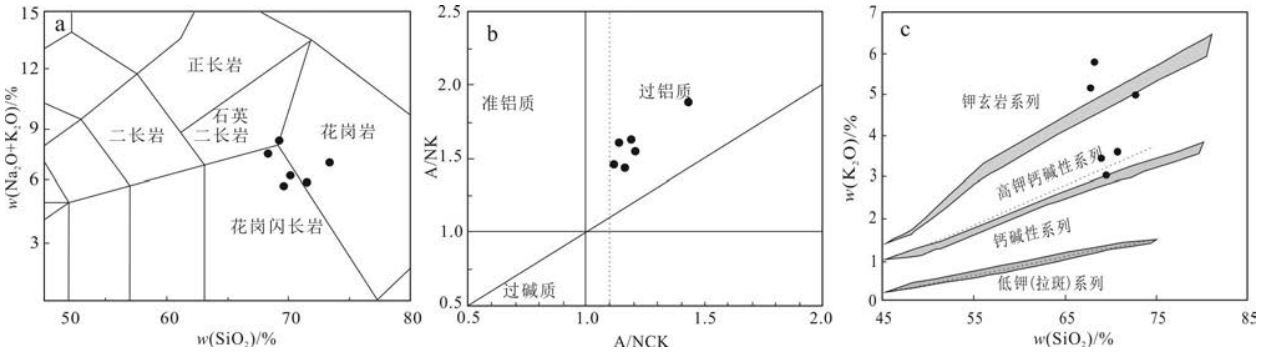

图7 东风岩体花岗岩TAS图解(a, 底图据Le Bas, 1986)、ANK-ACNK图解(b, 底图据Rollinson, 1993)和$w(K_2O)$-$w(SiO_2)$图解(c,底图据Maniar et al., 1989)

Fig. 7 TAS diagram (a, base map after Le Bas et al., 1986), ANK-ACNK diagram (b, base map after Rollinson, 1993) and $w(K_2O)$-$w(SiO_2)$ diagram (c, base map after Maniar et al., 1989) of the Dongfeng monzogranite

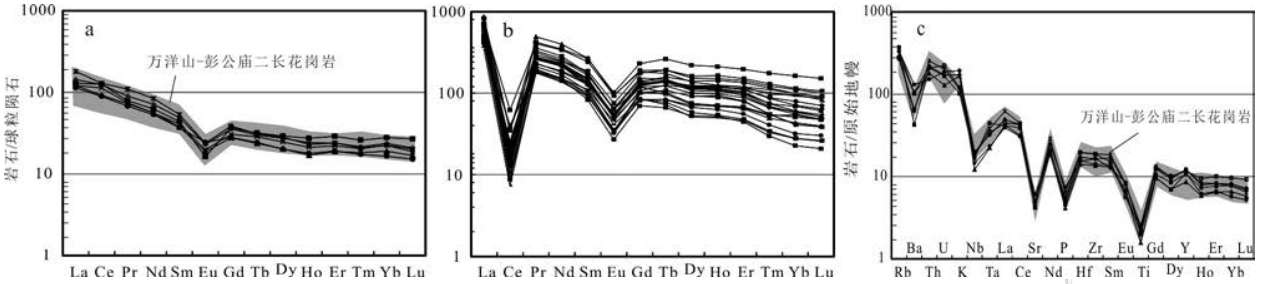

图8 东风岩体花岗岩基岩(a)、风化层(b)稀土元素球粒陨石标准化图和东风岩体花岗岩基岩微量元素原始地幔标准化蛛网图(c)(标准化值据Boynton, 1984; Sun et al., 1989)

万洋山岩体、彭公庙岩体二长花岗岩数据来源自柏道远等,2006;伍光英等,2008;陈迪等,2016;风化层数据源自湖南省核工业地质局301队,2018

Fig. 8 Chondrite-normalized REE patterns for the Dongfeng monzogranite (a) and REE ore body (b), and primitive mantle-normalized trace element spider diagram for the Dongfeng monzogranite (c) (chondrite and mantle values after Boynton, 1984; Sun et al., 1989)

Wanyangshan and Penggongmiao data are from Bai et al., 2006; Wu et al., 2008; Chen et al., 2016; REE values in Ore body from 301 Brigade of Hunan Nuclear Geological Bureau, 2018

陨石演化线之下(Wu et al., 2006;吴福元等,2007),由此可推断东风岩体花岗岩为古老地壳物质部分熔融的产物。二阶段模式年龄介于1714~1882 Ma,样品DF01的继承锆石(点07)的形成年龄也在此范围内,与前人统计得到的华夏板块Hf同位素二阶段模式年龄(Xu et al., 2007; Yu et al., 2010; Zhao et al., 2013)一致,而明显区别于扬子地块(Liu et al., 2008; Zhao et al., 2013)。

综上所述,东风岩体的微量元素特征、锆石Hf同位素特征以及继承锆石的形成年龄均表明东风岩体成岩物质来源于华夏地块古老地壳物质的部分熔融。尽管岩浆结晶锆石没有显著幔源特征的Hf同位素记录,但是计算显示东风岩体花岗岩具有较高的"锆石饱和温度"(Watson et al., 1983)(789.5~824.9℃,平均810℃,表3),暗示地幔岩浆很可能为花岗岩的形成提供了热源(王涛等, 2013; 任飞等, 2021)。

前人对华南地区加里东期构造环境的研究表明,460~440 Ma期间扬子地块和华夏地块发生陆内俯冲和汇聚挤压,造山带发生快速褶皱缩短和逆冲加厚(舒良树等,2008)而形成岩石圈山根。其后岩石圈地幔与软流圈之间对流,引起岩石圈拆沉和上地幔的隆起,导致幔源岩浆的产生和底侵,引起下地壳的部分熔融,同时后碰撞构造环境下深大断裂(本区为茶陵—郴州大断裂,图1a)伸展松弛促使中下地壳减压熔融,从而诱发了南岭在440~420 Ma期间的

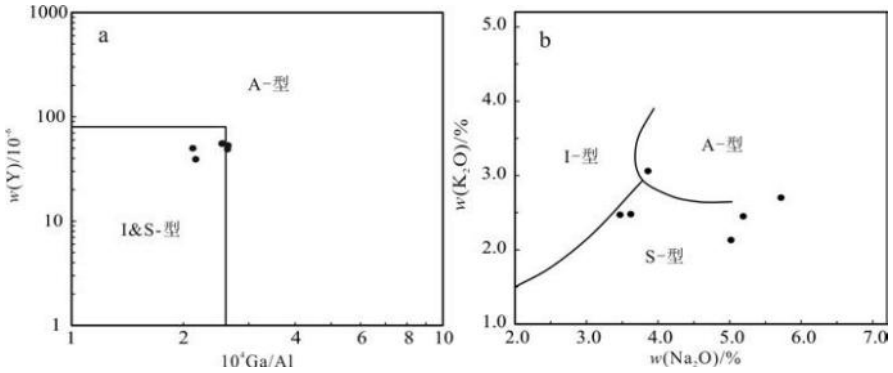

图 9　东风岩体花岗岩的 w(Y)-Ga/Al 图解(a,底图据 Whalen et al., 1987)和 $w(K_2O)$-$w(Na_2O)$图解(b,底图据 Collins et al., 1982)

Fig. 9　w(Y)-Ga/Al diagram (a, base map after Whalen et al., 1987) and $w(K_2O)$-$w(Na_2O)$ diagram (b, base map after Collins et al., 1982) of the Dongfeng monzogranite

大面积中酸性岩浆(本区为万洋山—彭公庙等岩体)的侵入活动(徐先兵等,2009;Wang et al., 2007b; 2010; Wan et al., 2010; Li et al., 2010; 张菲菲等,2010;程顺波等,2013;2016;Chen et al., 2019)。

在微量元素构造判别图解(图 10)中,东风岩体与邻区万洋山岩体、彭公庙岩体加里东期花岗岩一样,所有数据点均落入后碰撞区域(Post-CLOG),进一步表明东风岩体形成于后碰撞环境。

综上所述,东风岩体形成于扬子板块与华夏板块陆内汇聚后的后碰撞伸展环境,为增厚地壳减压熔融和软流圈地幔上涌诱发古老地壳物质发生重熔作用形成的S型花岗岩。

5.3　东风稀土矿床特征

近年来对南岭地区风化壳离子吸附型稀土矿的研究显示,加里东期(王彦斌等,2010;孙艳等,2012;赵芝等,2012)、印支期(于扬等,2012;张爱梅等,2010;郑国栋等,2012)和燕山期(陈正宏等,2008;Li et al., 2003; 李建康等,2012)的花岗岩均可作为稀土矿床的成矿母岩(王登红等,2013;赵芝等,2014),因此,离子吸附型稀土矿床的形成对花岗岩的时代没有选择性。原岩中稀土元素的含量则对矿床的形成起到关键性的作用,花岗岩岩体原岩中稀土元素丰度愈高,对成矿愈有利,稀土矿床的母岩在成岩过程中一般经历过稀土元素的预富集过程(周美夫等,2020)。南岭离子吸附型稀土元素矿体一般比基岩中的稀土元素含量富集2~5倍,因此,在基岩的稀土丰度大于150×10^{-6}的情况下就可形成离子吸附型稀土矿床(苏晓云等,2014)。一般富轻稀土元素的花岗岩母岩经风化后形成轻稀土型风化壳,富重稀土

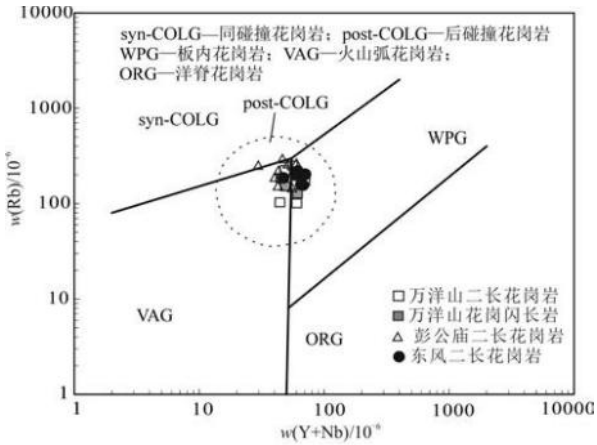

图 10　东风岩体构造判别图解(底图据 Pearce et al., 1984; 1996)

万洋山岩体、彭公庙岩体数据引自柏道远等,2006;伍光英等,2008;陈迪等,2016

Fig. 10　Tectonic setting discrimination diagram of the Dongfeng pluton (base map after Pearce et al., 1984; 1996)

Wanyangshan and Penggongmiao data are from Bai et al., 2006; Wu et al., 2008; Chen et al., 2016

元素者则风化形成重稀土风化壳,但近年在赣南地区也有轻稀土矿床中有重稀土矿体的报道(王登红等,2017;陈斌锋等,2019;赵芝等,2022)。

东风岩体花岗岩基岩中的稀土元素总量∑REE为$(184.2\sim264.2)\times10^{-6}$(表3),要高于南岭地区已知的4个含稀土矿的徐敦、竹州、宁化、益将加里东期花岗岩体的稀土元素含量($(124\sim224)\times10^{-6}$,地矿部南岭项目组,1989;王彦斌等,2010)。LREE/HREE值介于1.72~2.22,显示出轻稀土元素富集的特征,其中,岩体中的w(Y)非常高,为$(39.1\sim55.3)\times10^{-6}$(表

3)，Y/∑REE=21%~26%，属于高Y型花岗岩(张旗等，2022)，因此，东风稀土矿床的母岩属稀土元素含量较高的高Y轻稀土型花岗岩。风化壳矿体中的LREE/HREE值多介于0.50~1.00，Y/∑REE=36%~52%(湖南省核工业地质局301队，2018)，显示出花岗岩母岩在经历风化作用后，重稀土元素特别是Y得到了高程度的富集。对比基岩与稀土矿体的特征，不难看出东风稀土矿床是一典型的由富轻稀土元素的母岩经风化后形成的重稀土矿床。

风化壳离子吸附型稀土矿的形成一般经历了内生作用(成矿母岩)和外生作用(风化过程)两阶段(裴秋明等，2015；张恋等，2015)。东风岩体具显著的内生作用成矿：花岗岩起源于古老地壳物质重熔，分异指数Di(80.38~86.95)及微量元素特征反映岩浆有一定的分离结晶作用，矿物的显微岩相学特征则表明花岗岩内部经历了蚀变作用和重结晶作用(图2b~f)，而结晶分异作用可促成重稀土元素的富集(张恋等，2015)，热流体的蚀变作用(图2e)可致黑云母等矿物减少、稀土元素矿物的形成，从而导致稀土元素的分馏和富集(吴澄宇等，1990；张恋等，2015)。总体来说，相对南岭地区其他离子吸附型HREE矿床的原岩通常为高分异的花岗岩类(毛景文等，2022)，东风岩体花岗岩的分异程度并不高，这也与在岩体内基本未见到石英脉及细晶岩脉的地质现象相符(吴福元等，2017)。与高分异花岗岩中较低的稀土元素含量相比，东风岩体分异程度不高的花岗岩相对更富含稀土元素，为后期次生富集形成稀土矿床提供了物质基础，同时，母岩体中的高Y含量更是可以形成重稀土矿床的关键。

东风岩体具有良好的外生作用成矿条件，岩体所处地理位置为亚热带季风性湿润气候区(目前年降水量为1500 mm左右)，属海拔在400~600 m、地形较缓的丘陵-低山区，此为离子吸附型稀土矿形成的十分有利的气候和地形地貌条件(王登红等，2013；范飞鹏等，2014；裴秋明等，2015；张民等，2022)，万洋山岩体和彭公庙岩体内与东风岩体地形地貌条件相似的部位也发现了一批离子吸附型稀土矿床(图1a)。东风岩体含稀土矿风化壳具有明显的层状分带特征，由上往下可分为腐殖层、残坡积层、全风化层和半风化层(图3)。由腐殖层至半风化层，伴随大气降水淋滤作用的逐渐减弱，其pH值逐渐升高。在腐殖层和残坡积层中，除Ce元素易由Ce^{3+}氧化成Ce^{4+}以方铈矿的形式富集于表层外(Li et al., 2017；王长兵等，2021)，稀土元素(尤其为重稀土元素)在较低的pH值环境下迁移能力强(范飞鹏，2014)，部分稀土元素从稀土元素矿物中分解释放出来在大气降水的淋滤作用下发生向下迁移。全风化层中随着pH值升高，稀土元素迁移能力减弱，黏土矿物对稀土元素离子的吸附能力增强，本层以及从风化壳上部(腐殖层、残坡积层)释放迁移来的稀土元素离子大部分被黏土矿物吸附，尤其是在表生环境中迁移能力十分强的Y元素(裴秋明等，2015)，在本层得到高度富集而形成有工业价值的稀土矿体。东风矿区全风化层厚度达10~38 m(图3)，不仅为稀土矿的成矿作用提供了物质来源，也提供了稀土矿体的储存空间。而半风化层中淋滤作用相对很弱，稀土元素得不到迁移，其品位一般与基岩相当，不具工业价值。因此，华南地区高钇轻稀土型母岩花岗岩在风化后可形成重稀土矿床，在今后风化壳离子吸附型稀土矿床的找矿工作中应引起重视。

6 结 论

(1) 2件二长花岗岩的锆石U-Pb定年结果分别为(433.5±2.6)Ma和(432.0±2.5)Ma，表明东风岩体形成于加里东晚期。

(2) 岩石主、微量元素地球化学以及锆石Hf同位素等特征表明，东风岩体形成于在扬子板块与华夏板块陆内汇聚后的后碰撞伸展环境，为增厚地壳减压熔融和软流圈地幔上涌诱发古老地壳物质重熔所形成的S型花岗岩。

(3) 东风稀土矿床为一由富轻稀土元素的母岩经风化后形成的重稀土矿床，分异程度不高、富含稀土元素的高Y型花岗岩为矿床的形成提供了关键的物质基础，东风岩体所处地理位置的气候及地形地貌特征为稀土元素的淋滤迁移和吸附富集提供了重要保证。

致 谢 二位匿名审稿专家对本文进行了辛勤细致的审查，提出的宝贵意见促进了本文的进一步完善与提高，在此表示衷心感谢。

References

Amelin Y, Lee D C, Halliday A N and Pidgeon R T. 1999. Nature of the earth's earliest crust from hafnium isotopes in single detrital

zircons[J]. Nature, 399(6733): 252-255.

Andersrn T. 2002. Correction of common lead in U-Pb analyses that do not report ^{204}Pb[J]. Chemical Geology, 192: 59-79.

Bai D Y, Huang J Z, Ma T Q and Wang X H. 2006. Geology and geochemistry of the Silurian Penggongmiao granitic pluton in the Southeastern Hunan Province and its implication for tectonic setting[J]. Geoscience, 20(1): 130-140(in Chinese with English abstract).

Ballouard C, Poujol M, Boulvais P, Branquet Y, Tartèse R and Vigneresse J L. 2016. Nb-Ta fractionation in peraluminous granites: A marker of the magmatic-hydrothermal transition[J]. Geology, 44: 231-234.

Bau M. 1996. Controls on the fractionation of isovalent trace elements in magmatic and aqueous systems: Evidence from Y/Ho, Zr/Hf, and lanthanide tetrad effect[J]. Contribution to Mineralogy and Petrology, 123: 323-333.

Bea F, Mazhari A, Montero P, Amini S and Ghalamghash J. 2011. Zircon dating, Sr and Nd isotopes, and element geochemistry of the Khalifan pluton, NW Iran: Evidence for Variscan magmatism in a supposedly Cimmerian superterrane[J]. Journal of Asian Earth Sciences, 40: 172-179.

Blichert-Toft J and Albarède F. 1997. The Lu-Hf isotope geochemistry of chondrites and the evolution of the mantle-crust system[J]. Earth and Planetary Science Letters, 148: 243-258.

Boynton W V. 1984. Cosmochemistry of the rare earth elements: meteorites studies[A]. In: Henderson P, ed. Rare earth element geochemistry[C]. Elsevier: Amsterdam. 63-114.

Chappell B W and White A J R. 1992. I- and S-type granites in the Lachlan Fold Belt[J]. Transactions of the Royal Society of Edinburgh: Earth and Environmental Science, 83: 1-26.

Chen B F, Zou X Y, Peng L L, Qi F Y, Que X H, Zhang Q and Zhou X H. 2017. Geological characteristics and heavy Rare earth ore prospecting potential of Qingxi pluton Rare earth deposit[J]. Chinese Rare Earths, 40 (4): 20-31(in Chinese with English abstract).

Chen D, Ma A J, Liu Y R and Ni Y J. 2013.Research on U-Pb chronology in Xitian pluton of Hunan Province[J]. Geoscience, 27(4): 819-830(in Chinese with English abstract).

Chen D, Ma T Q, Liu W, Liu Y R, Ma A J and Ni Y J. 2016. Zircon SHRIMP U-Pb age, petrogenesis and tectonic implication of Wanyangshan pluton in Southeast Hunan Province[J]. Geotectonica et Metallogenia, 40(4): 873-890(in Chinese with English abstract).

Chen D, Liu J Y, Wang X H, Yang J, Ma T Q and Luo L. 2017. The petrogeochemistry, SHRIMP zircon U-Pb age, and Hf isotope character of Wufengxian pluton in Hunan Province[J]. Geological Science and Technology Information, 36(6): 1-12(in Chinese with English abstract).

Chen J F, Shen D, Shao Y J, Zhang J X, Liu Z F, Wei H T, Yang Q D, Luo X Y and Du Y. 2019. Silurian S-type granite-related W-(Mo) mineralization in the Nanling Range, South China: A case study of the Pingtan W-(Mo) deposit[J]. Ore Geology Reviews, 107: 186-200.

Chen X M, Wang R C, Liu C S, Hu H, Zhang W L and Gao J F. 2002. Isotopic dating and genesis for Fogang biotite granites of Conghua area, Guangdong Province[J]. Geological Journal of China Universities, 8(3): 293-307(in Chinese with English abstract).

Chen Z H, Li J Y, Xie P S, Zeng W and Zhou H W. 2008. Approaching the age problem for some metamorphosed Precambrain basement rocks and Phanerozoic granitic bodies in the Wuyishan area: The application of EMP monazite age dating[J]. Geological Journal of China Universities, 14(1): 1-15(in Chinese with English abstract).

Cheng S B, Fu J M, Ma L Y, Chen X Q, Zhang L G and Lu Y Y.2013. Geochemical characteristics, petrogenesis and ore potential evaluation of Caledonian granitoids in Nanling Range, South China[J]. Geology and Mineral Resources of South China, 29(1): 1-11(in Chinese with English abstract).

Cheng S B, Fu J M, Ma L Y, Lu Y Y, Kou X H, Zhang L G and Huang H L. 2016. Origin of the Yuechengling caledonian granitic Batholith, northeastern Guangxi: Constraint from Zircon U-Pb geochronology, geochemistry and Nd-Hf isotopes[J]. Geotectonica et Metallogenia, 40(4): 853-872(in Chinese with English abstract).

Collins W J, Beams S D, White A J R and Chappell B W. 1982. Nature and origin of A type granites with particular reference to sourheastern Australia[J]. Contributions to Mineralogy and Petrology, 80(2): 189-200.

Dong G C, Mo X X, Zhao Z D, Zhu D C, Goodman R C, Kong H L and Wang S. 2013. Zircon U-Pb dating and the petrological and geochemical constraints on Lincang granite in western Yunnan, China: Implications for the closure of the Paleo-Tethys Ocean[J]. Journal of Asian Earth Sciences, 62: 282-294.

Fan F P, Xiao H L, Chen L Z, Bao X M, Cai Y T, Zhang J and Zhu Y P. 2014. Mineralization and geological characteristics of elution-deposited rare earth ore from weathering crust in Pitou region, southern Ganzhou[J]. Journal of the Chinese Society of Rare Earths, 32(1): 101-107(in Chinese with English abstract).

Feng Y G, Liu S W, Lü Y J, Zhang C, Shu G M and Wang C Q. 2008. Monazite age mapping of Longhua S-type granites in the northern margin of the North China Craton[J]. Acta Petrologica Sinica, 24 (1): 104-114(in Chinese with English abstract).

Griffin W L, Pearson N J, Belonsova E, Jackson S E, Achterherah E V, O'Reilly S Y and Shee S R. 2000. The Hf isotope composition of cratonic mantle: LA-MC-ICPMS analysis of zircon megacrysts in kimberlites[J]. Geochimica et Cosmochimica Acta, 64: 133-147.

Griffin W L, Wang X, Jackson S E, Pearson N J, O'Reilly S Y, Xu X S and Zhou X M. 2002. Zircon chemistry and magma mixing, SE China: In-situ analysis of Hf isotopes, Tonglu and Pingtan igneous complexes[J]. Lithos, 61: 237-269.

Griffin W L, Pearson N J, Belousova E A and Saeed A. 2006. Comment: Hf-isotope heterogeneity in zircon 91500[J]. Chemical Geology, 23: 358-363.

Guo A M, Chen B H, Chen J F, Si C S and Zheng Z F. 2017. Zircon SHRIMP U-Pb geochronology of granitoids from northern Zhuguangshan granitic composite batholith, Hunan Province[J]. Geo-

logy in China, 44(4): 781-792 (in Chinese with English abstract).

Hoskin P W O and Schaltegger U. 2003. The composition of zircon and igneous and metamorphic petrogenesis[J]. Reviews of Mineralogy and Geochemistry, 53: 27-62.

Hu Z C, Liu Y S, Gao S, Liu W G, Zhang W, Tong X R, Lin L, Zong K Q, Li M, Chen H H, Zhou L and Yang L. 2012. Improved in situ Hf isotope ratio analysis of zircon using newly designed X skimmer cone and jet sample cone in combination with the addition of nitrogen by laser ablation multiple collector ICP-MS[J]. Journal of Analytical Atomic Spectrometry, 27: 1391-1399.

Hunan Institute of Geological Survey. 1972. 1∶200 000 Yongxing regional geological survey report[R]. 1-112(in Chinese).

Hunan Institute of Geological Survey. 2005. 1∶250 000 Hengyang regional geological survey report[R]. 1-324(in Chinese).

Hunan Institute of Geological Survey. 2014. Regional geology and mineral resources prospect survey report in Chaling-Ninggang district, Hunan[R]. 1-149(in Chinese).

Hunan Institute of Geological Survey. 2018. 1∶50 000 Regional geology and mineral resources survey report in Huanxi district, Hunan[R]. 1-236(in Chinese).

Le Bas M J, Le Maitre R W, Streckeisen A and Zanettin B. 1986. A chemical classification of volcanic rocks based on the total alkali-silica system[J]. Journal of Petrology, 27: 745-750.

Li C N. 1992. Trace element in igneous rock[M]. Wuhan: China University of Geosciences. 1-187(in Chinese).

Li J K, Chen Z Y, Chen Z H, Hou K J and Zhao Z. 2012. The dating and analysis of ore-forming conditions for Hanfang granite intrusions in Ganxian, Jiangxi Province[J]. Rock and Mineral Analysis, 31(4): 717-723 (in Chinese with English abstract).

Li T, Yuan H Y and Wu S X. 1998. On the average chemical composition of granitodis in China and the world[J]. Geotectonica et Metallogenia, 22(1): 29-34 (in Chinese with English abstract).

Li X H, Chen Z G, Liu D Y and Li W X. 2003. Jurassic gabbro-granite-syenite suites from southern Jiangxi Province, SE China: Age, origin, and tectonic significance[J]. International Geology Review, 45: 898-921.

Li Y H M, Zhao W W and Zhou M F. 2017. Nature of parent rocks, mineralization styles and ore genesis of regolith-hosted REE deposits in South China: An integrated genetic model[J]. Journal of Asian Earth Sciences, 148: 65-95.

Li Z X, Li X H, Wartho J A, Clark C, Li W X and Zhang C L. 2010. Magmatic and metamorphic events during the Early Paleozoic Wuyi-Yunkai orogeny, southeastern South China: New age constraints and pressure-temperature conditions[J]. Geological Society of America Bulletin, 122(5-6): 772-793.

Liang X Q, Dong C G, Jiang Y, Wu S C, Zhou Y, Zhu H F, Fu J G, Wang C and Shan Y H. 2016. Zircon U-Pb, molybdenite Re-Os and muscovite Ar-Ar isotopic dating of the Xitian W-Sn polymetallic deposit, eastern Hunan Province, South China and its geological significance[J]. Ore Geology Reviews, 78: 85-100.

Liu Y S, Hu Z C, Gao S, Günther D, Xu J, Gao C G and Chen H H. 2008. In situ analysis of major and trace elements of anhydrous minerals by LA-ICP-MS without applying an internal standard[J]. Chemical Geology, 257: 34-43.

Liu Y S, Gao S, Hu Z C, Gao C G, Zong K Q and Wang D B. 2010. Continental and oceanic crust recycling-induced melt-peridotite interactions in the Trans-North China Orogen: U-Pb dating, Hf isotopes and trace elements in zircons of mantle xenoliths[J]. Journal of Petrology, 51 (1-2): 537-571.

Ludwig K R. 2003. ISOPLOT 3.00: A Geochronological Toolkit for Microsoft Excel[M]. Berkeley Geochronology Center, California, Berkeley: 39.

Ma T Q, Bai D Y, Kuang J and Wang X H. 2005. Zircon SHRIMP dating of the Xitian granite pluton, Chaling southeastern Hunan, and its geological significance[J]. Geological Bulletin of China, 24(5): 415-419(in Chinese with English abstract).

Maniar P D and Piccoli P M. 1989. Tectonic discrimination of granitoids[J]. Geological Society of America Bulletin, 101: 635-643.

Mao J W, Song S W, Liu M and Meng J Y. 2022. REE deposits: Basic characteristics and global metallogeny[J]. Acta Geologica Sinica, 96(11): 3675-36972(in Chinese with English abstract).

Niu R, Liu Q, Hou Q L, Sun J F, Wu S C and Zhang H Y, Guo Q Q and Wang Q. 2015. Zircon U-Pb geochronology of Xitian granitic pluton in Hunan Province and its constraints on the metallogenic ages of the tungsten-tin deposit[J]. Acta Petrologica Sinica, 31(9): 2620-2632(in Chinese with English abstract).

No.301 Brigade of Hunan Nuclear Geological Bureau. 2018. General investigation geological report of Dongfeng REE deposit in Yanling Country, Hunan Province[R]. 1-71(in Chinese).

Patino D A E and Johnston A D. 1991. Phase equilibria and melt productivity in the pelitic system: Implications for the origin of peraluminous granitoids and aluminous granites[J]. Contributions to Mineralogy and Petrology, 107: 202-218.

Patino D A E and Beard J S. 1995. Dehydration-melting of biotitegneiss and quartz amphibolite from 3 to 15 Kbar[J]. Journal of Petrology, 36: 707-738.

Pearce J A, Harris N B W and Tindle A G. 1984 .Trace element discrimination diagrams for the tectonic interpretation of granitic rocks[J]. Journal of Petrology, 25(4): 956-983.

Pearce J A. 1996. Sources and settings of granitic rocks[J]. Episodes, 19: 120-125.

Pei Q M, Liu T Q, Yuan H Q, Cao H W, Li S H and Hu X K. 2015. Geochemical characteristics of trace elements of ion adsorption type rare elements deposit in Guposhan region, Guangxi, China[J]. Journal of Chengdu University of Technology(science and technology edition), 42(4): 451-462(in Chinese with English abstract).

Ren F, Yin F G, Xu B, Liu H L, Fan B L, Xu C H, and Bai J G. 2021. Zircon U-Pb age and Hf isotope of Early Paleozoic granite from the Jitang area in eastern Tibet and its insight into the evlution of the evolution of the Proto-Tethys Ocean[J]. Geological Bulletin of China, 40(11): 1865-1876(in Chinese with English abstract).

Rollinson H R. 1993. Using geochemical data: Evaluation, presenta-

tion, interpretation[M]. New York: Longman Scientific & Technical. 1-352.

Segal I, Halicz L and Platzner I T. 2003. Accurate isotope ratio measurements of ytterbium by multiple collection inductively coupled plasma mass spectrometry applying erbium and hafnium in an improved double external normalization procedure[J]. Journal of Analytical AtomicSpectrometry, 18: 1217-1223.

Shen W Z, Zhang F R, Shu L S, Wang L J and Xiang L. 2008. Formation age, geochemical characteristics of the Ninggang granite body in Jiangxi Province and its tectonic significance[J]. Acta Petrologica Sinica, 24(10): 2244-2254(in Chinese with English abstract).

Shu L S. 2006. Predevonian tectonic evolution of South China: From Cathaysian Block to Caledonian period folded orogenic Belt[J]. Geological Journal of China Universities, 12(4): 418-431(in Chinese with English abstract).

Shu L S, Yu J H, Jia D, Wang B, Shen W Z and Zhang Y Q. 2008. Early Paleozoic orogenic belt in the eastern segment of South China[J]. Geological Bulletin of China, 27(10): 1581-1593(in Chinese with English abstract).

Soderlund U, Patchett P J, Vervoort J D and Isachsen C E. 2004. The ^{176}Lu decay constant determined by Lu-Hf and U-Pb isotope systematics of Precambrian mafic intrusions[J]. Earth and Planetary Science Letters, 219: 311-324.

Su X Y, Guo C L, Chen Z Y, Zhao Z, Guo N X and Zhao Z. 2014. Zircon U-Pb age, geochemistry and mineralization prospective of the Caledonian Doushui granitic pluton in southern Jiangxi Province[J]. Geotectonica et Metallogenia, 38(2): 334-346(in Chinese with English abstract).

Sun S S and McDonough W F. 1989. Chemical and isotopic systematics of oceanic basalts: Implications for mantle composition and processes[J]. Geological Society, London, Special Publications, 42: 313-345.

Sun Y, Li J K, Chen Z Y, Chen Z H, Hou K J and Zhao Z. 2012. LA-MC-ICP-MS Zircon U-Pb dating and rare earth potential of the Longshe granite in Ganzhou, Jiangxi Province[J]. Geotectonica et Metallogenia, 36(3): 422-426(in Chinese with English abstract).

The Granitoid Resrarch Group of the Nanling Project, MGMR. 1989. Geology of granitoids of Nanling region and their petrogenesis and mineralization[M]. Beijing: Geological Publishing House. 1-437(in Chinese with English abstract).

Vervoort J D, Pachelt P J, Gehrels G E and Nutman A P. 1996. Constraints on Early Earth differentiation from hafnium and neodymium isotopes[J]. Nature, 379: 624-627.

Wan Y S, Liu D Y, Wilde S A, Cao J J, Chen B, Dong C Y, Song B and Du L L. 2010. Evolution of the Yunkai Terrane, South China: Evidence from SHRIMP zircon U-Pb dating, geochemistry and Nd isotope[J]. Journal of Asian Earth Sciences, 37(2): 140-153.

Wang C B, Ni G Q, Qu L, Wu R L, Li C Q, Ma X, Zhang Z J and Yang C P. 2021. Ce geochemical characteristics of granite weathering crust and its prospecting significance: A case study of Chahe ion adsorption rare earth deposit in western Yunnan[J]. Mineral Deposits, 40(5): 1013-1028(in Chinese with English abstract).

Wang D H, Zhao Z, Yu Y, Zhao T, Li J K, Dai J J, Liu X X and He H H. 2013. Progress, problems and research orientation of ion-adsorption type rare earth resources[J]. Rock and Mineral Analysis, 32(5): 796-802(in Chinese with English abstract).

Wang D H, Zhao Z, Yu Y, Wang C H, Da J J, Sun Y Zhao T, Li J K, Huang F, Chen Z Y, Zeng Z L, Deng M C, Zou X Y, Huang H G, Zhou H and Feng W J. 2017. A review of the achievements in the survey and study of ion-adsorption type REE deposits in China[J]. Acta Geoscientica Sinica, 38(3): 317-325(in Chinese with English abstract).

Wang T and Liu S. 2013. Zircon saturation temperatures of granites in the Jiaonan area and their geological significations[J]. Bulletin of Mineralogy, Petrology and Geochemistry, 32(5): 619-624(in Chinese with English abstract).

Wang Y B, Wang D H, Han J, Chen Z H and Wang Q L. 2010. U-Pb dating and Hf isotopic characteristics of zircons from quartz-diorite in the Yijiang REE-Sc deposit, Rucheng County, Hunan: Constraints on the timing of Caledonian magmatic activity in South China[J]. Geology in China, 37(4): 1062-1070(in Chinese with English abstract).

Wang Y J, Fan W M, Sun M, Liang X Q, Zhang Y H and Peng T P. 2007a. Geochronological, geochemical and geothermal constraints on petrogenesis of the the Indosinian peraluminous granites in the South China Block: A case study in the Hunan Province[J]. Lithos, 96(3): 475-502.

Wang Y J, Fan W M, Zhao G C, Ji S C and Peng T P. 2007b. Zircon U-Pb geochronology of gneissic rocks in the Yunkai Massif and its implications on the Caledonian event in the South China Block[J]. Gondwana Research, 12(4): 404-416.

Wang Y J, Zhang F F, Fan W M, Zhang G W, Chen S Y, Peter A C and Zhang A M. 2010. Tectonic setting of the South China Block in the Early Paleozoic: Resolving intracontinental and ocean closure models from detrital zircon U-Pb geochronology[J]. Tectonics, 29. doi: 10.1029/ 2010TC002750.

Watson E B and Harrison T M. 1983. Zircon saturation revisited: Temperature and composition effects in a variety of crustal magma types[J]. Earth and Planetary Science Letters, 64: 295-304.

Whalen J B, Currie K L and Chappell B W. 1987. A-type granites: Geochemical characteristics, discrimination and petrogenesis[J]. Contributions to Mineralogy and Petrology, 95: 407-419.

Wu C Y, Huang D H, Bai G and Ding X S. 1990. Differentiation of Rare earth elements and origin of granitic rocks, Nanling Mountain area[J]. Acta Petrologica et Mineralogica, 9(2): 106-117(in Chinese with English abstract).

Wu F Y, Yang Y H, Xie L W, Yang J H and Xu P. 2006. Hf isotopic compositions of the standard zircons and baddeleyites used in U-Pb geochronology[J]. Chemical Geology, 234: 105-126.

Wu F Y, Li X H. Zheng Y F and Gao S. 2007. Lu-Hf isotopic systematics and their applications in petrology[J]. Acta Petrologica Sinica,

23(2): 185-220(in Chinese with English abstract).

Wu F Y, Liu X C, Ji W Q, Wang J M and Yang L. 2017. Highly fractionated granites: Recognition and research[J]. Science China Earth Sciences, 60: 1201-1219(in Chinese).

Wu G Y, Ma T Q, Feng Y F, Yan Q R, Liu F G and Bai D Y. 2008. Geological and geochemical character istics and genesis of the Caledonian Wanyangshan granite in the Nanling Mountains, South China[J]. Geology in China, 35(4): 608-617(in Chinese with English abstract).

Wu Q H, Cao J Y, Kong H, Shao Y J, Li H, Xi X S and Deng X T. 2016. Petrogenesis and tectonic setting of the Early Mesozoic Xitian granitic pluton in the middle Qin-Hang Belt, South China: Constraints from zircon U-Pb ages and bulk-rock trace element and Sr-Nd-Pb isotopic compositions[J]. Journal of Asian Earth Sciences, 128: 130-148

Wu Y B and Zheng Y F. 2004. Genesis of zircon and its constraints on interpretation of U-Pb age[J]. Chinese Science Bulletin, 49(16): 1589-1604(in Chinese).

Xu X, O'Reilly S Y, Griffin W L, Wang X, Pearson N J and He Z. 2007. The crust of Cathaysia: Age, assembly and reworking of two terranes[J]. Precambrian Research, 158(1-2): 51-78.

Xu X B, Zhang Y Q, Shu L S, Jia D, Wang R R and Xu H Z. 2009. Zircon La-ICPMS U-Pb dating of the Weipu granitic pluton in Southwest Fujian and the Changpu migmatite in South Jiangxi: Constrains to the timing of Caledonian movement in Wuyi mountains[J]. Geology Review, 55(2): 277-285(in Chinese with English abstract).

Yao Y, Chen J, Lu J J and Zhang R Q. 2013. Geochronology, Hf isotopic compositions and geochemical characteristics of Xitian A-type granite and its geological significance[J]. Mineral Deposits, 32(3): 467-488(in Chinese with English abstract).

Yu J H, O'Reilly S Y, Wang L, Griffin W L, Zhou M F, Zhang M and Shu L. 2010. Components and episodic growth of Precambrian crust in the Cathaysia Block, South China: Evidence from U-Pb ages and Hf isotopes of zircons in Neoproterozoic sediments[J]. Precambrian Research, 181(1-4): 97-114.

Yu Y, Chen Z Y, Chen Z H, Hou K J, Zhao Z, Xu J X, Zhang J J and Zeng Z L. 2012. Zircon U-Pb dating and mineralization prospective of the Triassic Qingxi Pluton in southern Jiangxi Province[J]. Geotectonica et Metallogenia, 36(3): 413-421(in Chinese with English abstract).

Zhang A M, Wang Y J, Fan W M, Zhang F F and Zhang Y Z. 2010. LA-ICPMS zircon U-Pb geochronology and Hf isotopic compositions of Caledonian granites from the Qingliu area, Southwest Fujian[J]. Geotectonica et Metallogenia, 38(3): 408-418(in Chinese with English abstract).

Zhang F F, Wang Y J, Fan W M, Zhang A M and Zhang Y Z. 2010. LA-ICPMS zircon U-Pb geochronology of Late Early Paleozoic granites in eastern Hunan and western Jiangxi Province, South China[J]. Geochimica, 39(5): 414-426 (in Chinese with English abstract).

Zhang F R, Shu L S, Wang D Z, Yu J H and Shen W Z. 2009. Discussions on the tectonic setting of Caledonian granitoids in the eastern segment of South China[J]. Earth Science Frontiers, 16(1): 248-260 (in Chinese with English abstract).

Zhang L, Wu K X, Chen L K, Zhu P and Ouyang H. 2015. Overview of metallogenic features of ion-adsorption type REE deposits in southern Jiangxi Province[J]. Journal of the Chinese Society of Rare Earths, 33(1): 10-17(in Chinese with English abstract).

Zhang M, Tan W, He X C, Zhao F F and Luo L Y. 2022. Analysis on geological characteristics and discussion about metallogenic process for ion-adsorption type REE deposit in Lancang County, Yunnan Province[J]. Mineral Deposits, 41(3): 567-584(in Chinese with English abstract).

Zhang Q, Zhai M G, Wei C J, Zhou L G, Chen W F, Jiao S T, Wang Y and Yuan F L. 2022. Innovative petrogennetic classification of granitoids: Perspective from metamorphic anatexis and big data[J]. Earth Science Frontiers, 29(4): 319-329(in Chinese with English abstract).

Zhang W L, Wang R C, Lei Z H, Hua R M, Zhu J C, Lu J J, Xie L, Che X D, Zhang R Q, Yao Y and Chen J. 2011. Zircon U-Pb dating confirms existence of a Caledonian scheelite bearing aplitic vein in the Penggongmiao granite batholith, South Hunan[J]. Chinese Science Bulletin, 56: 1448-1454(in Chinese).

Zhao K D, Jiang S Y, Sun T, Chen W F, Ling H F and Chen P R. 2013. Zircon U-Pb dating, trace element and Sr-Nd-Hf isotope geochemistry of Paleozoic granites in the Miao'ershan-Yuechengling batholith, South China: Implication for petrogenesis and tectonic-magmatic evolution[J]. Journal of Asian Earth Sciences, 74: 244-264.

Zhao Z, Chen Z Y, Chen Z H, Hou K J, Zhao Z, Xu J X, Zhang J J and Zeng Z L. 2012. Zircon U-Pb dating, tectonic setting and ore-bearing properties evaluation of the Caledonian Yangbu pluton in South Jiangxi[J]. Rock and Mineral Analysis, 31(3): 530-535(in Chinese with English abstract).

Zhao Z, Wang D H, Chen Z Y, Guo N X, Liu X X and He H H. 2014. Metallogenic specialization of rare earth mineralized igneous rocks in the eastern Nanling Region[J]. Geotectonica et Metallogenia, 38(2): 255-263(in Chinese with English abstract).

Zhao Z, Wang D H and Zou X Y. 2022. The genesis and diversity of ion adsorption REE mineralization in the Zhaibei deposit, Jiangxi Province, South China[J]. Acta Petrologica Sinica, 38(2): 365-370 (in Chinese with English abstract).

Zheng G D, Li J K, Chen Z Y, Chen Z H, Hou K J and Zhao Z. 2012. U-Pb dating of zircon from Jibu Huangsha intrusions in southern Jiangxi Province and its geological significances[J]. Rock and Mineral Analysis, 31(4): 711-716(in Chinese with English abstract).

Zhou M F, Li X X, Wang Z C, Li X C and Liu J C. 2020. The genesis of regolith-hosted rare earth element and scandium deposits: Current understanding and outlook to future prospecting[J]. Chinese Science Bulletin, 65(33): 3809-3824(in Chinese).

Zhou Y, Liang X Q, Wu S C, Jiang Y, Wen S N and Cai Y F. 2013. Geo-

chronology and geochemical characteristics of the Xitian tungsten-tin-bearing A-type granites, Hunan Province, China[J]. Geotectonica et Metallogenia, 37(3): 511-529(in Chinese with English abstract).

Zhou Y, Liang X Q, Wu S C, Cai Y F, Liang X R, Shao T B, Wang C, Fu J G and Ying J. 2015. Isotopic geochemistry, zircon U-Pb ages and Hf isotopes of A-type granites from the Xitian W-Sn deposit, SE China: Constraints on petrogenesis and tectonic significance[J]. Journal of Asian Earth Sciences, 105: 122-139.

附中文参考文献

柏道远, 黄建中, 马铁球, 王先辉. 2006. 湘东南志留纪彭公庙花岗岩体的地质地球化学特征及构造背景[J]. 现代地质, 20(1): 130-140.

陈斌锋, 邹新勇, 彭琳琳, 漆富勇, 阙兴华, 张青, 周兴华. 2019. 清溪岩体稀土矿床地质特征及重稀土找矿潜力[J]. 稀土, 40(4): 20-31.

陈迪, 马爱军, 刘伟, 刘耀荣, 倪艳军. 2013. 湖南锡田花岗岩体锆石 U-Pb 年代学研究[J]. 现代地质, 27(4): 819-830.

陈迪, 马铁球, 刘伟, 刘耀荣, 马爱军, 倪艳军. 2016. 湘东南万洋山岩体的锆石 SHRIMP U-Pb 年龄、成因及构造意义[J]. 大地构造与成矿, 40(4): 873-890.

陈迪, 刘珏懿, 王先辉, 杨俊, 马铁球, 罗来. 2017. 湖南五峰仙岩体岩石地球化学、SHRIMP U-Pb 年龄及 Hf 同位素特征[J]. 地质科技情报, 36(6): 1-12.

陈小明, 王汝成, 刘昌实, 胡欢, 张文兰, 高剑锋. 2002. 广东从化佛冈(主体)黑云母花岗岩定年和成因[J]. 高校地质学报, 8(3): 293-307.

陈正宏, 李寄嵎, 谢佩姗, 曾雯, 周汉文. 2008. 利用 EMP 独居石定年法探讨浙闽武夷山地区变质基底岩石与花岗岩的年龄[J]. 高校地质学报, 14(1): 1-15.

程顺波, 付建明, 马丽艳, 陈希清, 张利国, 卢友月. 2013. 南岭地区加里东期花岗岩地球化学特征、岩石成因及含矿性评价[J]. 华南地质与矿产, 29(1): 1−11.

程顺波, 付建明, 马丽艳, 卢友月, 寇晓虎, 张利国, 黄惠兰. 2016. 桂东北越城岭岩体加里东期成岩作用: 锆石 U-Pb 年代学、地球化学和 Nd-Hf 同位素制约[J]. 大地构造与成矿学, 40(4): 853-872.

地矿部南岭项目花岗岩专题组. 1989. 南岭花岗岩地质及其成因和成矿作用[M]. 北京: 地质出版社. 1-437.

范飞鹏, 肖惠良, 陈乐柱, 鲍晓明, 蔡逸涛, 张洁, 朱意萍. 2014. 赣南陂头一带风化壳淋积型稀土矿成矿地质特征[J]. 中国稀土学报, 32(1): 101-107.

凤永刚, 刘树文, 吕勇军, 张臣, 舒桂明, 王长秋. 2008. 华北克拉通北缘隆化地区 S 型花岗岩的独居石年龄图谱[J]. 岩石学报, 24(1): 104-114.

郭爱民, 陈必河, 陈剑锋, 司程山, 郑正福. 2017. 南岭诸广山北体复式花岗岩锆石 SHRIMP U-Pb 定年及地质意义[J]. 中国地质, 44(4): 781-792.

湖南省地质调查院. 1972. 1∶20 万永兴幅区域地质报告[R]. 1-112.

湖南省地质调查院. 2005. 1∶25 万衡阳市幅区域地质调查报告[R]. 1-324.

湖南省地质调查院. 2014. 湖南茶陵-宁岗地区矿产远景调查成果报告[R]. 1-149.

湖南省地质调查院. 2018. 湖南浣溪地区 1∶5 万地质矿产综合调查成果报告[R]. 1-236.

湖南省核工业地质局三〇一大队. 2018. 湖南省炎陵县东风矿区稀土矿普查地质报告[R]. 1-71.

黎彤, 袁怀雨, 吴胜昔. 1998. 中国花岗岩类和世界花岗岩类平均化学成分的对比研究[J]. 大地构造与成矿学, 22(1): 29-34.

李昌年. 1992. 火成岩微量元素岩石学[M]. 武汉: 中国地质大学出版社. 1-187.

李建康, 陈振宇, 陈郑辉, 侯可军, 赵正. 2012. 江西赣县韩坊岩体的成岩时代及成矿条件分析[J]. 岩矿测试, 31(4): 717-723.

马铁球, 柏道远, 邝军, 王先辉. 2005. 湘东南茶陵地区锡田岩体锆石 SHRIMP 定年及其地质意义[J]. 地质通报, 24(5): 415-419.

毛景文, 宋世伟, 刘敏, 孟健寅. 2022. 稀土矿床:基本特点与全球分布规律[J]. 地质学报, 96(11): 3675-3697.

牛睿, 刘庆, 侯泉林, 孙金凤, 伍式崇, 张宏远, 郭谦谦, 王麒. 2015. 湖南锡田花岗岩锆石 U-Pb 年代学及钨锡成矿时代的探讨[J]. 岩石学报, 31(9): 2620-2632.

裴秋明, 刘图强, 苑鸿庆, 曹华文, 李社宏, 胡昕凯. 2015. 广西姑婆山离子吸附型稀土矿床微量元素地球化学特征[J]. 成都理工大学学报 (自然科学版), 42(4): 451-462.

任飞, 尹福光, 徐波, 刘恒麟, 樊炳良, 徐长昊, 白景国. 2021. 藏东吉塘地区早古生代花岗岩锆石 U-Pb 年龄、Hf 同位素及其对原特提斯洋演化的启示[J]. 地质通报, 40(11): 1865-1876.

沈渭洲, 张芳荣, 舒良树, 王丽娟, 向磊. 2008. 江西宁冈岩体的形成时代、地球化学特征及其构造意义[J]. 岩石学报, 24(10): 2244-2254.

舒良树. 2006. 华南前泥盆纪构造演化: 从华夏地块到加里东期造山带[J]. 高校地质学报, 12(4): 418-431.

舒良树, 于津海, 贾东, 王博, 沈渭洲, 张岳桥. 2008. 华南东段早古生代造山带研究[J]. 地质通报, 27(10): 1581-1593.

苏晓云, 郭春丽, 陈振宇, 赵正, 郭娜欣, 赵芝. 2014. 赣南加里东期陡水岩体的锆石 U-Pb 年龄、地球化学特征及其稀土含矿性探讨[J]. 大地构造与成矿学, 38(2): 334-346.

孙艳, 李建康, 陈振宇, 陈郑辉, 侯可军, 赵正. 2012. 江西新丰桐木稀土矿区龙舌岩体的成矿时代及成矿条件分析[J]. 大地构造与成矿学, 36(3): 422-426.

王长兵, 倪光清, 瞿亮, 伍荣林, 李灿清, 马鑫, 张子军, 杨春鹏. 2021. 花岗岩风化壳中 Ce 地球化学特征及其找矿意义——以滇西岔河离子吸附型稀土矿床为例[J]. 矿床地质, 40(5): 1013-1028.

王登红, 赵芝, 于扬, 赵汀, 李建康, 代晶晶, 刘新星, 何晗晗. 2013. 离子吸附型稀土资源研究进展、存在问题及今后研究方向[J]. 岩矿测试, 32(5): 796-802.

王登红, 赵芝, 于扬, 王成辉, 代晶晶, 孙艳, 赵汀, 李建康, 黄凡, 陈振宇, 曾载淋, 邓茂春, 邹新勇,黄华谷, 周辉, 冯文杰. 2017. 我国离子吸附型稀土矿产科学研究和调查评价新进展[J]. 地球学报, 38(3): 317-325.

王涛, 刘燊. 2013. 胶南花岗岩锆石饱和温度及其地质意义[J]. 矿物岩石地球化学通报, 32(5): 619-624.

王彦斌, 王登红, 韩娟, 陈郑辉, 王清利. 2010. 湖南益将稀土-钪矿的

石英闪长岩锆石U-Pb定年和Hf同位素特征: 湘南加里东期岩浆活动的年代学证据[J]. 中国地质, 37(4): 1062−1070.

吴澄宇, 黄典豪, 白鸽, 丁孝石. 1990. 南岭花岗岩类起源与稀土元素的分馏[J]. 岩石矿物学杂志, 9(2): 106-117.

吴福元, 李献华, 郑永飞, 高山. 2007. Lu-Hf同位素体系及其岩石学应用[J]. 岩石学报, 23(2): 185-220.

吴福元, 刘小驰, 纪伟强, 王佳敏, 杨雷. 2017. 高分异花岗岩的识别与研究[J]. 中国科学: 地球科学, 47: 745-765

吴元保, 郑永飞. 2004. 锆石成因矿物学研究及其对U-Pb年龄解释的制约[J]. 科学通报, 49(16): 1589-1604.

伍光英, 马铁球, 冯艳芳, 闫全人, 刘富国, 柏道远. 2008. 南岭万洋山加里东期花岗岩地质地球化学特征及其成因[J]. 中国地质, 35(4): 608-617.

徐先兵, 张岳桥, 舒良树, 贾东, 王瑞瑞, 许怀智. 2009. 闽西南玮埔岩体和赣南菖蒲混合锆石LA-ICPMS U-Pb年代学: 对武夷山加里东运动时代的制约[J]. 地质论评, 55(2): 277-285.

姚远, 陈骏, 陆建军, 章荣清. 2013. 湘东锡田A型花岗岩的年代学、Hf同位素、地球化学特征及其地质意义[J]. 矿床地质, 32(3): 467-488.

于扬, 陈振宇, 陈郑辉, 侯可军, 赵正, 许建祥, 张家菁, 曾载淋. 2012. 赣南印支期清溪岩体的锆石U-Pb年代学研究及其含矿性评价[J]. 大地构造与成矿学, 36(3): 413-421.

张爱梅, 王岳军, 范蔚茗, 张菲菲, 张玉芝. 2010. 闽西南清流地区加里东期花岗岩锆石U-Pb年代学及Hf同位素组成研究[J]. 大地构造与成矿学, 34(3): 408−418.

张芳荣, 舒良树, 王德滋, 于津海, 沈渭洲. 2009. 华南东段加里东期花岗岩类形成构造背景探讨[J]. 地学前缘, 16(1): 248-260.

张菲菲, 王岳军, 范蔚茗, 张爱梅, 张玉芝. 2010. 湘东-赣西地区早古生代晚期花岗岩的LA-ICPMS锆石U-Pb定年研究[J]. 地球化学, 39(5): 414-426.

张恋, 吴开兴, 陈陵康, 朱平, 欧阳怀. 2015. 赣南离子吸附型稀土矿床成矿特征概述[J]. 中国稀土学报, 33(1): 10-17.

张民, 谭伟, 何显川, 赵甫峰, 罗莲英. 2022. 云南省澜沧县离子吸附型稀土矿床地质特征分析与成矿过程探讨[J]. 矿床地质, 41(3): 567-584.

张旗, 翟明国, 魏春景, 周李岗, 陈万峰, 焦守涛, 王跃, 袁方林. 2022. 一个新的花岗岩成因分类:基于变质岩深熔作用理论与大数据的证据[J]. 地学前缘, 29(4): 319-329.

张文兰, 王汝成, 雷泽恒, 华仁民, 朱金初, 陆建军, 谢磊, 车旭东, 章荣清, 姚远, 陈骏. 2011. 湘南彭公庙加里东期含白钨矿细晶岩脉的发现[J]. 科学通报, 56: 1448-1454.

赵芝, 陈振宇, 陈郑辉, 侯可军, 赵正, 许建祥, 张家菁, 曾载淋. 2012. 赣南加里东期阳埠(坦子下)岩体的锆石年龄、构造背景及其含矿性评价[J]. 岩矿测试, 31(3): 530-535.

赵芝, 王登红, 陈振宇, 郭娜欣, 刘新星, 何晗晗. 2014. 南岭东段与稀土矿有关岩浆岩的成矿专属性特征[J]. 大地构造与成矿学, 38(2): 255-263.

赵芝, 王登红, 邹新勇. 2022. “寨背式”离子吸附型稀土矿床多类型稀土矿化及其成因[J]. 岩石学报, 38(2): 356-370.

郑国栋, 李建康, 陈振宇, 陈郑辉, 侯可军, 赵芝. 2012. 赣南吉埠黄沙岩体的锆石U-Pb法年代学研究及其地质意义[J]. 岩矿测试, 31(4): 711-716.

周美夫, 李欣禧, 王振朝, 李晓春, 刘嘉成. 2020. 风化壳型稀土和钪矿床成矿过程的研究进展和展望[J]. 科学通报, 65(33): 3809-3824.

周云, 梁新权, 梁细荣, 伍式崇, 蒋英, 温淑女, 蔡永丰. 2013. 湖南锡田含W-Sn A型花岗岩年代学与地球化学特征[J]. 大地构造与成矿学, 37(3): 511-529.

Original Research Article

GREENHOUSE GASES SCIENCE AND TECHNOLOGY

A method to classify coal pore system by using cumulative amplitude ratio and its dynamic variation

Mingjun Zou, College of Geosciences and Engineering, North China University of Water Resources and Electric Power, Zhengzhou, China
Ningbo Cai, China University of Geosciences, Wuhan, China and New Geological Energy Exploration and Development Engineering Technology Research Center of Hunan, Changsha, China
Keying Wang, New Geological Energy Exploration and Development Engineering Technology Research Center of Hunan, Changsha, China and Geophysics and Geochemistry Survey Institute of Hunan, Changsha, China
Zibin Ding and Linlin Yao, College of Geosciences and Engineering, North China University of Water Resources and Electric Power, Zhengzhou, China

Abstract: As coal pore development is decisive for choosing the engineering site and predicting the CO_2 storage capacity, this paper provides a new method to define the double T_2 cutoff values by using cumulative amplitude ratio measured by nuclear magnetic resonance measurements, classifies the coal pore systems, and analyzes the influences on cumulative amplitude ratio. The following cognitions are achieved. The minimum ratio always varies narrowly and ranges from 0.9 to 1.1, which is quite stable and approximately equals to 1. Ranges of maximum and average ratios are 1.2–3.5 and 1.1–1.8, respectively. T_{2c1} represents the dividing point of diffusion pore and permeation pore, and its average value is about 4.1 ms. T_{2c2} represents the dividing point of permeation pore and cleat, with an average value of about 81.9 ms. The volumetric proportions of diffusion pore range from 1.5% to 76.2%, with an average value of 34.6%; the volumetric proportions of permeation pore are from 14.9% to 98.5%, with an average of 46.8%; while the volumetric proportions of cleat are between 8.4% and 57.5%, with an average of 26.6%. According to the different influencing degrees on maximum and average ratios, three types of parameters can be divided. The first type is strong correlation parameters and includes permeability, volumetric percentage of cleat, and relative volumetric percentage of cleat. The second type is medium correlation parameters, such as volumetric percentage of diffusion pore. The third type is weak correlation parameters, including T_2 cutoff values, porosity, and maximum vitrinite reflectance.

Keywords: T_2 cutoff value; cumulative amplitude ratio; coal pore system; CO_2 geological storage; CO_2 storage capacity

Correspondence to: Mingjun Zou, College of Geosciences and Engineering, North China University of Water Resources and Electric Power, Zhengzhou 450045, China.
E-mail: zoumingjun2008@163.com
Keying Wang, New Geological Energy Exploration and Development Engineering Technology Research Center of Hunan, Changsha, 410019, China.
E-mail: 744491522@qq.com
Received May 23, 2023; revised July 6, 2023; accepted July 17, 2023
Published online at Wiley Online Library (wileyonlinelibrary.com). DOI: 10.1002/ghg.2240

Introduction

CO_2 geological storage is of great significance for reducing CO_2 emission and protecting the atmosphere.[1,2] Regarding all types of geological reservoirs, coal is essential for its wide distribution and abundant resource, and CO_2 storage in coal can also be used for enhancing coalbed methane (CBM) recovery.[3,4]

Coal pores are complexly developed within the matrix by organic, inorganic, or tectonic origins.[5–8] The development of coal pores influences the behavior of coal as a reservoir rock for coalbed methane or CO_2 adsorption,[9–11] and a migration channel for CO_2 injection as well.[2,12–13] Therefore, coal pore development needs to be investigated in detail to help choose the engineering site and predict the CO_2 storage capacity.

Coal pores distribute in a wide range in the matrix.[14,15] According to various migration patterns, coal pore systems are thereby classified as diffusion pore, permeation pore, and cleat.[16] Generally, gas always diffuses in the diffusion pore,[17] permeates in permeation pore, and finally drains out via cleat.[18] While for water, diffusion pores are totally filled with irreducible water; cleats are totally filled with movable water; and two types of water are both filled in permeation pores.[19] As a result, the accuracy of coal pore system classification influences the gas migration and water occurrence.

Researchers presented different classification methods for coal pores by using routine measurements of mercury intrusion porosimetry, nitrogen adsorption isotherm, or scanning electron microscopy, as found in Refs.[17,20–22] Different classification results are thereby obtained, and three pore systems of diffusion pore, permeation pore, and cleat are then classified. Recently, nuclear magnetic resonance (NMR) technology has been widely used in pore structure analysis and pore size distribution since it is nondestructive and convenient.[16,23–25] T_2 cutoff value is used to classify the pore system to diffusion pore, permeation pore, and cleat, which is the puzzle during classification. Yao et al.[23,26] classified coal pore systems according to peak distributions of T_2 spectra. Zou et al.[25] classified coal pore systems by using irreducible water saturation curve. Zheng et al.[27] determined pore systems by using a multifractal-based method.

Cumulative amplitude ratio is introduced in this article, and then we proposed an accurate and convenient NMR dual T_2 cutoff determination method for coal samples. Coal pore systems for 10 samples are then classified, and the influences of parameters on cumulative amplitude ratio are deeply investigated.

Samples and experiment

Sample preparation

Ten coal samples sized 250 mm × 250 mm × 100 mm are collected from the underground coal mines in Qinshui basin of Shanxi Province of China. The maximum vitrinite reflectance of 10 coal samples varies from 1.24% to 2.33%. More information is listed in Table 1. It should be noted that basic information of samples QBSX01-05 has been presented in authors' former studies in Refs. 16, 19, 25.

All the samples were prepared as cylinder samples with the diameter of 25 mm and the height of 30 to 50 mm, and they were used for routine analyses of porosity and permeability and NMR measurements under the fully water saturated and centrifuged conditions.

Experimental theory

Routine analyses

Helium porosity and air permeability were both tested. The measurements were simulated under situ stress conditions using a triaxial cell with an isotropic ambient pressure of 2.5 MPa. Porosity was measured using helium expansion while absolute permeability was measured using a bubble flowmeter that used flowing air through the core sample until the variation of permeability became stable, as discussed in Zou et al.[25] in detail.

NMR measurement

Detailed theories of mercury intrusion porosimetry (MIP) and NMR measurements can be found in Refs.[25,28,29] It establishes a linear relationship between pore radius and transverse relaxation time as listed in the following equation:

$$1/T_2 = \rho_2(S/V) \tag{1}$$

where, T_2 is the transverse relaxation time, referring to the relaxation time of fluid; ρ_2 is a constant representing the transverse relaxation strength; S/V is the surface to volume ratio related to the pore radius.

Equation (1) supports the theory basis for coal pore analyzing by NMR. Before measurements, the cylinder

Table 1. Basic information of 10 coal samples.

Sample ID	Coal mine	Location	Coal seam	Geological time[a]	Buried depth/ m	$R_{o,max}$/%
QBSX01	Malan coal mine	Gujiao County, Taiyuan City	8	C	200	1.40
QBSX02	Xiqu coal mine	Gujiao County, Taiyuan City	2	P	130	1.57
QBSX03	Fanshigou coal mine	Gujiao County, Taiyuan City	2	P	200	1.55
QBSX04	Zhenchengdi coal mine	Gujiao County, Taiyuan City	8	C	300	1.32
QBSX05	Dangdangling coal mine	Lingshi County, Jinzhong City	10	C	180	1.24
QBSX06	Xinjing coal mine	Yangquan City	3	P	500	2.17
QBSX07	Shibangou coal mine	Xiangyuan County, Changzhi City	3	P	320	1.97
QBSX08	Xinzhuang coal mine	Gaoping County, Jincheng City	3	P	280	1.88
QBSX09	Xialiang coal mine	Xiangyuan County, Changzhi City	3	P	390	2.04
QBSX10	Xinyuan coal mine	Shouyang County, Jinzhong City	3	P	580	2.33

[a]P-Permian; C-Carboniferous.

samples were dried for 24 h in a drying oven at 70°C, pumped in a vacuum for 8 h, and then saturated in distilled water for 8 h. These fully water saturated samples were tested by NMR measurements to obtain pore distributions. After that, the fully water-saturated samples were centrifuged under the centrifugal pressure of 200 psi (absolute) according to Refs.[24–26] Finally, NMR measurements under the centrifuged condition were conducted to obtain irreducible water situation.

The NMR instrument has a constant magnetic field strength of 1200 gauss and a resonance frequency of 2.38 MHz. The measurement parameters were set as follows: echo spacing, 0.6 ms; waiting time, 5 s; echo numbers, 2,048; numbers of scans, 64.

Table 2. Results of routine analyses for 10 samples.

Sample ID	Helium porosity/%	Air permeability/ mD
QBSX01	4.56	0.159
QBSX02	3.88	0.064
QBSX03	4.49	0.044
QBSX04	4.10	0.047
QBSX05	5.36	0.091
QBSX06	5.18	0.055
QBSX07	4.12	0.102
QBSX08	3.23	0.078
QBSX09	3.62	0.089
QBSX10	2.12	0.025

Result and discussion

Results for routine analyses

Results of routine analyses for 10 samples are listed in Table 2. Helium porosity varies between 2.12% and 5.36%, while air permeability ranges from 0.025 to 0.159 mD. As the smaller diameter of molecular nitrogen compared with the water molecule cluster, the porosity analyzed by helium injection is a little higher than that by water saturation.[25] It indicates that helium porosity is more effective and accurate than the general water porosity. Air permeability here is the core permeability. Because lots of big cleats are not involved in the core sample caused by the limited sample size, core permeability is generally lower than reservoir permeability. In the field situation, well testing is always used to obtain the reservoir permeability. However, core permeability is a guide to study the CBM geology as it is much convenient to test. Meanwhile, core permeability combined with simulated big cleats is also adopted in reservoir simulation to make the core permeability close with the reservoir permeability.

T_2 spectra

NMR measurements of the 10 coal samples at fully water-saturated and centrifuged conditions yield NMR

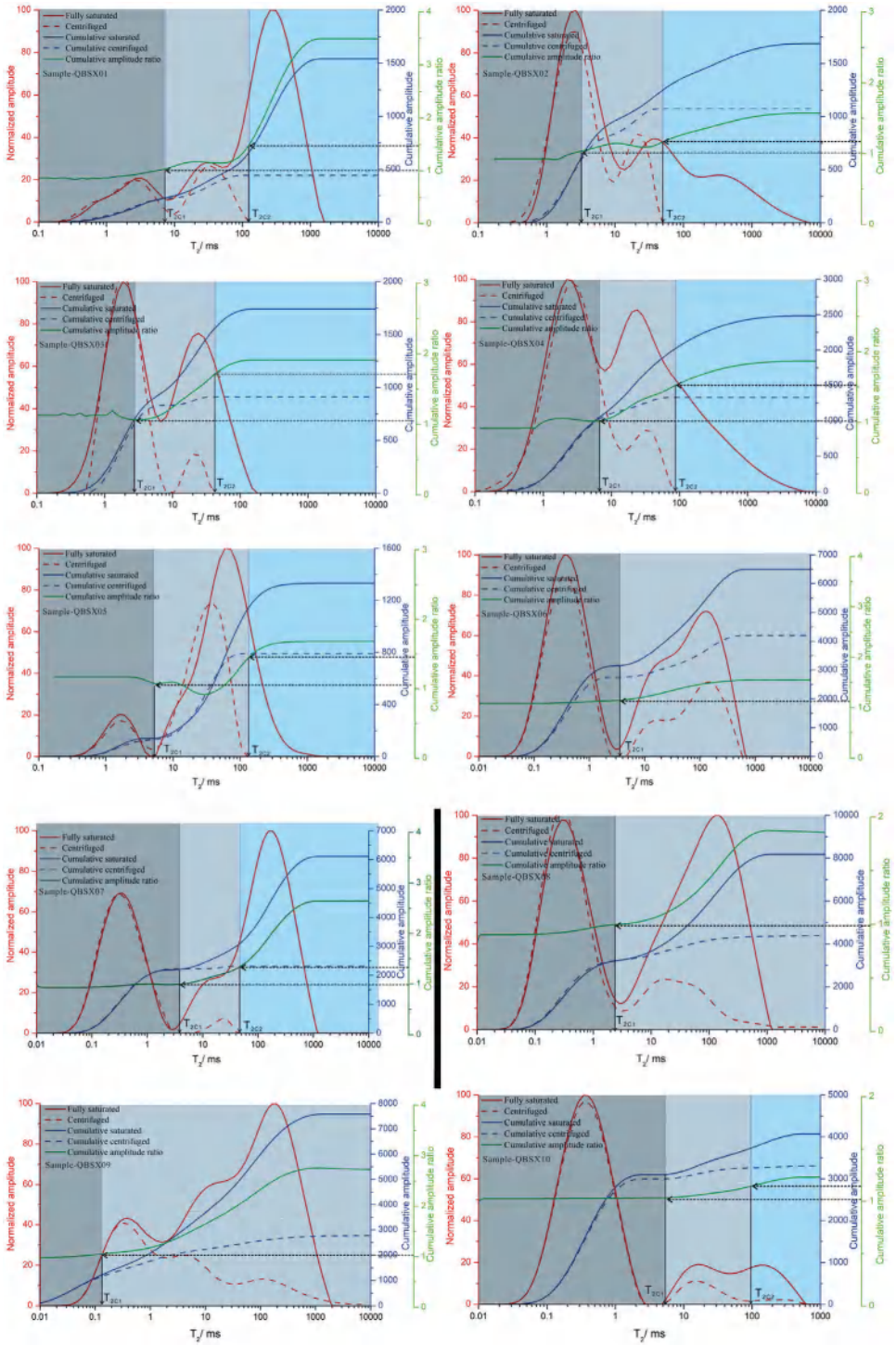

Figure 1. T_2 spectra for ten samples and T_2 cutoff value determination.

T_2 spectra, which are shown as red solid and dot lines in Fig. 1, respectively. To facilitate comparison, the highest amplitude is set artificially to 100, and other amplitudes are transferred based on the ratio. Then the amplitude is normalized. It should be noted that the T_2 spectra at fully water saturated and centrifuged conditions for samples QBSX01-05 have presented in authors' former studies in Ref. 16, 19, 25, and they are modified and analyzed in this paper for the coal pore system classification.

The T_2 distribution in fully water saturated condition represents the distribution of coal pore size, with the smaller pores having shorter relaxation times; while the T_2 distribution in centrifuged condition represents the distribution of irreducible water within coal pores. The amplitude is a measure of the number of pore volume, and the continuity of the T_2 spectrum depicts the connectivity of each coal pore.

Several findings are shown from Fig. 1. First, the 10 samples generally have good connectivity, and their T_2 spectra always show as two or three peaks. In the spectra with three peaks, the amplitudes at two conditions coincide in the left peak, separate in the middle peak, while the centrifuged T_2 spectra disappears in the right peak, such as in samples QBSX01, QBSX02, and QBSX10, which corresponds to the feature of irreducible water occurrence in different pore systems.[16] Second, centrifuged amplitudes are always lower than the fully water-saturated values because producible water can be partly centrifuged. However, several abnormal cases show that centrifuged amplitudes have increase just a little compared with fully water-saturated amplitudes, such as in samples QBSX02, QBSX05, and QBSX08. Al-Mahrooqi et al.[30] suggested that the poor connection of the sample caused water to be retained at the surface or inside the adsorption pores after centrifuging, leading to the increase of relaxation time amplitude.

Cumulative amplitude ratio and its dynamic variation

Generally, fluid in diffusion pores cannot be centrifuged, but it can be partly centrifuged in permeation pores, and can be entirely centrifuged in cleats.[31,32] Then, diffusion pores are totally filled with irreducible water; cleats are totally filled with movable water; while two types of water are both filled in permeation pores. Thus, T_{2c2} locates at the position when the centrifuged amplitude disappears permanently, which is easy to be identified as shown in Fig. 1. It should be pointed out that when the cleat system lacks in some samples, leading to the collective disappearances of centrifuged amplitude and fully saturated amplitude. Then, no T_{2c2} is marked, such as in samples QBSX06, QBSX08 and QBSX09. T_{2c1} is quite difficult to distinguish. Cumulative amplitude ratio is introduced in this paper, which equals to the ratio of cumulative amplitude in fully water-saturated condition and centrifuged condition expressed as follows:

$$r^i = \frac{\sum_0^i A_c^i}{\sum_0^i A_f^i} \tag{2}$$

where, i is the T_2 time, ms; r^i is the cumulative amplitude ratio at the T_2 time of i; $A_c{}^i$ is the normalized amplitude under centrifuged condition at the T_2 time of i; $A_f{}^i$ is the normalized amplitude under fully saturated water condition at the T_2 time of i.

The cumulative fully saturated amplitude concerns diffusion pore, permeation pore and cleat; while the cumulative centrifuged amplitude only concerns the diffusion pore. Therefore, the cumulative amplitude ratio for diffusion pore is 1, and a ratio above 1 is for permeation pore and cleat systems. Thus, the dividing location for cumulative amplitude ratio of approximate 1 and above 1 can thus be defined as T_{2c1}.

Curves of cumulative amplitude ratio for 10 coal samples are calculated as shown in the green lines in Fig. 1, and the values are listed and plotted in Fig. 2. It should be noted that the average ratio in the table is calculated by all ratios within the entire T_2 range for each sample.

For three types of values in Fig. 2, the minimum ratio varies narrowly for 10 samples, ranging from 0.9 to 1.1. Therefore, the minimum ratio is quite stable and approximately equals to 1, which also indicates that approximate 1 and above 1 for cumulative amplitude ratio can be set as the dividing location of T_{2c1} as discussed above. Ranges of maximum and average ratios are 1.2–3.5 and 1.1–1.8, respectively.

T_2 cutoff values

Observing the cumulative amplitude ratios in Fig. 1, except sample QBSX05, the other samples quite perfectly satisfy the theory in cumulative amplitude ratio and its dynamic variation section, and there is an obvious dividing point of cumulative amplitude ratio between approximate 1 and above 1 in each of these samples, as revealed in Fig. 3. It should be noted that the zigzag line in the figure indicates that the T_{2c1} locations for all samples are different. For this type of T_2 spectrum, T_{2c1} is easy to identify.

The cumulative amplitude ratio of sample QBSX05 is special. There is still a cumulative amplitude ratio region with values approximately equal to 1 at the beginning of the T_2 spectrum. However, an unstable

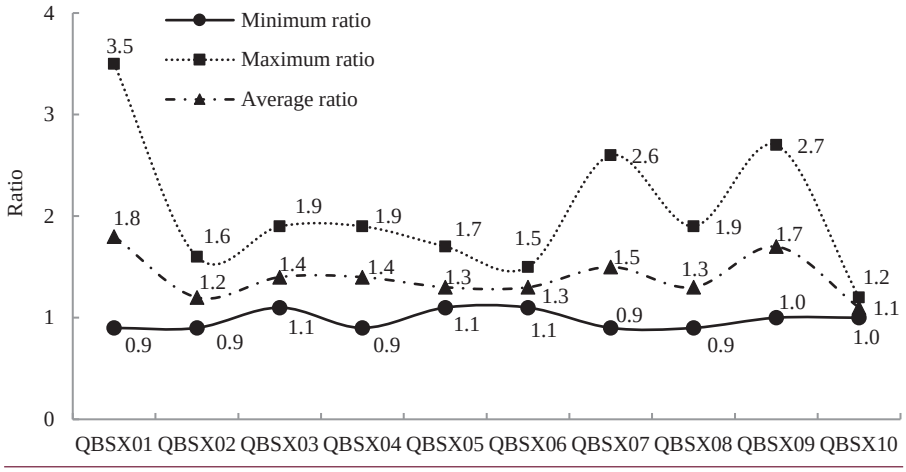

Figure 2. Cumulative amplitude ratio for each coal sample.

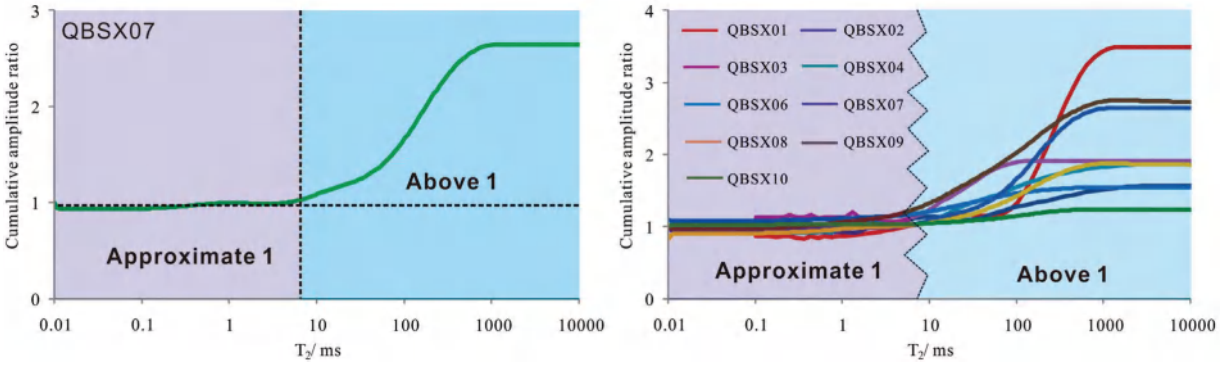

Figure 3. T_{2c1} identifications for sample QBSX07 (left) and all samples except QBSX05 (right).

Table 3. T_2 cutoff values for each coal sample.

Sample ID	T_{2c1}/ ms	T_{2c2}/ ms	Sample ID	T_{2c1}/ ms	T_{2c2}/ ms
QBSX01	7.2	124.5	QBSX06	3.6	-[a]
QBSX02	3.2	50.0	QBSX07	3.8	47.7
QBSX03	2.8	41.6	QBSX08	2.4	-
QBSX04	6.9	86.4	QBSX09	0.1	-
QBSX05	5.2	124.5	QBSX10	5.5	98.5

[a] - indicates that no value is identified.

stage with an initial decrease and then increase in ratio follows, which is distinct with other samples. It may be caused by the poor connection and complex pore structure of some pores in the sample. Therefore, the dividing point of amplitude ratio between values approximately equal to 1 and unstable values is roughly set as T_{2c1}.

Finally, T_{2c1} and T_{2c2} are both identified for all the samples as shown in Fig. 1, and their values are listed in Table 3. T_{2c1} ranges from 0.1 to 7.2 ms with an average of 4.1 ms; while T_{2c2} is between 41.6 and 124.5 ms, with an average value of 81.9 ms.

Pore type classification

Based on the T_2 cutoff values in Table 3, volumetric proportions of diffusion pore, permeation pore, and cleat for 10 samples are calculated as shown in Fig. 4. It can be seen from the figure that the volumetric

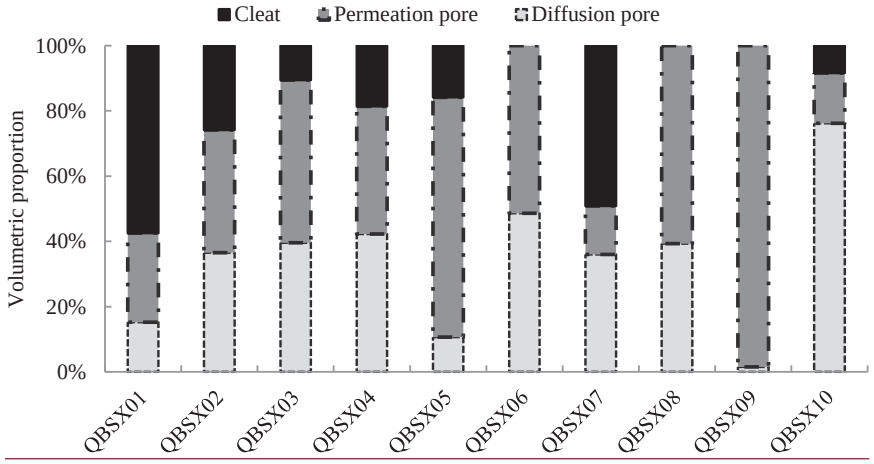

Figure 4. Volumetric proportion for ten samples.

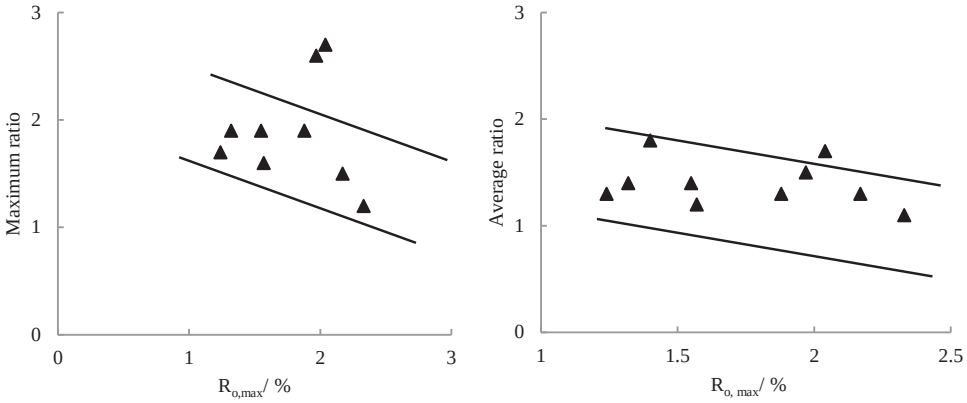

Figure 5. Scatter diagram of $R_{o,\,max}$ versus maximum ratio (left) and average ratio (right).

proportions of diffusion pore range from 1.5 to 76.2%, with an average value of 34.6%; the volumetric proportions of permeation pore are from 14.9% to 98.5%, with an average of 46.8%; while the volumetric proportions of cleat are between 8.4% and 57.5% exclude samples QBSX06, QBSX08, and QBSX09, with an average of 26.6%. It is also revealed that the permeation pore is the most developed for 10 samples.

Influence on cumulative amplitude ratio

Cumulative amplitude ratio is critical in this study. As can be seen from Fig. 2, the maximum and average ratios vary complexly, while the minimum ratio is quite stable. To discuss the factors influencing the maximum and average ratios, the following analyses are conducted.

Maximum vitrinite reflectance

Scatter diagrams of maximum vitrinite reflectance versus maximum and average ratios are shown in Fig. 5. The relationships in the figure indicate that the maximum vitrinite reflectance has a weak and negative influence on both maximum and average ratios. Maximum ratio reflects the development of permeation pore or cleat. As the minimum ratio is quite stable, the average ratio is mainly influenced by the maximum ratio. Hence, both the maximum and average ratios represent the development of permeation pore or cleat system. Maximum vitrinite reflectance concerns the development of the entire pore system including diffusion pores within the matrix, therefore its influences on both the maximum and average ratios are relatively weak.

Porosity and permeability

Scatter diagrams of porosity and permeability versus maximum and average ratios are shown in Fig. 6. The relationships in Fig. 6 indicate that the porosity has a weak and positive influence on the two ratios, while the

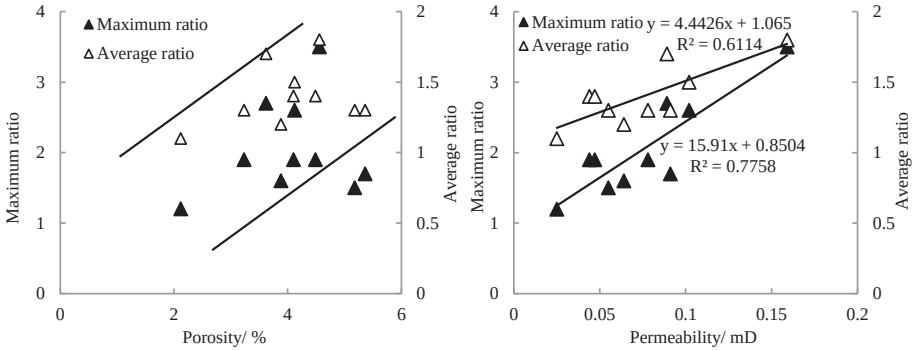

Figure 6. Scatter diagrams of porosity (left) and permeability (right) versus maximum and average ratios.

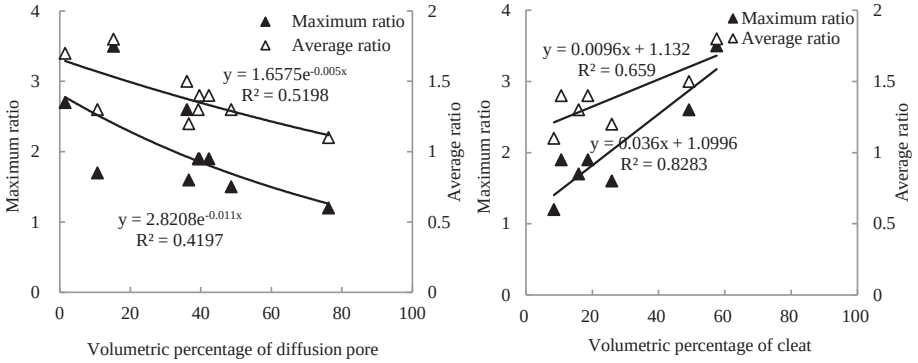

Figure 7. Scatter diagrams of volumetric percentages of diffusion pore (left) and cleat (right) versus maximum and average ratios.

permeability has a strongly and positively linear relationship with both the maximum and average ratios, of which the fitting degrees are 0.78 and 0.61, respectively.

As a result, permeability is the critical factor for maximum and average ratios, while the impacts of porosity on both the maximum and average ratios are relatively weak. As discussed above, both the maximum and average ratios represent the development of permeation pore or cleat system. Porosity concerns the development of the entire pore system, therefore its influences on both the maximum and average ratios are relatively weak. The maximum and average ratios are both strongly influenced by permeability, which could be attributed to the permeation mainly occurring within the permeation pore or cleat system.

Volumetric percentages of different pore systems

Scatter diagrams of volumetric percentages versus maximum and average ratios are shown in Fig. 7. The figure indicates that the volumetric percentage of diffusion pore has strongly and negatively exponential correlations with both the maximum and average ratios with fitting degrees of about 0.51 and 0.54, respectively; while the volumetric percentage of cleat system has strongly and positively linear relationships with both the maximum and average ratios, with fitting degrees of about 0.83 and 0.66, respectively.

As discussed above, both the maximum and average ratios represent the development of permeation pore or cleat system. Therefore, the volumetric percentage of cleat system has strong and positive relationships with both the maximum and average ratios. Conversely, the volumetric percentage of diffusion pore system has negative correlations with both the maximum and average ratios.

To deep investigate relationships of volumetric percentage of pore system versus maximum and average ratios, a relative volumetric percentage of cleat is defined in this paper as expressed follows,

$$V_{rc} = \frac{V_c}{V_d + V_p} \tag{3}$$

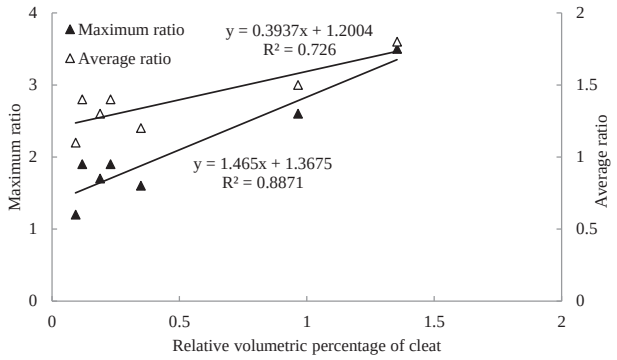

Figure 8. Scatter diagram of relative volumetric percentage of cleat versus maximum and average ratios.

where, V_{rc} is the relative volumetric percentage of cleat, decimal; V_c is the volumetric percentage of cleat,%; V_d is the volumetric percentage of diffusion pore,%; V_p is the volumetric percentage of permeation pore,%.

The scatter diagram of relative volumetric percentage of cleat versus maximum and average ratios is shown in Fig. 8. The figure indicates that the relative volumetric percentage of cleat has strong and positive linear correlations with both the maximum and average ratios, which is caused by the fact that the cleat has positive relationships with the two ratios and that the diffusion pore has negative relationships with both the ratios. Compared with the relationships in Fig. 7, the relationships in Fig. 8 are obviously stronger and clearer, with higher fitting degrees, which indicate that the relative volumetric percentage of cleat is the most important parameter among all the volumetric percentage values.

T_2 cutoff values

Scatter diagrams of T_2 cutoff values versus maximum ratio and average ratio are shown in Fig. 9. The figure indicates that T_{2c1} has a negative relationship with maximum or average ratio, while T_{2c2} has a positive relationship with maximum or average ratio, although the correlations are relatively weak.

T_{2c1} represents the volumetric percentage of diffusion pore, while T_{2c2} represents the volumetric percentage of cleat. Therefore, T_{2c1} has negative relationships with both the two ratios, and T_{2c2} has positive relationships with both the two ratios, as discussed in the volumetric percentages of different pore systems section.

Influencing degree analysis

The above analyses indicate that these parameters have different influencing degrees on cumulative maximum and average ratios. According to the influencing degrees, the parameters can be divided into three types. The first type is strong correlation parameters, referring to those parameters that have high influencing degrees with two ratios (generally close to or higher than 0.8), including permeability, volumetric percentage of cleat, and relative volumetric percentage of cleat. The second type is medium correlation parameters, referring to those parameters that have medium influencing degrees with two ratios (generally around 0.6), such as volumetric percentage of diffusion pore. The third type is weak correlation parameters, representing those parameters that only have positive or negative tendencies with low fitting degrees, such as T_2 cutoff values, porosity, and maximum vitrinite reflectance.

In conclusion, maximum and average ratios mainly concern developments of the permeation pore and cleat system, while they have relatively weak correlations with those parameters representing developments of the entire pore system. Meanwhile, T_2 cutoff values are defined with relative values of cumulative amplitude ratios for each NMR spectrum, but have weak correlations with absolute values of maximum and average ratios for different NMR spectra.

Conclusions

This paper introduces a new term of cumulative amplitude ratio by using NMR measurements under the fully saturated water and centrifuged conditions. Based on the cumulative amplitude ratio, the double T_2 cutoff values are defined, and coal pore systems are classified in this paper. The following cognitions are achieved.

Ten samples generally have good connectivity, and their T_2 spectra always show two or three peaks. Centrifuged amplitudes are always lower than the fully water saturated values because producible water can be partly centrifuged. However, several abnormal cases are caused by the poor connection of some pores in the samples. The minimum ratio varies narrowly and ranges from 0.9 to 1.1, and it is quite stable and approximately equals to 1. Ranges of maximum and average ratios are 1.2–3.5 and 1.1–1.8, respectively.

T_{2c1} represents the dividing point of diffusion pore and permeation pore, and its average value is about 4.1 ms. T_{2c2} represents the dividing point of permeation pore and cleat, with an average value of about 81.9 ms. The volumetric proportions of diffusion pore range from 1.5% to 76.2%, with an average value

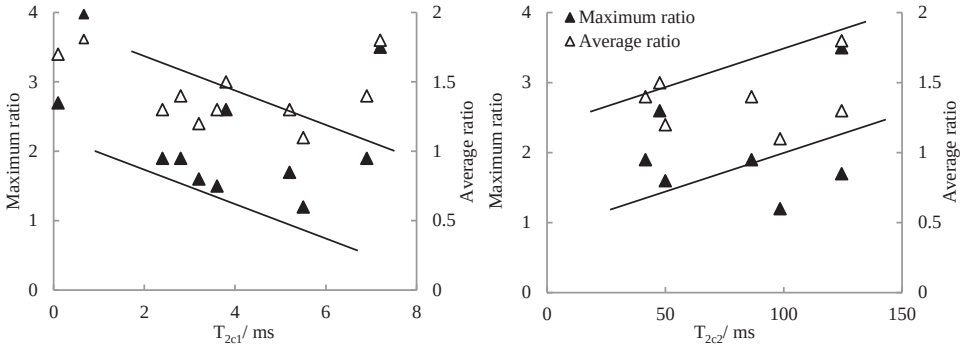

Figure 9. Scatter diagrams of T_{2c1} (left) and T_{2c2} (right) versus maximum and average ratios.

of 34.6%; the volumetric proportions of permeation pore are from 14.9 to 98.5%, with an average of 46.8%; while the volumetric proportions of cleat are between 8.4% and 57.5%, with an average of 26.6%.

Three types of parameters are divided according to the different influencing degrees on maximum and average ratios. The first type is strong correlation parameters, including permeability, volumetric percentage of cleat, and relative volumetric percentage of cleat. The second type is medium correlation parameters, such as volumetric percentage of diffusion pore. The third type is weak correlation parameters, such as T_2 cutoff values, porosity, and maximum vitrinite reflectance.

Author Contribution

Mingjun Zou: was involved in conceptualization, methodology, formal analysis, writing original draft, supervision, project administration and funding acquisition. **Ningbo Cai**: was involved in the methodology, software, validation, and formal analysis. **Keying Wang**: was involved in conceptualization, formal analysis, and writing. **Zibing Ding**: was involved in sample collection, laboratory experiments, and data analysis. **Linlin Yao**: Sample collection, laboratory experiments, and data analysis.

Conflict of Interest

The authors declare no conflict of interest.

References

1. Ajayi T, Awolayo A, Gomes JS, Parra H, Hu J. Large scale modeling and assessment of the feasibility of CO_2 storage onshore Abu Dhabi. Energy. 2019;185:653–70.
2. Zou M, Yao L, Zhang M, Huang Z, Xu R, Ding Z, et al. Hydraulic fracture to enhance coalbed methane recovery by using coated ceramsite. Greenhouse Gas Sci Technol. 2022;12:751–63.
3. Viete DR and Ranjith PG. The effect of CO_2 on the geomechanical and permeability behavior of brown coal: implications for coal seam CO_2 sequestration. Int J Coal Geol. 2006;66(3):204–16.
4. Su E, Liang Y, Zou Q, Niu F, Li L. Analysis of effects of CO_2 injection on coalbed permeability: implications for coal seam CO_2 sequestration. Energ Fuel. 2019;33(7):6606–15.
5. Xue G, Liu H, Li W. Deformed coal types and pore characteristics in Hancheng coalmines in Eastern Weibei coalfields. Int J Min Sci Techno. 2012;22(5):681–6.
6. Jin K, Cheng Y, Wang L, Dong J, Guo P, An F, et al. The effect of sedimentary redbeds on coalbed methane occurrence in the Xutuan and Zhaoji Coal Mines, Huaibei Coalfield, China. Int J Coal Geol. 2015;137:111–23.
7. Li Y, Zhang C, Tang D, Gan Q, Niu X, Wang K, et al. Coal pore size distributions controlled by the coalification process: an experimental study of coals from the Junggar, Ordos and Qinshui basins in China. Fuel. 2017;206: 352–63.
8. Li J, Huang Q, Wang G, Wang E, Ju S, Qin C. Experimental study of effect of slickwater fracturing on coal pore structure and methane adsorption. Energy. 2022;239:122421.
9. Bustin RM and Clarkson CR. Geological controls on coal bed methane reservoir capacity and gas content. Int J Coal Geol. 1998;38:3–26.
10. Crosdale PJ, Beamish BB, Valix M. Coalbed methane sorption related to coal composition. Int J Coal Geol. 1998;35:147–58.
11. Radlinski AP, Mastalerz M, Hinde AL, Hainbuchner M, Rauch H, Baron M, et al. Application of SAXS and SANS in evaluation of porosity, pore size distribution and surface area of coal. Int J Coal Geol. 2004;59:245–71.
12. Chen J, Cheng W, Wang G, Li H. Correlation mechanism between the law of ultrasonic propagation in coal samples and the migration of water. Fuel. 2022;310:122264.
13. Wang G, Chen X, Wang S, Chen H. Influence of fracture connectivity and shape on water seepage of low-rank coal based on CT 3D reconstruction. J Nat Gas Sci Eng. 2022;102:104584.
14. Spitzer Z. Mercury porosimetry and its application to the analysis of coal pore structure. Powder Technol. 1981;29(1):177–86.
15. Sakurovs R, He L, Melnichenko YB, Radlinski AP, Blach T, Lemmel H, et al. Pore size distribution and accessible pore

size distribution in bituminous coals. Int J Coal Geol. 2012;100:51–64.
16. Zou M, Wei C, Huang Z, Zhang M, Lv X. Experimental study on identification diffusion pores, permeation pores and cleats of coal samples. J Energ Resour-ASME. 2016;138: 021201.
17. Gong G, Xie Q, Zheng Y, Ye S, Chen Y. Regulation of pore size distribution in coal-based activated carbon. New Carbon Mater. 2009;24(2):141–6.
18. Wei Z and Zhang D. Coupled fluid flow and geomechanics for triple-porosity /dual-permeability modeling of coalbed methane recovery. Int J Rock Mech Min Sci. 2010;47(8):1242–53.
19. Zou M, Liu Y, Huang Z, Zhang M, Zhang P. Geological control of irreducible water within the coal matrix and its quantified evaluation model. ACS Omega. 2020;5: 9540–9.
20. Hodot BB. Outburst of coal and coalbed gas (Chinese Translation). Beijing: China Coal Industry Press; 1966.
21. Gan H, Walker PL, Nandi SP. Nature of porosity American coals. Fuel. 1972;51(2):272–7.
22. Fu X, Qin Y, Zhang W, Wei C, Zhou R. Fractal classification and natural classification of coal pore structure based on migration of coal bed methane. Chinese Sci Bull. 2005;50:66–71.
23. Yao Y, Liu D, Che Y, Tang D, Tang S, Huang W. Petrophysical characterization of coals by low-field nuclear magnetic resonance (NMR). Fuel. 2010;89(7):1371–80.
24. Li S, Tang D, Xu H, Yang Z. Advanced characterization of physical properties of coals with different coal structures by nuclear magnetic resonance and X-ray computed tomography. Comput Geosci. 2012;48:220–7.
25. Zou M, Wei C, Zhang M, Shen J, Chen Y, Qi Y. Classifying coal pores and estimating reservoir parameters and nuclear magnetic resonance and mercury intrusion porosimetry. Energ Fuel. 2013;27: 3699–708.
26. Yao Y, Liu D, Cai Y, Li J. Advanced characterization of pores and fractures in coals by nuclear magnetic resonance and X-ray computed tomography. Sci China Earth Sci. 2010;53(6):854–62.
27. Zheng S, Sang X, Yao Y, Liu D, Liu S, Wang M, et al. A multifractal-based method for determination NMR dual T2 cutoffs in coals. J Petrol Sci Eng. 2022;214:110488.
28. Kleinberg RL and Farooqui SA. T1/T2 ratio and frequency dependence of NMR relaxation in porous sedimentary rocks. J Colloid Interf Sci. 1993;158:195–8.
29. Timur A. Nuclear magnetic resonance study of carbonates rocks. Log Analyst. 1972;13:3–11.
30. Al-Mahrooqi SH, Grattoni CA, Moss AK, Jing XD. An investigation of the effect of wettability on NMR characteristics of sandstone rock and fluid systems. J Petrol Sci Eng.. 2003;39(3-4):389–98.
31. Yao Y and Liu D. Comparison of low-field NMR and mercury intrusion porosimetry in characterizing pore size distributions of coals. Fuel. 2012;95:152–8.
32. Zou Q, Zhang T, Ma T, Tian S, Jia X, Jiang Z. Effect of water-based SiO_2 nanofluid on surface wettability of raw coal. Energy. 2022;254:124228.

Mingjun Zou

is an associate professor in North China University of Water Resources and Electric Power. He received his BSc and PhD degrees from China University of Mining & Technology, in 2009 and 2014, respectively, and he is involved in coalbed methane geology and carbon storage technology.

Ningbo Cai

is a senior engineer in Hunan Geophysical and Geochemical Survey Institute. He received his MSc degree from China University of Geosciences in 2012. He is involved in coalbed methane geology.

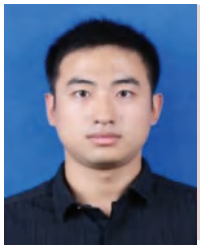

Keying Wang

is a senior engineer in Hunan Geophysical and Geochemical Survey Institute. He received his MSc degree from China University of Mining & Technology in 2014. He is involved in coalbed methane geology.

Zibin Ding

is a master's degree candidate in North China University of Water Resources and Electric Power, and he received his BSc degree in 2022 from this college. He is involved in carbon storage technology.

Linlin Yao

is a master's degree candidate in North China University of Water Resources and Electric Power, and he received his BSc degree in 2021 from this college. He is involved in reservoir reconstruction.

陈剑锋,杜云,熊伊曲等. 2023. 南岭加里东期钨锡矿床成矿机制研究:以湘西南落家冲矿床为例. 岩石学报,39(06): 1693-1716, doi: 10.18654/1000-0569/2023.06.07

南岭加里东期钨锡矿床成矿机制研究:以湘西南落家冲矿床为例*

陈剑锋[1,2,3] 杜云[2] 熊伊曲[3**] 管申进[4] 何红生[1,5] 周立同[2] 陆文[2] 石金江[2]

CHEN JianFeng[1,2,3], DU Yun[2], XIONG YiQu[3**], GUAN ShenJin[4], HE HongSheng[1,5], ZHOU LiTong[2], LU Wen[2] and SHI JinJiang[2]

1. 湖南省地球物理地球化学调查所,长沙 410116
2. 湖南省地质调查所,长沙 410116
3. 中南大学,有色金属成矿预测与地质环境监测教育部重点实验室,长沙 410083
4. 昆明理工大学国土资源工程学院,昆明 650093
5. 湖南省地质新能源勘探开发工程技术研究中心,长沙 410116

1. *Geophysical and Geochemical Survey Institute of Hunan, Changsha* 410116, *China*
2. *Geological Survey Institute of Hunan Province, Changsha* 410116, *China*
3. *MOE Key Laboratory of Metallogenic Prediction of Nonferrous Metals and Geological Environment Monitoring, Central South University, Changsha* 410083, *China*
4. *Faculty of Land Resource Engineering, Kunming University of Science and Technology, Kunming* 650093, *China*
5. *Engineering Technology Research Center for Geological New Energy Exploration and Development of Hunan Province, Changsha* 410116, *China*

2022-09-24 收稿, 2023-01-04 改回.

Chen JF, Du Y, Xiong YQ, Guan SJ, He HS, Zhou LT, Lu W and Shi JJ. 2023. Ore-forming mechanism of Caledonian W-Sn deposit in the Nanling Range: A case study from the Luojiachong deposit, sourthwestern Hunan Province. *Acta Petrologica Sinica*, 39(6): 1693-1716, doi: 10.18654/1000-0569/2023.06.07

Abstract Recently, many Caledonian W-Sn deposits have been discovered in the Nanling Range, whereas their ore-forming mechanism are still unclear. The Luojiachong deposit in the northwestern Miao'ershan batholith, southwestern Hunan Province, is a newly-discovered Caledonian W-Sn deposit. It is considered to be a promising tungsten-tin reserve, whilst the fluids evolution processes and ore genesis of the deposit still remain enigmatic. Based on detailed geological observation, the mineralization process can be divided into four ore-forming stages, namely altered granite-scheelite stage (Ⅰ), greisen-scheelite-cassiterite stage (Ⅱ), quartz-scheelite stage (Ⅲ) and quartz-sulfide stage (Ⅳ). We present new cassiterite and zircon U-Pb ages and zircon Hf isotopes of stage Ⅰ, as well as detailed fluid inclusion, H-O isotopic studies of quartz in all stages to constrain the ore genesis of the Luojiachong deposit. The cassiterite Tera-Wasserburg U-Pb age (433.0±11Ma, MSWD=0.75) is consistent with the zircon $^{206}Pb/^{238}U$ weighted mean age (430.7±2.3Ma, MSWD=0.05) of biotite monzogranite, suggesting that the W-Sn mineralization is spatial-temporally associated with the Late Caledonian biotite monzogranite. Fluid inclusion microthermometry shows that the homogenization temperatures of the fluid inclusions decrease from stage Ⅰ to stage Ⅳ (260~380℃ for stage Ⅰ, 260~320℃ for stage Ⅱ, 200~320℃ for stage Ⅲ and 180~220℃ for stage Ⅳ, respectively), whereas the salinities of the fluid inclusions drastically decrease from stages Ⅰ to Ⅱ and within a narrow range from stages Ⅱ to Ⅳ (ave. 16.9%, 3.9%, 4.8% and 3.7% NaCleqv, respectively). The ages of granite emplacement and mineralization, the characterics of ore-forming fluids, combined with zircon $\varepsilon_{Hf}(t)$ values (−7.6~−5.0) and two-stage model ages t_{DM2} (1565~1711 Ma), the $\delta^{18}O_{H_2O}$ value of quartz decreses from stage Ⅰ (3.97~5.34‰) to stage Ⅳ (−4.99~−5.10‰), as well as the reported geochemical analysis of Miao'ershan batholith, we suggest that the ore-forming material in

* 本文受湖南省自然科学基金项目(2021JJ30387)、中国地质调查局二级项目(DD20230055)、湖南省创新团队项目(2021RC4055)和中国地质调查局花岗岩成岩成矿地质研究中心开放基金(PMGR202006)联合资助.

第一作者简介: 陈剑锋,男,1985 年生,博士,高级工程师,矿物学、岩石学、矿床学专业,E-mail: chenjianfeng021041@163.com

** **通讯作者**:熊伊曲,男,1988 年生,副教授,博士后,从事矿床学的教学和科研工作,E-mail: xiongyiqu@126.com

Luojiachong deposit is derived from the partial melting of Proterozoic crustal which experiences highly fractionation. The fluid boiling and temperature reduction are the effective ore-forming mechanisms for the Luojiachong W-Sn deposit.

Key words Zircon and cassiterite U-Pb age; Fluid inclusions; H-O isotopes; Ore genesis; Caledonin W-Sn deposit

摘 要 近来南岭地区加里东期钨锡找矿勘查取得较大突破,但其成因机制研究仍相对缺乏。湘西南苗儿山岩体西北部的落家冲矿床是近年新发现的加里东期钨锡矿床,具有良好的钨锡多金属矿找矿前景,其成矿流体的特征和成矿机制有待查明。在详细的野外地质调查基础上,落家冲矿床的成矿过程可划分为四个阶段:蚀变花岗岩-白钨矿阶段(Ⅰ)、云英岩-白钨矿-锡石阶段(Ⅱ)、石英脉-白钨矿阶段(Ⅲ)和石英脉-硫化物阶段(Ⅳ)。本文选取第Ⅰ阶段的锆石和锡石开展了 U-Pb 定年和锆石 Hf 同位素分析,对四个成矿阶段的石英矿物进行了流体包裹体以及 H-O 同位素的研究。获得的锡石 U-Pb 反等时线年龄(433.0±11Ma)与蚀变花岗岩锆石 U-Pb 年龄(430.7±2.3Ma)在误差范围内一致,表明矿区的成岩成矿作用均发生于加里东晚期。流体包裹体研究显示第Ⅰ阶段到第Ⅳ阶段,均一温度分别集中在 260~380℃、260~320℃、200~320℃和 180~220℃之间,呈逐渐降低的趋势,盐度则表现为由第Ⅰ阶段到第Ⅱ阶段陡降,第Ⅱ阶段到第Ⅳ阶段总体变化不大的特点(平均值分别为 16.9%、3.9%、4.8%和 3.7% NaCleqv)。成岩成矿定年结果、各成矿阶段的成矿流体特征,结合锆石 $\varepsilon_{Hf}(t)=-7.6\sim-5.0$、$t_{DM2}=1565\sim1711$Ma,和石英矿物的 $\delta^{18}O_{H_2O}$ 值从第Ⅰ阶段(3.97‰~5.34‰)到第Ⅳ阶段(-4.99‰~-5.10‰)逐渐降低的特点,以及区域岩体的地球化学特征,本文认为落家冲钨锡矿床是加里东期起源于元古宙地壳重熔的岩浆在经历了高分异演化作用后,流体的沸腾作用以及温度下降造成成矿流体中钨锡等矿质的沉淀所形成。

关键词 锆石和锡石 U-Pb 定年;流体包裹体;H-O 同位素;成矿机制;加里东期钨锡矿床

中图法分类号 P597; P618.44; P618.67

南岭地区是我国重要的钨锡金属矿集区,长期以来,这些钨锡多金属矿床以及与之成因相关的多时代花岗岩类(Mao *et al.*, 2013a, b, 2019; 陈懋弘等, 2015, 2020; Yuan *et al.*, 2018a; Zhao *et al.*, 2022a; 毛景文等, 2023; 吴福元等, 2023)一直是矿床学研究领域的热点,其中该区与燕山期花岗岩(180~80Ma)相关的"成矿作用大爆发"(华仁民和毛景文, 1999; 华仁民等, 2005; 毛景文等, 1999, 2007)更是得到了长期高度的关注(Mao *et al.*, 2013a, 2019, 2021a; 袁顺达等, 2012a, b; Yuan *et al.*, 2015, 2019; 毛景文等, 2018; Zhao *et al.*, 2018; 蒋少涌等, 2020),取得了一系列瞩目成果。随着钨锡成矿作用的研究与地质找矿工作的持续推进,该区钨锡成矿理论不断得到丰富,同时也推动了南岭钨(锡)矿床找矿工作的重大突破(陈郑辉等, 2015; 盛继福等, 2015; 袁顺达, 2017; 袁顺达等, 2020; 毛景文等, 2020; 蒋少涌等, 2020),如湘南荷花坪、川口、水源山、江西青山、仙鹅塘以及广西栗木、李贵福等一批中大型钨锡多金属矿床均已被证实形成于印支期(蔡明海等, 2006; 刘善宝等, 2008; 杨锋等, 2009; Zhang *et al.*, 2015; 彭能立等, 2017; Zhao *et al.*, 2018; Qin *et al.*, 2020),其成矿时代多发生于230~210Ma之间(谢桂青等, 2021)。

南岭地区加里东期的花岗岩在出露规模上仅次于燕山期(华仁民等, 2013; Mao *et al.*, 2021b),华仁民等(2013)指出加里东期花岗岩在成矿方面的重要贡献是为燕山期钨锡成矿作用的大爆发提供预富集,其晚期分异演化充分的花岗岩也可直接形成钨锡矿床。最初李晓峰等(2006)在南岭西段识别出加里东期的钨锡成矿作用,其获得广西桂岭岩体白石顶钼(钨)矿床的辉钼矿 Re-Os 年龄为 424.6±5.7Ma;随后在大瑶山地区陆续有关于加里东期钨多金属矿床的系列报导,如高精度的测年结果显示该区玉坡、社垌、武界、上木水等钨多金属矿床(点)的成矿年龄多介于 446~432Ma 之间(陈懋弘等, 2011, 2012; Jiang *et al.*, 2017; Dang *et al.*, 2018, 2020)。近年在苗儿山-越城岭岩体内新发现的独石岭、李家、牛塘界、平滩等大中型钨锡多金属矿床同样被证实形成于加里东期(Yang *et al.*, 2014; 豆浩然等, 2018; Chen *et al.*, 2019; 张强和陆建军, 2019; Li *et al.*, 2019),其成矿年龄多介于 430~410Ma。因此,大瑶山地区和苗儿山-越城岭地区是南岭目前已知的两个重要加里东期钨(锡)多金属矿集区(Zhang *et al.*, 2017; 陈懋弘等, 2020)。尽管以往围绕南岭地区加里东期钨锡矿床的成矿作用有了系列研究,但总体上关于加里东期钨锡矿床的成矿机制仍较模糊,有待进一步的精细厘定。

位于南岭西段苗儿山岩体西北部的落家冲钨锡矿床在成矿类型上具有多样性,包括有蚀变花岗岩型、云英岩型和石英脉型,在整个南岭地区加里东期的矿床中具有很强的代表性。本文选取落家冲钨锡矿床为研究对象,在详细的野外调查基础上,利用锆石和锡石 U-Pb 定年获得矿床准确的成岩成矿时代,通过系统研究矿床石英矿物中流体包裹体的岩相学、显微测温、激光拉曼成分等特征,结合各阶段石英的 H-O 同位素组成,以揭示落家冲钨锡矿床成矿流体的来源及演化过程,为探讨南岭地区加里东期钨锡矿床的成矿机制提供有利信息。

1 区域地质与矿区地质特征

苗儿山-越城岭岩体位于南岭西段,在大地构造上属华夏地块与扬子地块结合部位的西侧,该岩体为一出露面积大于 3000km^2、主要由加里东期和印支期花岗岩组成的复式花岗岩基(程顺波等, 2016),新-资超大型断裂带把其分为西

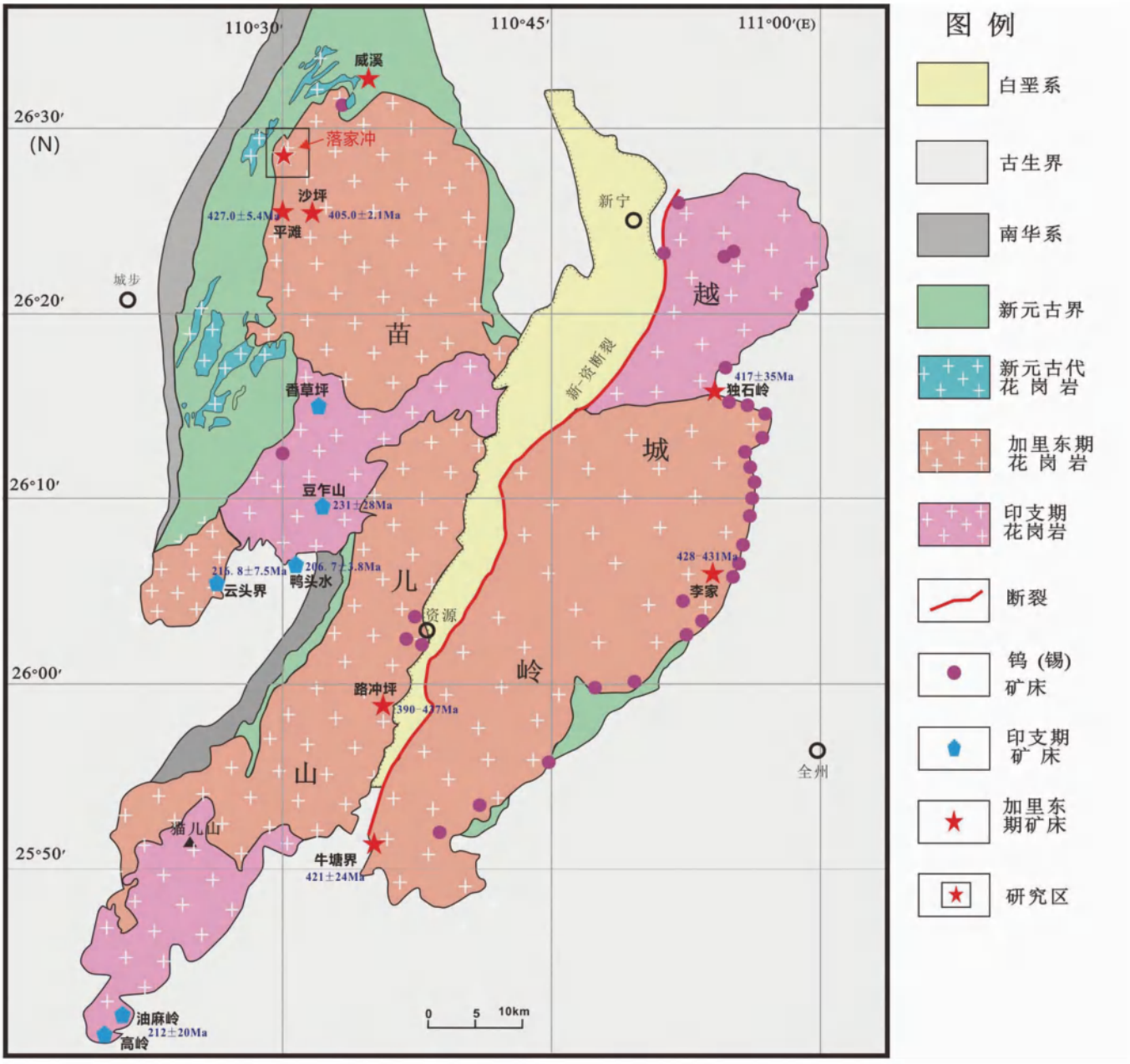

图 1 苗儿山-越城岭岩体地质简图（据 Chen *et al.*，2019；Li *et al.*，2019 修改）

Fig. 1 Simplified geological map of the Miao'ershan-Yuechengling pluton (modified after Chen *et al.*, 2019; Li *et al.*, 2019)

侧的苗儿山岩体和东侧的越城岭岩体（图 1）。岩体与（前）志留系呈侵入接触关系，与泥盆系-白垩系呈沉积接触。在该岩基周边或内部陆续发现有百余个钨锡矿床（点）（Yang *et al.*，2014；Chen *et al.*，2016），是南岭地区印支-加里东期重要的钨锡矿集区（Zhang *et al.*，2017）。其中越城岭岩体内部的独石岭铜钨矿、李家锡矿以及牛塘界钨矿床均形成于加里东期（Yang *et al.*，2014；Chen *et al.*，2016；张强和陆建军，2019；Li *et al.*，2019；Zhu *et al.*，2020），而与之相邻的苗儿山岩体中印支期和加里东期的钨锡矿床均有产出：印支期的云头界钨钼矿床和高岭（油麻岭）钨矿床（伍静等，2012；张迪等，2015）；加里东期的路冲坪、平滩、落家冲、沙坪等钨锡多金属矿床（Zhang *et al.*，2017；Chen *et al.*，2019；杜云等，2022；周立同等，2022）。

落家冲钨锡矿床位于湘西南苗儿山岩体西北部，该矿床以钨锡矿为主，伴生铜、钼等矿化，其钨锡矿的远景资源量可达大型规模（杜云等，2022）。地层主要出露于西北部，为青白口纪黄狮洞组粉砂质板岩、绢云母板岩、云母石英片岩等，总体走向为北东，倾向北西（290°～330°），倾角 45°～65°。区内断裂发育，主要分为 NE 向和近 EW 向的两组，其中 NE 向的断裂是区内最主要的一组断裂，倾向以南东为主，次为北西，倾角多介于 60°～80°。该组断裂多产于花岗岩体内部，规模较大者对花岗岩有明显切割破坏作用（图 2）。近 EW 向断裂，倾向北，倾角 70°～80°，可见其切割岩体与青白口系，致地层与岩体接触界线在断层处发生明显位错。

矿区岩浆岩发育，新元古代中粒片麻状黑云母二长花岗岩局部出露于矿区西北部，多见初糜棱岩化，绿泥石化、绢云

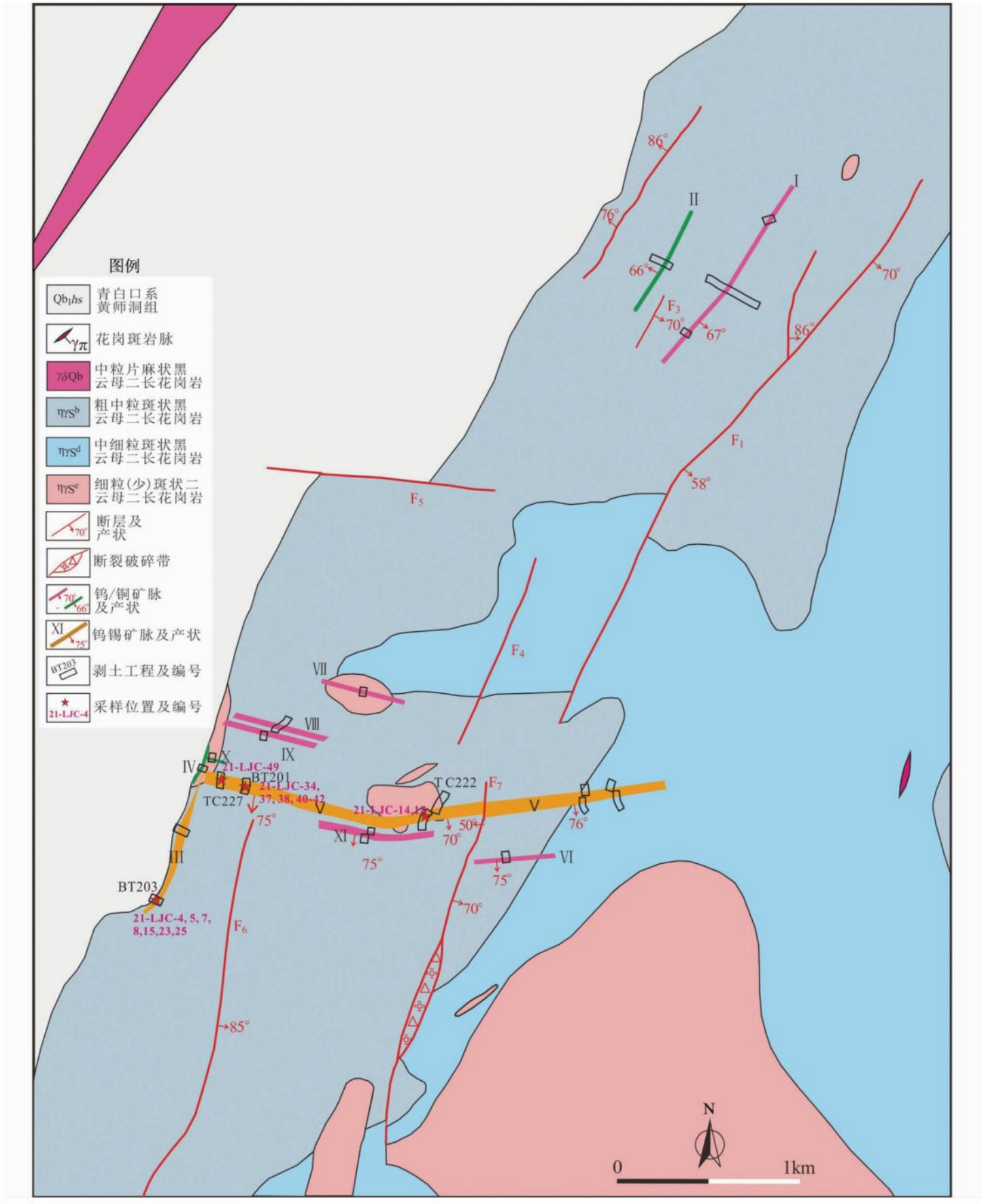

图 2 落家冲钨锡矿区地质简图(据杜云等, 2022 修改)

Fig. 2 Simplified geological map of the Luojiachong W-Sn deposit (modified after Du *et al.*, 2022)

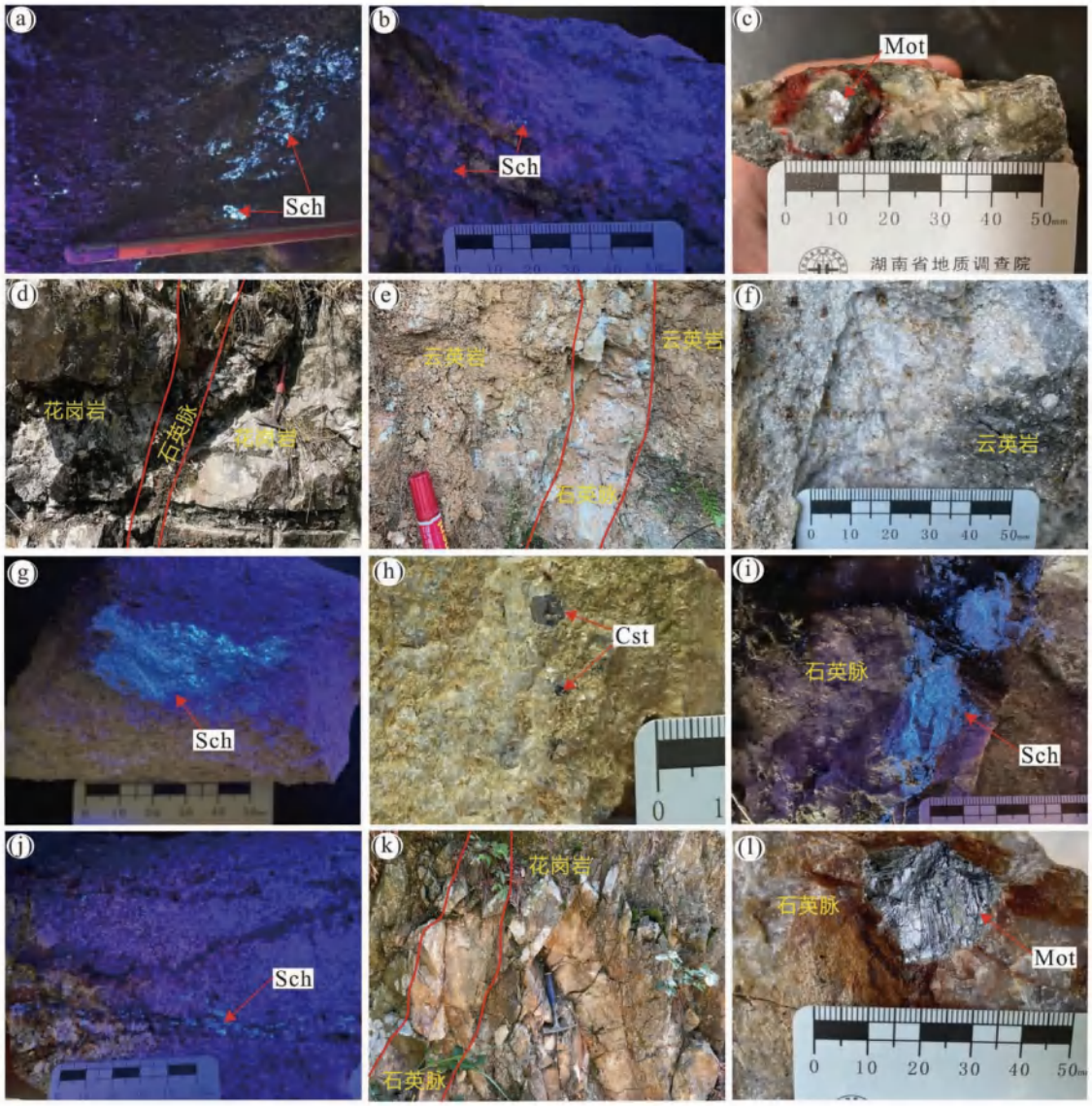

图 3 落家冲钨锡矿区岩(矿)石手标本特征

(a)第Ⅰ阶段蚀变花岗岩中的集合体状白钨矿；(b)第Ⅰ阶段蚀变花岗岩中的浸染状白钨矿；(c)第Ⅰ阶段蚀变花岗岩中的辉钼矿；(d)第Ⅲ阶段石英脉侵入于第Ⅰ阶段的蚀变花岗岩中；(e)第Ⅲ阶段石英脉侵入于第Ⅱ阶段的云英岩中；(f)云英岩；(g)云英岩中的白钨矿；(h)云英岩中的锡石；(i)石英脉中的白钨矿；(j)石英细脉中的白钨矿；(k)第Ⅳ阶段石英脉侵入于第Ⅰ阶段蚀变花岗岩中；(l)第Ⅳ阶段石英脉中的辉钼矿. Cst-锡石；Sch-白钨矿；Mot 辉钼矿

Fig. 3 Alteration and mineralization characteristics of the ore-hosting granite and tungsten ore in Luojiachong deposit

(a) scheelite aggregate in the altered granite of stage Ⅰ; (b) disseminated scheelite in the altered granite of stage Ⅰ; (c) molybdenite mineralization in the altered granite of stage Ⅰ; (d) quartz vein of stage Ⅲ intruded in altered granite of stage Ⅰ; (e) quartz vein of stage Ⅲ intruded in greisen of stage Ⅱ; (f) greisen; (g) scheelite mineralization in greisen; (h) cassiterite mineralization in greisen; (i) scheelite mineralization in quartz vein; (j) scheelite mineralization in quartz veinlet; (k) quartz vein of stage Ⅳ intruded in altered granite of stage Ⅰ; (l) molybdenite mineralization in quartz vein of stage Ⅳ. Cst-cassiterite; Sch-scheelite; Mot-molybdenite

母化等蚀变较强。加里东期花岗岩大面积出露于矿区西南部，可分为三个期次，从早到晚分别为：粗中粒斑状黑云母二长花岗岩($\eta\gamma S^b$)、中细粒斑状二云母花岗岩($\eta\gamma S^d$)和细粒(少斑状)二云母二长花岗岩($\eta\gamma S^e$)。其中粗中粒斑状黑云母二长花岗岩为矿区的主要赋矿围岩(图 3a-c)，主要呈似斑状花岗结构，块状构造，岩石斑晶主要为斜长石和石英(8% ~12%)，粒径多介于 8 ~20mm 之间，基质主要为斜长石(20% ~25%)、钾长石(25% ~35%)、石英(30% ~40%)和黑云母(6% ~10%)，副矿物主要有磷灰石、锆石、独居石、金红石等。岩石局部(特别是矿化部位)见有明显的绿泥石化、绢云母化、绿帘石化等蚀变(图 4a)。中细粒斑状二云母花岗岩与粗中粒斑状黑云母二长花岗岩的矿物组成基本相同，但粒径差别较大(图 3j)。细粒二云母二长花岗岩的斑晶主要为斜长石和石英(<5%)，粒径多介于 4 ~8mm 之间，基质主要包括斜长石(25% ~30%)、钾长石(25% ~30%)、石英(25% ~35%)、黑云母(6% ~8%)和白云母(2% ~5%)，粒

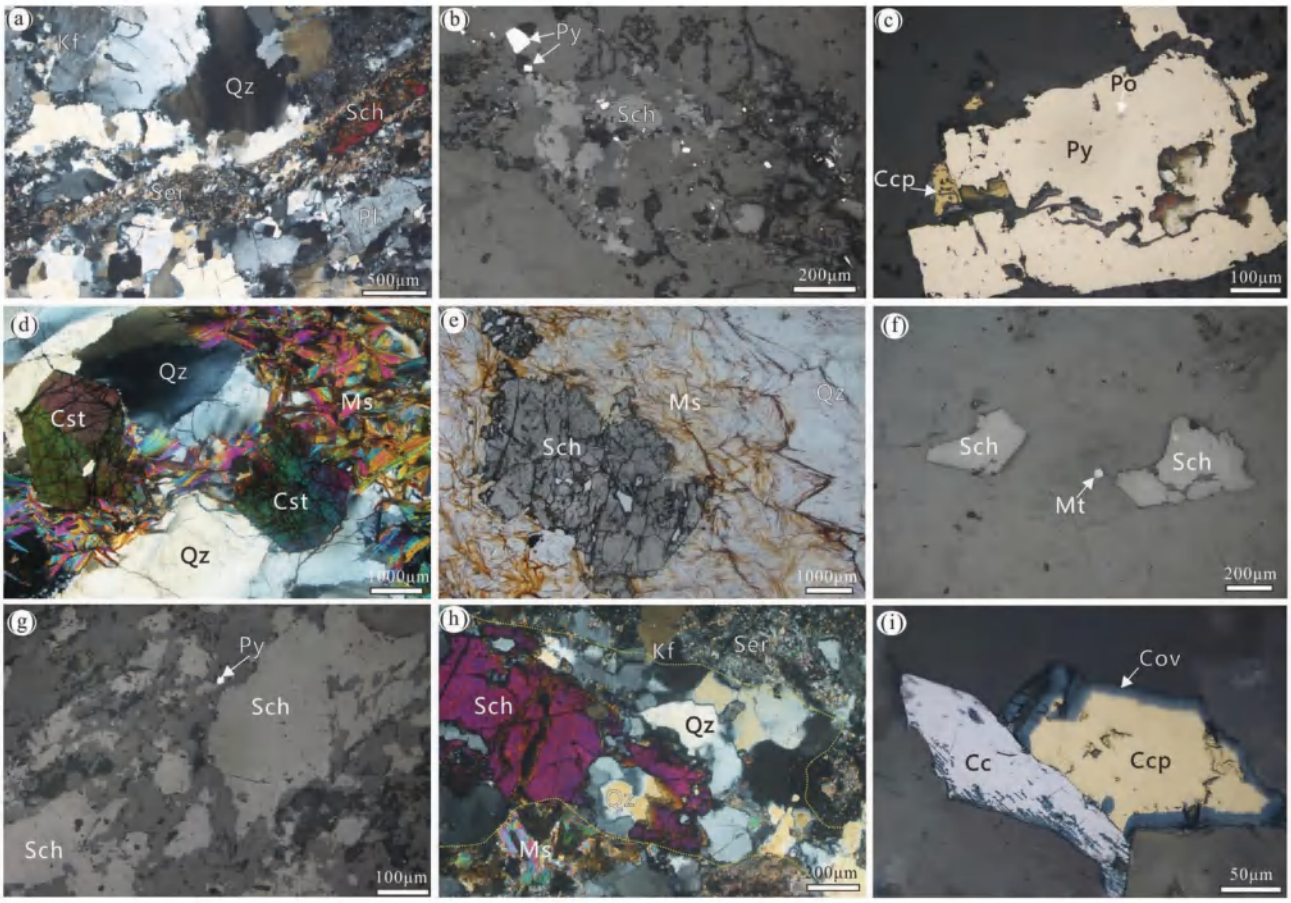

图 4 落家冲钨锡矿区矿物显微镜下特征

(a)蚀变花岗岩中的绢云母化和白钨矿;(b)蚀变花岗岩中白钨矿与黄铁矿共生;(c)蚀变花岗岩中黄铁矿、磁黄铁矿与黄铜矿共生;(d)云英岩中的锡石;(e)云英岩中的白钨矿;(f)石英脉中白钨矿与磁铁矿;(g)石英脉中的白钨矿与黄铁矿;(h)石英细脉中的白钨矿;(i)石英脉中的黄铜矿、铜蓝和辉铜矿. Cc-斑铜矿;Ccp-黄铜矿;Cov-铜蓝;Kf-钾微斜长石;Mt-磁铁矿;Ms-白云母;Pl-斜长石;Po-磁黄铁矿;Py-黄铁矿;Qz-石英;Ser-绢云母

Fig. 4 Photomicrographs of the ores from the Luojiachong W-Sn deposit

(a) sericite and scheelite in altered granite ore; (b) scheelite coexisting pyrite in altered granite ore; (c) pyrite coexisting pyrrhotite and chalcopyrite in altered granite ore; (d) cassiterite mineralization in greisen; (e) scheelite mineralization in greisen; (f) scheelite and magnetite in quartz vein; (g) scheelite and pyrite in quartz vein; (h) scheelite in quartz veinlet; (i) chalcopyrite coexisting covellite and chalcocite in quartz vein. Cc-chalcocite; Ccp-chalcopyrite; Cov-covellite; Kf-K-feldspar; Mt-magnetite; Ms-muscovite; Pl-plagioclase; Po-pyrrhotite; Py-pyrite; Qz-quartz; Ser-sericite

径均小于2mm;副矿物有金红石、锆石、独居石、磷灰石、电气石等,同时岩石有明显的绿泥石化、绢云母化、绿帘石化等蚀变。

矿区内的矿体均产于岩体内部,矿体呈脉状产出,共发现钨锡多金属矿脉共11条(图2),矿脉的走向与矿区内的断裂走向相似,矿(化)体厚度介于0.6~100m之间,矿体真厚度介于0.5~30.8m之间,地表探槽、剥土所揭露矿体的WO_3平均品位为0.120%~0.446%,Sn平均品位为0.234%~0.317%,Cu的平均品位为0.280%~0.760%。3号和5号矿脉为矿区规模最大的两条钨锡矿脉,3号矿脉走向北东,倾向北西,倾角多大于70°,地表工程控制其走向长大于1.0km,达工业品位的矿体厚度为2.0~14.1m,其矿化类型以蚀变花岗岩型为主(图3a-d),次为石英脉型和云英岩型;5号脉走向近东西,倾向南,倾角多介于70°~80°,地表工程对其控制走向长大于2.5km,达工业品位的矿体厚度为0.9~30.8m,矿化类型以云英岩型(图3e-h)和石英脉型为主(图3i, j),蚀变花岗岩型少见。矿区内的矿石矿物主要为白钨矿与锡石,伴生黄铜矿和辉钼矿(图3c)。脉石矿物中的金属矿物见有黄铁矿、磁铁矿、磁黄铁矿、毒砂等,非金属矿物主要有石英、钾长石、斜长石,白云母,其次为绿泥石、绢云母、黑云母、绿帘石、褐帘石等。

根据野外观察到的矿脉间的相互穿插关系及矿物共生组合,本文将矿区的成矿过程划分为四个阶段(图5):其中第Ⅰ阶段为蚀变花岗岩-白钨矿阶段,该阶段金属矿物主要有白钨矿(图3a, b),见有少量锡石、辉钼矿、黄铁矿、黄铜矿、磁黄铁矿和闪锌矿(图3c、图4b, c),非金属矿物主要有石英、钾长石、斜长石,其次为绢云母、绿泥石、黑云母、绿帘石、褐帘石等,白钨矿主要呈浸染状或集合状(图3a, b),半

图 5 落家冲矿区各成矿阶段矿物生成顺序图

Fig. 5 Paragenetic sequence of minerals from the Luojiachong deposit

自形-他形，粒径 1 ~ 4mm；第Ⅱ阶段为云英岩-白钨矿-锡石阶段，见云英岩呈近直立脉状穿插于蚀变花岗岩内部，脉宽 0.6 ~ 2.0m，该阶段金属矿物主要有锡石和白钨矿（图 3d-h、图 4d，e），含少量黄铁矿、金红石、磁铁矿和赤铁矿等，非金属矿物主要为石英和白云母，含少量绿泥石，锡石多为自形-半自形，可见有明显的生长环带（图 3h、图 4d），粒径介于 0.1 ~ 5.0mm 间，白钨矿呈他形粒状或集合状分布于石英及白云母等的粒间（图 3g、图 4e），矿物粒径多介于 0.2 ~ 3mm；第Ⅲ阶段为石英脉-白钨矿阶段，该阶段石英脉有两种形式，其一为呈大脉状（宽 5 ~ 90cm）侵入于云英岩或蚀变花岗岩中（图 3i），其二为呈密集细脉状（ < 1cm）分布于花岗岩内部（图 3j），该阶段金属矿物主要为白钨矿，见少量黄铁矿、毒砂、黄铜矿、钛铁矿、金红石等（图 4f-h），非金属矿物主要为石英，白钨矿主要呈他形粒状或集合状，粒径多介于 0.1 ~ 3.0mm 间（图 3i，j）；第Ⅳ阶段为石英脉-硫化物阶段，该阶段金属矿物主要为黄铜矿和辉钼矿（图 3k，l），其次为黄铁矿、斑铜矿、铜蓝（图 4i）等，非金属矿物主要为石英。其中第Ⅰ阶段为北东向矿脉的主要成矿阶段，第Ⅱ阶段和第Ⅲ阶段为近东西向矿脉的主要成矿阶段。

2 采样和测试方法

用于锆石 U-Pb 定年（21-LJC-4）以及锡石 U-Pb 定年（21-LJC-15）的样品采集于矿区的 3 号矿脉，地表 BT203 内，其经纬度位置为 110°29′59.5″E、26°29′21.0″N；不同成矿阶段用于流体包裹体显微测温和 H-O 同位素分析的石英样品采集于矿区具典型代表性的 3 号和 5 号矿脉，详细采样位置及样品特征见图 2 和表 1。

锆石单矿物是在无污染的环境下用人工重砂方法分离（包括手工碎样、水洗、磁选），然后在双目镜下挑选，选出晶形较好、具代表性的锆石用环氧树脂充分固定、抛光，制成样品靶。锡石样品采用常规重选法粗选，然后在双目镜下挑选出粒度较大、透明度较好的锡石颗粒进行制靶。锆石和锡石的制靶、透射光、反射光和阴极发光（CL）在河北省欣航测绘院岩矿实验测试中心完成。锆石的 U-Pb 定年以及 Hf 同位素分析和锡石的 U-Pb 定年均在武汉上谱分析科技有限责任公司完成，分析数据的离线处理（包括对样品和空白信号的选择、同位素质量分馏校正）均采用软件 ICPMSDataCal（Liu *et al.*，2008）完成。流体包裹体的岩相学观察、显微测温在武汉地质调查中心流体包裹体实验室完成，激光拉曼探针成分分析在昆明理工大学国土资源工程学院完成。石英 H、O 同位素的分析测试在中国科学院地球化学研究所矿床地球化学国家重点实验室完成。

2.1 锆石 U-Pb 定年和 Hf 同位素分析

锆石 U-Pb 同位素定年利用 LA-ICP-MS 分析完成。

表 1 落家冲钨锡矿区测试样品相关信息表

Table 1 Information of analytical samples in Luojiachong deposit

样品号	成矿阶段	采样位置	样品测试	样品描述
21-LJC-4	Ⅰ	BT203	锆石 U-Pb 定年和 Hf 同位素分析	含白钨矿、黄铁矿的蚀变花岗岩
21-LJC-7		BT203	流体包裹体显微测温、激光拉曼	含白钨矿、黄铁矿的蚀变花岗岩
21-LJC-8		BT203	流体包裹体显微测温、激光拉曼	含白钨矿、黄铁矿的蚀变花岗岩
21-LJC-15		BT203	锡石 U-Pb 定年	含白钨矿、锡石的蚀变花岗岩
21-LJC-23		BT203	H-O 同位素	含白钨矿、黄铁矿的蚀变花岗岩
21-LJC-25		BT203	H-O 同位素	含白钨矿、黄铁矿的蚀变花岗岩
21-LJC-14	Ⅱ	TC222	流体包裹体显微测温、H-O 同位素	含白钨矿、锡石的云英岩,穿插于第Ⅰ阶段
21-LJC-18		TC222	H-O 同位素	
21-LJC-34		BT201	流体包裹体显微测温、激光拉曼	
21-LJC-37	Ⅲ	BT201	H-O 同位素	含白钨矿石英脉,穿插于第Ⅱ阶段
21-LJC-38		BT201	H-O 同位素	
21-LJC-40		BT201	流体包裹体显微测温、激光拉曼	
21-LJC-41		BT201	流体包裹体显微测温	
21-LJC-5	Ⅳ	BT203	H-O 同位素	含黄铜矿、辉钼矿石英脉
21-LJC-42		BT201	H-O 同位素	
21-LJC-49		TC227	流体包裹体显微测温、激光拉曼	

GeolasPro 激光剥蚀系统由 COMPexPro 102 ArF 193 nm 准分子激光器和 MicroLas 光学系统组成,ICP-MS 型号为 Agilent 7900。本次分析的激光束斑和频率分别为 44μm 和 8Hz。U-Pb 同位素定年和微量元素含量处理中采用锆石标准 91500 和玻璃标准物质 NIST610 作外标分别进行同位素和微量元素分馏校正。原始测试数据用 ICPMSDataCal 软件进行处理(Liu *et al.*, 2008)。普通 Pb 校正方法参照 Andersen (2002),^{206}Pb-^{238}U 加权平均年龄与谐和图解由 ISOPLOT 软件获得(Ludwig, 2003),单个数据点误差均为 1σ。

锆石 Hf 同位素测试所用激光剥蚀系统为 Geolas HD, MC-ICP-MS 为 Neptune Plus。分析过程同时配备了信号平滑装置以提高信号稳定性和同位素比值测试精密度(Hu *et al.*, 2015)。激光输出能量密度为 7.0J/cm^2。采用单点剥蚀模式,束斑固定为 44μm。详细仪器操作条件和分析方法参照文献(Hu *et al.*, 2012)。为确保分析数据的可靠性,Plešovice、91500 和 GJ-1 三个国际锆石标准与实际样品同时分析(Zhang and Hu, 2020),Plešovice 用于进行外标校正以进一步优化分析测试结果。

2.2 锡石 U-Pb 定年

锡石 U-Pb 同位素定年使用的 GeolasPro 激光剥蚀系统由 COMPexPro 102 ArF 193 nm 准分子激光器和 MicroLas 光学系统组成,ICP-MS 型号为 Agilent 7900。本次分析的激光束斑、频率和能量密度分别为 44μm、3Hz 和 5J/cm^2,锆石 91500(Wiedenbeck *et al.*, 1995)作为外标以进行 Pb/U 分馏和质量歧视校正,锡石 AY-4 作为未知样品进行分析。在本研究中,AY-4 的 9 次分析中获得的$^{206}Pb/^{238}U$ 年龄加权平均值为 159.6±2.5Ma,与参考年龄 158.2±0.4Ma 在误差范围内一致(Yuan *et al.*, 2011)。玻璃标准物质 NIST610 作外标进行微量元素含量校正(Liu *et al.*, 2010)。锡石样品的 U-Pb 年龄图件运用 Isoplot 4.1(Ludwig, 2012)完成,将实验数据运用 Tera Wasserburg 图解(Tera and Wasserburg, 1972)得到的纵轴交点及普通铅$^{207}Pb/^{206}Pb$ 的比值,下交点即为锡石的形成年龄。

2.3 流体包裹体测温

实验使用的仪器是英国产的 Linkam THMS 600 型冷热台,可测温度为 -196 ~ +600℃。实验过程中为防止包裹体在加热过程中爆裂,先进行冷冻测温。0 ~ 600℃ 的精度为 ±2℃,0 ~ -196℃ 的精度为 ±0.1℃,气液两相包裹体均一温度测试在冰点值附近升温速率为 0.2℃/min,达到均一时的升温速率为 0.5℃/min。对于含子矿物包裹体,在升温过程中仔细观察气、液、固三相的变化,并记录其子矿物消失温度及均一温度,当温度接近相变点时,升温速率为 0.2 ~ 0.5℃/min。

2.4 激光拉曼探针分析

激光拉曼探针成分分析使用 Renishaw in Via 型显微共焦激光拉曼光谱仪,激光功率为 25mW,激光波长为 514.53nm,空间分辨率为 1 ~ 2μm,积分时间一般为 30 ~ 60s,1000 ~ 4000cm^{-1} 全波段一次取峰。采用激光束斑直径约为 1μm,光谱分辨率为 1 ~ 2cm^{-1}。主要对矿区四个成矿阶段石英矿物中的流体包裹体的气相、液相及子矿物成分进行了分析。

2.5 H-O 同位素分析

氢、氧同位素组成分别利用 MAT-253 型气体同位素质谱仪和 Delta v advantage 气体同位素质谱仪测定,氢同位素组成分析精度为 ±2‰,氧同位素组成分析精度为 0.2‰。

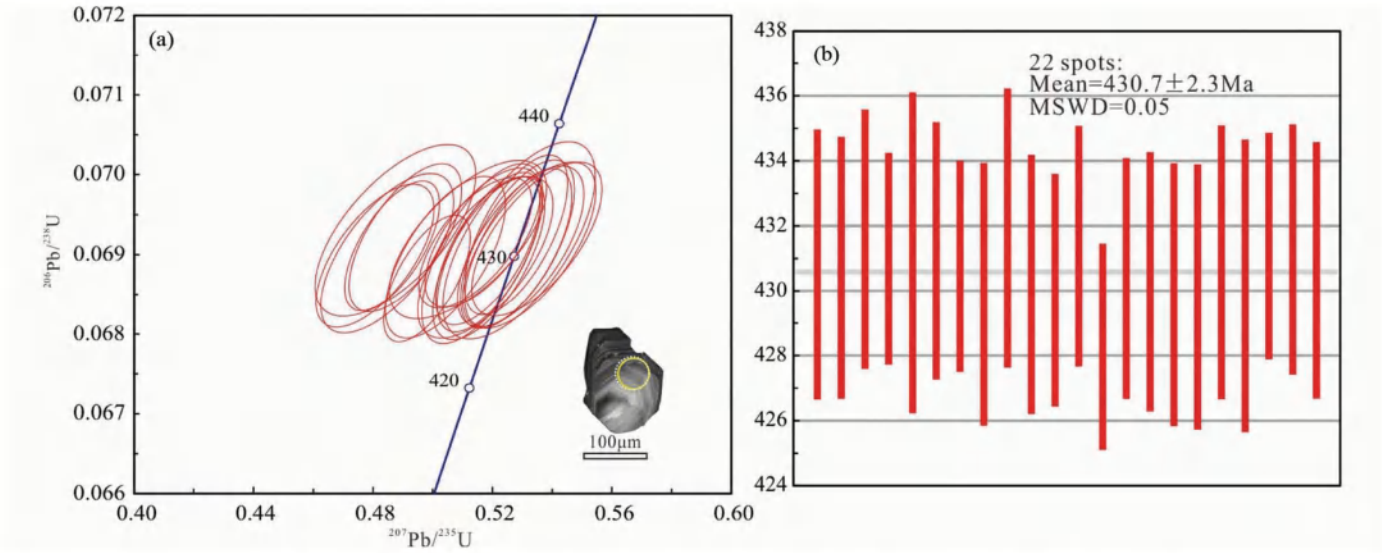

图 6 落家冲钨锡矿区黑云母二长花岗岩(样品 21-LJC-4)的 U-Pb 年龄谐和图(a)和加权平均年龄图(b)

Fig. 6 U-Pb concordia age plot (a) and weighted average diagram (b) of the Luojiachong biotite monzogranite (Sample 21-LJC-4)

表 2 落家冲钨锡矿区黑云母二长花岗岩(样品 21-LJC-4)LA-ICP-MS 锆石 U-Pb 定年结果

Table 2 Zircon U-Pb dating results of the Luojiachong biotite monzogranite (Sample 21-LJC-4)

测点号	含量($\times10^{-6}$)		Th/U	同位素比值						年龄(Ma)					
	^{232}Th	^{238}U		$\frac{^{207}Pb}{^{206}Pb}$	1σ	$\frac{^{207}Pb}{^{235}U}$	1σ	$\frac{^{206}Pb}{^{238}U}$	1σ	$\frac{^{207}Pb}{^{206}Pb}$	1σ	$\frac{^{207}Pb}{^{235}U}$	1σ	$\frac{^{206}Pb}{^{238}U}$	1σ
-01	1669	3224	0.52	0.05530	0.00158	0.53229	0.01471	0.06912	0.00069	433.4	60.2	433.3	9.8	430.8	4.2
-02	1644	1830	0.90	0.05522	0.00155	0.52951	0.01396	0.06910	0.00067	420.4	58.3	431.5	9.3	430.7	4.0
-03	3892	7334	0.53	0.05471	0.00115	0.52794	0.01140	0.06924	0.00066	466.7	50.9	430.4	7.6	431.6	4.0
-04	2340	5217	0.45	0.05352	0.00133	0.51426	0.01248	0.06915	0.00054	350.1	55.6	421.3	8.4	431.0	3.3
-05	1379	1057	1.30	0.05546	0.00180	0.52893	0.01683	0.06918	0.00082	431.5	67.6	431.1	11.2	431.2	4.9
-06	4160	1779	2.34	0.05358	0.00187	0.51184	0.01737	0.06919	0.00066	353.8	79.6	419.7	11.7	431.2	4.0
-07	4612	5001	0.92	0.05091	0.00108	0.48639	0.01047	0.06911	0.00054	235.3	48.1	402.4	7.2	430.8	3.2
-08	5434	2098	2.59	0.05297	0.00131	0.50427	0.01327	0.06896	0.00067	327.8	25.0	414.6	9.0	429.9	4.0
-09	1761	1341	1.31	0.05108	0.00187	0.48752	0.01777	0.06930	0.00071	242.7	80.5	403.2	12.1	431.9	4.3
-10	6922	2451	2.82	0.05103	0.00150	0.48479	0.01469	0.06901	0.00066	242.7	68.5	401.4	10.1	430.2	4.0
-11	2396	3064	0.78	0.05057	0.00133	0.48068	0.01303	0.06898	0.00059	220.4	56.5	398.5	8.9	430.0	3.6
-12	2708	2906	0.93	0.05144	0.00127	0.49085	0.01244	0.06921	0.00061	261.2	52.8	405.5	8.5	431.4	3.7
-13	7038	13954	0.50	0.05248	0.00103	0.49810	0.00957	0.06870	0.00052	305.6	44.4	410.4	6.5	428.3	3.2
-14	1833	3687	0.50	0.05429	0.00118	0.51849	0.01153	0.06904	0.00061	383.4	43.5	424.1	7.7	430.4	3.7
-15	5049	8888	0.57	0.05417	0.00113	0.51902	0.01160	0.06903	0.00066	388.9	50.9	424.5	7.8	430.3	4.0
-16	955	2068	0.46	0.05420	0.00162	0.51763	0.01493	0.06896	0.00067	388.9	73.1	423.6	10.0	429.9	4.0
-17	2564	3694	0.69	0.05421	0.00132	0.51878	0.01237	0.06895	0.00068	388.9	55.6	424.3	8.3	429.8	4.1
-18	5305	2535	2.09	0.05506	0.00135	0.52841	0.01260	0.06913	0.00070	413.0	55.6	430.8	8.4	430.9	4.2
-19	1212	1978	0.61	0.05403	0.00144	0.51664	0.01336	0.06901	0.00074	372.3	61.1	422.9	9.0	430.2	4.5
-20	2768	2063	1.34	0.05365	0.00136	0.51680	0.01276	0.06921	0.00058	366.7	57.4	423.0	8.5	431.4	3.5
-21	2371	1426	1.66	0.05556	0.00152	0.53487	0.01440	0.06919	0.00064	435.2	61.1	435.0	9.5	431.3	3.8
-22	2573	4101	0.63	0.05488	0.00121	0.52869	0.01184	0.06909	0.00065	405.6	45.4	430.9	7.9	430.6	3.9

3 测试结果

3.1 锆石 U-Pb 定年结果

本次研究从蚀变粗中粒斑状黑云母二长花岗岩(样品 21-LJC-4)中分离出来的锆石呈自形、长柱状、透明-半透明(图 6a),粒径多介于 100 ~ 150μm 之间,在阴极发光条件下显示出岩浆锆石所特有的韵律环带(吴元保和郑永飞,2004),锆石 Th/U 比值基本大于 0.5(表 2),这些特征表明属于岩浆型锆石(Hoskin and Schaltegger, 2003; 吴元保和郑永

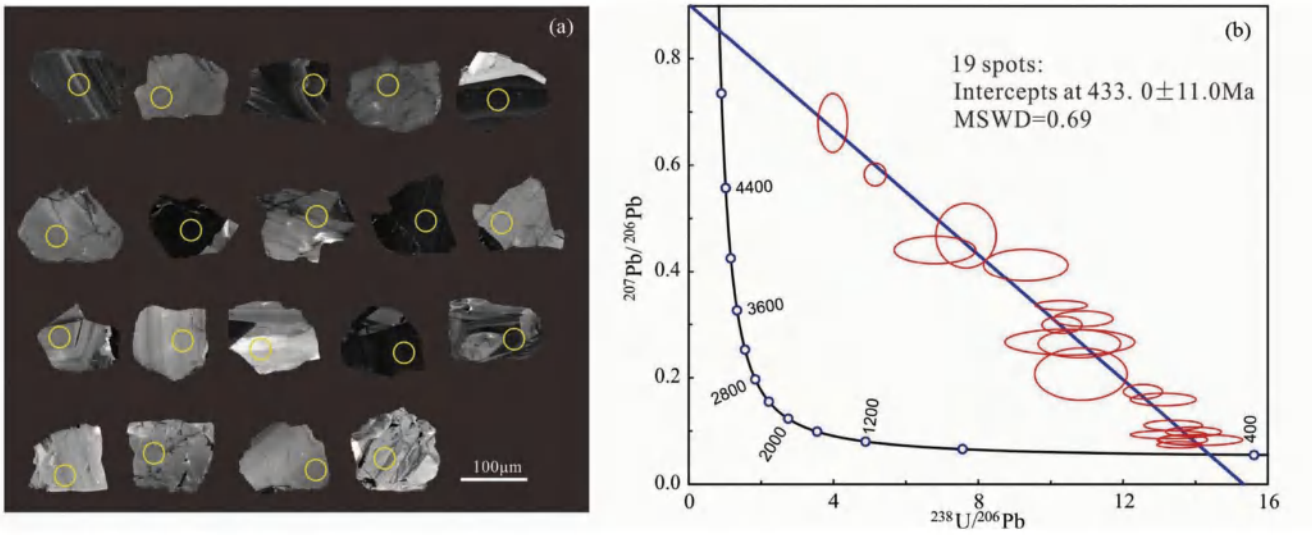

图 7 落家冲钨锡矿区蚀变花岗岩(样品 21-LJC-15)锡石阴极发光(a)和反等时线年龄图(b)

Fig. 7 Cassiterite CL images (a) and U-Pb age plot (b) of the Luojiachong altered granite (Sample 21-LJC-15)

飞, 2004)。

本次共计进行了 22 个点的锆石 U-Pb 年龄分析。这些锆石中的普通铅含量普遍很低,所有测试点在 U-Pb 年龄曲线图上都表现有较好的谐和度,均位于谐和线上或其附近(图 6a),且$^{206}Pb/^{238}U$ 年龄值非常集中,获得这 22 组锆石数据的$^{206}Pb/^{238}U$ 加权平均值为 430.7 ± 2.3Ma(MSWD = 0.05)(图 6b)。

3.2 锡石 U-Pb 定年结果

含白钨矿锡石的蚀变花岗岩(样品 21-LJC-15)中的锡石颗粒粒径均大于 100μm,在 CL 条件下均显示有明显的环带结构(图 7a),本次共计进行了 19 个点的 U-Pb 年龄分析(表 3),得到 Tera Wasserburg 的下交点年龄为 433.0 ± 11.0Ma (MSWD = 0.69)(图 7b)。

3.3 锆石 Hf 同位素分析

对落家冲矿区蚀变粗中粒斑状黑云母二长花岗岩(样品 21-LJC-4)已完成 U-Pb 测年的部分锆石打点部位选择 16 个点进行了 Hf 同位素分析测试,得到该样品锆石的$^{176}Yb/^{177}Hf$ 和$^{176}Lu/^{177}Hf$ 比值范围分别为 0.013810 ~ 0.071330 和 0.000465 ~ 0.002318(表 4),除点 21-LJC-4-21 外,其它测点$^{176}Lu/^{177}Hf$ 比值均小于 0.002,表明这些锆石在形成以后,仅具有较少放射成因 Hf 的积累,因而可以用初始$^{176}Hf/^{177}Hf$ 比值来代表锆石形成时的$^{176}Hf/^{177}Hf$ 比值(Wu *et al.*, 2006),从而能够有效示踪岩浆源区。样品的$f_{Lu/Hf}$的平均值为 -0.97,明显小于铁镁质地壳的$f_{Lu/Hf}$(-0.34, Amelin *et al.*, 1999)以及硅铝质地壳的$f_{Lu/Hf}$(-0.72, Vervoort *et al.*, 2004),因此二阶段模式年龄(t_{DM2})更能反映源区物质从亏损地幔抽取的时间(或其源区物质在地壳的平均存留年龄)。

16 颗锆石的 Hf 同位素成分均一,其$^{176}Hf/^{177}Hf$ 的变化范围在 0.282298 ~ 0.282354 之间(平均值为 0.282336,表 4),对应的 $\varepsilon_{Hf}(t)$ 变化范围在 -7.6 ~ -5.0 之间,平均值 -6.3;地壳模式年龄 t_{DM2} 变化范围在 1565 ~ 1711Ma 之间,平均值为 1635Ma(表 4)。

3.4 流体包裹体的岩相学特征及显微测温结果

3.4.1 岩相学特征

本次对落家冲钨锡矿床石英中的流体包裹体镜下观察与实验测温结果显示,矿区流体包裹体的初融温度分布于 -20.6 ~ -22.4℃之间,表明其属 NaCl-(KCl)-H_2O 体系,根据流体包裹体的分类准则(Roedder, 1984; 卢焕章等, 2004)及室温下流体包裹体相的组成特征、冷冻/升温过程中相变行为,本次将矿区石英中的原生流体包裹体分为富液相(L 型)、富气相(V 型)和含子晶三相包裹体(S 型)三种类型。

L 型包裹体:该类型包裹体成分以液相为主,是四个成矿阶段中最常见的包裹体类型,气相成分一般 < 60%,包裹体形态以负晶型、椭圆形、以及不规则状等为主,常呈单个孤立存在或集群分布,大小集中在 8 ~ 18μm 之间,少数可达 20μm 以上,加热后均一至液相,该类型包裹体约占原生包裹体总数的 80%(图 8a, c-e, g, i, j, l)。

V 型包裹体:该类型包裹体成分以气相为主,包括富气相和纯气相包裹体,气相成分一般 > 65%,包裹体多呈负晶形和椭圆形,呈单个孤立或集群分布,大小多集中在 9 ~ 15μm 之间,加热后均一至气相,约占包裹体总数的 15%(图 8a, b, h, k)。

S 型包裹体:该类型包裹体组成包括子晶矿物、液相成分和气泡,气相分数一般 5% ~ 25%,大小集中在 10 ~ 18μm 之间,这类包裹体多主要见于第 I 阶段,约占第 I 阶段流体包裹体总数的 15%,一类子晶呈立方体状者为石盐(NaCl)(图 8a, c, d),在升温过程中子晶先消失(290 ~ 350℃),最

表 3 落家冲钨锡矿区蚀变花岗岩(样品 21-LJC-15) LA-ICP-MS 锡石 U-Pb 测试结果

Table 3 Csssiterite U-Pb dating results of the Luojiachong altered granite (Sample 21-LJC-15)

测点号	含量($\times10^{-6}$)			Th/U	同位素比值						rho
	Pb	^{232}Th	^{238}U		^{207}Pb/^{206}Pb	1σ	^{207}Pb/^{235}U	1σ	^{206}Pb/^{238}U	1σ	
-01	1.39	0.0035	17.60	0.0002	0.08112	0.00632	0.75393	0.04600	0.07375	0.00223	0.49580
-02	0.21	0.0051	1.35	0.0038	0.14036	0.03320	2.62975	0.45967	0.09228	0.00718	0.44529
-03	0.86	0.0029	10.75	0.0003	0.10234	0.01277	0.84329	0.06592	0.07317	0.00236	0.41272
-04	0.63	0.0055	5.89	0.0009	0.21052	0.02222	1.67251	0.11096	0.07626	0.00348	0.68761
-05	0.79	0.0023	9.04	0.0003	0.12645	0.01129	1.13935	0.07915	0.07470	0.00297	0.57214
-06	0.89	0.0328	4.57	0.0072	0.40477	0.03293	4.49750	0.22033	0.09712	0.00445	0.93505
-07	2.09	0.0000	17.96	0.0000	0.17798	0.01051	1.90806	0.11194	0.07968	0.00226	0.48381
-08	2.66	0.3413	3.81	0.0896	0.68185	0.07362	23.54222	2.03257	0.25139	0.01700	0.78341
-09	1.32	0.0287	7.22	0.0040	0.34787	0.02731	3.99903	0.19942	0.09697	0.00344	0.71038
-10	0.16	0.0483	0.90	0.0535	0.11911	0.02636	3.49417	0.44617	0.09497	0.01069	0.88157
-11	0.43	0.0083	4.94	0.0017	0.12567	0.01604	0.96789	0.07290	0.07537	0.00397	0.69860
-12	0.19	0.0062	2.48	0.0025	0.07561	0.01455	0.81229	0.07987	0.07079	0.00391	0.56245
-13	0.14	0.0000	0.42	0.0000	0.11990	0.02326	8.93936	1.03632	0.14703	0.01607	0.94264
-14	0.74	0.1558	3.86	0.0404	0.38515	0.04107	3.93000	0.23017	0.09174	0.00457	0.85107
-15	0.30	0.0712	1.21	0.0589	0.33556	0.04139	6.10116	0.58342	0.10738	0.00887	0.86413
-16	3.30	0.1880	5.86	0.0321	0.60465	0.02351	15.58923	0.71069	0.19407	0.00751	0.84834
-17	3.04	0.0506	8.66	0.0058	0.41592	0.03003	8.41506	0.94047	0.13053	0.00939	0.64373
-18	0.67	0.0024	7.90	0.0003	0.10918	0.00939	0.97328	0.06817	0.07170	0.00261	0.51989
-19	0.20	0.0213	1.15	0.0185	0.16540	0.02631	3.36926	0.32216	0.09264	0.00646	0.72874

表 4 落家冲钨锡矿区黑云母二长花岗岩(样品 21-LJC-4)锆石 Hf 同位素分析结果

Table 4 Zircon Hf isotopic data of the Luojiachong biotite monzogranite (Sample 21-LJC-4)

测点号	t(Ma)	^{176}Yb/^{177}Hf	^{176}Lu/^{177}Hf	^{176}Hf/^{177}Hf	2σ	$\varepsilon_{Hf}(0)$	$\varepsilon_{Hf}(t)$	t_{DM1}(Ma)	t_{DM2}(Ma)	$f_{Lu/Hf}$
-01	430.7	0.035647	0.001191	0.282298	0.000032	-16.77	-7.64	1353	1711	-0.96
-03		0.022543	0.000745	0.282311	0.000014	-16.31	-7.05	1320	1679	-0.98
-04		0.034945	0.001128	0.282329	0.000013	-15.68	-6.52	1308	1650	-0.97
-05		0.043562	0.001485	0.282348	0.000021	-15.01	-5.96	1294	1619	-0.96
-07		0.029467	0.000953	0.282345	0.000014	-15.11	-5.91	1279	1616	-0.97
-08		0.013810	0.000465	0.282323	0.000013	-15.88	-6.54	1293	1651	-0.99
-09		0.035745	0.001165	0.282320	0.000031	-15.99	-6.85	1322	1668	-0.96
-11		0.037489	0.001206	0.282318	0.000015	-16.05	-6.92	1325	1672	-0.96
-12		0.028797	0.000976	0.282334	0.000017	-15.50	-6.31	1296	1638	-0.97
-15		0.026660	0.000925	0.282346	0.000019	-15.06	-5.85	1276	1613	-0.97
-16		0.053704	0.001849	0.282354	0.000029	-14.78	-5.83	1297	1612	-0.94
-17		0.017186	0.000596	0.282349	0.000023	-14.97	-5.67	1262	1603	-0.98
-19		0.015344	0.000522	0.282338	0.000013	-15.34	-6.02	1274	1622	-0.98
-20		0.018211	0.000640	0.282368	0.000038	-14.28	-4.99	1236	1565	-0.98
-21		0.071330	0.002318	0.282337	0.000027	-15.39	-6.58	1339	1653	-0.93
-22		0.014245	0.000498	0.282352	0.000017	-14.86	-5.52	1254	1595	-0.98

注：$\varepsilon_{Hf}(t)=10{,}000\times(\{[(^{176}Hf/^{177}Hf)_S-(^{176}Lu/^{177}Hf)_S\times(e^{\lambda t}-1)]/[(^{176}Hf/^{177}Hf)_{CHUR,0}-(^{176}Lu/^{177}Hf)_{CHUR}\times((e^{\lambda t}-1)]-1\}$. $t_{DM}=1/\lambda\times\ln\{1+[(^{176}Hf/^{177}Hf)_S-(^{176}Hf/^{177}Hf)_{DM}]/[(^{176}Hf/^{177}Hf)_S-(^{176}Hf/^{177}Hf)_{DM}]\}$. $t_{DM}^{C}=t_{DM}-(t_{DM}-t)\times[(f_{cc}-f_s)/(f_{cc}-f_{DM})]$. $f_{Lu/Hf}=(^{176}Lu/^{177}Hf)_S/(^{176}Lu/^{177}Hf)_{CHUR}-1$, $\lambda=1.867\times10^{-11}$/yr (Söderlund *et al.*, 2004); $(^{176}Lu/^{177}Hf)_S$ 和 $(^{176}Hf/^{177}Hf)_S$ 为样品测试值; $(^{176}Lu/^{177}Hf)_{CHUR}=0.0332$ and $(^{176}Hf/^{177}Hf)_{CHUR,0}=0.282772$ (Blichert-Toft and Albarède, 1997); $(^{176}Lu/^{177}Hf)_{DM}=0.0384$ and $(^{176}Hf/^{177}Hf)_{DM}=0.28325$ (Griffin *et al.*, 2000); $(^{176}Lu/^{177}Hf)_{mean\ crust}=0.015$; $f_{cc}=[(^{176}Lu/^{177}Hf)_{mean\ crust}/(^{176}Lu/^{177}Hf)_{CHUR}]-1$; $f_s=f_{Lu/Hf}$; $f_{DM}=[(^{176}Lu/^{177}Hf)_{DM}/(^{176}Lu/^{177}Hf)_{CHUR}]-1$; t = 锆石结晶年龄

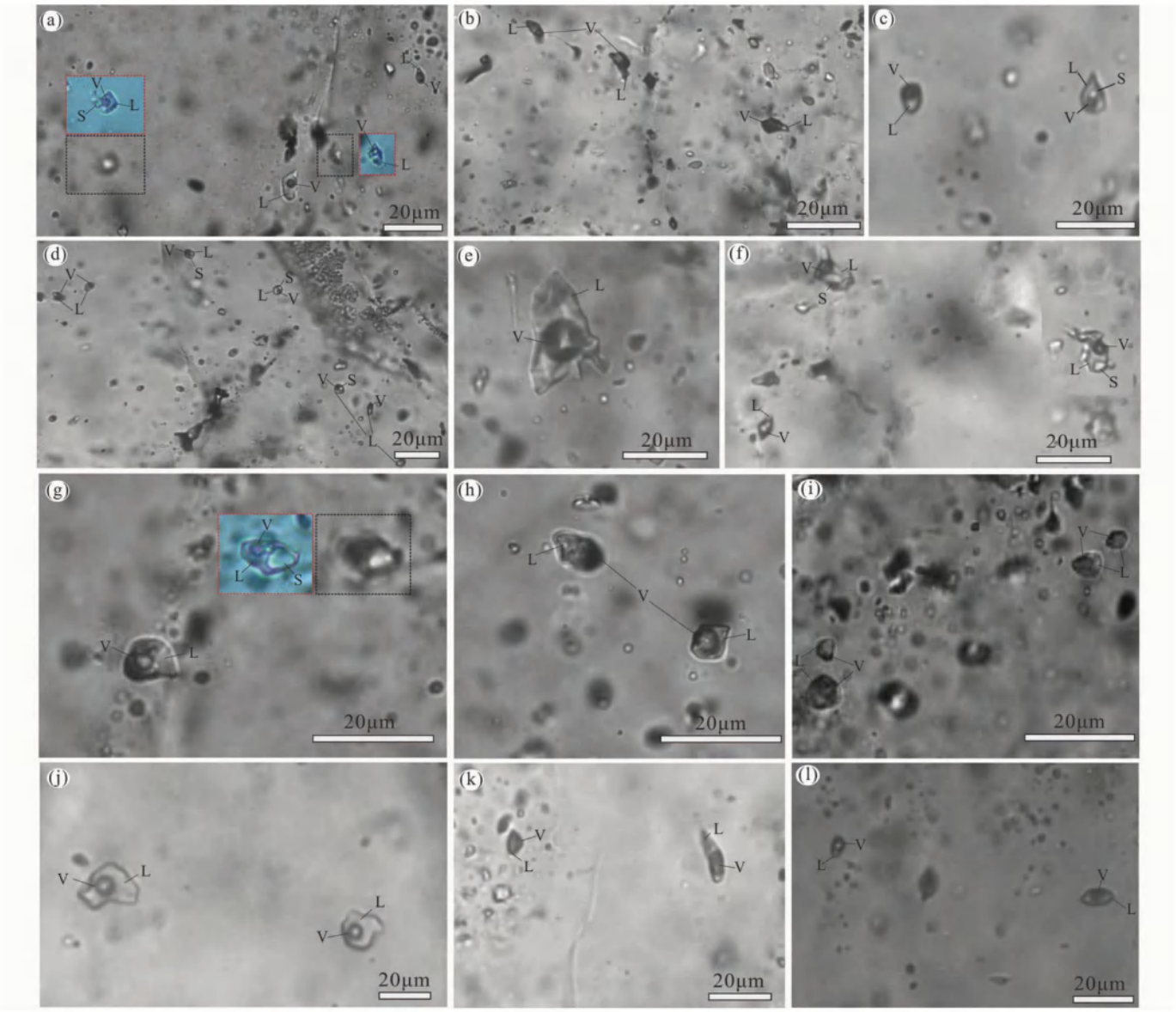

图 8 落家冲钨锡矿区石英中的代表性包裹体类型及特征

第Ⅰ阶段的 L 型、V 型和 S 型包裹体(a)、L 型和 V 型包裹体(b)、L 型和 S 型包裹体(c)、L 型和 S 型类包裹体(d)、L 型包裹体(e)、L 型和 S 型包裹体(f);第Ⅱ阶段的 L 型和 S 型包裹体(g)、V 型包裹体(h)、L 型包裹体(i);第Ⅲ阶段的 L 型包裹体(j)、V 型包裹体(k);(l)第Ⅳ阶段的 L 型包裹体. 相邻虚线框代表同一包裹体在不同焦距下的特征. L-液相;V-气相;S-子晶

Fig. 8 Typical microphtographs of fluid inclusions in Luojiachong deposit

Type L, V and S fluid inclusion (a), Type L and V fluid inclusion (b), Type L and S fluid inclusion (c), Type L and S fluid inclusion (d), Type L fluid inclusion (e), Type L and S fluid inclusion (f) of stage Ⅰ; Type L and S fluid inclusion (g), Type V fluid inclusion (h), Type L fluid inclusion (i) of stage Ⅱ; Type L fluid inclusion (j), Type L fluid inclusion (k) of stage Ⅲ; (l) Type L fluid inclusion of stage Ⅳ. Adjcaent dotted frame were shows the characteristics of the same inclusion in differents focal length. L-liquid phase; V-vapor phase; S-solid

后气泡消失达到均一,激光拉曼检测不到其成分。另一类中见有呈他形、不规则状的矿物(图 8f, g),经激光拉曼检测显示其为云母类矿物(图 9a),该类矿物应为包裹体形成时直接捕获的矿物,而不是降温析出的子晶。

3.4.2 显微测温结果

本次研究对落家冲钨锡矿区的四个成矿阶段进行测温研究,测温结果见表 5,其中 L 型和 V 型包裹体的盐度利用冰点-盐度关系表(Bodnar, 1994)获得,S 型含石盐子晶包裹体的盐度则利用相关的公式计算获得(Hall *et al.*, 1988)。

第Ⅰ阶段的 L 型包裹体均一温度介于 237 ~ 361℃之间,主要集中在 280 ~ 360℃之间,平均温度为 314℃(图 10a、图 11a),盐度范围为 8.7% ~ 17.5% NaCleqv(图 10b、图 11a),主要集中在 10.0% ~ 17.0% NaCleqv 之间,平均值为 13.6% NaCleqv;V 型包裹体均一温度介于 317 ~ 367℃之间,平均值为 333℃,盐度介于 8.3% ~ 12.7% NaCleqv,平均值为 10.7% NaCleqv;S 型包裹体均一温度介于 270 ~ 342℃之间,子晶溶解温度介于 298 ~ 324℃,对应的盐度为 38.1% ~ 40.1% NaCleqv(图 10b、图 11a),平均值为 38.9%。

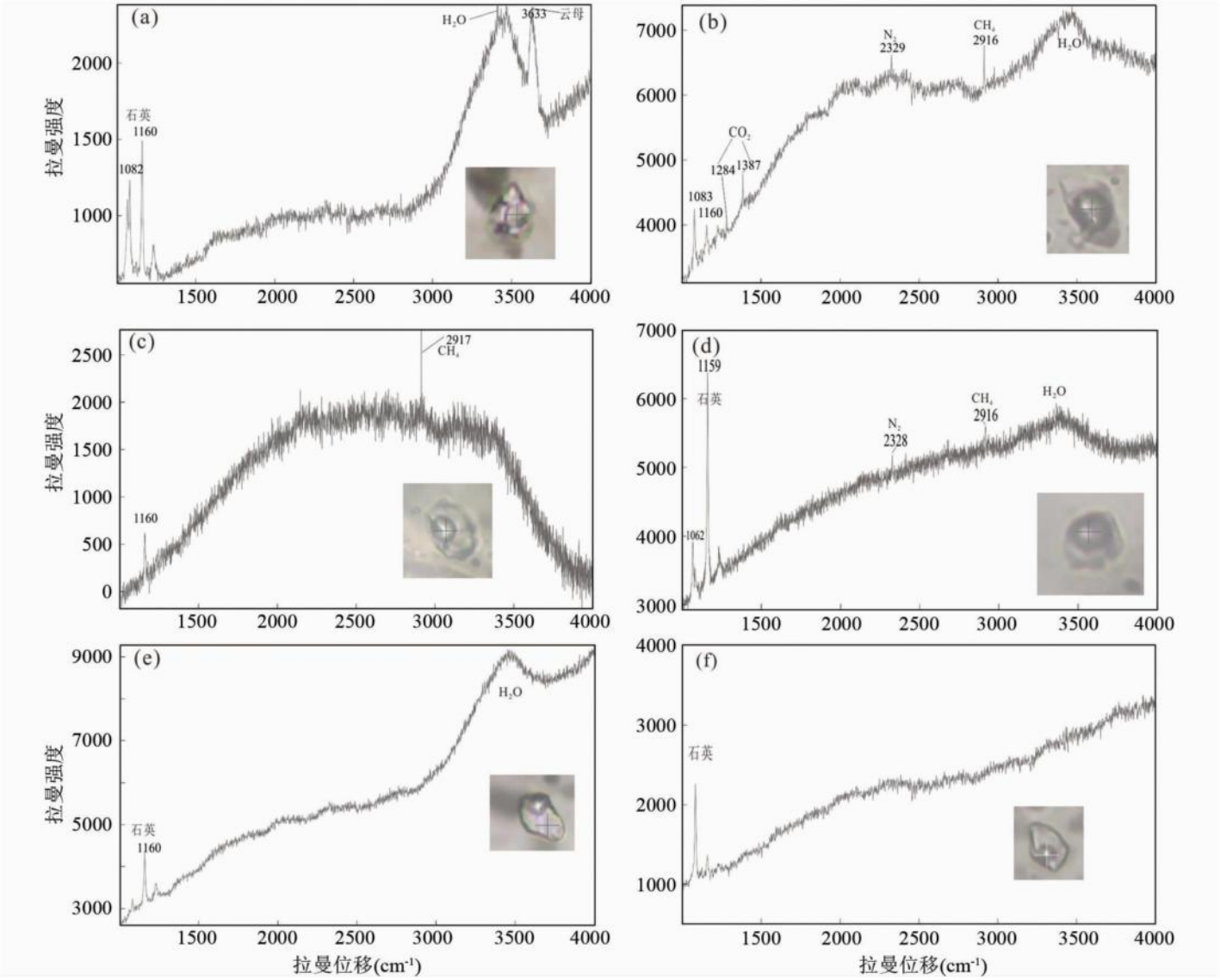

图 9 落家冲钨锡矿区石英流体包裹体激光拉曼图谱

Fig. 9 Raman spectra of fluid inclusion in quartz of Luojiachong deposit

表 5 落家冲钨锡矿床石英中流体包裹体显微测温结果

Table 5 Summary of microthermometric data of fluid inclusions in quartz from the Luojiachong W-Sn deposit

阶段	初溶温度(℃)	类型	数量	大小(μm)	V/(V+L)(%)	Tm,冰点(℃)	Tm,石盐(℃)	Th(平均值)(℃)	盐度(平均值)(% NaCleqv)
Ⅰ		L	68	8~20	5~50	-5.6~-13.7		237~361 (314)	8.7~17.5 (13.6)
		V	10	7~14	65~85	-5.3~-8.8		317~367 (333)	8.7~12.7 (10.7)
		S	13	8~18	10~25		298~324	270~342 (312)	38.1~40.1 (38.9)
Ⅱ	-20.6~-22.4	L	81	8~16	5~55	-0.9~-4.3		222~375 (289)	1.6~6.9 (3.9)
		V	14	8~15	65~80	-1.5~-2.8		267~332 (308)	2.6~4.7 (3.3)
Ⅲ		L	95	8~20	10~50	-0.9~-4.9		188~352 (257)	1.6~7.7 (4.8)
		V	7	6~15	65~80	-2.2~-3.9		258~332 (303)	3.7~6.1 (4.9)
Ⅳ		L	51	6~18	10~50	-1.1~-4.1		161~225 (202)	1.1~6.6 (3.7)
		V	3	8~10	65~70	-1.8~-2.9		185~273 (239)	3.0~4.7 (3.7)

第Ⅱ阶段的 L 型包裹体均一温度介于 222~375℃之间，大多集中于 260~320℃之间，平均值为 289℃（图 10c、图 11b），盐度范围为 1.6%~6.9% NaCleqv，主要集中在 2.0%~6.0% NaCleqv 之间，平均值为 3.9% NaCleqv（图 10d、图 11b）；V 型包裹体均一温度介于 267~332℃之间，大多集中于 300~320℃之间，平均值为 308℃，盐度范围为 2.6%~4.7% NaCleqv（图 10d、图 11b），平均值为 3.3% NaCleqv。

第Ⅲ阶段的 L 型包裹体均一温度介于 188~352℃之间，

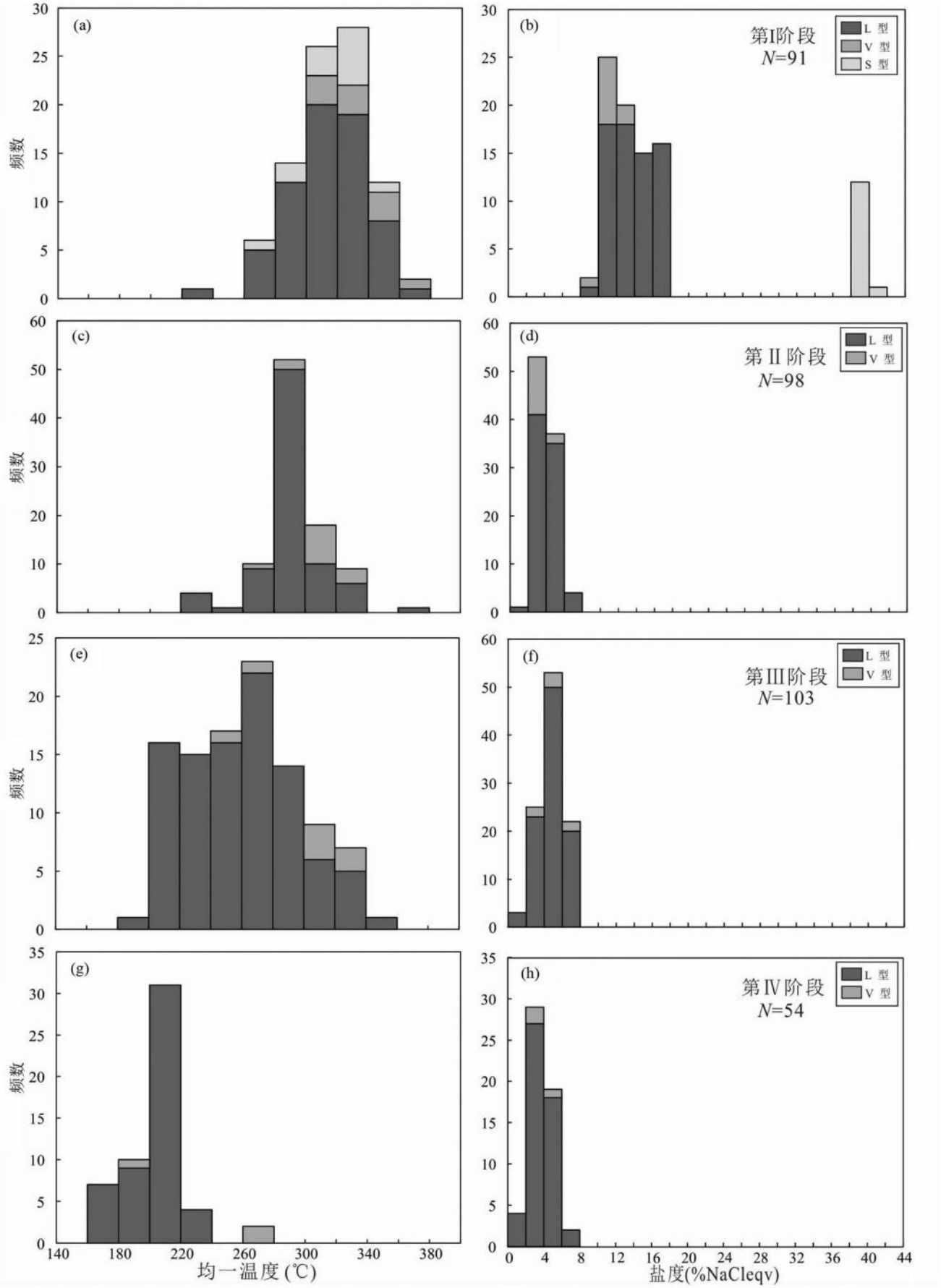

图 10 落家冲矿区石英中的流体包裹体温度和盐度直方图

Fig. 10 Histograms of the homogenization temperature and salinity of fluid inclusions in quartz of the Luojiachong deposit

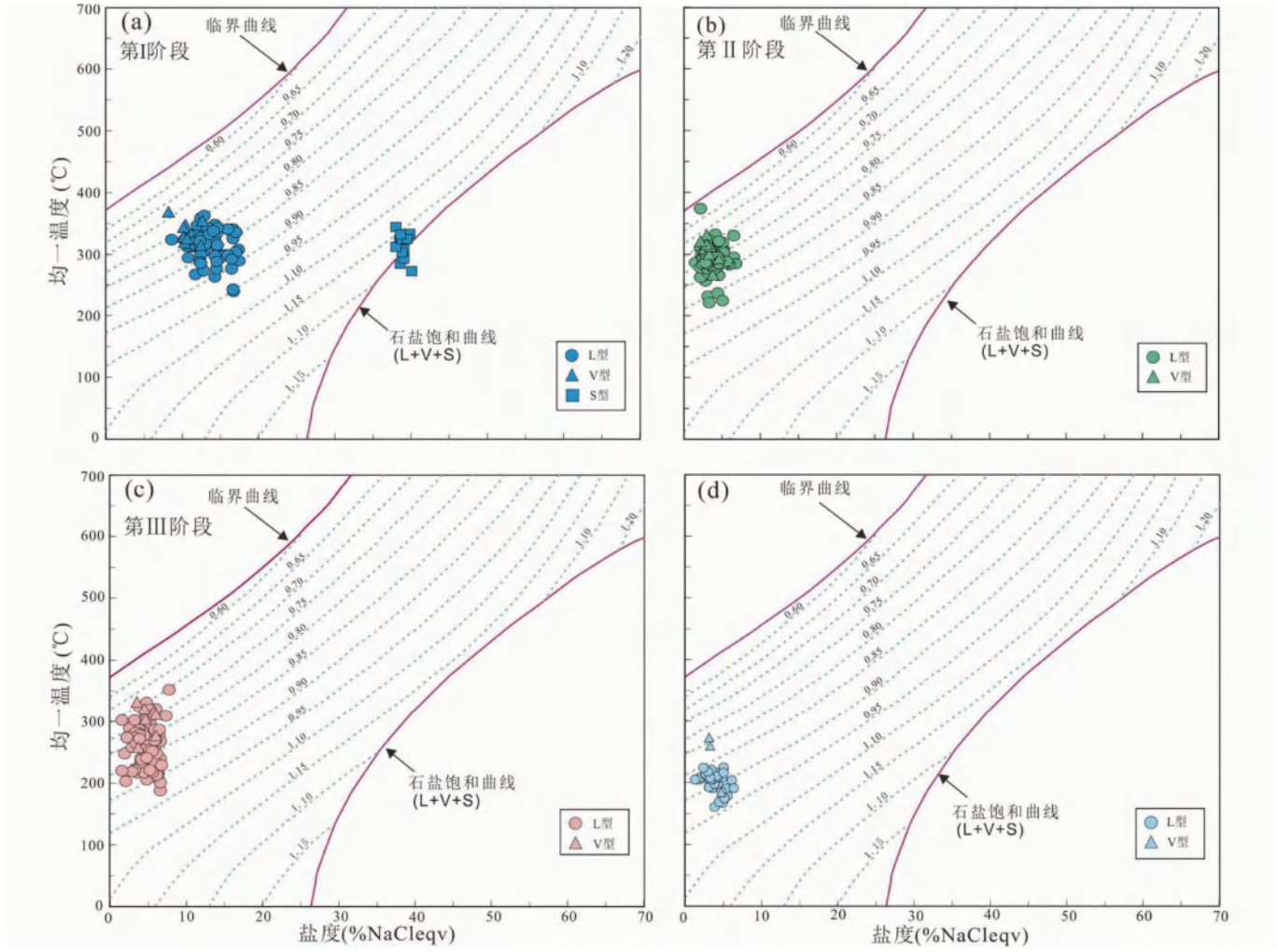

图 11 落家冲钨锡矿区石英流体包裹体均一温度-盐度图(据 Bodnar, 1994)

Fig. 11 Plots of homogenization temperature vs. salinity of ore fluids in quartz of the Luojiachong deposit (after Bodnar, 1994)

平均值为 257℃(图 10e、图 11c),盐度范围为 1.6% ~7.7% NaCleqv,平均值为 4.8% NaCleqv;V 型包裹体均一温度介于 258 ~332℃之间,平均值为 303℃,盐度范围为 3.7% ~6.1% NaCleqv(图 10f、图 11c)。

第Ⅳ阶段的 L 型包裹体均一温度介于 161 ~225℃之间,平均值为 202℃(图 10g、图 11d),盐度范围为 1.1% ~6.6% NaCleqv(图 10h、图 11d),平均值为 3.7% NaCleqv;V 型包裹体在该阶段很少,仅见三个。

3.5 激光拉曼成分分析

本次对落家冲钨锡矿区的四个成矿阶段石英中的流体包裹体进行了激光拉曼分析测试,结果显示,这四个阶段的包裹体在气相成分上有区别,其中第Ⅰ阶段包裹体的气相成分除主要为 H_2O 外,还检测到存在少量有 CO_2、N_2、CH_4(图 9b),第Ⅱ阶段和第Ⅲ阶段石英中流体包裹体的气相成分除 H_2O 外,有检测到少量 CH_4 和 N_2(图 9c, d),第Ⅳ阶段石英中的气相成分和四个阶段的液相成分主要为 H_2O(图 9e,f)。

3.6 H-O 同位素测试结果

落家冲钨锡矿床石英氢、氧同位素分析结果见表 6,石英 $\delta D_{V\text{-}SMOW}$ 为 -71.65‰ ~ -59.31‰,$\delta^{18}O_{V\text{-}SMOW}$ 为 6.60‰ ~ 11.55‰,均属于正常岩浆水的范围(Sheppard, 1986; Hedenquist and Lowenstern, 1994; 郑永飞等, 2000),利用石英与水体系同位素平衡方程:$\delta^{18}O_Q$-$\delta^{18}O_{H_2O} \approx 3.38 \times 10^6/T^2$-3.40(Clayton *et al.*, 1972),其中温度(T)为绝对温度,可根据各阶段石英矿物中包裹体测温得到的均一温度平均值(图 10)计算所得,继而可计算获得石英与水平衡时的 $\delta^{18}O_{H_2O}$ 值,结果显示,落家冲钨锡矿床各成矿阶段石英矿物中的 $\delta^{18}O_{H_2O}$ 值介于 -5.10‰ ~ +5.34‰。

4 讨论

4.1 成岩成矿时代

锆石 U-Pb 定年是目前岩浆岩类同位素年代学研究中最

表 6 落家冲钨锡矿区石英中的氢、氧同位素组成分析结果

Table 6 Hydrogen and oxygen isotope data of quartz from the Luojiachong deposit

成矿阶段	样品号	$\delta D_{V\text{-}SMOW}$(‰)	$\delta^{18}O_{V\text{-}SMOW}$(‰)	$\delta^{18}O_{H_2O}$(‰)	温度(℃)
Ⅰ	21-LJC-23	-70.67	11.55	5.34	320
	21-LJC-25	-68.51	10.18	3.97	
Ⅱ	21-LJC-14	-71.65	7.24	-0.41	280
	21-LJC-18	-69.84	9.34	1.69	
Ⅲ	21-LJC-37	-60.19	8.08	-0.41	260
	21-LJC-38	-59.31	7.87	-0.62	
Ⅳ	21-LJC-42	-61.39	6.71	-4.99	200
	21-LJC-5	-62.18	6.60	-5.10	

常用和有效的方法,而锡石 U-Pb 测年已成为钨锡矿床研究中确定成矿时代的重要方法之一(Yuan *et al.*, 2008, 2011; Xie *et al.*, 2019; Fei *et al.*, 2020; Xiong *et al.*, 2020; 熊峥嵘等, 2021; 张志远等, 2021)。本次研究利用 LA-ICP-MS 获得落家冲钨锡矿区北东向矿脉内(第Ⅰ阶段)蚀变粗中粒斑状黑云母花岗岩的锆石 U-Pb 年龄为 430.7±2.3Ma,同时得到锡石的 U-Pb 年龄为 433.0±11Ma,显示出成岩和成矿时代在误差范围内一致的特征,表明落家冲钨锡矿床成岩成矿时代均属加里东晚期。

距落家冲钨锡矿区南部仅 5km(图 1)的平滩钨矿,为同样形成于加里东期的白钨矿床,其成矿类型具有与落家冲钨锡矿区北东向矿脉(3 号矿脉)相同的特点,Chen *et al.* (2019)获得平滩矿区蚀变粗中粒黑云母花岗岩锆石 U-Pb 年龄以及辉钼矿的 Re-Os 年龄分别为 431.0±1.8Ma 和 427.0±5.4Ma,认为矿床的形成与矿区黑云母二长花岗岩相关(Chen *et al.*, 2019);位于湘中矿集区白马山岩体东北部的杨家山钨锡矿床是另一被证实形成于加里东期的矿床,成矿类型主要为石英脉型和云英岩型,其黑云母二长花岗岩锆石的 U-Pb 年龄为 406.6±2.8Ma,锡石 U-Pb 定年结果为 406.8±5.6Ma(Xie *et al.*, 2019),该矿床也被认为与黑云母二长花岗岩具有成因联系。由上可知,落家冲矿区 3 号矿脉与平滩白钨矿床、杨家山钨锡矿床具有在成岩成矿年代学上相似的特征,即这三个形成于加里东期的矿床均与黑云母二长花岗岩具有成因上的联系(Chen *et al.*, 2019; Xie *et al.*, 2019; 张志远等, 2021)。同时,湘西南地区钨锡矿床的成岩成矿年代(427~433Ma)要早于湘中地区(~406Ma)。结合广西境内的大瑶山地区加里东期钨多金属矿床的成矿时代多介于 446~432Ma(陈懋弘等, 2011, 2012; Jiang *et al.*, 2017; Dang *et al.*, 2018)的特征,可以看出在区域上从南到北,加里东期花岗岩的成岩成矿时代整体表现出越来越年轻的特征。

4.2 成矿流体特征

前人的研究显示,黑钨矿较与之共生石英相比,其内部流体包裹体的均一温度要高 40~100℃(Wei *et al.*, 2012; Ni *et al.*, 2015a),而白钨矿与共生石英矿物中流体包裹体的形成条件则相同(郭志军等, 2016; Wang *et al.*, 2016; Li *et al.*, 2021),因此,石英矿物中的流体特征可代表共生白钨矿的形成条件。

本次研究获得落家冲矿区第Ⅰ阶段石英中的包裹体均一温度主要集中在 260~380℃之间,平均温度为 315℃,而盐度变化范围较大,主要集中在 10%~18.0% NaCleqv 与 38.0%~40.0% NaCleqv 之间分布,平均盐度为 16.9% NaCleqv;第Ⅱ阶段石英中的流体包裹体均一温度主要集中在 240~320℃之间,平均值为 291℃,盐度主要集中在 2.0%~6.0% NaCleqv 之间,平均盐度为 3.9% NaCleqv;第Ⅲ阶段的流体包裹体均一温度主要在 200~320℃之间,平均值为 260℃,盐度主要分布在 2.0%~8.0% NaCleqv 的范围内,平均值为 4.8% NaCleqv;第Ⅳ阶段的流体包裹体均一温度主要分布于 180~220℃之间,平均值为 202℃,盐度主要集中于 2.0%~6.0% NaCleqv,平均值为 3.7% NaCleqv。表明从第Ⅰ阶段到第Ⅳ阶段,落家冲矿区石英中的流体包裹体温度是逐渐降低的(图 10、图 11),而盐度则表现为由第Ⅰ阶段到第Ⅱ阶段急剧下降,后由第Ⅱ阶段到第Ⅳ阶段总体变化不大的特点,显示出经过早期第Ⅰ阶段后,成矿流体的盐度趋于相对稳定的特征。

第Ⅰ阶段为落家冲矿区北东向矿脉的主要成矿阶段,显示出成矿流体为中高温、中高盐度的特点,具有与加里东期同类型的平滩白钨矿床成矿流体相似的特征(陈剑锋, 2019; 陈剑锋等, 2020);第Ⅱ阶段和第Ⅲ阶段是矿区近东西向矿脉的主要成矿阶段,显示出成矿流体为中温、低盐度的特征,这两个阶段与在成矿类型(云英岩型和石英脉型)上一致的湘中地区加里东期杨家山钨锡矿床(Xie *et al.*, 2019; Li *et al.*, 2021)相比较,其温度偏高而盐度偏低,温度偏高可能是由于落家冲矿区的钨锡矿体围岩为花岗岩而在杨家山矿区则为地层,受矿体距母岩的远近不同以及围岩环境的影响所致;盐度偏低则可能是由于落家冲矿区在发生了高盐度的成矿作用(第Ⅰ阶段)后,成矿流体的含盐矿物大量沉淀而致后期成矿流体盐度大幅降低。

4.3 成岩、成矿的物源

落家冲矿区黑云母二长花岗岩花岗岩样品中单颗粒锆

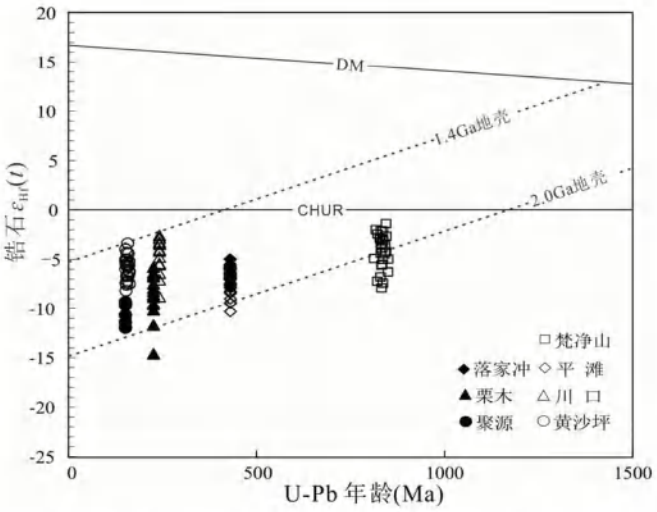

图 12 华南各时代代表性致矿花岗岩类锆石的 $\varepsilon_{Hf}(t)$-t 关系图

数据来源于张怀峰等，2014；丁腾，2016；Chen *et al.*，2019；苏晔等，2020；Lü *et al.*，2021 及本文

Fig. 12 Zircon $\varepsilon_{Hf}(t)$ value versus cryatallization age diagram for differents stages mineralization granitoid in South China

Data from Zhang *et al.* (2014), Ding *et al.* (2016), Chen *et al.* (2019), Su *et al.* (2020), Lü *et al.* (2021) and this study

石的 Hf 同位素组成具有与平滩矿区花岗岩（Chen *et al.*，2019，图 12）相似的特征，其 $\varepsilon_{Hf}(t)$ 值（集中于 -8 ~ -5 之间）与 Hf 同位素二阶段模式年龄（1.57 ~ 1.71Ga 之间）变化范围均较小。Hf 同位素的特征表明 $\varepsilon_{Hf}(t)<0$，且在 $\varepsilon_{Hf}(t)$-t 图解上（图 12）样品点均落于球粒陨石演化线（CHUR）及亏损地幔线（DM）之下，可推测矿区花岗岩为元古代古老地壳物质部分熔融的产物（Griffin *et al.*，2002；Vervoort *et al.*，2004）。越来越多的研究显示，华南各时代的花岗岩均有发生 W-Sn-Nb-Ta 的成矿作用，如贵州梵净山与广西元宝山新元古代花岗岩体内及周围发育有与之成因相关的 W-Sn-Nb-Ta 矿床（Lv *et al.*，2021；Xiang *et al.*，2018）、湘西南地区的平滩和落家冲钨锡多金属矿床的形成与加里东期花岗岩相关（Chen *et al.*，2019），广西栗木 W-Sn-Nb-Ta 矿床和湘南川口钨矿床均与印支期花岗岩类具有成因联系（张怀峰等，2014；罗鹏等，2021），湘南黄沙坪钨多金属矿床和赣中聚源钨矿床的形成均与燕山期花岗岩类相关（丁腾，2016；苏晔等，2020），各时代致矿花岗岩具有相类似的锆石 Hf 同位素特征（图 12），指示了不同时代的致矿花岗岩物源均起源于元古宙地壳，且随着成岩成矿时代愈年轻，其物源也具有相对更年轻的特点（图 12），这可能是时代更年轻的花岗岩浆在上侵时混入了更多的新生地壳物质（也包含早期的花岗岩）（华仁民等，2013），同时造成钨锡等成矿元素的活化和再富集，促使侵入时代晚的花岗岩发生了更大规模的成矿作用。

本次获得落家冲矿区第Ⅰ阶段石英中流体包裹体具有较高的均一温度，且该阶段含有一定比例的高盐度子晶包裹体（图 8a，c，d、图 10a，b），暗示矿床的成矿流体来源于岩浆。在 δD-$\delta^{18}O_{H_2O}$ 图解上（图 13），落家冲矿区石英中成矿流体的 H、O 同位素特征具有与平滩（Chen *et al.*，2019）、杨家山（Xie *et al.*，2019）相似的特点，这几个加里东期矿床在成矿早阶段（第Ⅰ阶段）均紧邻岩浆水的部位，而随着成矿作用的演化至成矿晚阶段，其氢、氧同位素组成逐渐有向雨水线靠近的趋势（图 13）。因此，与平滩及杨家山相类似，落家冲钨锡矿区早阶段的成矿流体主要来源于岩浆水，而在后期有不同比例的大气降水的混入。

4.4 成矿机制探讨

在钨锡矿床的成矿机制方面，前人的研究认为流体的减压“沸腾”（王旭东等，2012a；盛继福等，2015）、流体的不混溶（Graupner *et al.*，1999；王旭东等，2012b，2013；Xiong *et al.*，2017）、岩浆水与大气降水的混合作用（魏文凤等，2011a，b；Ni *et al.*，2015a）、自然冷却（董少花等，2011；黄惠兰等，2015；Ni *et al.*，2015a；Peng *et al.*，2018）以及水岩反应（Lecumberri-Sanchez *et al.*，2017）等均可使钨锡金属从岩浆热液流体中释放出来，发生矿质的沉淀。

落家冲钨锡矿床第Ⅰ阶段成矿流体的盐度在高盐度和低盐度区间都有分布（图 10b），且在相同的温度区间内，流体具有低盐度和高盐度包裹体共存的特点（图 11a）。第Ⅰ阶段石英矿物中的 S 型包裹体约占其总包裹体数的 15%，这些含石盐子晶的流体包裹体可直接从长英质岩浆中出溶形成（Cline and Bodnar，1994；杨志明等，2005）或通过流体不混溶（或者沸腾作用）来实现（Bodnar，1994；Wilkinson，2001）。本次研究利用激光拉曼检测到第Ⅰ阶段的成矿流体中有少量 CO_2 的存在（图 9b），但在室温条件下各成矿阶段均未观察到含 CO_2 相的流体包裹体，说明 CO_2 的占比很小（小于 0.1%，Einaudi *et al.*，1981），因此它在成矿过程的作用可忽略，同时也表明在成矿流体的演化过程中并没有发生不混溶作用（Ni *et al.*，2015a，b）。而在同一视域背景下，第Ⅰ阶段流体包裹体存在有 L 型、V 型和 S 型包裹体共存的现象（图 10a-d），表明第Ⅰ阶段的成矿流体有发生明显的沸腾作用（卢焕章，2000；Li *et al.*，2011；陈剑锋等，2020），这是造成第Ⅰ阶段相同温度区间内高密度和低密度包裹体共存的原因，同时也导致了成矿流体发生盐度的骤降以及 CO_2 的逸失。

第Ⅱ阶段和第Ⅲ阶段是矿区近东西向矿脉的主要成矿阶段，第Ⅱ阶段的成矿流体较第Ⅲ阶段其流体温度明显降低而盐度变化不大（图 10、图 11），H-O 同位素特征显示两个成矿阶段成矿流体中均有大气降水的混入（图 13），大气降水等外来流体的加入以及自然冷却均可致成矿流体温度的降低，温度降低是这两个阶段钨锡等矿质沉淀的主要原因（Wood and Samson，2000；Wang *et al.*，2020）。

到第Ⅳ阶段，随着该区成矿作用接近尾声，成矿流体中

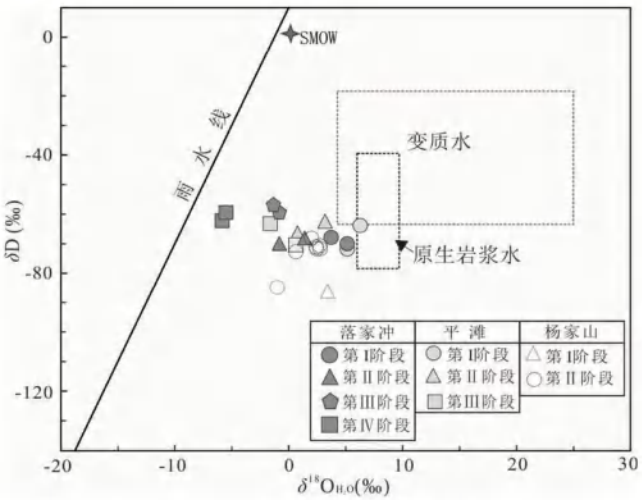

图 13 落家冲钨锡矿区流体的 δD-$\delta^{18}O_{H_2O}$ 图解(据 Taylor, 1979)

Fig. 13 δD vs. calculated $\delta^{18}O_{H_2O}$ of fluid inclusions in quartz of the Luojiachong deposit (after Taylor, 1979)

混入了更多量的大气降水,造成温度以及盐度持续降低,同时伴随了矿区黄铜矿、辉钼矿等硫化物的进一步沉淀。

4.5 对找矿勘查的启示

岩浆源区成矿元素的预富集被认为是钨锡矿床形成的必要条件(Zhao *et al.*, 2022b),因此,南岭地区大量钨(锡)矿床的形成一般与花岗岩体内(晚期)高度演化的小岩株(枝)密切相关,而大面积出露的花岗岩(岩基)基本不能直接形成钨锡矿床(袁顺达, 2017; Zhao *et al.*, 2022c),如位于南岭中段的彭公庙及诸广山岩基内的几个钨矿床,即使矿床围岩为加里东期的花岗岩,但成矿作用却均被证实发生于燕山期(Yuan *et al.*, 2018a, b; 于玉帅等, 2022)。本次研究的落家冲钨锡矿床,与湘西南地区平滩白钨矿床(Chen *et al.*, 2019; 陈剑锋等, 2020)和湘中地区的杨家山钨锡矿床(Xie *et al.*, 2019; Li *et al.*, 2021),均位于加里东期大型花岗岩基内或周缘,三个矿床的形成均与加里东期(早侵入次)的黑云母二长花岗岩相关。黑云母二长花岗岩为苗儿山岩体加里东期花岗岩的主要岩性,全岩地球化学组成显示其 Nb/Ta 值介于 3.36 ~ 9.89 之间(平均为 5.41),Zr/Hf 比值介于 18.4 ~ 35.6(平均为 24.6)(杜云等, 2021),表明花岗岩经历了较高程度的分异作用(Bau, 1996; Ballouard *et al.*, 2016; 吴福元等, 2017)。南岭西段的加里东期花岗岩从广西境内的海洋山、大宁岩体往北到湘桂交界处的苗儿山-越城岭岩体,它们具有起源于同一岩浆房并表现出分异程度从南到北逐渐升高的特点(李文杰等, 2006),因此,湘西南苗儿山岩体内这些即使是早侵入次的花岗岩也经历了较明显的分异作用(Chen *et al.*, 2019),促使钨锡等矿质得到富集,为直接成矿提供了充足的物质来源。因此,在南岭西段加里东期花岗岩岩基内同样具有寻找钨锡矿床的潜力。此外,在成矿系统研究的基础上,也应注意 Nb-Ta 等稀有金属(毛禹杰等, 2021)和外围的 Pb-Zn 矿床(Xiong *et al.*, 2019)的找矿勘查。

落家冲钨锡矿区的北东向矿脉与平滩白钨矿床具有在成矿类型、矿体空间的展布等方面一致的特征,本次研究显示两者在成岩成矿年代、成矿流体物源以及矿化机制等方面更是具有相似性,暗示两者有可能是同一条矿脉在南北不同地段的展现,目前该区的找矿勘查工作程度过低,在两矿床之间的空白区域是否存在相同类型的矿脉有待后续工作查验。

5 结论

(1)落家冲钨锡矿区蚀变粗中粒斑状黑云母花岗岩的锆石 U-Pb 年龄为 430.7 ± 2.3Ma,锡石的 U-Pb 年龄为 433.0 ± 11Ma,两者在误差范围内一致,表明落家冲钨锡矿床成岩成矿时代均为加里东晚期,矿床的形成与苗儿山加里东期黑云母二长花岗岩相关。

(2)落家冲钨锡矿床经历了四个主要成矿阶段:蚀变花岗岩-白钨矿阶段(第Ⅰ阶段)、云英岩-白钨矿-锡石阶段(第Ⅱ阶段)、石英脉-白钨矿阶段(第Ⅲ阶段)和石英脉-硫化物阶段(第Ⅳ阶段),成矿流体主要来源于岩浆,后期有大气降水的混入。

(3)流体的沸腾作用造成了第Ⅰ阶段钨等矿质沉淀,温度的降低是引起第Ⅱ阶段和第Ⅲ阶段钨锡金属沉淀的主要原因。

致谢 衷心感谢二位匿名审稿专家及编辑部老师对本文辛勤细致的审查,所提出的宝贵意见促进了本文的进一步完善与提高。

References

Amelin Y, Lee DC, Halliday AN and Pidgeon RT. 1999. Nature of the Earth's earliest crust from hafnium isotopes in single detrital zircons. Nature, 399(6733): 252 – 255

Andersen T. 2002. Correction of common lead in U-Pb analyses that do not report ^{204}Pb. Chemical Geology, 192(1 – 2): 59 – 79

Ballouard C, Poujol M, Boulvais P, Branquet Y, Tartèse R and Vigneresse JL. 2016. Nb-Ta fractionation in peraluminous granites: A marker of the magmatic-hydrothermal transition. Geology, 44(3): 231 – 234

Bau M. 1996. Controls on the fractionation of isovalent trace elements in magmatic and aqueous systems: Evidence from Y/Ho, Zr/Hf, and lanthanide tetrad effect. Contributions to Mineralogy and Petrology, 123(3): 323 – 333

Blichert-Toft J and Albarède F. 1997. The Lu-Hf isotope geochemistry of chondrites and the evolution of the mantle-crust system. Earth and Planetary Science Letters, 148(1 – 2): 243 – 258

Bodnar RJ. 1994. Synthetic fluid inclusions: Ⅻ: The system H_2O NaCl. Experimental determination of the halite liquidus and isochores for a 40wt% NaCl solution. Geochimica et Cosmochimica Acta, 58(3):

1053 – 1063

Cai MH, Chen KX, Qu WJ, Liu GQ, Fu JM and Yin JP. 2006. Geological characteristics and Re-Os dating of molybdenites in Hehuaping tin-polymetallic deposit, southern Hunan Province. Mineral Deposits, 25(3): 263 – 268 (in Chinese with English abstract)

Chen JF. 2019. Research on the metallogenic mechanism of the Pingtan scheelite deposit in Chengbu County, Hunan Province. Ph. D. Dissertation. Changsha: Central South University, 1 – 119 (in Chinese with English abstract)

Chen JF, Sheng D, Shao YJ, Zhang JX, Wei HT, Yang QD, Luo XY and Du Y. 2019. Silurian S-type granite-related W-(Mo) mineralization in the Nanling Range, South China: A case study of the Pingtan W-(Mo) deposit. Ore Geology Reviews, 107: 186 – 200

Chen JF, Shao YJ, Dai XL, Sheng D, Guan SJ, Wen CH, Zhang JX, Lin BH and Tian L. 2020. Ore-forming fluid inclusion of Pingtan Caledonian tungsten deposit in the Nanling Range, South China. The Chinese Journal of Nonferrous Metals, 30(7): 1714 – 1729 (in Chinese with English abstract)

Chen MH, Mo CS, Huang ZZ, Li B and Huang HW. 2011. Zircon LA-ICP-MS U-Pb ages of granitoid rocks and molybdenite Re-Os age of Shedong W-Mo deposit in Cangwu County of Guangxi and its geological significance. Mineral Deposits, 30(6): 963 – 978 (in Chinese with English abstract)

Chen MH, Huang ZZ, Li B and Huang HW. 2012. Geochemistry of granitoid rocks of Shedong W-Mo deposit district in Cangwu County, Guangxi and its relation to mineralization. Acta Petrologica Sinica, 28(1): 199 – 212 (in Chinese with English abstract)

Chen MH, Li ZY, Li Q, Wei ZR, Huang HW, Zhang ZQ and Xiao LY. 2015. A preliminary study of multi-stage granitoids and related metallogenic series in Dayaoshan area of Guangxi, China. Earth Science Frontiers, 22(2): 41 – 53 (in Chinese with English abstract)

Chen MH, Dang Y, Zhang ZQ, Chen G, Huang ZZ and Ye YL. 2020. Caledonian tungsten deposits in Dayaoshan area of South China. Mineral Deposits, 39(4): 647 – 685 (in Chinese with English abstract)

Chen WD, Zhang WL, Wang RC, Chu ZY, Xiao R, Zhang D and Che XD. 2016. A study on the Dushiling tungsten-copper deposit in the Miao'ershan-Yuechengling area, northern Guangxi, China: Implications for variations in the mineralization of multi-aged composite granite plutons. Science China (Earth Sciences), 59(11): 2121 – 2141

Chen ZH, Wang DH, Sheng JF, Ying LJ, Liang T, Wang CH, Liu LJ and Wang YL. 2015. The metallogenic regularity of tin deposits in China. Acta Geologica Sinica, 89(6): 1026 – 1037 (in Chinese with English abstract)

Cheng SB, Fu JM, Ma LY, Lu YY, Kou XH, Zhang LG and Huang HL. 2016. Origin of the Yuechengling Caledonian granitic batholith, northeastern Guangxi: Constraint from zircon U-Pb geochronology, geochemistry, and Nd-Hf isotopes. Geotectonica et Metallogenia, 40(4): 853 – 872 (in Chinese with English abstract)

Cline JS and Bodnar RJ. 1994. Direct evolution of brine from a crystallizing silicic melt at the Questa, New Mexico, molybdenum deposit. Economic Geology, 89(8): 1780 – 1802

Clayton RN, O'Neil JR and Mayeda TK, 1972. Oxygen isotope exchange between quartz and water. Journal of Geophysical Research, 77(17): 3057 – 3067

Dang Y, Chen MH, Fu B, Mao JW, Fanning CM and Li ZY. 2018. Petrogenesis of the Yupo W-bearing and Dali Mo-bearing granitoids in the Dayaoshan area, South China: Constraints of geochronology and geochemistry. Ore Geology Reviews, 92: 643 – 655

Dang Y, Chen MH, Mao JW and Fu B. 2020. Weakly fractionated I-type granitoids and their relationship to tungsten mineralization: A case study from the Early Paleozoic Shangmushui deposit, Dayaoshan area, South China. Ore Geology Reviews, 117: 103281

Ding T. 2016. Geochemical study on metallogenetic relationship between Mesozoic granitoids and polymetallic deposits in southeastern Hunan, China. Ph. D. Dissertation. Nanjing: Nanjing University, 1 – 150 (in Chinese with English abstract)

Dong SH, Bi XW, Hu RZ, Chen YW and Chen H. 2011. Characteristics of ore-forming fluid in Yaogangxian quartz-vein wolframite deposit, Hunan Province. Journal of Mineralogy and Petrology, 31(2): 54 – 60 (in Chinese with English abstract)

Dou HR, Zhang WL, Wang RC and Chen WD. 2018. Chronology, metallogenic fluid properties and evolution of the Niutangjie tungsten deposit, northern Guangxi, China. Acta Geologica Sinica, 92(11): 2269 – 2300 (in Chinese with English abstract)

Du Y, Guo AM, Lu YY, Tian L, Wang JY, Zhou LT, Fan H and Luo XY. 2021. Petrogenesis of the Caledonian granites in the northern part of Miaoershan pluton, southwestern Hunan Province: Evidence from petrology, geochemistry and zircon U-Pb age. Geology in China, 48(5): 1540 – 1561 (in Chinese with English abstract)

Du Y, Tian L, Zheng ZF, Chen JF, Zhang XQ, Wang JY, Zhou LT, Fan H and Li C. 2022. Sm-Nd dating of scheelite in Luojiachong W-Sn deposit, Miaoershan area, southwestern Hunan Province: Implications for polycyclic tectonic-magmatic activities and metallogenesis in South China. Geological Bulletin of China, 41(5): 886 – 902 (in Chinese with English abstract)

Einaudi MT, Meinert LD and Newberry RJ. 1981. Skarn deposits. In: Skinner BJ (ed.). Seventy-Fifth Anniversary Volume. Society of Economic Geologists, 317 – 391

Fei GC, Menuge JF, Li YQ, Yang JY, Deng Y, Chen CS, Yang YF, Yang Z, Qin LY, Zheng L and Tang WC. 2020. Petrogenesis of the Lijiagou spodumene pegmatites in Songpan-Garze Fold Belt, West Sichuan, China: Evidence from geochemistry, zircon, cassiterite and coltan U-Pb geochronology and Hf isotopic compositions. Lithos, 364 – 365: 105555

Graupner T, Kempe U, Dombon E, Pätzold O, Leeder O and Spooner ETC. 1999. Fluid regime and ore formation in the tungsten (-yttrium) deposits of Kyzyltau (Mongolian Altai): Evidence for fluid variability in tungsten-tin ore systems. Chemical Geology, 154(1 – 4): 21 – 58

Griffin WL, Pearson NJ, Belousova E, Jackson SE, van Achterbergh E, O'Reilly SY and Shee SR. 2000. The Hf isotope composition of cratonic mantle: LAM-MC-ICPMS analysis of zircon megacrysts in kimberlites. Geochimica et Cosmochimica Acta, 64(1): 133 – 147

Griffin WL, Wang X, Jackson SE, Pearson NJ, O'Reilly SY, Xu XS and Zhou XM. 2002. Zircon chemistry and magma mixing, SE China: In-situ analysis of Hf isotopes, Tonglu and Pingtan igneous complexes. Lithos, 61(3 – 4): 237 – 269

Guo ZJ, Li JW, Huang MH, Guo WJ, Dong XZ, Tian J, Yang YC, She HQ, Xiang AP and Kang YJ. 2016. Characteristics of ore-forming fluid in Honghuaerji scheelite deposit, Inner Mongolia. Mineral Deposits, 35(1): 1 – 17 (in Chinese with English abstract)

Hall DL, Sterner SM and Bodnar RJ. 1988. Freezing point depression of NaCl-KCl-H_2O solutions. Economic Geology, 83(1): 197 – 202

Hedenquist JW and Lowenstern JB. 1994. The role of magmas in the formation of hydrothermal ore deposits. Nature, 370(6490): 519 – 527

Hoskin PWO and Schaltegger U. 2003. The composition of zircon and igneous and metamorphic petrogenesis. Reviews in Mineralogy and Geochemistry, 53(1): 27 – 62

Hu ZC, Liu YS, Gao S, Liu WG, Zhang W, Tong XR, Lin L, Zong KQ, Li M, Chen HH, Zhou L and Yang L. 2012. Improved in situ Hf isotope ratio analysis of zircon using newly designed X skimmer cone and Jet sample cone in combination with the addition of nitrogen by laser ablation multiple collector ICP-MS. Journal of Analytical Atomic Spectrometry, 27(9): 1391 – 1399

Hu ZC, Zhang W, Liu YS, Gao S, Li M, Zong KQ, Chen HH and Hu SH. 2015. "Wave" signal-smoothing and mercury-removing device for laser ablation quadrupole and multiple collector ICPMS analysis: Application to lead isotope analysis. Analytical Chemistry, 87(2): 1152 – 1157

Hua RM and Mao JW. 1999. A preliminary discussion on the Mesozoic

metallogenic explosion in East China. Mineral Deposits, 18(4): 300 – 307 (in Chinese with English abstract)

Hua RM, Chen PR, Zhang WL and Lu JJ. 2005. Three major metallogenic events in Mesozoic in South China. Mineral Deposits, 24(2): 99 – 107 (in Chinese with English abstract)

Hua RM, Zhang WL, Chen PR, Zhai W and Li GL. 2013. Relationship between Caledonian granitoids and large-scale mineralization in South China. Geological Journal of China Universities, 19(1): 1 – 11 (in Chinese with English abstract)

Huang HL, Chang HL, Tan J, Li F, Zhang CH and Zhou Y. 2015. Contrasting infrared microthermometry study of fluid inclusions in coexisting quartz, wolframite and other minerals: A case study of Xihuashan quartz-vein tungsten deposit, China. Acta Petrologica Sinica, 31(4): 925 – 940 (in Chinese with English abstract)

Jiang SY, Zhao KD, Jiang H, Su HM, Xiong SF, Xiong YQ, Xu YM, Zhang W and Zhu LY. 2020. Spatiotemporal distribution, geological characteristics and metallogenic mechanism of tungsten and tin deposits in China: An overview. Chinese Science Bulletin, 65(33): 3730 – 3745 (in Chinese with English abstract)

Jiang XZ, Kang ZQ, Xu JF, Feng ZH, Pang CJ, Fang GC, Wu JC and Xiong SQ. 2017. Early paleozoic granodioritic plutons in the Shedong W-Mo ore district, Guangxi, southern China: Products of re-melting of middle Proterozoic crust due to magma underplating. Journal of Asian Earth Sciences, 141: 59 – 73

Lecumberri-Sanchez P, Vieira R, Heinrich CA, Pinto F and Wälle M. 2017. Fluid-rock interaction is decisive for the formation of tungsten deposits. Geology, 45(7): 579 – 582

Li JD, Li XF and Xiao R. 2019. Multiple-stage tungsten mineralization in the Silurian Jiepai W skarn deposit, South China: Insights from cathodoluminescence images, trace elements, and fluid inclusions of scheelite. Journal of Asian Earth Sciences, 181: 103898

Li JX, Li GM, Qin KZ and Xiao B. 2011. High-temperature magmatic fluid exsolved from magma at the Duobuza porphyry copper-gold deposit, Northern Tibet. Geofluids, 11(2): 134 – 143

Li W, Xie GQ, Mao JW and Zhang HC. 2021. Mineralogy, fluid inclusion and isotope signatures: Implications for the genesis of the Early Paleozoic Yangjiashan scheelite-quartz vein deposit, South China. Ore Geology Reviews, 134: 104136

Li WJ, Liang JC, Feng ZM, Zhang GL, Chen MH and Yuan AP. 2006. Judging for characterstics of geochemical and structural environment of several Caledonian granitoids in Northeast Guangxi. Mineral Resources and Geology, 20(4 – 5): 353 – 360 (in Chinese with English abstract)

Li XF, Feng ZM, Li RS, Tang ZH, Qu WJ and Li JC. 2009. Silurian Mo mineralization at Baishiding molybdenum deposit in northern Guangxi: Constraints from zircon SHRIMP U-Pb and molybdenite Re-Os ages. Mineral Deposits, 28(4): 403 – 412 (in Chinese with English abstract)

Liu SB, Wang DH, Chen YC, Li JK, Ying LJ, Xu JX and Zeng ZL. 2008. $^{40}Ar/^{39}Ar$ ages of muscovite from different types tungsten-bearing quartz veins in the Chong-Yu-You concentrated mineral area in Gannan Region and its geological significance. Acta Geologica Sinica, 82(7): 932 – 940 (in Chinese with English abstract)

Liu YS, Hu ZC, Gao S, Günther D, Xu J, Gao CG and Chen HH. 2008. In situ analysis of major and trace elements of anhydrous minerals by LA-ICP-MS without applying an internal standard. Chemical Geology, 257(1 – 2): 34 – 43

Liu YS, Gao S, Hu ZC, Gao CG, Zong KQ and Wang DB. 2010. Continental and oceanic crust recycling-induced melt-peridotite interactions in the Trans-North China Orogen: U-Pb dating, Hf isotopes and trace elements in zircons from mantle xenoliths. Journal of Petrology, 51(1 – 2): 537 – 571

Lu HZ. 2000. High temperature, salinity and high concentrated ore metal magmatic fluids: An example from Grasberg Cu-Au porphyry deposit. Acta Petrologica Sinica, 16(4): 465 – 472 (in Chinese with English abstract)

Lu HZ, Fan HR, Ni P, Ou GX, Shen K and Zhang WH. 2004. Fluid Inclusion. Beijing: Science Press, 1 – 487 (in Chinese)

Ludwig KR. 2003. Isoplot 3.00: A Geochronological Toolkit for Microsoft Excel. Berkeley: Berkeley Geochronology Center, 1 – 39

Ludwig KR. 2012. User's manual for Isoplot version 3.75 – 4.15: A geochronological toolkit for Microsoft Excel. Berkeley Geochronological Center Special Publication, 5: 1 – 56

Luo P, Chen D, Yang J, Ling YX and Luo L. 2021. Petrogenesis of the Late Triassic Chuankou granite and implications for tungsten mineralization, Hunan Province. South China Geology, 37(3): 247 – 264 (in Chinese with English abstract).

Lü ZH, Chen J, Zhang H and Tang Y. 2021. Petrogenesis of Neoproterozoic rare metal granite-pegmatite suite in Jiangnan Orogen and its implications for rare metal mineralization of peraluminous rock in South China. Ore Geology Reviews, 128: 103923

Mao JW, Hua RM and Li XB. 1999. A preliminary study of large-scale metallogenesis and large clusters of mineral deposits. Mineral Deposits, 18(4): 291 – 299 (in Chinese with English abstract)

Mao JW, Xie GQ, Guo CL and Chen YC. 2007. Large-scale tungsten-tin mineralization in the Nanling region, South China: Metallogenic ages and corresponding geodynamic processes. Acta Petrologica Sinica, 23(10): 2329 – 2338 (in Chinese with English abstract)

Mao JW, Cheng YB, Chen MH and Pirajno F. 2013a. Major types and time-space distribution of Mesozoic ore deposits in South China and their geodynamic settings. Mineralium Deposita, 48(3): 267 – 294

Mao JW, Xie GQ, Yuan SD, Liu P, Meng XY, Zhou ZH and Zheng W. 2018. Current research progress and future trends of porphyry-skarn copper and granite-related tin polymetallic deposits in the Circum Pacific metallogenic belts. Acta Petrologica Sinica, 34(9): 2501 – 2517 (in English with Chinese abstract)

Mao JW, Ouyang HG, Song SW, Santosh M, Yuan SD, Zhou ZH, Zheng W, Liu H, Liu P, Cheng YB and Chen MH. 2019. Geology and metallogeny of tungsten and tin deposits in China. Economic Geology (Special Publications), 22: 411 – 482

Mao JW, Wu SH, Song SW, Dai P, Xie GQ, Su QW, Liu P, Wang XG, Yu ZZ, Chen XY and Tang WX. 2020. The world-class Jiangnan tungsten belt: Geological characteristics, metallogeny, and ore deposit model. Chinese Science Bulletin, 65(33): 3746 – 3762 (in Chinese with English abstract)

Mao JW, Zheng W, Xie GQ, Lehmann B and Goldfarb R. 2021a. Recognition of a Middle-Late Jurassic arc-related porphyry copper belt along the southeast China coast: Geological characteristics and metallogenic implications. Geology, 49(5): 592 – 596

Mao JW, Liu P, Goldfarb RJ, Goryachev NA, Pirajno F, Zheng W, Zhou MF, Zhao C, Xie GQ, Yuan SD and Liu M. 2021b. Cretaceous large-scale metal accumulation triggered by post-subductional large-scale extension, East Asia. Ore Geology Reviews, 136: 104270

Mao JW, Song SW, Liu P, Liu M, Zhao PL and Yuan SD. 2023. Current progress and development trend of the research on tin deposits. Acta Petrologica Sinica, 39(5): 1233 – 1240 (in Chinese with English abstract)

Mao YJ, Shao YJ, Xiong YQ, Jiang SY and Wen CH. 2021. Magmatic-hydrothermal metallogenic system in Nb-Ta-W-Sn-Pb-Zn Dengfuxian orefield, eastern Hunan: Constraint from U-Pb geochronology of columbite-tantalite. Journal of Central South University (Science and Technology), 52(9): 2959 – 2972 (in Chinese with English abstract)

Mao ZH, Cheng YB, Liu JJ, Yuan SD, Wu SH, Xiang XK and Luo XH. 2013b. Geology and molybdenite Re-Os age of the Dahutang granite-related veinlets-disseminated tungsten ore field in the Jiangxi Province, China. Ore Geology Reviews, 53: 422 – 433

Ni P, Wang XD, Wang GG, Huang JB, Pan JY and Wang TG. 2015a. An infrared microthermometric study of fluid inclusions in coexisting quartz and wolframite from Late Mesozoic tungsten deposits in the Gannan metallogenic belt, South China. Ore Geology Reviews, 65: 1062 – 1077

Ni P, Wang GG, Chen H, Xu YF, Guan SJ, Pan JY and Li L. 2015b. An Early Paleozoic orogenic gold belt along the Jiang-Shao Fault, South China: Evidence from fluid inclusions and Rb-Sr dating of

quartz in the Huangshan and Pingshui deposits. Journal of Asian Earth Sciences, 103: 87 – 102

Peng NL, Wang XH, Yang J, Chen D, Luo L, Luo P and Liu TY. 2017. Re-Os dating of molybdenite from Sanjiaotan tungsten deposit in Chuankou area, Hunan Province, and its geological implications. Mineral Deposits, 36(6): 1402 – 1414 (in Chinese with English abstract)

Peng NJ, Jiang SY, Xiong SF and Pi DH. 2018. Fluid evolution and ore genesis of the Dalingshang deposit, Dahutang W-Cu ore field, northern Jiangxi Province, South China. Mineralium Deposita, 53(8): 1079 – 1094

Qin JH, Wang DH, Li C, Chen YC and Cai FC. 2020. The molybdenite Re-Os isotope chronology, in situ scheelite and wolframite trace elements and Sr isotope characteristics of the Chuankou tungsten ore field, South China. Ore Geology Reviews, 126: 103756

Roedder E. 1984. Fluid Inclusions: Reviews in Mineralogy. Washington: Mineralogical Society of America, 12: 644

Sheng JF, Chen ZH, Liu LJ, Ying LJ, Huang F, Wang DH, Wang JH and Zeng L. 2015. Outline of metallogeny of tungsten deposits in China. Acta Geologica Sinica, 89(6): 1038 – 1050 (in Chinese with English abstract)

Sheppard SMF. 1986. Characterization and isotopic variations in natural waters. In: Valley JW, Taylor HP and O'Neil JR (eds.). Stable Isotopes in High Temperature Geological Processes. Reviews in Mineralogy. Washington: Mineralogical Society of America, 165 – 184

Söderlund U, Patchett PJ, Vervoort JD and Isachsen CE. 2004. The ^{176}Lu decay constant determined by Lu-Hf and U-Pb isotope systematics of Precambrian mafic intrusions. Earth and Planetary Science Letters, 219(3 – 4): 311 – 324

Su Y, Li GL, Tang A, Li CX, Wei XL and Yin XY. 2020. Zircon U-Pb age, petrochemistry, Sr-Nd-Hf isotopic features and genesis of granite porphyry from Juyuan tungsten deposit in central Jiangxi Province. Geotectonica et Metallogenia, 44(5): 971 – 985 (in Chinese with English abstract)

Taylor Jr HP. 1979. Oxygen and hydrogen isotope relationships in hydrothermal mineral deposit. In: Barnes HL (ed.). Geochemistry of Hydrothermal Ore Deposits. 2nd Edition. New York: Wiley, 236 – 277

Tera F and Wasserburg GJ. 1972. U-Th-Pb systematics in three Apollo 14 basalts and the problem of initial Pb in lunar rocks. Earth and Planetary Science Letters, 14(3): 281 – 304

Vervoort JD, Patchett PJ, Söderlund U and Baker M. 2004. Isotopic composition of Yb and the determination of Lu concentrations and Lu/Hf ratios by isotope dilution using MC-ICPMS. Geochemistry, Geophysics, Geosystems, 5(11): Q11002

Wang H, Feng CY, Zhao YM, Zhang MY, Chen RS and Chen JL. 2016. Ore genesis of the Lunwei granite-related scheelite deposit in the Wuyi metallogenic belt, Southeast China: Constraints from geochronology, fluid inclusions, and H-O-S isotopes. Resource Geology, 66(3): 240 – 258

Wang XD, Ni P, Yuan SD and Wu SH. 2012a. Characteristics of fluid inclusions of the Muziyuan tungsten deposit in Southern Jiangxi Province and their geological implications. Geology in China, 39(6): 1790 – 1797 (in Chinese with English abstract)

Wang XD, Ni P, Yuan SD and Wu SH. 2012b. Fluid inclusion studies of the Huangsha quartz-vein type tungsten deposit, Jiangxi Province. Acta Petrologica Sinica, 28(1): 122 – 132 (in Chinese with English abstract)

Wang XD, Ni P, Yuan SD and Wu SH. 2013. Fluid inclusion studies of Dajishan tungsten deposit in Jiangxi Province. Mineral Deposits, 32(2): 308 – 322 (in Chinese with English abstract)

Wang XL, Qiu Y, Lu JJ, Chou IM, Zhang WL, Li GL, Hu WX, Li Z and Zhong RC. 2020. In situ Raman spectroscopic investigation of the hydrothermal speciation of tungsten: Implications for the ore-forming process. Chemical Geology, 532: 119299

Wei WF, Hu RZ, Bi XW, Su WC, Song SQ and Shi SH. 2011a. Fluid evolution in Xihuashan tungsten deposit, southern Jiangxi Province, China. Acta Mineralogica Sinica, 31(2): 201 – 210 (in Chinese with English abstract)

Wei WF, Hu RZ, Peng JT, Bi XW, Song SQ and Shi SH. 2011b. Fluid mixing in Xihuashan tungsten deposit, southern Jixangxi Province: Hydrogen and oxygen isotope simulation analysis. Geochimica, 40(1): 45 – 55 (in English with Chinese abstract)

Wei WF, Hu RZ, Bi XW, Peng JT, Su WC, Song SQ and Shi SH. 2012. Infrared microthermometric and stable isotopic study of fluid inclusions in wolframite at the Xihuashan tungsten deposit, Jiangxi Province, China. Mineralium Deposita, 47(6): 589 – 605

Wiedenbeck M, Allé P, Corfu F, Griffin WL, Meier M, Oberli F, Von Quadt A, Roddick JC and Spiegel W. 1995. Three natural zircon standards for U-Th-Pb, Lu-Hf, trace element and REE analyses. Geostandards Newsletter, 19(1): 1 – 23

Wilkinson JJ. 2001. Fluid inclusions in hydrothermal ore deposits. Lithos, 55(1 – 4): 229 – 272

Wood SA and Samson IM. 2000. The hydrothermal geochemistry of tungsten in granitoid environments: Ⅰ. Relative solubilities of ferberite and scheelite as a function of T, P, pH, and mNaCl. Economic Geology, 95(1): 143 – 182

Wu FY, Yang YH, Xie LW, Yang JH and Xu P. 2006. Hf isotopic compositions of the standard zircons and baddeleyites used in U-Pb geochronology. Chemical Geology, 234(1 – 2): 105 – 126

Wu FY, Liu XC, Ji WQ, Wang JM and Yang L. 2017. Highly fractionated granites: Recognition and research. Science China (Earth Sciences), 60(7): 1201 – 1219

Wu FY, Guo CL, Hu FY, Liu XC, Zhao JX, Li XF and Qin KZ. 2023. Petrogenesis of the highly fractionated granites and their mineralizations in Nanling Range, South China. Acta Petrologica Sinica, 39(1): 1 – 36 (in Chinese with English abstract)

Wu J, Liang HY, Huang WT, Wang CL, Sun WD, Sun YL, Li J, Mo JH and Wang XZ. 2012. Indosinian isotope ages of plutons and deposits in southwestern Miaoershan-Yuechengling, northeastern Guangxi and implications on Indosinian mineralization in South China. Chinese Science Bulletin, 57(9): 1024 – 1035

Wu YB and Zheng YF. 2004. Genesis of zircon and its constraints on interpretation of U-Pb age. Chinese Science Bulletin, 49(15): 1554 – 1569

Xiang L, Wang RC, Erdmann S, Sizaret S, Lu JJ, Zhang WL, Xie L, Che XD and Zhang RQ. 2018. Neoproterozoic mineralization in a hydrothermal cassiterite-sulfide deposit at Jiumao, northern Guangxi, South China: Mineral-scale constraints on metal origins and ore-forming processes. Ore Geology Reviews, 94: 172 – 192

Xie GQ, Mao JW, Li W, Fu B and Zhang ZY. 2019. Granite-related Yangjiashan tungsten deposit, southern China. Mineralium Deposita, 54(1): 67 – 80

Xie GQ, Mao JW, Zhang CQ, Li W, Song SW and Zhang RQ. 2021. Triassic deposits in South China: Geological characteristics, ore-forming mechanism and ore deposit model. Earth Science Frontiers, 28(3): 252 – 270 (in Chinese with English abstract)

Xiong YQ, Shao YJ, Zhou HD, Wu QH, Liu JP, Wei HT, Zhao RC and Cao JY. 2017. Ore-forming mechanism of quartz-vein-type W-Sn deposits of the Xitian district in SE China: Implications from the trace element analysis of wolframite and investigation of fluid inclusions. Ore Geology Reviews, 83: 152 – 173

Xiong YQ, Shao YJ, Mao JW, Wu SC, Zhou HD and Zheng MH. 2019. The polymetallic magmatic-hydrothermal Xiangdong and Dalong systems in the W-Sn-Cu-Pb-Zn-Ag Dengfuxian orefield, SE China: Constraints from geology, fluid inclusions, H-O-S-Pb isotopes, and sphalerite Rb-Sr geochronology. Mineralium Deposita, 54(8): 1101 – 1124

Xiong YQ, Shao YJ, Cheng YB and Jiang SY. 2020. Discrete Jurassic and Cretaceous mineralization events at the Xiangdong W (-Sn) deposit, Nanling Range, South China. Economic Geology, 115(2): 385 – 413

Xiong ZR, Li XN, Qi C and Xiong YQ. 2021. Geochronology of cassiterite and trace element compositions of wolframite: Constraints to the ore genesis of Jiguanshi tungsten deposit, eastern Hunan

Province. Acta Petrologica Sinica, 37(3): 769 – 780 (in Chinese with English abstract)

Yang F, Li XF, Feng ZM and Bai YP. 2009. $^{40}Ar/^{39}Ar$ dating of muscovite from greisenized granite and geological Significance in Limu tin deposit. Journal of Guilin University of Technology, 29(1): 21 – 24 (in Chinese with English abstract)

Yang Z, Wang RC, Zhang WL, Chu ZY, Chen J, Zhu JC and Zhang RQ. 2014. Skarn-type tungsten mineralization associated with the Caledonian (Silurian) Niutangjie granite, northern Guangxi, China. Science China (Earth Sciences), 57(7): 1551 – 1566

Yang ZM, Xie YL, Li GM, Xu JH and Wang BH. 2005. Study of fluid inclusions from Tinggong porphyry copper deposit in Gangdese Belt, Tibet. Mineral Deposits, 24(6): 584 – 594 (in Chinese with English abstract)

Yu YS, Zhou Y, Niu ZJ, An ZH and Liu AS. 2022. Geochemical characteristics, age and W-Sn metallogenic potential of Penggongmiao pluton, Hunan Province. Acta Petrologica et Mineralogica, 41(4): 695 – 713 (in Chinese with English abstract)

Yuan SD, Peng JT, Hu RZ, Li HM, Shen NP and Zhang DL. 2008. A precise U-Pb age on cassiterite from the Xianghualing tin-polymetallic deposit (Hunan, South China). Mineralium Deposita, 43(4): 375 – 382

Yuan SD, Peng JT, Hao S, Li HM, Geng JZ and Zhang DL. 2011. In situ LA-MC-ICP-MS and ID-TIMS U-Pb geochronology of cassiterite in the giant Furong tin deposit, Hunan Province, South China: New constraints on the timing of tin-polymetallic mineralization. Ore Geology Reviews, 43(1): 235 – 242

Yuan SD, Zhang DL, Shuang Y, Du AD and Qu WJ. 2012a. Re-Os dating of molybdenite from the Xintianling giant tungsten-molybdenum deposit in southern Hunan Province, China and its geological implications. Acta Petrologica Sinica, 28(1): 27 – 38 (in Chinese with English abstract)

Yuan SD, Liu XF, Wang XD, Wu SH, Yuan YB, Li XK and Wang TZ. 2012b. Geological characteristics and ^{40}Ar-^{39}Ar geochronology of the Hongqiling tin deposit in southern Hunan Province. Acta Petrologica Sinica, 28(12): 3787 – 3797 (in Chinese with English abstract)

Yuan SD, Mao JW, Cook NJ, Wang XD, Liu XF and Yuan YB. 2015. A Late Cretaceous tin metallogenic event in Nanling W-Sn metallogenic province: Constraints from U-Pb, Ar-Ar geochronology at the Jiepailing Sn-Be-F deposit, Hunan, China. Ore Geology Reviews, 65: 283 – 293

Yuan SD. 2017. Several crucial scientific issues related to the W-Sn metallogenesis in the Nanling Range and their implications for regional exploration: A review. Bulletin of Mineralogy, Petrology and Geochemistry, 36(5): 736 – 749 (in Chinese with English abstract)

Yuan SD, Williams-Jones AE, Mao JW, Zhao PL, Yan C and Zhang DL. 2018a. The origin of the Zhangjialong tungsten deposit, South China: Implications for W-Sn mineralization in large granite batholiths. Economic Geology, 113(5): 1193 – 1208

Yuan SD, Williams-Jones AE, Romer RL, Zhao PL and Mao JW. 2019. Protolith-related thermal controls on the decoupling of Sn and W in Sn-W metallogenic provinces: Insights from the Nanling region, China. Economic Geology, 114(5): 1005 – 1012

Yuan SD, Zhao PL and Liu M. 2020. Some problems involving in petrogenesis and metallogenesis of granite-related tin deposits. Mineral Deposits, 39(4): 607 – 618 (in Chinese with English abstract)

Yuan YB, Yuan SD, Mao JW, Zhao PL, Yan C, Zhao HJ, Zhang DL, Shuang Y and Peng JT. 2018b. Recognition of Late Jurassic W-Sn mineralization and its exploration potential on the western margin of the Caledonian Guidong granite batholith, Nanling Range, South China: Geochronological evidence from the Liuyuan Sn and Zhuyuanli W deposits. Ore Geology Reviews, 93: 200 – 210

Zhang D, Zhang WL, Wang RC, Chu ZY, Gong MW and Jiang GX. 2015. Quartz-vein type tungsten mineralization associated with the Indosinian (Triassic) Gaoling granite, Miao'ershan area, northern Guangxi. Geological Review, 61(4): 817 – 834 (in Chinese with English abstract)

Zhang HF, Lu JJ, Wang RC, Ma DS, Zhu JC and Zhang RQ. 2014. Petrogenesis of the concealed Daqiling intrusion in Guangxi and its tectonic significance: Constraints from geochemistry, zircon U-Pb dating and Nd-Hf isotopic compositions. Science China (Earth Sciences), 57(8): 1723 – 1740

Zhang Q and Lu JJ. 2019. Caledonian W-Sn mineralization in Miao'ershan-Yuechengling region. In: Proceedings of the Symposium Proceedings for 9th Metallogenic theory and Prospecting in China. Nanjing: 53 – 54 (in Chinese)

Zhang RQ, Lu JJ, Wang RC, Yang P, Zhu JC, Yao Y, Gao JF, Li C, Lei ZH, Zhang WL and Guo WM. 2015. Constraints of in situ zircon and cassiterite U-Pb, molybdenite Re-Os and muscovite ^{40}Ar-^{39}Ar ages on multiple generations of granitic magmatism and related W-Sn mineralization in the Wangxianling area, Nanling Range, South China. Ore Geology Reviews, 65: 1021 – 1042

Zhang W and Hu ZC. 2020. Estimation of isotopic reference values for pure materials and geological reference materials. Atomic Spectroscopy, 41(3): 93 – 102

Zhang WL, Che XD, Chen WD, Wang RC and Zhang D. 2017. A new potential Caledonian-Indosinian ore concentration area: Evidence from diagenesis and mineralization ages of the Miao'ershan-Yuechengling region. Acta Geologica Sinica, 91(2): 743 – 744

Zhang ZY, Xie GQ and Li W. 2021. Muscovite ^{40}Ar-^{39}Ar and LA-ICP-MS cassiterite U-Pb dating of Yangjiashan quartz scheelite deposit, Xiangzhong ore district and its geological significance. Acta petrologica Sinica, 37(3): 794 – 804 (in Chinese with English abstract)

Zhao PL, Yuan SD, Williams-Jones AE, Romer RL, Yan C, Song SW and Mao JW. 2022a. Temporal separation of W and Sn mineralization by temperature-controlled incongruent melting of a single protolith: Evidence from the Wangxianling area, Nanling region, South China. Economic Geology, 117(3): 667 – 682

Zhao PL, Zajacz Z, Tsay A and Yuan SD. 2022b. Magmatic-hydrothermal tin deposits form in response to efficient tin extraction upon magma degassing. Geochimica et Cosmochimica Acta, 316: 331 – 346

Zhao PL, Chu X, Williams-Jones AE, Mao JW and Yuan SD. 2022c. The role of phyllosilicate partial melting in segregating tungsten and tin deposits in W-Sn metallogenic provinces. Geology, 50(1): 121 – 125

Zhao Z, Zhao WW, Lu L and Wang HY. 2018. Constraints of multiple dating of the Qingshan tungsten deposit on the Triassic W(-Sn) mineralization in the Nanling Region, South China. Ore Geology Reviews, 94: 46 – 57

Zheng YF, Long XB and Zhou GT. 2000. Geochemical studies of stable isotopes in minerals. Earth Science Frontiers, 7(2): 299 – 320 (in Chinese with English abstract)

Zhou LT, Chen JF, Du Y, Lu W and Shi JJ. 2022. Monazite U-Pb geochronology of granites in the Shaping tungsten deposit, western Nanling metallogenic belt and its geological significance. South China Geology, 38(3): 486 – 495 (in Chinese with English abstract)

Zhu YT, Li XF, Xiao R, Yu Y and Wang CZ. 2020. Multistage magmatic-hydrothermal activity and W-Cu mineralization at Jiepai, Guangxi, South China: Constraints from geochronology and Nd-Sr-Hf-O isotopes. Ore Geology Reviews, 121: 103492

附中文参考文献

蔡明海, 陈开旭, 屈文俊, 刘国庆, 付建明, 印建平. 2006. 湘南荷花坪锡多金属矿床地质特征及辉钼矿 Re-Os 测年. 矿床地质, 25(3): 263 – 268

陈剑锋. 2019. 湖南省城步县平滩白钨矿床成矿机制研究. 博士学位论文. 长沙: 中南大学, 1 – 119

陈剑锋, 邵拥军, 戴雪灵, 盛丹, 管申进, 文春华, 张锦煦, 林碧海,

田磊．2020．南岭地区平滩加里东期钨矿床成矿流体特征．中国有色金属学报，30(7)：1714－1729

陈懋弘，莫次生，黄智忠，李斌，黄宏伟．2011．广西苍梧县社洞钨钼矿床花岗岩类锆石 LA-ICP-MS 和辉钼矿 Re-Os 年龄及其地质意义．矿床地质，30(6)：963－978

陈懋弘，黄智忠，李斌，黄宏伟．2012．广西苍梧社洞钨钼矿床花岗岩类岩石的地球化学特征及其与成矿关系．岩石学报，28(1)：199－212

陈懋弘，李忠阳，李青，韦子任，黄宏伟，张志强，肖柳阳．2015．初论广西大瑶山地区多期次花岗质岩浆活动与成矿系列．地学前缘，22(2)：41－53

陈懋弘，党院，张志强，陈港，黄智忠，叶有乐．2020．华南大瑶山地区加里东期钨矿床．矿床地质，39(4)：647－685

陈郑辉，王登红，盛继福，应立娟，梁婷，王成辉，刘丽君，王永磊．2015．中国锡矿成矿规律概要．地质学报，89(6)：1026－1037

程顺波，付建明，马丽艳，卢友月，寇晓虎，张利国，黄惠兰．2016．桂东北越城岭岩体加里东期成岩作用：锆石 U-Pb 年代学、地球化学和 Nd-Hf 同位素制约．大地构造与成矿学，40(4)：853－872

丁腾．2016．湘东南中生代花岗岩与多金属矿床成因关系的地球化学研究．博士学位论文．南京：南京大学，1－150

董少花，毕献武，胡瑞忠，陈佑纬，陈恒．2011．湖南瑶岗仙石英脉型黑钨矿床成矿流体特征．矿物岩石，31(2)：54－60

豆浩然，张文兰，王汝成，陈文迪．2018．桂北牛塘界加里东期钨矿床年代学、成矿流体性质及其演化．地质学报，92(11)：2269－2300

杜云，郭爱民，卢友月，田磊，王敬元，周立同，樊晖，罗小亚．2021．湘西南苗儿山岩体北段加里东期花岗岩成因：来自岩石学、地球化学和锆石 U-Pb 年代学的证据．中国地质，48(5)：1540－1561

杜云，田磊，郑正福，陈剑锋，张小强，王敬元，周立同，樊晖，李超．2022．湘西南落家冲钨锡矿床加里东期成岩成矿年龄的测定：对华南多旋回构造-岩浆活动与成矿作用的启示．地质通报，41(5)：886－902

郭志军，李进文，黄蒙辉，郭万军，董旭舟，田京，杨郧城，佘宏全，向安平，康永建．2016．内蒙古红花尔基白钨矿矿床流体包裹体研究．矿床地质，35(1)：1－17

华仁民，毛景文．1999．试论中国东部中生代成矿大爆发．矿床地质，18(4)：300－307

华仁民，陈培荣，张文兰，陆建军．2005．论华南地区中生代3次大规模成矿作用．矿床地质，24(2)：99－107

华仁民，张文兰，陈培荣，翟伟，李光来．2013．初论华南加里东花岗岩与大规模成矿作用的关系．高校地质学报，19(1)：1－11

黄惠兰，常海亮，谭靖，李芳，张春红，周云．2015．共生黑钨矿与石英等多种矿物中流体包裹体的红外显微测温对比研究——以江西西华山石英脉钨矿床为例．岩石学报，31(4)：925－940

蒋少涌，赵葵东，姜海，苏慧敏，熊索菲，熊伊曲，徐耀明，章伟，朱律运．2020．中国钨锡矿床时空分布规律、地质特征与成矿机制研究进展．科学通报，65(33)：3730－3745

李文杰，梁金城，冯佐海，张桂林，陈懋弘，袁爱平．2006．桂东北地区几个加里东期花岗岩体的地球化学特征及其构造环境判别．矿产与地质，20(4－5)：353－360

李晓峰，冯佐海，李容森，唐专红，屈文俊，李军朝．2006．华南志留纪钼的矿化：白石顶钼矿锆石 SHRIMP U-Pb 年龄和辉钼矿 Re-Os 年龄证据．矿床地质，28(4)：403－412

刘善宝，王登红，陈毓川，李建康，应立娟，许建祥，曾载淋．2008．赣南崇义-大余-上犹矿集区不同类型含矿石英中白云母$^{40}Ar/^{39}Ar$年龄及其地质意义．地质学报，82(7)：932－940

卢焕章．2000．高盐度、高温和高成矿金属的岩浆成矿流体——以格拉斯伯格 Cu-Au 矿为例．岩石学报，16(4)：465－472

卢焕章，范宏瑞，倪培，欧光习，沈昆，张文淮．2004．流体包裹体．北京：科学出版社，1－487

罗鹏，陈迪，杨俊，凌跃新，罗来．2021．湖南川口印支期花岗岩成因及与钨成矿关系．华南地质，37(3)：247－264

毛景文，华仁民，李晓波．1999．浅议大规模成矿作用与大型矿集区．矿床地质，18(4)：291－299

毛景文，谢桂青，郭春丽，陈毓川．2007．南岭地区大规模钨锡多金属成矿作用：成矿时限及地球动力学背景．岩石学报，23(10)：2329－2338

毛景文，谢桂青，袁顺达，刘鹏，孟旭阳，周振华，郑伟．2018．环太平洋成矿带斑岩-矽卡岩型铜矿和与花岗岩有关的锡多金属矿研究现状与展望．岩石学报，34(9)：2501－2517

毛景文，吴胜华，宋世伟，戴盼，谢桂青，苏蔷薇，刘鹏，王先广，于忠珍，陈祥云，唐维新．2020．江南世界级钨矿带：地质特征、成矿规律和矿床模型．科学通报，65(33)：3746－3762

毛景文，宋世伟，刘鹏等，刘敏，赵盼捞，袁顺达．2023．锡矿床研究现状及发展趋势．岩石学报，39(5)：1233－1240

毛禹杰，邵拥军，熊伊曲，蒋少涌，文春华．2021．湘东邓阜仙 Nb-Ta-W-Sn-Pb-Zn 岩浆热液成矿系统：铌钽锰矿 U-Pb 年代学约束．中南大学学报(自然科学版)，52(9)：2959－2972

彭能立，王先辉，杨俊，陈迪，罗来，罗鹏，刘天一．2017．湖南川口三角潭钨矿床中辉钼矿 Re-Os 同位素定年及其地质意义．矿床地质，36(6)：1402－14147

盛继福，陈郑辉，刘丽君，应立娟，黄凡，王登红，王家欢，曾乐．2015．中国钨矿成矿规律概要．地质学报，89(6)：1038－1050

苏晔，李光来，唐傲，李成祥，韦星林，尹晓燕．2020．赣中聚源钨矿区花岗斑岩锆石 U-Pb 年代学、岩石地球化学和 Sr-Nd-Hf 同位素特征及成因探讨．大地构造与成矿学，44(5)：971－985

王旭东，倪培，袁顺达，吴胜华．2012a．赣南木梓园钨矿流体包裹体特征及其地质意义．中国地质，39(6)：1790－1797

王旭东，倪培，袁顺达，吴胜华．2012b．江西黄沙石英脉型钨矿床流体包裹体研究．岩石学报，28(1)：122－132

王旭东，倪培，袁顺达，吴胜华．2013．江西大吉山钨多金属矿床流体包裹体研究．矿床地质，32(2)：308－322

魏文凤，胡瑞忠，毕献武，苏文超，宋生琼，石少华．2011a．赣南西华山钨矿床成矿流体演化特征．矿物学报，31(2)：201－210

魏文凤，胡瑞忠，彭建堂，毕献武，宋生琼，石少华．2011b．赣南西华山钨矿床的流体混合作用：基于 H、O 同位素模拟分析．地球化学，40(1)：45－55

吴福元，刘小驰，纪伟强，王佳敏，杨雷．2017．高分异花岗岩的识别与研究．中国科学(地球科学)，47(7)：745－765

吴福元，郭春丽，胡方泱，刘小池，赵俊兴，李晓峰，秦克章．2023．

南岭高分异花岗岩成岩与成矿. 岩石学报, 39(1): 1 – 36

伍静, 梁华英, 黄文婷, 王春龙, 孙卫东, 孙亚莉, 李晶, 莫济海, 王秀璋. 2012. 桂东北苗儿山-越城岭南西部岩体和矿床同位素年龄及华南印支期成矿分析. 科学通报, 57(13): 1126 – 1136

吴元保, 郑永飞. 2004. 锆石成因矿物学研究及其对 U-Pb 年龄解释的制约. 科学通报, 49(16): 1589 – 1604

谢桂青, 毛景文, 张长青, 李伟, 宋世伟, 章荣清. 2021. 华南地区三叠纪矿床地质特征、成矿规律和矿床模型. 地学前缘, 28(3): 252 – 270

熊峥嵘, 李信念, 祁程, 熊伊曲. 2021. 锡石年代学和黑钨矿微量元素对湘东鸡冠石钨矿床的成因约束. 岩石学报, 37(3): 769 – 780

杨锋, 李晓峰, 冯佐海, 白艳萍. 2009. 栗木锡矿云英岩化花岗岩白云母$^{40}Ar/^{39}Ar$ 年龄及其地质意义. 桂林工学院学报, 29(1): 21 – 24

杨志明, 谢玉玲, 李光明, 徐九华, 王葆华. 2005. 西藏冈底斯斑岩铜矿带厅宫铜矿床流体包裹体研究. 矿床地质, 24(6): 584 – 594

于玉帅, 周云, 牛志军, 安志辉, 刘阿睢. 2022. 湖南彭公庙岩体地球化学特征、时代及钨锡成矿潜力. 岩石矿物学杂志, 41(4): 695 – 713

袁顺达, 张东亮, 双燕, 杜安道, 屈文俊. 2012a. 湘南新田岭大型钨钼矿床辉钼矿 Re-Os 同位素测年及其地质意义. 岩石学报, 28(1): 27 – 38

袁顺达, 刘晓菲, 王旭东, 吴胜华, 原垭斌, 李雪凯, 王铁柱. 2012b. 湘南红旗岭锡多金属矿床地质特征及 Ar-Ar 同位素年代学研究. 岩石学报, 28(12): 3787 – 3797

袁顺达. 2017. 南岭钨锡成矿作用几个关键科学问题及其对区域找矿勘查的启示. 矿物岩石地球化学通报, 36(5): 736 – 749

袁顺达, 赵盼捞, 刘敏. 2020. 与花岗岩有关锡矿成岩成矿作用研究若干问题讨论. 矿床地质, 39(4): 607 – 618

张迪, 张文兰, 王汝成, 储著银, 龚名文, 蒋桂新. 2015. 桂北苗儿山地区高岭印支期花岗岩及石英脉型钨成矿作用. 地质论评, 61(4): 817 – 834

张怀峰, 陆建军, 王汝成, 马东升, 朱金初, 章荣清. 2014. 广西栗木大岐岭隐伏花岗岩的成因及其构造意义: 岩石地球化学、锆石 U-Pb 年代学和 Nd-Hf 同位素制约. 中国科学(地球科学), 44(5): 901 – 918

张强, 陆建军. 2019. 苗儿山-越城岭地区加里东期钨锡成矿作用. 见: 第九届全国成矿理论与找矿方法学术讨论会摘要. 南京: 53 – 54

张志远, 谢桂青, 李伟. 2021. 湘中矿集区杨家山石英脉白钨矿床的白云母^{40}Ar-^{39}Ar 和 LA-ICP-MS 锡石 U-Pb 年龄及其地质意义. 岩石学报, 37(3): 794 – 804

郑永飞, 徐宝龙, 周根陶. 2000. 矿物稳定同位素地球化学研究. 地学前缘. 7(2): 299 – 320

周立同, 陈剑锋, 杜云, 陆文, 石金江. 2022. 南岭西段沙坪钨矿区花岗岩独居石 U-Pb 定年及地质意义. 华南地质, 38(3): 486 – 495

Ore Geology Reviews 153 (2023) 105276

Contents lists available at ScienceDirect

Ore Geology Reviews

journal homepage: www.elsevier.com/locate/oregeorev

Petrogenesis of Mesozoic Li-, Cs-, and Ta-rich (LCT) pegmatites from the Neoproterozoic Jiangnan Orogenic Belt, South China: An alternative origin model for the LCT type pegmatite

Jian-Feng Chen [a,b,c], Chun-Hua Wen [b], Zheng-Hang Lv [d,e,*], Jian-Zhong Huang [b], Jin-Xu Zhang [b], Yong Tang [d], Yun Du [b], Chuang-Hua Cao [b]

[a] Geophysical and Geochemical Survey Institute of Hunan, Changsha 410116, PR China
[b] Hunan Institute of Geological Survey, Changsha 410116, PR China
[c] Key Laboratory of Metallogenic Prediction of Nonferrous Metals and Geological Environment Monitoring, Ministry of Education, Central South University, Changsha 410083, PR China
[d] Institute of Geochemistry, Chinese Academy of Sciences, Guiyang 55081, PR China
[e] Key Laboratory of Critical Minerals Metallogeny in University of Yunnan Province, School of Earth Sciences, Yunnan University, Kunming 650500, PR China

ARTICLE INFO

Keywords:
Petrogenesis
Mesozoic
LCT pegmatite
Parallel differentiation model
Jiangnan Orogenic Belt

ABSTRACT

According to the classical petrogenesis model, Li-, Cs-, and Ta-rich (LCT) pegmatites juxtaposed in the same regional zonation are generally formed by unidirectional successive crystallization differentiation of the common parental granitic melt. However, this model cannot explain the origin of the Mesozoic LCT pegmatites from the East Jiangnan Orogenic Belt (JOB), South China. Herein, we studied the geology, zircon U–Pb ages, Hf isotope compositions, monazite U–Th–Pb ages, and Nd isotope compositions of three types of pegmatites in Renli, East JOB, South China to reveal their petrogenesis. The Renli pegmatites distributed in or around the Mufushan batholith, show mineralization zoning with distance from the batholith. The studied pegmatites were formed at the Early Cretaceous, with a decreasing trend from ca. 141 Ma for two-mica microcline pegmatite (type I) to 134 Ma for muscovite–albite–spodumene pegmatite (type III). The Renli pegmatites have coupled Hf–Nd isotope compositions and consistent Hf isotope compositions with the Mufushan granites. From the spatial–temporal, source and differentiation relationships between the Renli pegmatites and the Mufushan granites, we propose that type I pegmatites originates from biotite monzogranite while type II (muscovite–microcline–albite pegmatite) and type III pegmatites originate from the two-mica monzogranite and muscovite monzogranite, respectively, indicating a new model of parallel differentiations of triple granitic melts for the origin of LCT pegmatites in South China. The Renli pegmatites have a similar Hf isotope composition to the Neoproterozoic granitoids and the backarc sedimentary rocks of the Lengjiaxi Group formed during the Jiangnan orogeny. Combining with previous studies, we suggest that the Mesozoic Renli LCT pegmatites originated from reworking materials of the Neoproterozoic JOB caused by slab roll back of the paleo-Pacific Ocean plate during subduction.

1. Introduction

Granitic pegmatites (hereinafter referred to as pegmatites) have garnered immense attention because of their rare-earth element enrichment namely Li, Be, Nb, Ta, and Cs, which are listed as strategic mineral sources by many countries. Although the favorable tectonic settings of pegmatites still remain under debate, the Li-, Cs-, Ta-rich (LCT) pegmatites appear dominantly in convergent orogenic belts and correlate with orogenic, especially postorogenic, magmatisms (Černý, 1991; Černý et al., 2012) and supercontinent assembly temporally (e.g., McCauley and Bradley, 2014; Tkachev, 2011). In China, LCT pegmatites are widely exposed in the Altai, East Tianshan, West Kunlun, and Songpan–Ganzi Orogenic Belts, and most of them have been proposed to form in a postorogenic extension stage after accretion or collision orogeny (e.g., Lv et al., 2012, 2021a; Li et al., 2020a; Fei et al., 2020; Wang et al., 2020; Yan et al., 2022).

The Jiangnan Orogenic Belt (JOB), South China, is a convergence zone formed by Yangtze and Cathaysia block collision during the

* Corresponding author at: Institute of Geochemistry, Chinese Academy of Sciences, No. 99 Lincheng West Street, Guiyang 55081, PR China.
E-mail address: lvzhenghang@vip.gyig.ac.cn (Z.-H. Lv).

https://doi.org/10.1016/j.oregeorev.2022.105276
Received 25 June 2022; Received in revised form 6 December 2022; Accepted 27 December 2022
Available online 28 December 2022

Neoproterozoic (e.g.,Wang et al., 2014a, 2017; Zhou et al., 2009). Thus far, two periods of rare-metal pegmatites have been verified in the JOB. The early-one is represented by the Neoproterozoic pegmatite exposed only in the Fanjingshan area, West JOB. It comprises tens of pegmatites with limited Nb–Ta–Sn mineralization, which genetically relates to the Fanjingshan muscovite granite, and is formed by the partial melting of sedimentary rocks and high degrees of fractional crystallization of granitic melts after continental collision at ca. 830 Ma (Lv et al., 2021a). The late one is comprises of>1000 pegmatites distributed in or around the Yanshanian Mufushan batholith (YMB), East JOB. Recent exploration reveals that plenty of pegmatites have large potential for rare-metal (Nb–Ta ± Li ± Be) mineralizations, especially those exposed in the Renli mining area, South YMB (Zhou et al., 2019a, b) (Fig. 1). The YMB mainly comprises granodiorite, biotite monzogranite (BMG), and two-mica monzogranite (TMG) (Wang et al., 2014b), and the highly fractionated granitic phase, such as muscovite granite, is almost absent. In addition, lots of the pegmatites are widely distributed in the granodiorite, BMG and TMG (Fig. 1), and they have distinct mineral assemblages and mineralizations. These granite-hosted pegmatites also differ to those emplaced in sedimentary rocks. According to the classical model, a successive and (sub)vertical fractionation sequence of a granitic melt, normally featured by a lower biotite granite, an intermediate two-mica granite, and an upper muscovite granite, is essential for pegmatite regional zonation generation, and the most fractionated granite phase is directly responsible for all types of pegmatites in the same zonation (e.g., Černý, 1991; London, 2018). Moreover, pegmatites derived from the upper fractionated granitic melt are impossible to emplace in the lower granitic phase. Therefore, the classical model is hard to explain the pervasive occurrence of pegmatites in various granitoids. Were they originated from a common granitic source or multiple sources, still remains unanswered?

Although some studies have been conducted on the granites and adjacent pegmatites in the Mufushan area, especially the geochronology (Li et al., 2019, 2020b; Xiong et al., 2020; Zhou et al, 2020), mineralizing mechanism (Liu et al., 2019; Zhou et al., 2019a), and magma ecolution (Wang et al., 2019; Yang et al., 2019; Zhou et al., 2019b) studies of the Renli No.5 pegmatite, which is the most remarkable Nb–Ta mineralization dike in the Mufushan area, it is not enough to reveal the petrogenesis of various pegmatites, especially the relationship between pegmatites and granitoids. Herein, monazite and zircon U–(Th)–Pb chronology was used to study the formation ages of the three types of pegmatites, including the Nos. 7, 2, 3, and 47 pegmatites, distributed in the Renli mining area, South YMB, and Nd–Hf isotope compositions to determine their source, aiming to decipher the petrogenesis of LCT pegmatite that formed in the JOB, South China.

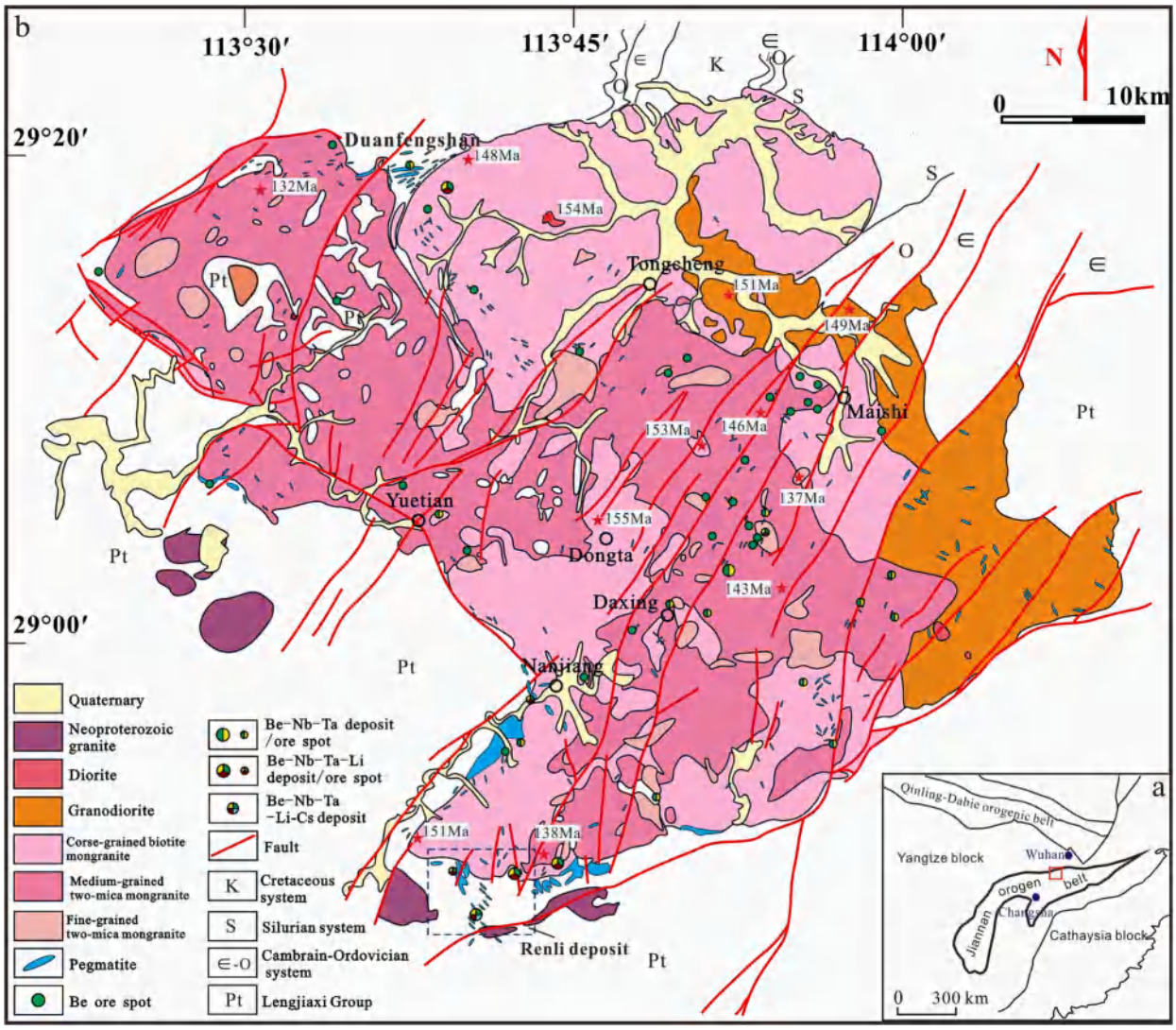

Fig. 1. Tectonic outline of the JiangnanOrogen Belt(a) and the geological sketch map of the Mufushan area (b) (modified from Li et al., 2021).

2. Geological setting

The Renli pegmatite-type rare-metal deposit is located in the Mufushan region, the central–eastern segment of the JOB in South China (Fig. 1a). The JOB, also referred to as the Jiangnan Orogen, Jiangnan paleocontinent, Jiangnan block, and Jiangnan fold belt (Cawood et al., 2013;Shu et al., 1994; Wang et al., 2006; Xu et al., 2017;Yao et al., 2014; Yu et al., 2021), was formed by the Neoproterozoic amalgamation of the Yangtze and Cathaysia blocks due to the subduction and collision processes before ca. 820 Ma (Li, 2006; Li et al., 2009; Shan et al., 2017; Wang et al., 2014a; Zhao et al., 2011) and reactivated at ~ 130 Ma because of the paleo-Pacific plate subduction toward the Eurasic plate (Shu and Zhou, 2002; Wang and Zhou, 2002; Wang and Shu, 2012). The central–eastern JOB is an important polymetallic metallogenic belt in South China and hosts large amounts of Au, Sb, W, Cu, Co, Pb, Zn, and even Be, Nb, and Ta ore deposits/spots(Deng et al., 2017; Hu and Peng, 2018; Lv et al., 2021a; Wang et al., 2017a; Wen et al., 2021; Xiong et al., 2020; Xu et al., 2017; Zhou et al., 2019b; Zou et al., 2018).

The Mufushan complex massif, located at the junction of Hunan, Hubei, and Jiangxi Provinces with an exposure area of>2000 km^2, is composed of the extensive Yanshanian granitoid batholith (ca.158–138 Ma) (Ji et al., 2017, 2018; Li, 2017, Li et al., 2020b; Wang et al., 2014b; Xu et al., 2019a,b; Xiong et al., 2020) and local Neoproterozoic granitic stocks (ca. 838–816 Ma) (HIGS, 2009; Shan et al., 2017) in the western and southwestern regions (Fig. 1).The YMB comprises several periods of intrusions (Fig. 1), including diorite(154 Ma,Wang et al., 2014b), granodiorite (151–149 Ma; Ji et al., 2018; Wang et al., 2014b), BMG (155–148 Ma; HIGS, 2009; Ji et al., 2017, 2018; Li et al., 2017; Wang et al., 2014b; Xiong et al., 2020), medium-grained TMG (146–138 Ma, Ji et al., 2017; Li et al., 2020b; Wang et al., 2014b), and fine-grained TMG (137 Ma; HIGS, 2009), with a decreasing trend in age from the reported zircon U–Pb ages.

Exposed as strata around the YMB (except northeast) or as fragmentation isolated in the batholith is the Lengjiaxi Group of the Neoproterozoic Qingbaikou system, which is ~ 6,700–10,127 m thick comprising sericitized slate, carbonaceous sericite silty slate, graywacke, and schist (Gao et al., 2011; Yang et al., 2020); schist occurs in the exocontact zone of the YMB within 0–6 km. Moreover, the lower Paleozoic Cambrian, Ordovician, and Silurian systems are found in the northeast.

Several ore deposits distributed around the YMB can be found, namely, the Taolin and Lishan large-scale Pb–Zn–fluorite deposits (Ding and Rees, 1984; Shan et al., 2017; Yu et al., 2021) and Duanfengshan and Renli Nb–Ta–(Li) rare-metal deposits. The latter two are the newly discovered, large-superlarge scale rare-metal deposits situated in the north and south of Mufushan batholiths, respectively(Li et al., 2017; Li et al., 2018; Li et al., 2020a; Li et al., 2021; Wei et al., 2021; Zhou et al., 2019b). Moreover, high amounts of rare-metal (Be, Nb, and Ta) pegmatites (Fig. 1) were found in the exocontact zone of the YMB.

3. Ore deposit geology

Located within the contact zone between the southern YMB and Lengjiaxi metasedimentary strata, the Renli rare metal ore deposit (Fig. 2) is the largest known granitic pegmatite rare-metal deposit with high-grade Ta and Nb (10791 t of Ta_2O_5, average grade at 0.036 wt%;

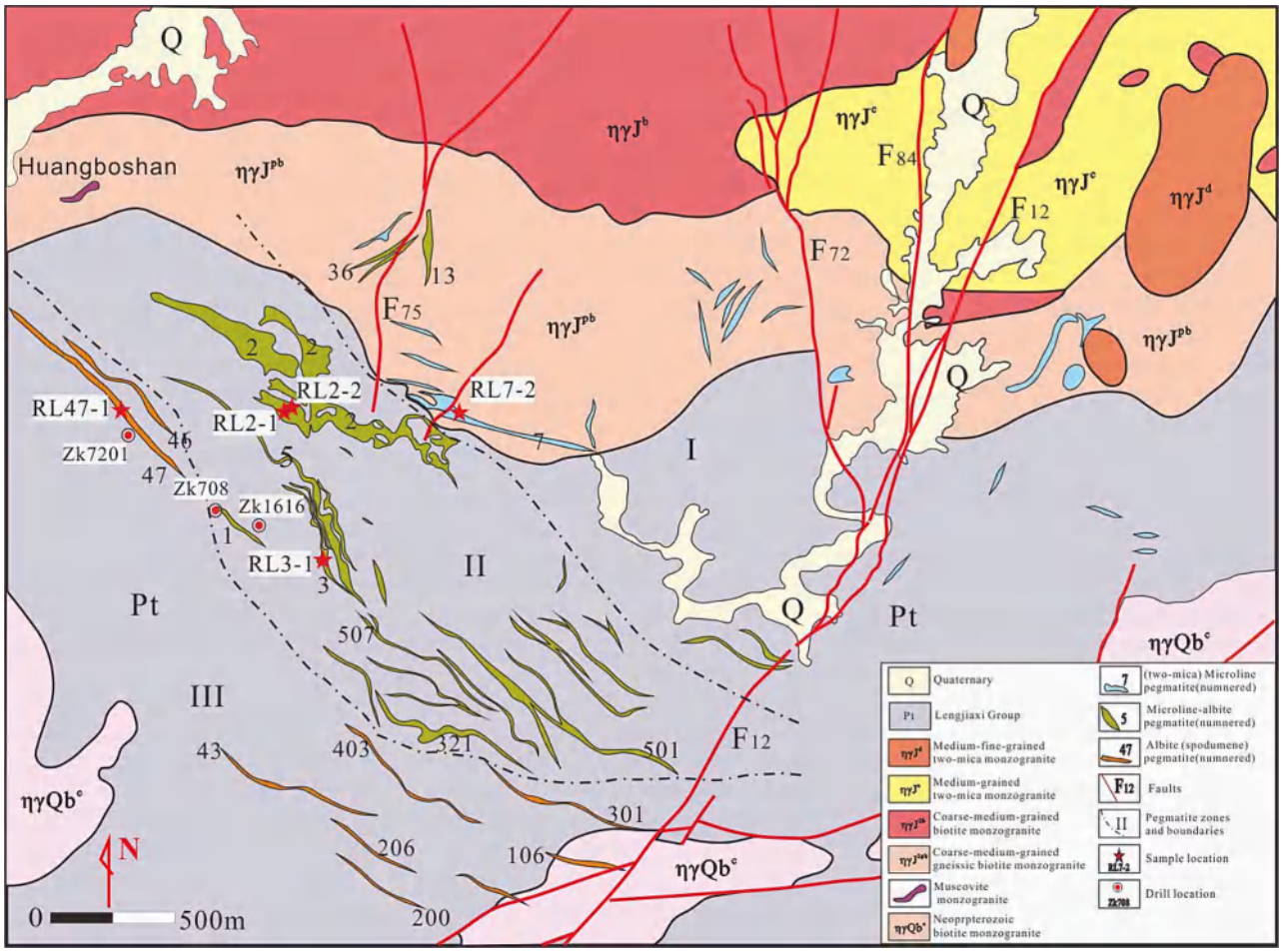

Fig. 2. Geological map of the Renli rare-metal deposit (modified from Li, 2017). Pegmatite spatial zonation: type I–microcline pegmatite; type II–microcline-albite pegmatite; and type III–albite pegmatite.

14057 t of Nb_2O_5, average grade at 0.047 wt%; Zhou et al., 2019b). The exposed strata in the south of the mining area belongs to the Neoproterozoic Lengjiaxi Group (Fig. 2) and comprises garnet-bearing two-mica schist, sericite schist, and banded slate, with NW-trending and NW-dipping (dip angles 20–50°). The fault structures in the mining area are mainly NE-oriented, with a smaller number of NNE-oriented faults, which cut the metasedimentary rocks, granites, and pegmatites (Li et al., 2020a,b, Li et al., 2021; Xiong et al., 2020).

Neoproterozoic and Yanshanian granitic intrusive rocks are extensively exposed in the Renli mining area (Fig. 2). The former is medium- to fine-grained and weakly gneissic biotite plagioclase granite that occurs in the southwestern and southern regions of the district. The latter is composed of (1) coarse- to medium-grained BMG occurring in the north with a gneissoid margin, (2) medium- and fine-grained TMG occurring in the northeast, (3) a small amount of fine- to medium-grained muscovite monzogranite (MMG) dikes, and (4) plenty of pegmatite dikes/veins. Precious zircon U–Pb age analysis shows that the granites exposed in the Renli district have consistent zircon U–Pb ages of 140–138 Ma (Li et al., 2020b; Xiong et al., 2020) while the BMG samples obtained from the drillings of ZK708, ZK1616, and ZK7201 (locations in Fig. 2) show an older age of ca.146 Ma (Li et al., 2017).

Several hundreds of pegmatite dikes are found in the Renli mining

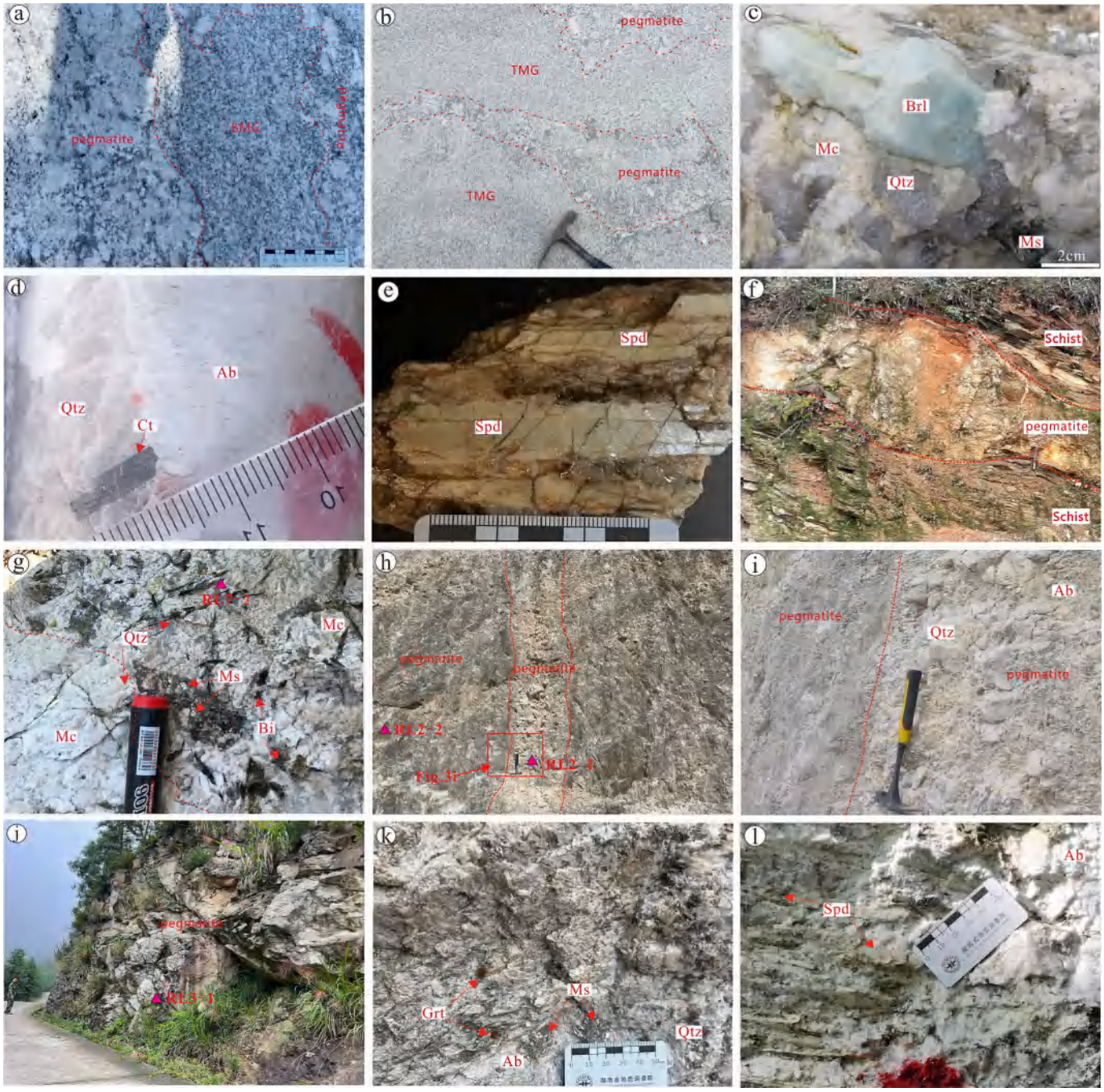

Fig. 3. Field photographs of pegmatites in the Renli mining area. Outcrop of type I pegmatites in BMG (a); outcrop of type II pegmatites in TMG (b); beryl-bearing pegmatite (c); coltan-bearing pegmatite samples (d); spodumene-bearing pegmatite(e); outcrop of spodumene–albite pegmatite of the No.47 (f); outcrop of two mica-microcline pegmatite of the No.7 pegmatite (g); outcrop of microcline–albite pegmatite of the No.2 pegmatite (h, i) and the later pegmatite intrusion (h); outcrop of microcline–albite pegmatite of the No.3 pegmatite (j, k); spodumene–albite pegmatite of the No.47 (l). Ab = albite; Brl = Beryl; Bi = Biotite; Mc = microcline; Ms = Muscovite; Qtz = quartz; Grt = Garnet; Spd = spodumene.

area. About 140 dikes have large sizes (width > 1 m): 95 hosted in the YMB and 45 dikes emplaced in the Lengjiaxi Group as an intrusion. The pegmatites show diverse mineral assemblages and mineralizations with distance from the YMB. Almost all the pegmatite dikes hosted in the BMG belong to biotite–muscovite–microcline pegmatite (type I) (Fig. 3a) and basically lack rare-metal minerals, but occasionally some beryl or small needle-like coltan. The pegmatites in the TMG belong to muscovite–microcline–albite pegmatite (type II) (Fig. 3b), and contain a certain amount of beryl (Fig. 3c) and coltan (Fig. 3d). These pegmatites emplaced in granites generally exhibit irregular shapes, unconstant strikes and limited scales. There are two classifications of pegmatite dikes in the Lengjiaxi Group (Fig. 3f). The first is muscovite–microcline–albite pegmatite (type II) and locates in an ~ 1–1.7 km-wide contact zone between the YMB and schist (Fig. 2). It is featured by significant Nb and Ta mineralizations, such as Nos. 2, 3, and 5 pegmatite dikes, containing 15 %, 13 %, and 58 % of the total Ta_2O_5 and 17 %, 13 %, and 53 % of the total Nb_2O_5 in the Renli Nb–Ta ore deposit, respectively. Coltan is the main rare-metal mineral and appears as needle-like or euhedral tabular crystals, with 0.1–1.5 cm grain sizes and intergrowth with quartz and albite (Fig. 3d and 4c). The second classification is muscovite–albite–spodumene pegmatite (type III), which locates in the southern and southwestern parts of the mining area and is identified by the presence of spodumene (Fig. 3e and 4d, e) and few lepidolite (Fig. 4e) and less coltan (Fig. 4f) compared to type II. With distance from the batholith, the dominant alkaline elements of pegmatite change from K to K + Na and then to Na(+Li), and the rare-metal mineralization type changes from Be to (Be +)Nb + Ta and then to (Be +)Nb + Ta + Li. The above geology and mineralization characteristics indicate the Li–Cs–Ta (LCT) affinity of the Renli pegmatites.

4. Sampling

Zircon separation, U–Pb dating, and Hf isotope analysis, were performed on the RL7-2, RL2-2, and RL47-1 samples collected from Nos. 7, 2, and 47 pegmatites, respectively (Fig. 2). Monazite separation, U–Pb dating, and Nd isotope analysis were performed on the RL2-1, RL2-2, and RL3-1 collected from Nos. 2, and 3 pegmatites, respectively (Fig. 2).

4.1. RL7-2

RL7-2 was collected from No.7 pegmatite, which is the largest type I pegmatite in the Renli mining area. The outcrop of the No. 7 pegmatite is 2000-m long and 80–140-m wide, with a strike and dip angles of 330°–350° and 50°–80°, respectively. The pegmatite has simple internal zonation, i.e., a graphic pegmatite zone, a biotite–muscovite–microcline–quartz zone, and a locally developed blocky microcline zone. RL7-2 was collected from the biotite-muscovite-microcline-quartz zone with a composition of 60 % microcline, 25 % quartz, 10 % muscovite, and 4 % biotite (Fig. 3g).

4.2. RL2-1 and RL2-2

RL2-1 and RL2-2 were collected from No.2 pegmatite, which is the largest type II pegmatite in the Renli mining area. It shows three large outcrops with average length of 2900 m and width of 50 m. The largest outcrop of the pegmatite shows a complex shape featuring branch and recombination, with strike and dip angles of 310°–330° and 25°–40°, respectively. and was intrusion of a late small pegmatite vein with a sharp contact (Fig. 3h, i). The No.2 pegmatite is almost homogeneous in mineralogy and texture with no evident internal zonation. For comparison, the later intrusion vein is uneven in mineral proportion and size. RL2-2 was collected from the foot wall of the No. 2 pegmatite (Fig. 3h) and has a composition of 25 % microcline, 35 % albite, 30 % quartz, and 8 % muscovite (Fig. 4a, b). RL2-1 was collected from the later pegmatite intrusion in the No. 2 pegmatite (Fig. 3h) and has a composition of 10 % microcline, 35 % albite, 40 % quartz, and 12 % muscovite and is identified by remarkable Nb–Ta mineralization.

4.3. RL3-1

RL3-1 was collected from the No. 3 pegmatite (Fig. 3j), which also belongs to the type II pematite. It is located near the No. 5 pegmatite

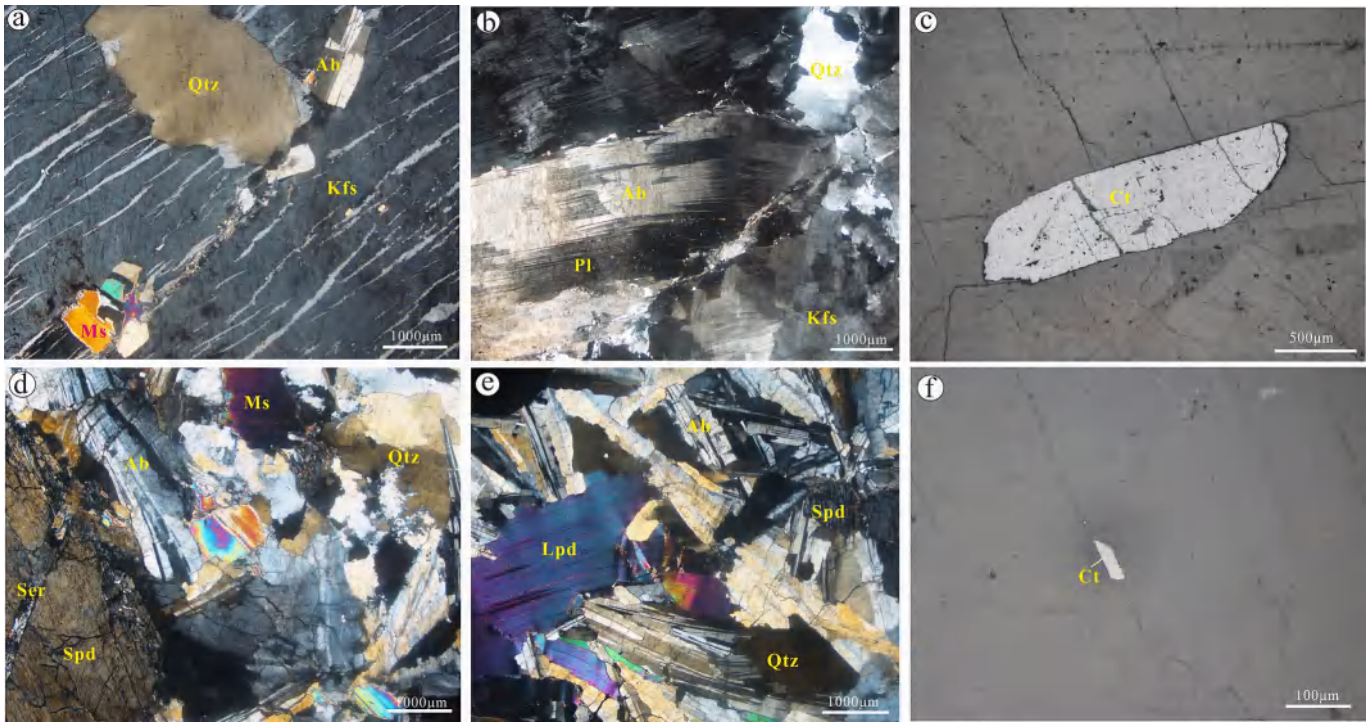

Fig. 4. Photomicrographs of pegmatite samples from the Renli deposit. muscovite–microcline–albite pegmatite (type II) (a, b); euhedral coltan in type II pegmatite (c); muscovite–albite–spodumene pegmatite (type III) (d, e); euhedral coltan in type III pegmatite (f).

(Fig. 2) featured by large-scale Nb–Ta mineralization. It shows a tabular shape in outcrop (Fig. 3j) and has a length of 1280 m and a width of 2–6 m, with general strike and dip angles of 280°–310° and 25°–35°, respectively. The No. 3 pegmatite also shows simple mineralogy and internal zonation including only a graphic zone and a muscovite–quartz–albite zone. RL3-1 was collected from the muscovite–quartz–albite zone and is composed of 10 % microcline, 40 % albite, 30 % quartz, and 18 % muscovite (Fig. 3k). Coltan is the dominant ore-forming mineral (Fig. 4c).

4.4. RL47-1

RL47-1 was collected from the No.47 pegmatite (Fig. 3f), which is the largest spodumene-rich pegmatite of the type III pegmatite exposed in the Renli mining area. The pegmatite is located in the western part of the Renli mining area and intruded into the schist of the Lengjiaxi Group (Fig. 2). It is ca.2000-m long and 1.5–7.0-m wide with a strike of NNW 300–310° and a dip angle of 25–35°. The No.47 pegmatite also shows simple internal zonation that mainly comprises an albite–spodumene zone and a muscovite-quartz zone. The RL47-1 sample was collected from the albite–spodumene zone with rock-forming minerals of 40 % albite, 30 % spodumene, 20 % quartz, and 8 % muscovite (Fig. 3l).

5. Analytical methods

All preparatory and analytical works were performed at the State Key Laboratory of Ore Deposit Geochemistry (SKLODG), Institute of Geochemistry, Chinese Academy of Sciences. The work details are as follows.

5.1. Zircon U–Pb dating and Hf isotope analysis

Zircons were separated from the pegmatites using conventional density and magnetic separation techniques and then hand-picked under a binocular microscope. Zircons were mounted onto epoxy and polished to about half their thickness. Transmitted and reflected light microscopy and cathodoluminescence (CL) imaging were performed on the zircons to reveal their internal structure (Fig. 5).

Zircon U–Pb dating was performed using laser ablation inductively coupled plasma mass spectrometry (LA–ICP–MS; GeoLasPro laser ablation system) coupled with an Agilent 7700ICP-MS system. A 193-nm ArF excimer laser, homogenized by a set of beam delivery systems, was focused on a zircon surface with 10 J/cm^2 flux under conditions of 32 μm spot size, 30 kV accelerating voltage, and 5 Hz repetition rate for 40 s. Helium was used as a carrier gas to transport the aerosol to the ICP–MS system. Zircon 91,500 was used as an external standard for the correction of instrumental mass discrimination and elemental fractionation (Wiedenbeck et al., 1995). Zircon GJ-1 and Plešovice were treated as quality control references for geochronology. Zircon common Pb concentration was externally calibrated against NIST SRM 610 with Si as an internal standard, whereas Zr served as the internal standard for the other trace elements (Hu et al., 2011; Liu et al., 2010a). Data reduction was performed offline with ICPMSDataCal (Liu et al., 2010b).

Hf isotope compositions were subsequently obtained from the same zircon spots previously analyzed for U–Pb dating, as guided by CL images. Zircon Hf isotopic analyses were performed using a Nu Plasma high resolution multiple-collector (MC)-ICP-MS (Nu Instruments ltd., UK) equipped with a GeoLas 2005 193 nm ArF excimer laser ablation system at the SKLODG, GIGCAS under conditions of 60 μm spot size, 10 Hz repetition rate, 15–20 J/cm^2 energy density, and He carrier gas. Raw count rates for ^{172}Yb, ^{173}Yb, ^{175}Lu, ^{176}(Hf + Yb + Lu), ^{177}Hf, ^{178}Hf, ^{179}Hf, and ^{180}Hf were collected simultaneously. The correction of the isobaric interference of ^{176}Lu on ^{176}Hf was done by measuring the intensity of an interference-free ^{175}Lu isotope, and ^{176}Lu/^{177}Hf ratios were calculated using a recommended ^{176}Lu/^{175}Lu ratio of 0.02669. Similarly, correction of the interference of ^{176}Yb on ^{176}Hf was done by measuring an interference-free ^{172}Yb isotope, and ^{176}Hf/^{177}Hf ratios were calculated using a ^{176}Lu/^{172}Yb ratio of 0.5886 (Chu et al., 2002).

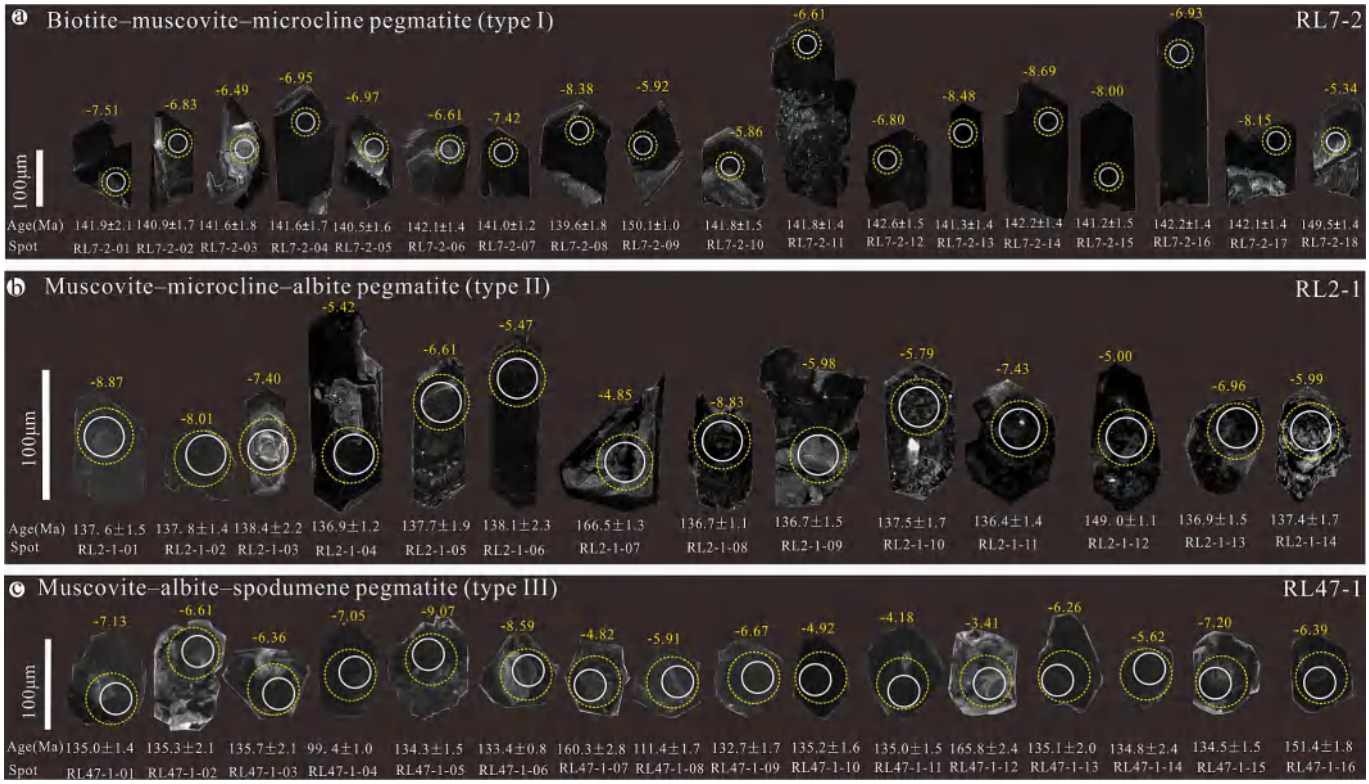

Fig. 5. Cathodoluminescence (CL) images of zircons from the Renli pegmatite. White and yellow circles indicate the laser spots of U–Pb dating and Hf isotope analysis, respectively.

The correction of time-dependent drifts of Lu–Hf isotopic ratios was performed via linear interpolation based on the variations of 91,500 and Penglai. For data quality evaluation, 91,500 and GJ-1 were reanalyzed as unknowns. The obtained $^{176}Hf/^{177}Hf$ ratios were 0.282295 ± 0.000027 (n = 14, 2σ) for 91,500 and 0.282904 ± 0.000006 (n = 30, 2σ) for Penglai, which is in good agreement with the recommended $^{176}Hf/^{177}Hf$ ratios within 2σ (0.282307 ± 58 and 0.282906 ± 0.000010; Griffin et al., 2006; Li et al., 2010).

A decay constant for ^{176}Lu of $1.865 \times 10^{-11}a^{-1}$ (Scherer et al., 2001) and chondritic ratios of $^{176}Hf/^{177}$ Hf = 0.282772 and $^{176}Lu/^{177}Hf$ = 0.0332 (Blichert-Toft and Albarède, 1997) were adopted for the calculation of the initial $^{176}Hf/^{177}Hf$ and $\varepsilon_{Hf}(t)$ values. Depleted mantle Hf model ages (T_{DM}) were calculated from the measured $^{176}Lu/^{177}Hf$ and $^{176}Hf/^{177}Hf$ ratios of the zircons, assuming a present $^{176}Hf/^{177}Hf$ ratio of 0.283250 and a $^{176}Lu/^{177}Hf$ ratio of 0.0384 for the depleted mantle (Griffin et al., 2002). The average crustal $^{176}Lu/^{177}Hf$ value of 0.015 was adopted for the calculation of the two stage model ages (Griffin et al., 2002).

5.2. Monazite U–Pb dating and Nd isotope analyses

Monazite U–Th–Pb dating was done by LA-ICP-MS. Laser sampling was performed using a GeolasPro LA system comprising a COMPexPro 102ArF excimer laser (193 nm wavelength and 200 mJ maximum energy) and a MicroLas optical system. ICP–MS (Agilent 7700e ICP–MS instrument) was performed for acquiring ion-signal intensities. Helium was used as the carrier gas and argon was used as the make-up gas; both were mixed using a *T*-connector before they were entered into the ICP–MS instrument. A "wire" signal smoothing device was included in this LA system through which smooth signals are produced even at very low laser rates down to 1 Hz (Hu et al., 2008). The spot size of the laser was set to 24 μm, and the frequency of the laser was 5 Hz. Monazite standard Harvard 117,531 (272 ± 2 Ma; Tomascak et al., 1996) and glass NIST610 were used as external standards for U–Th–Pb dating and trace element calibration, respectively. The pegmatite monazite standards Coqueiro and Paraíso (Goncalves et al., 2016) were used as a secondary standard to monitor data quality. Each analysis incorporated a background acquisition of ~ 20–30 s followed by 50 s of data acquisition from the sample. The Excel-based software ICPMSDataCal was used to perform offline selection and integration of background and analyzed signals, time-drift correction, and quantitative calibration for trace element analysis and U–Th–Pb dating. Concordia diagrams were constructed, and Isoplot 4.15 was used to performed weighted mean calculations (Ludwig, 2011).

In situ monazite Nd isotope measurements were conducted using a Nu Plasma III MC–ICP–MS (Nu Instruments) that was attached to a RESOlution-155 ArF 193 nm laser ablation system (Australian Scientific Instruments). Monazite was ablated in a mixture of helium (350 mL/min) and nitrogen (2 mL/min) atmospheres at 30 s baseline time, 40 s ablation time, 60 μm spot size, 6 Hz repetition rate, and 6 J/cm^2 energy density. The interference of ^{144}Sm on ^{144}Nd was derived from the ^{147}Sm intensity using a natural $^{144}Sm/^{147}Sm$ ratio of 0.205484 (Isnard et al., 2005). The mass bias factor of Sm with a true value of 1.08680 was calculated from the measured isotopic ratio of $^{147}Sm/^{149}Sm$ (Isnard et al., 2005). The mass bias of $^{143}Nd/^{144}Nd$ was normalized to $^{146}Nd/^{144}Nd$ of 0.7129 with an exponential law. One apatite standard Durango every-five samples and other two apatite standards (AP1 and MAD) every 30 unknown samples were treated as quality control. The measured $^{143}Nd/^{144}Nd$ ratio for the apatite standard AP1 was 0.512342 ± 0.000014 (n = 12), near the recommended value (AP1: 0.512352 ± 0.000024) (Yang et al., 2014).

6. Analytical results

6.1. CL and Th–U features of zircon samples

For the RL7-2 sample, the zircons are euhedral (Fig. 5a) and transparent or translucent. Zircons lengths are from 100 to 300 μm, with length/width ratios of 2:1–4:1. Most zircons exhibit weak oscillatory growth zoning, and a few of them are almost black (grains 12–16) in their CL images (Fig. 5a). Their Th and U contents are in the ranges of 82–620 and 5154–21886 ppm, respectively, with consistent Th/U ratios of 0.02–0.03 (Table 1).

For the RL2-2 sample, the zircons are euhedral to subhedral and translucent and 80–120-μm long, with length/width ratios of 1:1 to 3:1 (Fig. 5b). Some zircons exhibit weak (grains 1, and 2) to clear (grains 3, 4, 5, 6, and 9) oscillatory growth zoning, and some (grains 7, 10, 11, 12, 13, and 14) show a blurred and spongy inner core and weak oscillatory growth zoning in outer rims. Their Th and U contents are 293–3749 and 4292 to 45588 ppm, respectively, with Th/U ratios of 0.02–0.09 (Table 1).

For the RL47-1 sample, the zircons are subhedral and translucent, with crystal sizes 70–110-μm long, with length/width ratios of 1:1–1.5:1. All the zircon grains exhibit irregular and weak oscillatory growth zoning (Fig. 5c). Their Th and U contents are 235 –30401 and 4012–74993 ppm, respectively, with Th/U ratios of 0.03–0.41 (Table 1).

6.2. CL and Th–U features of monazite samples

The monazites from the RL2-1, RL2-2, and RL3-1 samples exhibit almost the same feature, as shown in the CL images (Fig. 6a, b, c); they are euhedral to subhedral, 80–130-μm long, and 40–100-μm wide with low length/width ratios. In addition, most of the grains lack oscillatory growth zoning in their CL images. They contain high Th (118,000–266,000 ppm) and U (18,000–83,000 ppm) contents and relatively low Pb (1200–3000 ppm) contents (Table 2).

6.3. Zircon U–Pb ages

For the RL7-2 sample of microcline pegmatite, U–Pb age determination was performed on 18 zircons (Fig. 5a). Nos. 9 and 18 grains yielded old $^{206}Pb/^{238}U$ ages of 150.1 ± 1.0 and 149.5 ± 1.4 Ma, respectively, indicating the occurrence of zircon xenocryst. The other 16 zircons yielded $^{206}Pb/^{238}U$ ages of 139.6–142.6 Ma, with a lower intercept age of 141.8 ± 1.1 Ma (MSWD = 0.21) and a weighted mean $^{206}Pb/^{238}U$ age of 141.5 ± 0.8 Ma (MSWD = 0.22, Fig. 7a, b; Table 1), which may represent the crystallization age.

For the RL2-1 sample of microcline–albite pegmatite, 14 zircon grains were analyzed (Fig. 5b). Nos. 7 and 12 grains yielded $^{206}Pb/^{238}U$ ages of 166.5 ± 1.3 and 149.0 ± 1.1 Ma, respectively, indicating the occurrence of zircon xenocryst. The age obtained from the No. 02 grain largely deviated from the concordia diagram owing to the effect of common Pb on the $^{207}Pb/^{235}U$ age. The other 11 zircon grains yielded consistent $^{206}Pb/^{238}U$ ages of 136.4–138.4 Ma, with a lower intercept age of 137.0 ± 1.0 Ma (MSWD = 0.13) and a weighted mean $^{206}Pb/^{238}U$ age of 137.1 ± 0.8 Ma (MSWD = 0.15, Fig. 7c, d; Table 1), indicating the crystallization age.

For the RL47-1 sample of spodumene–albite pegmatite, 16 zircons were analyzed. Nos. 07, 12, and 16 grains yielded old $^{206}Pb/^{238}U$ ages of 151.4–165.8 Ma, consistent with those of the inherited zircons from the RL7-2 and RL2-1 samples within error. Nos. 04 and 08 grains yielded young $^{206}Pb/^{238}U$ ages of 99.4 and 111.4 Ma, respectively, probably caused by significant Pb loss due to metamictization. The other 11 zircon grains yielded a $^{206}Pb/^{238}U$ age population of 132.7–135.7 Ma, with a lower intercept age of 134.3 ± 1.6 Ma (MSWD = 0.43) and a weighted mean $^{206}Pb/^{238}U$ age of 134.5 ± 0.8 Ma (MSWD = 0.38, Fig. 7e, f; Table 1), representing the crystallization age.

Table 1
Zircon U-Pb dating results of the Renli pegmatite.

Spot.no.	Content (ppm)		Th/U	Isotopic ratios and 1σ errors						Corrected ages and ± 1σ errors(Ma)					
	^{232}Th	^{238}U		^{207}Pb/^{206}Pb	1σ	^{207}Pb/^{235}U	1σ	^{206}Pb/^{238}U	1σ	^{207}Pb/^{206}Pb	1σ	^{207}Pb/^{235}U	1σ	^{206}Pb/^{238}U	1σ
RL7-2–01	262	13,681	0.02	0.04837	0.00078	0.15049	0.00285	0.02226	0.00034	116.8	37.0	142.3	2.5	141.9	2.1
RL7-2–02	301	13,301	0.02	0.05058	0.00077	0.15711	0.00295	0.02210	0.00026	220.4	35.2	148.2	2.6	140.9	1.7
RL7-2–03	515	17,752	0.03	0.04824	0.00075	0.15012	0.00273	0.02221	0.00029	109.4	37.0	142.0	2.4	141.6	1.8
RL7-2–04	481	16,973	0.03	0.04808	0.00080	0.14968	0.00274	0.02221	0.00027	101.9	38.9	141.6	2.4	141.6	1.7
RL7-2–05	540	20,961	0.03	0.05069	0.00076	0.15738	0.00293	0.02203	0.00026	233.4	35.2	148.4	2.6	140.5	1.6
RL7-2–06	494	19,119	0.03	0.04850	0.00069	0.15208	0.00242	0.02229	0.00023	124.2	33.3	143.7	2.1	142.1	1.4
RL7-2–07	149	5161	0.03	0.04925	0.00081	0.15278	0.00247	0.02211	0.00019	166.8	38.9	144.4	2.2	141.0	1.2
RL7-2–08	301	13,432	0.02	0.05040	0.00081	0.15519	0.00285	0.02189	0.00028	213.0	37.0	146.5	2.5	139.6	1.8
RL7-2–09	394	16,175	0.02	0.05055	0.00080	0.16774	0.00248	0.02355	0.00015	220.4	37.0	157.5	2.2	150.1	1.0
RL7-2–10	392	16,224	0.02	0.05180	0.00085	0.16231	0.00280	0.02225	0.00024	276.0	41.7	152.7	2.4	141.8	1.5
RL7-2–11	240	11,569	0.02	0.04818	0.00082	0.15121	0.00269	0.02224	0.00023	109.4	34.3	143.0	2.4	141.8	1.4
RL7-2–12	369	15,831	0.02	0.04890	0.00077	0.15424	0.00260	0.02237	0.00024	142.7	41.7	145.6	2.3	142.6	1.5
RL7-2–13	620	21,886	0.03	0.05154	0.00080	0.16062	0.00237	0.02217	0.00021	264.9	37.0	151.2	2.1	141.3	1.4
RL7-2–14	312	15,240	0.02	0.04861	0.00073	0.15284	0.00250	0.02230	0.00023	127.9	32.4	144.4	2.2	142.2	1.4
RL7-2–15	502	21,170	0.02	0.04856	0.00073	0.15161	0.00247	0.02215	0.00023	127.9	30.6	143.3	2.2	141.2	1.5
RL7-2–16	442	16,775	0.03	0.04775	0.00070	0.14996	0.00237	0.02230	0.00023	87.1	35.2	141.9	2.1	142.2	1.4
RL7-2–17	369	15,769	0.02	0.04951	0.00077	0.15532	0.00285	0.02228	0.00029	172.3	4.6	146.6	2.5	142.1	1.8
RL7-2–18	82.2	5354	0.02	0.04914	0.00086	0.16172	0.00272	0.02346	0.00023	153.8	36.1	152.2	2.4	149.5	1.4
RL2-1–01	1260	28,673	0.04	0.05500	0.00092	0.16485	0.00280	0.02157	0.00024	413.0	37.0	154.9	2.4	137.6	1.5
RL2-1–02	2725	33,633	0.08	0.09234	0.00217	0.27988	0.00774	0.02160	0.00023	1475.9	44.4	250.6	6.1	137.8	1.4
RL2-1–03	1037	21,431	0.05	0.05782	0.00164	0.17659	0.00637	0.02171	0.00034	524.1	61.1	165.1	5.5	138.4	2.2
RL2-1–04	3749	45,584	0.08	0.05347	0.00104	0.16133	0.00308	0.02146	0.00020	350.1	42.6	151.9	2.7	136.9	1.2
RL2-1–05	1969	27,434	0.07	0.05237	0.00123	0.15892	0.00387	0.02159	0.00030	301.9	49.1	149.8	3.4	137.7	1.9
RL2-1–06	744	16,729	0.04	0.04984	0.00103	0.15199	0.00342	0.02166	0.00036	187.1	48.1	143.7	3.0	138.1	2.3
RL2-1–07	1387	31,138	0.04	0.05088	0.00093	0.18810	0.00326	0.02617	0.00021	235.3	42.6	175.0	2.8	166.5	1.3
RL2-1–08	2150	24,766	0.09	0.04930	0.00074	0.14827	0.00246	0.02143	0.00018	161.2	35.2	140.4	2.2	136.7	1.1
RL2-1–09	1521	28,848	0.05	0.05134	0.00103	0.15250	0.00322	0.02143	0.00024	257.5	46.3	144.1	2.8	136.7	1.5
RL2-1–10	421	17,567	0.02	0.04980	0.00100	0.14930	0.00355	0.02156	0.00027	187.1	46.3	141.3	3.1	137.5	1.7
RL2-1–11	293	4292	0.07	0.05138	0.00115	0.15323	0.00366	0.02138	0.00022	257.5	51.8	144.8	3.2	136.4	1.4
RL2-1–12	456	20,229	0.02	0.05375	0.00102	0.17597	0.00367	0.02338	0.00017	361.2	75.0	164.6	3.2	149.0	1.1
RL2-1–13	799	29,160	0.03	0.04877	0.00081	0.14700	0.00257	0.02147	0.00024	200.1	38.9	139.3	2.3	136.9	1.5
RL2-1–14	1003	22,893	0.04	0.05293	0.00089	0.16040	0.00318	0.02154	0.00027	324.1	38.9	151.1	2.8	137.4	1.7
RL47-1–01	346	7482	0.05	0.05070	0.00097	0.14909	0.00300	0.02116	0.00021	228	72.2	141.1	2.7	135.0	1.4
RL47-1–02	332	4012	0.08	0.06548	0.00175	0.19309	0.00585	0.02120	0.00033	791	62	179.3	5.0	135.3	2.1
RL47-1–03	448	13,133	0.03	0.05061	0.00110	0.14980	0.00406	0.02128	0.00033	233	50.0	141.7	3.6	135.7	2.1
RL47-1–04	1224	33,028	0.04	0.05088	0.00086	0.10979	0.00195	0.01554	0.00015	235	38.9	105.8	1.8	99.4	1.0
RL47-1–05	1487	11,614	0.13	0.05534	0.00102	0.16236	0.00360	0.02105	0.00024	433	40.7	152.8	3.1	134.3	1.5
RL47-1–06	801	12,531	0.06	0.05459	0.00078	0.15895	0.00225	0.02090	0.00013	394	31.5	149.8	2.0	133.4	0.8
RL47-1–07	6425	17,515	0.37	0.05287	0.00081	0.18498	0.00374	0.02518	0.00045	324	39.8	172.3	3.2	160.3	2.8
RL47-1–08	1635	15,312	0.11	0.05734	0.00099	0.13847	0.00266	0.01743	0.00028	506	38.9	131.7	2.4	111.4	1.7
RL47-1–09	30,401	74,933	0.41	0.05350	0.00105	0.15668	0.00424	0.02080	0.00027	350	44.4	147.8	3.7	132.7	1.7
RL47-1–10	1023	19,724	0.05	0.05333	0.00101	0.15812	0.00327	0.02119	0.00025	343	42.6	149.1	2.9	135.2	1.6
RL2-47–11	2868	24,224	0.12	0.04814	0.00073	0.14221	0.00236	0.02116	0.00023	106	32.4	135.0	2.1	135.0	1.5
RL2-47–12	235	6880	0.03	0.05085	0.00101	0.18425	0.00379	0.02605	0.00038	235	46.3	171.7	3.3	165.8	2.4
RL2-47–13	674	19,012	0.04	0.05968	0.00112	0.17783	0.00471	0.02117	0.00031	591	40.7	166.2	4.1	135.1	2.0
RL2-47–14	3366	19,083	0.18	0.06209	0.00176	0.18821	0.00940	0.02113	0.00037	676	63.9	175.1	8.0	134.8	2.4
RL2-47–15	1359	24,812	0.05	0.05697	0.00096	0.16756	0.00259	0.02108	0.00024	500	37.0	157.3	2.3	134.5	1.5
RL2-47–16	553	18,075	0.03	0.05391	0.00111	0.17891	0.00390	0.02377	0.00029	369	46.3	167.1	3.4	151.4	1.8

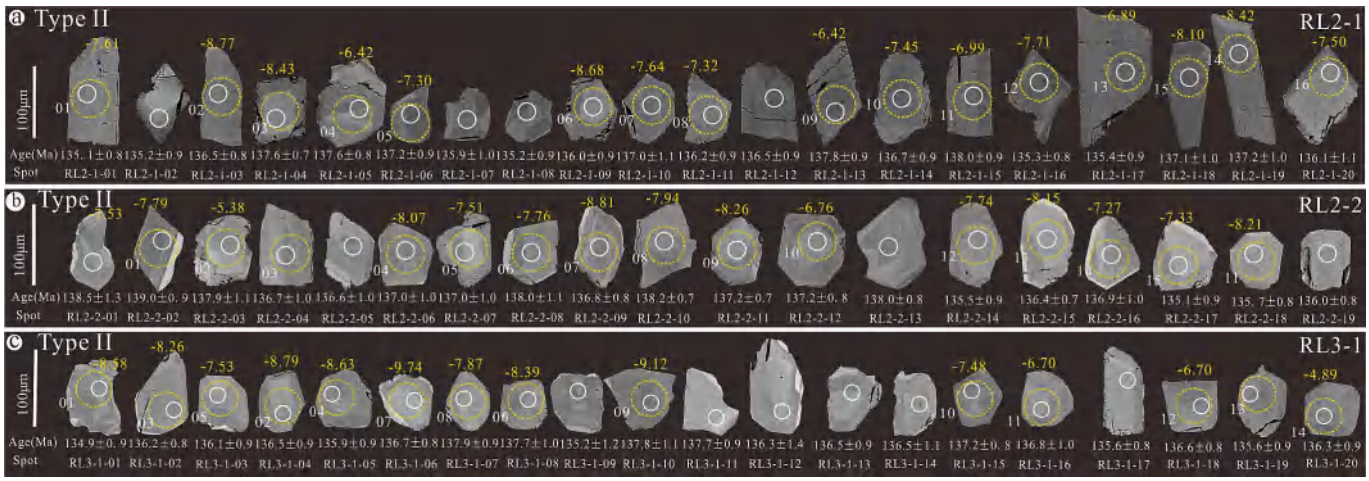

Fig. 6. CL images of monazites the Renli pegmatite. White and yellow circles indicate the laser spots of U–Th–Pb dating and Nd isotope analysis, respectively.

6.4. Monazite U–Th–Pb ages

Although monazite incorporates significant amounts of ^{230}Th into its structure during crystallization, the effect of excess ^{206}Pb from the decay of initial ^{230}Th (Schärer, 1984) can be avoided by using of the Th–Pb system. Monazites typically contain a relatively low amount of radiogenic ^{207}Pb, affording ^{207}Pb/^{235}U ages less precise than ^{206}Pb/^{238}U and ^{208}Pb/^{232}Th ages. The analyzed monazites contain abundant ^{232}Th (Table 2) and significant ^{208}Pb, with high Th/U ratios of 2.6 to 37.2 (average 9.8). Because Th–Pb dating of monazite has advantages over the U–Pb dating because of better counting statistics and smaller proportion of common ^{208}Pb, we adopted the ^{208}Pb/^{232}Th age as the best candidate for the crystallization time of monazite (e.g., Ayers et al., 2002; Cottle et al., 2015; Xiong et al., 2020; Ying et al., 2017).

LA–ICP–MS U–Th–Pb dating was performed on the three groups of monazite samples from microcline–albite pegmatite (RL2-1, RL2-2, and RL3-1) (Fig. 6). Table 2 lists the dating results.

Twenty monazite grains from the RL2-1 sample yielded consistent ^{208}Pb/^{232}Th ages of 135.1–138.0 Ma, with a weighted mean ^{208}Pb/^{232}Th age of 136.5 ± 0.4 Ma (MSWD = 1.12, Fig. 8a, b; Table 2). Nineteen spots on 19 monazite grains from the RL2-2 sample defined a ^{208}Pb/^{232}Th age population of 135.1–139.0 Ma, with a weighted mean ^{208}Pb/^{232}Th age of 137.0 ± 0.5 Ma (MSWD = 1.5, Fig. 8c, d; Table 2). Twenty spots on 20 monazite grains from the RL3-1 sample yielded ^{208}Pb/^{232}Th ages between 134.9 and 137.9 Ma, with a weighted mean ^{208}Pb/^{232}Th age of 136.5 ± 0.4 Ma (MSWD = 0.82, Fig. 8a, b; Table 2).

6.5. Zircon Hf isotope composition

The zircons analyzed for U–Pb age were chosen for Hf isotopic composition analysis. Fig. 5 shows the specific ablation spots, and Table 3 lists the results.

The zircons from RL7-2 have ^{176}Lu/^{177}Hf and ^{176}Hf/^{177}Hf ratios of 0.000673–0.002803 and 0.282443–0.282523, respectively. According to the U–Pb ages, the ε_{Hf}(t) values are calculated to be − 8.69 to − 5.86 (average − 7.29), the $f_{Lu/Hf}$ values are measured to be − 0.98 to − 0.92, and the T_{DM2} ages are calculated to be 1535 to 1740 Ma (average 1652 Ma).

For RL2-2, the Hf isotope compositions of the zircons from RL2-2 are similar to those of RL7-2: ^{176}Lu/^{177}Hf ratios of 0.000048–0.001929, ^{176}Hf/^{177}Hf ratios of 0.282436–0.282533, ε_{Hf} (t) values of − 8.87 to − 5.42 (average − 6.58), $f_{Lu/Hf}$ from − 1.00 to − 0.94, and T_{DM2}ages of 1513–1748 Ma (average 1606 Ma).

Zircons from RL47-1 have ^{176}Lu/^{177}Hf and ^{176}Hf/^{177}Hf ratios of 0.000031–0.000122 and 0.282432–0.282570, respectively. The calculated ε_{Hf} (t) values are − 9.07 to − 4.18 (average − 6.26), the $f_{Lu/Hf}$ values are − 1.00, and the T_{DM2}ages are 1451–1759 Ma (average 1582 Ma).

6.6. Monazite Nd isotope composition

Sm–Nd isotope composition analysis was conducted on euhedral or large monazite grains with concordant U–Th–Pb age from the RL2-1, RL2-2, and RL3-1 samples, with the ablation site overlying the U–Th–Pb spots (Fig. 6). Table 4 lists the results.

For the RL2-1 sample, 16 monazites were analyzed (Fig. 6a). The results are as follows. ^{143}Nd/^{144}Nd ratios of 0.512153–0.512309 with ^{147}Sm/^{144}Nd ratios of 0.13–0.20, ε_{Nd}(t) of − 8.77 to − 6.42 (average − 7.60), and T_{DM2} ages of 1452–1643 Ma (average 1548 Ma).

For the RL2-2 sample, 15 monazites were analyzed (Fig. 6b). The results are as follows. ^{143}Nd/^{144}Nd ratios of 0.512144–0.512322 with ^{147}Sm/^{144}Nd ratios of 0.13–0.17. The corresponding ε_{Nd} (t) values are between − 8.81 and − 5.38 (average − 7.62), and T_{DM2} ages are 1368–1647 Ma (average 1549 Ma).

For the RL3-1 sample, the results for the Nd isotope compositions of the monazite grains are as follows: ^{147}Sm/^{144}Nd ratios of 0.512093–0.512387 with ^{147}Sm/^{144}Nd ratios of 0.14–0.20, ε_{Nd}(t) values of − 9.74 to − 4.89 (average − 7.94), and T_{DM2} ages of 1328 to 1721 Ma (average 1575 Ma).

7. Discussion

7.1. Geochronology of the Renli pegmatite

Granitic pegmatites commonly contain certain amounts of accessory and ore minerals, such as zircon, apatite, monazite, and columbite group minerals, which are adaptable for dating. Zircon and monazite were chosen because of the high closure temperature of the U–Pb system (>600 °C; Mezger et al., 1989; Sevigny and Hanson, 1992) and the wide application of zircon Hf and monazite Nd isotope compositions. The zircon grains collected from RL7-2, RL2-1, and RL47-1 display weak luminescence (Fig. 3), high U and Th contents, and low Th/U ratios (Table 1), which are distinct from the typical magmatic zircon described by Hoskin and Schaltegger (2003). However, it is difficult to exclude the magmatic origin of these zircons by the features mentioned above. For instance, the weak luminescence of zircon probably results from the suppression of CL emission caused by high U^{4+} abundance and its radiation damage on the crystal lattice (Nasdala et al., 2003). In addition, the very low Th/U ratio can be ascribed to the preferential incorporation of U^{4+} into zircon owing to its small ionic radius compared to Th^{4+} and the large partition coefficient of U compared to Th in H_2O-rich fluids (Rollinson and Windley, 1980). In addition, some zircons from the RL7-

Table 2
Monazite U-Th-Pb dating results of theRenli pegmatite.

Spot.no.	Content (ppm)			Common Pb	Isotopic ratios and 1σ errors						Corrected ages and ± 1σ errors(Ma)							
	Pb(Total)	^{232}Th	^{238}U		^{207}Pb/^{235}U	1σ	^{206}Pb/^{238}U	1σ	^{208}Pb/^{232}Th	1σ	^{207}Pb/^{206}Pb	1σ	^{207}Pb/^{235}U	1σ	^{206}Pb/^{238}U	1σ	^{208}Pb/^{232}Th	1σ
RL2-1–01	1582	195,894	24,197	0.5	0.15150	0.00290	0.02124	0.00017	0.00671	0.00004	333.4	40.7	143.2	2.6	135.5	1.0	135.1	0.8
RL2-1–02	1327	146,232	25,447	5.8	0.15004	0.00262	0.02120	0.00016	0.00671	0.00004	253.8	38.9	141.9	2.3	135.2	1.0	135.2	0.9
RL2-1–03	1554	179,255	27,157	6.8	0.14876	0.00250	0.02131	0.00015	0.00678	0.00004	220.4	37.0	140.8	2.2	135.9	1.0	136.5	0.8
RL2-1–04	2030	232,388	35,883	4.6	0.14753	0.00212	0.02130	0.00013	0.00683	0.00004	211.2	31.5	139.7	1.9	135.9	0.8	137.6	0.7
RL2-1–05	1667	175,314	34,534	5.6	0.14587	0.00237	0.02103	0.00017	0.00683	0.00004	205.6	35.2	138.3	2.1	134.2	1.1	137.6	0.8
RL2-1–06	1469	172,576	25,033	3.3	0.14798	0.00242	0.02138	0.00015	0.00681	0.00004	198.2	33.3	140.1	2.1	136.4	0.9	137.2	0.9
RL2-1–07	1050	115,539	21,221	2.8	0.15051	0.00288	0.02082	0.00020	0.00675	0.00005	298.2	41.7	142.4	2.5	132.9	1.3	135.9	1.0
RL2-1–08	1390	172,499	22,215	3.8	0.14945	0.00265	0.02115	0.00016	0.00671	0.00004	255.6	37.0	141.4	2.3	134.9	1.0	135.2	0.9
RL2-1–09	1784	199,284	34,676	3.0	0.14961	0.00233	0.02114	0.00017	0.00675	0.00004	253.8	31.5	141.6	2.1	134.8	1.1	136.0	0.9
RL2-1–10	1439	178,569	22,456	9.6	0.14919	0.00292	0.02155	0.00021	0.00680	0.00005	211.2	44.4	141.2	2.6	137.5	1.3	137.0	1.1
RL2-1–11	1589	207,782	22,035	9.0	0.14826	0.00263	0.02141	0.00019	0.00676	0.00005	205.6	37.0	140.4	2.3	136.6	1.2	136.2	0.9
RL2-1–12	1444	171,205	24,788	0.8	0.14860	0.00252	0.02130	0.00015	0.00678	0.00004	220.4	37.0	140.7	2.2	135.9	1.0	136.5	0.9
RL2-1–13	1569	171,543	30,348	0.4	0.14971	0.00228	0.02141	0.00017	0.00684	0.00005	233.4	31.5	141.7	2.0	136.5	1.1	137.8	0.9
RL2-1–14	1546	185,470	25,637	2.3	0.15034	0.00285	0.02135	0.00016	0.00679	0.00004	239.0	40.7	142.2	2.5	136.2	1.0	136.7	0.9
RL2-1–15	1230	150,858	19,069	4.4	0.15261	0.00277	0.02135	0.00017	0.00685	0.00005	279.7	40.7	144.2	2.4	136.2	1.1	138.0	0.9
RL2-1–16	1523	155,648	33,273	1.7	0.14854	0.00238	0.02123	0.00018	0.00672	0.00004	233.4	31.5	140.6	2.1	135.4	1.1	135.3	0.8
RL2-1–17	1259	164,672	17,338	6.4	0.15234	0.00303	0.02129	0.00016	0.00672	0.00005	276.0	42.6	144.0	2.7	135.8	1.0	135.4	0.9
RL2-1–18	1656	191,548	29,525	4.1	0.14331	0.00250	0.02111	0.00016	0.00681	0.00005	153.8	37.0	136.0	2.2	134.7	1.0	137.1	1.0
RL2-1–19	1920	240,717	28,038	3.2	0.14766	0.00249	0.02143	0.00017	0.00681	0.00005	190.8	39.8	139.8	2.2	136.7	1.1	137.2	1.0
RL2-1–20	1744	208,827	28,865	7.3	0.14968	0.00257	0.02123	0.00016	0.00676	0.00005	242.7	37.0	141.6	2.3	135.4	1.0	136.1	1.1
RL2-2-01	1428	148,079	30,104	10.9	0.15842	0.00299	0.02161	0.00018	0.00688	0.00006	344.5	36.1	149.3	2.6	137.8	1.2	138.5	1.3
RL2-2-02	1710	182,486	34,749	9.0	0.15253	0.00237	0.02138	0.00018	0.00690	0.00005	333.4	31.5	144.1	2.1	136.3	1.1	139.0	0.9
RL2-2-03	1685	211,484	25,320	4.7	0.15321	0.00264	0.02169	0.00019	0.00684	0.00005	253.8	43.5	144.7	2.3	138.3	1.2	137.9	1.1
RL2-2-04	1683	180,693	34,789	7.5	0.14592	0.00239	0.02131	0.00016	0.00678	0.00005	176.0	37.0	138.3	2.1	135.9	1.0	136.7	1.0
RL2-2-05	1504	179,008	25,851	3.6	0.15034	0.00257	0.02145	0.00018	0.00678	0.00005	231.6	69.4	142.2	2.3	136.8	1.1	136.6	1.0
RL2-2-06	1547	152,283	35,912	5.8	0.14628	0.00240	0.02115	0.00017	0.00680	0.00005	211.2	35.2	138.6	2.1	134.9	1.1	137.0	1.0
RL2-2-07	1899	244,897	26,679	7.5	0.15062	0.00281	0.02171	0.00019	0.00680	0.00005	211.2	37.0	142.5	2.5	138.5	1.2	137.0	1.0
RL2-2-08	1380	173,150	20,850	9.9	0.15149	0.00288	0.02133	0.00024	0.00685	0.00006	264.9	36.1	143.2	2.5	136.0	1.5	138.0	1.1
RL2-2-09	1898	222,870	32,919	4.2	0.14783	0.00240	0.02151	0.00016	0.00679	0.00004	187.1	35.2	140.0	2.1	137.2	1.0	136.8	0.8
RL2-2-10	1240	175,933	12,313	7.4	0.14928	0.00356	0.02190	0.00015	0.00686	0.00004	164.9	53.7	141.3	3.1	139.6	1.0	138.2	0.7
RL2-2-11	1900	215,446	34,884	5.7	0.14644	0.00207	0.02145	0.00013	0.00681	0.00004	168.6	−0.9	138.8	1.8	136.8	0.8	137.2	0.7
RL2-2-12	1638	222,032	19,589	5.0	0.14961	0.00272	0.02152	0.00018	0.00681	0.00004	213.0	40.7	141.6	2.4	137.3	1.2	137.2	0.8
RL2-2-13	1216	138,250	21,826	5.8	0.14630	0.00236	0.02137	0.00014	0.00685	0.00004	176.0	35.2	138.6	2.1	136.3	0.9	138.0	0.8
RL2-2-14	1806	219,452	28,946	7.4	0.13863	0.00235	0.02116	0.00017	0.00672	0.00005	76.0	35.2	131.8	2.1	135.0	1.1	135.5	0.9
RL2-2-15	1510	177,188	25,681	6.3	0.13872	0.00250	0.02095	0.00014	0.00677	0.00004	101.9	38.9	131.9	2.2	133.6	0.9	136.4	0.7
RL2-2-16	1267	160,468	18,109	3.9	0.14090	0.00288	0.02096	0.00019	0.00679	0.00005	139.0	45.4	133.8	2.6	133.7	1.2	136.9	1.0
RL2-2-17	1661	202,878	26,530	8.3	0.13225	0.00241	0.02070	0.00016	0.00670	0.00004	20.5	40.7	126.1	2.2	132.1	1.0	135.1	0.9
RL2-2-18	1612	188,794	27,938	5.0	0.13175	0.00233	0.02046	0.00016	0.00674	0.00004	53.8	43.5	125.7	2.1	130.5	1.0	135.7	0.8
RL2-2-19	1448	175,624	23,354	6.2	0.13043	0.00245	0.02035	0.00017	0.00675	0.00004	39.0	−162.0	124.5	2.2	129.9	1.1	136.0	0.8
RL3-1–01	1258	118,772	30,843	4.0	0.14805	0.00253	0.02103	0.00016	0.00670	0.00004	239.0	32.4	140.2	2.2	134.1	1.0	134.9	0.9
RL3-1–02	1670	156,337	41,618	6.0	0.14451	0.00213	0.02088	0.00015	0.00676	0.00004	211.2	31.5	137.1	1.9	133.2	0.9	136.2	0.8
RL3-1–03	1382	135,250	32,966	6.5	0.14842	0.00232	0.02103	0.00016	0.00676	0.00005	255.6	33.3	140.5	2.1	134.2	1.0	136.1	0.9
RL3-1–04	1720	143,535	48,759	9.0	0.14519	0.00213	0.02087	0.00015	0.00678	0.00004	209.3	25.0	137.7	1.9	133.2	1.0	136.5	0.9
RL3-1–05	1561	132,416	43,555	6.8	0.14913	0.00228	0.02104	0.00017	0.00675	0.00005	257.5	26.9	141.1	2.0	134.2	1.1	135.9	0.9
RL3-1–06	1810	185,408	41,443	11.5	0.14803	0.00210	0.02103	0.00015	0.00679	0.00004	239.0	62.0	140.2	1.9	134.2	1.0	136.7	0.8
RL3-1–07	1918	180,318	48,187	6.7	0.14734	0.00236	0.02107	0.00017	0.00685	0.00005	233.4	33.3	139.6	2.1	134.4	1.0	137.9	0.9
RL3-1–08	1781	166,380	45,575	7.4	0.14780	0.00237	0.02077	0.00017	0.00684	0.00005	264.9	33.3	140.0	2.1	132.5	1.1	137.7	1.0
RL3-1–09	1699	143,574	48,894	15.3	0.14822	0.00269	0.02068	0.00022	0.00671	0.00006	283.4	34.3	140.3	2.4	132.0	1.4	135.2	1.2
RL3-1–10	1335	118,737	35,201	6.4	0.14894	0.00260	0.02116	0.00015	0.00684	0.00005	239.0	32.4	141.0	2.3	135.0	0.9	137.8	1.1
RL3-1–11	3054	265,815	82,616	10.0	0.15005	0.00206	0.02103	0.00017	0.00684	0.00004	333.4	25.9	142.0	1.8	134.2	1.0	137.7	0.9
RL3-1–12	2401	199,801	67,957	5.9	0.15032	0.00262	0.02088	0.00023	0.00677	0.00007	300.1	35.2	142.2	2.3	133.2	1.4	136.3	1.4
RL3-1–13	2496	209,077	70,659	7.8	0.14621	0.00211	0.02068	0.00017	0.00678	0.00004	250.1	29.6	138.6	1.9	132.0	1.1	136.5	0.9
RL3-1–14	2585	202,549	77,270	12.4	0.14716	0.00246	0.02069	0.00021	0.00678	0.00005	261.2	31.5	139.4	2.2	132.0	1.3	136.5	1.1
RL3-1–15	1723	158,458	43,236	10.1	0.15145	0.00264	0.02114	0.00015	0.00681	0.00004	276.0	39.8	143.2	2.3	134.9	0.9	137.2	0.8
RL3-1–16	1865	180,899	44,475	4.8	0.14795	0.00240	0.02104	0.00017	0.00679	0.00005	239.0	30.6	140.1	2.1	134.2	1.1	136.8	1.0
RL3-1–17	2824	254,639	75,144	6.2	0.14576	0.00194	0.02051	0.00013	0.00673	0.00004	261.2	24.1	138.2	1.7	130.9	0.8	135.6	0.8
RL3-1–18	1726	165,226	41,774	6.5	0.14771	0.00243	0.02089	0.00014	0.00678	0.00004	250.1	35.2	139.9	2.2	133.3	0.9	136.6	0.8
RL3-1–19	1787	166,262	45,280	7.8	0.14290	0.00209	0.02078	0.00016	0.00673	0.00004	187.1	25.0	135.6	1.9	132.6	1.0	135.6	0.9
RL3-1–20	1998	192,709	48,407	2.8	0.14678	0.00237	0.02070	0.00016	0.00676	0.00004	253.8	31.5	139.1	2.1	132.1	1.0	136.3	0.9

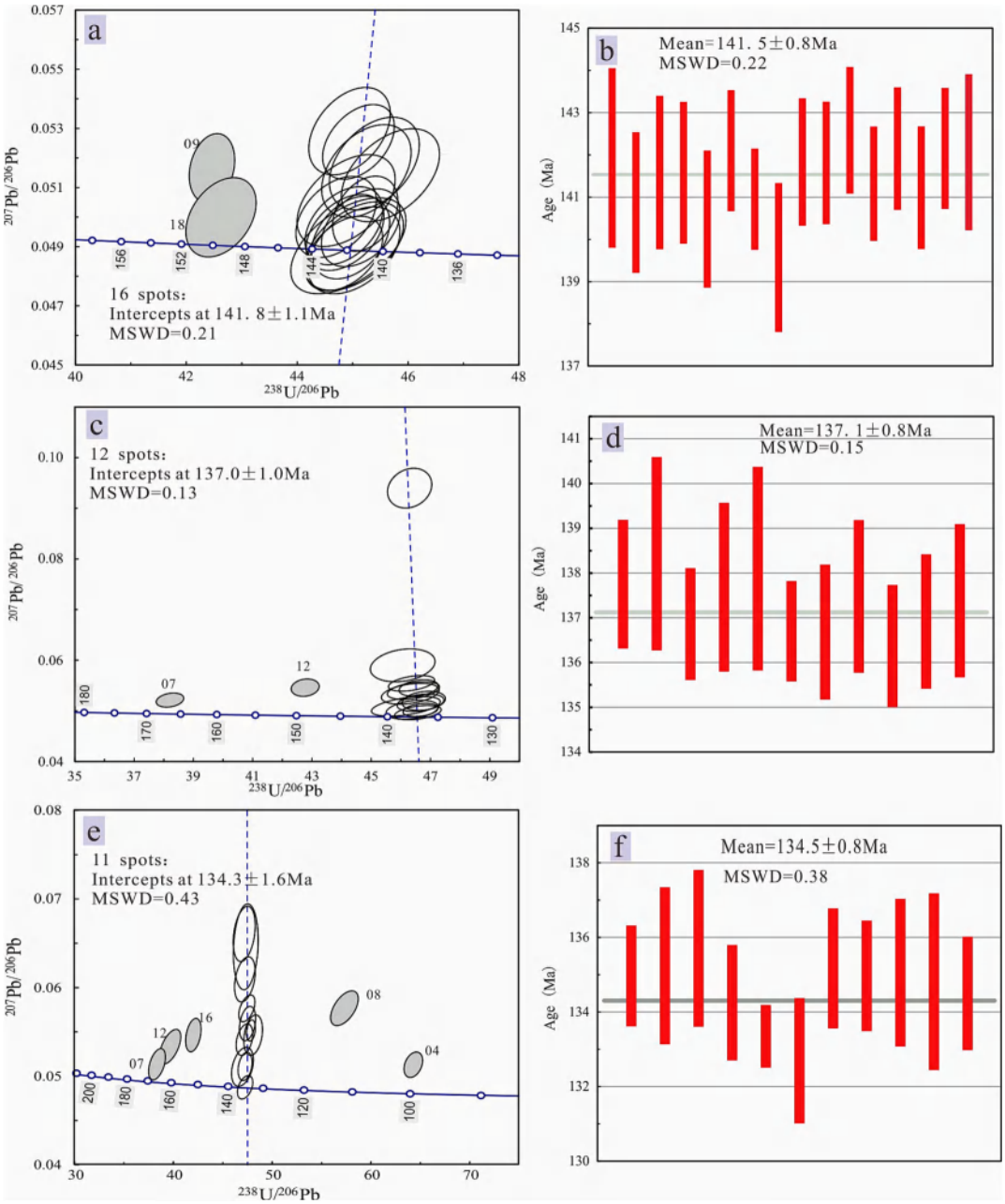

Fig. 7. Tera-Wasserburg of zircon U–Pb age plots (a, c, and e) and weighted average age diagrams (b, d, and f) of the Renli Nos. 7, 2 and 47 pegmatites, respectively.

2, RL2-1, and RL47-1 samples feature growth zoning in CL images, which supports a magmatic origin.

However, most zircons from the Nos. 2, 7 and 47 pegmatites are highly rich in U (4012–33028 ppm), with low Th/U ratios (mostly below 0.1) (Table 1), and weak or mosaic luminescence (Fig. 5), indicating that they suffered from later reworking event(s). A high abundance of U and its radioactive decay destroys the zircon lattice, i.e., metamictization, and make zircons susceptive to fluid alteration, leaching, and recrystallization, which is featured by spongy texture and mosaic luminescence. The loss of radiogenic Pb daughters lose from metamict zircons occurs through diffusion because their large ionic radius will induce younger U-Pb ages. In addition, the $^{206}Pb/^{238}U$ and $^{207}Pb/^{235}U$ ages obtained from metamict zircons reworked by later fluids could be discordant in most cases, with discordant younger ages owing to Pb-losing induced by fluid leaching or older ages owing to the incorporation of common Pb in zircon. The recrystallization effect on U-Pb age depends on the degree and time of recrystallization: the former affects the age concordance and the latter determines whether it can be distinguished from zircon crystallization age under specific conditions of analysis technique. However, mostly concordant $^{206}Pb/^{238}U$ and $^{207}Pb/^{235}U$ ages are obtained from the zircons (with concordance > 90 %), indicating limited effect from Pb losing and acquisition. In addition, zircons from the early pegmatites, such as the No. 7 pegmatite (type I) and the No. 2 pegmatite (type II), have distinct $^{206}Pb/^{238}U$ ages from those of the late pegmatites, such as the No. 47 pegmatite (type III), indicating the limited effect from multistage magmatic activities. Zircons from RL2-1 pegmatite show a weighted average $^{206}Pb/^{238}U$ age of 137.1 ± 0.8 Ma, which is consistent with that obtained from the monazite of the same sample (137.0 ± 0.5 Ma). These ages are evidently older than the upper age limit of the same type of pegmatite represented by the Ar–Ar (125.0 ± 1.40 Ma) and Re–Os ages (130.1 ± 1.1 Ma), such as the No.5 pegmatite, Considering the high closure temperatures of U-Pb system in zircon and monazite (>600 °C, Cherniak and Watson, 2000; Compeland, 1990) as compared to those of muscovite Ar-Ar

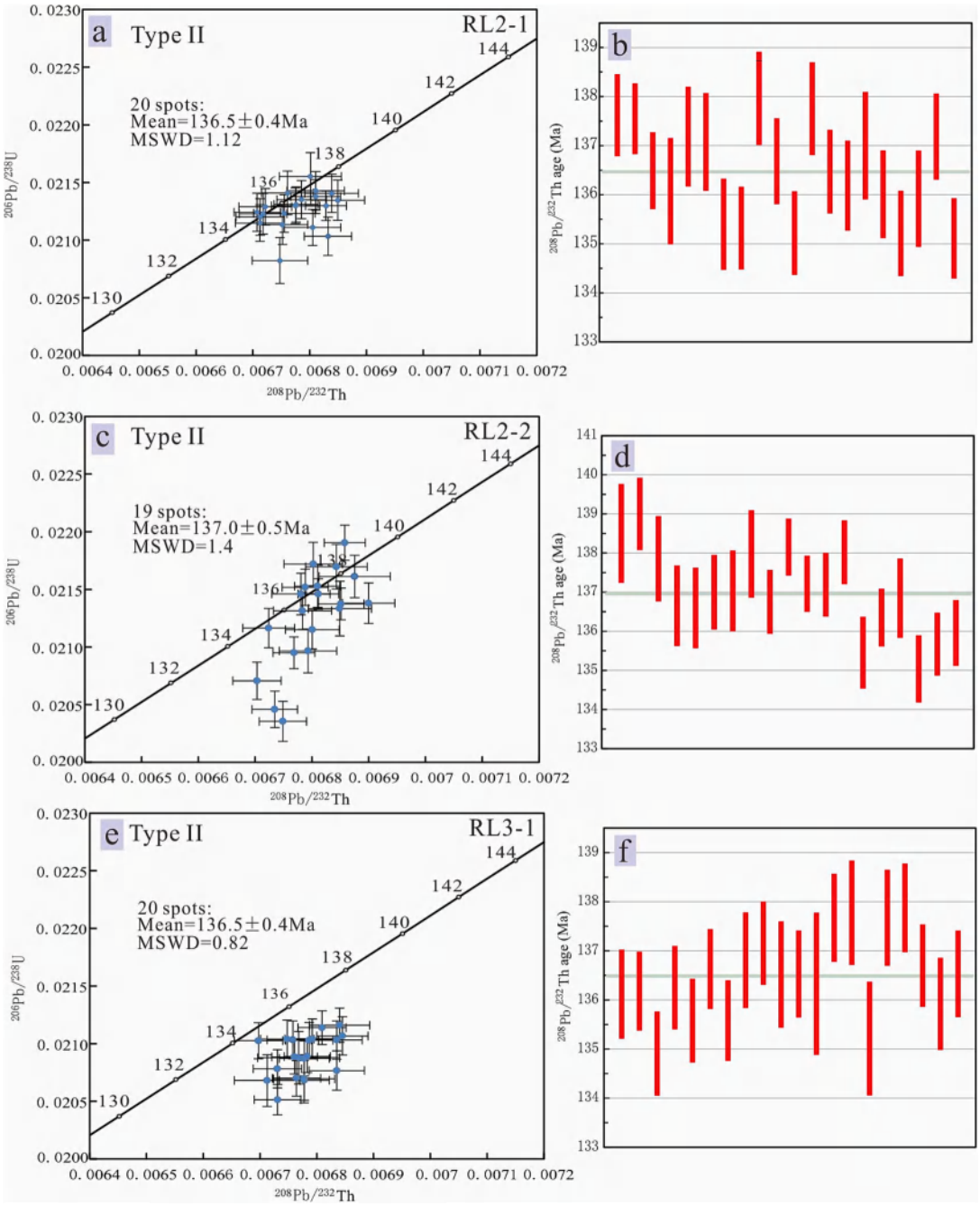

Fig. 8. Monazite U–Th–Pbconcordia age plots (a, c, and e) and weighted average diagrams (b, d, and f) of the Renli No. 2, later intrusion dike, and No. 3 pegmatites, respectively.

(425 °C, Harrison et al., 2009) and molybdenite re-Os (500 °C, Suzuki et al., 1996), there is no doubt that the zircon U-Pb ages were free from late thermal events.

In some cases, metamictization could magnify the apparent age because of a "high U effect" (Williams and Hergt, 2000; Li et al., 2013). In Fig. 9, the apparent $^{206}Pb/^{238}U$ ages do not show a positive or negative correlation with the U contents of zircon (Fig. 9a); similarly, the apparent $^{208}Pb/^{232}Th$ ages are independent of the U and Th contents of monazite (Fig. 9b and c), implying limited effects of high U and Th contents on the apparent $^{206}Pb/^{238}U$ and $^{208}Pb/^{232}Th$ ages, respectively. It has been demonstrated that a high U effect is mainly observed in the dating results by secondary-ion mass spectrometry rather than LA–ICP–MS (Zhao et al., 2014; Zhang et al., 2017), and the $^{208}Pb/^{232}Th$ ages obtained from Th-rich monazite are also consistent with the zircon or coltan U–Pb age proven by another group (Xiong et al., 2020) and this study (see ages of RL2-2 in Fig. 7c and 8c). Therefore, our zircon and monazite U–Pb ages can represent the formation times of the studied pegmatites.

To ensure the accuracy of the U–Pb ages for the different types of pegmatite in the Renli mining area, both zircon U–Pb and monazite U–Th–Pb geochronology studies were performed on the Renli pegmatites. The RL2-2 from the No. 2 pegmatite (type II) gave a zircon U–Pb age of 137.1 ± 0.8 Ma (Fig. 7c, d), Which is consistent with the monazite Th–Pb age of 137.0 ± 0.5 Ma (Fig. 8c, d) within the range of error, indicating that both zircon U–Pb and monazite Th–Pb ages are mutually supportive and convincible. The RL7-2 sample from the No. 7 pegmatite (type I) gave a zircon $^{206}Pb/^{238}U$ age of 141.5 ± 0.8 Ma (Fig. 7a, b), while the RL47-1 sample from the No. 47 pegmatite (type III) gave a

Table 3
Zircon Hf isotopic compositions of the Renli pegmatites.

Spot no.	Age (Ma)	$^{176}Yb/^{177}Hf$	$^{176}Lu/^{177}Hf$	$^{176}Hf/^{177}Hf$	2σ	εHf(0)	εHf(t)	T_{DM1}	T_{DM2}	$f_{Lu/Hf}$
RL7-2–01	141.9	0.039240	0.001114	0.282475	0.000011	−10.52	−7.51	1102	1666	−0.97
RL7-2–02	140.9	0.020978	0.000629	0.282493	0.000008	−9.86	−6.83	1063	1622	−0.98
RL7-2–03	141.6	0.021658	0.000721	0.282503	0.000013	−9.52	−6.49	1052	1601	−0.98
RL7-2–04	141.6	0.034302	0.001013	0.282490	0.000009	−9.96	−6.95	1077	1630	−0.97
RL7-2–05	142.8	0.045529	0.001350	0.282490	0.000008	−9.98	−6.97	1088	1633	−0.96
RL7-2–06	142.1	0.040751	0.001235	0.282500	0.000009	−9.61	−6.61	1070	1609	−0.96
RL7-2–07	141.0	0.025670	0.000673	0.282477	0.000011	−10.45	−7.42	1087	1659	−0.98
RL7-2–08	139.6	0.029114	0.000793	0.282451	0.000009	−11.37	−8.38	1127	1719	−0.98
RL7-2–09	150.1	0.014481	0.000487	0.282513	0.000007	−9.16	−5.92	1031	1572	−0.99
RL7-2–10	141.8	0.049005	0.001607	0.282523	0.000009	−8.82	−5.86	1048	1561	−0.95
RL7-2–11	141.8	0.066265	0.002248	0.282503	0.000008	−9.51	−6.61	1095	1609	−0.93
RL7-2–12	142.6	0.040757	0.001247	0.282495	0.000009	−9.81	−6.80	1078	1622	−0.96
RL7-2–13	141.3	0.082928	0.002748	0.282452	0.000009	−11.32	−8.48	1186	1726	−0.92
RL7-2–14	142.2	0.054018	0.001652	0.282443	0.000008	−11.65	−8.69	1164	1740	−0.95
RL7-2–15	141.2	0.052622	0.001616	0.282462	0.000008	−10.95	−8.00	1135	1696	−0.95
RL7-2–16	142.2	0.029245	0.000832	0.282490	0.000009	−9.97	−6.93	1072	1629	−0.97
RL7-2–17	142.1	0.072106	0.002803	0.282461	0.000010	−11.01	−8.15	1175	1706	−0.92
RL7-2–18	149.5	0.023870	0.000613	0.282530	0.000010	−8.56	−5.34	1011	1535	−0.98
RL2-1–01	137.6	0.002218	0.000048	0.282436	0.000007	−11.88	−8.87	1125	1748	−1.00
RL2-1–02	137.8	0.008493	0.000259	0.282461	0.000010	−11.01	−8.01	1097	1695	−0.99
RL2-1–03	138.4	0.005733	0.000143	0.282477	0.000009	−10.42	−7.40	1071	1656	−1.00
RL2-1–04	136.9	0.005691	0.000133	0.282534	0.000012	−8.41	−5.42	993	1530	−1.00
RL2-1–05	137.7	0.015539	0.000405	0.282513	0.000013	−9.15	−6.16	1028	1578	−0.99
RL2-1–06	138.1	0.023182	0.000523	0.282533	0.000009	−8.45	−5.47	1004	1534	−0.98
RL2-1–07	166.5	0.026489	0.000607	0.282534	0.000008	−8.43	−4.85	1006	1516	−0.98
RL2-1–08	136.7	0.055431	0.001686	0.282442	0.000010	−11.67	−8.83	1166	1745	−0.95
RL2-1–09	136.7	0.009392	0.000238	0.282519	0.000009	−8.95	−5.98	1017	1565	−0.99
RL2-1–10	137.5	0.019882	0.000372	0.282524	0.000011	−8.77	−5.79	1013	1554	−0.99
RL2-1–11	136.4	0.057849	0.001929	0.282482	0.000010	−10.25	−7.43	1116	1657	−0.94
RL2-1–12	149.0	0.008457	0.000143	0.282539	0.000009	−8.25	−5.00	987	1513	−1.00
RL2-1–13	136.9	0.050026	0.001795	0.282495	0.000010	−9.80	−6.96	1094	1627	−0.95
RL2-1–14	137.4	0.056076	0.001722	0.282522	0.000010	−8.85	−5.99	1053	1566	−0.95
RL47-1–01	135.0	0.004557	0.000122	0.282487	0.000008	−10.08	−7.13	1057	1637	−1.00
RL47-1–02	135.3	0.002929	0.000074	0.282502	0.000009	−9.57	−6.61	1036	1604	−1.00
RL47-1–03	135.7	0.002723	0.000069	0.282508	0.000010	−9.33	−6.36	1027	1589	−1.00
RL47-1–04	99.4	0.002653	0.000067	0.282511	0.000010	−9.23	−7.05	1023	1605	−1.00
RL47-1–05	134.3	0.002000	0.000058	0.282432	0.000010	−12.01	−9.07	1130	1759	−1.00
RL47-1–06	133.4	0.002177	0.000054	0.282446	0.000009	−11.51	−8.59	1111	1728	−1.00
RL47-1–07	160.3	0.003288	0.000076	0.282537	0.000010	−8.33	−4.82	988	1510	−1.00
RL47-1–08	111.4	0.005039	0.000110	0.282536	0.000012	−8.34	−5.91	989	1542	−1.00
RL47-1–09	132.7	0.002462	0.000063	0.282501	0.000009	−9.58	−6.67	1036	1606	−1.00
RL47-1–10	135.2	0.002296	0.000061	0.282549	0.000010	−7.88	−4.92	970	1498	−1.00
RL47-1–11	135.0	0.003875	0.000105	0.282570	0.000014	−7.14	−4.18	942	1451	−1.00
RL47-1–12	165.8	0.005089	0.000129	0.282573	0.000014	−7.03	−3.41	939	1425	−1.00
RL47-1–13	135.1	0.002555	0.000075	0.282511	0.000009	−9.22	−6.26	1022	1582	−1.00
RL47-1–14	134.8	0.002742	0.000080	0.282530	0.000009	−8.57	−5.62	997	1541	−1.00
RL47-1–15	134.5	0.001104	0.000031	0.282485	0.000010	−10.15	−7.20	1057	1641	−1.00
RL47-1–16	151.4	0.001460	0.000034	0.282498	0.000010	−9.71	−6.39	1040	1603	−1.00

$\varepsilon_{Hf}(t) = 10{,}000 \times (\{[(^{176}Hf/^{177}Hf)_S - (^{176}Lu/^{177}H\,f)_S \times (e^{\lambda t} - 1)] / [(^{176}Hf/^{177}Hf)_{CHUR,\,0} - (^{176}Lu/^{177}Hf)_{CHUR} \times ((e^{\lambda t} - 1)] - 1\}$. $T_{DM} = 1/\lambda \times \ln\{1 + [(^{176}Hf/^{177}Hf)_S - (^{176}Hf/^{177}Hf)_{DM}] / [(^{176}Hf/^{177}Hf)_S - (^{176}Hf/^{177}Hf)_{DM}]\}$. $T_{DM\,C} = T_{DM} - (T_{DM} - t) \times [(f_{cc} - f_s) / (f_{cc} - f_{DM})]$. $fLu/Hf = (^{176}Lu/^{177}Hf)_S / (^{176}Lu/^{177}Hf)_{CHUR} - 1$, where, $\lambda = 1.867 \times 10^{-11}$/a (Soderlund et al., 2004); $(^{176}Lu/^{177}Hf)_S$ and $(^{176}Hf/^{177}Hf)_S$ are the measured values of the samples; $(^{176}Lu/^{177}Hf)_{CHUR} = 0.0332$ and $(^{176}Hf/^{177}Hf)_{CHUR,0} = 0.282772$ (Blichert-Toft and Albarède, 1997); $(^{176}Lu/^{177}Hf)_{DM} = 0.0384$ and $(^{176}Hf/^{177}Hf)_{DM} = 0.28325$ (Griffin et al., 2000); $(^{176}Lu/^{177}Hf)_{mean\ crust} = 0.015$; $f_{cc} = [(^{176}Lu/^{177}Hf)_{mean\ crust} / (^{176}Lu/^{177}Hf)_{CHUR}] - 1$; fs = fLu/Hf; $f_{DM} = [(^{176}Lu/^{177}Hf)_{DM} / (^{176}Lu/^{177}Hf)_{CHUR}] - 1$; t = crystallization time of zircon.

zircon $^{206}Pb/^{238}U$ age of 134.5 ± 0.8 Ma (Fig. 7e, f). In addition, the RL3-1 from the No. 3 pegmatite (type II) gave a monazite weighted mean $^{208}Pb/^{232}Th$ age of 136.5 ± 0.4 Ma (Fig. 8e, f), and the RL2-1 sample from the late pegmatite intrusion in the No. 2 pegmatite yielded a monazite $^{208}Pb/^{232}Th$ age of 136.5 ± 0.4 Ma (Fig. 8a, b), consistent with the zircon and monazite U–Th–Pb ages of the No. 2 pegmatite within error, indicating the two stages of magma activities in the No.2 pegmatite at least in a very short period of time. In summary, our dating results suggest that (1) the pegmatites were gradually formed from type I to type III with distance from the YMB and with time from ca. 141 to 134 Ma; and (2) the formation ages are virtually unanimous for the same type of pegmatite but evidently distinguishable for different types of pegmatite.

7.2. Genetic relationship between pegmatite and granite

It has been suggested that rare-metal pegmatites can be formed by the anatexis of sedimentary rocks without parental granites (Barros and Menuge, 2016; Dill, 2015, 2016; Knoll et al., 2018; Lv et al., 2018, 2021b; Müller et al., 2017; Zhang et al., 2019); meanwhile, it is commonly believed that pegmatites originate from the crystallization differentiation of granitic magmas (Černy and Ercit, 2005; Černy et al., 2012; London, 2014, 2018, London et al., 2020; Roda-Robles et al., 2018). The pegmatite regional zoning around the Mufushan batholith in the Renli area (Fig. 2) suggests a closely spatial relationship between the Mufushan granites and Renli pegmatites. In addition, previous chronology studies and the dating results herein suggest a successive activity timeline for the igneous rocks in the YMB (Table 5; Fig. 10). The diorite, granodiorite, BMG, two-mica granite, and MMG have zircon U–Pb ages of 154.0 ± 1.9, 151.5 ± 1.3, 154–140, 146–138, and 141.0 ± 1.2 Ma,

Table 4
Monazite Nd isotopic data of the Renli pegmatite.

spot	Age(Ma)	$^{147}Sm/^{144}Nd$	$^{143}Nd/^{144}Nd$	2σ	εNd(0)	εNd(t)	T_{DM}	T_{DM2}
RL2-1–01	136.5	0.1525427	0.5122086	0.000028	−8.38	−7.61	2342	1549
RL2-1–02	136.5	0.1569837	0.5121531	0.00003	−9.46	−8.77	2672	1643
RL2-1–03	136.5	0.1500268	0.5121642	0.000024	−9.24	−8.43	2355	1615
RL2-1–04	136.5	0.1961955	0.5123087	0.000024	−6.42	−6.42	7226	1452
RL2-1–05	136.5	0.1671111	0.5122375	0.000023	−7.81	−7.30	2975	1524
RL2-1–06	136.5	0.1652963	0.5121652	0.000023	−9.22	−8.68	3089	1635
RL2-1–07	136.5	0.1550979	0.5122091	0.000023	−8.37	−7.64	2442	1552
RL2-1–08	136.5	0.1622110	0.5122321	0.000026	−7.92	−7.32	2710	1525
RL2-1–09	136.5	0.1450644	0.5122629	0.000029	−7.32	−6.42	1969	1452
RL2-1–10	136.5	0.1501454	0.5122145	0.000024	−8.26	−7.45	2240	1536
RL2-1–11	136.5	0.1480716	0.5122366	0.000024	−7.83	−6.99	2119	1498
RL2-1–12	136.5	0.1464113	0.5121981	0.000021	−8.58	−7.71	2153	1557
RL2-1–13	136.5	0.1520852	0.5122452	0.000021	−7.66	−6.89	2235	1490
RL2-1–14	136.5	0.1368375	0.5121532	0.000022	−9.46	−8.42	1975	1614
RL2-1–15	136.5	0.1661190	0.5121958	0.000022	−8.63	−8.10	3046	1588
RL2-1–16	136.5	0.1389485	0.5122022	0.000024	−8.50	−7.50	1931	1540
RL2-2–01	137.0	0.1611028	0.5122201	0.000024	−8.15	−7.53	2688	1543
RL2-2–02	137.0	0.1565784	0.5122030	0.000021	−8.49	−7.79	2521	1564
RL2-2–03	137.0	0.1521509	0.5123223	0.00004	−6.16	−5.38	2048	1368
RL2-2–04	137.0	0.1508650	0.5121834	0.000043	−8.87	−8.07	2340	1586
RL2-2–05	137.0	0.1557368	0.5122163	0.00004	−8.23	−7.51	2450	1541
RL2-2–06	137.0	0.1469657	0.5121958	0.000026	−8.63	−7.76	2176	1561
RL2-2–07	137.0	0.1489083	0.5121437	0.000021	−9.64	−8.81	2363	1647
RL2-2–08	137.0	0.1461180	0.5121856	0.000024	−8.82	−7.94	2172	1576
RL2-2–09	137.0	0.1390080	0.5121632	0.000023	−9.26	−8.26	2012	1602
RL2-2–10	137.0	0.1501978	0.5122501	0.000023	−7.57	−6.76	2157	1480
RL2-2–11	137.0	0.1470500	0.5121727	0.00003	−9.08	−8.21	2231	1598
RL2-2–12	137.0	0.1498649	0.5122133	0.000021	−8.28	−7.47	2233	1538
RL2-2–13	137.0	0.1533907	0.5121815	0.000026	−8.90	−8.15	2442	1593
RL2-2–14	137.0	0.1520429	0.5122256	0.000025	−8.04	−7.27	2282	1521
RL2-2–15	137.0	0.1530462	0.5122232	0.000024	−8.09	−7.33	2325	1527
RL3-1–01	136.5	0.1437782	0.5121508	0.000023	−9.50	−8.58	2175	1628
RL3-1–02	136.5	0.1628774	0.5121573	0.000023	−9.38	−8.79	2967	1645
RL3-1–03	136.5	0.1489253	0.5121720	0.000023	−9.09	−8.26	2297	1602
RL3-1–04	136.5	0.1606525	0.5121633	0.000031	−9.26	−8.63	2826	1632
RL3-1–05	136.5	0.1570257	0.5122168	0.000024	−8.22	−7.53	2504	1542
RL3-1–06	136.5	0.1943988	0.5122060	0.000039	−8.43	−8.39	7346	1612
RL3-1–07	136.5	0.1452257	0.5120930	0.000025	−10.63	−9.74	2348	1721
RL3-1–08	136.5	0.1515641	0.5121946	0.000022	−8.65	−7.87	2339	1570
RL3-1–09	136.5	0.1648371	0.5121420	0.000026	−9.68	−9.12	3132	1672
RL3-1–10	136.5	0.1606383	0.5122224	0.000024	−8.11	−7.48	2658	1538
RL3-1–11	136.5	0.1638258	0.5122651	0.000026	−7.27	−6.70	2698	1475
RL3-1–12	136.5	0.1500175	0.5121992	0.000031	−8.56	−7.75	2272	1560
RL3-1–13	136.5	0.1671529	0.5122302	0.000028	−7.95	−7.44	3002	1535
RL3-1–14	136.5	0.1966343	0.5123871	0.000031	−4.89	−4.89	6734	1328

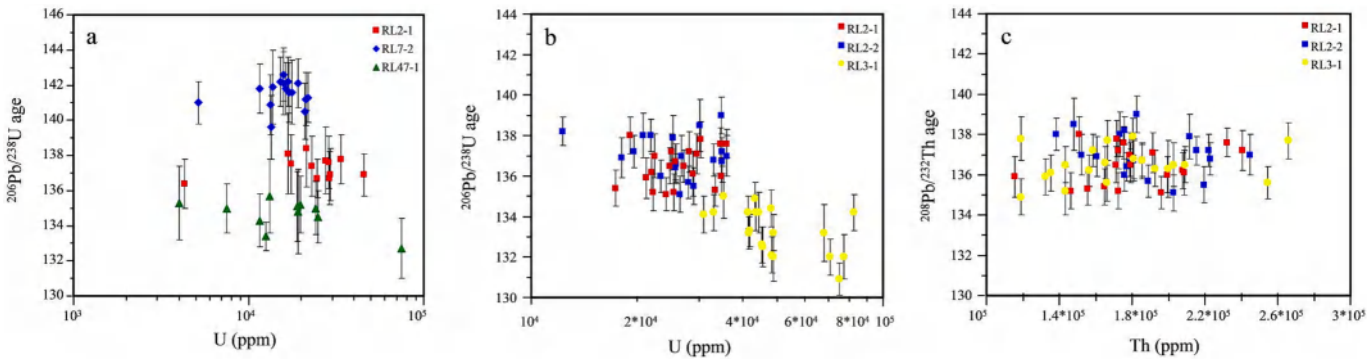

Fig. 9. Zircon $^{206}Pb/^{238}U$ age vs U (a), monazite $^{206}Pb/^{238}U$ age vs U (b), and monazite $^{208}Th/^{232}U$ age vs Th (c) diagrams of the Renli Nos. 2, 3, 7 and 47 pegmatites.

respectively (Li et al., 2019, 2020b; Wang et al., 2014b; Xiong et al., 2020). However, the disparate Hf and Nd isotope compositions do not support the genetic relationship between the intermediate rock and acid rock (Wang et al., 2014b). The prolonged magma activity from the Mufushan granite sequence (154–140 Ma) to the Renli pegmatite sequence (141.5–130.8 Ma) (Table 5; Fig. 10) supports a closely temporal relationship between them. In addition, Nos. 2, 7, and 47 pegmatites have consistent zircon Hf isotope compositions (this work) with the Mufushan BMG and TMG (Li et al., 2020a, b), with ε_{Hf} (t) values and two-stage model ages (T_{DM2}) in ranges of − 10 to − 5 (Table 3; Fig. 11b, c) and 1.5–1.8 Ga (Table 3; Fig. 11d), respectively, indicating a source connection.

However, the parental granite of the Renli pegmatites remains controversial. For example, Li (2016) suggested that the BMG is the

Table 5
The age statistics on igneous rocks from Mufushan area, South China.

Sample number	Lithology	Type	Age (Ma)	Dating method	Note	Reference
18RL-28	Pegmatite	Nb-Ta	140.2 ± 0.95	coltan U-Pb	No. 5	Xiong et al., 2020
18RL-8		Nb-Ta	140.7 ± 0.50	Monazite U-Pb	No. 5	
MRLm-4		Be-Nb-Ta	125.0 ± 1.40	Ar-Ar	No. 5	Li et al., 2019
RLN1-6		Nb-Ta	133.0 ± 2.60	coltan U-Pb		Li et al., 2020b
RL5		Nb-Ta	131.2 ± 2.40	zircon U-Pb	No. 5	
ZK1616-M1-4		Nb-Ta	130.1 ± 1.1	Re-Os	No. 5	Zhou et al., 2020
H17		Li	130.8 ± 0.9	Ar-Ar	No. 106	Liu et al., 2019
RL7-2		Barren	141.5 ± 0.8	zircon U-Pb	No. 7	This work
RL2-2		Nb-Ta	137.1 ± 0.8	zircon U-Pb	No. 2	
RL2-1		Nb-Ta	136.5 ± 0.4	Monazite U-Pb	No. 2	
RL2-2		Nb-Ta	137.0 ± 0.5	Monazite U-Pb	No. 2	
RL3-1		Nb-Ta	136.5 ± 0.4	Monazite U-Pb	No. 3	
RL47-1		Li	134.5 ± 0.8	zircon U-Pb	No. 47	
PJ-9–7-4		Be	130.5 ± 0.90	Ar-Ar	Daxing	Li et al., 2017
DFS3-3		Nb-Ta	127.7 ± 0.90	Ar-Ar	Duanfengshan	
07MFS25-2	Diorite	Diorite	154.0 ± 1.9	zircon U-Pb		Wang et al., 2014a
07MFS13-1	Granodiorite	Granodiorite	151.5 ± 1.3	zircon U-Pb		
07MFS01-1	Granite	Biotite monzogranite	148.3 ± 1.4	zircon U-Pb		
07MFS18-1		TW leucogranite	145.8 ± 0.9	zircon U-Pb		
QD49		Two-mica monzogranite	131.8 ± 1.5	zircon U-Pb		Ji et al., 2017
H16			141.0 ± 1.2	zircon U-Pb		Liu et al., 2019
RLG-2			138.3 ± 0.3	zircon U-Pb		Li et al., 2020b
RLG-3		Prophyritic biotite monzogranite	140.7 ± 0.7	zircon U-Pb		
RLG-4		Biotite monzogranite	140.3 ± 0.7	zircon U-Pb		
CQSK			142.9 ± 0.9	zircon U-Pb		Xu et al., 2019a,b
18RL-26			154.1 ± 0.98	zircon U-Pb		Xiong et al., 2020
18RL-10		Muscovite Monzogranite	141.0 ± 1.2	zircon U-Pb		

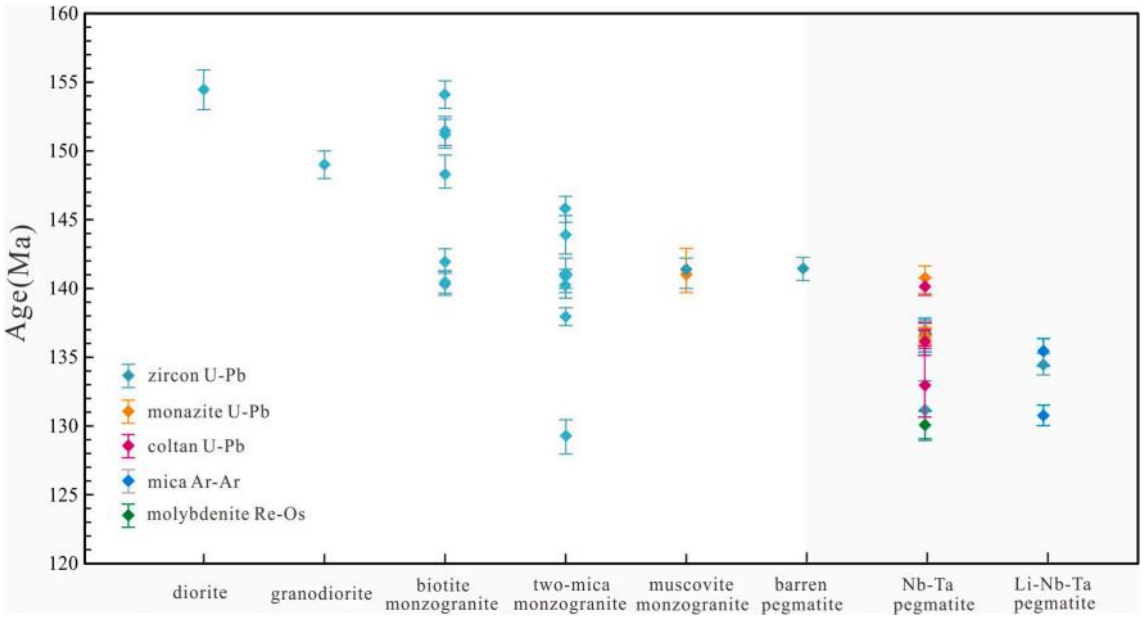

Fig. 10. Statistics on geochronological method and ages of the Mesozoic YMB and Renli rare-metal pegmatites, showing the time sequence of igneous rocks in the Mufushan area.

parental granite of type II pegmatite with Nb–Ta mineralization based on the locally spatial relationship between them. Xiong et al. (2020) hold that the Nb–Ta-mineralized pegmatite is genetically related to MMG rather than BMG according to the temporal-spatial relationship between them and the whole rock chemical compositions of the monzogranites. Li et al. (2021) have recently amended their previous proposal and suggested the closest petrogenetic relationship of TMG with the Renli rare-metal pegmatites based on the geochemical characteristics of muscovites from different types of pegmatites and granites in the Renli mining area.

From the classical model of LCT pegmatite (Černý, 1991; Shearer et al., 1992), the most fractionalized granitic phase in a common granite sequence (such as muscovite granite) is directly responsible for the origin of pegmatites exposed in the same regional zoning (Fig. 12a). However, the petrogenesis of the Renli pegmatite is difficult to explain using this model. First, the MMG shows a small quantity and limited scale and occurs as dikes in BMG (Wang et al., 2014b; Xiong et al., 2020), thus, it is difficult to provide abundant source materials for numerous pegmatites and sufficient Nb, Ta, and Li ore-forming elements for type II and III pegmatites, respectively. Moreover, the deep-buried majority of the MMG can be excluded because of the wide exposure of the lower phases (biotite granite and two-mica granite), indicating a high-level denudation of the YMB. Second, type I pegmatite generally occurs as veins and schlierens in the BMG (Fig. 3e) with a gradual

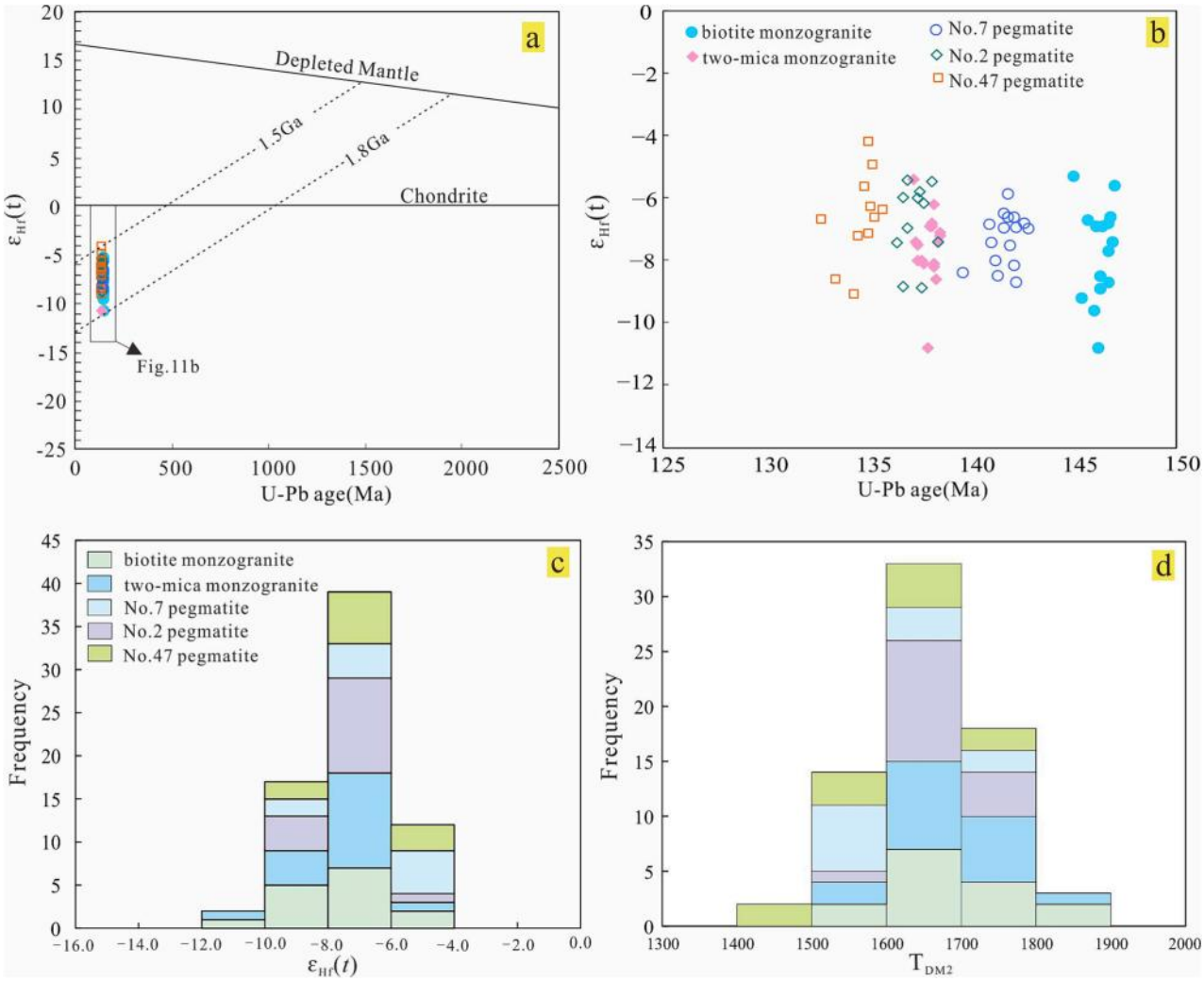

Fig. 11. Zircon $\varepsilon_{Hf}(t)$ vs U–Pb age diagram (a, b). Histogram of zircon $\varepsilon_{Hf}(t)$ values(c). Histogram of zircon Hf-isotope crust model age(T_{DM2}) (d). Zircon data of BMG and TMG are from Li et al. (2020a), Li et al. (2020b).

contact, and the ore-forming mineral of biotite in the BMG is absent in the MMG, indicating a sharp composition discontinuity. Third, no pegmatite regional zoning around the MMG in the Renli mining area and the periphery or interior of the Mufushan batholith is observed. Moreover, the possibility that all three types of pegmatites commonly sourced from the BMG can be excluded based on the following: (1) the occurrence of three phases of granite and three types of pegmatite indicates that fractional crystallization is the dominating mechanism for their formations. Further, it is impossible that, in this case, the type III pegmatite (muscovite–albite–spodumene pegmatite) originates from the BMG owing to a large composition gap between them; (2) the type I pegmatite hosted in the BMG evidently differs to the type II pegmatite hosted in the TMG in mineral assemblage and mineralization (e.g., the former is barren and contains a certain amount of biotite which is absent in the latter). Further, both types occur as schlierens, veins, branches, and pods in the BMG and TMG, without oriented distribution controlled by faults or joints, Further, there is no development of the chill border in the contact zone (Fig. 3a, b). All these evidences support the cogenetic relationship between the type I pegmatite and BMG and the type II and TMG. Accordingly, it is not possible that the type I pegmatite was sourced from a deep-buried biotite granite instead of the exposed BMG. The temporal–spatial and source relationships between the BMG and the type I pegmatite are confirmed herein; however, the occurrence of deep biotite granites in the Mufushan area is also denied by the geophysical study (Ji et al., 2018). Importantly, no other buried granitoids has been found in the depth of 15 km at least according to the forward gravity modeling along two trending profiles across the Dayunshan-Mufushan batholiths (Ji et al., 2018). With consideration of the effective derive distance of pegmatite from source granites (<10 km), it is meaningless for the pegmatites even if deep granites do exist with bury depth over 15 km.

Although lack of the physical connection of the type III pegmatite with specific granite, the type III pegmatite is close to the MMG in composition (similar rock-forming minerals of albite, quartz and muscovite) and formation age (ca. 135 Ma and 141 Ma, respectively; Table 5). In addition, an exposure of MMG has been demonstrated in Huangboshan area. The MMG has U-Pb age of 141 Ma (Xiong et al., 2020) and is close to the No.47 spodumene-rich pegmatite (no>1 km, Fig. 2), indicating a close temporal-spatial connection between them. More importantly, previous works demonstrated that the BMG and TMG belong to different batchs of granitic intrusion rather than the crystallization differentiation production of the same one batch of magma (Ji et al., 2018). The occurrence of MMG dyke in the BMG and TMG also supports that the MMG was the latest intrusion. Therefore, its reasonable that the majority of the MMG could be sealed in the early BMG and TMG or covered by Neoproterozoic sedimentary rocks due to its limited volume.

The BMG exposed in the Renli area was dated at 154.1 ± 2.5 Ma (Xiong et al., 2020) and 140.7 ± 0.7 Ma (Li et al., 2020a), and BMG host type I pegmatite in adjacent area of Renli was dated at 142.9 ± 0.9 Ma

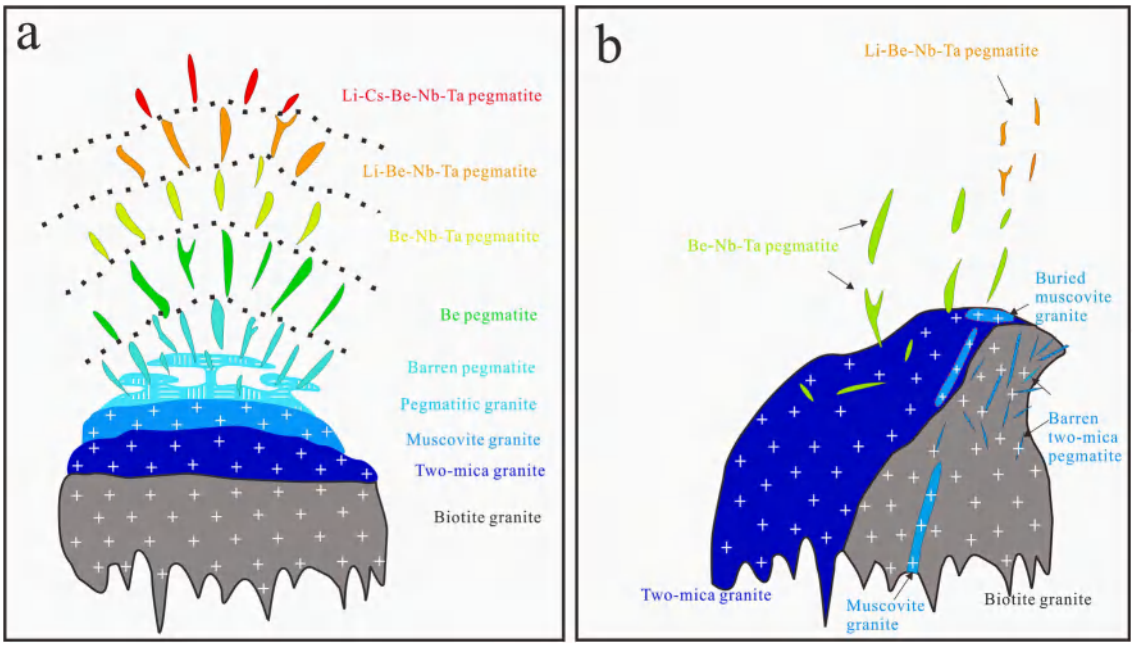

Fig. 12. Classical model for LCT pegmatite (a) (after Černý, 1991; Shearer et al., 1992) and a schematic model for Renli LCT pegmatites (b).

(Xu et al., 2019a,b), the latter two ages coincide with the U–Pb age of the No. 7 pegmatite (141.5 ± 0.8 Ma, this work) within range of error, indicating a temporal relationship. Moreover, the No. 7 pegmatite shows a similar zircon Hf isotope composition to the BMG (Fig. 11), indicating a source connection. Although the TMG shows similar U–Pb ages (141–138 Ma, Li et al., 2020b; Liu et al., 2019) and Hf isotope composition to the type I pegmatite (Fig. 11), it is excluded to be the parental rock of the latter because the type I pegmatite commonly occurs in the BMG as schlieren or vein, with a gradual contact, and it is almost absent in the TMG, indicating a close spatial connection of the type I pegmatite with the BMG. Importantly, the type I pegmatite has primitive components (higher K/Rb and Nb/Ta ratios and lower Li, Rb, and Cs contents) compared to the TMG from a previous study (Li et al., 2021).

The Nos. 2 and 3 pegmatites have zircon and monazite U–Th–Pb ages of 137.1 –136.5 Ma, and the No. 47 pegmatite was formed at ~ 134.5 Ma (Figs. 7, 8), which are slightly younger than the ages of the TMG (141–138.3 Ma, Li et al., 2020b; Liu et al., 2019). The TMG occupies a large proportion of the Mufushan batholith and hosts plenty of Be and Be–Nb–Ta-mineralized pegmatites, i.e., the type II, (Fig. 1). Similar to the type I pegmatite, the type II pegmatite occurs as veins and schlierens in the TMG with gradual contacts between them (Fig. 3b). Moreover, the studied types II pegmatite has consistent zircon Hf isotope compositions with the TMG (Fig. 11). The above mentioned evidence supports that the TMG could be the parental rock of types II pegmatite in the Renli mining area.

Hence, we propose a new parallel differentiation model for the generation of the Renli LCT pegmatites, i.e., the types I, II and III pegmatites were derived from the BMG, TMG and MMG, (Fig. 12b), respectively. In Black Hills, South Dakata, USA, plenty of pegmatites distributed in/around the Harney Peak Granite. Three trajectories of fractional crystallization were identified after analyzing a mass of composition data of potash feldspar from pegmatite and granite samples (Shearer, 1992). Except the pegmatites sharing a same trajectory of fractional crystallization with the Harney Peak Granite, the Li-, Rb-, Cs-enriched zoned pegmatites and F-, sn-, Be-enriched pegmatites show distinct differentiation trajectories to any specific granites. They could be formed by anatexis rather than fractional crystallization of granitic melts (Shearer, 1992). Although the pegmatites from Renli and Black Hills both have various origins and types, but they are essentially different in source. The types I, II, and III pegmatites from Renli have a common source indicated by their consistent Hf isotope compositions (Fig. 11b). In contrast, the three pegmatite arrays, i.e., the Harney Peak Granite-related pegmatites, Li-, Rb-, Cs-enriched zoned pegmatites and F-, sn-, Be-enriched pegmatites from Black Hills were derived from distinct sources (Shearer, 1992). In a nutshell, the differences among pegmatites in Renli resulted from the level of fractional crystallization of a common melt, and for the pegmatites from Black Hills, source and partial melting degree are dominating factors.

It is still unclear what factors control the differentiation of granitic melts, however, the differentiation mechanism considerably restricts the spatial relationship between pegmatite and parental granite. If crystal-melt fractionation was the dominating way, the interior residual melts were hard to accumulate and migrate adequately. Therefore, they were hard to extract from the source magma (Černý, 1991). Pegmatites originating from these melts are generally emplaced in their source rocks, such as the type I pegmatite in Renli. If melt fractionation was controlled by filter pressing and gravity convection–diffusion, the residual melts were inclined to accumulate in the uppermost domes of source melt (Černý, 1991), and emplaced commonly out of their parental rocks owing to low viscosity and sudden extractions promoted by the enrichment of volatiles and pressure variations, respectively, such as the type III pegmatite.

7.3. Source of the Renli pegmatite

Zircon has been used effectively as a proxy for tracing crust–mantle evolution by the combination of its U–Pb age and Hf isotope composition (Amelin et al., 1999; Griffin et al., 2002; Scharer et al., 1997). Zircons formed in pegmatites, especially those having rare-metal mineralizations, are commonly rich in Hf and transform to hafnon sometimes. High Hf content in pegmatite-forming melt endows the authority on provenance identification by Hf isotopes. It has been demonstrated that metamictization, recrystallization, and metasomatism hardly modify the original Hf isotope composition of zircon from highly differentiated pegmatite (Chen et al., 2018; Lv et al., 2012; Tang et al., 2017). Monazite is a common mineral and widely applied in chronology and isotope studies because of the Th, U, and light rare earth element enrichment and the high closure temperatures of U–Pb and Sm–Nd isotope systems (e.g., Cottle et al., 2019; Fisher et al., 2020; Liu et al., 2012; Pandur et al., 2020; Pearce et al., 1999).

Zircons from the Nos. 2, 7, and 47 pegmatites have almost the same Hf isotope composition, also coincident with those of the BMG (Li et al., 2020a) and TMG (Li et al., 2020b) in the Renli area (Fig. 9). The pegmatites show $\varepsilon_{Hf}(t)$ values − 10 to − 5 (Table 3; Fig. 9b, c) and T_{DM2} of 1.5–1.8 Ga (Table 3; Fig. 9d). Monazites from the Nos. 2 and 3 pegmatites in the Renli area have negative $\varepsilon_{Nd}(t)$ values (Table 4; Fig. 13a), with>90 % of the data in the range of − 10 and − 6 (Table 4; Fig. 13b), and the T_{DM2} of 1.4–1.7 Ga (Table 4; Fig. 13c), consistent with the zircon Hf isotope compositions of $\varepsilon_{Hf}(t)$ (−10 to − 5) and T_{DM2}(1.5–1.8 Ga) mentioned above. The monazites from the RL2-1 sample show $\varepsilon_{Nd}(t)$ values of − 6.42 to − 8.77 (Table 4), with corresponding $\varepsilon_{Hf}(t)$ values of − 5.78 to − 8.97 based on the conversion formula by Vervoort et al. (1999). These values are consistent with the $\varepsilon_{Hf}(t)$ values (−4.85 to − 8.87, Table 3) of zircons from the RL2-1 sample, indicating the coupled Nd–Hf isotope compositions of the Renli pegmatites.

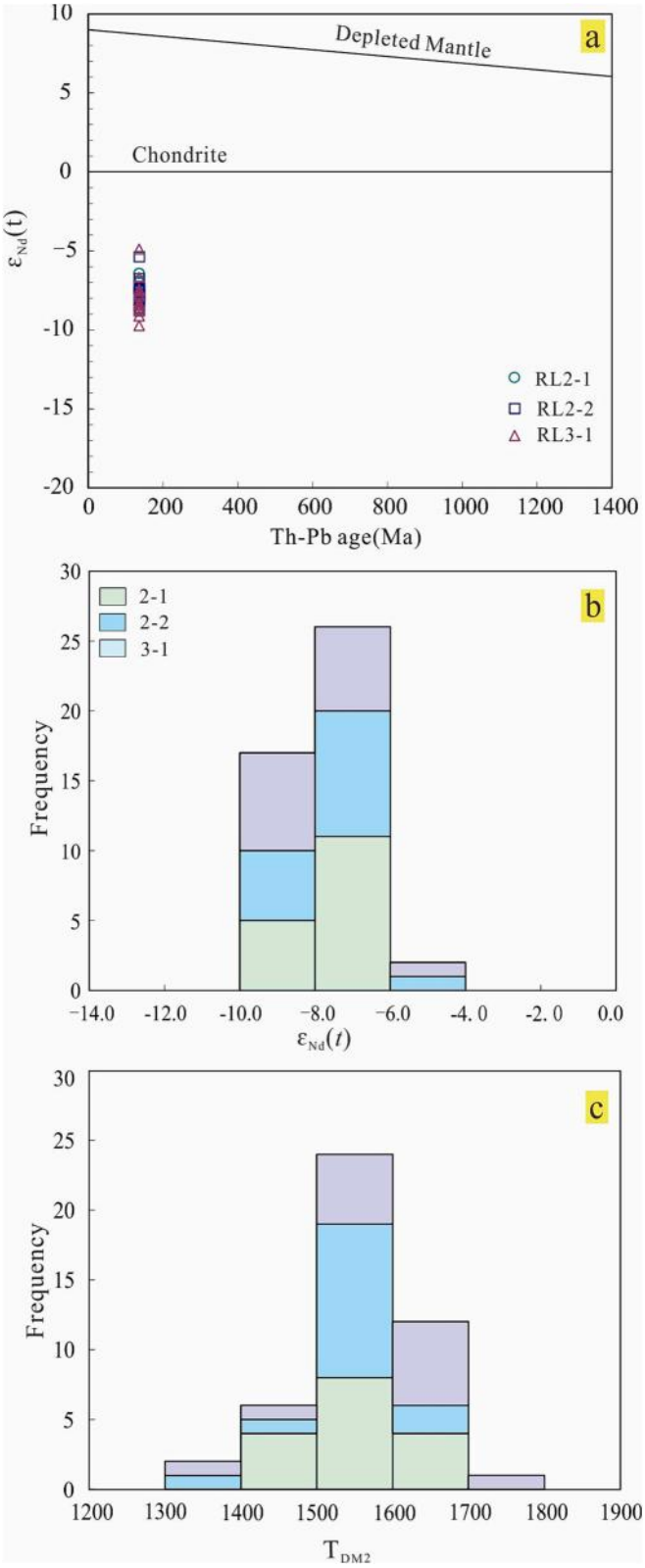

Fig. 13. Monazite $\varepsilon_{Nd}(t)$ vs Th–Pb age diagram(a). Histogram of monazite εNd (t) values(b). Histogram of monazite Nd-isotope crust model age (T_{DM2}) (c).

The JOB is a Neoproterozoic convergent orogen formed by Yangtze and Cathaysia block amalgamation (e.g., Wang et al., 2014a, 2017b; Zhou et al., 2009). Although a large number of granites were generated during orogenesis, only the Fanjingshan granite contributed to pegmatite formation and rare-metal mineralization in the western JOB. A systematic study of pegmatite, granite, and sedimentary rocks demonstrated that the Fanjingshan granite–pegmatite suite has Sn–Nb–Ta mineralization and originates from the partial melting of sedimentary rocks from the Fanjingshan Group at ca.830 Ma (Lv et al., 2021a). The Lengjiaxi Group exposed in the Renli area (Figs. 1 and 2) has a similar maximum deposit age (ca. 860–820 Ma) to the Fanjingshan Group and contemporaneous strata in the JOB (e.g., the Shuangqiaoshan Group in Jiangxi and the Sibao Group in Guangxi). They were formed by deposition in a backarc setting with varying sources from eastern to western JOB (e.g., Wang et al., 2014a, 2017b)and are regarded as the major source of Neoproterozoic granites (e.g., Li et al., 2003; Wu et al., 2006a, b; Zheng et al., 2007).

Compared to the Neoproterozoic Fanjingshan rare-metal granite–pegmatite suite ($\varepsilon_{Hf}(t)$ = +1.13 – −9.51, T_{DM2} = 2.31–1.65 Ga, Lv et al., 2021a), the Renli granite and pegmatite have relatively depleted zircon Hf isotope composition ($\varepsilon_{Hf}(t)$ = -3.0 – −10.8 T_{DM2} = 1.88–1.39 Ga, Fig. 14), indicating the contribution of more juvenile crust materials to the Renli granite and pegmatite. However, they totally match with the Neoproterozoic granitoids exposed in northeastern Hunan (Figs. 14 and 15) in zircon Hf isotope compositions, indicating their common source. Although the younger (T_{DM2} < 1.2 Ga) and older (T_{DM2} > 2.0 Ga) components of the Lengjiaxi Group are absent in the Renli granite and pegmatite according to the statistics of comparison of model age (Fig. 15), the Renli granite and pegmatite could be sourced from the sedimentary rocks of Lengjiaxi Group. Because a few of inherited zircons have been observed in the BMG and TMG of the YMB with dominating ages of 700–900 Ma (Li et al., 2020b; Wang et al., 2014b; Xiong et al., 2020), and these zircon U-Pb ages are totally consistent with the dominating age of detrital zircons (690–950 Ma, Li et al., 2020b) from the Lengjiaxi Group, indicating a strong source connection of the Mesozoic granite-pegmatite suite with the Neoproterozoic sedimentary rocks.

In conclusion, the Renli LCT pegmatites and their parental granites originate from the partial melting of the sedimentary rocks from the Neoproterozoic JOB.

7.4. Petrogenetic and mineralization model of the Renli pegmatite

Based on the distribution location of pegmatite worldwide, Dill (2015, 2016) summarized five types of geodynamic settings for pegmatite formation, namely, Alpine, Variscan, Rift, Andean, and island arc. Among them, the Variscan type orogen setting is the uppermost for pegmatite formation because of the largely thickened crust. A thinned crust and alkaline magmatism characterize the Rift setting (Dill, 2015), indicating a facilitated setting for Nb-, Y-, and F-rich pegmatite (Černý, 1991). In comparison, the Andean and island arc settings are averse to pegmatite formation, and pegmatites are generally formed in hinterland far away from the active continental margin (Dill, 2016). The Mesozoic geology of South China is different from that of the Andean subduction setting and Japan Island Arc (e.g., Mao et al., 2014). Tectonic studies

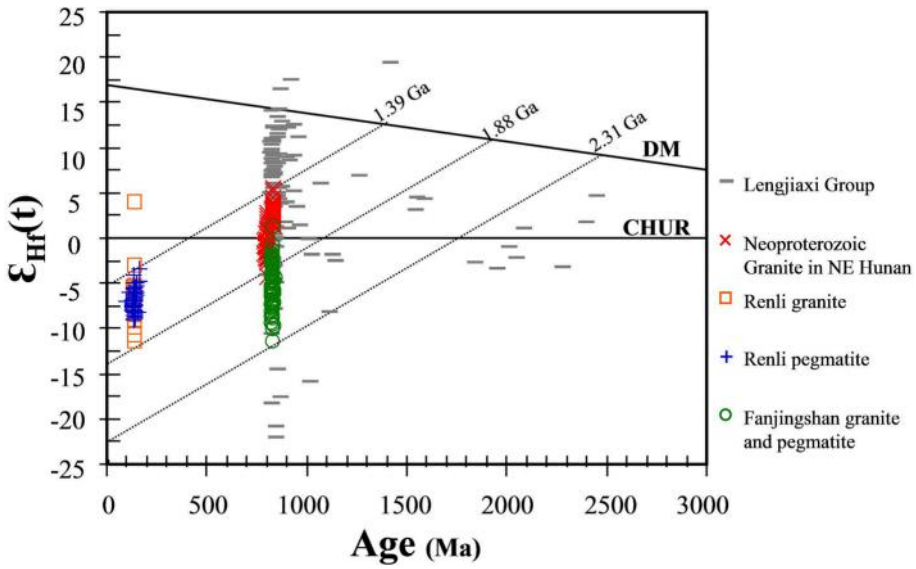

Fig. 14. Diagram of $\varepsilon_{Hf}(t)$ value vs crystallization ages of detrital and igneous zircons from the JOB. Data of zircon are from Li et al. (2020b), Lv et al. (2021a), Wang et al. (2011), Wang et al. (2014a), and this work.

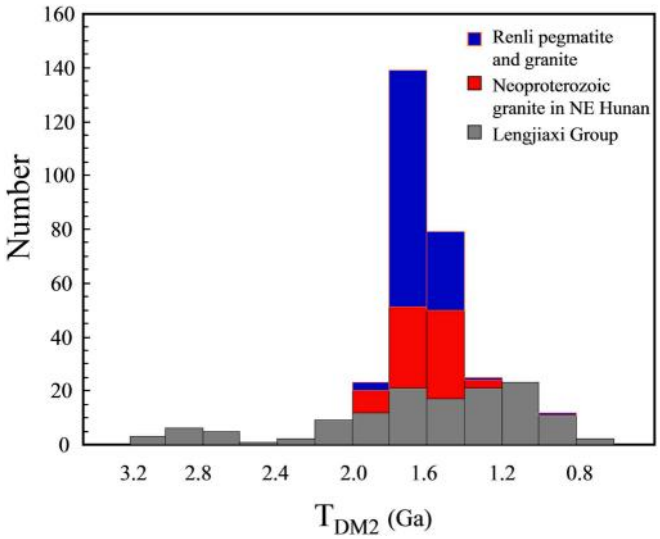

Fig. 15. Histogram of zircon Hf-isotope crust model age (T_{DM2}) of pegmatite, granite and schist from the Mufushan area and northeastern Hunan. Data of the Lengjiaxi Group from Wang et al. (2016) and Li et al. (2020a), , Li et al. (2020b); data of the Neoproterozoic granite from Ma et al.(2009) and Wang et al. (2014a); data of Renli pegmatite and granite from Li et al. (2020a, , Li et al. (2020b) and this work.

have indicated that the Mufushan granite and pegmatite might be formed in (1) a postorogenic setting after the early Triassic collision between South China and North China blocks (Li et al., 1993; Zhou et al., 2006), or (2) a *syn*-orogenic subduction setting induced by the subduction of the paleo-Pacific Ocean plate under the South China block (Li and Li, 2007; Jiang et al., 2009; Sun et al., 2012). However, the second setting is preferentially considered here owing to the face that (1) the activities of the Mufushan granite and pegmatite largely lag behind the postorogenic granites formed at 243–214 Ma after collision (e.g., Wang et al., 2007) and (2) the Middle Jurassic–Early Certaceous granites and related rare metal ore deposits mainly concentrate in the South China block (e.g., Wang et al., 2014b). Further, they show a NE-striking distribution vertical to the northwestward subduction. Although the syn–orogenic stage is commonly characterized by extrusion stress and thickened crust compressional setting, an extension setting is preferentially considered for the Mufushan granite and pegmatite during the Late-Jurassic to Early Cretaceous, according to the following. (1) the bimodal magmatic suites comprise gabbro and granite that have been confirmed in Mufushan area (Wang et al., 2014b; Chen et al., 2021), and the juxtaposing of gabbro and granite generally indicates extensional settings (Bonin, 2004; Pin and Paquette, 1997; Tang et al., 2013); (2) the pervasive Mesozoic granitoids and volcanic rocks in South China have been attributed to the production of lithospheric extension caused by the roll back of the paleo-Pacific Ocean plate (Zhou et al., 2006; Li and Li, 2007), especially for the Late Jurassic to the Early Cretaceous granitoids exposed in Mufushan and Lianyunshan (Wang et al., 2014; Wang et al., 2016; Ji et al., 2017). In addition, the Late Jurassic to Early Cretaceous lithospheric extension also promoted the generations of the Pb–Zn, W, and other rare-metal ore deposits in South China (Shu et al., 2021; Yu et al., 2020; Zhao et al., 2017). Combined with previous studies, we propose the following geodynamic scenario for the YMB during the early Yanshanian:

Lithospheric extension and intense magmatism in South China have been caused by the long-distance subduction the paleo-Pacific plate in the Late Jurassic to the Early Cretaceous (e.g., Li and Li, 2007; Shu et al., 2021). In the Mufushan area, the underplating of mantle magma causes the generation of high-Mg diorite at ca. 154 Ma and a large volume of granitic magma derived by the partial melting of the JOB crust at ca. 148 Ma (Wang et al., 2014b). The initial granite-forming melts of the BMG, TMG, and MMG were successively formed by the sufficient crystallization differentiation of the granitic magma because of the extended heat supply from the prolonged mantle magmatisms (154–137 Ma, Chen et al., 2021; Wang et al., 2014b). Meanwhile, the types I, II and III pegmatite-forming melts were derived by crystallization differentiation of the BMG, TMG and MMG melts, respectively. The type I melt had hardly escaped from its parental melt owing to the evident lack of volatile components. However, the types II and III pegmatite-forming melts were extracted from their parental magma and mostly emplaced in peripheral sedimentary rocks, i.e., the Lengjiaxi Group (Figs. 2, 12b).

Comparatively, *syn*-orogenic LCT pegmatites are rarer than those formed in the postorogenic extension setting (Černý, 1991; Lv et al., 2018). In the Chinese Altai, the Devonian *syn*-orogenic pegmatite was formed by the partial melting of Early Paleozoic accreted materials in a fore-arc extension setting caused by the subduction of the ocean ridge and the upwelling of the asthenosphere mantle (Lv et al., 2018), accompanied by with coeval high temperature metamorphism (e.g.,

720 °C–650 °C). Conversely, the Mufushan pegmatites were formed in inland far away from the active continental margin, and sourced from the backarc sedimentary materials accreted in the Neoproterozoic Jiangnan orogeny rather than the newly accreted materials during the subduction of paleo-Pacific Ocean. The specific reasons caused in these discrepancies are still unclear and need to be studied in the future. The prolonged heat supply may be critical to the differentiation of the rare-metal granite–pegmatite suite formed in a subduction setting. Moreover, the source inherited from ancient orogen and further enrichment of rare-metal elements caused by the cycling of ancient orogenic crust may contribute to the mineralization of the inland synorogenic peraluminous magmas. These factors may explain the barren property of the Neoproterozoic granites in Northeast Hunan Province although they have the same source as the YMB from the sedimentary rocks of the Lengjiaxi Group. However, future work on the migration and enrichment mechanisms of rare-metal elements during crust reworking and cycling should be done.

8. Conclusions

(1) The results of zircon U–Pb and monazite U–Th–Pb dating reveal that the Renli biotite–muscovite–microline pegmatite (type I) was formed at ca. 141 Ma, muscovite–microcline–albite pegmatite(type II) at ca. 137 Ma, and albite–spodumene pegmatite(type III) at ca. 134 Ma, with decreasing ages from the barren pegmatite to the Li mineralization pegmatite.
(2) The biotite–muscovite–microline pegmatite (type I) originates from the BMG, while the muscovite–microcline–albite pegmatite (types II) and albite–spodumene pegmatite (type III) may originate from the TMG and MMG, respectively, indicating a new petrogenesis model of parallel differentiations of triple source granitic melts for the LCT pegmatites in South China.
(3) The Renli LCT pegmatites have coupled Hf–Nd isotope compositions with model ages of 1.4–1.8 Ga, and the Hf isotope compositions are similar to that of the Neoproterozoic granitoids and match with the sedimentary rocks from the Neoproterozoic Lengjiaxi Group, indicating that the Renli LCT pegmatites originated from the reworking materials of the Neoproterozoic JOB.

Declaration of Competing Interest

The authors declare that they have no known competing financial interests or personal relationships that could have appeared to influence the work reported in this paper.

Data availability

Data will be made available on request.

Acknowledgments

We thank the Editor-in-Chief Prof. Chen H.Y. and Associate Editor Prof. Yang W.B. for handling this manuscript with expertness and efficiency, and four anonymous reviewers are also appreciated for their constructive comments. This study is jointly supported by the Key research and development program of Hunan Province, China (No. 2019SK2261), the Natural Science Foundation of Hunan Province, China (No. 2021JJ30387), and the National Natural Science Foundation of China (No. 41873030).

References

Amelin, Y., Lee, D.C., Halliday, A.N., Pidgeon, R.T., 1999. Nature of the Earth's earliest crust from hafnium isotopes in single detrital zircons. Nature 399, 252–255.
Ayers, J.C., Dunkle, S., Gao, S., Miller, C.F., 2002. Constraints on timing of peak and retrograde metamorphism in the Dabie Shan Ultrahigh-pressure Metamorphic Belt, east-Central China, using U-Th–Pb dating of zircon and monazite. Chem. Geol. 186, 315–331.
Barros, R., Menuge, J.F., 2016. The origin of spodumene pegmatites associated with the Leinster granite in Southeast Ireland. Can. Mineral. 54, 847–862.
Blichert-Toft, J., Albarède, F., 1997. The Lu-Hf isotope geochemistry of chondrites and the evolution of the mantle–crust system. Earth Planet. Sc. Lett. 148, 243–258.
Bonin, B., 2004. Do coeval mafic and felsic magmas in post-collisional to within-plate regimes necessarily imply two contrasting, mantle and crustal, sources? A review. Lithos 78, 1–24.
Cawood, P.A., Wang, Y., Xu, Y., Zhao, G., 2013. Locating South China in Rodinia and Gondwana: a fragment of greater India lithosphere? Geology 41, 903–906.
Černý, P., 1991. Rare element granitic pegmatites. Part II: Regional and global environments and petrogenesis. Geosci. Can. 18, 68–81.
Černy, P., Ercit, T.S., 2005. The classification of granitic pegmatites revisited. The Can. Mineral. 43, 2005–2026.
Černy, P., London, D., Novak, M., 2012. Granitic pegmatites as reflections of their sources. Elements 8, 289–294.
Chen, J.F., Zhang, H., Zhang, J.X., Ma, Y.H., 2018. Geochronology and Hf isotope of zircon for Koktokay No.3 granitic pegmatite in Xinjiang and its geological implications. China J. Nonfer. Metal. 28, 1832–1845 in Chinese with English abstract.
Chen, J.F., Wen, C.H., Huang, J.Z., Zhang, J.X., Wang, C., Tang, Y., Lv, Z.H., Zhou, F.C., Cao, C.H., Chen, Y.P., 2021. Characteristics of No.7 pegmatite and pyroxene diorite in Renli rare metal deposit, south margin of Mufushan batholiths and its geological implications. Geotec. Metal. 10 (5), 951–967 in Chinese with English abstract.
Cherniak, D.J., Watson, E.B., 2000. Pb diffusion in zircon. Chem. Geol. 172, 5–24.
Chu, N.C., Taylor, R.N., Chavagnac, V., Nesbitt, R.W., Boella, R.M., Milton, J.A., Burton, K., 2002. Hf isotope ratio analysis using multi-collector inductively coupled plasma mass spectrometry: An evaluation of isobaric interference corrections. J. Anal. Atom. Spectrom 17, 1567–1574.
Cottle, J., Lederer, G., Larson, K., 2019. The monazite record of pluton assembly: Mapping manaslu using Petrochronology. Chem. Geol. 530, 119309.
Cottle, J.M., Searle, M.P., Jessup, M.J., Crowley, J.L., Law, R.D., 2015. Rongbuk re-visited: Geochronology of leucogranites in the footwall of the South Tibetan Detachment System, Everest Region, Southern Tibet. Lithos 227, 94–106.
Deng, T., Xu, D.R., Chi, G.X., Wang, Z.L., Jiao, Q.Q., Ning, J.T., Dong, G.J., Zou, F.H., 2017. Geology, geochronology, geochemistry and ore genesis of the Wangu gold deposit in northeastern Hunan Province, JiangnanOrogen South China. Ore Geol. Rev. 88, 619–637.
Dill, H.G., 2015. Pegmatites and aplites: Their genetic and applied ore geology. Ore Geol. Rev. 69, 417–561.
Dill, H.G., 2016. The CMS classification scheme (Chemical composition-Mineral assemblage-Structural geology)-linking geology to mineralogy of pegmatitic and aplitic rocks. NeuesJahrbuchfürMineralogie-Abhandlungen. J. Mineral. Geochem. 193, 231–263.
Ding, T., Rees, C.E., 1984. The sulphur isotope systematics of the Taolin Lead-zinc ore deposit, China. Geochim. Cosmochim. Acta 48, 2381–2392.
Fisher, C.M., Bauer, A.M., Luo, Y., Sarkar, C., Hanchar, J.M., Vervoort, J.D., Tapster, S.R., Horstwood, M., Pearson, D.G., 2020. Laser ablation split-stream analysis of the Sm-Nd and U-Pb isotope compositions of monazite, titanite, and apatite–Improvements, potential reference materials, and application to the Archean Saglek Block genesis. Chem. Geol. 539, 119493.
Gao, L.Z., Chen, J., Ding, X.Z., Liu, Y.R., Zhang, C.H., Zhang, H., Liu, Y.X., Pang, W.H., Zhang, Y.M., 2011. Zircon SHRIMP U-Pb dating of the tuff bed of Lengjiaxi and Banxi groups, northeastern Hunan: constraints on the Wuling movement. Geol. Bull. China 30, 1001–1008 in Chinese with English abstract.
Goncalves, G.O., Lana, C., Scholz, R., Buick, I., Gerdes, A., Kamo, S.L., Corfu, F., Marinho, M.M., Chaves, A.O., Valeriano, C., Nalini, H.A., 2016. An assessment of monazite from the Itambé pegmatite district for use as U-Pb isotope reference material for microanalysis and implications for the origin of the "Moacyr" monazite. Chem. Geol. 424, 30–50.
Griffin, W.L., Pearson, N.J., Belonsova, E., Jackson, S.E., Achterherah, E.V., O'Reilly, S. Y., Shee, S.R., 2000. The Hf isotope composition of cratonic mantle: LA-MC-ICPMS analysis of zircon megacrysts in kimberlites. Geochim. Cosmochim. Acta 64, 133–147.
Griffin, W.L., Wang, X., Jackson, S.E., Pearson, N.J., O'Reilly, S.Y., Xu, X., Zhou, X., 2002. Zircon chemistry and magma mixing, SE China: In-situ analysis of Hf isotopes, Tonglu and Pingtan igneous complexes. Lithos 61, 237–269.
Griffin, W.L., Pearson, N.J., Belousova, E.A., Saeed, A., 2006. Comment: Hf-isotope heterogeneity in zircon 91500. Chem. Geol. 23, 358–363.
Harrison, T.M., Celerier, J., Aikman, A.B., Herman, J., Heiziler, M.T., 2009. Diffusion of ^{40}Ar in muscovite. Geochim. Cosmochim. Acta 73, 1039–1051.
Hunan Institute of Geological Survey (HIGS), 2009. 1:250000 Regional Geological Survey Report of Yueyang Area. Hunan Institute of Geological Survey, Changsha, 71 pp. (in Chinese).
Hoskin, P.W.O., Schaltegger, U., 2003. The composition of zircon and igneous and metamorphic petrogenesis. Rev. Mineral. Geochemi. 53, 27–62.
Hu, Z.C., Gao, S., Liu, Y.S., Hu, S.H., Chen, H.H., Yuan, H.L., 2008. Signal enhancement in laser ablation ICP-MS by addition of nitrogen in the central channel gas. J. Anal. Atom. Spectrom 23, 1093–1101.
Hu, Z., Liu, Y., Chen, L., Zhou, L., Li, M., Zong, K., Gao, S., 2011. Contrasting matrix induced elemental fractionation in NIST SRM and rock glasses during laser ablation ICP-MS analysis at high spatial resolution. J. Anal. Atom. Spectrom 26, 425–430.
Hu, A.X., Peng, J.T., 2018. Fluid inclusions and ore precipitation mechanism in the giant Xikuangshan mesothermal antimony deposit, South China: Conventional and infrared microthermometric constraints. Ore Geol. Rev. 95, 49–64.

Isnard, H., Brennetot, R., Caussignac, C., Caussignac, N., Chartier, F., 2005. Investigations for determination of Gd and Sm isotopic compositions in spent nuclear fuels samples by MC ICPMS. Int. J. Mass Spectrom. 246, 66–73.
Ji, W.B., Lin, W., Faure, M., Chen, Y., Xue, Z., 2017. Origin of the Late Jurassic to Early Cretaceous Peraluminous Granitoids in the Northeastern Hunan Province (middle Yangtze Region), South China: Geodynamic Implications for the Paleo-Pacific Subduction. J. Asian Earth Sci. 141, 174–193.
Ji, W.B., Faure, M., Wei, L., Yan, Y., Xue, Z., 2018. Multiple emplacement and exhumation history of the Late Mesozoic Dayunshan-Mufushan batholith in Southeast China and Its tectonic significance: 1. structural analysis and geochronological constraints. J. Geophys. Res-Sol. Ea. 123, 689–710.
Jiang, Y.H., Jiang, S.Y., Dai, B.Z., Liao, S.Y., Zhao, K.D., Ling, H.F., 2009. Middle to Late Jurassic felsic and mafic magmatism in southern Hunan Province, Southeast China: implications for a continental arc to rifting. Lithos 107, 185–204.
Knoll, T., Schuster, R., Huet, B., 2018. Spodumenepegmatites and related leucogranites from the Austroalpine Unit (Eastern Alps, Central Europe): field relations, petrography, geochemistry and geochronology. Can. Mineral. 56, 489–528.
Li, C.Y., 2016. The Genesis of Chuanziyuan Niobium-Tantalum-Lithium Rare Metal Deposit in Pingjiang Hunan: Master Dissertation. Central South Univ. 1–68 in Chinese with English abstract.
Li, X.H., Li, Z.X., Ge, W.C., Zhou, H.W., Li, W.X., Liu, Y., Wingate, M.T.D., 2003. Neoproterozoic granitoids in South China: crustal melting above a mantle plume at ca. 825 Ma? Precamb. Res. 122, 45–83.
Li, Z.X., Li, X.H., 2007. Formation of the 1300 km-wide intracontinental orogen and postorogenic magmatic province in Mesozoic South China: A flat-slab subduction model. Geology 35, 179–182.
Li, X.H., Li, W.X., Li, Z.X., Lo, C.H., Wang, J., Ye, M.F., Yang, Y.H., 2009. Amalgamation between the Yangtze and Cathaysia Blocks in South China: constraints from SHRIMP U-Pb zircon ages, geochemistry and Nd–Hf isotopes of the Shuangxiwu volcanic rocks. Precamb. Res. 174, 117–128.
Li, P., Li, J., Pei, R., Leng, S., Zhang, X., Zhou, F., 2017. Multistage magmatic evolution and cretaceous peak metallogenic epochs of Mufushan composite granite mass: constrains from geochronological evidence. Earth Sci. 42, 1684–1696 in Chinese with English abstract.
Li, P., Liu, X., Li, J.K., Huang, Z.B., Zhou, F.C., Zhang, L.P., 2019. Petrographic and geochemical characteristics of Renli-Chuanziyuan No. 5 pegmatite, NE Hunan, and its metallogenic age. Acta Geol. Sin. 93, 1374–1391 in Chinese with English abstract.
Li, P., Li, J.K., Liu, X., Li, C., Huang, Z.B., Zhou, F.C., 2020b. Geochronology and source of the rare-metal pegmatite in the Mufushan area of the Jiangnan orogenic belt: A case study of the giant Renli Nb–Ta deposit in Hunan, China. Ore Geol. Rev. 116, 103237.
Li, P., Li, J.K., Chen, Z.Y., Liu, X., Huang, Z.B., Zhou, F.C., 2021. Compositional evolution of the muscovite of Renli pegmatite-type rare-metal deposit, northeast Hunan, China: Implications for its petrogenesis and mineralization potential. Ore Geol. Rev. 138, 104380.
Li, X.H., Long, W.H., Li, Q., Liu, Y., Zheng, Y., Yang, Y.H., Chamberlain, K.R., Wan, D.F., Cuo, C.H., Wang, X.C., Tao, H., 2010. Penglai zircon megacrysts: a potential new working reference material for microbeam determination of Hf–O isotopes and U-Pb age. Geostand. Geoanal. Res. 34, 117–134.
Li, L.G., Wang, L.X., Tian, Y., Ma, C.Q., Zhou, F.C., 2018. Petrogenesis and rare-metal mineralization of the Mufushan granitic pegmatite, south China: insights from in situ mineral analysis. Earth Sci. 44, 2532–2550 in Chinese with English abstract.
Li, Q.L., Yang, Y., Liu, Y., Tang, G.Q., Hao, J.L., Zhang, J.C., Hu, S., Zhao, X.C., Chen, Y. L., Chu, X.L., Wang, Y., Jiang, Y., 2013. Ion microprobe microanalytical techniques and their applications in earth science. Bull. Mineral. Petrol. Geochem. 32, 310–327 in Chinese with English abstract.
Li, P., Zhou, F.C., Li, J.K., Liu, X., Huang, Z.B., Zhang, L.P., 2020a. Zircon U-Pb ages and Hf isotopic compositions of the concealed granite of Renli-Chuangziyuan deposit, NE Hunan and geological significance. Geotec. Metal. 44, 486–500 in Chinese with English abstract.
Li, P.C., 2006. Magmatism of Phanerozoic granitoids in southeastern Hunan Province, China and its evolution regularity. Beijing: Chinese Academy of Geological Sciences (doctoral dissertation), 35–44 (in Chinese with English abstract).
Liu, Y.S., Gao, S., Hu, Z.C., Gao, C.G., Zong, K., Wang, D., 2010a. Continental and oceanic crust recycling-induced melt–peridotite interactions in the trans-North China orogen: U-Pb dating, Hf isotopes and trace elements in zircons from mantle xenoliths. J. Petrol. 51, 537–571.
Liu, Y.S., Hu, Z.C., Zong, K.Q., Gao, C.G., Gao, S., Xu, J., Chen, H.H., 2010b. Reappraisement and refinement of zircon U-Pb isotope and trace element analyses by LA-ICP-MS. Chinese Sci. Bull. 55, 1535–1546 in Chinese with English abstract.
Liu, Z.C., Wu, F.Y., Yang, Y.H., Yang, J.H., Wilde, S.A., 2012. Neodymium isotopic compositions of the standard monazites used in U-Th-Pb geochronology. Chem. Geol. 334, 221–239.
Liu, X., Zhou, F.C., Li, P., Li, J.K., Huang, Z.B., Shi, W.K., Hunag, X.Q., Zhang, L.P., Su, J. N., 2019. Geological characteristics and metallogenic age of Renli rare metal orefield in Hunan and its prospecting significance. Miner. Depos. 38, 771–791 in Chinese with English abstract.
London, D., 2014. A petrologic assessment of internal zonation in granitic pegmatites. Lithos 184, 74–104.
London, D., 2018. Ore-forming processes within granitic pegmatites. Ore Geol. Rev. 101, 349–383.
London, D., Hunt, L., Schwing, C.R., Guttery, B.M., 2020. Feldspar thermometry in pegmatites: truth and consequences. Contrib. Mineral. Petr. 175, 8.
Ludwig, K.R., 2011. Isoplot v. 4. 15: A Geochronological Toolkit for Microsoft Exce. Berkely: Berkeley Geochronology Center Special Publication, 1–75.
Lv, Z.H., Zhang, H., Tang, Y., Guan, S.J., 2012. Petrogenesis and magmatic–hydrothermal evolution time limitation of Kelumute no. 112 pegmatite in Altay, Northwestern China: evidence from zircon U-Pb and Hf isotopes. Lithos 154, 374–391.
Lv, Z.H., Zhang, H., Tang, Y., Liu, Y.L., Zhang, X., 2018. Petrogenesis of syn-orogenic rare metal pegmatites in the Chinese Altai: Evidences from geology, mineralogy, zircon U-Pb age and Hf isotope. Ore Geol. Rev. 95, 161–181.
Lv, Z.H., Chen, J., Zhang, H., Tang, Y., 2021a. Petrogenesis of Neoproterozoic rare metal granite-pegmatite suite in JiangnanOrogen and its implications for rare metal mineralization of peraluminous rock in South China. Ore Geol. Rev. 128, 103923.
Lv, Z.H., Zhang, H., Tang, Y., 2021b. Anatexis origin of rare metal/earth pegmatites: Evidences from the Permian pegmatites from the Permian pegmatites Chinese Altai. Lithos 380–381, 105865.
Ma, T.Q., Chen, L.X., Bai, D.Y., Zhou, K.J., Li, G., Wang, X.H., 2009. Zircon SHRIMP dating and geochemical characteristics of Neoproterozoic granites in southeastern Hunan. Geol. China 36, 65–73 in Chinese with English abstract.
Mao, J.R., Li, Z.L., Ye, H.M., 2014. Mesozoic tectono-magmatic activities in South China: Retrospect and prospect. Sci. China: Earth Sci. 57, 2853–2877 in Chinese with English abstract.
McCauley, A., Bradley, D.C., 2014. The global age distribution of granitic pegmatites. Can. Mineral. 183–190.
Mezger, K., Hanson, G.N., Bohlen, S.R., 1989. U-Pb Systematics of garnet: Dating the growth of Garnet in the Late ArcheanPikwitonei Granulite Domain at Cauchon and Natawahunan Lakes, Manitoba, Canada. Contrib. Miner. Petrol. 101, 136–148.
Müller, A., Romer, R.L., Pedersen, R.B., 2017. The Sveconorwegian Pegmatite Province-Thousands of pegmatites without parental granites. Can. Mineral. 55, 283–315.
Nasdala, L., Zhang, M., Kempe, U., Panczer, G., Pltze, M., 2003. Spectroscopic methods applied to zircon. Rev. Mineral. Geochem. 53, 427–467.
Pandur, K., Ansdell, K.M., Eglington, B.M., Harper, C.T., Hanchar, J.M., McFarlane, C.R. M., 2020. In situ U-Pb geochronology, Lu-Hf and Sm-Nd isotope systematics of the Hoidas Lake REE deposit, northern Saskatchewan, Canada. Precamb. Res. 339, 105591.
Pearce, J.A., Kempton, P.D., Nowell, G.M., Noble, S.R., 1999. Hf–Nd element isotope perspective on the nature and provenance of mantle and subduction components in Western Pacific arc-basin systems. J. Petrol. 40, 1579–1611.
Pin, C., Paquette, J.L., 1997. A mantle-derived bimodal suite in the Hercynian belt: Nd isotope and trace element evidence for a subduction-related rift origin of the late Devonian Brevenne metavolcanics, Massif Central (France). Contrib. Mineral. Petrol. 129, 222–238.
Roda-Robles, E., Villaseca, C., Pesquera, A., Gil-Crespo, P.P., Vieira, R., Lima, A., Olave, I., 2018. Petrogenetic relationships between Variscangranitoids and Li-(F-P)-rich aplite-pegmatites in the Central Iberian Zone: Geological and geochemical constraints and implications for other regions from the European Variscides. Ore Geol. Rev. 95, 408–430.
Rollinson, H.R., Windley, B.F., 1980. Selective elemental depletion during metamorphism of Archean granulites. Contrib. Mineral Petrol. 72, 257–263.
Schärer, U., 1984. The effect of initial ^{230}Th disequilibrium on young U-Pb ages: the Makalucase, Himalaya. Earth Planet. Sci. Lett. 67, 191–204.
Scherer, E., Munker, C., Mezger, K., 2001. Calibration of the lutetium hafnium clock. Science (New York, N.Y.) 293, 683–687.
Sevigny, J.H., Hanson, G.N., 1992. U-Pb dating of garnets in Paleozoic leucogranites, southwestern New England Appalachians. Can. J. Anaesth. 51, 638.
Shan, L., Ke, X.Z., Pang, Y.C., Liu, J.J., Zhao, X.M., Wang, J., Kang, B., Zhang, K., 2017. Zircon LA-ICP-MS U-Pb chronology, Lu-Hf characteristics and its geological significance of the Neoproterozoic magma activity in Lishan area from the northeastern Hunan Province. Geol. Sci. Tech. Infor. 36, 32–42 in Chinese with English abstract.
Shearer, C.K., Papike, J.J., Jolliff, B.L., 1992. Petrogenetic links among granites and pegmatites in the Harney Peak rare-element granite-pegmatite system, Black Hills, South Dakota. Can. Mineral. 30, 785–809.
Shu, L., Zhou, G., Shi, Y., Yin, J., 1994. Study of the high pressure metamorphic blueschist and its late Proterozoic age in the eastern Jiangnan belt. Chin. Sci. Bull. 39, 1200–1204.
Shu, L.S., Zhou, X.M., 2002. Late Mesozoic tectonism of Southeast China. Geol. Rev. 48, 249–260 in Chinese with English abstract.
Shu, L.S., Zhu, W.B., Xu, Z.Q., 2021. Geological settings and metallogenetic conditions of the granite-type lithium ore deposits in South China. Acta Geol. Sin. 95, 3099–3114.
Soderlund, U., Patchett, P.J., Vervoort, J.D., Isachsen, C.E., 2004. The ^{176}Lu decay constant determined by Lu-Hf and U-Pb isotope systematics of Precambrian mafic intrusions. Earth Planet. Sc. Lett. 219, 311–324.
Sun, W.D., Yang, X.Y., Fan, W.M., Wu, F.Y., 2012. Mesozoic large scale magmatism and mineralization in South China: Preface. Lithos 150, 1–5.
Suzuki, K., Shimizu, H., Masuda, A., 1996. Re-Os dating of molybdenites from ore deposits in Japan: implication for the closure temperature of the Re-Os system for molybdenite and the cooling history of molybdenum ore deposits. Geochim. Cosmochim. Acta 60 (16), 3151–3159.
Tang, L., Chen, H., Dong, C., Yang, S.F., Shen, Z.Y., Chen, X.G., Fu, L.L., 2013. Middle triassic post-orogenic extension on Hainan Island: Chronology and geochemistry constraints of bimodal intrusive rocks. Sci. China Earth Sci. 56, 783–793.
Tang, Y., Zhao, J.Y., Zhang, H., Cai, D.W., Lv, Z.H., Liu, Y.L., Zhang, X., 2017. Precise columbite-(Fe) and zircon U-Pb dating of the Nanping No. 31 pegmatite vein in northeastern Cathaysia Block, SE China. Ore Geol. Rev. 83, 300–311.
Tkachev, A.V., 2011. Evolution of metallogeny of granitic pegmatites associated with orogens throughout geological time. Geol. Soc. Lond. Spec. Publ. 350, 7–23.

Tomascak, P.B., Krogstad, E.J., Walker, R.J., 1996. U-Pb monazite geochronology of granitic rocks from Maine: implications for late Paleozoic tectonics in the Northern Appalachians. J. Geol. 104, 185–195.
Vervoort, J.D., Patchett, P.J., Blichert-Toft, J., Albarède, F., 1999. Relationships between Lu-Hf and Sm-Nd isotopic systems in the global sedimentary system. Earth Planet. Sc. Lett. 168, 79–99.
Wang, Z., Chen, Z.Y., Li, J.K., Xiong, X., Yang, H., Zhou, F.C., 2019. Indication of mica minerals for magmatic-hydrothermal evolution of Renli rare metal pegmatite deposit. Miner. Depos. 38, 1039–1814 in Chinese with English abstract.
Wang, L.X., Ma, C.Q., Zhang, C., Zhang, J.Y., Marks, M.A.W., 2014a. Genesis of leucogranite by prolonged fractional crystallization: A case study of the Mufushan complex, South China. Lithos 206–207, 147–163.
Wang, D., Shu, L., 2012. Late Mesozoic basin and range tectonics and related magmatism in southeast China. Geosci. Front. 3, 109–124 in Chinese with English abstract.
Wang, Z.L., Xu, D.R., Chi, G.X., Shao, Y.J., Lai, J.Q., Deng, T., Guo, F., Wang, Z., Dong, G. J., Ning, J.T., Zou, S.H., 2017b. Mineralogical and isotopic constraints on the genesis of the Jingchong Co-Cu polymetallic ore deposit in northeastern Hunan Province, South China. Ore Geol. Rev. 88, 638–654.
Wang, D.Z., Zhou, X.M., 2002. Genesis of Late Mesozoic Volcanic-Intrusive Complex of Southeast China and Crustal Evolution. Science Press, Beijing, pp. 1–295 in Chinese.
Wang, X., Zhou, J., Qiu, J., Zhang, W., Liu, X., Zhang, G., 2006. LA-ICP-MS U-Pb zircon geochronology of the Neoproterozoic igneous rocks from Northern Guangxi, South China: implications for tectonic evolution. Precamb. Res. 145, 111–130.
Wang, X.L., Zhou, J.C., Griffin, W.L., Zhao, G.C., Yu, J.H., Qiu, J.S., Zhang, Y.J., Xing, G. F., 2014b. Geochemical zonation across a Neoproterozoicorogenic belt: Isotopic evidence from granitoids and metasedimentary rocks of the Jiangnan orogeny, China. Precamb. Res. 242, 154–171.
Wang, X.L., Zhou, J.C., Chen, X., Zhang, F.F., Sun, Z.M., 2017a. Formation and evolution of the JinagnanOrogen. Bull. Mineral. Petrol. Geochem. 36, 714–734 in Chinese with English abstract.
Wei, J.Q., Zhu, D., Wang, F., Li, J., Lu, L., Pan, S.X., 2021. Mineralogical chcracteristics and occurrence state of niobium and tantalum in the Duanfengshan Nb-Ta deposit in Hubei Province, China. Acta Mineral. Sin. 41, 319–326 in Chinese with English abstract.
Wen, C.H., Shao, Y.J., Xiong, Y.Q., Li, J.K., Jiang, S.Y., 2021. Ore genesis of the Baishawo Be-Li-Nb-Ta deposit in the northeast Hunan Province, south China: Evidence from geological, geochemical, and U-Pb and Re-Os geochronologic data. Ore Geol. Rev. 129, 103895.
Wiedenbeck, M., Alle, P., Corfu, F., Griffin, W.L., Meier, M., Oberli, F., Vonquadt, A., Roddick, J.C., Speigel, W., 1995. Three natural zircon standards for U-Th–Pb, Lu–Hf, trace element and REE analyses. Geostandard. Newslett. 19, 1–23.
Williams, I.S., Hergt, J.M., 2000. U–Pb dating of Tasmanian dolerites: a cautionary tale of SHRIMP analysis of high-U zircon. in: Woodhead, J.D., Hergt, J.M., Noble, W.P. (Eds.), Beyond 2000: New Frontiers in Isotope Geoscience: Lorne, pp. 185–188.
Wu, F.Y., Yang, Y.H., Xie, L.W., Yang, J.H., Xu, P., 2006a. Hf isotopic compositions of the standard zircons and baddeleyites used in U-Pb geochronology. Chem. Geol. 234, 105–126.
Wu, R.X., Zheng, Y.F., Wu, Y.B., Zhao, Z.F., Zhang, S.B., Liu, X.M., Wu, F.Y., 2006b. Reworking of juvenile crust: element and isotope evidence from neoproterozoicgranodiorite in south China. Precam. Res. 146, 179–212.
Xiong, Y.Q., Jiang, S.Y., Wen, C.H., Yu, H.Y., 2020. Granite-pegmatite connection and mineralization age of the giant Renli Ta-Nb deposit in South China: Constraints from U-Th-Pb geochronology of coltan, monazite, and zircon. Lithos 358–359, 05422.
Xu, D., Deng, T., Dong, G., Ning, J., Wang, Z., Zhang, J., Zou, F., Zhou, Y., Chen, G., Yu, D., Ye, T., 2017. Zircon U-Pbgeochronological and geochemical characteristics of the Lianyunshan two-mica monzogranites in northeastern Hunan province: implications for petrogenesis and tectonic setting associated with polymetallic mineralization. Earth Sci. Front. 24, 104–122 in Chinese with English abstract.
Xu, D.R., Deng, T., Chi, G.X., Wang, Z.L., Zou, F.H., Zhang, J.L., Zou, S.H., 2019b. Gold mineralization in the JiangnanOrogenic Belt of South China: Geological, geochemical and geochronological characteristics, ore deposit-type and geodynamic setting. Ore Geol. Rev. 88, 565–618.
Xu, C., Li, J.K., Shi, G.H., Li, P., Liu, X., Zhang, L.P., 2019a. Zircon U-Pb age and Hf isotopic composition of porphyaceous biotite granite in south margin of Mufushan and their geological implications. Miner. Depos. 38 (5), 1053–1068 in Chinese with English abstract.
Yan, Q.H., Wang, H., Chi, G.X., Wang, Q., Hu, H., Zhou, K.L., Zhang, X.Y., 2022. Reconnition of a 600-km-long late Triassic rare metal (Li-Rb-Be-Nb-Ta) pegmatite belt in the Western Kunlun orogenic belt, western China. Econ. Geol. 117 (1), 213–236.
Yang, H., Chen, Z.Y., Li, J.K., Li, P., Xiong, X., Wang, Z., Zhou, F.C., 2019. Relation between the mineralization and evolution of mica and feldspar components of Renli-Chuangziyuan No. 5 pegmatite, northeast Hunan. Miner. Depos. 38, 851–866 in Chinese with English abstract.
Yang, Y.H., Wu, F.Y., Yang, J.H., Chew, D.M., Xie, L.W., Chu, Z.Y., Huang, C., 2014. Sr and Nd isotopic compositions of apatite reference materials used in U-Th–Pb geochronology. Chem. Geol. 385, 35–55.
Yang, X., Zhang, Y.Z., Cui, X., Yu, P.P., Xu, W.J., 2020. Geochemistry and detrital zircon U-Pb ages of sedimentary rocks from NeoproterozoicLengjiaxi group in NE Hunan Province. Earth Sci. 45, 3461–3474 in Chinese with English abstract.
Yao, J., Shu, L., Santosh, M., 2014. Neoproterozoic arc–trench system and breakup of the South China Craton: constraints from N-MORB type and arc-related mafic rocks, and anorogenic granite in the Jiangnanorogenic belt. Precamb. Res. 247, 187–207.
Ying, Y., Chen, W., Lu, J., Jiang, S., Yang, Y., 2017. In situ U-Th–Pb ages of the Miaoyacarbonatite complex in the South Qinlingorogenic belt, Central China. Lithos 290–291, 159–171.
Yu, D.S., Xu, D.R., Wang, Z.L., Xu, K., Huang, Q.Y., Zou, S.H., Zhao, Z.X., Deng, T., 2021. Trace element geochemistry and O-S-Pb-He-Ar isotopic systematics of the LishanPb-Zn-Cu hydrothermal deposit, NE Hunan, South China. Ore Geol. Rev. 133, 104091.
Zhang, R., Lu, J., Lehmann, B., Li, C., Li, G., Zhang, L., Guo, J., Sun, W., 2017. Combined zircon and cassiterite U-Pb dating of the Piaotang granite-related tungsten–tin deposit, southern Jiangxi tungsten district, China. Ore Geol. Rev. 82, 268–284.
Zhang, H., Lv, Z.H., Tang, Y., 2019. Metallogeny and prospecting model as well as propecting direction of pegmatite-type rare metal ore deposits in Altay orogenic belt, Xinjiang. Miner. Depos. 38, 792–814 in Chinese with English abstract.
Zhao, K., Jiang, S., Ling, H., Palmer, M.R., 2014. Reliability of LA-ICP-MS U-Pb dating of zircons with high U concentrations: a case study from the U-bearing Douzhashan Granite in South China. Chem. Geol. 389, 110–121.
Zhao, J.H., Zhou, M.F., Yan, D.P., Zheng, J.P., Li, J.W., 2011. Reappraisal of the ages of Neoproterozoic strata in South China: no connection with the Grenvillian orogeny. Geology 39, 299–302.
Zheng, Y.F., Zhang, S.B., Zhao, Z.F., Wu, Y.B., Li, X.H., Li, Z.X., Wu, F.Y., 2007. Contrasting zircon Hf and O isotopes in the two episodes of Neoproterozoicgranitoids in South China: implications for growth and reworking of continental crust. Lithos 96, 127–150.
Zhou, F.C., Li, J.K., Liu, X., Li, P., Huang, Z.B., Shi, W.K., Su, J.N., Chen, H., Huang, X.Q., 2019a. Geochemical characteristics and genetic significance of orebodies in Renli Nb-Ta deposit, Hunan Province. Acta Geol. Sin. 93, 1392–1404 in Chinese with English abstract.
Zhou, F.C., Liu, X., Li, J.K., Huang, Z.B., Xiao, G.Q., Li, P., Zhou, H.X., Shi, W.K., Tan, L. M., Su, J.N., Chen, H., Wang, X.M., 2019b. Metallogenic characteristics and propecting direction of Renli super-large rere metal deposit in Hunan Province, China. Geotec. Metal. 43, 77–91 in Chinese with English abstract.
Zhou, F.C., Huang, Z.B., Liu, X., Su, J.N., Huang, X.Q., Wang, Z., Chen, H., Zhang, Z.D., Nuo, X.R., Li, J.B., Li, Z.H., Zhang, L.P., Zeng, L., Li, X.M., 2020. Re-Os dating of molybdenite from the RenliNb-Ta Deposit, Hunan Peovince, and its geological significance. Geotec. Metal. 44, 476–485 in Chinese with English abstract.
Zhou, X.M., Sun, T., Shen, W.Z., Shu, L.S., Niu, Y.L., 2006. Petrogenesis of Mesozoic granitoids and volcanicrocks in South China: A response to tectonicevolution. Episodes: English edition 29, 26–33.
Zhou, J.C., Wang, X.L., Qiu, J.S., 2009. Geochronology of Neoproterozoic mafic rocks and sandstones from northeastern Guizhou, South China: coeval arc magmatism and sedimentation. Precamb. Res. 170, 27–42.
Zou, S.H., Zou, F.H., Ning, J.T., Deng, T., Yu, D.S., Ye, T.W., Xu, D.R., Wang, Z.L., 2018. A. stand-alone Co mineral deposit in northeastern Hunan Province, South China: Its timing, origin of ore fluids and metal Co, and geodynamic setting. Ore Geol. Rev. 92, 42–60.

Further reading

Dill, H.G., 2018. Geology and chemistry of Variscan-type pegmatite systems (SE Germany) with special reference to structural and chemical pattern recognition of felsic mobile components in the crust. Ore Geol. Rev. 92, 205–239.
Schärer, U., Corfu, F., Demaiffe, D., 1997. U-Pb and Lu–Hf isotopes in baddeleyite and zircon megacrysts from the Mbuji-Mayikimberlite: constraints on the subcontinental mantle. Chem. Geol. 143, 1–16.